SEISMICALLY INDUCED EFFECTS AND SLOPE STABILITY IN URBANIZED AREAS VIA NUMERICAL MODELING

Gisela Domej

Thesis

for the acquisition of the academic degree

Doctor of the Université Paris-Est
Specialty: Geotechnical Engineering

SEISMICALLY INDUCED EFFECTS AND SLOPE STABILITY IN URBANIZED AREAS VIA NUMERICAL MODELING

presented by

Gisela Domej

(IFSTTAR - GERS - SV & SRO)

on the 29th of October 2018 to the jury:

Bertrand Maillot	Professor, Université de Cergy - Pontoise	reporter
Christian Sue	Professor, Université de Franche - Comté	reporter
Irini Djeran-Maigre	Professor, INSA Lyon	examiner/president
Patrick Meunier	Maître de Conférences, École Normale Supérieure	examiner
Jean-François Semblat	Professor, ENSTA ParisTech	thesis director
Luca Lenti	Chargé de Recherche, IFSTTAR - GERS - SV	thesis director
Céline Bourdeau	Chargé de Recherche, IFSTTAR - GERS - SRO	supervisor
Salvatore Martino	Associate Professor, Università Sapienza di Roma	supervisor
José Delgado	Professor, Universidad de Alicante	guest

IFSTTAR

ÉCOLE DOCTORALE UNIVERSITÉ PARIS-EST
Sciences, Ingénierie et Environnement

Start by doing what is necessary,
then do what is possible,
and suddenly you are doing the impossible.

Francis of Assisi (1181-1226)

für meine Erika

die sich immer über mich gefreut hat

Statement of Authorship

I hereby declare that I am the sole author of this thesis and that I have not used any sources other than those listed in the bibliography and identified as references. I further declare that I have not submitted this thesis at any other institution in order to obtain a degree.

Data included in the database does not belong to me, the co-authors of the published article or to my supervising institutions. References do not include publications associated to the individual landslides. However, it is possible at any time to provide a full list of evaluated literature for every landslide.

Champs-sur-Marne, 29th of October 2018

(Gisela Domej)

Acknowledgments

At first, I would like to express my recognition to my directory and supervising team for the opportunity of this thesis. Recruiting a geologist and risk engineer for a geotechnical doctorate posed a number of challenges for them as well as for me, but eventually I am grateful for the experience of the last three years at IFSTTAR and I thank all permanent staff and colleagues for the good time together. In particular, I am thankful for Luca Lenti's richness of ideas, Céline Bourdeau's sereneness and Salvatore Martino's imperturbable optimism. Moreover, I thank Jean-François Semblat for the main supervision of my thesis and Emmanuel Bougreois for his ever good-humored support.

One of the most extraordinary events just one month before the end of the thesis was the excursion to the Diezma Landslide to which I was invited by José Delgado during a visit in Alicante.

Furthermore, I express my thanks to those people who play – either personally or scientifically - an important role in my life and who support(ed) me in whatever circumstances: Erika Hassler, my Algerian family, Robert Faber, Abdourahmane Haibawi, Agatha and Ernst Kaltenegger, Petros Koutsovitis, Xiaoqiu Li, Ahmed Lijji, Qian Liu, Kacper Pluta, Kristian Tuovinen and Syed Ali Turab.

Retention wall of the Diezma Landslide (9th of September 2018).

Finally I thank the members of the jury – the two reporters Bertrand Maillot and Christian Sue and the tow examiners Irini Djeran-Maigre and Patrick Meunier – for conducting the exam.

Contents

CHAPTER 1
INTRODUCTION TO THE THESIS

1.1. Scope of the Thesis

Landslides are worldwide common phenomena triggered by a variety of causes such as heavy precipitation, strong storms, natural seismic activity, artificial load changes, clay involvement, or even blasts. Often causes interfere with each other and combined triggers are not scarce. On a global scale, the role of water, seismic and volcanic activity seem to have the most relevant effects (USGS, 2004). Depending on the size of an event, consequences can be minor to disastrous causing loss of life and considerable damage to infrastructure, property and the environment (BIRD & BOMMER, 2004). One main reason for more frequent catastrophes is the growth of population which entails extending urbanization to areas with high landslide potential (PETLEY, 2012).

Throughout literature, reports and case studies on seismically induced mass movements are abundant. In terms of fatalities the most disastrous example might be the rock avalanche at Nevado Huascarán, Peru, which was triggered by the Peruvian Earthquake (or Ancash Earthquake; M_W = 7.9) on the 31st of May 1970 and buried the towns of Yungai and Ranrahirca causing 54,000 victims (KUROIWA et al., 1970; LOMNITZ, 1970; RODRÍGUEZ et al., 1999). Also three more recent mass movement events drew a line of catastrophic destruction and a high rate of loss of life. The El Salvador Earthquake on the 13th of January 2001 (M_W = 7.6) triggered several landslides in Santa Tecla and Comasagua killing 500 people (EVANS & BENT, 2004). During the Hattian Bala rock avalanche triggered by the Kashmir Earthquake (M_W = 7.6) on the 8th of October 2005 around 25,000 residents of the Jhelum Valley, Pakistan, lost their lives (DUNNING et al., 2007). An equally high number of victims (20,000) amounts from the landslide series in and around Beichuan, China, after the Sichuan Earthquake (or Wenchuan Earthquake; M_W = 7.9) on the 12th of May 2008 (YIN et al., 2009). In contrast to such deadly events, there are also mass movements that initially claim a rather low number of fatalities but pose a long term secondary threat to the environment and the local population. For instance, the Sarez Earthquake of the 18th of February 1911 (M_W = 7.2) triggered a giant landslide that finally blocked the Murghab River, Tajikistan, creating a natural dam. This dam appears to be the largest natural dam and it permanently poses the threat of a leakage or deluge (PREOBRAZHENSKY, 1920; SCHUSTER, ALFORD, 2004; AMBRASEYS & BILHAM, 2012). Multi-hazard chain effects are also documented in historic chronicles. The Calabria Earthquake (or Messina Earthquake; M_W = 6.2) on the 6th of February 1783 is reported to have triggered the Scilla Landslide that slid into the sea. The hereby induced tsunami wave caused 1500 casualties at a nearby coastline agglomeration (BOZZANO et al., 2011).

Over time, the long-living assumption of mass movements being simply secondary effects of earthquakes was revised and the topic became a focus of interest. In many cases the damage and loss of life resulting from a mass movement exceed those of the earthquake itself. The tragic example of Jhelum Valley, Pakistan, shows that most of the victims did not die from the earthquake, but from the triggered rock avalanches (DUNNING et al., 2007) which also erased building stock and infrastructure preventing fast and adequate disaster management in the aftermath.

Therefore, research on the effect of seismic shaking to slopes is of particular importance, be it with respect to natural or artificial slopes such as – for example – excavations, road cuts, dams and mining pits. The better scientists understand the relation between impacting seismic waves and the slope response, the better will be predictions on surface deformation as well as environmental and socio-economic impact estimation. Risk management becomes more accurate; analysis on the occurrence probability of events, resilience and vulnerability assessment and hazard mapping gain in precision.

Research on seismically induced mass movements is extensive and a broad spectrum of methods for characterizing and modeling slope deformation is available (cf. 5., 6., 7.). In the very beginning, empiric approaches attempted to statistically correlate characteristics of earthquakes with those of mass movements (cf. 2.5.3., 3.1., 3.3.1.). In many – but by far not all cases – relations appeared to be non-satisfactory due to site effects (cf. 1.2.) and demands raised for more complex approaches. Today, methods range from pseudo-static and rigid-block-based

approaches (cf. 5.) to numerical models (cf. 6., 7.). The majority is limited to 2D modeling since more sophisticated approaches in 3D are still under development or need calibration. However, it must be kept in mind that due to the heterogeneity of nature one will never – neither with the best 3D-model – reproduce an exact replica of the real site conditions and as EBERHARDT (2003) states:

> *"[…] Numerical modelling is a tool and not a substitute for critical thinking and judgement." (p. 2)*

How difficult the evaluation of slope response is, becomes apparent when briefly introducing types of approaches to characterize the behavior of the slope. The linear approach is based on the hypothesis that material as well as damping parameters are constant over time and that the biggest amplifications of the incoming seismic signal is expected at the fundamental frequency of the mass movement body (cf. 6.3.1., Excursus – 6.4.2.; KAHIL, 2015).
In contrast, non-linear approaches take into account that relevant material and damping parameters are not constant over time and that non-linear slope behavior can change the response considerably. For example, as deformation increases with time, the shear modulus ($G = \rho \cdot v_s^2$) and thus the shear wave velocity (v_s) decrease. Subsequently, the fundamental frequency – as function of the shear wave velocity (v_s) – is also not constant. Inversely, the damping (ξ) becomes stronger with increasing deformation countering amplification (KAHIL, 2015).
This thesis focuses on linear slope behavior; i.e. all applied methods – the NEWMARK-Method (1965; cf. 5.), the modal recombination analysis (cf. 6.) and the analysis with the finite difference code FLAC (cf. 7.) – are based on the hypothesis of constant material and damping parameters.

1.2. Site Effects

Generally speaking, site effects influence the amplitude, the frequency content and the duration of an incoming seismic signal at a specific location. They depend on the local geological setting, the geometrical features within the underground and the properties of the involved material in combination with the characteristics of the incoming waves.
Usually site effects are noticed when it comes to extraordinary amplification of the signal and when damage is higher than expected. Already in 1824 MACMURDO noted that buildings were not damaged to the same extent after the Rann of Kutch Earthquake, India, on the 16th of June 1819 (M_W = 8.2); buildings located on rock were less affected. It took a century until GUTENBERG (1927) presented for the first time amplification factors related to subsurface conditions. Today, the creation, propagation and impact of seismic waves are no longer considered as mystery or even a "divine punishment"; the phenomena rather follow physical principles.
After a rupture has taken place, primary and secondary waves (longitudinal/P- and shear/S-waves; cf. Fig. 1.1) radiate from the hypocenter (cf. Fig. 1.3). Assuming that geologic layers become less dense with progressively shallower depths, waves undergo reflection and refraction at every interface according to Snell's Law (cf. Fig. 1.2a-c); the term "refraction" implies transmission of the wave to the less dense medium with a smaller angle from the perpendicular:

$$\frac{\sin(\alpha_1)}{v_1} = \frac{\sin(\alpha_2)}{v_2}$$

where α_1 and α_2 are the angles towards the perpendicular
and v_1 and v_2 the wave propagation velocities in the respective media

P-waves vibrate along the direction of propagation; they are also polarized in the direction of propagation. The direction of propagation and the vertical axis define the plane of incidence which corresponds in Fig. 1.2a-c to the plane of the images themselves.

The vibration of S-waves is perpendicular to the direction of propagation; their polarizations can have two orientations:

- in the polarization plane and the plane of incidence (cf. Fig. 1.2a)
- in the polarization plane and perpendicular to the incidence plane (cf. Fig. 1.2c)

Respectively the two types of S-waves are called SV-waves (cf. Fig. 1.2a) and SH-waves (cf. 1.2b). Incident P- or SV-waves scatter at an interface to reflected and transmitted P- and SV-waves. Reflected and transmitted P-waves always have a bigger angle to the perpendicular due to their higher velocities; S-waves are slower than P-waves in the same medium. SH-waves cannot change their nature by being reflected or transmitted (cf. Fig. 1.2a-c).

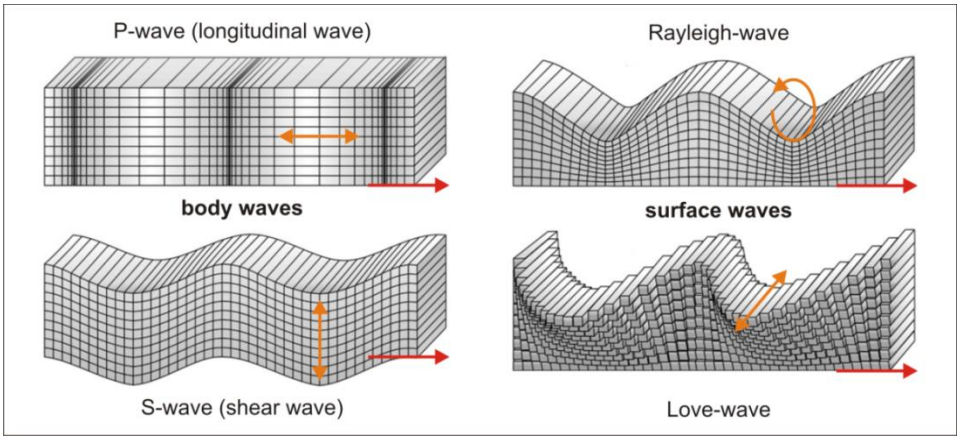

Fig. 1.1. Types of body waves and surface waves. The particle motion is indicated in orange, the direction of wave propagation in red (after CLAUSER, 2014).

Due to the phenomenon described by Snell's Law, it is apparent that waves tend to reach the surface with an almost right angle (cf. Fig. 1.3). The free surface causes total reflection and the creation of surface waves that travel across the ground surface. These latter waves are called Rayleigh- and Love-waves and form through interference of P- and SV-waves and two SH-waves respectively. Since the focus of this thesis is to analyze the response of the underground – in this case of landslides – the main interest is on S-waves. After the process of "curving upwards" they have a shearing character parallel to the surface and hence cause eminent "left-right" or "forward-backward" displacements inside the underground. In section 4.4. the choice of applied signals will be explained. All of them are x-components of registered accelerograms and supposed to represent SV-waves that shear the landslide mass in the plane of its longitudinal cross section (cf. Fig. 4.8).

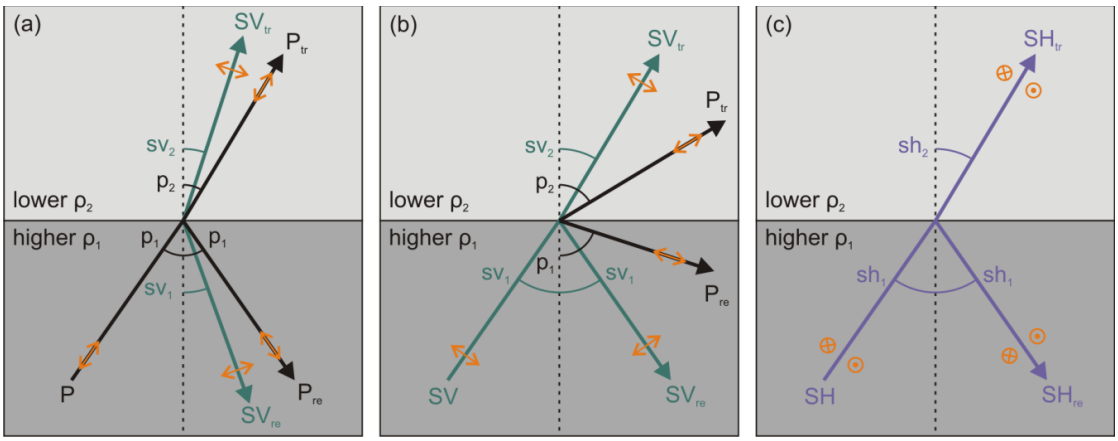

Fig. 1.2a-c. Wave reflection and refraction (transmission) at interfaces between two media.
Abbreviations with capital letters refer to waves (P, SH and SV), those with small letters to angles (p, sh and sv).
Orange arrows indicate the direction of vibration which is not to be confounded with the direction of propagation.

Besides of local geology, also the topography plays an important role for site effects (cf. Fig. 1.3). This becomes obvious when comparing accelerograms of the same earthquake that were registered at different sites. The accelerogram originating from the station at the bedrock serves as the reference. In comparison, accelerograms of concave topographies – such as depressions or valleys – tend to have lower amplitudes and shorter durations due to signal dispersion. Convex topographies – such as mountain ridges or crests – can trap incoming waves causing amplification through constructive interference; signals also become longer in duration. The biggest amplification and prolongation of the signal is to be expected in basins that are filled with non-consolidated sediments.

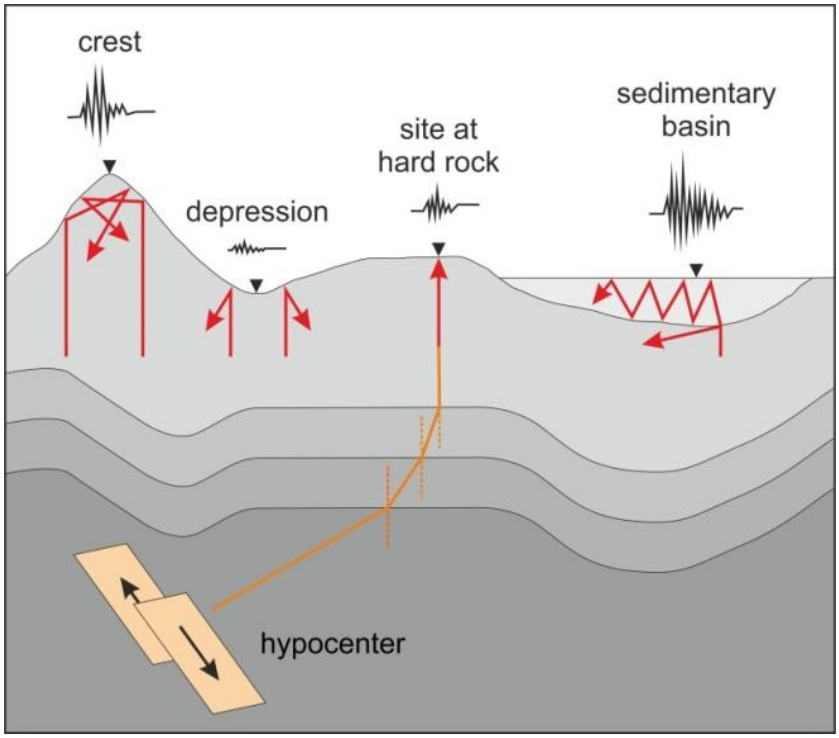

Fig. 1.3. Schematic representation of site effects (after ZACEK, 1996).

The impedance ($Z = \rho \cdot v_s$) of a medium is a property defining its resistance to wave transmission; the stronger the impedance contrast between the sediments and the underlying bedrock is, the bigger become the entrained effects. One can easily recognize the reason via the principle of elastic wave energy conservation; if the shear wave velocity (v_s) and the density (ρ) decrease while the energy flux ($\rho \cdot v_s \cdot \dot{u}^2$) remains the same, the particle velocity ($\dot{u}$) must increase (KRAMER, 1996), and as NEWMARK (1965) summarizes:

> *"One of the most important special conditions [...] is a relatively soft sedimental deposit of fairly great depth and wide extent. When such a soil deposit is set into motion at its contact with the bedrock, there is a tendency for the resultant motions of the soil to reflect the natural frequency of the bowl of soil. This has an effect of increasing the magnitude of surface displacements and velocities, but it also causes the resultant motion to be more periodic [...]. A structure built on such a material [...] will generally have a larger response than it would have if it were subjected to motions of the bed rock." (p. 141)*

Two of the most cited examples for extreme amplification and signal prolongation at sedimentary basins are the Mexico City Earthquake on the 19th of September 1985 (M_W = 8.0) and the Loma Prieta Earthquake on the 19th of October 1989 (M_W = 6.9). In the case of Mexico, the epicenter was around 350 km away and experienced only moderate damage. The spectral accelerations in Mexico City, however, were up to ten times higher and the time of shaking lasted much longer (DOBRY & VUCETIC, 1987; STONE et al., 1987). Also in the second case of the San

Francisco Bay Area in California, USA, the epicenter was located at a distance (100 km) and the effect of signal amplification is illustrated by the collapse of the Cypress Viaduct in Oakland (cf. Fig. 1.4). The structure was founded on muddy sediments (SEED et al., 1990).

Fig. 1.4. Collapsed Cypress Viaduct in Oakland (LEWIS, 1989).

Having dedicated several paragraphs on wave propagation, topographic effects and sedimentary basins, one might ask what the relation to landslides is. Put simply, landslides are to be seen as masses of unconsolidated material, however with a limited spatial extent and an inclination with respect to the horizontal. As such, they experience seismic shaking, they are affected by topographic effects and like sedimentary basins they show a significant impedance contrast to the underlying bedrock. Thus, they are likewise prone to be affected by site effects and for this very reason the mentioned empiric correlations of earthquakes characteristics with those of mass movements (cf. 1.1.) do not always fit.

Over the last years research on the topic has made great progression. BRAY (1998) showed that expected co-seismic displacements are dependent on particular parameters of the seismic event. BOURDEAU & HAVENITH (2012) as well as ALFARO et al. (2012) demonstrated that the angle of incidence of seismic waves have an influence on the amplification. LENTI & MARTINO (2012) conducted parametric studies which revealed that the seismic response of landslides is a function of the dimensions and sequences of layers it contains.

The aim of this thesis is to contribute to the overall topic of seismically induced landslides, site effects and the prediction of expected surface deformation across slopes.

In order to assess and compare expected displacements across slope surfaces a series of different seismic scenarios was applied to one particular site using three different methods: the NEWMARK-Method (1965) being the only type of analysis based on the limit-equilibrium principle, simple estimation by modal recombination in the frequency domain with the finite-element codes CESAR-LCPC 2D and CESAR-LCPC 3D under visco-elastic conditions, and analysis in the time domain with the finite-difference codes FLAC 2D and FLAC 3D under elasto-plastic conditions.

The thesis finally discusses results from the three mentioned methods with respect to relevant earthquake and landslide parameters on the one hand, and permits a critical view on the suitability of the different methods for deformation analyses of seismically induced landslide on the other hand. The next section (cf. 1.3.) gives a short overview of each chapter of the thesis.

1.3. Guide to the Reader

Including this introduction, the thesis is partitioned in eight chapters. The following overview serves as a guide to the reader and sums up the main contents of each chapter.

CHAPTER 2 / LANDSLIDE DATABASE

Chapter 2 presents the landslide database with its contents and properties as well as its potential of usage for statistical and numerical analyses. The chapter is not necessary for understanding the scientific context of the analysis conducted based on data from the database; it is rather a reference manual for the database itself.

CHAPTER 3 / STATISTICAL ANALYSES OF THE DATABASE

Chapter 3 describes statistical analyses that were carried out on data from the database and resumes those descriptions of the database that are essential for understanding the scientific context. The chapter corresponds in most of its parts to the article published by DOMEJ et al. (2017).

CHAPTER 4 / DIEZMA LANDSLIDE & APPLIED SIGNALS

Chapter 4 explains the choice of the Diezma Landslide as site of interest to which all 2D- and 3D- methods of displacement analysis were applied. It shows how simplified and fine geometries in 2D and 3D were built and what possibilities of analysis exist. In its second part, the chapter presents the applied seismic scenarios to the Diezma Landslide.

CHAPTER 5 / NEWMARK-ANALYSIS

Chapter 5 discusses in its first part the topics of static and seismic slope stability to trace back the NEWMARK-Method (1965) to its basic principles of Limit Equilibrium Analysis and the factor of safety. The second part describes the application of the method to the Diezma Landslide and discusses results and the suitability of the methods.

CHAPTER 6 / MODAL RECOMBINATION ANALYSIS

Chapter 6 is dedicated to the first of two numerical methods to analyze seismically induced slope deformation. It gives a general overview on numerical modeling and on those principles of structural dynamics on which the method of modal recombination is based. The second part describes the application of the method to the Diezma Landslide.

CHAPTER 7 / FINITE DIFFERENCE ANALYSIS

Chapter 7 is dedicated to the second of two numerical methods to analyze seismically induced slope displacements. It gives an overview on the functionality of the finite difference codes FLAC 2D and FLAC 3D. The second part describes the application of the method to the Diezma Landslide.

CHAPTER 8 / DISCUSSION OF 3 METHODS, CONCLUSIONS & PERSPECTIVES

Chapter 8 compares the seismically induced displacements across the slope of the Diezma Landslide that were obtained from the NEWMARK-Analysis (1965), the modal recombination analysis and the analysis with the finite difference code FLAC. It draws conclusions on the methods advantages and drawbacks and finally sets perspectives for future work.

CHAPTER 2
LANDSLIDE DATABASE

2.1. Introduction

In the course of this thesis a global chronological database was created to study and compare 2D- and 3D-geometries of landslides – i.e. of landslides properly sliding on a rupture surface. It contains 277 distinct seismically and non-seismically triggered landslides whose rupture masses were measured in all available details allowing for statistical analyses of their shapes and to create numerical models thereupon based.
This chapter presents in the first part the database itself in all its details. First, the chapter explains the construction strategy and the properties of the database, its functionality and contents and what processes were involved to deal with the great amount of information. Second, it presents the separate components of the database and their interconnections. A third section describes the combination of these components into a Microsoft Access database, which allows for efficient data handling and therefore is a convenient tool for statistical analyses and data preparation for numerical modeling. Advantages and some drawbacks will be discussed.

The main aim of this chapter is to provide a "**reference manual**" for other users allowing them to understand, use and eventually complete it. It can be skipped while reading the thesis, since it is not necessary to understand the scientific context of the thereupon based statistical and numerical analyses. A summary of the essential contents is to be found in the beginning of next chapter (cf. 3.1., 3.2.).

2.2. Abbreviations and Punctuation

Common abbreviations used throughout the database are:

EQ	earthquake	MM	mass movement
M	magnitude	LS	landslide
ID	identification	DA	debris avalanche
f	frequency	DF	debris flow
f_{res}	resonance frequency	RA	rock avalanche
LCS	longitudinal cross section	RF	rock fall
TCS	transversal cross section	EF	earth flow
GW(T)	ground water (table)	MF	mud flow
PW(P)	pore water (pressure)	LF	loess flow
SF	factor of safety	DSGM	deep seated gravitational movement

The left column of abbreviations is of less peculiarity; the combinations are rather straightforward. The right column of abbreviations is of interest when classifying mass movements (cf. 2.2., 2.4.1., 3.3.3.). A notable detail is, that literature often reports loess flows instead of earth flows which is contradictory in the way that loess is – according to CRUDEN & VARNES (1996) – a type of earth. Nevertheless, loess is a very special material and thus often takes a particular place among earth types. It is a homogeneous, unstratified, yellow-gray, aeolian sediment that consists mainly of silt with a certain carbonate percentage. Also, the mechanical behavior of loess is different in comparison to other soil types as DANNEELS et al. (2008) definition of loess states:

> *"Due to its specific microstructure, loess can sustain nearly vertical slopes in dry and non-seismic conditions. However, under strong seismic shaking, this microstructure may break and the loess then behaves as a cohesionless material, creating very rapid loess flows with a long runout zone. The stability of loess slopes is also highly dependent on the water content." (p. 17; after ZHANG & WANG, 1995)*

The creation of the abbreviation DSGM is a mixture of mass movement designations that appear in literature; it is not to be considered as an official term (cf. 2.2., 2.4.1., 3.3.3.). Whereas many of

those official terms also include dynamical or material related aspects (e.g. “deep seated rock creep”) the term DSGM simply should relate to the big dimension of the mass movement. More details about the landslides dynamics and material are to be found in other sections of the survey charts.
Abbreviations of scientific corporations – such as for instance the USGS (United States Geological Survey) or the IAEG (International Association of Engineering Geology) – are not listed here because the geoscientific community is supposed to be familiar with them.
Punctuation throughout the report is as it is customary in English; however, because the used Microsoft Office Package is a French version, attention has to be paid to the fact that for instance in Excel-files punctuation is in European Style:

e.g.	1,000,000 m^3	1.5 km	in this thesis
e.g.	1.000.000 m^3	1,5 km	in Excel-files

2.3. Strategy of Construction

One component of a thesis – and of scientific work in general – is the creation of data that will be evaluated at a later stage. The more accurate the dataset is, the better is its evaluation and the wider is the variety of possibilities to make use of it. However, to ensure such a successful outcome, one has to adopt a strategy for data creation – in the present case, for the creation of a database.

2.3.1. Strategy for the Database

Initially, the main idea was to collect scientific publications about landslides that preferentially contain both a map and a LCS to retrieve the geometry of the rupture zone as well as the overall properties of the landslide. Scientific publications of interest fall under the categories of articles, conference proceedings and scientific abstracts, web-based articles, book chapters, theses, etc. The starting point for the collection of publications was three articles that appeared due to different reasons:

DELGADO et al. (2015)	Unconventional pseudostatic stability analysis on the Diezma landslide (Granada, Spain) based on a high-resolution engineering-geological model.
EVANS, et al. (2009)	Landslides triggered by the 1949 Khait earthquake, Tajikistan, and associated loss of life.
DEWITTE & DEMOULIN (2005)	Morphology and kinematics of landslides inferred from precise DTMs in West Belgium.

The first article served as reference example since it reports one of the research projects of the supervising team. The second article has a direct relation to my Master thesis and displays research of one of my Tajik supervisors. The third article helped to define the prototype of a rupture zone geometry required for the database.
Based on those three articles further literature was systematically explored in a – figuratively speaking – “explosion-like” way: After designing one publication as suitable for the database, all its promising references were checked; then again, every newly found publication was examined for suitability and its references were explored.
Doing so, for each appearing publication of interest an entry was made in the Excel-sheet named “BIB-List” (cf. 2.3.3.). This process was finished at the moment where no more pertinent cases were found because publications in a confined field of science tend to cite each other. Nonetheless, this procedure can never claim to be exhaustive. The main online platforms used for literature research are:

AGU Publications	https://publications.agu.org/
EGU Publications	http://www.egu.eu/publications/
Google	https://www.google.com/
Google Scholar	https://scholar.google.com/
Oxford Journals	https://www.oxfordjournals.org/
Researchgate	https://www.researchgate.net/
Science Direct	http://www.sciencedirect.com/
Springer Link	http://link.springer.com/
USGS	https://www.usgs.gov/products/publications/
WikipediA	https://www.wikipedia.org/
Wiley Online Library	http://onlinelibrary.wiley.com/

While conducting literature research in this "explosive" style several authors appeared repeatedly and hence working groups became apparent – not least by mutual referencing. Also a "hall of fame" emerged (cf. Tab. 2.1) – a number of authors that worked during the last century on the phenomena of naturally and seismically induced landsliding.
Certainly this list of pertinent authors does not claim completeness; one reason therefore is the fact that some authors tend to publish in journals that are not accessible for different reasons (cf. 2.6.), a second reason might be a matter of constant evolution of science. For each of the authors a separate literature research was conducted; publication lists were checked on the personal web pages of authors or on their portraits at the institutions they are affiliated to.
Moreover, several separate landslide inventories were checked regarding their cases and references. These inventories emerged during the process of literature collection; they appear as simple list grouping landslides according to distinct characteristics and locality or as so-called "database papers" presenting analysis on sets of documented landslides. Inventories of the following sources were checked:

OMIV (2016)	publications on the Séchilienne Landslide
USGS (2016)	Catastrophic Landslides of the 20th Century.
BIRD & BOMMER (2004)	Earthquake losses due to ground failure.
BOMMER & RODRÍGUEZ (2002)	Earthquake-induced landslides in Central America.
DELGADO et al. (2011)	On far field occurrence of seismically induced landslides.
DELGADO et al. (2011)	Seismically-induced landslides in the Betic Cordillera (S Spain).
KEEFER (1984)	Landslides caused by earthquakes.
KEEFER (2002)	Investigating Landslides Caused by Earthquakes – A Historical Review.
RODRÍGUEZ et al. (1999)	Earthquake-induced landslides: 1980–1997.
XU et al. (2014)	Landslides triggered by the 12 January 2010 Port-au-Prince, Haiti, M_W = 7.0 earthquake: visual interpretation, inventory compiling, and spatial distribution statistical analysis.

New publications were always processed in the same "explosive" way as indicated above. Finally, the last part of the literature research consisted in the evaluation of the proceedings of the 12th International Symposium on Landslides held from the 12th to the 19th of June 2016 in Naples, Italy, which appeared under the title "Landslides and Engineered Slopes – Experience, Theory and Practice" (AVERSA et al., 2016). Based on this publication 28 new cases could be added to the database, but in agreement with the supervising team further references were not checked any more to bring the literature research to an end.

Alfaro P.	Cruden D. M.	Havenith H. B.	Martino S.
Angeli M. G.	Del Gaudio V.	Hutchinson J. N.	Meunier P.
Aringoli D.	Delgado J.	Ischuk A.	Moro M.
Barla G.	Demoulin A.	Ishihara K.	Moulin C.
Bommer J. J.	Di Maio C.	Jibson R. W.	Rodríguez-Peces M. J.
Bozzano F.	Dunning S. A.	Jongmans D.	Sassa K.
Brückl E.	Eberhardt E.	Keefer D. K.	Sepúlveda S. A.
Chigira M.	Esposito E.	Kieffer D. S.	Strom A.
Cotecchia F.	Evans S. G.	Korup O.	Torgoev I.
Crosta G. B.	Glade T.	Lenti L.	Torgoev A.
Crozier M. J.	Harp E. L.	Liu Q.	Wasowski J.

Tab. 2.1. Authors working on landslides.

Tab. 2.2. Relevant scientific journals.

At this point it should be mentioned that the hereby established literature collection is far from covering all interesting or more relevant landslides and that much more literature is available on the Internet and in diverse libraries and archives. Due to the initial objective to collect cases over the period of half a year and to the fact that data creation for a thesis has to come to an end at a certain stage, the following sources remained unexplored, although they are surely promising; there is no other reason than the time issue for not having them checked as well.

AGU Landslide Blog	http://blogs.agu.org/landslideblog/
CERI Catalog	http://www.ceri.uniroma1.it/index.php/web-gis/cedit/
EERI Publications	https://www.eeri.org/
USGS Publications	https://www.usgs.gov/products/
Landslides of the World	SASSA (1999)
Landslides	CLAGUE & STEAD (2014)
List of Landslides	WIKIPEDIA (2016a)

Another very broad and time-consuming approach to collect landslide case studies might have been the systematic search by keyword in pertinent journals. After the "explosion" approach and the therewith connected creation of a separate reference list (cf. 2.3.3.) the journals listed in Tab. 2.2 appeared to be most relevant. Appropriate keywords and their combinations might have been: landslide(s), mass movement(s), earthquake(s), 2D/3D, numerical model(ing), seismically induced, site effects, etc.

2.3.2. Survey Charts

In total the landslide database counts 277 distinct cases whose accuracy of documentation extends from very low to very high – a fact depending on the quality of related literature.
To facilitate literature evaluation per case a survey chart was created. It regroups information in different categories that are necessary to describe a landslide event and its rupture zone geometry with the aim of enabling statistical analysis on a later stage. Thereby obtained values can then be used for numerical modeling.
Initially the survey chart was supposed to serve only as aide memoire to keep an order amongst individual cases; its first version (v. 1 – blue charts) existed even in the form of a simple Word-file to be filled in manually. Since, however, literature evaluation is an evolutionary process itself, and due to the fast increase in registered cases, an Excel-file was created (v. 2 – red charts). The expected advantage was to allow for cell-wise export of entries to a professional database tool later on (cf. 2.5.). In the course of amelioration, standardization and bug fixing even a third version (v. 3 – green charts) in the form of an Excel-file was developed. It is this latter survey chart that serves now as basis of the entire database; an example of a survey chart of version 3 is shown in the appendix (cf. A.1.). Every landslide owns a separate Excel-file only named with the number of its case:

e.g. 078.00 Tortum → 078.00.xls

Details about entries in the survey chart are discussed in section 2.4. of this chapter. Units follow the SI-system with one exception and numbers can have up to two decimals (cf. Tab. 2.3).

page	type of Information	unit	decimals
landslide ID (page 1)	location	km	1
	location (Google Earth) – m.a.s.l	m	-
	sliding Direction – degrees	°	1
	φ	°	-
landslide geometry (page 2)	volume(s)	m^3	-
	area(s)	m^2	-
	ratios	-	2
	map – all	m	-
	LCS – all	m / °	-
	TCS – all	m / °	-

Tab. 2.3. Units and decimals as they appear on the survey charts.

2.3.3. Other Elements of the Database

BIB-List

Generally, the BIB-List is a register in the form of an Excel-file that references all publications relevant for this thesis – not only those for the database. The majority of publications is also stored as a PDF-file. Two separate folders are to be found in the BIB-List:

Papers & Chapters	format described in Tab. 2.4
Books & Entire Journals	format described in Tab. 2.5

LS#	000	landslide ID
	x20	landslide ID (Alaska)
	LS-E	landslide example
	LS-E-T	landslide e. & theory
	LS-G	landslide geometry
	LS-G-T	landslide g. & theory
	LS-T	landslide theory
	none	no landslides
	no paper	no paper
SE	SE-E	site effect example
	SE-E-T	site effect e. & theory
	SE-T	site effect theory
	none	no site effects
	no paper	no paper
REF	checked	checking completed
	stop	checking stopped
	no ref	checking impossible
	no paper	no paper
version	digital	PDF-copy available
	no paper	no copy available
	only abstract	abstract available
	only part	partly available
author	Abc A. B.	name
et al.	Abc A. B.	name
	Abc A. B., Abc A. B., …	names
	none	no co-author
year	…	year of publication
title	… .	title
	… . In: Abc A. B. et al. (Eds.). … .	title in a compendium
journal, conference, webpage or editor	…	name of journal
	…	name of editor
	Proceedings of …, City, Country	name of proceedings
	Service (webpage)	name of service
volume	…	volume number
	…	publication number
	xx	no information
pages	… p.	number of pages
	p. …-…	pages from … to …
	…	publication number
	xx	no information

Tab. 2.4. Formats of "Papers & Chapters" listed in the BIB-List (cf. 2.3.3.).

Of particular interest is the first column of the "Papers & Chapters" folder since it contains a number via which references are linked to individual landslides cases (cf. Landslide Number - 2.4.1.). The folder "Books and Entire Journals" does not have such a number because the amount of entire books or journals on the subject of one single mass movement is relatively small; references are here made manually.
The exception of numbering concerns the USGS Professional Papers (No. 541-546, with subdivisions) on the Alaska 1964 Earthquake. Between 1964 and 1970 a multitude of reports and maps were published by authors working for the USGS. By simply according the number 020 to all of them, there would not be enough space in the box of Related Papers (cf. 2.4.1.) on the survey charts. Thus they bear the special number x20 and usually the separate reports are cited as "USGS (several authors), 1964-1970".

version	digital	PDF-copy available
	none	no copy available
author or editor	Abc A. B.	name
et al.	Abc A. B.	name
	Abc A. B., Abc A. B., …	names
	none	no co-author/-editor
year	…	year of publication
title	… .	title
editor or entire journal	… .	name of editor
	… .	name of journal
	Proceedings of …, City, Country.	name of proceedings
	Thesis type, University.	origin of thesis
volume	…	volume number
	…	publication number
	xx	no information
pages	… p.	number of pages
	p. …-…	pages from … to …
	…	publication number
	xx	no information

Tab. 2.5. Formats of "Books and Entire Journals" listed in the BIB-List (cf. 2.3.3.).

EQMM-List: Earthquake Part (EQ-List)

Year / Month / Day

Unlike mass movements which might persistently go on, earthquakes are unique events. The date indicated in the first three columns of the EQ-List corresponds in its format to the second date box on the survey charts (cf. Date - 2.4.1.). Usually, when an earthquake or another seismic event clearly triggered a mass movement their two date entries are the same.

M type / M value

Entries for magnitude types and values correspond to what is indicated under Landslide Cause (cf. 2.4.1.).

#EQ / EQ /Alternative Name of EQ

For clear identification throughout the database, a distinct identification number was attributed to every earthquake or seismic input. It has the format "EQ.000.00" (cf. Earthquake - 2.4.1.).

Some listed earthquakes have a number but do not relate to a mass movement. The reason for this is simple. Either they are famous and it is "smart" to keep them in mind, or they were noted to use the entry at a later stage when additional literature might be available to link a mass movement to the respective earthquake. Examples for such famous or useful entries are:

e.g.	EQ.083.00 Guatemala	on 04/02/1976
e.g.	EQ.157.01 San Francisco 1906	on 18/04/1906
e.g.	EQ.166.00 Sumatra 2004	on 26/12/2004

Names of earthquakes and other seismic inputs appear in the same format as mentioned under Earthquake (cf. 2.4.1.). If the earthquake is also known under one or more different names, they are marked in the respective adjacent box.

Notes to EQ

Additional remarks to an earthquake can be made under Notes to EQ. Such remarks help to distinguish cases or state what a certain event is famous for. Notes might cite special constructions, destroyed localities, tsunamis, fire, etc.

#MM / related MM / other MM

Related mass movements together with their corresponding identification numbers are reported under #MM and related MM. It should be noted that several mass movement events can be triggered by the same earthquake or seismic event; they are then listed in ascending order in both boxes.
If literature reports other mass movements triggered by a distinct seismic event an entry of the following form is made under other MM. However, those mass movements are not separately considered in the MM-List (cf. 2.3.3.).

e.g.	MM according to KEEFER (1984)
e.g.	MM according to KEEFER (2002)

EQMM-List: Mass Movement Part (MM-List)

Year / Month / Day

As mentioned under Date (cf. 2.4.1.) mass movements are either unique or ongoing events; further detailed explanation is given in the referring later section of the report. The date indicated in the first three columns of the MM-List corresponds in its format to the second date box on the survey charts.

#MM / MM /Alternative Name of MM

For clear identification throughout the database, a distinct identification number was attributed to every mass movement. It can have one of the three following formats (cf. Landslide Number - 2.4.1.):

000.00	landslides with survey chart
N.000.00	landslides without survey chart
X.000.00	other mass movements (DF, RA, etc.) without survey chart

The reason for listing also mass movements that do not have a survey chart or other mass movements that are no actual landslides is analogous to the reason for noting earthquakes without mass movements. Either they are famous and it is "smart" to keep them in mind, or they

were noted to use the entry at a later stage when additional literature might be available to create a new survey chart and thus add the landslide to the database. Examples for such famous or useful entries are:

e.g.	N.004.00 Zhashkava	on 29/04/1991	EQ.152.00 Racha
e.g.	N.023.00 Flims	9480 years ago	no EQ
e.g.	X.028.01 Nevado Huascaran I	on 10/01/1962	no EQ
e.g.	X.028.02 Nevado Huascaran II	on 31/05/1970	EQ.034.00 Ancash

Names of mass movements appear in the same format as mentioned under Name (cf. 2.4.1.). If the mass movement is also known under one or more different names, they are marked in the respective adjacent box.

Notes to MM

Additional remarks to a mass movement can be made under Notes to MM. Such remarks help to distinguish cases or state what a certain case is famous for. Notes might cite special constructions, destroyed localities, etc.
Attention has to be paid to the entry "unsure MM-EQ-relation". Sometimes it is not sure if a mass movement was indeed triggered by an earthquake or another seismic event (cf. Landslide Cause - 2.4.1.). For cases with a survey chart this unsure relation is mentioned on the survey chart and in the Details-List. However, for entries without a survey chart an uncertain MM-EQ-relation is marked here.

#EQ / related EQ

Related earthquakes and other seismic events together with their corresponding identification numbers are reported under #EQ and related EQ. It should be noted that only one earthquake or seismic event can be the trigger and reactivation triggers are not considered.

Details-List

The Details-List is an Excel-file that contains for each of the 277 landslides information stored in 29 columns. Since it regroups types of information and characterizations that equally appear in the survey charts, its importance is of rather technical origin – namely the standardization of entries. Only three columns do not appear on the survey charts:

wind rose	with possible entry "yes" or "no"
coordinates	with possible entry "yes" or "no"
LCS over peak	with possible entry "over peak" or "no"

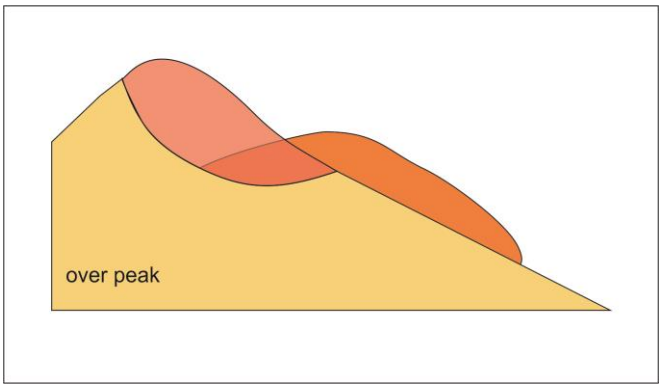

Fig. 2.1. LCS with "over peak" setting.

Entries about the wind rose and the coordinates specify respectively, if for a given case the sliding direction and if the location could be determined (cf. Sliding Direction - 2.4.1.). If a LCS displays a slope including the peak or a local elevation of the mountain ridge the entry "over peak" is made (cf. Fig. 2.1); this might be of interest when defining geometries of rupture zones for numerical modeling.

Google Earth Markers

Another component of the database is the kmz-file created in Google Earth that contains the geographical coordinates of all landslides – except for the two landslides that could not be localized (cf. Location (Google Earth) – 2.4.1., Location Problem - 2.4.1.). Details about the way of setting pins and their accuracy are to be found in these later sections of this report.
Landslides are marked with yellow pins and bear the name in the format "(000.00) [name]" (cf. Landslide Number - 2.4.1.). Interestingly, when examining the distribution of pins around the globe (cf. Fig. 2.2a-e), it seems that distribution patterns mainly follow mountainous or seismic zones or both on the one hand, and on the other hand pins tend to accumulate in areas where research on landslides is a priority – i.e. where means are available and where imminent danger is an issue. It might not be a coincidence that most of the reported cases are from Canada, China, Italy and the United States.

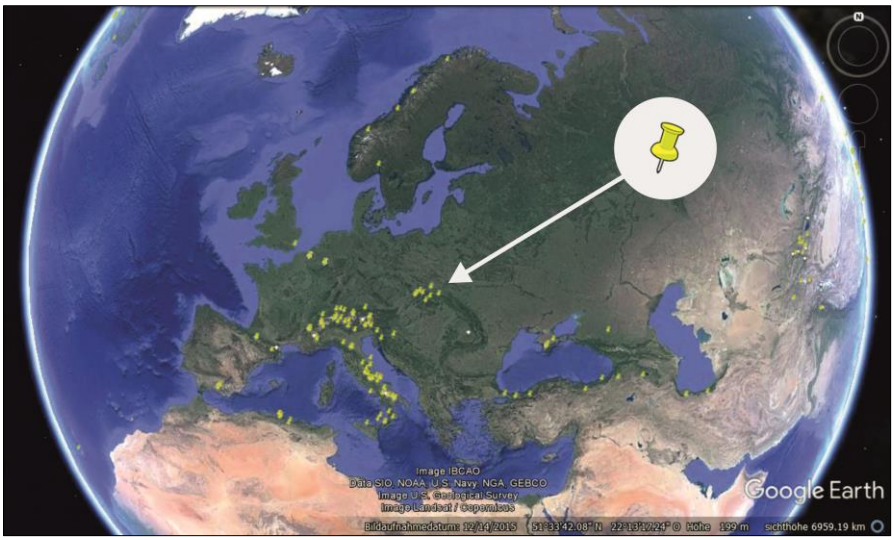

Fig. 2.2a. Pin distribution in Europe; example of a yellow pin (after GOOGLE EARTH, 2016).

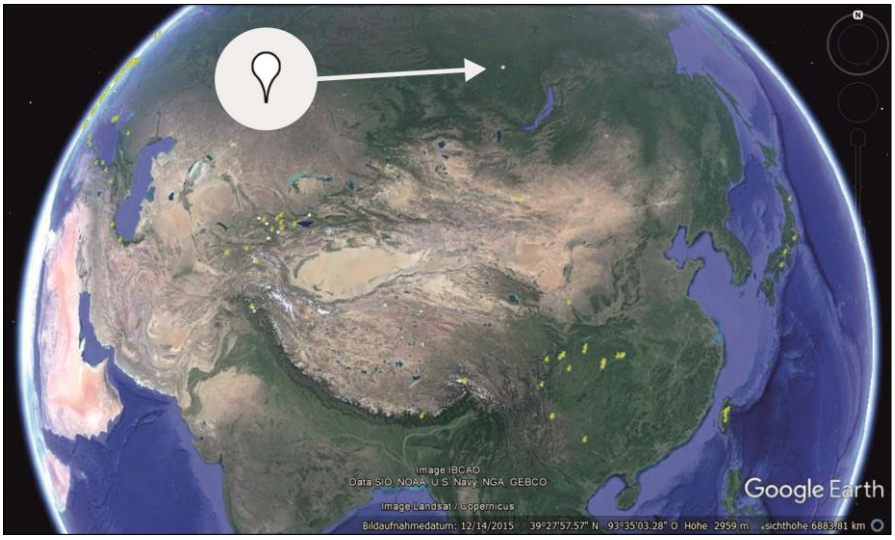

Fig. 2.2b. Pin distribution in Asia; example of a white droplet (after GOOGLE EARTH, 2016).

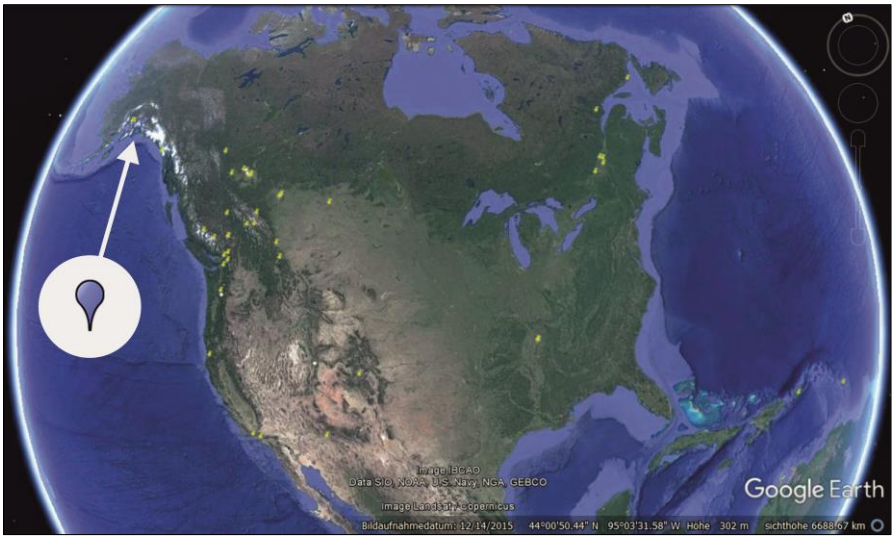

Fig. 2.2c. Pin distribution in North America; example of a blue droplet (after GOOGLE EARTH, 2016).

Fig. 2.2d. Pin distribution in Oceania; example of a red pin (after GOOGLE EARTH, 2016).

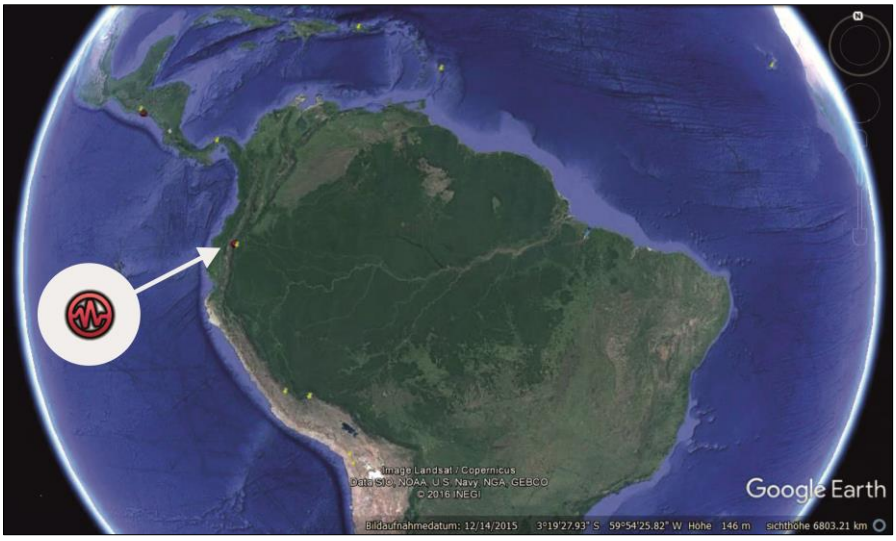

Fig. 2.2e. Pin distribution in South America; example of an earthquake pin (after GOOGLE EARTH, 2016).

For consistency it should be noted that the kmz-file also contains coordinates of mass movements that are famous for different reasons or whose position was worth to keep. They are marked with white droplets (cf. Fig. 2.2b) and bear only their name without any number.
A third type of markers are blue droplets (cf. Fig. 2.2c). They mark the positions of mass movements triggered by the Alaska 1964 Earthquake. The source citing these mass movements is a series of Professional Papers published by the USGS between 1964 and 1970 (No. 541-546 with subdivisions). It should be mentioned that the blue droplets do not mark all of the herein mentioned mass movements, i.a. because nine of them are included in the database and hence own a yellow pin (No. 020.02 – 020.09).
Red pins (cf. Fig. 2.2e) are only located on the Earth's South Pole; they stand for landslides with an unknown location. Those earthquakes that triggered landslides (cf. 2.5.3.) own a pin showing a red wave (cf. Fig. 2.2d).

Carton Box

The carton box is indeed a physical item containing numbered printouts of maps and LCS of the landslides appearing in the database. Since almost all geometrical measurements (cf. Fig. 3.3) were retrieved manually on these printouts, it is of great importance to carefully keep this collection to allow for backtracking if necessary at a later stage. Moreover, many handwritten notes appear on the margins of the printouts.

2.3.4. Strategy as proposed by the IAEG

In the 1990s the objective of the IAEG was to build a World Landslide Inventory. Therefore, a working party at the UNESCO was entrusted with the elaboration of a strategy of construction and a suitable tool for manipulation.
The working party consisted of 39 members in – at that time – 29 different countries or political entities (UNESCO, 1990) around the world and until 1995 five guidelines were published on how to build the World Landslide Inventory:

No. 41 - A Suggested Method for Reporting a Landslide.	(UNESCO, 1990)
No. 43 - A Suggested Method for a Landslide Summary.	(UNESCO, 1991)
No. 47 - A Suggested Method for Describing the Activity of a Landslide.	(UNESCO, 1993)
No. 50 - A Suggested Method for Reporting a Landslide Cause.	(UNESCO, 1994)
No. 52 - A Suggested Method for Describing the Rate of Movement of a L.	(UNESCO, 1995)

The main principle of these guidelines is the creation of nation-wide datasets in a standardized way so that those datasets could be gathered in an international inventory (cf. No. 41 & 43). Although the current landslide database is not designed to meet international levels, the strategy of construction is very similar to the one proposed by the IAEG. This is particularly interesting inasmuch as the guidelines of the IAEG appeared at a rather late stage of literature research and therefore could not serve as model. However, after having designed an own strategy of construction they confirmed its required soundness.
The landslide reports of the IAEG likewise focus on position, date, type, geometry, volume and damage. Further parallels are for instance the attribution of identification numbers to each landslide, the separate reference file liked to the individual cases via numbers, one reference point in the form of coordinates, the standardization to numbers or "yes/no-choices" to enable the transfer to a database tool or the type and material classifications according to international standards (e.g. VARNES, 1978). Other overlaps concerning the activity (cf. No. 47), the rate of movement (cf. No. 52) and possible causes of a landslide (cf. No. 50) are discussed under Dynamics (cf. 2.4.1.) and Landslide Cause (cf. 2.4.1.).
Moreover, the IAEG draws an obvious comparison to earthquake studies; distribution patterns of landslide occurrence would lead to better predictive models and risk alleviation – one of the main ideas of which this thesis consists.

Still, there are differences between the concept of the IAEG and the one adopted for the database construction. For example, a landslide to be included is by the definition of the IAEG one that meets at least one of the following three criteria, whereas the database does not require one or more of them:

- volume bigger than 1.000.000 m^3
- loss of human life
- significant direct or indirect damage

Furthermore, the reference coordinate (cf. Location (Google Earth) - 2.4.1.) does not necessarily point to the crown or toe to the nearest second; it is simply set "somewhere" on the landslide. The time of occurrence does not indicate the most rapid displacement, but the time when the displacement started in general regardless of the fact that a landslide might start out slowly to experience much faster events at a later stage. The names of reporters as well as the damage in terms of local currency are not recorded in the database.
Stunningly, research on the Internet solely leads back to the five Bulletins of the IAEG, but the World Landslide Inventory does not appear at any point. A conjecture might be that it was built before the era of digital globalization. However, it would be of great interest to have access to the dataset of the IAEG.

2.4. Survey Charts

2.4.1. Descriptive Part (Page 1)

Landslide ID

Landslide Number

The box at the upper right corner of the survey charts contains the landslide number – a unique number attributed to every distinct landslide. Numbers have the format "000.00"; two ways of numbering are to be distinguished:

e.g.	154.00	individual case
e.g.	023.01	cases that are either linked by location,
	023.02	by cause or by the fact that they are mentioned
	023.03	in the same publication and hence form a series

Name

Naming of landslides is – similarly to earthquakes – not trivial. Often, one event is known under different names. Landslide names were chosen either in accordance to the initial publication or to the most frequent naming throughout available literature. For consistency names do not contain the word "landslide" or any other designation of mass movements, what sometimes leads to unusual names as for example:

e.g.	CN50.9 Landslide	→	CN50.9
e.g.	Hope Slide	→	Hope
e.g.	Number 1 Ancient Slide	→	Number 1

If a landslide does not have a name it is marked with "[name]". Alternative names of landslides are to be found in the EQMM-List (cf. 2.3.3.).

MM Type

Probably the most difficult task during the creation of the database was the classification of mass movements themselves (cf. 3.2.). There are no distinct thresholds according to which a type of movement can be defined and thus transitions are gradual (cf. Fig. 3.1).
Although classification systems distinguish the big types of movement – even in a rather rough way – the term "slide" is very common and in a great number of cases authors equalize slides with any other kind of mass movement. VARNES (1978) writes on this subject:

> *"The term landslide is widely used and, no doubt, will continue to be used as an all-inclusive term for almost all varieties of slope movements, including some that involve little or no true sliding. Nevertheless, improvements in technical communication require a deliberate and sustained effort to increase the precision associated with the meaning of the words, and therefore the term slide will not be used to refer to movements that do not include sliding." (p. 11)*

He even adapted his own classification first proposed in 1958 referring to "slope movements" rather than to "landslides" since – for instance – neither a flow nor a fall show the same physical and mechanical behavior like a slide. However, he also points out that movements as well as material are both very variable due to location and time and that right classification might still remain an issue (VARNES, 1978). Hence, confusing classification is very common (cf. Fig. 2.3a, Fig. 2.3b) and great attention had to be paid while collecting literature for the database.

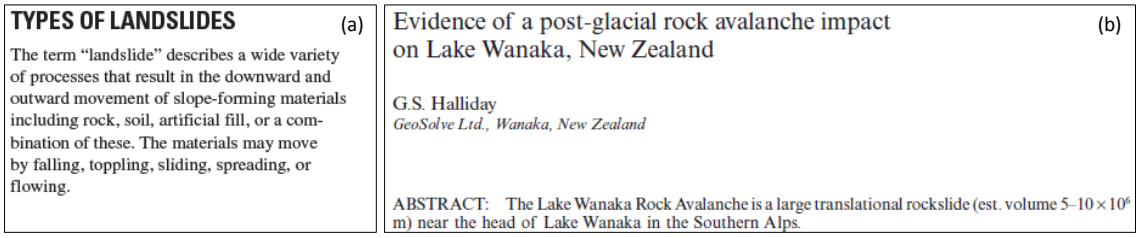

Fig. 2.3a-b. Unclear mass movement classification (after USGS, 2004; after HALLIDAY, 2016).

Clearly, the database is supposed to contain only landslides, but due to the above mentioned difficulties of classification it happened that some mass movements entered the database although they are no landslides. One of those cases is the Slumgullion Earthflow (082.00) which is frequently called "Slumgullion Landslide" in literature.
Other types of mass movements that are very similar in their behavior but still slightly different from common landslides are deep seated deformations of slopes. About 10% of the documented cases fall in this category.
To summarize, the box of mass movement types can have one of the tree entries listed below. It should be noted that, when speaking about landslides in this report, generally one of those three terms is meant, although a flow is not a slide as already mentioned.

LS	landslide
DSGM	deep seated gravitational movement
EF	earth flow

It should be noted that in chapter 3. the abbreviation "DSGSD" (deep seated gravitational slope displacement; cf. 3.3.3.) is used for "DSGM". In scientific publications "DSGSD" is more common though.

Earthquake

Also the naming of earthquakes is not trivial. It appears to be very common that one single event is known under different names. Earthquake names – like landslide names – were chosen either in accordance to the initial publication or to the most frequent naming throughout available literature. Alike, names do not contain the word "earthquake" or any other designation of seismic sources, what sometimes leads as well to unusual names as for example:

e.g.	Great Peruvian Earthquake	→	Great Peruvian

Some earthquakes bear exactly the same name because they happened in the same place. In this case the year of occurrence is kept behind the name. If two events happened in the same place and the same year Latin numbers are added to the name:

e.g.	Alaska Earthquake	09/07/1958	→	Alaska 1958
e.g.	Alaska Earthquake	27/03/1964	→	Alaska 1964
e.g.	Hindukush Earthquake	03/03/2002	→	Hindukush 2002 I
e.g.	Hindukush Earthquake	25/03/ 2002	→	Hindukush 2002 II

Earthquakes belonging to earthquake sequences are marked as follows; many of them have an alternative name which makes identification easier and which is to be found in the EQMM-List (cf. 2.3.3.).

e.g.	New Madrid Sequence (1st event)	→	New Madrid Seq. 1

Generally earthquakes or other seismic sources can have the following names:

e.g.	Boumerdès	single event
e.g.	Northern Italy Seq. 1	event of a sequence
	volcanic eruption	other natural seismic source
	volcanic intrusion	other natural seismic source
	tremors	other natural seismic source
	blast	only artificial seismic source

If an earthquake does not have a name it is marked with "[name]". Earthquakes are given numbers in a format similar to landslides (cf. Landslide Number - 2.4.1.), but their numbers appear only in the EQMM-List (cf. 2.3.3.).

MM ⇆ EQ

The abbreviation "MM ⇆ EQ" stands for the relation between the mass movement and the earthquake. If literature cites with certainty an earthquake (or another seismic source such as for example tremors or blasts) as trigger for a mass movement, the relation is marked as "sure". If their relation is only suspected, it will be marked as "unsure". This applies mainly to paleo-landslides or to times in history where exact records were rare. It should be noted that in the EQMM-List (cf. 2.3.3.) all "mass-movement-earthquake-couples" appear as if they were surely linked and remarks on uncertainty exist only in the survey charts and in the Details-List (cf. 2.3.3.).
In case of mass movements without seismic cause, the relation box contains "no EQ".

Date

Date indications have to be read with care. Precise information on the occurrence of the landslide is to be found in the second box. It can have the following formats, where the time

specification can designate either the moment of a unique event or the moment when continuous movement started:

e.g.	2001/2/3	on/since 03/02/2001
e.g.	1999/10	in/since October 1999
e.g.	1600	in/since the year 1600
e.g.	15th cent.	during/since the 15th century
	paleo	during/since ancient geological times
	postglacial	after/since the last glaciation
	?	at/since an unknown time

Additional indications on major events of a landslide appear in the first box in the formats below; they give information about times before and after the main event:

e.g.	since 2000	landslide moving since 2000 (before main event)
e.g.	earlier in 2000	event in 2000 (before to main event)
e.g.	earlier in 07/2000	event in July 2000 (before to main event)
e.g.	earlier on 10/05/2000	event on 10/05/2000 (before to main event)
e.g.	later in 2005	event in 2005 (after main event)
e.g.	later in 07/2005	event in July 2005 (after main event)
e.g.	later on 10/05/2005	event on 10/05/2005 (after main event)

Fatalities

The marked number refers to human loss. Only in some very rare cases animals are mentioned; this is the case when a significant herd died. It should be noted that no value can mean that literature either does not report a number or that there was no fatality.

Damage

Similarly to Fatalities (cf. 2.4.1.) damage reports on survey charts are always incomplete, so they should serve only as overview on the impact of the event. An empty box under Damage can mean that either no damage happened or that no damage is reported. Also, if for example infrastructure is not mentioned, it does not mean that infrastructure remained undamaged. For cases with existing damage reports losses are cited in a simple way, but standardized only to some extent:

e.g.	A-92	damage to a motorway
e.g.	road	damage to any other road
e.g.	Khait	damage to a whole village or a part of it
e.g.	building stock	damage to houses of all types
e.g.	infrastructure	damages to lifelines of all types

The formation of dams is not considered as damage; however it is a very common and important consequence after landsliding and hence marked here. The notation “dam” indicates that due to the landslide a dam had formed; it does not say if the dam is still retaining a lake, if a spillway was dug for drainage or if the dam broke by itself. The notation “dam possible” refers either to cases of paleo-landslides where the formation of a dam was likely but no evidence was found so far, or to slowly moving landslides that might be triggered in future and then form a dam.

Location

Basic geographical information on a landslide locality is stored under Location. For each landslide its position is noted in the following way using four boxes in a row:

e.g.	box 1:	2.5	distance in km
e.g.	box 2:	ENE	wind direction
e.g.	box 3:	Old Hissar	geographical locality
e.g.	box 4:	TJ	country code

Fig. 2.4. Rough distance measurement by direct connection (after GOOGLE EARTH, 2016).

These four types of information read out as "The landslide is located 2.5 km ENE of Old Hissar in Tajikistan." (cf. Fig. 2.4). For economizing space and correct country identification the standard code ISO 3166-1 alpha-2 was used (WIKIPEDIA, 2016b). Disputed territories are cited according to this standard code and hence do not reflect any other consideration on geopolitical affiliation.

Location (Google Earth)

A second headline named Location (Google Earth) refers to an exact position of a landslide. It is given by latitude and longitude coordinates retrieved from Google Earth (cf. Fig. 2.5) and appears in the following form:

	000°00'00.00'' N	(or S)	for latitudes
	000°00'00.00'' E	(or W)	for longitudes
e.g.	1000		for meters above sea level

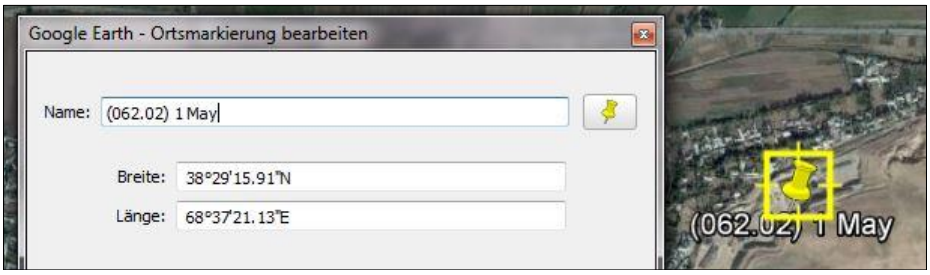

Fig. 2.5. Retrieving coordinates for a landslide (after GOOGLE EARTH, 2016).

In many cases exact positioning of landslides in Google Earth is a time-consuming and difficult task because satellite images have to be compared with maps given in literature. Besides, recent slope reconstruction and terrain modifications (cf. Slope Modification - 2.4.1.), which are visible on more recent satellite images, complicate the identification of original landslide locations. In this context the "Google Earth time machine" is a useful tool but still cannot solve the issue in most of the problematic cases since older satellite imagery usually has a lower resolution and less quality.
Almost all landslides possess a pin in Google Earth from which latitude and longitude values were taken. Also the altitude value in meters above sea level corresponds to the respective pin.
It should be noted that a pin does not mark the center of the rupture zone of a landslide; it rather serves to localize the landslide in Google Earth or on another map. Thus pin information should not be used for any calculation. Also, the geographical information mentioned above is given with reference to pins and therefore distances and wind direction from other geographical localities might differ especially if the landslide is large.

Another issue that makes correct positioning difficult is the fact that locations in China are not in alignment with Google Earth satellite imagery (cf. Fig. 2.6). According to the State Bureau of Surveying and Mapping Chinese maps use the GCJ-02 geodetic datum, which introduces random offsets in both the latitude and the longitude by using an obfuscation algorithm (WIKIPEDIA, 2016c). Thus, pins in China were very difficult to set and some might not show the actual landslide site.

Fig. 2.6. Random geodetic offset in China (after GOOGLE EARTH, 2016).

Dynamics

Landslides can be either active or inactive, and the active state can be further divided. On the survey charts the following boxes can be ticked to display the dynamic behavior of a landslide:

active – constant / slow	for landslides in constant slow motion (e.g. creeps)
active – sudden / fast	for occasionally fast moving landslides
no activity	for landslides that are actually stable

It has to be noted that a combination between "active – constant / slow" and "active – sudden / fast" is possible when constantly moving landslides experience sudden ruptures due to seasonal precipitation or seismic activity for instance. Furthermore, "no activity" only means that the landslide is currently inactive (at the time of the creation of the database); it might have been an active paleo-landslide or it might be active in future.

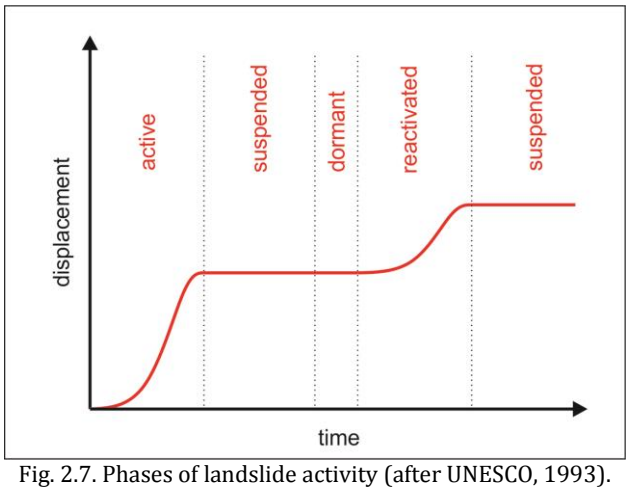

Fig. 2.7. Phases of landslide activity (after UNESCO, 1993).

An interesting and detailed concept of activity documentation is presented by the IAEG (UNESCO, 1993); it refers to state, distribution and style of activity of a landslide and it is partially based on the work of VARNES (1978). Summarizing, Fig. 2.7 shows a graph that is

described as particularly suitable to trace the dynamic behavior of a landslide over time. Indeed, it clearly depicts phases of activity (where the gradient is not 0) and inactivity (where the gradient is 0). However, for the database differences were not made for all 4 possible states and correspondences between the here presented state divisions and the ones of the IAEG are given in Tab. 2.6.

IAEG	database
active	active - constant / slow
reactivated	sudden / fast
dormant	no activity
suspended	

Tab. 2.6. Comparison of dynamic phases of landslides.

Also the rate of movement of a landslide is described by the IAEG (UNESCO, 1995). It is proposed to retain division of VARNES (1978) into speed groups ranging from extremely slow to extremely fast. Concerning speed though, the only interest in this database is how to distinguish a rapid event from a slope in slow motion.

Material Classification

One of the most popular classifications for mass movements is the one of VARNES (1978) which combines types of movement with types of material as shown in Tab. 2.7.

mass movement classification		material type		
		rock	debris	soil
movement type	fall	rock fall	debris fall	earth fall
	topple	rock topple	debris topple	earth topple
	slide – rotational	rock slump	debris slump	earth slump
	slide – translational	rock slide	debris slide	earth slide
	lateral spread	rock spread	debris spread	earth spread
	flow	rock flow	debris flow	earth flow
	complex	combinations		

Tab. 2.7. Mass movement classification (after VARNES, 1978).

Since the overall aim of the database is to assemble landslides – and thus the movement type is defined –, simple classification of material was adopted from VARNES (1978); namely the discrimination between rock, debris and soil. Lately, HUNGR et al. (2014) recommended a change of nomenclature of material type in the classification of VARNES (1978) to make it more compatible with geological and geotechnical terminology. The new classification only distinguishes rock and soil, where the involvement of debris is mentioned under "soil" based on its grain sizes:

e.g.	rock slide	for rock slides
e.g.	gravel/sand/silt slide	for debris or soil slides

Although the newly proposed modification is surely legitimate in terms of better overlap to geological and geotechnical terminology, material distinction throughout the database was still made according to the older classification of VARNES (1978). On the one hand it is still widely used and changes as proposed by HUNGR et al. (2014) did not yet find their way to the overall geoscientific community, on the other hand, rock, debris and soil have very distinct physical properties and show significantly different dynamic behavior when undergoing seismic shaking. Hence, in order to make use of the database for numerical modeling, it is of great advantage to

be able to distinguish quickly involved material types without trailing off in subgroups and relying on a classification that is still the most popular among scientists.

Sliding Direction

Sliding directions of landslides are given in wind directions and degrees based on the principle of "dip angle and dip direction" in structural geology (cf. Fig. 2.9) by comparing the ground surface of the landslide mass to the horizontal. The dip is replaced by the slope angle α (cf. Fig. 3.3) and the dip direction corresponds to the average sliding direction.
Sliding directions are rounded to the 16 main wind directions (cf. Fig. 2.8, Tab. 2.8). By inserting a wind direction to the respective box on a survey chart the corresponding degree appears automatically. Also the green arrow switches to the correct position.

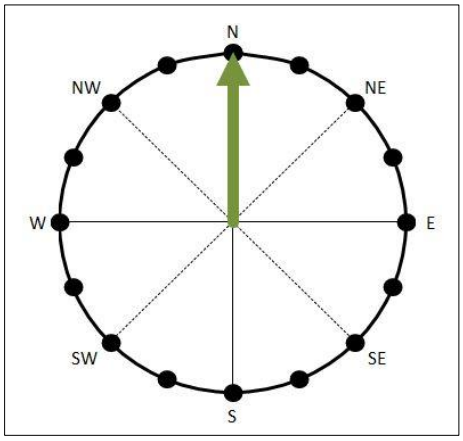

Fig. 2.8. Wind rose.

N	0.0°	E	90.0°	S	180.0°	W	270.0°
NNE	22.5°	ESE	112.5°	SSW	202.5°	WNW	292.5°
NE	45.0°	SE	135.0°	SW	225.0°	NW	315.0°
ENE	67.5°	SSE	157.5°	WSW	247.5°	NNW	337.5°

Tab. 2.8. Wind directions in degrees.

For cases without known sliding direction – mostly due to an unknown location of the landslide (cf. Location Problem - 2.4.1.) – the wind direction box remains empty, hence the degrees box shows "wrong" and the arrow remains on the north position.

φ

The emplacement of a LCS on a map is not always obvious. Usually it should be indicated with a line or point-to-point mark on the map, and ideally it is taken along the average sliding direction. Sometimes, especially when access to the terrain is restricted, or when scientists have special interest in features offside the line along the average sliding direction, a LCS can be placed with a diverting angle – the angle "φ" (cf. Fig. 2.10a, 2.11a)
The "φ-box" can contain one of the following values; it is measured from maps manually with an angle meter and does not show decimals.

	0	no deviation or no LCS available
e.g.	8	deviation up to 20°
e.g.	35	deviation bigger than 20°

Geometrical Correction

For a while, during the database construction, the possibility of geometrical correction for LCS diverting by more than 20° from the average sliding direction was discussed. The main idea was to make use of the principle of angle correction first published by PALMER (1919) which is a common tool in structural geology and geologic cartography. In the following the principle itself as well as its possible application to landslide geometries is presented.
In structural geology separating interfaces such as shear surfaces, bedding planes or slickenside surfaces are very common. Their orientation is defined by either the strike or the dip direction measured respective to north and the dip respective to the horizontal (cf. Fig. 2.9); dip direction and dip indicate the direction of the orientation of the highest gradient and its value in degrees. However, very often measures exist only for cross sections with an angular offset from the dip direction; dip and dip direction are then only apparent and do not correspond to the actual values. Figure 2.9 shows the relation of real and apparent parameters where:

strike	strike direction (± 90° from dip direction)
dir_r	real dip direction
dip_r	real dip
dir_a	apparent dip direction
dip_a	apparent dip
φ	angle between apparent dip direction and real dip direction
δ	angle between apparent dip direction and strike direction
d	depth value for comparison
x	depth value for comparison

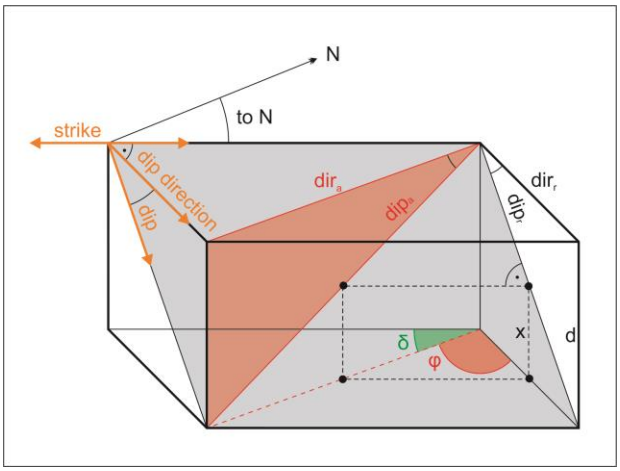

Fig. 2.9. Relation between real and apparent dips and dip directions.

Considering some trigonometric equations, real and apparent dips are related as shown below.

$$\text{from} \quad \tan(dip_r) = \frac{d}{dir_r} \quad \text{and} \quad \tan(dip_a) = \frac{d}{dir_a} \quad \text{follows}$$

$$\tan(dip_a) = \frac{dir_r}{dir_a} \cdot \tan(dip_r) \quad \text{and with} \quad \sin(90 - \varphi) = \frac{dir_r}{dir_a} \quad \text{one obtains}$$

$$dip_a = \tan^{-1}(\tan(dip_r) \cdot \sin(90 - \varphi)) \quad \text{and}$$

$$dip_r = \tan^{-1}\left(\frac{\tan(dip_a)}{\sin(90-\varphi)}\right)$$

Using these relations it can be seen that by progressive deviation of the apparent dip direction from the real dip direction the apparent dips become smaller, i.e. the surface appears less steep (cf. Fig. 2.10a, Tab. 2.9).

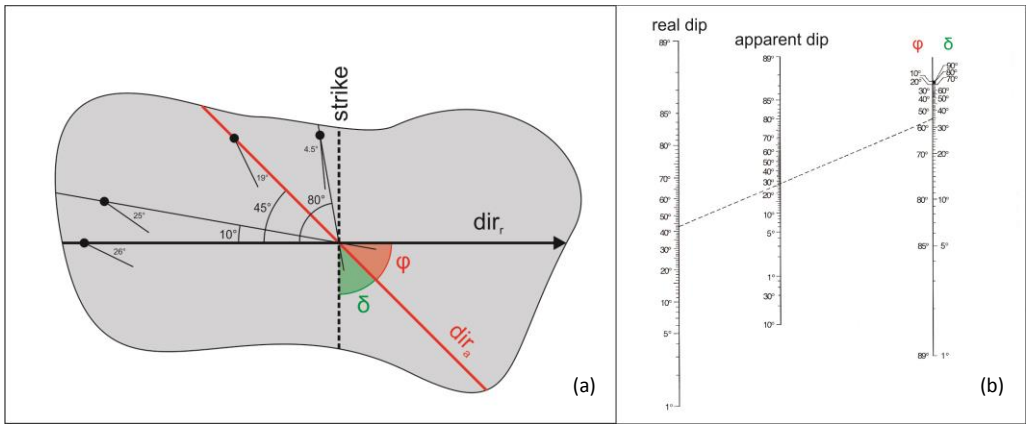

Fig. 2.10a-b. Relation between real and apparent dips and dip directions (after PALMER, 1919).

real dip (°)	apparent dip (°)	φ
26	26	0
26	25	10
26	19	45
26	4.5	80
26	0	90

Tab. 2.9. Example values for Fig. 2.10a-b.

Based on this relation PALMER (1919) published a chart linking real dip, apparent dip and φ (or δ as the complement of φ to 90°); it is a straightforward tool for geological fieldwork enabling angle corrections without calculation (cf. Fig. 2.10b).
Since this chart can easily be used for the correction of angles on a plane interface, the initial idea was to make use of it to adjust values for δ_1, δ_2, δ_3, δ_4, and δ_E. At the five main positions (cf. Fig. 3.3) those five angles define the inclination of a tangent plane towards the horizontal, and the bigger the angle φ becomes, the more significant is the difference between real and apparent dip angles. As threshold value for required geometrical correction φ was set to 20°, meaning that LCS with a φ ≤ 20° could be evaluated as given, whereas LCS with φ > 20° should be corrected using PALMER's (1919) chart. In theory, the approach would be (cf. Fig. 2.11a):

1) localize the apparent LCS
2) mark the real LCS along the average sliding direction
3) measure φ between both LCS
4) divide the apparent LCS in 4 equal parts
5) project those 4 parts to the real LCS (cf. for right angle in Fig. 2.11a)
6) attribute corrected angles to the five main positions along the real LCS

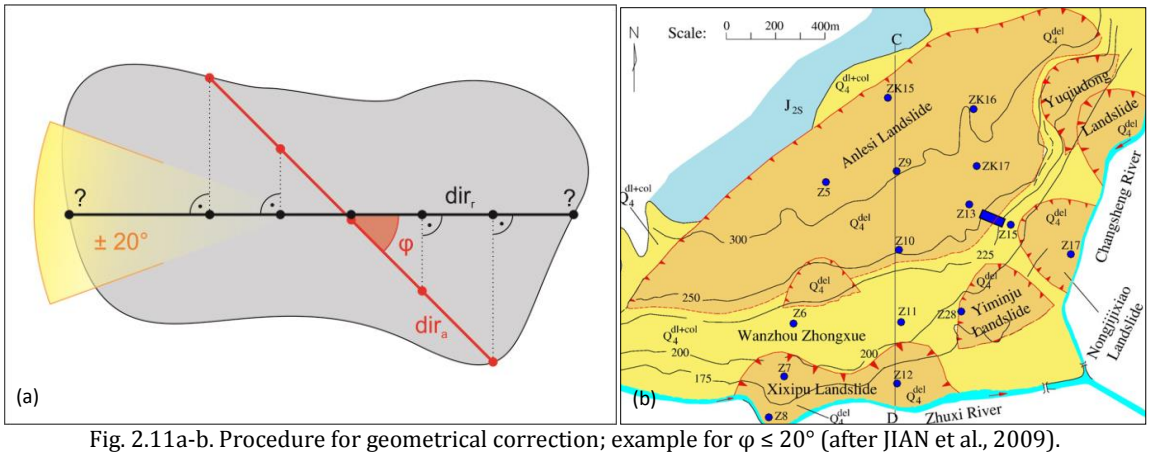

Fig. 2.11a-b. Procedure for geometrical correction; example for φ ≤ 20° (after JIAN et al., 2009).

Even though this way of angle correction seems to be rather simple and straightforward, it has a number of drawbacks and potential error sources.
One problem arises by projecting positions from the apparent to the real LCS. Since the type of projection is a normal projection, positions 1-3 remain inside the landslide mass (cf. case of Fig. 2-11a), but positions 0 and E move from the landslide border to its interior. This latter circumstance provokes a wrong angle attribution.
Another issue is applicability of procedures for both translational and rotational landslides. Considering the formerly mentioned problem with projections, it is obvious that angle correction is possible for the inner positions 1-3 of a perfectly flat and equally thick translational landslide. However, angles at positions 0 and E of the rupture surface cannot be properly corrected. Even more complex – or actually impossible – is the correction of rotational landslides because depth values of the five main positions cannot be assumed to be equal (cf. x in Fig. 2.9) and usually rotational landslides tend to have either deeper or completely irregular depths in the center of the main body.
Furthermore, it must be kept in mind that usually a LCS is only an interpretation of soundings or borehole data. Thus, every image of a LCS contains some error and defining a real LCS to measure φ also introduces further uncertainty.
Due to the interplay of drawbacks and error sources it seems that after all PALMER's (1919) principle remains a useful tool only for purposes related to structural geology, but not for defining landslide geometries. Especially the fact that it is only partially applicable to translational landslides, but not to rotational landslides, is a strong argument against the use for angle correction of LCS; for consistency both – and also mixed – types of landslides should be able to be corrected.
As a conclusion, for landslide cases with $\varphi > 20°$ the respective φ value is shown and the Geometrical Correction box contains "yes". This means that due to the deviation a correction would be needed, but it was not performed. Further information on LCS is given under Notes (cf. 2.4.1.) as in cases where LCS exist, but exact parameters were not measured. If the box contains "no", no correction is needed because $\varphi \leq 20°$.

Landslide Imagery

Map

This box can contain either "yes", "no" or "map cut off". Respectively those abbreviations mean:

yes	in at least one of the listed references there is an exploitable map
n	in none of the listed references there is an exploitable map
map cut off	the exploitable map does not show the entire landslide

In case there is an exploitable map, its image number is shown in Assumption for Map (cf. 2.4.1.); otherwise the box contains "n". For the handling of cut off maps refer to Other Notes (cf. 2.4.1.).

LCS

This box can contain either "yes", "no", "LCS cut off" or "LCS $\varphi > 20°$". Respectively those abbreviations mean:

yes	in at least one of the listed references there is an exploitable LCS
n	in none of the listed references there is an exploitable LCS
LCS cut off	the exploitable LCS does not show the entire landslide
LCS $\varphi > 20°$	the exploitable LCS diverts by more than 20° from the sliding direction

In case there is an exploitable LCS, its image number is shown in Assumption for LCS (cf. 2.4.1.); otherwise the box contains "n". For the handling of cut off LCS refer to Other Notes (cf. 2.4.1.).

If literature displays LCS that divert by 20° or more from the average sliding direction, LCS information is given under Notes (cf. 2.4.1.), but exact parameters were not measured (cf. Geometrical Correction - 2.4.1.). Hence, the geometrical earnings of cases with "LCS φ > 20°" and of those without any LCS is the same.

3D

This box can contain either "yes" or "no". Respectively those abbreviations mean:

yes	in at least one of the listed references there is a figure in 3D
n	in none of the listed references there is figure in 3D

Photo

This box can contain either "yes" or "no". Respectively those abbreviations mean:

yes	in at least one of the listed references there is a photo
n	in none of the listed references there is a photo

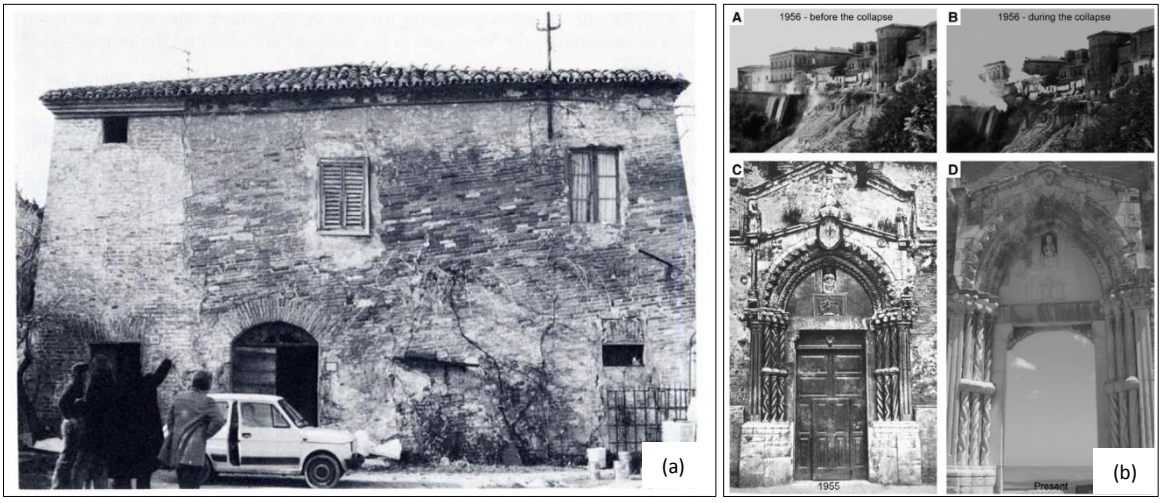

Fig. 2.12a-b. Photos showing damage of the Post House (Ancona Landslide, 035.01) and of the S. Pietro Church (Vasto Landslide, 102.00) (after COLTORTI et al., 1985; after DELLA SETA et al., 2013).

It should be noted that photos not necessarily show the landslide; they might also show damage, small scale features or outcrops (cf. Fig. 2.12a-b). An example for a landslide where all four types of imagery (cf. Fig. 2.13a-d) are present is the La Clapière Landslide (036.00).

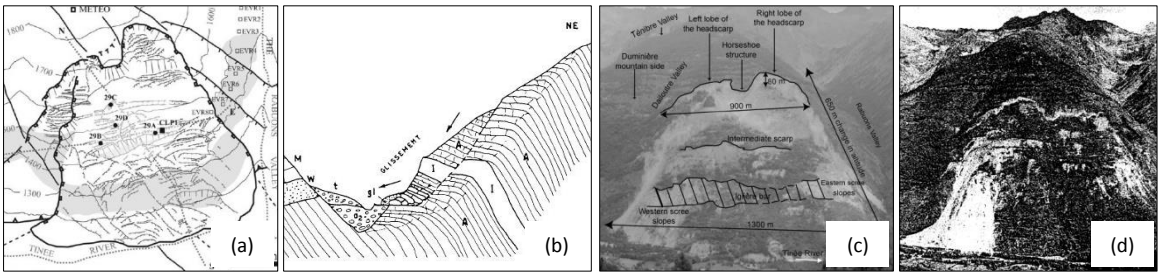

Fig. 2.13a-d. Map, LCS, 3D figure and photo of La Clapière Landslide (after GAFFET et al., 2010 ; after BLANC et al., 1987 ; after CASSO et al., 2003 ; after BLANC et al., 1987).

Landslide Cause

Similar to landslide dynamics (cf. Dynamics - 2.4.1.) the IAEG proposes a method for reporting landslide causes (UNESCO, 1994). The latter can be very wide spread and usually a slope failure is a result of several interlinked causes. At this, the IAEG mentions a distinction between preparatory and triggering causes, which – however – is not of great importance in the present database since it is not trivial to clearly separate them. In any case, the requirement for failure is a factor of safety (SF) smaller than 1 (cf. 5.2.1.). This implies that the sum of all internal and external landslide causes in the form of applied forces exceeds the combination of all forces operating against failure.

$$FS = \frac{holding\ forces}{driving\ forces}$$

Such internal or external causes may be categorized in three groups (cf. Tab. 2.10); however the causes for the most damaging landslides worldwide are the involvement of water and seismic and volcanic activity (USGS, 2004). During the assessment of the individual landslides special emphasis was given to the first two major causes.

geological causes	morphological causes	anthropogenic causes
weak materials	tectonic uplift	excavation work
sensitive materials	glacial retreat	overload
weathered materials	erosion & leaching	reservoir drawdown
adverse discontinuities	vegetation removal	irrigation & leakage
permeability contrast	freeze-thaw cycles	mining
stiffness contrast	shrink-swell cycles	vibration & explosions

Tab. 2.10. Geological, morphological and anthropogenic landslide causes (after UNESCO, 1994; after USGS, 2004).

Earthquake

Around a third of the database consists of landslides caused by earthquakes or other seismic triggers. Names of seismic events are given under Earthquake (cf. 2.4.1.) and the certitude of the relation is indicated under MM ⇆ EQ (cf. 2.4.1.) next to it. Earthquakes are given numbers in a format similar to landslides (cf. Landslide Number - 2.4.1.). Numbers appear only in the EQMM-List (cf. 2.3.3.), but not on the survey charts.

e.g. EQ.127.00 for the Manjil-Rudbar Earthquake

More detailed information on earthquakes that triggered a landslide appears under Magnitude, Time Lag and General Seismic Area.

* m	unified magnitude	* $M_{J=JMA}$	magnitude of the JMA
* m_B	body wave magnitude	* M_m	mantle magnitude
* m_b	short period m_B	* M_L	local magnitude
* M_d	duration magnitude	* M_S	surface wave magnitude
* M_E	energy magnitude	* M_W	moment magnitude

Tab. 2.11. Magnitude types.

The information on magnitude contains firstly the magnitude type and secondly the respective value. So far, type and value are stored as they were found in literature. However, it should be noted that according to the magnitude type (cf. Tab. 2.11; WIKIPEDIA, 2016d) the value can change. Magnitude types that appear in the database are marked with an asterisk (*); if the

magnitude type or the value could not be determined throughout literature, the survey chart contains a "?" in the respective box. For completeness and to avoid confusion, it should be noted that M_0 is not a magnitude but the seismic moment and therefore not listed in Tab. 2.11.
Especially for magnitude distance comparisons with respect to possible landslide triggering (KEEFER, 1984) it is important to use magnitudes of the same type (cf. 1.5.3., 3.3.1.).
Landslides can either be triggered by the main seismic impact or at a later stage due to the effect of ground weakening and pore pressure redistribution. The box of Time Lag indicates the behavior of a landslide in terms of time that passed between the triggering seismic event and the main landslide event. The following abbreviations are used:

co	co-seismic triggering of the landslide
post	post-seismic triggering of the landslide
co-post	co seismic-triggering of the landslide, ongoing events in the aftermath
no EQ	landslide without seismic trigger

The information on the overall seismicity of a region is a rather subjective estimate comparing locations of occurrence to global seismic maps such as the one in Fig. 2.14. Three classifications were made:

currently seismic	for locations with actual strong seismic activity
seismic in past	for locations with strong seismic activity in the past
rather non-seismic	for locations with low (or almost no) seismic activity

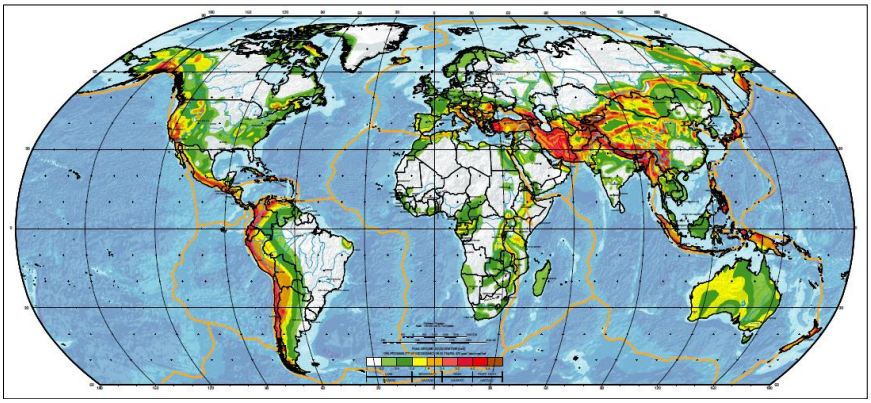

Fig. 2.14. Global seismic hazard map (after GIARDINI et al., 2013).

It should be noted that no area on the Earth is completely free of seismic activity and that in theory earthquakes can occur all over the globe, but with different magnitude and probability. Also, non-seismically triggered landslides can occur in seismically active regions; "no EQ" hence does not necessarily imply "rather non-seismic".

Other

Landslide causes other than seismic triggering mostly relate to water, strong storm events, phenomena of physical weakening and weathering or a combination of factors. Per landslide case, factors are sorted according to the best-fit-principle to the following four categories as most suitable and using the keywords:

water	for precipitation, pore pressure effects, drainage, groundwater, etc.
wind	for hurricanes, thunderstorms, etc.
else	for erosion, lithology, structural geology, anthropogenic influence, etc.
suspicion	for assumed causes

However, it is important to keep in mind that one factor might concern two categories although it is noted in only one of the boxes; for instance, a thunderstorm represents a wind and rain event at the same time, and toe erosion by a river displays a physical decomposition caused by a water course. Furthermore, notations in this section are not standardized and cannot be used for statistical purposes because they only sum up what literature reported and in reality many more unmentioned factors might play a role in the triggering process.

Unknown

In some very rare cases the landslide cause is not reported in literature. This concerns mainly case studies conducted for technical issues such as road construction, tunneling, mining, etc. The box named Unknown is only ticked, when there is not even a suspicion about the triggering cause.

Notes

Assumption for Map

If in at least one of all listed references there is an exploitable map, its image number is shown under Assumption for Map; otherwise the box contains "n".

Assumption for LCS

If in at least one of all listed references there is an exploitable LCS, its image number is shown under Assumption for LCS; otherwise the box contains "n". Some LCS bear an index or a point-to-point mark. These are put in brackets behind the image number as follows:

e.g.	Fig. 3 (A-A')	for LCS exploited from Fig. 3, cross section A-A'
e.g.	Fig. 29 (S4)	for LCS exploited from Fig. 29, cross section S4

Location Problem

As indicated in the section of Location (Google Earth) (cf. 2.4.1.) correct positioning of landslides can be difficult. The box of Location Problem contains either "no" if there is no difficulty to locate a landslide, or one of the following notes:

1 pin for several MM	cf. a)
pin somewhere close	cf. b)
right location found?	cf. c)
unknown location	cf. d)

a) If a series of landslides is unable to be localized and their position is approximately known, one pin is set for the whole series. Thus, all landslides from that series have the same coordinates. Also for the geographical information this pin is taken as reference.

b) If one single landslide is unable to be localized and its position is approximately known, the pin is set somewhere in the environs. Also for the geographical information this pin is taken as reference.

c) In some cases the right position of a landslide is believed to be found. Then the pin is set on the assumed position. Also for the geographical information this pin is taken as reference.

d) In some very rare cases landslides are not to be localized at all. For them the pin is set on the Earth's South Pole and the box of Location (Google Earth) (cf. 2.4.1.) contains:

090°00'0.00"S	for latitudes
000°00'0.00"E	for longitudes
?	for meters above sea level

The geographical information is then given in the following format:

e.g. box 1: 0.0		distance in km, always on 0.0
e.g. box 2: N		wind direction, always on N
e.g. box 3: Otsu		geographical locality if known, otherwise empty
e.g. box 4: JP		country code

Slope Modification

Slope modification is also a rather broad term and refers to any artificial change of the slope of a landslide such as complete reconstruction or land use change in case a landslide took place in urbanized areas, replacement of roads and other infrastructure components, installation of protection measures such as for example retaining walls or earthworks such as excavations or landfills. Furthermore, the mark "slope reshaped" can also mean that a slope in constant slow motion is densely inhabited, that the landslide happened for instance due to construction work after tunneling activity or that the landslide is a result of wrong geotechnical constructions.
In case of no relevant slope modification the box contains "n", but it should be noted that literature might not mention every detail about the artificial evolution of a slope.

MM includes / became

After a mass movement is triggered, it is very common for it to undergo transformation to another type or at least to include one at some location. For example, a landslide consisting of rock triggered in high mountainous terrain might easily transform to a rock avalanche after leaving the rupture zone; or a sliding mass mainly consisting of loess – thus soil – might mix with precipitation and turn into an earth flow. Some landslides, which keep their landslide characteristics, only show flow features at their toe when touching a water course or they trigger rock falls or involve toppling on their side flanks.
The overall mass movement type is defined under MM Type (cf. 2.4.1.); the inclusion or the transformation to another mass movement type is mentioned in the box of MM includes / became. In the following common types are listed with their abbreviations; however this list is not complete since classification of mass movements is generally difficult (cf. 2.2., 2.4.1., 3.3.3., Fig. 3.1). In terms of material, this abbreviation system corresponds partially to the mass movement classification of CRUDEN & VARNES (1996) to which reference is made under Material Classification (cf. 2.4.1.).

DA	debris avalanche
DF	debris flow
RA	rock avalanche
RF	rock fall
EF	earth flow
LF	loess flow

Landslides without any transformation or inclusion of other mass movement types are marked simply with "LS"; DSGM also do not change their behavior; the same marking is applied to them:

LS	landslide
DSGM	deep seated gravitational movement (cf. 2.2., 2.4.1., 3.3.3.)

LCS

The section named LCS documents detailed information on the quality and characteristics of LCS. Relations and if-then-conclusions are frequent and will be discussed below. As mentioned under LCS (cf. 2.4.1.) in the section describing the available landslide imagery, LCS with a φ equal or bigger than 20° information is retrieved, but exact parameters were not measured. If literature does not show LCS, all boxes will contain "no LCS" with the exception of the last one; the LCS is then considered as if it was self-placed and hence φ is 0°.
The following five features are of main interest when judging the quality and characteristics of LCS:

knickpoints	cf. a)
XZ-scale	cf. b)
rupture zone	cf. c)
pre-LS surface	cf. c)
self-placed	cf. d)

a) Knickpoints in LCS are usually unpractical to handle, but due to reasons such as access in the terrain or significant change of the sliding direction they appear in literature from time to time. Throughout the database LCS with up to three knickpoints exist; the number per respective LCS is given in the box of knickpoint followed by one of the three possible remarks indicating how the existence of knickpoints was dealt with:

bent straight	LCS straightened to a line	(cf. Fig. 2.15a)
point-to-point line	new line created linking positions 0 and E	(cf. Fig. 2.15b)
segmented	LCS accepted in segmented form	(cf. Fig. 2.15c)

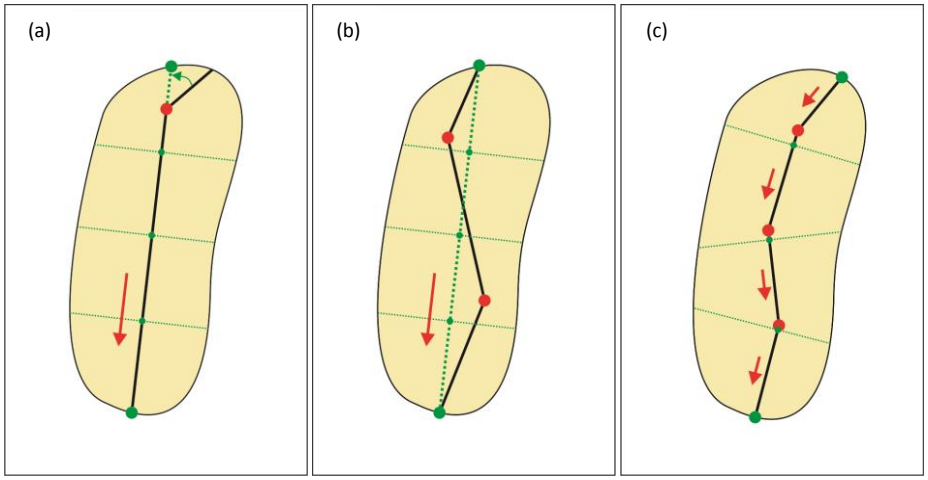

Fig. 2.15a-c. Examples for 1, 2 and 3 knickpoints and the handling of bending straight, drawing a point-to-point line and segmentation.

The entries would respectively appear in the survey chart as follows:

e.g.	1 (bent straight)	for Fig. 2.15a
e.g.	2 (point-to-point line)	for Fig. 2.15b
e.g.	3 (segmented)	for Fig. 2.15c

It should be noted that such transpositions facilitate the geometrical evaluation of LCS, but also introduce an error. However, transpositions are judged individually and they are only made when the error is expected to be almost insignificant.
A special case is the Stewart Landslide (009.01). Its LCS does not contain knickpoints but it is composed of three different parts located with a parallel offset. It is exceptionally marked with "3 separate parts", but since the average direction of those three parts diverts by more than 20° from the main sliding direction of the landslide, the LCS could not be exploited in any case.
If a LCS does not contain knickpoints the box contains "n".

b) Another factor of difficulty during LCS evaluation is axis exaggeration. This refers to vertical axis (here called Z-axis) where exaggeration is measured in relation to the horizontal axis (here called X-axis).

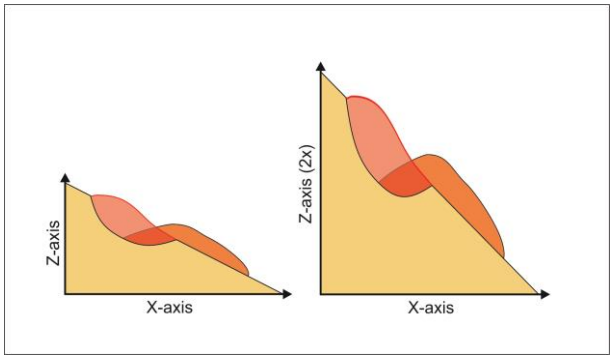

Fig. 2.16. Exaggeration of the vertical axis.

Indeed, exaggerated Z-axes might show more details of the underground structures inside a slope, but it also causes more error when evaluating geometrical parameters by analogue measuring. At positions 0, 1, 2, 3 and E (cf. Fig. 3.3) depths have to be scaled back and for angle values tangent calculations are necessary (cf. Fig. 2.16).
Exaggerated LCS are marked with "unequal", whereas those without exaggeration show the note "same scale" in the box of XZ-scale.

c) Two LCS characteristics closely linked to each other are the definitions of the rupture zone and the pre-landslide surface; one requires the other for precise geometrical dimensioning.
Generally, only the dimension of the rupture zone (cf. shaded green areas in Fig. 2.17a-c) of a landslide is of interest for the database since it is the base entry for stability modeling. Hence, great attention has to be paid to its dimensions. Often this is not trivial because literature reports cases in different states. Landslides can be just in the course of leaving the rupture zone – a very common state for constantly slowly moving landslides featuring for instance "drunken trees", displaced fences or disrupted brickwork (cf. Fig. 2.17a). Single fast moving events may display a state where the landslide material is partially deposited inside and partially outside of the rupture zone (cf. Fig. 2.17b). For very steep topographies landslide material can even be deposited entirely outside of the rupture zone (cf. Fig. 2.17c). Also mixed states are possible.

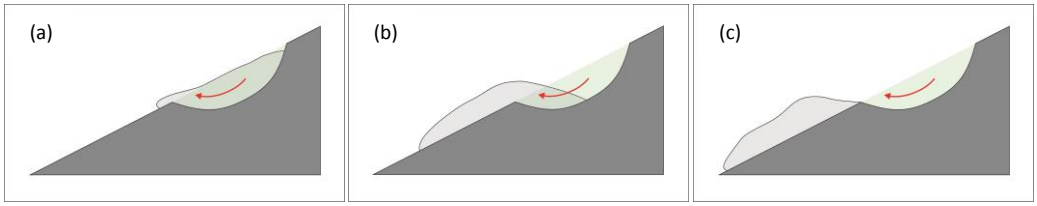

Fig. 2.17a-c. Different states of a landslide according to the deposit of the rupture mass.

If a rupture zone is properly defined, the next issue is the proper definition of its limits in terms of thickness. Therefore a LCS should indicate a pre-landslide ground surface (cf. Fig. 2.18a). For LCS displaying a clear rupture surface and a pre-landslide surface, geometrical parameters are taken with respect to the latter. In case of LCS showing a clear rupture surface and a post-landslide surface a line between positions 0 and E is drawn and geometrical parameters are taken with respect to this line, which is – as indicated under Slope Angle α (cf. 2.4.2.) – the average gradient of the slope above the rupture surface (cf. Fig. 2.18b). Throughout the entire database this straight is simply called "line". Assuming the original slope surface being a line of course introduces some error, but it seems to be a reasonable compromise between expected topography and a standardized procedure applicable to the concerned cases. To summarize, and if a rupture surface is clear, the following options are possible to appear in the boxes of rupture zone and pre-LS surface:

clear	surface	cf. Fig. 2.18a
clear	taken as line	cf. Fig. 2.18b
unclear	unclear	cf. Fig. 2.18c

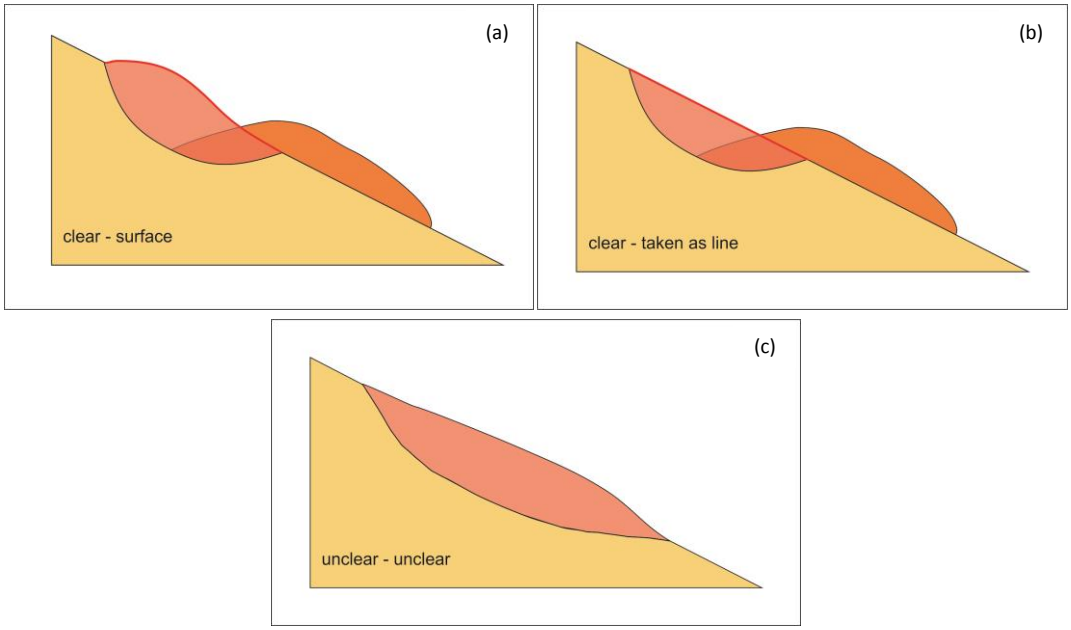

Fig. 2.18a-c. Examples for clear and unclear rupture zones and the assumptions for the ground surface.

Unfortunately literature sometimes contains LCS that do not indicate if they show the pre- or the post-landslide state (cf. Fig. 2.18c), i.e. the LCS can either show the rupture surface with its dimensions confined by a sliding surface and a pre-landslide ground surface, or the LCS displays the post-landslide state and the dimensions refer to the landslide deposit which is of no use for the database. The rupture zones and pre-landslide surfaces of those cases are marked thus as "unclear" (cf. above).

d) The last point in the LCS characteristics list is a rather technical indication about its emplacement. Some articles clearly report the LCS location by a line on a map; in this case the LCS is not self-placed, the box contains "n" and the box of φ (cf. 2.4.1.) gives the deviation from the average sliding direction (cf. Fig. 2.11a).
Other articles display a LCS but without showing the emplacement on the corresponding map; in this case the LCS is self-placed, the box contains "yes" and the box of φ (cf. 2.4.1.) shows 0° because – for simplification and due to the lack of information – it is assumed

that the LCS is taken along the average sliding direction (cf. Fig. 2.10a). Also for articles without LCS the box of self-placed contains "yes" and φ is set to 0°.

Other Notes

Three boxes on the survey chart are kept free for additional notes. They are rather not standardized and might contain memoranda, mentionable facts, curiosities or "memory hook" for distinction and better characterization of single cases. Also assumptions and the employment of numerical codes for model generation are noted at this place. The latter is of great importance when geometries are retrieved from modeled LCS. If literature reports the use of FLAC a note is made – either "FLAC" or "FLAC 3D".
Some few standardized indications come along with cut off or incomplete maps and LCS in the following forms:

map cut off: adjusted manually to what seems logic	cf. a) and Fig. 2.19a
map cut off: no measurements possible	cf. b) and Fig. 2.19b
map cut off: end of frame	cf. c) and Fig. 2.19c
LCS cut off: adjusted manually to what seems logic	cf. d) and Fig. 2.20

a) With the help of Google Earth and/or with experience the dimension of the landslide on a map could be completed. Geometrical parameters are based on the new dimension.

b) Google Earth and/or experience do not help to complete the dimension of the landslide on a map. No geometrical parameters are retrieved.

c) The outline of the landslide is not fully shown on the map because the display window is too small. Under some rare and exceptional conditions the dimension of the landslide is defined by the end of the image frame.

d) With the help of Google Earth and/or with experience the dimension of the landslide on a LCS could be completed. Geometrical parameters are based on the new dimension.

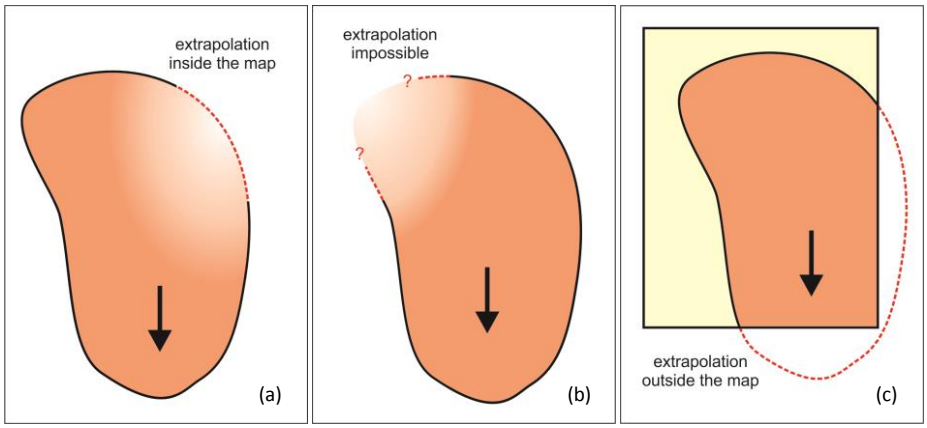

Fig. 2.19a-c. Examples for cut-off maps.

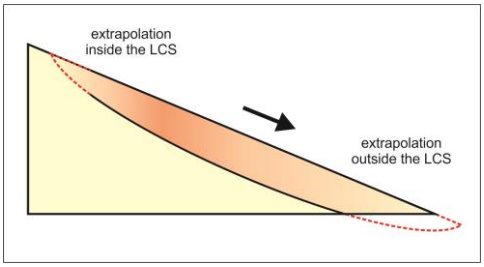

Fig. 2.20. Example for cut-off LCS.

Some seismically triggered landslides are post-seismic, meaning that the event happened with some time delay after the earthquake. If the time lag (cf. Time Lag - 2.4.1.) thus is "post", additional information on the time span is given in the form of:

e.g.	time lag: 30 minutes	for a single post-seismic event after 30 minutes
e.g.	time lag: during 1 year	for consequent activity over one year

It appears that some landslides are in relation with other events. Such options might be:

related event: 000.00 ([name]) on 00/00/0000
related event: EQ.000.00 ([name]) on 00/00/0000
related event: 000.00 ([name]) due to EQ.000.00 ([name]) on 00/00/0000

Respectively the three options have the following meanings: first, another mass movement happened at the location of the landslide on a certain date without the influence of seismic events; second, another earthquake shook the location of the landslide on a certain date either before or after the main landslide event, but without causing any other mass movements; third, another earthquake shook the location of the landslide on a certain date either before or after the main landslide event and caused another mass movement.

Related Papers

Usually a landslide is not only described once in literature; in most cases articles, book chapters, conference proceedings etc. can be found for the same landslide. In the course of the construction of the data base the so-called BIB-List (cf. 2.3.3.) was built which attributes the same number to all publications concerning the same landslide:

e.g.	004	Martino S.	et al.	2016	concerning 004.00 (Büyükçekmece)
e.g.	004	Bourdeau C.	et al.	2015	concerning 004.00 (Büyükçekmece)
e.g.	004	Dogan U.	et al.	2013	concerning 004.00 (Büyükçekmece)

It should be noted that the box of Related Papers lists not only literature related to the landslide itself, but also cites publications on related earthquakes or for example the region of interest. For instance, the survey chart of the Büyükçekmece Landslide (004.00) contains the three above listed entries of which the first two refer to the landslide itself and the third one to the concerned region.
Attention has to be paid at landslide series (cf. Landslide Number - 2.4.1.). Since in the BIB-List (cf. 2.3.3.) only the main number is attributed to publications, the box of Related Papers of series contains all concerned references:

e.g.	007	Djerbal L.	Melbouci B.	2012	all publications with the
e.g.	007	Guirous L.	et al.	2014	number 007 are listed in
e.g.	007	Djerbal L.	Bahar R.	2016	each survey chart of the
e.g.	007	Djerbal L.		2015	series (i.e. in 007.01,
e.g.	007	Bouaziz N.	Melbouci B.	2015	007.02, 007.03 and 007.04)

Also information on landslide imagery is based on all available publications (cf. BIB-List - 2.3.3.); the availability of related publications is indicated by the following notes:

digital	PDF-copy available, citation in the BIB-List
only part	PDF-copy of part available, citation in the BIB-List
only abstract	PDF-copy of abstract available, citation in the BIB-List
no paper	no PDF-copy available, citation in the BIB-List

Citations in survey charts have the following format:

e.g.	Laurel S., 1921	for 1 author
e.g.	Laurel S., Hardy O., 1921	for 2 authors
e.g.	Laurel S. et al., 1921	for more than 2 authors

2.4.2. Geometry Part (Page 2)

A first international nomenclature of landslide parameters was published by the IAEG (1990). It describes 19 distinct features and 7 dimensions of landslides and defines their characteristics. Since this database aims solely to collect geometries of rupture zones the following dimensions were of particular interest; their definitions are copied from the publication (IAEG, 1990):

(10) rupture surface	the projection of the main scarp surface under the displaced material of a landslide
(19) flank	the side of the landslide (Compass directions are preferable in describing the side but if left and right are used, they refer to the slide viewed from the crown.)
(L_r) length of rupture surface	the distance from the toe of the rupture surface to the crown
(W_r) width of rupture surface	the maximum width between the flanks of the landslide, perpendicular to the length L_r
(D_r) depth of rupture surface	the maximum depth of the rupture surface below the original ground surface measured perpendicular to the original ground surface

Based on this nomenclature a more detailed set of landslide parameters was elaborated; it contains more than 50 parameters that are listed in Tab. 3.2. An illustrating graphic is shown in Fig. 3.3.
A special case of landslide geometry derivation arises when a case is reported without LCS, and when at the same time the map indicates a landslide towards a water body. Even if the assumption might be not entirely true, the rupture zone of the landslide is then assumed to end where the water body starts. Concerned water bodies might be rivers, lakes, reservoirs or the sea.
The database is not designed to include underwater landslides because modeling software that will be used on a later stage does not cope with water submersion. Only two half subaqueous cases found their way to the database and thus are marked with “offshore”:

022.00	Degirmendere (offshore)
177.03	Finneidfjord (offshore)

It should be noted that both the Degirmendere Landslide and the Finneidfjord Landslide have LCS, so here the question of the dimension of the rupture zone does not arise.

Principal Geometry

The database distinguished only rotational, translational and roto-translational landslides and respectively notes “rot”, “trans” or “roto-trans” in the box of Principal Geometry (cf. Fig. 2.21). It should be noted that the type of principal geometry was preferably adopted from literature of a particular case. If no type is mentioned in literature, types were chosen according to what fits best. In case of indeterminable principal geometries the type was set to “roto-trans”. However attention has to be paid, since literature also reports roto-translational landslides and best-fit-assumptions might result in roto-translation as well; so “roto-trans” is not a term exclusively referring to indeterminable geometries.

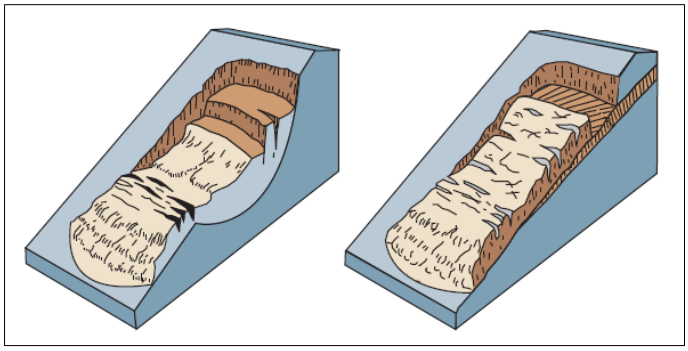

Fig. 2.21. Rotational (left) and translational (right) landslides (after USGS, 2004).

Volume

Volume reports of landslides are of great interest but not trivial. The first question when retrieving volume values from literature is the one of its type. Often literature indicates the deposit volume which is by far easier to determine after a landslide event. However the deposit volume is usually bigger than the rupture volume due to water entrainment and air inclusion in the deposit mass. The factor by which the deposit volume increases is called swell factor.
For the database only rupture volumes are of interest; according to CRUDEN & VARNES (1996) they can be approximated by calculating the volume of half an ellipsoid as shown below (cf. Fig. 2.22, 3.2.). For consistency it should be noted that also deposit volumes are to be approximated by this equation with respective greater parameters.

$$V_{half\ ell} = \frac{1}{2} \cdot \left(\frac{4}{3} \cdot \pi \cdot a \cdot b \cdot c \right) = \frac{1}{2} \cdot \left(\frac{4}{3} \cdot \pi \cdot \frac{L}{2} \cdot \frac{W}{2} \cdot D \right)$$

$$V = \frac{1}{6} \cdot \pi \cdot L \cdot D \cdot W$$

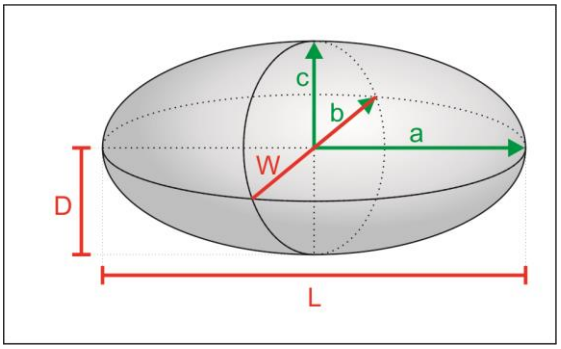

Fig. 2.22. Ellipsoid with geometric parameters.

Usually the equation presented by CRUDEN & VARNES (1996) fits best for perfectly rotational landslides with a very flat original surface topography. The more the rupture geometry deviates from this perfect half ellipsoid the more the equation overestimates the volume. Especially for shallow translational – sheet shaped – landslides the equation does not deliver trustable results. Thus, attention has to be paid when evaluating volumes and the equation should only be considered for rotational cases. A more recent approach to calculate volumes is presented by GUZETTI et al. (2009).
For comparison survey charts report two types of volumes:

according to literature	reported volume (tending to store mentioned maximum)
according to equation	calculated volume (as half ellipsoid)

Area

Area values of landslides can have two formats:

A	area of a landslide across the slope
A_h	area of a landslide in horizontal projection

If no area is given in literature, both area boxes will remain empty as A_h is calculated using the slope angle α (cf. 2.4.2.). Similarly to landslide volumes, also indications on area have to be recorded with care; literature might give the area of the rupture zone only or the entire area concerned by landslide activity which tends to be much larger.

Ratios

This section comprises three ratios commonly used in landslide science (cf. below). It should be noted that in the statistical analysis presented in section 3.3.3. a similar (but not identical) set of ratios is used: d_{av}/L, w_{av}/L_h, H_{0E}/L_h and d_{av}/w_{av}.

D/L	depth over length, cf. a)
w_{av}/L_h	width over length, cf. b)
H_{max}/L_h	height over length, cf. c)

a) The first ratio puts in relation the maximum depth D of a landslide and its length L across the slope. It is hence an indicator for the thickness of a landslide as the following example shows – the higher the ratio, the thicker it is:

e.g.	$D/L = 1/4 = 0.25$	thinner	(cf. Fig. 2.23a)
e.g.	$D/L = 2/4 = 0.5$	average	(cf. Fig. 2.23b)
e.g.	$D/L = 3/4 = 0.75$	thicker	(cf. Fig. 2.23c)

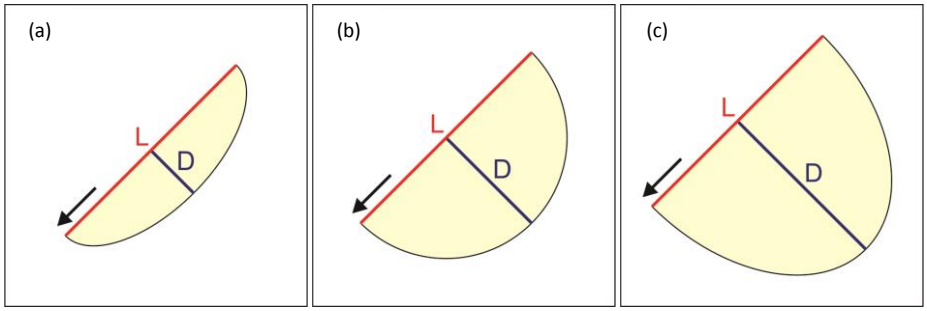

Fig. 2.23a-c. Depth-over-length ratio.

b) The second ratio puts in relation the average width w_{av} of a landslide and its length L_h projected to a horizontal plane. It is hence an indicator for the roundness of a landslide as the following example shows – the higher the ratio, the broader it is:

e.g.	$w_{av}/L_h = 2/4 = 0.5$	longer	(cf. Fig. 2.24a)
e.g.	$w_{av}/L_h = 2/2 = 1$	round	(cf. Fig. 2.24b)
e.g.	$w_{av}/L_h = 4/2 = 2$	broader	(cf. Fig. 2.24c)

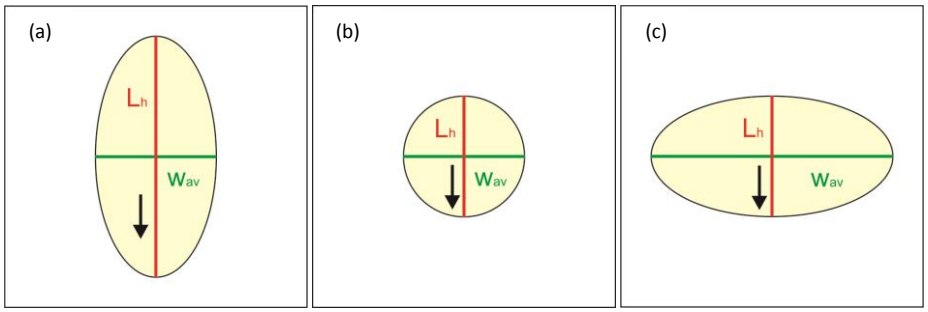

Fig. 2.24a-c. Width-over-length ratio.

c) The third ratio puts in relation the maximum height h_{max} of a landslide and its length L_h projected to a horizontal plane. It is hence an indicator for the steepness of a landslide as the following example shows – the higher the ratio, the steeper it is:

e.g. $h_{max}/L_h = 1/2 = 0.5$ flatter (cf. Fig. 2.25a)

e.g. $h_{max}/L_h = 2/2 = 1$ 45° (cf. Fig. 2.25b)

e.g. $h_{max}/L_h = 3/2 = 1.5$ steeper (cf. Fig. 2.25c)

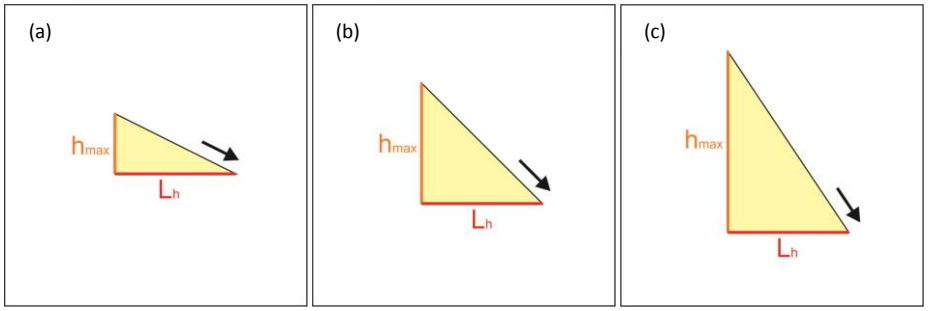

Fig. 2.25a-c. Height-over-length ratio.

Work on statistical patterns of L/W-ratios is presented by TAYLOR et al. (2015). The authors examined elliptical shapes of complete landslide inventories after the Northridge Earthquake on the 17th of January 1994 and after the Hurricane Mitch in 1998. It should be noted that here – as commonly in literature – the ratio reporting the relation of length and width is given by L/W, whereas in the present database it is inversely w_{av}/L_h.

Longitudinal Cross Section

The section named LCS comprises the parameters referring to lengths, depths, heights and angles to be measured from cross sections along the average sliding direction.

Length

Lengths values are:

L	length of a landslide across the slope (between positions 0 and E)
$l_1 = \ldots = l_4$	L divided into 4 equal parts

Depth

Depth values are:

D	maximum depth of a landslide
d_0	depth at position 0
d_1	depth at position 1
d_2	depth at position 2
d_3	depth at position 3
d_E	depth at position E, always set to 0
d_{av}	average depth of a landslide (average of the 5 main positions)

Depth Parts

Another section referring to depth values is the one showing depth parts. More precisely, the depth value at a certain position consists of two parts – the depth part below and above the line (cf. Fig. 3.3).
In order to reproduce accurate cross sections for modeling purposes it is important to know at least one part to calculate the complement and finally to generate proper depth plots. The depth value alone would not be enough, because it would remain unclear at what point the line intersects the depth vertical. Depth part values are:

$d_{0\text{-}ab}$	depth above the line at position 0, always set to 0
$d_{1\text{-}ab}$	depth above the line at position 1
$d_{2\text{-}ab}$	depth above the line at position 2
$d_{3\text{-}ab}$	depth above the line at position 3
$d_{E\text{-}ab}$	depth above the line at position E, always set to 0
$d_{0\text{-}bel}$	depth below the line at position 0
$d_{1\text{-}bel}$	depth below the line at position 1
$d_{2\text{-}bel}$	depth below the line at position 2
$d_{3\text{-}bel}$	depth below the line at position 3
$d_{E\text{-}bel}$	depth below the line at position E

A tool included in the survey charts is the automatic regeneration of LCS. This plot needs only L_h, H_{0E}, d_0, d_1, d_2, d_3, $d_{1\text{-}ab}$, $d_{2\text{-}ab}$, and $d_{3\text{-}ab}$ to be inserted; $d_{0\text{-}bel}$, $d_{1\text{-}bel}$, $d_{2\text{-}bel}$, $d_{3\text{-}bel}$ and $d_{E\text{-}bel}$ are calculated. Example values and the thereby created LCS are shown in Tab. 2.12. and Fig. 2/26.

example values		L_h	50
d_0	3	H_{0E}	25
d_1	10	$d_{1\text{-}ab}$	2
d_2	18	$d_{2\text{-}ab}$	4
d_3	8	$d_{3\text{-}ab}$	- 3

Tab. 2.12. Example values for Fig. 2.26.

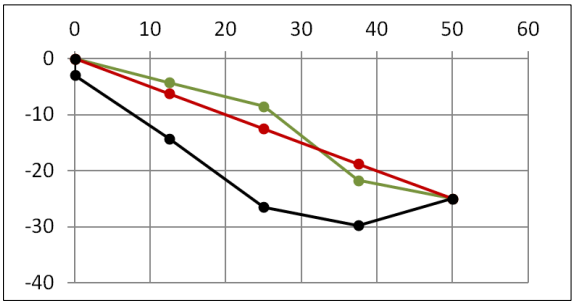

Fig. 2.26. Automatically regenerated LCS on a survey chart. Length and depth are in meters.

This example illustrates two special features. First, if d_0 is greater than 0, the landslide has not only a simple scar but a whole trough structure, which becomes visible only after the main landslide event. Second, if a depth part referring to an above segment of the depth vertical is negative, it means that the ground surface before the main landslide event passed under the line (cf. red and green dots in Fig. 2.26).
The advantage of this tool is to quickly verify manually measured parameters by comparing the hereby generated LCS to the LCS given in literature. If shapes do not fit, a parameter might not be properly retrieved what on a later stage of modeling would cause problems.

Height

The database stores two types of heights:

H_{0E}	height of a landslide (between positions 0 and E)
H_{max}	maximum height of a landslide

Especially rotational and roto-translational landslides often have rupture surfaces that curve up before reaching the position E (cf. Fig. 3.3) H_{max} then gives the greatest height difference a landslide can have. In case rupture surfaces do not curve up H_{max} equals H_{0E}. In general, H_{0E} can never be bigger than H_{max} (i.e. $H_{0E} \leq H_{max}$).
For some landslides literature only gives maps. In those cases exact height information is difficult to be retrieved; H_{0E} was then taken as height difference between positions 0 and E from Google Earth or – if applicable – by interpolating contour lines on the map. Because no depth information is available in those cases, H_{max} was also set to H_{0E}. Surely this latter assumption might not be fully true in every case – especially for deep rotational landslides –, but generally H_{max} is of lower importance for statistical evaluation.

Slope Angle α

For comparison the database includes two values for the slope angle:

according to literature	slope angle cited in literature (averaged if several values)
according to equation	calculated slope angle

One of the most important entries in the database is the calculated slope angle α. It is obtained by the first of the following equations. For length and area projections from or to the horizontal plane α is crucial as the second of the following equations shows.

$$\alpha = \tan^{-1}\left(\frac{H_{0E}}{L_h}\right) \qquad \cos(\alpha) = \frac{L_h}{L} = \frac{A_h}{A}$$

To avoid confusion, it should be noted that projections for length and area are made contrariwise; the reason is simply the fact that literature more often reports an effective area across the slope whereas lengths are more suitable to measure from maps:

L_h projects with α to L
A projects with α to A_h

As mentioned in LCS (cf. 2.4.1.), the straight line between positions 0 and E is simply called “line” throughout the database (cf. red line in Fig. 2.26).

Angles along Rupture Surface

At each of the five main positions the angle between a tangent plane and the horizontal is measured in the direction of sliding. This leads to positive and negative values of which the latter indicates an "up curving" rupture surface (cf. Fig. 2.27). Angles along the rupture surface are:

δ_0	angle at position 0
δ_1	angle at position 1
δ_2	angle at position 2
δ_3	angle at position 3
δ_E	angle at position E

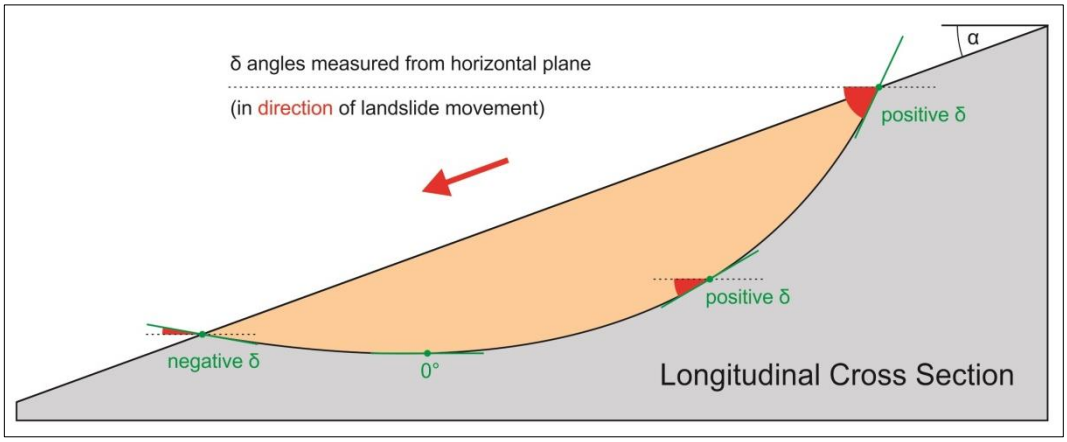

Fig. 2.27. Definition of angles along the rupture surface.

Initially, an idea was to use the angles along the rupture surface to regenerate LCS (cf. Fig. 2.26). However, it quickly became apparent that manual alignment with an angle meter can introduce a great error, especially when the vertical axis is exaggerated (cf. Fig. 2.16) and angles have to be calculated via trigonometry. It appears thus that the depths at positions 0, 1, 2, 3 and E are much more stable for regenerating LCS, even if values have to be deskewed.

Map

The section named Map only comprises the parameters referring to widths and lengths projected to a horizontal plane. Especially the latter is of great importance since it defines together with H_{0E} (the height between positions 0 and E) the slope angle α.

Length

Lengths values are:

L_h	length of a landslide in horizontal projection (between positions 0 and E)
$l_{h1} = \ldots = l_{h4}$	L_h divided into 4 equal parts

Width

Width values are:

W	maximum width of a landslide
w_0	width at position 0
w_1	width at position 1
w_2	width at position 2

w_3	width at position 3
w_E	width at position E
w_{av}	average width of a landslide (average of the 5 main positions)

Transversal Cross Section I, II & III

The sections named TCS I, II & III comprise the parameters referring to depths and angles to be measured from cross sections perpendicular to the average sliding direction. Ideally TCS I, TCS II and TCS III display cross sections at positions 1, 2 and 3 respectively (cf. Fig. 3.3). However, it should be noted that given TCS almost never correspond exactly to one of the positions 1, 2 or 3. TCS are thus assigned to the closest fitting position.
In general reported TCS are sparse, and in most of the reported landslide cases only a LCS is available. Throughout the whole database in only two cases one or more TCS appear:

004.00	Büyükçekmece Landslide
062.02	Okuli Landslide

Due to the low number of cases with TCS figure indications do not appear in a separate box similar to Assumption for Map (cf. 2.4.1.) or Assumption for LCS (cf. 2.4.1.), but they are noted under Other Notes (cf. 2.4.1.) in the format:

e.g. T1 for TCS I, T2 for TCS II and T3 for TCS III

Width

Width values are copied automatically from Map (cf. 2.4.2.):

w_1 / w_2 / w_3	widths at positions 1, 2 and 3

Depth

The box of Depth contains two types of values, of which the first one is automatically copied from LCS (cf. 2.4.2.):

d_1 / d_2 / d_3	depths at positions 1, 2 and 3
d_{1t} / d_{2t} / d_{3t}	centered depths at position 1, 2 and 3

As indicated in Fig. 3.3, a depth d is the depth that is retrieved from a LCS; it is the maximum depth under one of the three inner positions (1, 2 or 3) of a LCS. Naturally, due to the "imperfect" shape of a landslide, the position of d in a TCS does not necessarily coincide with the real centered depth d_t – the depth under the point that bisects w. For comparison, both d and d_t are noted in the survey chart.

Flank Angles

Flank angles refer to the right and left angles between an imaginary tangent plane touching the sliding surface and the horizontal as indicated in Fig. 2.28d. Attention has to be paid to the fact, that in the database "left and right" are defined by looking upwards to the landslide crest, whereas inversely the IAEG (1990) defines "left and right" by looking downwards to the landslide toe.

γ_{1L} / γ_{2L} / γ_{3L}	left flank angles at positions 1, 2 and 3
γ_{1R} / γ_{2R} / γ_{3R}	right flank angles at positions 1, 2 and 3

Rough Width Shape

Flank angles alone do not give sufficient information to outline a TCS and rough width shapes are obligatory to complete this lack of information. This circumstance becomes apparent when comparing Fig. 2.28a and Fig. 2.28c. Flank angles on both sides are very similar (around 140°), but thereby defined shapes can range from wedges to shallow tubs. The boxes of Rough Width Shape give a shape estimation according to how the TCS appears in literature. Four main shape types are distinguished:

V	TCS with a wedge shape	(cf. Fig. 2.28a)
[	TCS with a rectangle shape	(cf. Fig. 2.28b)
(	TCS with a shallow tub shape	(cf. Fig. 2.28c)
U	TCS with a deep tub shape	(cf. Fig. 2.28d)

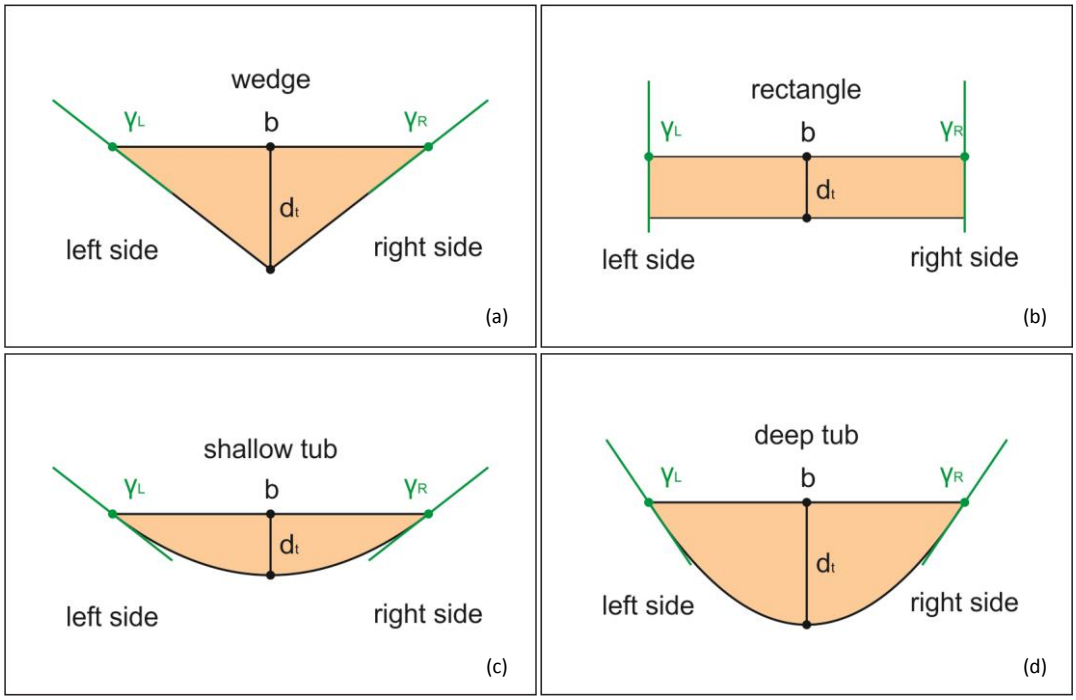

Fig. 2.28a-d. TCS shapes: wedge, rectangle, shallow tub and deep tub.

2.5. Microsoft Access

2.5.1. Creation and Purpose of the Access Database

Most of the data is stored in Excel-files. However, this approach proved to be insufficient in terms of maintenance and processing. On the one hand, the big number of information and relations between data is a source of potential mistakes and data inconsistency. On the other hand, Microsoft Excel does not have a built-in controlling tool for data insertion and updating at multiple places, and thus learning from relations is extremely difficult. Also, sophisticated filtering is laborious in Microsoft Excel; it is not easy to answer questions as for example: How many seismically triggered landslides are translational and consist only of soil and rock?
Software dedicated to the class of problems being considered are relational databases using SQL (Structured Query Language) to compute, filter and retrieve data from the database. The previously stated question can be quickly answered with a simple query in SQL.

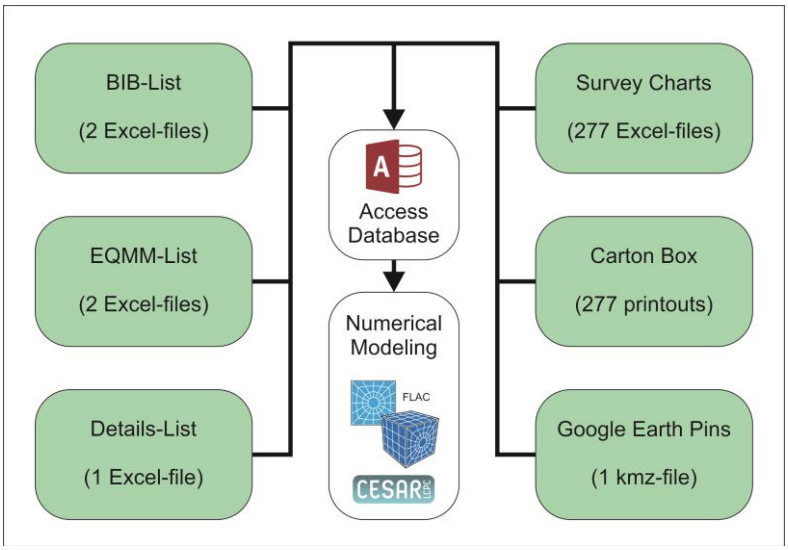

Fig. 2.29. Role of Microsoft-Access for handling the database
(after ITECH, IFSTTAR, 2016; after ITASCA, 2016; after WIKIPEDIA, 2016e).

For this database project Microsoft Access was chosen. It provides many tools that are broadly useable also for non-database specialists, of which the two most important are: the query builder (providing a graphical user interface to define queries without SQL) and the reporting module (defining reports based on SQL queries).
Another reason for the choice of Microsoft Access is the fact that all established data existed in Microsoft Excel, and import to Microsoft Access using VBA (Visual Basic for Applications) was much easier than to other types of software.
The aim of the database in Microsoft Access is to enable statistical analysis of parameters and relations. It is possible to quickly filter datasets to create data for numerical modeling, or – if necessary – to re-filter datasets to update or modify models. In Microsoft Excel it would take much more time to sort columns to create input data and the probability of making mistakes is high.

2.5.2. Easy Statistics

The so-called "easy statistics" shows some simple filter applications; at the same time those filtered output values illustrate a few basic characteristics of the database. More complex queries are presented in the next chapter (cf. 3.). For consistency it should be noted that the following statistical charts do not have own numbers. One particular statistical application – the comparison of data to the work of KEEFER (1984) – is presented in the next section (cf. 2.5.3., 3.3.1.).

Main sliding mechanism

The database distinguishes rotational, translational and roto-translational landslides; each of them accounts for around one third.

102	rotational
87	translational
88	roto-translational

277	

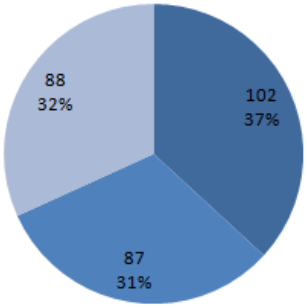

Landslide material

The involved material is classified in groups according to VARNES (1958): soil, rock, debris, or a combination. It appears that more than half of all cases consist or involve soil, what is typical for "classic" landslides.

78	soil
37	rock
1	debris
43	soil and rock
33	soil and debris
68	rock and debris
17	soil, rock and debris

277	

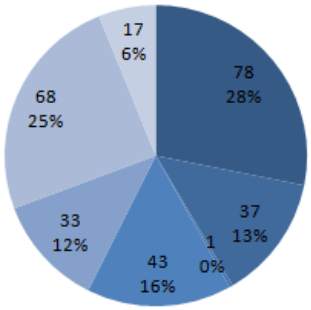

Availability of maps

Throughout literature, the availability of maps showing the respective landslide is high. Almost 80% of all evaluated cases dispose of a map, of which some miss out a part of the landslide.

206	available
10	map cut off
61	not available

277	

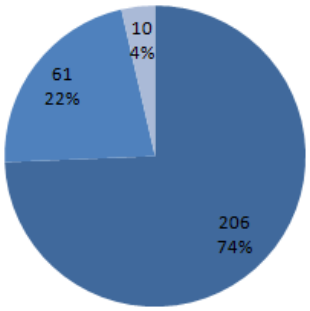

Availability of LCS

Throughout literature, the availability of LCS is also high. Around 70% of all evaluated cases dispose of a LCS, of which some are not placed along the main sliding direction or miss out a part of the landslide.

179	available
015	LCS cut off
075	not available
008	LCS with φ > 20°

277	

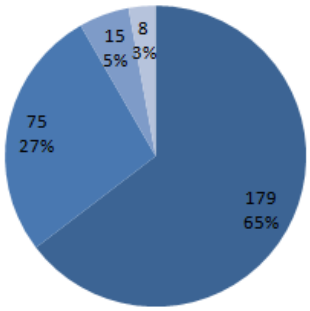

Outline of rupture zone

An important fact when evaluating LCS is the clear outline of the landslide mass. Of all cases with LCS, 95% have a clear outline; the remaining 5% were not to be used for geometric evaluation.

137	clear, surface shown
47	clear, taken as line
10	unclear

194	

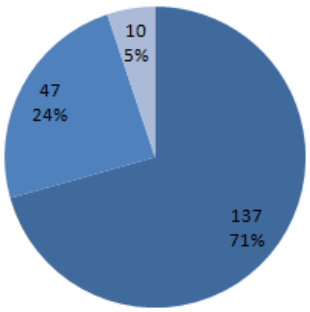

φ

In 70% of the cases the LCS is placed along the main sliding direction or with an angular deviation smaller than 20° from it. The cases with a deviation of more than 20° were not to be used for geometric evaluation.

161	φ = 0°
75	φ = 0° (no LCS)
33	φ < 20° (cf. chart below)
8	φ > 20° (cf. chart below)

277	

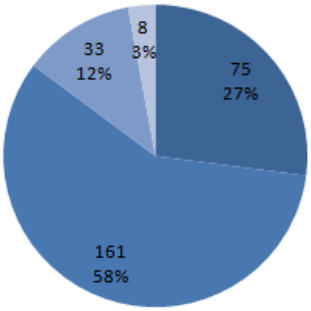

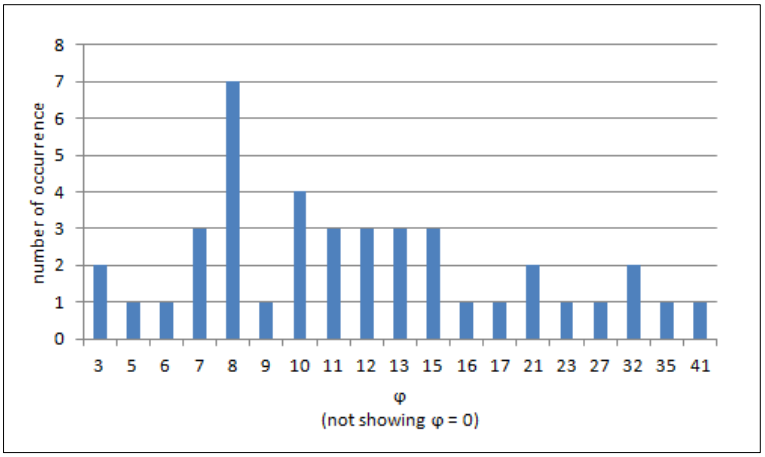

Occurrences of angular deviations (φ) from the main sliding direction in degrees.

2.5.3. KEEFER's Curves

Based on a set of 40 seismically triggered mass movements, KEEFER (1984) published the relation of magnitudes and the maximum distances at which the mass movements occurred. More precisely, he divided the mass movements into three groups and drew for every group an enveloping curve over the concerned set of scattered points (cf. Fig. 2.30):

disrupted slides and falls	→	black curve	
coherent slides	→	red curve	(only curve shown in Fig. 3.4)
lateral spreads and flows	→	blue curve	

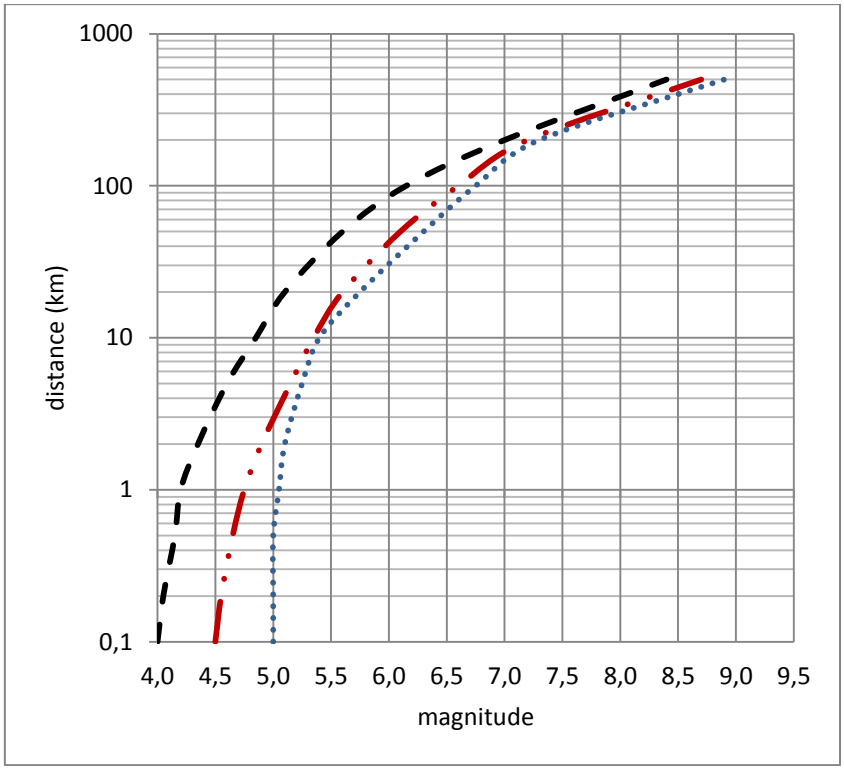

Fig. 2.30. Digitized KEEFER's (1984) curves.

A simple but interesting question was, if the seismically triggered landslides included in the database fit to the relation proposed by KEEFER. To answer this question an overlay of his curves and points computed from the database was plotted. The procedure was not straightforward and is explained in detail in the following.

As first step, KEEFER's curves had to be digitized since so far they are only available as figure in the publication of 1984. For this purpose the summarizing figure (Fig. 2D in KEEFER, 1984) was simply magnified to size A4 and the curves were traced manually reading the magnitude (with an accuracy of 0.05) for each distance step. Even though the first axis (magnitudes) shows more steps, readings were taken from the second axis (distances) because of the latter being logarithmic and hence more difficult to scale manually. Plots were realized in Excel.
KEEFER's (1984) plot shows 40 points which refer to earthquakes of different magnitudes as the following footnote (KEEFER, 1984) states:

> *"With a few exceptions noted in Tab. 1, M < 7.5 are Richter surface-wave magnitudes (M_S), and M ≥ 7.5 are moment magnitudes (M_W) of KANAMORI (1977)." (p. 407)*

On the one hand it is surely not ideal to use two different types of magnitudes within the same plot. On the other hand however, M_S saturates at high values and very big earthquakes are rather to be covered by using M_W.
In order to plot the database cases into KEEFER's (1984) diagram the issue of sorting was of great importance. Magnitudes throughout the database show all kinds of magnitude types, whereas KEEFER (1984) only used M_S and M_W. It became hence essential to know for each earthquake at least one of those two magnitude types.
Transforming magnitudes by using equations is tricky because they are empirical and bond to a distinct region of the world. An example might be the equation of TOBYÁS & MITTAG (1991):

$$M_S = -3.2 + 1.45 \cdot M_L$$

Since there is no globally applicable equation for transforming M_S and M_W into each other, the solution was to check each earthquake separately in seismological catalogs that provide different reviewed magnitude types per earthquake.
In total the database contains 99 seismically triggered landslides, of which 74 surely have an earthquake or volcanic activity as trigger. For those 72 surely seismically triggered landslides M_S and M_W (and if possible body wave magnitudes m_B) were retrieved from the below listed catalogs and sub-sources.

ISC Bulletin (International Seismological Center)
↳ NEIC (National Earthquake Information Center)
↳ ISC (International Seismological Centre)
↳ HRVD (Harvard University)
↳ MOS (Geophysical Survey of the Russian Academy of Sciences)
↳ ABE1 (unknown source)
↳ DENG (unknown source)
↳ P&S (printed publications)

AHEAD (European Archive of Historical Earthquake Data)

WikipediA (for 4 exceptional cases nowhere else listed)
↳ EQ.038.01 Armenian 1679 (WIKIPEDIA, 2016f)
↳ EQ.100.00 Kangding-Luding (WIKIPEDIA, 2016g)
↳ EQ.140.01 New Madrid Seq. 1 (WIKIPEDIA, 2016h)
↳ EQ.140.02 New Madrid Seq. 1 (WIKIPEDIA, 2016h)

Finally, after a systematic search in the ISC Bulletin and the AHEAD catalog, and after completing the dataset with information from other sources, earthquakes of the following magnitude types were found. The dataset is shown in the appendix (cf. A.2.).

29 earthquakes	of	M_W	triggered	62 landslides
4 earthquakes	of	M_S	triggered	8 landslides
1 earthquake	of	M_{ukn}	triggered	2 landslides
34 earthquakes				72 landslides

It appeared that the majority of earthquakes is reported with M_W and as a matter of consistency no further sorting was done. The main reason for this decision was the fact that M_W is directly based on the seismic moment M_0 – thus, on the released energy (HANKS & KANAMORI, 1979). Its advantage is that it does not need to account for the location of the rupture surface, wave types or the duration.

$$M_W = \frac{2}{3} \cdot log_{10}(M_0) - 6.07$$

As a result – and differently to KEEFER's (1984) sorting – the dataset contains:

62 landslides	triggered by an earthquake reported in	M_W	(dots)
8 landslides	triggered by an earthquake reported in	M_S	(triangles)
2 landslides	triggered by an earthquake reported in	M_{ukn}	(squares)
72 landslides			

Exact distance measurements require coordinates for every earthquake and landslide. Besides depth values (of the hypocenters), latitudes and longitudes of earthquake locations were retrieved in a similar way as magnitudes (cf. below). Landslide locations were known already (cf. Location - 2.4.1., Location (Google Earth) - 2.4.1.).

ISC Bulletin (International Seismological Center)

AHEAD (European Archive of Historical Earthquake Data)

WikipediA (for 2 exceptional cases nowhere else listed)
↳ EQ.038.01 Armenian 1679 (WIKIPEDIA, 2016f)
↳ EQ.100.00 Kangding-Luding (WIKIPEDIA, 2016g)

Publication (for 2 exceptional cases nowhere else listed)
↳ EQ.140.01 Stewart (JIBSON & KEEFER, 1994)
↳ EQ.140.02 Campbell (JIBSON & KEEFER, 1994)

Unexpectedly MATLAB turned out to be the perfect tool for distance calculations. The command

```
[arclen,az] = distance(lat1,lon1,lat2,lon2,referenceEllipsoid('wgs84'))
```

computes the shortest distance across the Earth's surface between two points given in decimal degrees. The distance is given in meters, and many different reference ellipsoids are available. In this case the World Geodetic System 1984 (WGS 84) was selected; it is one of the most frequently used standard datums worldwide and also the datum of Google Earth where all landslides were marked.
KEEFER (1984) published two types of curves; one type relates to the epicenter, the other to the fault rupture zone.
For the present plot the epicenter diagram was chosen because depth values are only reported for earthquakes listed in the ISC Bulletin and entries of the 22 historical earthquakes do not show depths.

This assumption can be criticized because epicenter-landslide distances and hypocenter-landslide distances might vary significantly especially if the earthquake is deep or if the fault zone is large. However, only two of those earthquakes having a depth record appeared to be deep (cf. below) and all other earthquakes do not exceed the Mohorovičić Discontinuity, which is the border between the Earth's crust and mantle at on average 30 km.

EQ.074.00	El Salvador	82.9 km
EQ.161.00	Sanriku-Minami	71.2 km

The three points referring to the greatest distances are:

EQ.053.00 Cerda	$M_W = 5.2$	10.0 km (depth)
EQ.105.00 Kherrata	$M_W = 5.9$	9.6 km (depth)
EQ.118.02 Lisbon 1755	$M_W = 8.5$	unknown (depth)

Interestingly all three of them have an offshore epicenter, and the first two are rather shallow. In general the plots seem to overlap well and the scatter is similarly wide (cf. 3.3.1.).

2.6. Drawbacks

Naturally the creation of an entire database brings along a multitude of difficulties. Simply by imposing a highly standardized system on the very variable natural phenomenon of landsliding many uncertainties arise. At some point, hence, one has to remain in accord with the fact that, first, even the most detailed descriptive system (such as a database) or the best elaborated numerical model will never show the true characteristics of a natural phenomenon, and second, that assumptions and imprecisions cannot be avoided.
Many of those uncertainties, difficulties, assumptions and imprecisions are already discussed throughout the report in the respective sections. Examples might be for instance the mass movement classification and nomenclature or the quality and completeness of a documented case. At this, it is very obvious that judgments might be subjective to some extent since it is impossible to visit every landslide site and it is thus necessary to rely on information offered by available literature.
Another issue is the manual measurements of dimensions on maps and cross sections. Clearly, every map and cross section contains already an error because it will never be possible for authors to produce images of a concerned site that are representative for 100%. By taking manual measures from printouts another bias will be added and – as a result – it should be kept in mind that numerical models created after statistical analysis of dimensions remain in any case conceptual.

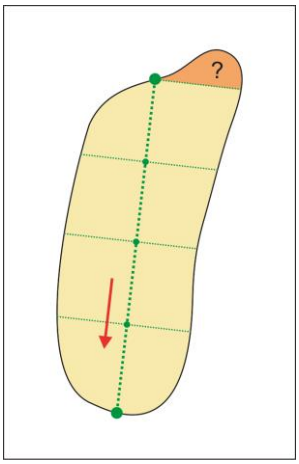

Fig. 2.31. Shape error.

Also, procedure standardization may lead to the creation of bias. An example might be the evaluation of geometric parameters (cf. Fig. 3.3). By definition the length L_h is taken along the main sliding direction and positions 0-E then are obtained by dividing L_h by four. If the landslide has a very elliptical shape the concerned area A_h is very easy to approximate; whereas, if the landslide has an unusual shape – such as in Fig. 2.31 – the area approximation will be rather incorrect.

A general drawback might be the selection of literature. During the "explosion-like" literature research focus was mainly on English publications, what – of course – does not imply that literature in other languages may have less quality. Russian publications on landslides, for instance, have very good quality. However, English publications are by far more accessible and (also due to my own laziness) much of non-English literature was left aside. One also could question the choice of publication sources. It is very much legitimate to criticize the completeness of the literature collection and, linked to that, worldwide case distribution. The drawback here is simply that not every high standard journal is accessible – for instance one needs to purchase articles of the Canadian Geotechnical Journal whose case studies are usually of excellent quality and completeness.

Certainly many more points of criticism can be found by delving into the database; thus no claims for perfection are raised and comments, discussions as well as suggestions for improvements will be always welcome.

CHAPTER 3
STATISTICAL ANALYSES OF THE DATABASE

3.1. Introduction

The aim of this chapter is to describe the statistical analyses that were carried out using data from the database (cf. 2.). As the chapter will show, one particular approach of evaluation was followed which of course does not claim to be the only proper procedure. Doubtlessly, many more aspects could be investigated and for this purpose the previous chapter describes the database in much more detail so that in future one can make use of it.
In this chapter the emphasis is, however, on the adopted approach of evaluation, whereas the description of the database – although present – takes up less space. This is due to several circumstances and considerations:
First, the statistical analysis was published as such in the form of a scientific article in the Italian Journal of Engineering Geology and the Environment and two posters at the General Assembly of the European Geoscience Union (DOMEJ et al., 2017; DOMEJ et al., 2018):

DOMEJ G., BOURDEAU C., LENTI L., MARTINO S. & PLUTA K.
Mean landslide geometries inferred from a global database of
earthquake- and non-earthquake-triggered landslides.
Italian Journal of Engineering Geology and the Environment, vol. 17/2, p. 87-107
DOI: 10.4408/IJEGE.2017-02.O-05

To allow for an easy and coherent reading flow in logic order it seems more suitable not to disassemble the article structure. Thus, the chapter is a one-to-one copy of the article starting from the fourth paragraph of the introduction (cf. 3.1.1.). The remaining parts of the article such as the abstract, the Italian extended abstract and the first three paragraphs of the introduction are to be found in a modified form in the first chapter of this thesis (cf. 1.).
Second, this chapter is also supposed to serve as a stand-alone short version of the previous chapter. It should explain to the reader only relevant contents and properties of the database without getting lost in unnecessary details that do not concern the applied statistical procedures.
However, by keeping a one-to-one copy, some overlaps cannot be avoided. General aspects of the database (cf. 2.3., 2.4., 2.5.2.) reappear in subsection 3.2. and the outcome of the data comparison to KEEFER's (1984; cf. 2.5.3.) magnitude-distance-relations of earthquakes and landslides are discussed in subsection 3.3.1. as first statistical analysis. To economize space and with the aim of a better reading flow of this chapter Fig. 3.1, Fig. 3.3 and Fig. 3.4 were moved from the previous to this chapter; in contrast to other chapters of this thesis there are no cross references in the text body.

3.1.1. Introductory Part of the Article

To establish correlations between mass movement features and the characteristics of their causes scientists established databases. The first and most cited of its kind is a set of 40 seismically triggered landslides presented by KEEFER in 1984. He empirically related magnitudes of earthquakes to the maximum distance at which the respective mass movements occurred; similarly, he also correlated area affected by mass movement events to the respective magnitude of the earthquake. In 1999 RODRÍGUEZ et al. published an extension of this work. Other studies associate landslide volumes with moment magnitudes M_W and seismic moments M_0 (KEEFER, 1994; MARTINO et al., 2014) or with the affected area (GUZZETTI et al., 2009). In contrast to global catalogs, event-based databases often try to relate landslide volumes to a variety of parameters. For instance, XU et al. (2016) estimate the total volume of all landslides triggered by the Sichuan Earthquake by evaluating six distinct landslide parameters and the peak ground acceleration.
Sharing the aim of data creation for comparative statistical analyses and numerical modeling of seismically triggered landslides to shed light on the causes of such events a new global landslide database was built. This chapter presents in the first part the database itself; properties, the way

of construction, advantages and some drawbacks will be discussed. The second part shows the statistical analyses that were carried out using the database and it presents nine mean landslide geometries inferred from the database.
These simplified landslide geometries will be useful for later studies to predict slope stability considering mechanical and geometrical properties as well as the properties of the potential seismic event. The contributions of trapped seismic waves to the displacement of the landslide mass can then be numerically modeled by different approaches in 2D and 3D.

3.2. Construction and Properties of the Database

Usually two types of databases for mass movements are to be distinguished – event-based and chronological databases. The first type ideally represents a complete inventory of mass movements after a certain triggering event such as intense rainfall, severe storms (like hurricanes and typhoons) or earthquakes. The second type inventorizes mass movements characterized by more than one trigger chronologically according to their occurrences. For both types completeness is a crucial factor because statistical analyses of event-based databases in particular might lead to false conclusions when dealing with incomplete or inaccurately assessed datasets (MALAMUD et al., 2004).
The database presented in this chapter is of chronological nature and also does not claim completeness. It contains a set of globally distributed mass movements with different triggers of which a third are earthquakes. It should be noted that the term "landslide" is wide-spread throughout literature designing rock falls, rock avalanches, debris flows, toppling and different types of slope failure. The more general term "mass movement" also includes soil settlements and liquefaction. This database focuses on proper "sliding" mechanisms according to the classification of VARNES (1978). Unfortunately, because of different scientific viewpoints and gradual transitions between mass movement types (cf. Fig. 3.1), landslide classification is not always trivial and hence might be misleading as it will be discussed in the following.

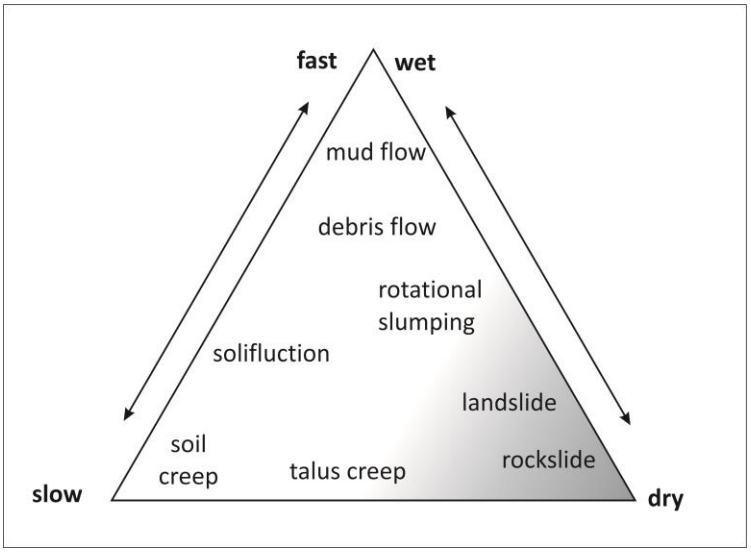

Fig. 3.1. Mass movement triangle (after CARSON & KIRKBY, 1972). The focus of the here presented database is on the shaded area referring to proper sliding mechanisms.

For the construction of the database, documented landslide cases in the available literature were evaluated as suitable or the opposite when coming across them in no particular order and without pre-selection. At the present stage the database contains 277 landslides in 40 countries (cf. A.3., Tab. 3.1) – a sufficient number for relevant statistical analyses.

country	each
Italy	50
Canada	29
Belgium	27
China, USA	22
Chile, Spain	10
Switzerland	8
France, Kyrgyzstan	7
Algeria, Japan, New Zealand, Tajikistan, Turkey, Ukraine	6
Austria, Norway, Taiwan	5
Czech Republic, Slovakia	4
Iran, Peru	3
Australia, Croatia, Poland	2
Armenia, Barbados, Bhutan, Cape Verde, Ecuador, El Salvador, Germany, Liechtenstein, Mongolia, Pakistan, Panama, Russia, Slovenia, United Kingdom	1
total	277

Tab. 3.1. Landslide distribution per modern-day country displaying also the availability of landslide data in different regions.

The main concept of data collection followed the suggestions by the INTERNATIONAL GEOTECHNICAL SOCIETIES' UNESCO WORKING PARTY ON WORLD LANDSLIDE INVENTORY (1990, 1991, 1993, 1994; cited as UNESCO) and the INTERNATIONAL UNION OF GEOLOGICAL SCIENCES WORKING GROUP ON LANDSLIDES (1995; cited as UNESCO) that indicate how to establish landslide reports and summaries and how the activity, the rate of movement and the causes of a landslides should be described. Based on these suggestions a "survey chart" with many more landslide characteristics was developed. As example, the survey chart of the Diezma Landslide is presented in the appendix (cf. A.1.).

The first section on the front page is dedicated to the identification of a landslide listing basic information such as name, its number in the database, precise location and sliding direction, date, fatalities and damage if reported and the relation to a seismic trigger. In contrast to the detailed activity phases described by the INTERNATIONAL GEOTECHNICAL SOCIETIES' UNESCO WORKING PARTY ON WORLD LANDSLIDE INVENTORY (1993; cited as UNESCO), the database presented in this chapter distinguishes only between active/slow, active/fast (both together 153 cases; 55%) and inactive (124 cases; 45%) landslides. The subsection of involved material is based on the classification of VARNES (1978) appointing rock, soil and/or debris as the three materials of which a landslide mass may be composed. Locations are given with respect to geographical references and as coordinate points. 220 landslides (79%) are located in currently seismic areas across the globe, 50 landslides (18%) are to be found in rather less or non-seismic areas and 7 landslides (8%) are situated in areas that used to be seismically active but came to tectonic stability.

Second, the section of landslide imagery gives information on how well literature documents a landslide visually – i.e. if publications show a map, a longitudinal cross section (LCS), a three-dimensional model and/or photographs. An interesting finding becomes apparent through graphical representation of the availability of landslide imagery (cf. Fig. 3.2). By far not for all landslides literature offers maps and LCS even though both of them are of great importance for the characterization of a landslide. For instance, only 216 cases (80%) have a map, for 202 cases (71%) a LCS is available and only 168 landslides (61%) are described by both a map and a LCS. Considering that the selection of cases and respective literature did not follow any preference, this leaves the general question about the average level of completeness of publications.

The third section refers to landslide causes and indicates the triggers of a landslide or their combinations. Of the 277 landslides 99 (36%) have or may have been seismically induced; the uncertainty is explained by the fact that – compared to recent seismically induced landslides with a well-documented time-history – for certain paleo-landslides a seismic trigger can only be

assumed but not confirmed. Of those 99 landslides 74 (75%) definitely have a seismic cause. 85 landslides (86%) are co-seismic, 11 landslides (11%) are post-seismic, and in the remaining 3 cases (3%) the main rupture process occurs over a longer period of time. It should be mentioned that the database considers earthquakes, blasts (5 cases) and repeated strong volcanic activity (2 cases) as seismic activity.

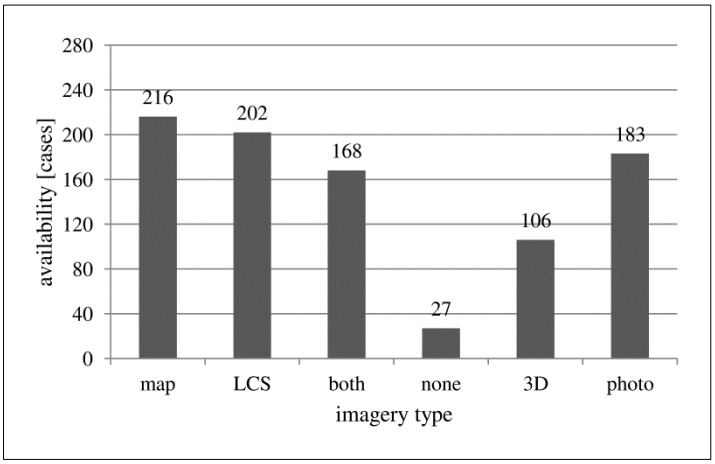

Fig. 3.2. Availability of landslide imagery in literature with respective numbers of cases (from left to right: map only, LCS only, map and LCS, neither map nor LCS, 3D representation, photography).

Finally, the fourth section lists all publications from which information was retrieved and introduced to the survey chart respecting the suggestion of the INTERNATIONAL GEOTECHNICAL SOCIETIES' UNESCO WORKING PARTY ON WORLD LANDSLIDE INVENTORY (1990; cited as UNESCO).

The back side of the survey chart is dedicated to the geometry of a particular landslide. Based on the suggested nomenclature for landslides proposed by the COMMISSION ON LANDSLIDES OF THE INTERNATIONAL ASSOCIATION OF ENGINEERING GEOLOGY (1990; cited as IAEG) a much more detailed set of parameters was elaborated which reports ideally – if literature is exhaustive enough – 66 single parameters and descriptive notes (cf. Fig. 3.3, Tab. 3.2) all referring to the rupture mass of a landslide, i.e. either the landslide mass confined by the rupture surface at the instance of the major sliding event, or the total moving mass in case of active landslides.

parameter	equation / note	description
principal geometry	rot, trans or rotrotrans	principal geometry type
V_{lit}		volume as by literature
V_{equ}	$= (1/6)\cdot\pi\cdot L\cdot D\cdot W$	volumes as by equation
A		area
A_h	$= A\cdot\cos(\alpha_{equ})$	area projected to horizontal
L	$= L_h/\cos(\alpha_{equ})$	length
L_h		length projected to horizontal
$l_1 = l_2 = l_3 = l_4$	$= L/4$	length parts
$l_{1h} = l_{2h} = l_{3h} = l_{4h}$	$= L_h/4$	length parts projected to horizontal
H_{max}		height between point 0 and deepest point
H_{0E}		height between point 0 and point E
W		maximum width
w_0		width at point 0
w_1		width at point 1
w_2		width at point 2
w_3		width at point 3
w_E		width at point E
w_{av}	$= (w_0+w_1+w_2+w_3+w_E)/5$	average width

D		maximum depth
d_0		depth at point 0 (if existing)
d_1		depth at point 1
d_2		depth at point 2
d_3		depth at point 3
d_E	always 0	depth at point E
d_{av}	$= (d_0+d_1+d_2+d_3+d_E)/5$	average depth
$d_{0\text{-}ab}$	always 0	depth part at point 0 (above line)
$d_{1\text{-}ab}$		depth part at point 1 (above line)
$d_{2\text{-}ab}$		depth part at point 2 (above line)
$d_{3\text{-}ab}$		depth part at point 3 (above line)
$d_{E\text{-}ab}$	always 0	depth part at point E (above line)
$d_{0\text{-}bel}$	$= d_0\text{-}d_{0\text{-}ab}$	depth part at point 0 (below line, if existing)
$d_{1\text{-}bel}$	$= d_1\text{-}d_{1\text{-}ab}$	depth part at point 1 (below line)
$d_{2\text{-}bel}$	$= d_2\text{-}d_{2\text{-}ab}$	depth part at point 2 (below line)
$d_{3\text{-}bel}$	$= d_3\text{-}d_{3\text{-}ab}$	depth part at point 3 (below line)
$d_{E\text{-}bel}$	$= d_E\text{-}d_{E\text{-}ab}$ = always 0	depth part at point E (below line)
δ_0		rupture surface inclination at point 0
δ_1		rupture surface inclination at point 1
δ_2		rupture surface inclination at point 2
δ_3		rupture surface inclination at point 3
δ_E		rupture surface inclination at point E
α_{lit} (literature)		mean slope angle as by literature
α_{equ} (equation)	$= \tan^{-1}(H_{0E}/L_h)$	mean slope angle as by equation
D/L (ratio)	= D/L	ratio “maximum depth / length”
w_{av}/L_h (ratio)	$= w_{av}/L_h$	ratio “average width / projected length”
H_{max}/L_h (ratio)	$= H_{max}/L_h$	ratio “maximum height / projected length”
d_{1t}, d_{2t}, d_{3t}		maximum depths of TCS I, II and III
γ_{1L}, γ_{2L}, γ_{3L}		left flank angles of TCS I, II and III
γ_{1R}, γ_{2R}, γ_{3R}		right flank angles of TCS I, II and III
rough width shape	to tick either V, (, [or U	rough width shapes of TCS I, II and III

Tab. 3.2. Full list of landslide geometry parameters. It should be noted that the survey chart cell of the principal geometry does not contain values but one out of three options to choose; for the rough width shapes one of four survey chart cells can be chosen. By definition, the content of the survey chart cells d_E, $d_{0\text{-}ab}$, $d_{E\text{-}ab}$, $d_{E\text{-}bel}$ are always 0. The “0” in the equation column and at indices of parameters is not to be confounded; one is a defined value, the other refers to the first of the five main geometry positions (Fig. 3.3).

The geometry section of the survey chart is separated into seven sections describing principal geometry, volume, area, LCS, map, transversal cross sections I-III (TCS I-III) and ratios. It also displays a small figure of the LCS according to the inserted respective values that served as a verification tool during the process of data assessment.
Distinction is made between rotational, translational and roto-translational landslides. This distinction becomes useful when calculating volumes of landslides. The volume of a landslide is an important parameter controlling its impact but it is also the most difficult to assess. In contrast to many landslide databases that report deposit volumes, for the database presented in this chapter only rupture volumes are of interest. According to CRUDEN & VARNES (1996) they can be approximated by calculating the volume of half an ellipsoid.

$$V = \left(\frac{1}{6}\right) \cdot \pi \cdot L \cdot D \cdot W$$

However, this equation fits best for perfectly rotational landslides with very flat original surface topographies. The more the rupture geometry deviates from this perfect half ellipsoid the more

the equation overestimates the volume and for translational and roto-translational landslides it might not deliver trustable results.

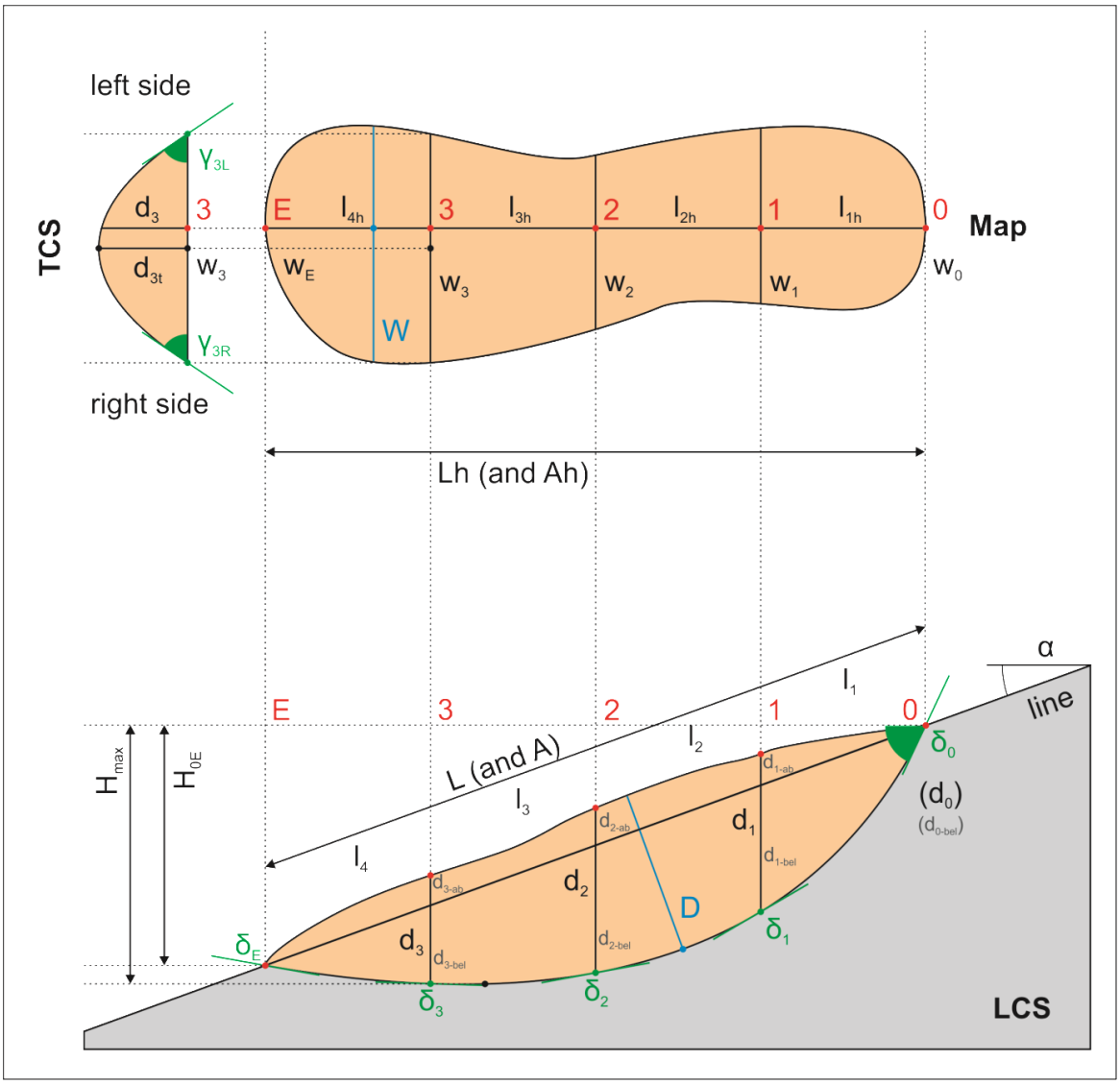

Fig. 3.3. Illustration of landslide geometry parameters in a plane view (map) and 2D cross sections (LCS & TCS). Abbreviations are described in Tab. 3.2. In contrast to the definition of "left and right" by the Commission on Landslides of the INTERNATIONAL ASSOCIATION OF ENGINEERING GEOLOGY (1990; cited as IAEG), the two sides are here defined by looking upwards to the landslide crest (i.e. from point E to point 0). The straight connection of the first main geometry point (0) and the last one (E) is simply entitled the "line"; with respect to the horizontal it defines the mean slope angle α. The two parameters d_0 and $d_{0\text{-bel}}$ are noted in brackets because they may or may not exist at a specific landslide since not every landslide mass detaches with a trench below point 0.

The volume section offers two cells: one cites the volume reported in literature, the other calculates the volume according to the equation proposed by CRUDEN & VARNES (1996).
Similarly, the section storing the area A of a landslide refers to the landslide area measured on the original topography before the sliding event. The horizontal projection A_h differs from A by the factor of the cosine of the mean slope angle α.
The section of the LCS is the most extensive and meaningful reporting lengths, depths, heights and angles along the average sliding direction with respect to the five main reference points 0, 1, 2, 3 and E (for "end"). Angles δ are measured between a tangent plane to the sliding surface and the horizontal in the direction of sliding; negative angles are possible when the sliding surface curves up (cf. Fig. 3.3).
The map section displays values measured from the horizontal projection of a landslide and the section of TCS I-III gives information on the lateral dimensions of a landslide. Ideally there would

be three clear TCS for every landslide indicating depths (d_{1t}, d_{2t} and d_{3t}) as well as the respective flank angles (γ_{1L}, γ_{1R}, γ_{2L}, γ_{2R}, γ_{3L} and γ_{3R}) to design a 3D enveloping confinement. Unfortunately TCS appear very seldom in literature and lateral shapes can only be assumed. For such assumptions the TCS section offers four cells where one of the following four shapes per TSC position can be chosen: "V" for V-shape, "(" for a flat concave shape, "[" for a drawer-like shape and "U" for a U-shape. Despite its great importance for assessing the behavior of a landslide mass under seismic shaking in 3D through numerical modeling this section is of less use since only 2 of 277 cases allow for complete TCS characterization.
The three proportions (D/L, wav/L_h and H_{max}/L_h) shown in the ratio sections serve for quick comparison of landslides. As analyses will show later, it seems though more suitable to use the rather uniform ratios d_{av}/L, w_{av}/L_h, d_{av}/w_{av} and H_{0E}/L_h as well as curvature values of landslides to compare their shapes.
To enable efficient and accurate data analyses, the complete content of the survey charts is stored in a Microsoft Access database. It allows for fast filtering and sorting to create data for statistical analyses.

3.3. Statistical Exploration of the Database

3.3.1. Magnitude-Distance-Relations comparing to KEEFER's Curve

Based on a set of 40 seismically induced landslides KEEFER (1984) related magnitudes of earthquakes to the maximum distances at which mass movements occurred. Distances relations are shown with respect to the epicenter and to the fault rupture zone locations separately. KEEFER (1984) distinguished disrupted falls and slides, coherent slides and lateral spreads and flows. To compare the data presented in this chapter to the proposed curves by KEEFER (1984) only the one of coherent slides was chosen as reference since it fits best the definition of landslides included in the here presented database.

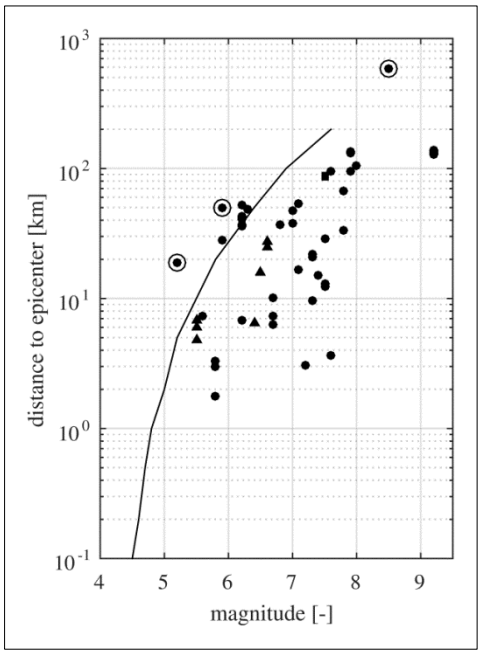

Fig. 3.4. Magnitude-distance relations of the 72 seismically induced landslides in the database caused by a specific earthquake. The curve represents the maximum distances from an epicenter at which coherent slides are to be expected according to KEEFER (1984) (dots for M_W, triangles for M_S, squares for M_{ukn}). Circled dots indicate the landslides of Laalam (M_W = 5.2), Cerda (M_W = 5.9) and Güevéjar (M_W = 8.5).

In total the database contains 99 seismically induced landslides of which 72 are proven to have an earthquake as trigger. For all of them either moment magnitudes (M_W) or surface wave magnitudes (M_S) were retrieved from the bulletin of the INTERNATIONAL SEISMOLOGICAL

CENTER (2016; cited as ISC) and the EUROPEAN ARCHIVE OF HISTORICAL EARTHQUAKE DATA (2016; cited as AHEAD). Indeed, it is not ideal to represent two types of magnitudes in the same graph, but since M_S saturates at higher values, big earthquakes are rather to be covered by using M_W. Also KEEFER (1984) used both magnitude types in his graphs. As a result, 62 landslides were triggered by an earthquake reported in M_W, 8 landslides were triggered by an earthquake reported in M_S and the remaining 2 landslides were triggered by an earthquake with unknown magnitude type (M_{ukn}; cf. Fig. 3.4).
Because there is no available information about the exact fault rupture location or the hypocenter for the 22 historical earthquakes among the set of 72, comparative magnitude-distance relations are limited to epicenter distances. Values refer to the length of the connecting line between the official epicenter and the landslide across the Earth's surface with respect to the World Geodetic System 1984 (WGS 84). It should be noted that epicenter-landslide distances might vary significantly from hypocenter-distances especially if the hypocenter is deep. However, only 2 of the 72 concerned earthquakes appear to be deep (El Salvador Earthquake on the 13th of January 2001, M_W = 7.6, 82.9 km; Sanriku-Minami Earthquake on the 26th of May 2003, M_W = 7.0, 71.2 km) whereas all other cases do not exceed the Mohorovičić Discontinuity.
In agreement to results of DELGADO et al. (2011), the scatter is big and some points reach the reference curve or even exceed it. Reasons might be topographic and/or lithological site effects, precipitation events and soil weakening earthquake swarms. Interestingly, two of the three points that lie highly above the curve are likewise described as outliers by DELGADO et al. (2011; cf. Tab. 3.3) and all three have an offshore epicenter.

date	earthquake	magnitude	landslide	distance
21st of March 2006	Kherrata	M_W = 5.2	Laalam	19 km
6th of September 2002	Cerda (or Palermo)	M_W = 5.9	Cerda	50 km
1st of November 1755	Lisbon 1755	M_W = 8.5	Güevéjar I	578 km

Tab. 3.3. The three seismically triggered landslides significantly exceeding the reference curve (Fig. 3.4).

3.3.2. Recurrence, Completeness and Distributions of Assessed Data

After completion of the data assessment raises the question about the data quality. Of particular interest are the recurrence of distinct parameters, the completeness of survey charts per dataset and the way values of parameters are distributed. The following sections describe each of the three qualitative and quantitative features separately.

Recurrence of Parameters

The recurrence of a distinct parameter refers to the question of how many times it is reported when comparing all 277 survey charts. For instance, in 165 cases literature reports the landslide volume, and hence the respective recurrence value amounts to 60%.
The second page of the survey chart contains in total 66 parameters. However, three of them – d_E, $d_{0\text{-}ab}$ and $d_{E\text{-}ab}$ – are always 0 by definition (cf. Tab. 3.2). Therefore the evaluation of parameter recurrence was carried out only for the other 63 parameters (cf. Tab. 3.4).
Among them there are direct and indirect – or calculated – parameters. The first type is reported directly from literature or measured from maps and cross sections, whereas the indirect parameters are those calculated by equations (cf. Tab. 3.2). Parameters of the second type thus create new values employing those of direct parameters under the condition that all necessary factors of the equation are available.
It is important to mention that: for the evaluation of the recurrence of parameters direct and indirect parameters were treated in the same way and no weighting was performed although one might argue that some parameters may be more suitable to describe landslides than others.
A special parameter is $d_{E\text{-}bel}$. It represents the only overlap between the group of indirect parameters and those that are always 0 since it is the difference between d_E and $d_{E\text{-}ab}$, both of

which are 0 by definition. To keep the number of exceptions low, $d_{E\text{-}bel}$ was nevertheless included in the set of 63 parameters. Its recurrence, though, is always 100%.

type	R < 5%	30 ≤ R < 70%	R ≥ 70%
direct parameters	d_{1t}, d_{2t}, d_{3t}, γ_{1L}, γ_{2L}, γ_{3L}, γ_{1R}, γ_{2R}, γ_{3R}, rough width shapes (12)	V_{lit}, A, α_{lit}	principal geometry (1), H_{max}, H_{0E}, L_h, W, w_0, w_1, w_2, w_3, w_E, D, d_0, d_1, d_2, d_3, $d_{1\text{-}ab}$, $d_{2\text{-}ab}$, $d_{3\text{-}ab}$, δ_0, δ_1, δ_2, δ_3, δ_E
indirect parameters		A_h	V_{equ}, α_{equ}, D/L, w_{av}/L_h, H_{max}/L_h, L, $l_{1\text{-}4}$, $l_{h1\text{-}h4}$, w_{av}, d_{av}, $d_{0\text{-}bel}$, $d_{1\text{-}bel}$, $d_{2\text{-}bel}$, $d_{3\text{-}bel}$, $d_{E\text{-}bel}$

Tab. 3.4. Recurrence (R) of the landslide parameters of page 2 of the survey chart (excluding d_E, $d_{0\text{-}ab}$ and $d_{E\text{-}ab}$ which are always 0 by definition).

Broadly speaking, it appears that direct and indirect parameters related to the delineation of maps and LCS reach higher percentages. The fact that they are reported more frequently throughout literature reflects also the way of investigation and analysis of landslides. For many engineering-geological purposes a map and a LCS are sufficient since 2D approaches remain the most widespread in slope stability assessment nowadays.
In contrast, TCS parameters are very rare and this evidence cannot be explained by impossible calculation because all TCS parameters are direct. Unfortunately, precisely those TCS features would be necessary for an exact definition of the 3D lateral confinement of a landslide mass and accurate stability analyses.
The indirect parameter with most complexly interlinked factors is the calculated volume V_{equ} (cf. 3.2.) including D, W, L_h and H_{0E}. Due to the requirement that all factors must be available to calculate such an indirect parameter, one might hence expect the respective recurrence to be very low. Strikingly, its recurrence amounts to 74% which is very satisfactory. The recurrence of V_{lit}, reaches only 60%. When comparing volumes at cases were both V_{equ} and V_{lit} exist, it appears that the ratios V_{lit}/V_{equ} oscillate well around 1 and hence no particular difference in order of magnitude can be detected between the two volume types.
Therefore, and because of its higher availability, V_{equ} is later used as a classification criterion for landslide magnitudes.

Completeness of Survey Charts

The completeness of a survey chart indicates the amount of available parameters. Likewise to the evaluation of the parameter recurrence, the reference number of parameters is 63 and an ideal case (where all parameters are available) would have a completeness of 100%.
Throughout the statistical analyses three datasets are defined of which two are in fact sub-sets:

- set “full” including all 277 landslides in the database
- set “SR” including all 220 landslides in seismic regions
- set “EQt” including all 99 landslides with a seismic trigger

The set “full” incorporates both the set “SR” and the set “EQt”, whereas the set “EQt” is only a part of the set “SR”. Especially for numerical modeling of landslides undergoing seismic shaking,

this separation is of particular importance allowing for comparison of the behavior of landslides in general, those being located in seismic regions and those having indeed a seismic trigger.
Figure 3.5 shows the completeness of survey charts for the three sets. It can be seen that within each set almost two thirds of the cases are complete to an extent of 50% to 70%. Also this result is very satisfactory since it testifies a high availability of parameters which in succession is required for the evaluation of the distributions of values of distinct parameters.

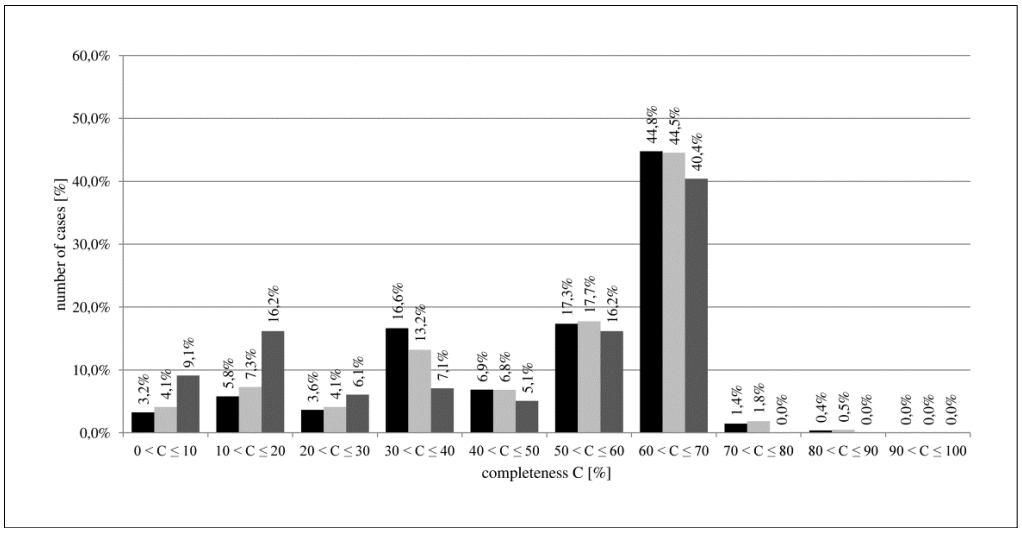

Fig. 3.5. Histograms showing the completeness (C) of the survey charts
(set "full" in black, set "SR" in light gray, set "EQt" in dark gray).

Combining the outcome of the evaluation of the parameter recurrence with the one of the survey chart completeness, it appears that a high completeness must be based on map- and LCS-related parameters. This reflects again the fact that obviously landslide studies are commonly limited to two dimensions, while full 3D representations which would allow for detailed 3D modeling are rather seldom.

Distributions of Parameters

Another major feature of parameters is their statistical behavior in terms of value distribution. Unlike mentioned in the above sections of recurrence and completeness of data, distributions can only be evaluated for 49 of the geometrical parameters appearing on the second page of the survey charts due to the fact that some parameters do not register values. The rubric of principal geometry stores a word and the rubric on rough width shapes of the TCS contain a checkbox. Moreover, the parameters always being 0 (d_E, $d_{0\text{-}ab}$, $d_{E\text{-}ab}$ as well as the above mentioned special case $d_{E\text{-}bel}$) are not included since their distributions would show only a zero line. For completeness, it is worth noting that the categories of the principal geometries are almost uniformly distributed within the database (32% rotational, 31% translational, 37% roto-translational).
Values for each individual parameter were grouped into histograms to fit different distribution curves on them in a second step. For all parameters histograms with 10, 30, 50 and 100 bins were computed, of which finally only the histograms with 30 bins were taken into consideration. It turned out that grouping to 10 bins results in a too coarse representation hindering accurate curve fitting, whereas 50 or 100 bins create a too detailed image making curve fitting difficult as well. By the means of the Curve Fitting Tool in MATLAB a normal, a power law and an exponential distribution were fitted to each set of values per parameter (cf. equations below). Best fits were chosen considering the coefficient of determination (R^2), the root mean square error (RMSE) and the best approximations of the coefficients a, b and c with 95% confidence bonds.

- normal distribution: $f(x) = a \cdot e^{-\left(\frac{x-b}{c}\right)^2}$
- power law distribution: $f(x) = a \cdot x^b$
- exponential distribution: $f(x) = a \cdot e^{b \cdot x}$

Applying this procedure to all 49 parameters for each of the three datasets ("full", "SR" and "EQt"), two types of statistical distributions emerge as suitable to characterize the histograms.
All values of dimension-related parameters manifest a clear decreasing exponential behavior, i.e. the histograms of 1D, 2D or 3D parameters show a progressively smaller number of occurrences with increasing parameter magnitude. This behavior is very common phenomenon in nature and comparable for example to the Gutenberg-Richter-Law relating the total number of earthquakes having a magnitude larger than a given magnitude in a given region and time period (GUTENBERG & RICHTER, 1956). The "exponential family" hence includes lengths, widths, depths (excluding the so-called "depth parts"), heights, surfaces and volumes (cf. Fig. 3.6c).

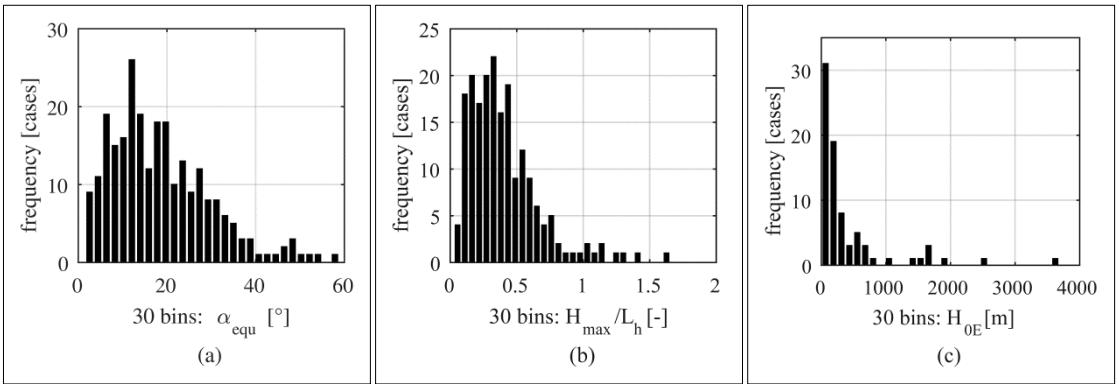

Fig. 3.6a-c. Examples of statistical distribution types. Histograms of angles as well as ratios were best fitted by normal distributions and are here exemplarily represented in a) by α_{equ} of the set "full" and in b) by H_{max}/L_h of the set "SR". Histograms of 1D, 2D and 3D parameters follow exponential distributions and are here exemplarily represented in c) by H_{0E} of the set "EQt".

By contrast, to all histograms of shape-related parameters normal distributions curves fit best; the angles along the rupture surface, the mean slope angle and the ratios form the "normal family" (cf. Fig. 3.6a-b). Curiously, also the "depth parts" belong to this family although they are 1D parameters. One possible explanation might be that the "depth parts" are by definition only parts of the entire depths at the five main positions of a landslide (cf. Fig. 3.3). They are created by intersecting a depth with the line of the mean slope angle, and therefore it is not unreasonable to believe that they could bear traits of proportions and hence rather belong to the "normal family".
In the course of statistical analyses the question arose, if large landslides affect the division of parameters into the two families. For instance, it was unclear if exceptional high values of volume elongate the tail of a decreasing exponential distribution curve and if the distribution is only therefore classified as such. Thus a temporary reduction of the biggest landslides was performed, removing all cases with $V_{lit} > 10^9$ m^3. Thereupon the procedure described above was carried out for the parameters L, A and V_{lit} of the dataset "full" to have a comparative histogram for a 1D, 2D and 3D parameter respectively. However, it turned out that the presence or absence of the biggest landslides in the histograms does not affect the results obtained by the Curve Fitting Tool in MATLAB and the distinction of families remains the same.

3.3.3. Mean Geometries of Landslides

Besides the consideration that dimension and shape of landslides might behave differently with increasing event size, there are also grounds for assumption that a landslide prototype could possibly be deduced from the database by averaging parameters and creating thereupon a mean geometry in the form of a LCS. Indeed, this is a promising approach for comparative studies

because mean LCS can hence be derived not only for landslides in general (set "full"), for landslides in seismic regions (set "SR") or for seismically induced landslides (set "EQt"), but also for any other sub-set according to the desired filtering.

Averaging of Parameters

Initially averaging of parameters was carried out for the three datasets separately, i.e. for each of the 49 parameters (cf. 3.3.2. - Distributions of Parameters) the mean value was calculated regardless of how many times they were reported or calculated as indirect parameters (cf. 3.3.2. - Recurrence of Parameters). It is important to mention that a mean value might thus be derived from a multitude of values or from only a few entries. Furthermore, mean values of different parameters are very likely to be derived from different pools of landslides since the completeness of the individual survey charts never reaches 100% (cf. 3.3.2. - Completeness of Survey Charts).
Unfortunately, this simple way of averaging did not show satisfactory results; most likely the landslide dimensions are by far too diverging to be represented by one single value per parameter. Proof for this assumption was provided by a simple multi-step test:

1) For all direct and indirect parameters mean values were calculated in Microsoft Access.
2) All "direct" mean values were inserted to a blank survey chart as if they represented values of a real case.
3) The survey chart automatically calculated from those "direct" mean values its own version of "indirect" mean values which at the end could be compared to the "indirect" mean values calculated initially by the Access database (cf. Fig. 3.7).

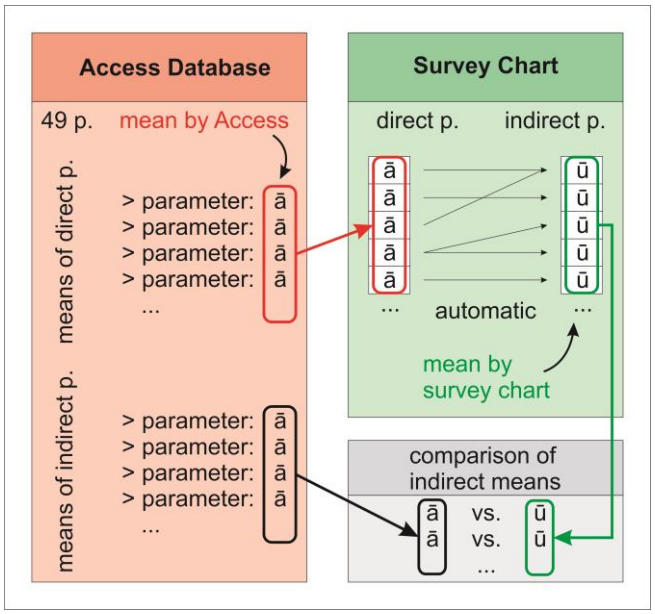

Fig. 3.7. Illustration of the test procedure to compare mean values of indirect parameters calculated by the database and mean values of indirect parameters calculated by the survey chart.

The differences between the two types of "indirect" mean values were more than obvious. Especially the mean values of A_h and V_{equ} appeared to be tremendously variable.
As simple averaging per dataset was apparently unsuitable for the definition of mean geometries, a more explicit distinction of the landslide dimension was necessary. Consequently landslides were grouped by order of magnitude (in decimal power) of their calculated volume V_{equ} (cf. Fig. 3.8a-b). This classification resulted in nine groups which were later united to three groups per dataset ($10^3 < V_{equ} \leq 10^6$, $10^6 < V_{equ} \leq 10^9$ and $10^9 < V_{equ} \leq 10^{12}$ in m^3) preserving the overall character of the statistical distribution.

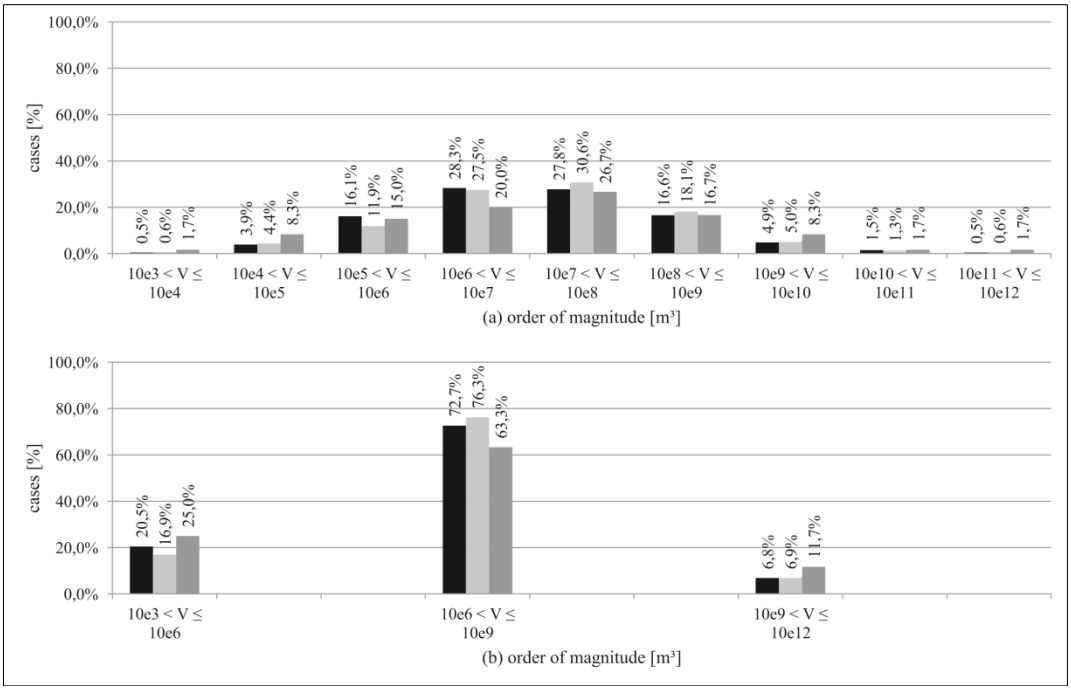

Fig. 3.8a-b. Number of landslides (in percent of the referring set) by order of magnitude of their calculated volume (V designing V_{equ}). The arrangement to 3 groups shown in b) preserves the statistical character of the distribution appearing in a).

Attention has to be paid to the fact that due to the grouping process only landslides with existent records of V_{equ} could be taken into account, and therefore only those could contribute their parameters for the later averaging procedure.

The fact that V_{equ} became the parameter according to which groups were formed requests more precision. Although often difficult to measure, the volume of a landslide is its most significant parameter of characterization. It directly relates to the event magnitude and subsequently to the consequences it may cause (MALAMUD et al., 2004). Thus, the grouping criterion was selected to be volume-based. Since the database theoretically reports V_{lit} and V_{equ} for every landslide – two occasionally quite different values – one of them had to be chosen. Among all 277 landslides in the database 165 report a V_{lit} and even though some of the landslides date back to times where digital elevation models (DEM) were not as accurate as today no significant over- or under-estimations of their volumes were found. On the contrary, 205 cases dispose of a V_{equ}. A strong argument against the choice of V_{equ} is the way of its calculation (cf. 3.2.); it is suitable for rotational landslides (CRUDEN & VARNES, 1996) while applying it to translational landslides it causes a volume loss and thus an underestimation of the actual volume. However, after comparing V_{lit} and V_{equ} at cases where both were available, differences appeared to be negligible and V_{equ} was adopted as the parameter according to which grouping should be performed.

With the new approach of grouping and averaging, mean values along with their respective standard deviations were obtained for the 49 concerned parameters and for the three datasets. This time, the results appear to be very satisfying as shown by the before described test procedure (cf. Fig. 3.7). "Indirect" mean values calculated by the survey charts came extremely close to the ones calculated by the Access database.

Representative for all 49 parameters, Fig. 3.9a-e shows the mean values for four 1D parameters (L, H_{0E}, w_{av}, d_{av}), the 2D parameter A, the 3D parameter V_{equ} as well as three shape-related parameters (α_{equ}, δ_0, δ_E) and four newly defined ratios (d_{av}/L, d_{av}/w_{av}, w_{av}/L_h, H_{0E}/L_h). Also a value for the curvature was created, which is by definition δ_0-δ_E, and whose mean values are represented likewise.

When comparing the behavior of these mean values with increasing magnitude group, one discovers that the mean values of all dimension-related parameters increase as it could be expected for progressively bigger landslides. From 1D to 3D parameters the increase itself

becomes more rapid and the standard deviation gaps become relatively larger. Surprisingly though, the mean values of all shape-related parameters are remarkably constant throughout the different orders of magnitude.

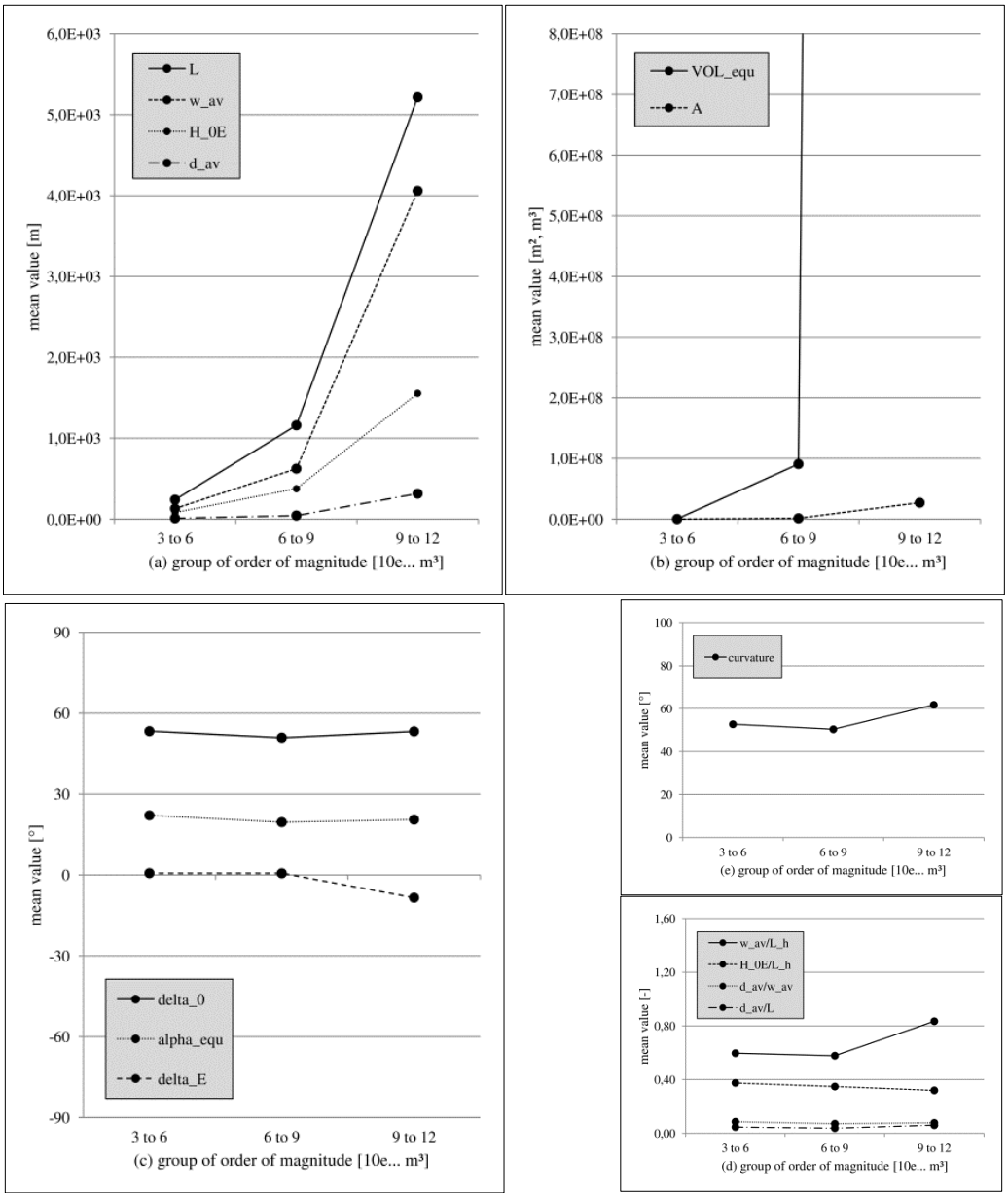

Fig. 3.9a-e. Development of mean values with increasing order of magnitude for the set "SR". Part a) shows the 1D parameters L, H_{0E}, w_{av}, d_{av}; part b) shows the 2D parameter A and the 3D parameter V_{equ}; part c) shows the shape-related parameters α_{equ}, δ_0, δ_E; part d) shows the four newly defined ratios d_{av}/L, d_{av}/w_{av}, w_{av}/L_h, H_{0E}/L_h and part e) shows the curvature.

The two findings apply without exception to all three datasets. Combining both of them, and at least on the basis of averaged landslides, one can conclude that with increasing magnitude of a landslide its dimension changes whereas its shape remains more or less the same.

An issue that deserves critical consideration is the inclusion of different mass movement types in the database and the question if "hiding" mass movements other than proper landslides could affect the statistical analyses. Ideally and based on the classification of VARNES (1978), only landslides composed of soil, rock and/or debris are appropriate to be included in the database.

Unfortunately it is not seldom that authors use terms describing mass movements in a very vague sense and cases that are described in one publication as a landslide might appear for

instance as an earth flow elsewhere. Gradual transitions between mass movement types support misleading nomenclature even more.
This discrepancy appears 37 times within the database; 33 cases can also be seen as a deep-seated gravitational slope deformation (DSGSD) and four cases might also be considered as earth flows. For each of them, literature indicated a clear surface of rupture separating the moving mass from the underlying bedding. – A fact, that favors – but does not justify – the interpretation as a landslide mass and hence the inclusion in the database.
Compared to landslides, earth flows as well as DSGSD – though to a lesser extent – are clearly different especially in terms of shapes. Their presence in the database must therefore be regarded with caution and two tests were carried out to estimate their statistical influence. First, plotting V_{equ} over the sequential numbers attributed to the individual cases, it turns out at all three datasets that calculated volumes of the DSGSD and the earth flows are by far not the greatest; the respective data points mix well among the ones of landslides. Second, based on the full dataset only and without subdivision into groups of order of magnitude, a mean value study similar to the above described procedure was conducted. This allowed for comparison of mean values obtained by the filtering options listed in Tab. 3.5. For DSGSD alone higher mean values of L, H_{0E} and thus of H_{0E}/L_h stand out and also δ_0 and the curvature are higher; the mean values for the earth flows depict lower mean values of δ_0 and the curvature as well as a higher L but lower w_{av} and thus a lower w_{av}/L_h. Both findings are in good agreement with typical DSGSD and earth flow masses. Differences to a characteristic landslide mass are therefore obvious.

filtering	meaning	cases
LS	landslides only	240
LS & DSGSD	landslides with DSGSD only	273
LS & EF	landslides with earth flows only	244
LS & DSGSD & EF	corresponding to the dataset “full”	277
DSGSD	DSGSD only	33
EF	earth flows only	4

Tab. 3.5. Numbers of cases obtained by filtering and combination of different mass movement types.

Nevertheless DSGSD and earth flows do not exceed landslides neither in terms of number nor of volume and it is unlikely that they influence the outcome of statistical analyses. Moreover, some of them might even be classified as landslide emphasizing this conclusion. In this case, “hiding” mass movements other than landslides are of lower importance to the overall outcome of analyzes. Though, the issue underlines the necessity of proper mass movement classification in literature in order to avoid misinterpretations.

Mean Geometries

The mean values per parameter can be used to draw averaged LCS. By combination of the three datasets and the three groups of orders of magnitude one obtains nine LCS which are called “mean geometries” for simplicity (cf. Fig. 3.10a-i).
As predicted by the mean value study, it can be seen that the dimension changes with increasing order of magnitude, but the shapes of the mean geometries are very similar throughout all magnitude groups. Only a slight increase of convexity becomes apparent at higher orders of magnitudes, which is probably an effect related to emerging topography. Naturally topography is more relevant at landslides with a length of several kilometers than at those being only several meters long. With respect to dimensions, the three smallest mean geometries stand out inasmuch as the LCS of the set “SR” is about 50 m longer and the LCS of the set “EQt” about 30 m shorter in comparison to the one of the set “full”. This evidence might seem significant at the first sight, but becomes negligible when considering length differences of up to around 100 m at the mean geometries of the intermediate magnitude group and of several hundreds of meters at those of the biggest magnitude group.

Furthermore, the shape does not change for different datasets; i.e. the mean geometry of all landslides does not differ from neither the one of the landslides in seismic regions nor the one of the seismically induced landslides.

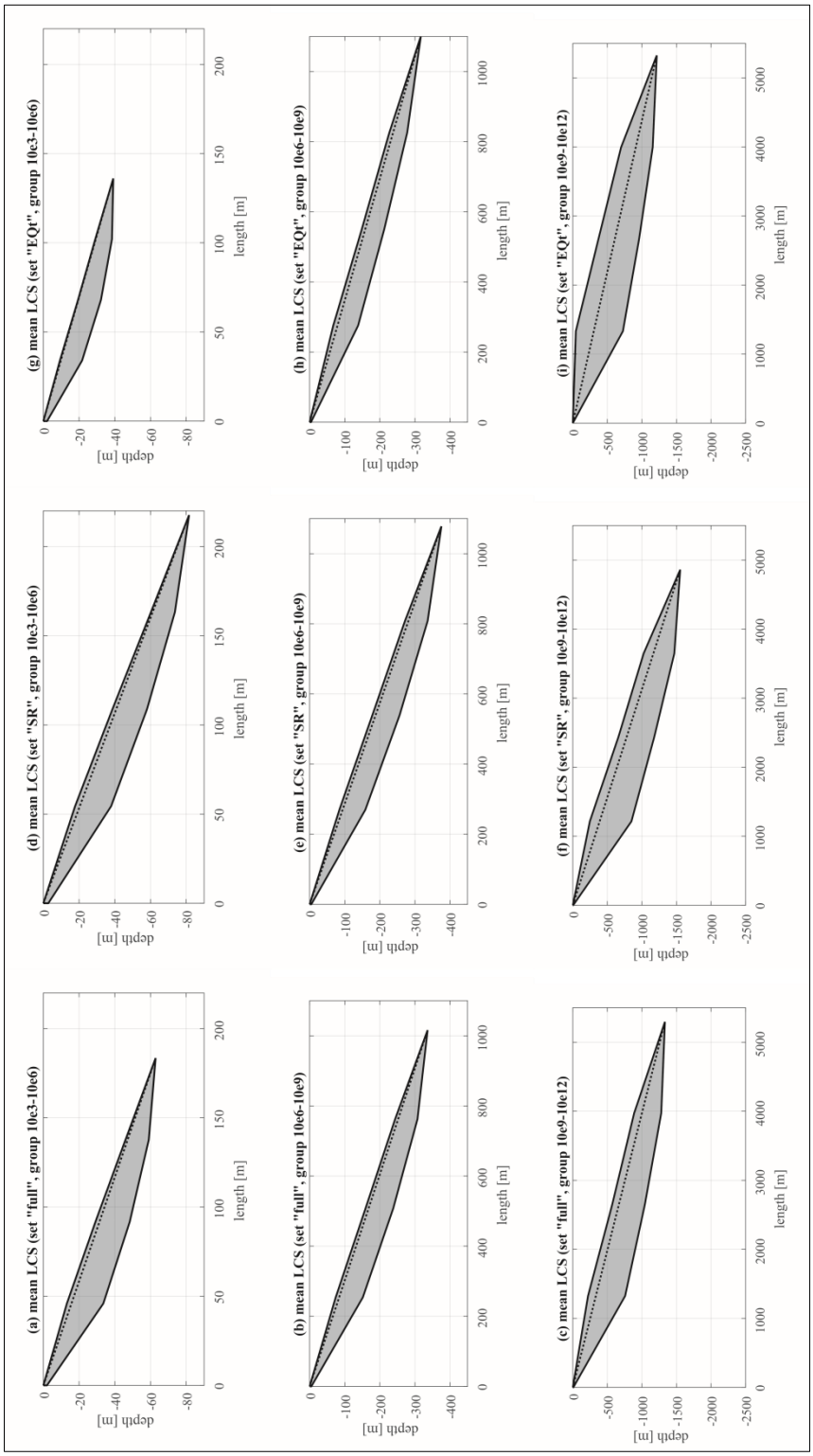

Fig. 3.10a-i. Mean geometries of landslide masses confined by topographic surface and surface of rupture. The dotted line indicates the mean slope angle and corresponds to the "line" (Fig. 3.3). The first column with the cross sections a), b) and c) refers to the set "full", the second column with the cross sections d), e) and f) refers to the set "SR" and the third column with the cross sections g), h) and i) refers to the set "EQt". The uppermost row is based on the smallest volume group (10^3-10^6 m^3), the middle row on the medium volume group (10^6-10^9 m^3) and the lowest row on the biggest volume group (10^9-10^{12} m^3). For completeness it should be mentioned that c) shows the only LCS without a trench (i.e. d_0 and thus $d_{0\text{-bel}}$ are not 0; Fig. 3.3).

3.4. Conclusions

A chronological database of landslides with various triggers was built. It contains 277 globally distributed cases of which one third has a seismic trigger. The term landslide refers to proper sliding mechanisms as defined by VARNES (1978).
By means of survey charts every landslide was comprehensively assessed giving general information such as location, date, triggering factors, material, sliding mechanism, event chronology, consequences and related literature on the one hand, and on the other hand information with respect to the landslide mass. The survey chart assured the maintenance of predefined standards during the acquisition process and it kept the bias as low as possible. The thereon appearing geometrical parameters are a further and more detailed development of the parameter set proposed by the INTERNATIONAL GEOTECHNICAL SOCIETIES' UNESCO WORKING PARTY ON WORLD LANDSLIDE INVENTORY (1990, 1991, 1993, 1994; cited as UNESCO) and the INTERNATIONAL UNION OF GEOLOGICAL SCIENCES WORKING GROUP ON LANDSLIDES (1995; cited as UNESCO). The entire content of all survey charts was introduced to a Microsoft Access database which now serves as a query tool to explore the data; it allows not only for data storing, but also for fast and efficient filtering, sorting and data preparation for statistical analyses of 2D and 3D landslide geometries.
Several statistical analyses were carried out to test the database itself in terms of qualitative and quantitative features, and to evaluate the data it contains. According to the type of analysis, the dataset of interest might either be the totality of all landslides (set "full", 277 cases), the sub-set of all landslides in seismic regions (set "SR", 220 cases) or the sub-set of all seismically induced landslides (set "EQt", 99 cases).
In a first step epicenter-to-landslide distances of cases included in the database were compared to maximum epicenter-to-landslide distances proposed by KEEFER (1984) for coherent slides. Data from the database appeared to fit very well to the proposed limits at different magnitudes, and even though the scatter is not to be neglected only 3 landslides clearly exceed the limit curve. Thus, the data of the database is in very good accordance with KEEFER'S (1984) proposition, which is highly satisfactory since the landslides in the database are randomly assessed on a global basis. The recurrence of distinct parameters in the database, i.e. the number of times the same geometrical parameter stores a value comparing all 277 survey charts, reveals that parameters related to the characterization of maps and LCS are more frequently assessed, whereas parameters related to TCS are very rare to show values. This result is promising for 2D modeling, but limits accurate 3D modeling due to the lack of information about the lateral confinement – and hence about the impedance contrast – of a landslide mass which is of particular interest when studying the soil response under seismic shaking. Strikingly, the calculated volume V_{equ} – even though being a parameter depending on many others – shows a very high recurrence. This emphasizes the choice of V_{equ} to be the parameter according to which landslides are grouped for further analysis.
The completeness of survey charts, i.e. the number of parameters storing a value per survey chart, shows that two thirds of all survey charts are complete to an extent of 50-70%. Roughly the same percentages are obtained for the three sets of interest which is again promising for 2D but less satisfactory for 3D modeling because full completeness is apparently not achieved at the expense of missing TCS information.
The combining of the results from the recurrence and the completeness studies, and the fact that the choice of landslides and their associated literature was random, reflects also the quality of landslide assessment in general. If more attention was paid to the widthwise characterization of a landslide, 3D models could be much more precise.
Later, values per parameter were grouped in histograms with 30 bins each to fit a normal, a power or an exponential distribution to them. Surely it is not ideal to fit distribution curves to histograms instead of ungrouped data, but unfortunately the values of a particular parameter have no dependency on the sequential numbers. Testing all parameters in the three sets, histograms of dimension-related parameters manifest an exponential decrease whereas

histograms of shape-related parameters were best fitted by normal distributions. The presence or absence of extremely large landslides did not affect the outcome.
The main request to the database was to delineate geometries that represent averaged shapes of rupture masses of landslides. After it turned out that averaging values of distinct parameters on the basis of whole sets is not suitable because of far too big and thus incomparable dimensions, a more explicit distinction was made. Landslides per set were united according to their calculated volume V_{equ} into three groups of the following orders of magnitude: $10^3 < V_{equ} \leq 10^6$, $10^6 < V_{equ} \leq 10^9$ and $10^9 < V_{equ} \leq 10^{12}$ in m^3. The result of this grouping (cf. Fig. 3.7) revealed a significant surplus of cases in the middle class leaving the question open if this distribution is globally representative implying a roll-over, or if – by chance – it is caused by the choice of landslides included in the database. The latter explanation remains arguable since the number of cases is high and no strategy was followed during the data assessment.
The grouping approach resulted in nine series of mean values of distinct parameters by combination of 3 sets and 3 classes of order of magnitude. Comparison of mean value behavior with increasing order of magnitude confirmed a different behavior of dimension- and shape-related parameters. Mean values of 1D, 2D and 3D parameters increase progressively with bigger orders of magnitude, whereas mean values of angles, ratios and the curvature remain rather constant. Using those mean values finally nine mean LCS in 2D (cf. Fig. 3.10a-i) were delineated which illustrate well the three major findings of the entire study:

1) statistically, dimensions and shapes do not behave in the same way with increasing order of magnitude
2) the shape is rather independent of the dataset
3) the shape is slightly dependent on the order of magnitude

The three facts are of particular importance to numerical modeling and the evaluation of seismically induced displacements of soils undergoing external dynamic loads, since the shape of a landslide mass governs the seismic interaction with the underlying bedrock, but the dimension controls the intensity of the expected seismic effects including induced displacements (LENTI & MARTINO, 2013). The different mean geometries serve hence as landslide prototypes of varying dimensions to explore differences between 2D and 3D models having the same framework conditions (geometry, material, etc.). On the basis of these examples, it will be possible to compare displacements predicted by traditional slope stability methods such as the Newmark Sliding Block Method (NEWMARK, 1965) and results from numerical methods considering characteristic periods T_l/T_m and T_s/T_m linked to longitudinal and vertical dimensions of a system. At this context, LENTI & MARTINO (2013) describe systematic under- and overestimations of displacements obtained with the NEWMARK-Method (1965) in comparison to results from numerical modeling. They also point out that horizontal displacements strongly depend on characteristic periods.
To conclude, it should be noted that, first, landslides are complex phenomena and averaged shapes of appearance like the ones presented in this study might serve for general research but cannot be used as representatives for the investigation of a particular site. Second, the statistical procedure presented in this chapter describes only one approach of evaluation with a specific focus of interest. Many other analyses may be conducted upon this vast and newly updated database and the creation of new input data for studies with different purposes is possible at any time.

CHAPTER 4
DIEZMA LANDSLIDE & APPLIED SIGNALS

4.1. Introduction

As described in the previous chapter (cf. 3.), statistical analyses of the database resulted in nine simplified mean geometries of landslides which can be used for numerical modeling and studies on slope stability. Using these simplified geometries, the contribution of trapped seismic waves to the displacement of the landslide mass can be modeled numerically and hence allows for analysis of potential seismic impacts.
Ideally, a comprehensive analysis of slope stability under seismic shaking would be carried out for all nine simplified landslide geometries using different 2D- and 3D-methods. Subsequently, comparisons of predicted displacements obtained by those different methods may demonstrate 2D-approaches to be sufficient for seismic slope stability predictions or they might justify the necessity of 3D numerical modeling (cf. Fig. 4.1).

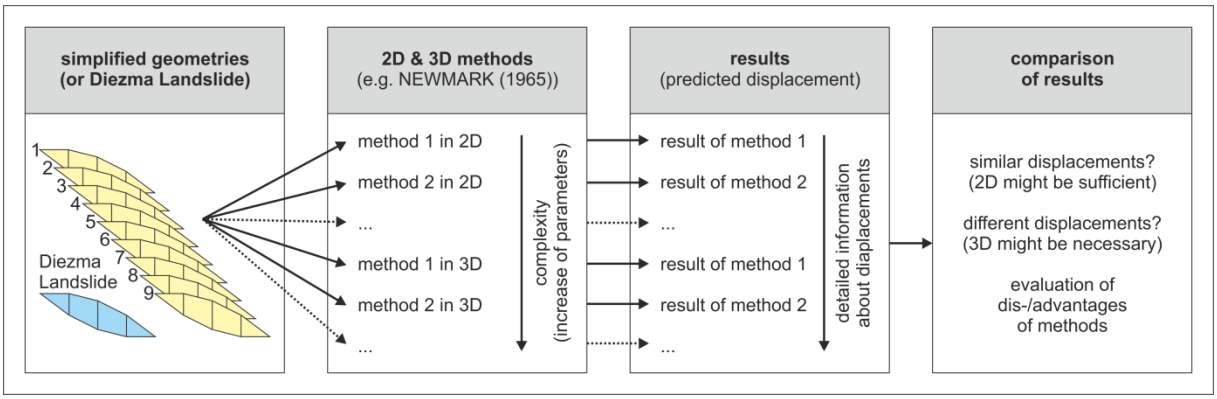

Fig. 4.1. Flow chart describing the process of comparative slope stability analyses using the nine simplified landslide geometries or the Diezma Landslide.

Unfortunately it turned out that within the restricted time frame of three years this comprehensive comparative analysis of all nine simplified landslide geometries is unfeasible. As alternative, all envisaged methods were applied to the real case of the Diezma Landslide. Thus, this thesis proposes an exemplary procedure that can be followed at a later stage for any other landslide or for the nine simplified geometries of the database. The Diezma Landslide was chosen as example for several reasons:

- Despite sophisticated and expensive protection measures the landslide is active since almost 30 years. It regularly damages the passing highway and other infrastructure facilities on the slope (AZAÑON et al., 2010; DELGADO et al., 2015; MARTINO et al., 2016).
- Even though the Diezma Landslide is not triggered by one particular earthquake, it is situated in a seismically active region regularly experiencing strong ground motion and it is affected by other vibratory sources such as traffic from the highway. Thus, the site is a very suitable example for the overall thesis topic of "studying seismically induced effects and slope stability in urbanized areas via numerical modeling".
- The Diezma Landslide is one of the main research sites of the working group and a wealth of geological and geotechnical data is available. Also, the engineering-geological development in terms of slope modification and protection measures is very well documented in the article by DELGADO et al. (2015).
- Several studies on the stability of the landslide were carried out in the past (DELGADO et al., 2015; MARTINO et al., 2016) and results of this thesis can now be compared to them. Such a "back-checking" evaluation would be impossible using the nine newly created mean geometries, what in return emphasizes the exemplarily procedure applied on the Diezma Landslide in the course of this thesis.

Several more advantages became apparent after the completion of the survey chart for the Diezma Landslide (cf. A.1.), which besides carries the number 001.00 in the database:

- The documentation is of very good quality. Concerning the landslide imagery (cf. 2.4.1.) all image types are available: a map and a LCS without lateral cut-offs, a 3D-representation and photographs. The Diezma Landslide is also one of the two cases throughout the whole database where exploitable TCS are available (cf. 2.4.1.).
- With a length of roughly 500 m the dimension of the landslide is to be located somewhere between the smallest and the medium group of simplified geometries. Since those both groups comprise most of the landslides (cf. Fig. 3.8), the Diezma Landslide appears to be a good representative.
- The volume reported in literature (1,200,000 m^3) differs of less than 1% of the calculated volume by the survey chart (1,191,338 m^3), which testifies to very accurate geometry evaluation. Only three cases in the database have equally close volumes. The reported (9°) and the calculated (10°) mean slope angle are also very similar.
- The Diezma Landslide is mainly translational, thus rather simple to perceive in 3D.
- It consists mainly of soil and debris, and having a rather low slope angle, this clearly excludes a rock slide or even rock fall. The Diezma Landslide represents hence a classic landslide without involvement of other mass movement types (cf. 3.3.)
- Unlike other cases, its LCS and TCS have no knickpoints. Lateral and vertical dimensions are represented in the same scale, the rupture mass is clearly outlined, the pre-landslide topography is shown in various stages and the positions of the LCS and the TCS are accurately indicated (cf. 2.4.).
- Although the position of the LCS does not correspond to the main sliding direction of the landslide, it is still considered as suitable for the depth assessment of the landslide. The angle between the azimuth of the LCS and the main sliding direction amounts to 11°. As mentioned in chapter 2.4.1., geometrical correction becomes necessary only at angles bigger than 20°. However, the issue of azimuthal deviation becomes relevant at the construction of the 3D-geometries and will be discussed in chapters 4.2.2. and 4.2.3. in greater detail.
- The second page of the survey chart assessing the landslide geometry is very complete; 71% of the parameters are available (cf. Fig. 3.5) which is one of the highest completeness values throughout the database.

Fig. 4.2. The Diezma Landslide besides the A-92 motorway
on a satellite picture taken on 27/07/2015 (after GOOGLE EARTH PRO, 2015).

The Diezma Landslide is located around 25 km north-east of Granada in the Sierra Nevada Range of the Betic Cordillera (Andalusia, Southern Spain) beside the highway A-92 (37°18'34.00''N, 3°22'08.70''W; cf. Fig. 4.2) whose construction is likely to have induced the landslide in the first place. The main failure occurred on the 18th of March 2001 after a period of intense rainfall (MARTINO et al., 2016), but smaller ground failures are reported since the 1990s. The site can therefore be described as an active landslide that moves constantly at low speed or even comes to stability for a certain period of time, but nevertheless it can experience fast and sudden failures after external impacts such as excavation work, intense rainfall and probably seismic activity.

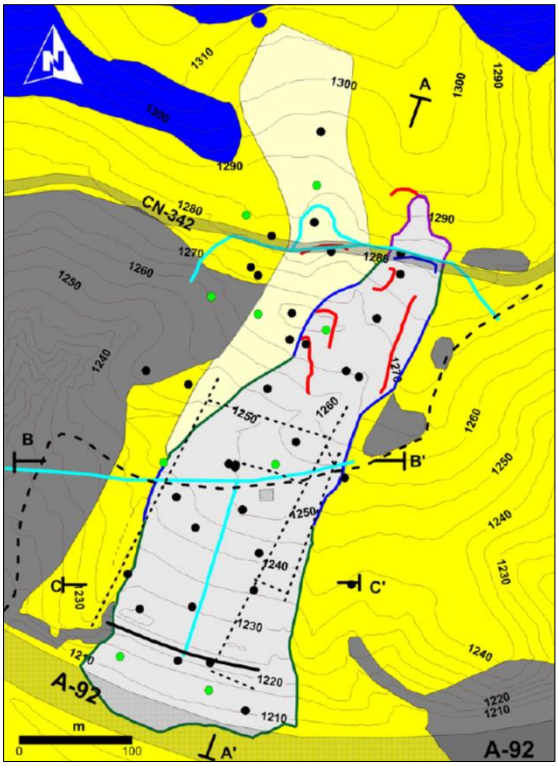

Fig. 4.3. Geological map: Numidoide Formation (yellow), Maláguide Complex (gray), South Iberian Domain (blue), debris (lightly shaded), landslide trace (blue lines – 1998, green lines – 2001, violet line – 2010), ground cracks (red lines), faults (black dotted lines), track (black dashed line), drainage system (light blue lines), boreholes (black dots), inclinometers (green dots), spring (blue dot), building (gray rectangle), wall (black line) (DELGADO et al., 2015).

As for the geologic emplacement, DELGADO et al. (2015) as well as RODRÍGUEZ-PECES et al. (2011) give very clear descriptions which are synthesized in the following. The Diezma Landslide consists of medium- to high-plasticity clays, silt and marls with embedded heterogenic limestone and dolostone blocks. This lithology belongs to a Cretaceous to Lower Miocene flysch formation (BOURGOIS et al., 1974) which is also called the "Neonumidian Flysch" (BOURGOIS, 1978) or the "Numidoide Formation" (OLIVIER, 1984). Having undergone intense deformation during the Alpine Orogeny, this formation appears today rather chaotic. At the location of the Diezma Landslide the Numidoide Formation lies on the Paleozoic to Triassic Maláguide Complex (Alborán Domain) consisting of shales, phyllites, sandstones and conglomerates. RODRÍGUEZ-PECES et al. (2011) report furthermore a smectite-rich clay layer in between the landslide mass and the underlying Maláguide Complex; this thin interlayer might be the actual sliding surface.
The Upper Jurassic South Iberian Domain is outcropping just north of the landslide. It was thrust onto the Maláguide Complex and consists of limestone and dolostone. Being composed of carbonate rock the South Iberian Domain acts as a karstic aquifer delivering water towards the south, and due to the less permeable material beneath the landslide the water table inside the landslide mass rises significantly after intense rainfall. Also several springs emerge at this unconformable tectonic contact between geological units in the northern vicinity of the landslide

of which one is shown in Fig. 4.3. Reactivation of the landslide mass after heavy rainfall is thus very likely, because of two reasons. First, the usual water table lies very deep and the landslide is almost unsaturated under normal conditions; a quick rise to a shallow water table hence causes a big difference of pore water pressure and shear strength reduction of the medium- to high-plasticity clays. Second, the installed drainage system appears to be less efficient and poorly maintained in some parts.
DELGADO et al. (2015) and RODRÍGUEZ-PECES et al. (2011) investigated the slope using geophysical and geotechnical methods to establish engineering-geological models and to characterize the landslide material. DELGADO et al. (2015) conducted three geophysical campaigns in 2012 and 2013 that included seismic noise measurements, Multi-channel Analyses of Surface Waves (MASW) and borehole testing. Laboratory tests on borehole samples of the Numidoide Formation show a high variability of parameters due to the fact that the formation itself is very heterogeneous. Based on the geological setting and the triggering conditions of the main slope failure in 2001 the authors "back-calibrated" these parameters using the JANBU-Method (JANBU, 1973) with a factor of safety (SF) of 1 and a Bishop Coefficient (r_u) of 0.22 – the latter representing the state of the landslide mass after intense rainfall. In Tab. 4.1 the obtained values are listed in comparison to the values published by RODRÍGUEZ-PECES et al. (2011). In this thesis the "back-calibrated" values of DELGADO et al. (2015) for the saturated unit weight (γ_{sat}), the residual cohesion (c_r) and the residual friction angle (Φ_r) were used (cf. 5.4.2.).
DELGADO et al. (2015) conclude from geophysical investigations a shear wave velocity (v_s) of 300 m/s for the landslide mass; MARTINO et al. (2016) indicate a Poisson's Ratio (υ) of 0.25 for the landslide mass and more than 750 m/s for the underlying bedrock.

author	unit	γ (kN/m^3)	γ_{sat} (kN/m^3)	c_p (kPa)	c_r (kPa)	Φ_p (°)	Φ_r (°)
D.	Numidoide Formation	19.00 (± 2.00)	-	46.00 (±23.00)	-	26.00 (± 6.00)	-
D.	Numidoide Formation	-	21.40 (calibr.)	-	4.00 (calibr.)	-	12.00 (calibr.)
R.-P.	Numidoide Formation	18.19 (± 0.91)	20.60	5.40 (± 3.20)	0.60 (± 0.50)	31.00 (± 4.00)	11.00 (± 3.00)
R.-P.	interlayer	15.24 (± 0.49)	17.66	1.30 (± 0.70)	0.40 (± 0.30)	21.00 (± 4.00)	8.00 (± 1.00)

Tab. 4.1. Values for the unit weight (γ), the cohesion (c) and friction angle (Φ) of the Numidoide Formation and the interlayer. The suffixes "sat", "p" and "r" mean "saturated", "residual" and "peak" respectively. It should be noted that literature reports the cohesion of 46.00 kPa without mentioning if it is the peak or the residual cohesion; however – due to the high value – it is more likely the peak cohesion and therefore marked as such (after DELGADO et al., 2015; after RODRÍGUEZ-PECES et al., 2011).

4.2. Creation of a 2D- and a 3D-Geometry

This chapter describes in detail the process of creating a 2D- and a 3D-geometry of the Diezma Landslide. The importance of precise documentation of the landslide will be discussed and it will be pointed out what difficulties arise in this context; a long and a short version of the landslide geometry will be presented. Section 4.2.2. shows a simplified geometry in 2D and 3D comparable to the nine simplified geometries retrieved from the landslide database (cf. Fig. 3.10a-i). Section 4.2.3. explains the creation of a fine 3D-geometry of which a fine 2D-geometry can be extracted.

4.2.1. Long and Short Version

The first question before designing a geometry for the Diezma Landslide was which volume should be considered. As mentioned in chapter 4.1., the slope has undergone significant natural and man-induced changes of shape. For the states in 1989, in 1990 and in 2013, the article by

DELGADO et al. (2015) and an appendant AutoCAD-file show cross sections with respective altimetric information for the sliding surface and the topography (cf. Fig. 4.5a-b, Fig. 4.13).
Since the main landslide event took place in 2001 after the terrace for the highway A-92 was cut, the volume of 1990 was accepted as reference. In contrast to the one of 1989 it shows already the terrace excavation (cf. Fig. 4.4).

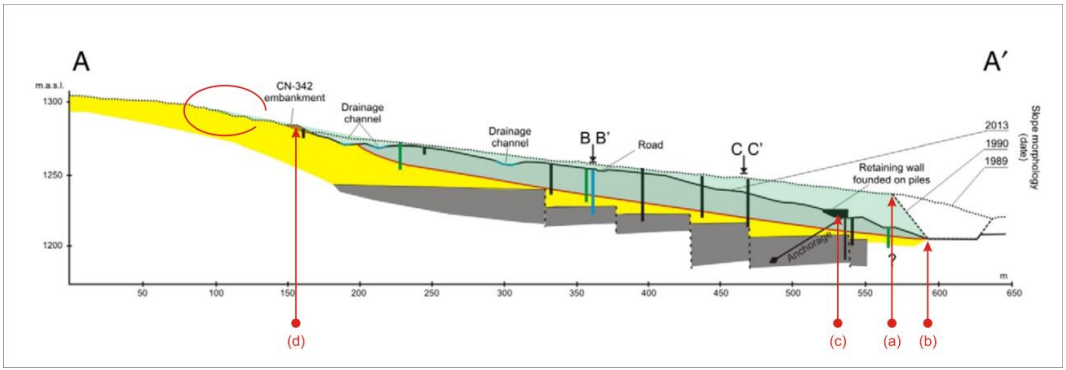

Fig. 4.4. LCS of the article. The shaded volume is the reference for the simplified 2D-geometry (cf. Fig. 4.3 for the legend). The red circle indicates the virtually added 50 m and letters a-d correspond to the discussed differences between this figure and Fig. 4.5a and Fig. 4.5b (after DELGADO et al., 2015).

AutoCAD-file	article	type	used as	notes
PT-5 = Profilio 5	-	LCS	-	
PT-1 = Profilio 1	-	LCS	-	
PT-6 = Profilio 6	A	LCS	A	Profilio 6: 2001 & 2013 (cf. Fig. 4.5a-b)
PT-9 = Profilio 9	-	LCS	-	
PT-8 = Profilio 8	-	TCS	N	newly named for the thesis
PT-4 = Profilio 4	-	TCS	-	
PT-3 = Profilio 3	B	TCS	B	
PT-7 = Profilio 7	C	TCS	C	
PT-2 = Profilio 2	-	TCS	M	newly named for the thesis

Tab. 4.2. Corresponding nomenclature of cross sections of the map and the AutoCAD-file (after DELGADO et al., 2015).

Another difficulty is the fact that the map and the LCS presented in the article of DELGADO et al. (2015) do not entirely correspond to the ones available in the AutoCAD-file. Thus, before taking measures to create 2D- or 3D-geometries, the differences had to be assessed. The first apparent difference is that the map of the article depicts only three cross sections (cf. Fig. 4.3) whereas the AutoCAD-file comprises nine cross sections. Corresponding nomenclature is given in Tab. 2. Of those nine cross sections only five were finally used because of their suitable emplacement.
Comparing the LCS shown in the article and the corresponding ones in the AutoCAD-file, altimetric information seems to be in rather good accordance. The simplified geometry overcomes a maximum elevation difference of 99 m (cf. Fig. 4.8) and the fine geometry of 98 m (cf. Tab. 4.6).
However laterally, major differences can be found (cf. Fig. 4.4, Fig. 4.5a-b); letters in the following alphabetic listing correspond to the letters indicated in the figures.

a) article: main cut from ~550 m to 580 m, ending at the highway
   AutoCAD: main cut from ~550 m to 580 m, ending at a terrace
b) article: highway from 580 m, at an altitude of 1210 m
   AutoCAD: highway from 640 m, at an altitude of 1210 m
c) article: wall at 540 m
   AutoCAD: wall at 570 m
d) article: old road at 160 m
   AutoCAD: old road at 195 m

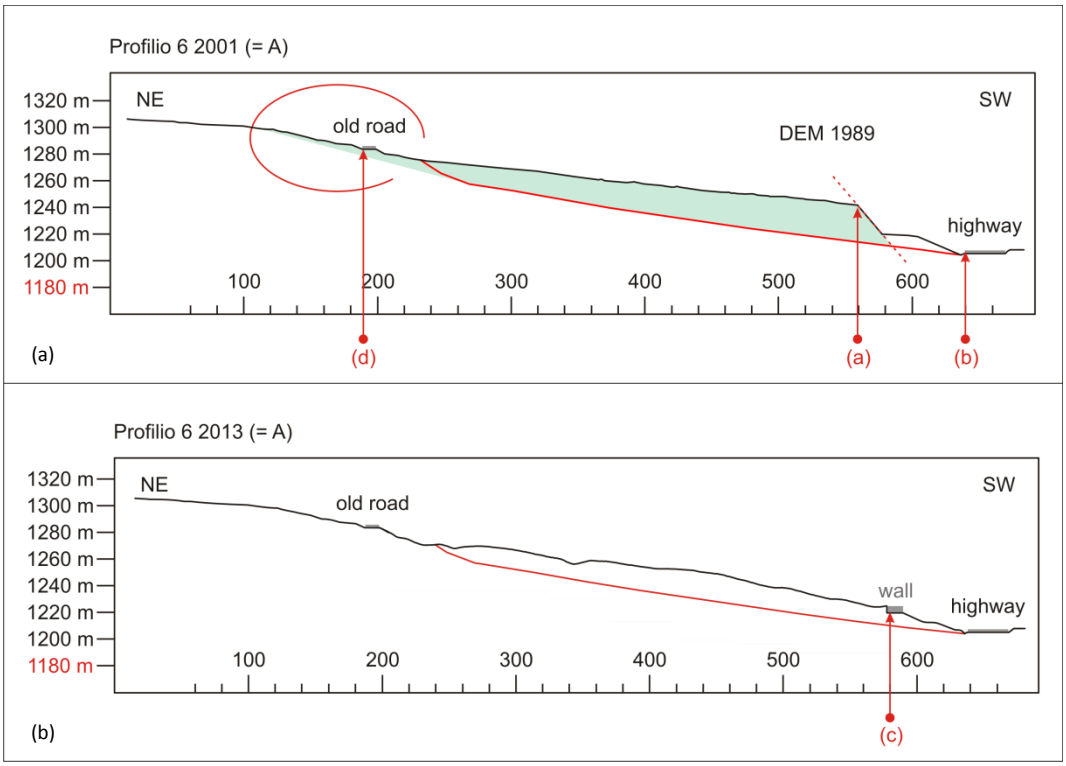

Fig. 4.5a-b. LCS of the AutoCAD-file. Letters a-d correspond to the discussed differences between this figure and Fig. 4.4 (after DELGADO et al., 2015).

Being aware of the fact that geological mapping and profiling is always a difficult task and that small deviations are always possible, a compromise between the two representations had to be found considering the following aspects. The compromise is reasonably compatible with the map presented in the article and the map of the AutoCAD-file.

a) The main cut starts in both cross sections at ~550 m; this position served as lateral reference for comparisons between the LCS from the article and the one from the AutoCAD-file. However, the cut ends once on the highway and once on the terrace. Also, the year given in the AutoCAD-file does not explain this difference. On the one hand, just next to the terrace appears the mark "DEM 1989" leading to the potential conclusion that – two years before the cut was completed – a rock mass was lying at this place. On the other hand, the profile carries the title "Profilio 6 2001" what might indicate that the terrace is the result of the main landslide event that took place on the 18th of March 2001. In this case though, one should ask oneself where this depositional terrace had slid from – the rest of the landslide mass is effectively the same as indicated in the article.
   Regardless of which interpretation is true, the cut in the LCS of the AutoCAD-file was extrapolated manually to meet the sliding surface and to come closer to the representation of the LCS in the article.
b) Following point a) it remains thus unclear why the highway is shifted by 60 m in the two LCS, unless the main excavation shown in the article is not the bed of the highway.
c) In effect, the wall is not of great importance to the volume of 1990 because it was not yet installed at that time. However, its position remains shifted by 30 m when comparing the LCS of the article and the LCS named "Profilio 6 2013" of the AutoCAD-file (cf. Fig. 4.5b). The TCS named "Profilio 2" also does not give evidence of the location of the wall since it is drawn in the cross section – and not behind or in front of the other geologic layers.
d) The old road – in contrast – existed in 1990 and its position is equally shifted by 25 m.

Other small issues at the interpretation of the AutoCAD-file are listed in the following. They are surely not insurmountable, but for the reader they might facilitate the understanding.

- Profilio 6 2001 & 2013: the first mark of altitude must be 1180 m
- Profilio 3, 7 & 8: E and W must be switched (comparing to contour lines)
- Profilio 2: NW to SE must be marked (comparing to contour lines)

Having found a compromise on the lower end of the landslide mass, the upper end still requires a closer look because the crown area is essential for the definition of the two geometry versions.

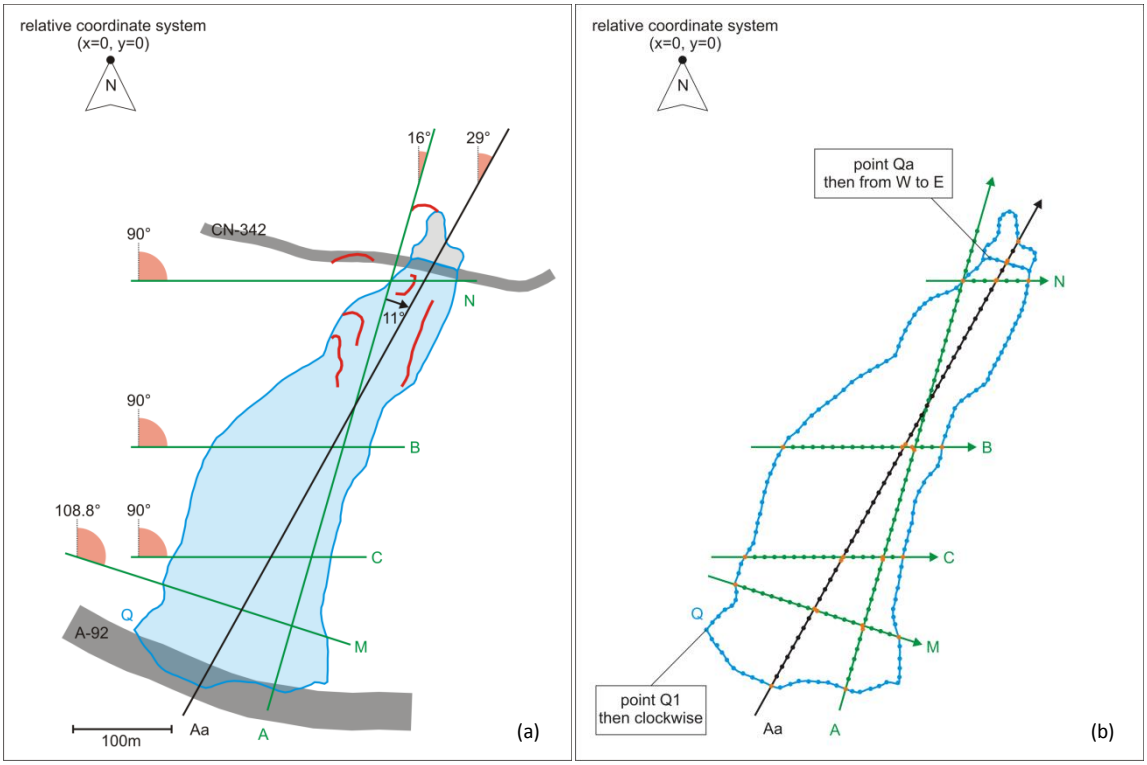

Fig. 4.6a-b. Emplacement of cross sections and point positions. Red lines indicate ground cracks. Arrows show the numbering direction of points per cross section and orange points design intersection or close neighbor points (after DELGADO et al., 2015). Both figures have the same scale.

The emplacement of a LCS is crucial; it should be positioned along the main sliding direction of the landslide. Due to accessibility in the terrain or special interest of scientists this is not always the case as at the site of the Diezma Landslide. The LCS diverts by 11° from the main sliding direction. In section 2.4.1. it was explained that azimuthal deviation angles (φ) of up to 20° are still acceptable to make use of the respective LCS. Values would be assessed along the given LCS and then attributed to an adopted LCS along the main sliding direction. In the case of Diezma, this procedure does not cause too many difficulties at the lower end of the landslide because the toe appears to be uniformly convex terminating on the same altitude of 1210 m. In the crown area though, this deviation of 11° makes a significant difference. As shown in Fig. 4.6a, LCS A exits the landslide at a much lower altitude than the adopted LCS Aa ("a" for "adopted"). The LCS represented in the article by DELGADO et al. (2015) is – surely accurate – but too short to cover the full length of LCS Aa.

The answer on the question if the full length has to be covered is not trivial either. The article by DELGADO et al. (2015) shows the landslide part above the old road in violet noting "2010 reactivation" (cf. Fig. 4.3). However, just at the uppermost point of the landslide trace ground cracks are marked in red without date indication which could let assume that the LCS of 1990 was that long. Also the LCS presented in the article of RODRÍGUEZ-PECES et al. (2011) shows a landslide mass exceeding by far the old road and dating the state to the time after the highway was constructed. Unfortunately, this article does not indicate the emplacement of its presented LCS, so – although a long extension to the north can be clearly identified – the exact direction remains unspecified (cf. Fig. 4.7).

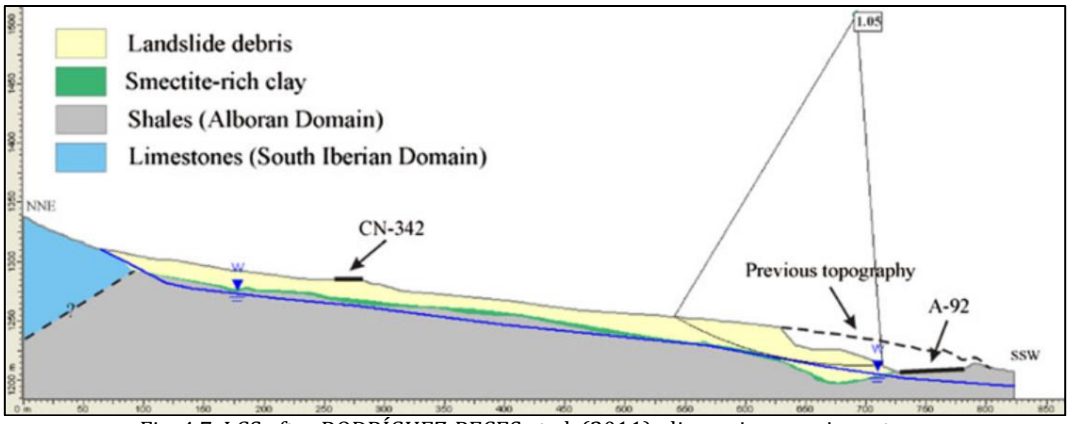

Fig. 4.7. LCS after RODRÍGUEZ-PECES et al. (2011); dimensions are in meters.

To avoid these non-trivial questions, two versions of possible geometries were created based on the map and LCS published by DELGADO et al. (2015) and the LCS of the AutoCAD-file:

- long version: extending roughly to the level of the red ground cracks
- short version: extending roughly to the level of the old road

For the short geometry, LCS Aa could simply adopt the values assessed at LCS A, whereas for the long geometry, LCS A had to be imaginarily prolonged first. This prolongation took into consideration that the uppermost crown area above the old road is very shallow. Already the last tens of meters of LCS A below the road do not show greater depths than a few meters. Available photographs in the articles of DELGADO et al. (2015) and RODRÍGUEZ-PECES et al. (2011) also indicate a very shallow landslide mass in the crown area. Thus, about 50 m above the old road were added to enable a depth assessment also for the long version of LCS A (cf. Fig. 4.4, Fig. 4.5a).
Certainly, this discrepancy is worth to take into consideration at the creation of 2D- and 3D-geometries because it has not only an influence on the factor of safety of the landslide but it also alters the resonance volume during seismic shaking. Luckily the volume difference is not very big (cf. Fig. 4.8) and as the analysis of the factor of safety in section 5.4.2. will show, the difference is almost negligible. Hence, all 2D- and 3D-methods applied to the Diezma Landslide were primarily based on the long geometries.

4.2.2. Simplified Geometry

This section describes extensively how a LCS is to be assessed and how a simplified 2D-geometry is created using values stored on the second page of the respective survey chart. It should be noted that due to the volume discrepancy there are also two versions of the simplified 2D-geometry (cf. Fig. 4.8) – both simplifying respectively LCS Aal ("l" for "long") and LCS Aas ("s" for "short").
Also a simplified 3D-geometry had to be created requiring TCS to be added to the simplified 2D-geometry. The only properly evaluable TCS – that represent also the landslide dimensions of 1990 – are the ones of the AutoCAD-file which were measured in great detail during the construction of the fine geometry. It is therefore advisable to

→ anticipate at this stage chapter 4.2.3.

to become familiar with the construction procedure, and especially with the particularities of the TCS. The thereupon based steps for the completion of the simplified 3D-geometry are listed in the following; some properties are summarized in Tab. 4.3.

The aim of this section is to provide a "**reference for construction**" for the geometries that represent the Diezma Landslide. This might be useful in future, in case the geometries have to be rebuild and introduced to another numerical modeling software or if changes in the geometry have to be made. The following steps 1-8 (cf. 4.2.2.) and steps 1-20 (cf. 4.2.3.) can be skipped while reading the thesis, since they are not necessary to understand the scientific context.

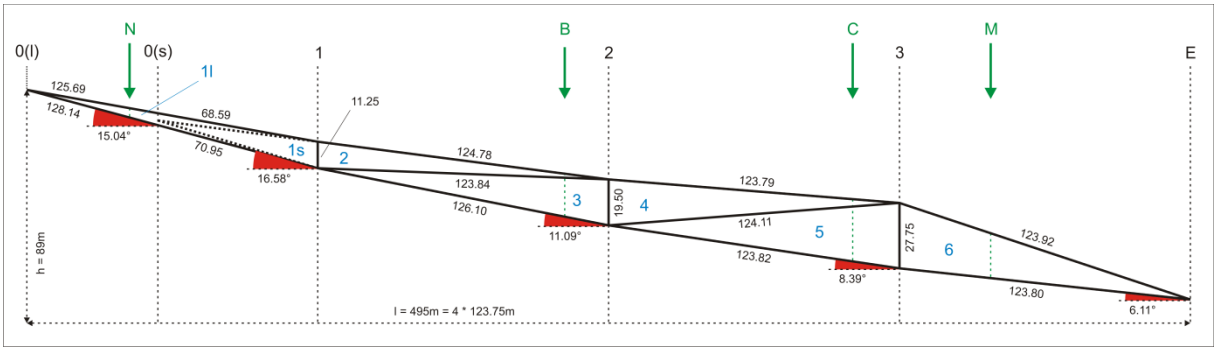

Fig. 4.8. Simplified 2D-geometry. The green arrows indicate the transposition of TCS intersections from Fig. 4.11 necessary for the creation of the simplified 3D-geometry. Blue numbers refer to the slice division used in the analysis of the factor of safety (cf. 5.4.2.). Dimensions are in meters.

TCS	direction	LCS to TCS	LCS to adopted TCS	intersection along LCS	intersection along TCS	intersection points
N	W→E	61.0°	29.0°	8.83%	50% (48.93%)	N2 = I1
B	W→E	61.0°	29.0°	46.23%	75% (76.17%)	B3 = I2
C	W→E	61.0°	29.0°	70.98%	62.08%	C2 or C3 ≠ I3
M	NW→SE	79.2°	10.2°	82.84%	50% (47.93%)	M2 = I4

Tab. 4.3. TCS properties of the simplified 3D-geometry.

1) Similar to the ideal simplified 2D-geometry for a LCS (cf. 2.4.2.), TCS were divided into four lengthwise equal slices that approximate the TCS shape. Since all four TCS were already assessed in great detail with an approximate spacing of 10 m for the fine geometry, there was no need to remeasure dimensions. The fine TCS geometries were already adjusted in height and shape to fit well to the landslide mass, and altimetric information for the topography and the sliding surface could simply be retrieved for steps at 0%, 25%, 50%, 75% and 100% of the TCS length. If existing steps did not correspond closely to either of those percentages intermediate values were adopted (as in the case of TCS N and TCS M). The thereby created simplified TCS are shown in Fig. 4.10a, Fig. 4.10b, Fig. 4.10c and Fig. 4.10d.
2) Ideally for every landslide there would be three TCS intersecting the LCS at the points 1, 2 and 3. In the case of the Diezma Landslide there are however four TCS which do not intersect the LCS at equal spacing neither with a right angle (cf. Tab. 4.3). This fact leads back to the question of what deviation angles φ between given and adopted cross sections are acceptable (cf. 2.4.1.). As Fig. 4.9 and Tab. 4.3 show, in three of four cases (TCS N, TCS B and TCS C) the angle between the LCS and the potentially adopted perpendicular TCS exceed 20°. According to section 2.4.1., this situation would need geometrical correction; however, one would have to decide if the correction would then be applied also to TCS M which actually would not need it.
   To keep things as simple as possible and comparable, the final decision on this issue was to leave the four TCS with their original intersections and original orientation relative to the LCS although the hereby created 3D-geometry does not correspond to the idealized geometry (cf. 2.4.3.).
3) More of an issue is the choice of a LCS to which the four TCS should be set in relation. On the one hand, the simplified 3D-geometry (with its four intersections) should be as

comparable as possible to the existing simplified 2D-geometry (which has only three intersections). On the other hand, all simplified TCS are taken from the AutoCAD-file and therefore a LCS (with four intersections) similar to the one presented at the end of chapter 4.2.3. would be preferable.
As a compromise, the spacing (in percent of the LCS length) between the extremities and four intersection points was transposed to the simplified 2D-geometry in order to retrieve altimetric information and to preserve the "slice-character" of the LCS (cf. Fig. 4.10e, Fig. 4.10f).

4) After equally distributing points 0-E along the TCS (in directions west to east and northwest to southeast) it became apparent that some of the points lie very close to the intersections along the LCS. Due to this vicinity TCS N, TCS B and TCS M adopted the position and altimetric information of intersections I1, I2 and I4 for their points N2, B3 and M2. In TCS C, both C2 and C3 are too far from I3, and hence C2, C3 and I3 exist separately (cf. Fig. 4.11, Tab. 4.3).
5) As explained in point 16 in chapter 4.2.3., also the altimetric information of the simplified 3D-geometry had to be adjusted in order to make close neighbor points fit to each other to preserve the local slope angles and the overall forms of the cross sections. Fortunately, here, this task was much easier than for the fine geometry and only at TCS N and TCS C slight corrections were necessary (sliding surface: N1 and N3 of 1 m downwards; topography: C1 and C3 of 4 m and 3m upwards (cf. Fig. 4.10g-l)).
6) The trace is a simple connection of all extreme points (cf. Fig. 4.11).
7) Again, a long and a short version of the landslide geometry are available.
8) Finally, x-y-coordinates had to be attributed to all points. Unlike as for the fine geometry, the relative coordinate origin was set to the first point of the LCS and the x-axis is the LCS itself. Cross sections to be used for the two volume versions are listed in Tab. 4.8.

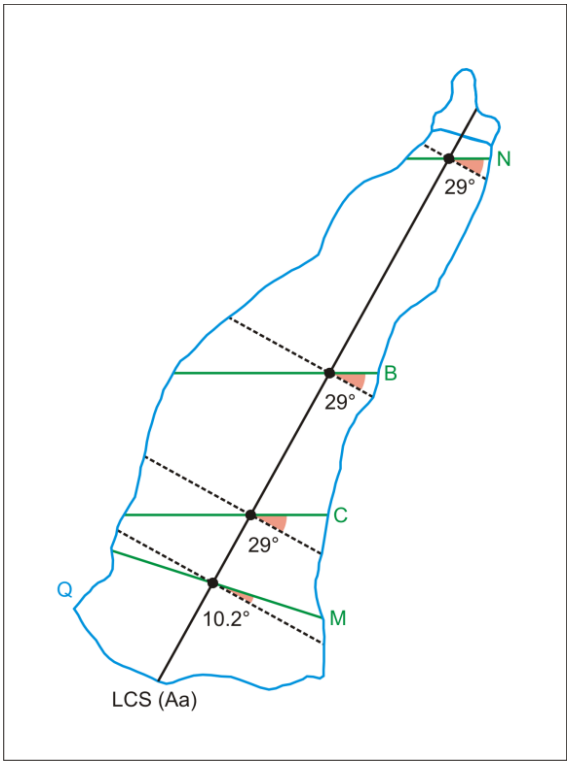

Fig. 4.9. Deviation angles between the given TCS and the potentially adopted TCS that would have to be perpendicular to LCS Aa (for the scale cf. Fig. 4.6a).

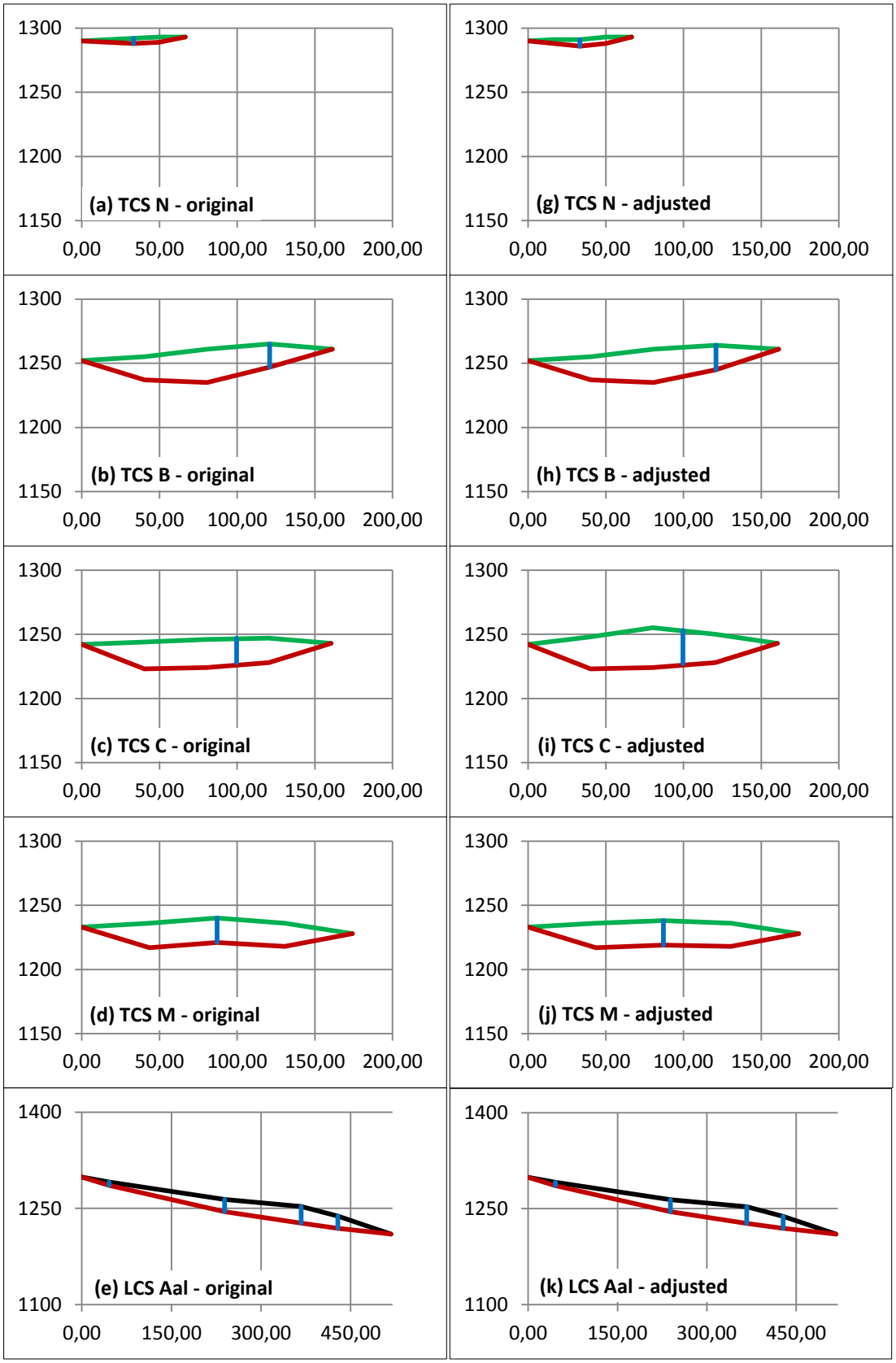
1300
1250
1200
1150
(a) TCS N - original
0,00 50,00 100,00 150,00 200,00
1300
1250
1200
1150
(g) TCS N - adjusted
0,00 50,00 100,00 150,00 200,00
1300
1250
1200
1150
(b) TCS B - original
0,00 50,00 100,00 150,00 200,00
1300
1250
1200
1150
(h) TCS B - adjusted
0,00 50,00 100,00 150,00 200,00
1300
1250
1200
1150
(c) TCS C - original
0,00 50,00 100,00 150,00 200,00
1300
1250
1200
1150
(i) TCS C - adjusted
0,00 50,00 100,00 150,00 200,00
1300
1250
1200
1150
(d) TCS M - original
0,00 50,00 100,00 150,00 200,00
1300
1250
1200
1150
(j) TCS M - adjusted
0,00 50,00 100,00 150,00 200,00
1400
1250
1100
(e) LCS Aal - original
0,00 150,00 300,00 450,00
1400
1250
1100
(k) LCS Aal - adjusted
0,00 150,00 300,00 450,00

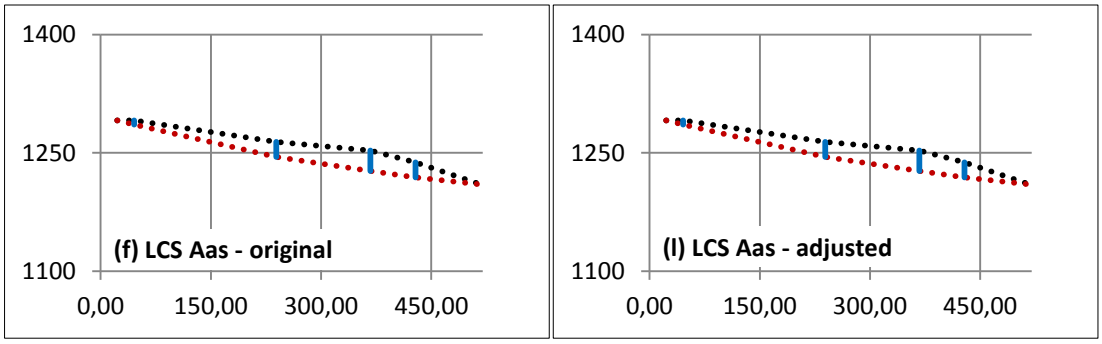

Fig. 4.10a-l. Original and adjusted cross sections for the simplified 3D-geometry (green and black lines for the topography, red lines for the sliding surface and blue lines for intersections). Dimensions are in meters.

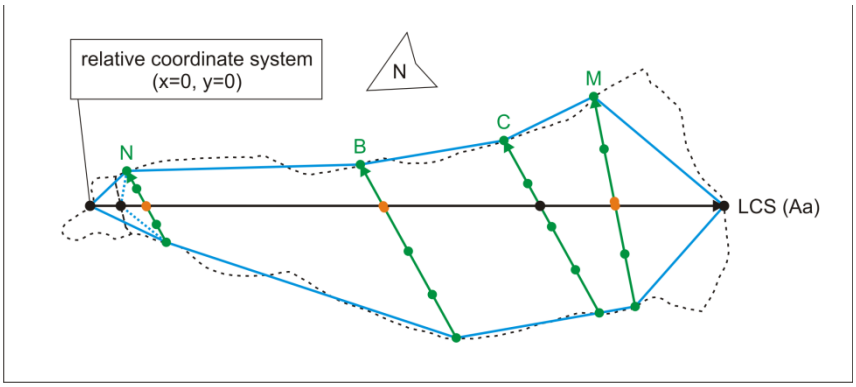

Fig. 4.11. Map of the simplified 3D-geometry (for the scale cf. Fig. 4.6a). Arrows show the numbering direction of points per cross section and orange points design intersection points. The dashed line shows the real landslide trace.

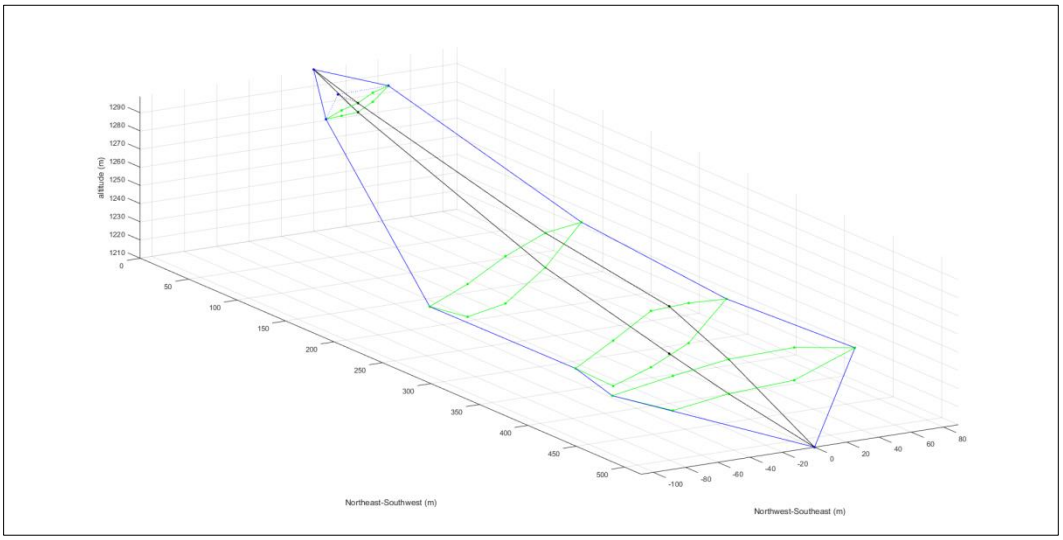

Fig. 4.12. Simplified 3D-geometry after adjustment.

At a first sight, this simplified 3D-geometry (cf. Fig. 4.12) seems very well tailored although it is clearly a sort of "hybrid". Its horizontal extents are based on the AutoCAD-file and the map, whereas its altimetric information originates from both the AutoCAD-file (for TCS) and the simplified 2D-geometry (for LCS).

By having a closer look nevertheless, a geometric misfit becomes apparent. From the simplified map (cf. Fig. 4.11) it is visible that the TCS intersect the LCS at certain percentages of the length; here reference is made to the length of the long geometry version. These percentages correspond to distances in meters as shown in Tab. 4.4. Also for the short geometry version, whose first LCS point is shifted by 22.57 m, the intersection positions remain the same and the intersection with TCS N lies – as expected – inside the short trace. However, applying the same

percentage calculation to the simplified 2D-geometry (Fig. 4.8), it appears that the intersection with TCS N lies outside of the short trace.

origin	point 0 (long)	point 0 (short)	intersect. to N	intersect. to B	intersect. to C	intersect. to M	point E
%	0.00%	-	8.83%	46.23%	70.98%	82.84%	100.00%
map	0.00 m	-	45.67 m	239.10 m	367.11 m	428.45 m	517.20 m
	-	22.57 m	45.67 m	239.10 m	367.11 m	428.45 m	517.20 m
simple 2D-geo.	0.00 m	-	43.71 m	228.84 m	351.35 m	410.06 m	495.00 m
	-	55.75 m	43.71 m	228.84 m	351.35 m	410.06 m	495.00 m

Tab. 4.4. Positions of the intersections of the LCS with the TCS for the simplified 3D-geometry.
Comparing the positions of points 0 (short) and N2 (= I1) the issue of the geometric misfit becomes apparent.

At the simplified 3D-geometry this misfit has no influence. Its length must correspond to the one of the map from which the coordinates were retrieved. Nonetheless it points out how important correct geological mapping and representation is. The small length difference of only 22.2 m is – in a figurative sense – able to displace a TCS out of the landslide mass.

4.2.3. Fine Geometry

Unlike at the simplified geometry, where the 3D effect was obtained by adding TCS later, the fine geometry was built first in 3D to extract the LCS. In the following the steps for the creation of the fine 3D-geometry will be explained; some properties are summarized in Tab. 4.5.

LCS/TCS	points	azimuth	AutoCAD	direction	end	length	spacing
N	1- 7	90.0°	61 m	W→E	fits	66.54 m	11.1 m
B	1- 17	90.0°	159 m	W→E	tight	161.28 m	10.1 m
C	1- 17	90.0°	163 m	W→E	tight	160.50 m	10.0 m
M	1- 19	108.8°	176 m	NW→SE	tight	174.16 m	9.7 m
Al	1- 47	16.0°	475 m	SW→NE	fits	484.55 m	10.5 m
As	1- 42	16.0°	424 m	SW→NE	fits	431.87 m	10.5 m
Aal	1- 47	29.0°	-	SW→NE	fits	517.12 m	11.2 m
Aas	1- 45	29.0°	-	SW→NE	fits	494.63 m	11.2 m
Ql	1-140	-	-	clockwise	-	-	~10.0 m
Qs	1-140	-	-	clockwise	-	-	~10.0 m

Tab. 4.5. LCS and TCS properties of the fine 3D-geometry.
It should be noted that in Qs points Qa-e replace points Q53-68 which exist only in Ql (cf. Fig. 4.6b).

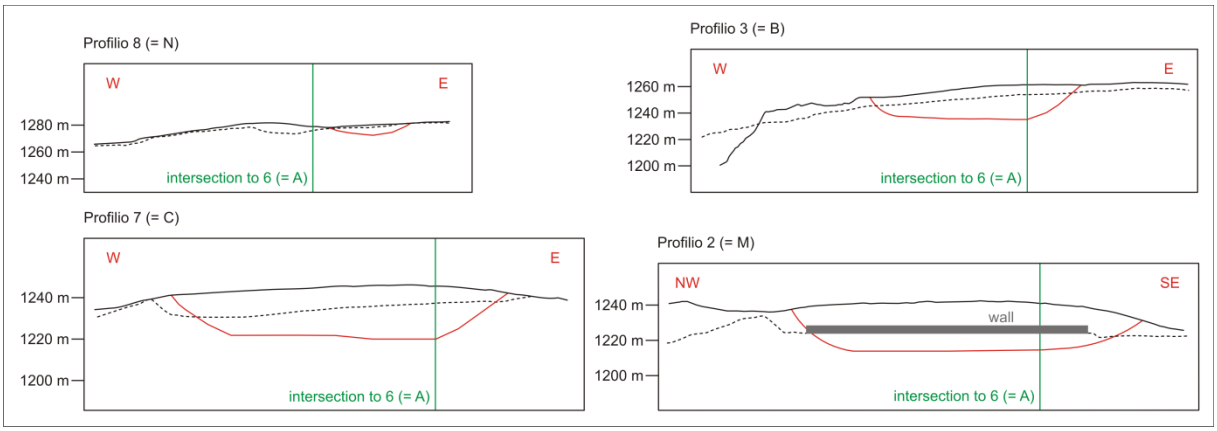

Fig. 4.13. TCS from the AutoCAD-file (after DELGADO et al., 2015).
The dotted line represents the recent topography; horizontal and vertical scales are the same.

The aim of this section is to provide a "**reference for construction**" for the geometries that represent the Diezma Landslide. This might be useful in future, in case the geometries have to be rebuild and introduced to another numerical modeling software or if changes in the geometry have to be made. The following steps 1-20 (cf. 4.2.3.) and steps 1-8 (cf. 4.2.2.) can be skipped while reading the thesis, since they are not necessary to understand the scientific context.

1) Initially the map presented in the article of DELGADO et al. (2015) was scanned to CorelDRAW and the landslide trace, the highway and the old road as well as the ground cracks were drawn as overlay (cf. Fig. 4.6a). LCS directions were aligned considering the azimuthal angles of the AutoCAD-file, which fitted well to the angles indicated in the map.
2) For simplicity, new names were given to the cross sections and the trace; according to the considered geometry version LCA A and LCS Aa are marked separately.
3) Since coordinates have to be readable from the CorelDRAW-file, and since the program is not a GIS-software, a relative coordinate system and a scale had to be defined. In the present case the relative origin was set to the top of the north arrow on the map; the x-axis is the direction west-east. As for the scale, 100 m correspond to 26 mm.
4) All cross sections from AutoCAD were printed on paper to mark the volume corresponding to the state of 1990 or before. For all TCS (cf. Fig. 4.13) this procedure was rather easy; at LCS A the issue of the final state of excavation (cf. Fig. 4.5a) had to be taken into consideration.
5) Subsequently, on each of the printed cross sections points were set every ten meters along the horizontal preferably from west to east or from south to north to extract the corresponding altimetric information. For every point, thus, there are two values available – one for the topography and one for the sliding surface. Only the first and last points of each cross section have one value because they define the intersection of the topography with the sliding surface (cf. Fig. 4.6b).
6) All points carry an identification number composed of the cross section name and their running number. Together with their corresponding altimetric information they were stored in an Excel-file.
7) For the landslide trace (named Ql or Qs according to the geometry version) points were set roughly every ten meters as well. In between additional points had to be inserted to preserve the outline of the landslide and the topographic character. Altimetric information was then manually retrieved from the geological map by interpolation between isometric lines.
8) As a matter of fact, a spacing of 10 m from one end of a cross section to the other might not necessarily result in equally spaced steps. It is even very likely that the last step will be shorter than all the previous ones. For the graphic reproduction of the respective cross section of the AutoCAD-file this fact is not disturbing; the depth value of the second last point can be taken as such and the overall shape of the cross section will be preserved. Difficulties arise when – as in the next step – equal spacing has to be introduced again. Then, all points slightly shift back towards the first point and the second last point would introduce a step altering the overall shape of the cross section (cf. Fig. 4.14).
   Luckily, only LCS B, LCS C and LCS M showed such a tight last step and to avoid the creation of depth steps of points B16 and C16 were shifted downwards by 3 m (B16: 1258 m to 1255 m; C16: 1238 m to 1235 m) in the original altimetric assessment. Point M18 was judged still acceptable.
9) Lengths of cross sections of the AutoCAD-file came very close to the lengths derived from the map. According to the number of points per cross section, the lengths obtained from the map were divided into equally spaced steps and the altimetric information was assigned to these newly located points.

10) Among all cross sections the adopted LCS Aa has a particular status. It is the only one that has no equivalent in the AutoCAD-file. Thus, it was placed manually keeping the same number of points as in LCS A so that altimetric information could transposed point by point later on. According to this, LCS A and LCS Aa have the same number of points with the same altimetric information, but a different spacing and different coordinates (cf. step 14).
11) Equal point distribution leaded to different spacing than 10 m at every cross section, but fortunately the differences were almost negligible (cf. Tab. 4.5).
12) Moreover, the new point distribution revealed points that either become intersections or lie so close to each other, that they must show the same altimetric value on the topography and on the sliding surface. Both types of points are summarized in Tab. 4.6.
13) Another particularity becomes apparent when having a closer look on the limits of LCS A and LCS Aa. According to the considered geometry version the respective LCS ends at different points, and thus the points A42 and Aa45 can be "open" or "closed". Table 4.7 specifies this fact comparing altimetric information of the sliding surface.
14) Finally, x-y-coordinates had to be retrieved for every point. They are stored with their altimetric information in the before mentioned Excel-file. A 3D-plot of the cross sections and the landslide trace was not perfect; height differences between intersection and close neighbor points were quite apparent (cf. step 4.12).

	point	12…m	point	12…m	point	12…m	corrected to
intersection points	Q8	25	M1	33			1233 m
	Q11	31	C1	42			1242 m
	Q23	45	B1	52			1252 m
	Q49	75	N1	78	A42	↑90/↓87	↑1290 m/↓1287 m
	Q64	88	Aa47	98			1298 m
	Q70	81	N7	81			1293 m
	Q93	57	B17	61			1261 m
	Q105	38	C17	43			1243 m
	Q113	23	M19	28			1228 m
	Q124	10	A1	10			1210 m
	Q132	10	Aa1	10			1210 m
	Qc	81	Aa45	↑96/↓94			↑1296 m/↓1294 m
close neighbor points	A7	↑45 ↓19	M15	↑35 ↓14			↑1236 m ↓1218 m
	A14	↑51 ↓28	C15	↑45 ↓30			↑1247 m ↓1228 m
	A25	↑64 ↓46	B14	↑61 ↓41			↑1264 m ↓1246 m
	Aa9	↑47 ↓21	M10	↑37 ↓12			↑1240 m ↓1221 m
	Aa14	↑51 ↓28	C11	↑46 ↓20			↑1247 m ↓1228 m
	Aa26	↑66 ↓47	B13	↑61 ↓37			↑1265 m ↓1247 m
	Aa43	↑92 ↓88	N4	↑80 ↓73			↑1292 m ↓1228 m

Tab. 4.6. Original and corrected altimetric information for intersection and close neighbor points. Arrows upwards and downwards refer to the topography and the sliding surface respectively. It should be noted that points A42 and Aa45 also have a "lower" value because they can be "open" or "closed" (cf. Tab. 4.7).

altimetry (m)	point 41	point 42	point 45	point 47
LCS	-	end As	end Aas	end Al & Aal
Al	↑1288 ↓1284	↑1290 ↓1287	↑1296 ↓1294	↑1298 ↓1298
As	↑1288 ↓1284	↑1290 ↓1290	- -	- -
Aal	↑1288 ↓1284	↑1290 ↓1287	↑1296 ↓1294	↑1298 ↓1298
Aas	↑1288 ↓1284	↑1290 ↓1287	↑1296 ↓1296	- -

Tab. 4.7. Differences between "open" and "closed" points along LCA A and LCA Aa.

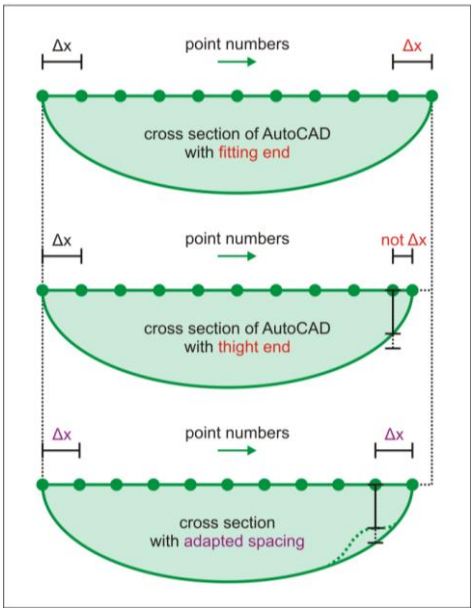

Fig. 4.14. Possible introduction and prevention of steps in the cross section by shifting points backwards during the process of equal spacing.

To bring intersection and close neighbor points together several further steps were necessary:

15) The trace Q was the most unproblematic to be shifted vertically. The altimetric information of the points had been obtained by isoline interpretation on the geological map (cf. Fig. 4.3), which shows a recent state of the slope, and hence the state that does not correspond any more to the one of 1990. Preferably, Q-points were shifted upwards accounting for the idea that the topography decreased with time due to sliding and excavation activity. Corrected altimetry information can be found in Tab. 4.6. For completion it should be noted, that the cross sections were less preferable to be shifted vertically since their altimetric information was retrieved from borehole loggings.
16) After the correction of the intersection points, also the ultimate neighbor points (not to be confounded with the close neighbor points of Tab. 4.6) of the shifted points had to be adjusted to preserve the local topography along the trace and the overall forms of the cross sections. The thereby created fine LCS and TCS are shown in Fig. 4.15a-h.
17) Contrasting to what is mentioned at step 15, TCS N had to be shifted upwards by about 12 m (cf. Fig. 4.15a, 4.15i). Comparing its position to LCS A, to LCS Aa and to the trace Q, it appears that it lies far too deep. Simple adjustment as explained in steps 15 and 16 and keeping the greatest depths in the middle of the cross section would significantly change the shape of the cross section. The crescent shape would turn into a U-shape causing the whole landslide to become gutter-like in the crown zone which is obviously not the case.

18) Also the close neighbor points (cf. Tab. 4.6) had to be adjusted in a similar way to avoid notches and spikes in the topography and in the sliding surface when creating a numerical model at a later stage. Here, TCS were modified more freely than the LCS. To optimize the comparability between geometries, differences between LCS thus have to be kept as low as possible (cf. Fig. 4.15i-p).
19) LCS A served initially only for the assessment of values that would later be attributed to LCS Aa. However, it indeed exists and during the process of adjustments it was considered like all other cross sections. Its short version (LCS As) can therefore be used as additional information when creating enveloping surfaces (i.e. sliding and ground surfaces). Cross sections to be used for the long and the short volume version are listed in Tab. 4.8.
20) Another 3D-plot of the cross sections and the landslide trace shows now a satisfying result (cf. Fig. 4.16).

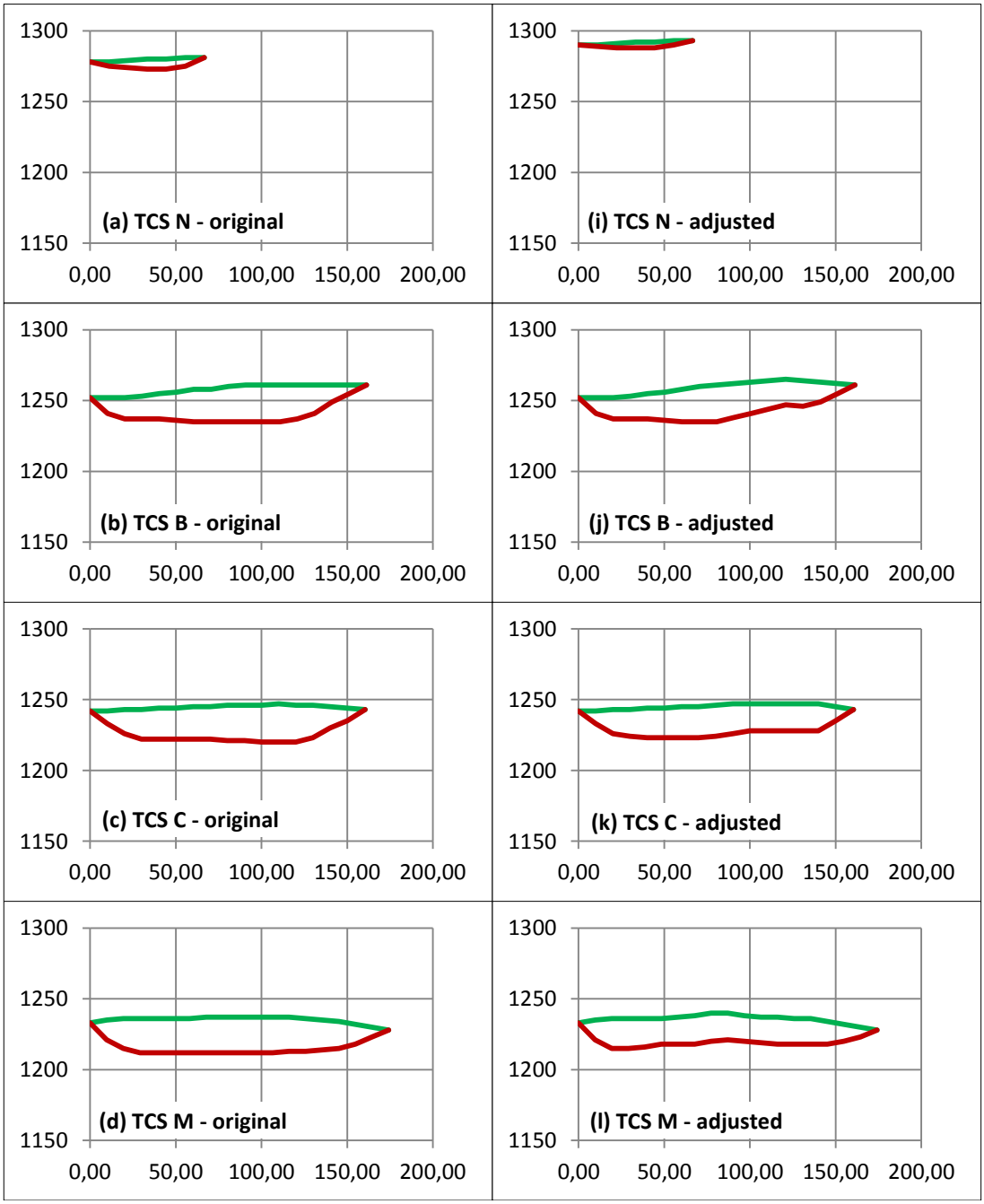

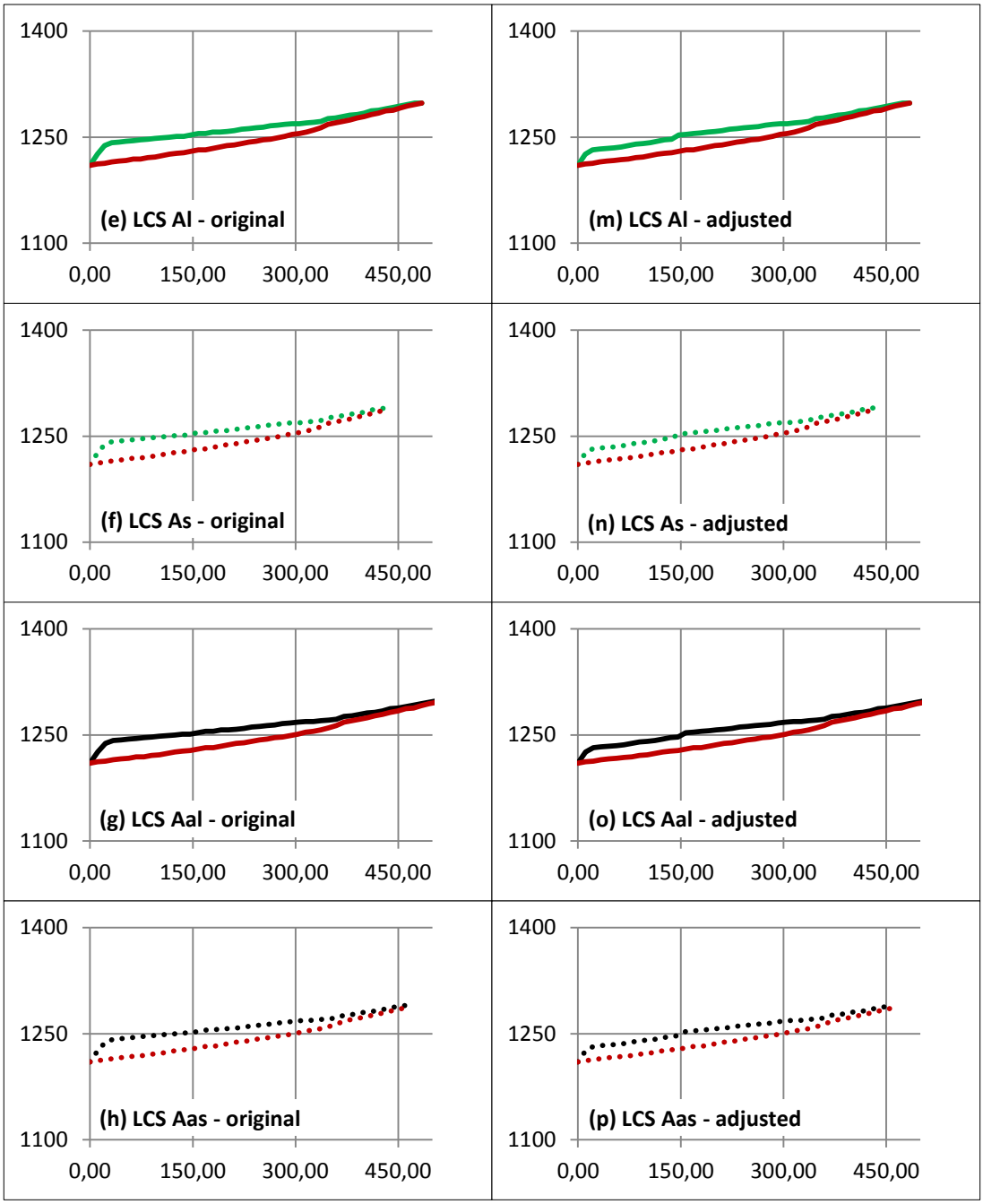

Fig. 4.15a-p. Original and adjusted cross sections for the fine 3D-geometry (green and black lines for the topography, red lines for the sliding surface and blue lines for intersections). Dimensions are in meters.

The LCS Aa for 2D-analyses can be simply extracted. According to the desired geometry version it looks either like LCS Aal or LCS Aas as presented in Fig. 4.15o and Fig. 4.15p. The long (LCS Aal) and the short version (LCS Aas) can be then seen as the fine counterparts to the long and the short simplified 2D-geometries described in the previous section (cf. Fig. 4.8).

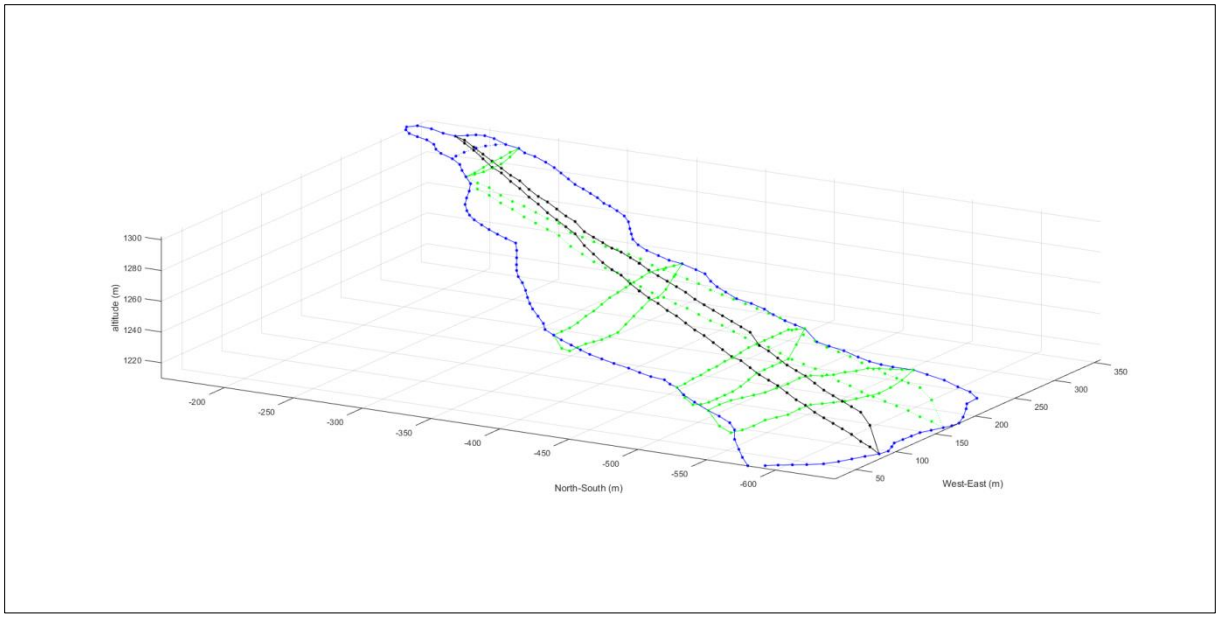

Fig. 4.16. Fine 3D-geometry after adjustment.

cross section	fine geometry		simplified geometry	
	long version	short version	long version	short version
N	✓	✓	✓	✓
B	✓	✓	✓	✓
C	✓	✓	✓	✓
M	✓	✓	✓	✓
Al	-	-	-	-
As	(✓)	(✓)	-	-
Aal	✓	-	✓	-
Aas	-	✓	-	✓
Ql*	✓	-	✓	-
Qs*	-	✓	-	✓

Tab. 4.8. Cross sections belonging to the long and the short geometry version.
Ql and Qs design the long and short version of the traces (*).

4.3. Possibilities to Analyze Displacement

In section 4.1. the Diezma Landslide was characterized as active and regularly affected by rising ground water within the landslide mass. It was mentioned that also earthquakes are considered as potential triggers to cause reactivation and sudden slope failures. In this thesis, the objective is to investigate the effects of earthquakes on the landslide mass by evaluating expected displacements with different methods. Detailed explanation of those methods will be given in the respective chapters.
Section 4.2. presented the different options to create geometries for the Diezma Landslide. Taking into account that a geometry can be long or short (cf. 4.2.1.), simplified or fine (cf. 4.2.2., 4.2.3.) and 2D or 3D (cf. 4.2.2., 4.2.3.), there are a variety of possibilities to analyze the expected displacement. According to the principles of the methods, suitable input geometries must be chosen; options are shown in Tab. 4.9 which represents the “task sheet” of the thesis and a figurative table of contents for the following chapters.

dimension and method		simplified geometry		fine geometry	
2D	NEWMARK (1965) (with SLAMMER)	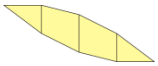 long ✓	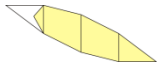 short ✓	 long not to be divided into slices	 short not to be divided into slices
2D	modal recombination (with CESAR-LCPC)	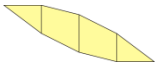 long ✓	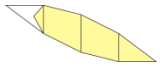 short too time-consuming	 long too time-consuming	 short too time-consuming
2D	finite difference analysis (with FLAC)	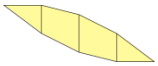 long ✓	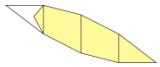 short ✓	 long ✓	 short ✓
3D	modal recombination (with CESAR-LCPC)	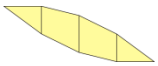 long ✓	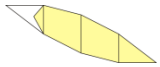 short too time-consuming	 long too time-consuming	 short too time-consuming
3D	finite difference analysis (with FLAC)	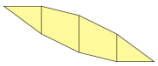 long ✓	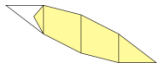 short ✓	 long ✓	 short ✓

Tab. 4.9. Options to analyze expected displacement under seismic shaking with different geometries. The shape of the LCS is only symbolic; i.e. it does not show real dimensions.

4.4. Applied Signals

To estimate ground displacements of the landslide during seismic shaking either synthetic signals or real accelerometric records can be used. In this thesis, earthquake signals were retrieved from European Strong-Motion Database (in the following abbreviated by ESMD; AMBRASEYS et al., 2004) – a database containing corrected acceleration, velocity and displacement time-histories of 462 triaxial strong-motion records of 110 earthquakes and 261 stations in Europe and the Middle East. Suitable accelerometric records were filtered from the ESMD with respect to the following criteria:

→ horizontal components — x- and y-records only (NS and WE respectively)
→ AI: 0.1-1 m/s — Arias Intensity expected in Southern Spain
→ M_W: 5.0-7.0 — moment magnitude expected in Southern Spain
→ PGA: 0.8-1.2 m/s^2 — peak ground acceleration expected in Southern Spain (0.1g ±20%)

These assumptions are in accordance with earthquake characteristics given by several authors (DELGADO et al., 2015; LENTI, MARTINO, 2012; MARTÍNEZ-SOLARES et al., 2013) and clearly display favorable conditions for a possible reactivation of the Diezma Landslide (MARTINO et al., 2016). MARTÍNEZ-SOLARES et al. (2013) indicate a PGA of 0.16g for a return period of 475

years while BENITO et al. (2010) give a critical acceleration (beyond which the landslide becomes unstable) of 0.10g. As section 5.4.4. will show, critical accelerations might be even lower than this estimation. RODRÍGUEZ-PECES et al. (2011) speak of significant hazard when earthquakes of M_W 4.0-5.0 might occur in a radius of 25 km. However, DELGADO et al. (2015) as well as MARTINO et al. (2016) indicate that no earthquake with $M_W > 5.0$ took place within a radius of 50 km since the main failure of the Diezma Landslide in 2001; according to the curves proposed by KEEFER (1984; cf. 3.3.1.) the distance at which epicenters for earthquakes with moment magnitudes between 5.0 and 7.0 could be located at a maximum distance of 100 km.
After applying the filter, characteristic earthquake periods (T_m) were calculated for the 13 obtained records using the equation proposed by SCHNABEL (1973) and RATHJE et al. (2004):

$$T_m = \frac{\sum {A_i}^2 \cdot \frac{1}{f_i}}{\sum {A_i}^2} = \frac{1}{F_m}$$

for $0.25\ \text{Hz} \leq f_i \leq 20\ \text{Hz}$
and where A_i is the spectral amplitude associated to the i^{th} value
of the Fast Fourier Transform (FFT) and f_i is the i^{th} frequency

(a)	ESMD ID	earthquake	date	time (UTC)	duration (s)	hypocenter (km)
A	000049x	Friuli	1976-05-06	20:00:13	19.91	7
B	000133x	Friuli (aftershock)	1976-09-15	03:15:19	10.24	5
C	000127x	Friuli (aftershock)	1976-09-15	03:15:19	5.76	5
D	000294x	Campano Lucano	1980-11-23	18:34:52	49.93	16
E	000335x	Alkion	1981-02-25	02:35:53	15.62	8
F	001875x	Griva	1990-12-21	06:57:43	7.75	1
G	006142x	Aigion	1995-06-15	00:15:51	23.27	10
H	000599x	Umbria Marche	1997-09-26	00:33:16	11.37	7
I	000612x	Umbria Marche	1997-09-26	09:40:30	29.70	6
J	000625x	Umbria Marche (ash.)	1997-10-06	23:24:00	15.29	7
K	005820x	Strofades	1997-11-18	13:07:41	16.43	10

(b)	ESMD ID	log M_0 (Nm)	M_W	M_S	PGA (m/s^2)	PGV (m/s)	PGD (m)	AI (m/s)	T_m (s)	F_m (Hz)
A	000049x	18.80	6.53	6.50	0.6141	0.0806	0.0151	0.12	0.6673	1.50
B	000133x	18.06	6.04	6.06	1.0714	0.0982	0.0191	0.12	0.6527	1.53
C	000127x	18.06	6.04	6.06	1.0333	0.0483	0.0043	0.14	0.3028	3.30
D	000294x	19.39	6.93	6.87	0.9122	0.1751	0.0601	0.27	1.0749	0.93
E	000335x	18.57	6.38	6.37	1.1449	0.1108	0.0338	0.22	0.7708	1.30
F	001875x	18.23	6.15	6.12	0.9766	0.1102	0.0110	0.13	0.5830	1.72
G	006142x	18.78	6.52	6.34	0.8039	0.1384	0.0428	0.19	0.9941	1.01
H	000599x	17.58	5.72	5.50	0.9615	0.0511	0.0068	0.13	0.3796	2.63
I	000612x	18.06	6.04	5.90	0.9278	0.1374	0.0489	0.23	1.1496	0.87
J	000625x	17.37	5.58	5.20	1.0460	0.0674	0.0076	0.12	0.4796	2.09
K	005820x	18.95	6.64	6.50	0.6954	0.0705	0.0159	0.13	0.7513	1.33

Tab. 4.10a-b. Properties of the 11 considered earthquakes. The Umbria Marche Earthquake (000599x) corresponds to the earthquake entry under number EQ.176.02 in the database of the thesis.
Peak ground acceleration, peak ground velocity and peak ground displacement are also shown in Fig. 4.18a-k.
Signals here are unfiltered; a comparison between unfiltered and filtered signals is to be found in Tab. 4.11.

For both the x-components as well as for the y-components of the triaxial records the T_m appeared to be almost equally distributed (0.30-1.15 and 0.33-1.26 respectively; cf. Fig. 4.19), so finally – and to keep the selection consistent within itself – only the x-components of the earthquake records were retained. Two of the 13 records were discarded because their Arias Intensities slightly did not fit to the mean value of the other 11 records (cf. Fig. 4.18a-k). Details and properties of those remaining 11 records are to be found in Tab. 4.10a and Tab. 4.10b. It should be noted that even though one filter criterion is a PGA between 0.8 m/s^2 and 1.2 m/s^2, two signals (000049x and 005820x) have a PGA smaller than that. The reason is that for every earthquake parameter the search tool of the ESMD filters according to the biggest value of all three components, i.e. here the PGA of the y-component is bigger than 0.8 m/s^2. The column "ID" indicates the signal name as it is used during the numerical modeling processes, whereas the ESMD ID is the identification code of the respective signal in the database. The duration refers to the time interval between the exceedances of the Arias Intensity at 5% and 95% (TRIFUNAC & BRADY, 1975).
Surely one might argue that all 11 earthquakes are rather distant and not linked to the tectonic setting of Southern Spain (cf. Fig. 4.17) and that therefore they might not be suitable to use for studying the Diezma Landslide. However, due to the above mentioned filtering, these 11 earthquakes are very comparable in terms of energy and frequency content to what can be expected in Southern Spain. The actual distance between the landslide and the epicenter and the duration became hence less important. Moreover, there are no recent records of strong earthquakes available as cited by DELGADO et al. (2015) and MARTINO et al. (2016). F_m-values appear to be reasonably variable representing close and distant sources; and also T_m-values – as the inverse of F_m – are covering an acceptable range necessary for comparative displacement studies according to the Characteristic Period Based Approach (MARTINO et al., 2016; cf. 6.4.2.).

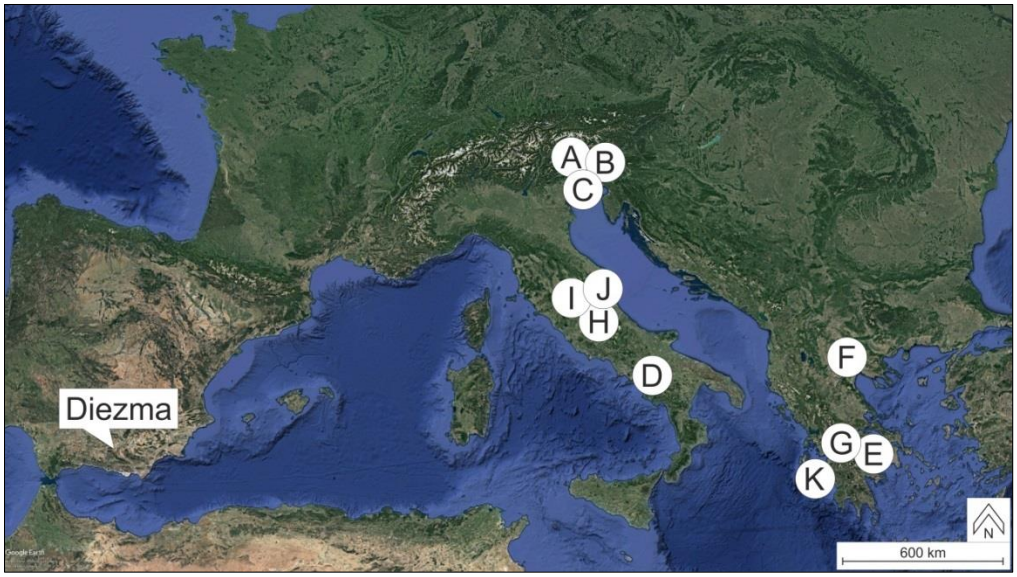

Fig. 4.17. Locations of the 11 considered earthquakes and the Diezma Landslide (after GOOGLE EARTH PRO, 2017).

Such parametric studies based on the Characteristic Period Based Approach of expected ground displacement were first carried out by LENTI & MARTINO (2013) and MARTINO et al. (2016). In the first mentioned publication the authors investigate the local seismic response of six theoretical slopes with different slope angles (15°, 35° and 45°) and two sliding mechanisms (translational and roto-translational). The height differences of all six slopes are of 100 m. Here, the Diezma Landslide is comparable to the setting of a roto-translational slide with a slope angle of 15°; its real height difference amounts to 100 m as well (cf. 4.2.1.). In the second mentioned publication the authors compare the Güevéjar Landslide and the Diezma Landslide as real cases. In both studies, the theoretical one and the real one, the LEMA_DES procedure (Levelled-Energy Multi-frequential Analysis for deriving Dynamic Equivalent Signals; LENTI & MARTINO, 2010) was applied. This procedure defines multi-frequential dynamic equivalent signals on the basis of

real accelerograms. It thus creates accelerometric time-histories that are less complex than the real accelerograms but nevertheless provides spectral, kinematic and energetic equivalence in terms of the Fourier Amplitude Spectrum, the phase and the response spectra, the Arias Intensity as well as the peak ground acceleration, the peak ground velocity and the peak ground displacement. Due to their straightforwardness such equivalent signals are particularly suitable for numerical geotechnical modeling of induced seismic effects. Soil sample testing, shaking table and centrifuge applications and numerical simulations become significantly less complicated and time-consuming (LENTI & MARTINO, 2010).
Nevertheless, in this thesis only real signals were used. This decisions is justifies by the fact that first, for one of the 11 remaining signals (001875x) the LEMA_DES signal transformation was not to be completed due to a non-convergence of the procedure. Second, comparing the original with the equivalent T_m-values an unsystematic shift appears between them; equivalent T_m-values are bigger than original ones (cf. Fig. 4.19). Moreover, it might be of interest if applying real signals to the Diezma Landslide delivers similar results to those obtained by MARTINO et al. (2016) who used the LEMA_DES procedure for studies at the same location.

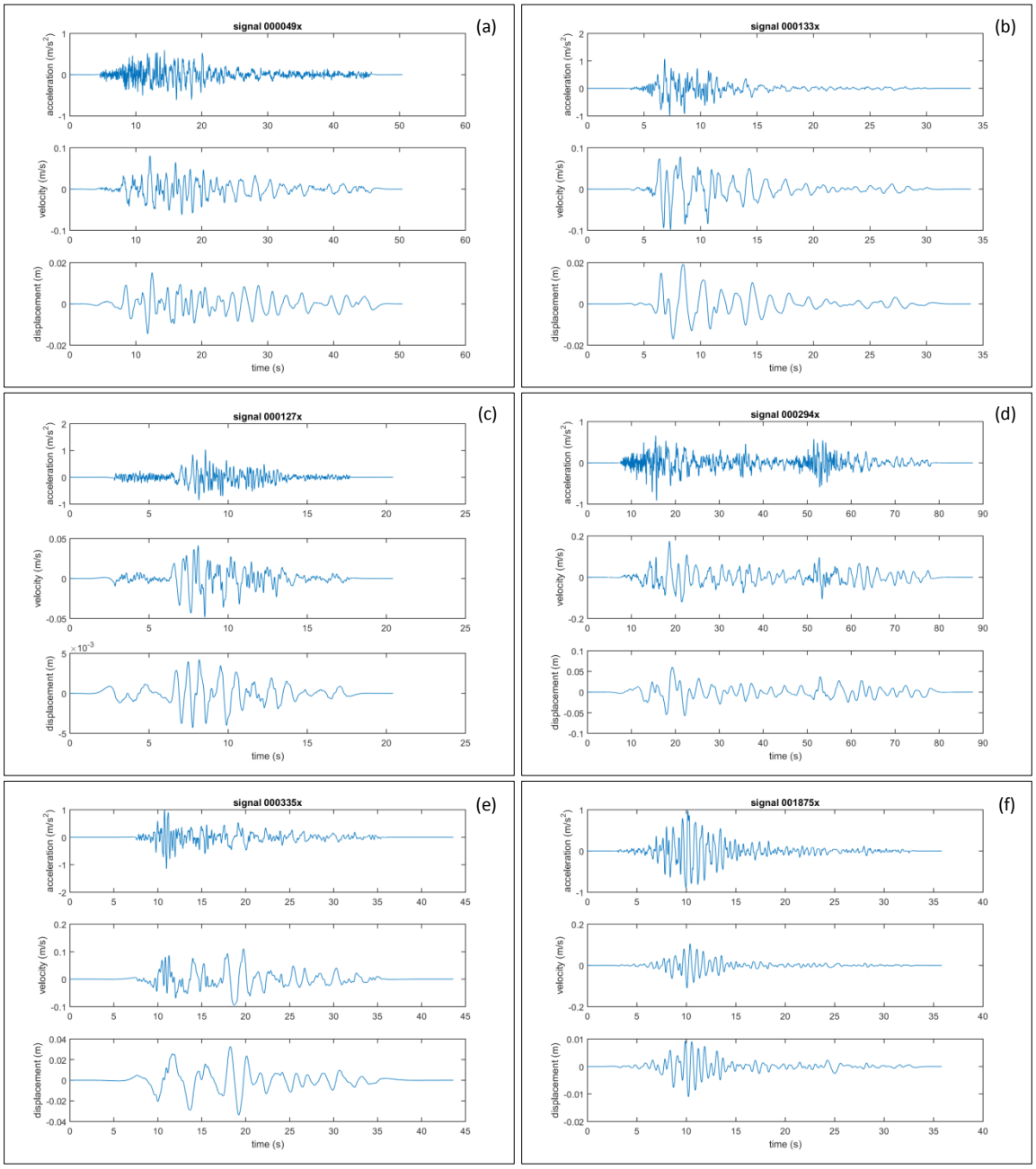

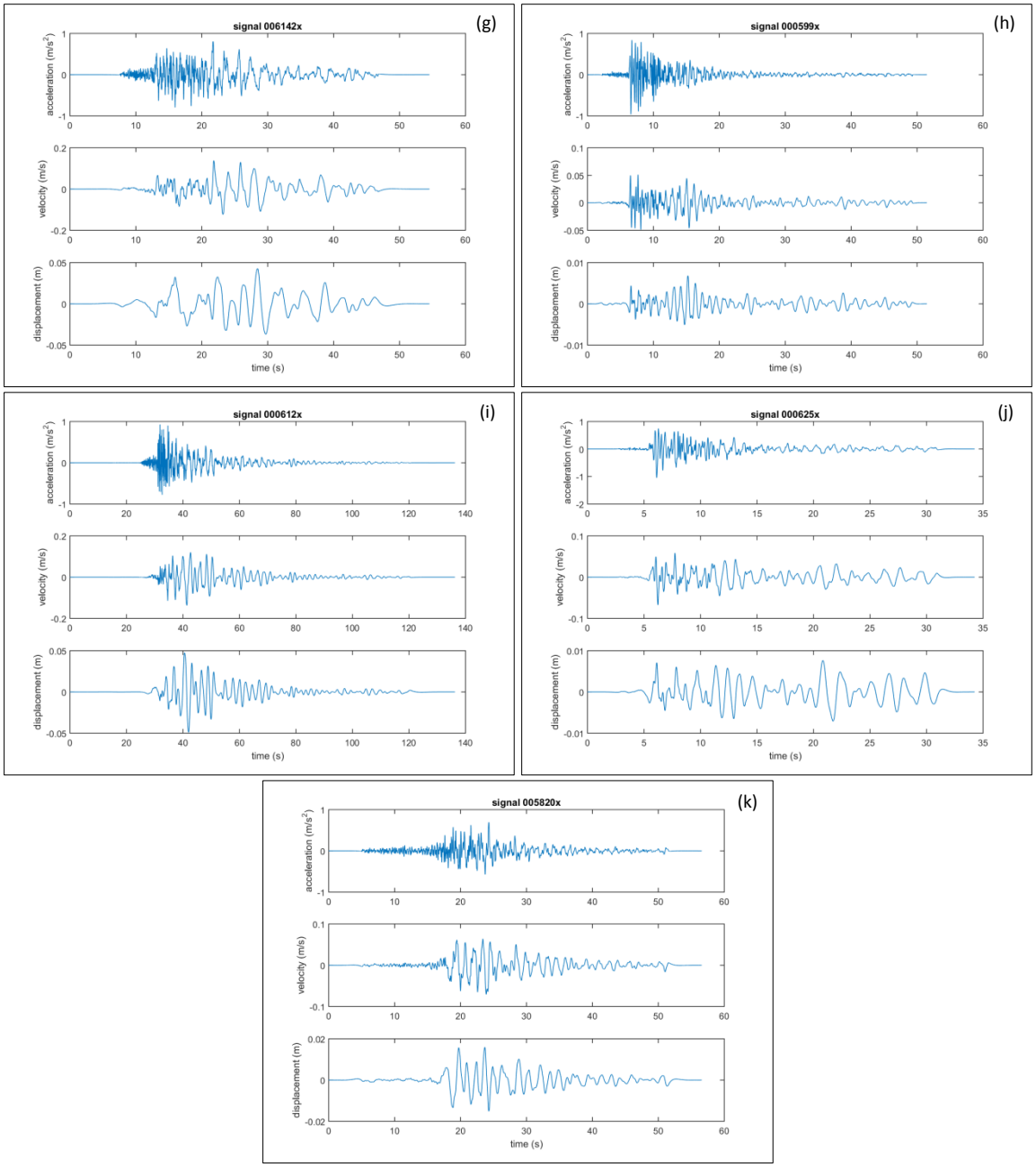

Fig. 4.18a-k. Original time-histories of the 11 considered earthquake signals. Peak ground acceleration, peak ground velocity and peak ground displacement are also shown in Tab. 4.10b. It should be noted that the filtered time-histories are so similar to these original ones, that a difference cannot be seen with bare eyes.

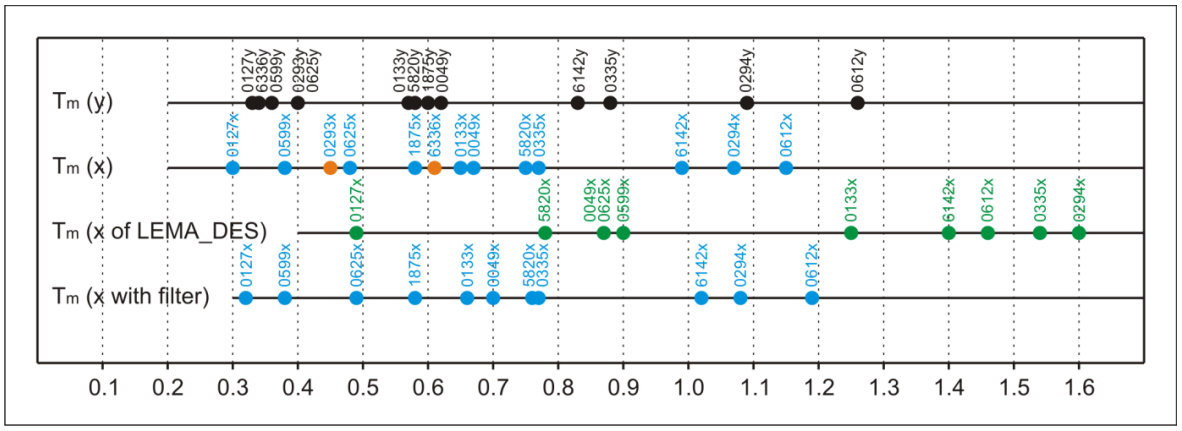

Fig. 4.19. Values of the characteristic period (T_m); the two orange dots refer to the discarded signals.

As Tab. 4.9 shows, the same set of signals is to be applied to the Diezma Landslide using three different methods to calculate ground displacement. Here, two issues are of particular importance. First, every method requires a different input:

- modal recombination (2D & 3D) needs displacement time-histories
- simplified Newmark (1965) (2D) needs acceleration & velocity time-histories
- traditional Newmark (1965) (2D) needs acceleration time-histories
- finite difference analysis (2D & 3D) needs velocity time-histories

Second, the methods have different requirements concerning the frequency content and the 11 signals must be suitably filtered to satisfy the conditions of all three methods. Unlike for the Newmark-Method (1965), for modal recombination analysis in CESAR-LCPC and especially in the finite difference software FLAC a mesh with a specific mesh-size has to be defined. To allow for correct wave propagation through the model without major disturbances this mesh-size is given by the following equation where Δl is the size of one element of the mesh which is linked to the maximum frequency of the applied signal and the minimum shear wave velocity.

$$\Delta l \leq \frac{v_{s\_min}}{10 \cdot f_{max}}$$

From section 4.1. it can be seen that the average shear wave velocity (v_s) is 300 m/s. This velocity will also be taken as minimum velocity for numerical models with FLAC (cf. 7.), whereas for modal recombination analysis the lowest velocity is 100 m/s (cf. 6.).
Returning to the above mentioned equation, and considering FLAC – being the most frequency sensitive method – a suitable element size and a maximum frequency can be found via the following consideration:

$$10\ m \leq \frac{300\ ^{m}/_{s}}{10 \cdot f_{max}\ Hz} \qquad \Delta l \leq \frac{300\ ^{m}/_{s}}{10 \cdot 10\ Hz}$$

$$f_{max} \leq 3\ Hz \qquad \Delta l \leq 3\ m$$

ID	ESMD ID	original signals				filtered signals				equivalence (%)			
		T_m	PGA	PGV	PGD	T_m	PGA	PGV	PGD	T_m	PGA	PGV	PGD
A	000049x	0.67	0.61	0.08	0.02	0.70	0.60	0.08	0.02	96	102	100	100
B	000133x	0.65	1.07	0.10	0.02	0.66	1.08	0.10	0.02	99	99	100	100
C	000127x	0.30	1.03	0.05	0.00	0.32	0.96	0.05	0.00	94	108	102	100
D	000294x	1.07	0.91	0.18	0.06	1.08	0.92	0.18	0.06	99	99	100	100
E	000335x	0.77	1.14	0.11	0.03	0.77	1.11	0.11	0.03	99	103	100	100
F	001875x	0.58	0.98	0.11	0.01	0.58	0.99	0.11	0.01	100	99	100	100
G	006142x	0.99	0.80	0.14	0.04	1.02	0.82	0.14	0.04	98	99	99	100
H	000599x	0.38	0.96	0.05	0.01	0.38	0.97	0.05	0.01	99	99	101	100
I	000612x	1.15	0.93	0.14	0.05	1.19	0.87	0.14	0.05	97	106	100	100
J	000625x	0.48	1.05	0.07	0.01	0.49	1.07	0.07	0.01	99	98	101	100
K	005820x	0.75	0.70	0.07	0.02	0.76	0.69	0.07	0.02	99	100	100	100

Tab. 4.11. Comparison between original and filtered signals. Units are the same as in Tab. 4.10a & Tab. 4.10b.

Adopting an element size of 10 m corresponding roughly to the resolution of the fine 3D-geometry (cf. 4.2.3.) would entail a maximum frequency of 3 Hz. However, the Fourier Amplitude Spectra (cf. Fig. 4.20a-k) show that a cut-off at 3 Hz is by far too low to comprise the relevant frequency content. In contrast, a maximum frequency of 10 Hz seems rather reasonable.

The element size in this case reduces to 3 m (or smaller) which is still acceptable. All 11 signals have thus undergone a 4th-order low-pass Butterworth Filter with a cut-off frequency of 10 Hz.

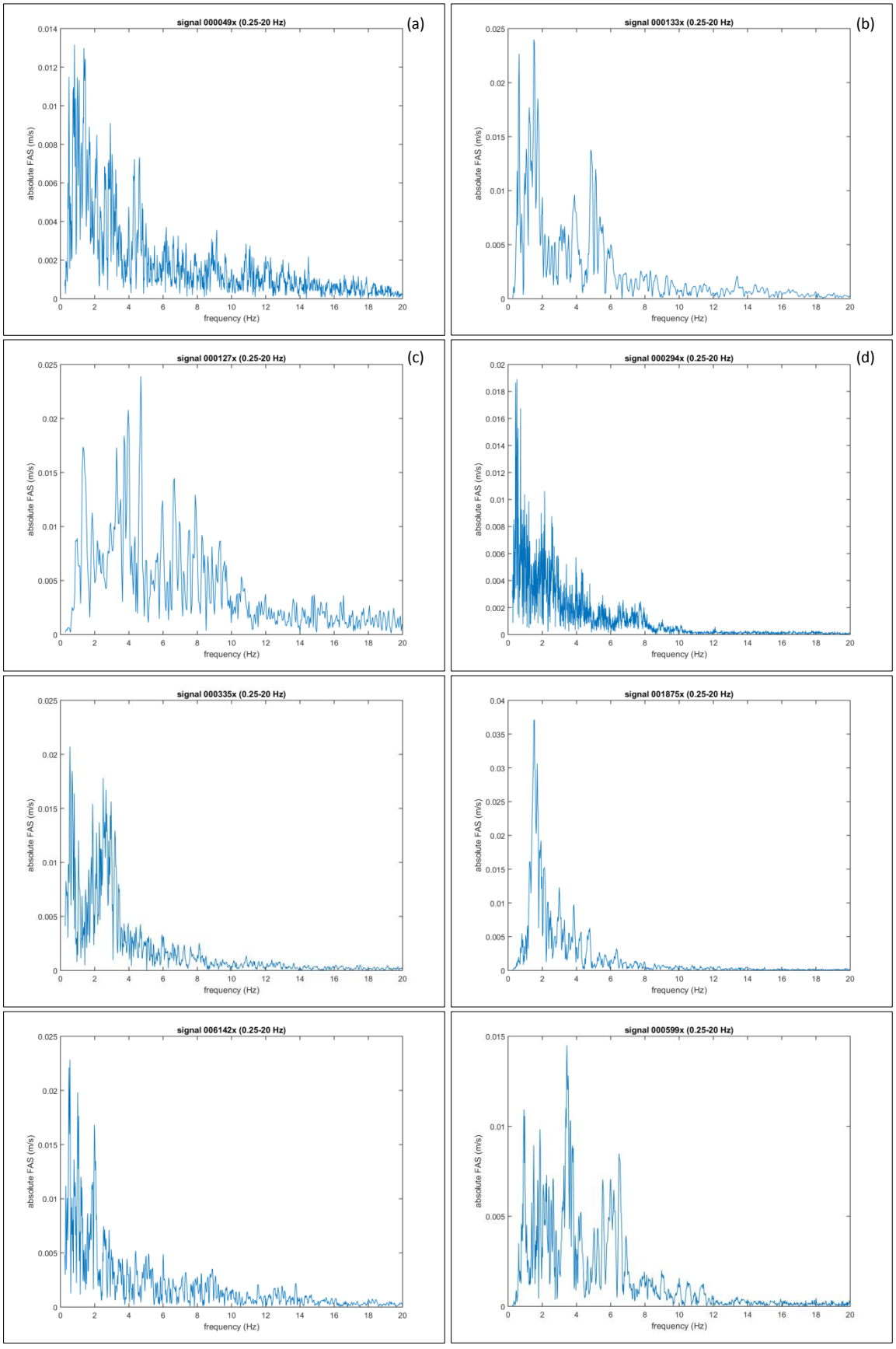

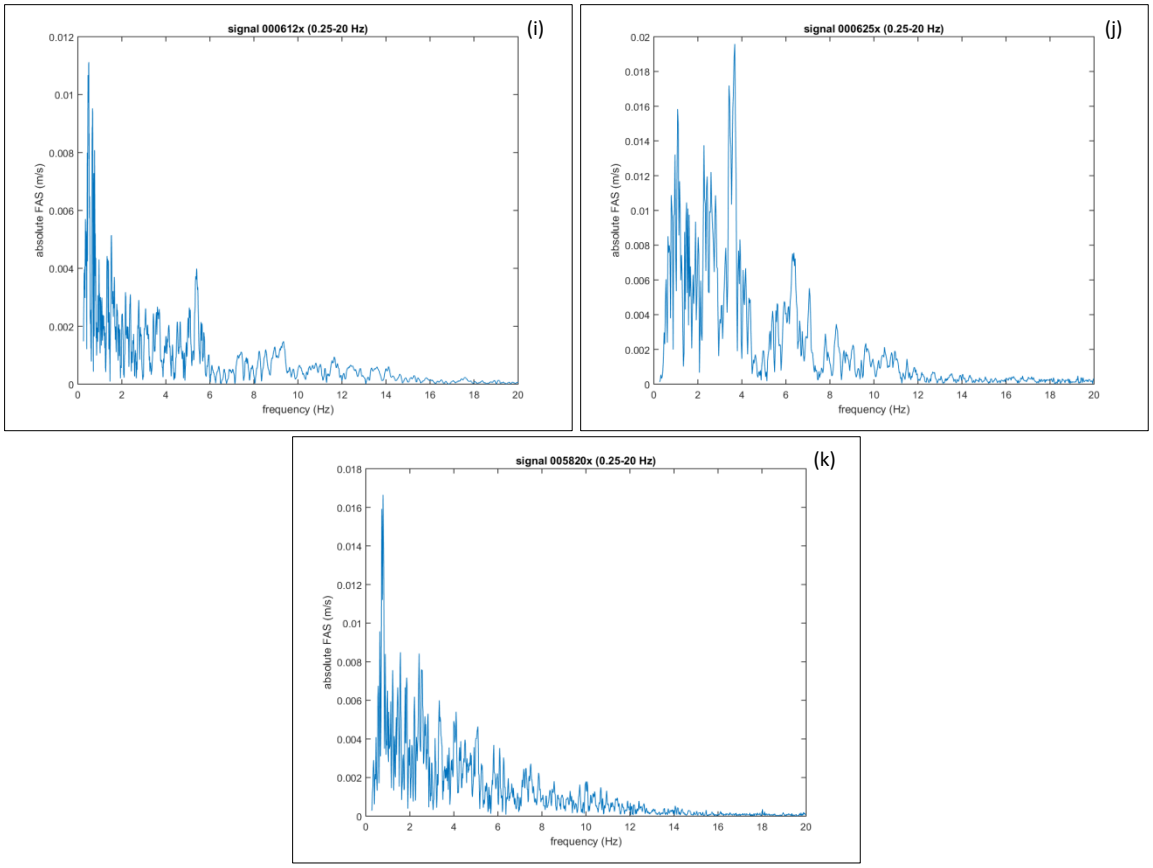

Fig. 4.20a-k. Fourier Amplitude Spectra of the original time-histories of the 11 considered earthquake signals. It should be noted that the Fourier Amplitude Spectra of the filtered time-histories are so similar to these original ones, that a difference cannot be seen with bare eyes.

To verify the equivalence between the original and the filtered signals values of T_m, PGA, PGV and PGD were compared (cf. Tab. 4.11, Fig. 4.19). It appeared that both signal types are very similar to each other and a difference cannot be seen with bare eyes neither in the time-histories nor in the Fourier Amplitude Spectra. Filtering with a cut-off frequency of 3 Hz would probably have caused significantly bigger changes.
In the following chapters (cf. 5., 6., 7.) as well as in the conclusive chapter (cf. 8.) all analyses are based on the filtered signals, and – once again – one should not confound the two types of filters presented in this chapter:

- the filter consisting of four criteria (cf. 4.4.) that was applied to the ESMD in order to retrieve the original 11 strong-motion records
- the 4th-order low-pass Butterworth Filter with a cut-off frequency of 10 Hz that those 11 strong-motion records have undergone

With "filtered signals" reference is made to the second filter – i.e. to the processed signals. However, since filtered time-histories and Fourier Amplitude Spectra are so similar to their original counterparts (cf. Fig. 4.18a-k, Fig. 4.20a-k), visual comparisons in the following chapters (cf. 5., 6., 7., 8.) are made to these "non-processed" (original) time-histories and Fourier Amplitude Spectra. Exceptionally, velocity-time-histories in Fig. 7.10a-f and Fig. 7.22a-d are shown indeed in their filtered versions.

CHAPTER 5
NEWMARK-ANALYSIS

5.1. Introduction

Static and seismic slope stability describes the potential of a slope to withstand or undergo movements. In particular, failures by sliding are of interest. The resistance to this kind of failure is determined by the regime of stress and strain within a concerned slope. An increase of shear stress (e.g. external loads, lateral pressure or transient forces) as well as a decrease of shear strength (e.g. weathering, toe cuts or changes of pore water pressure) might bring the stress-strain regime out of balance and induce a failure. For example, after a heavy rain event the pore water pressure across a sliding surface increases reducing normal stress and friction. At the same time the weight of the sliding mass itself increases due to water saturation. Both conditions then favor the triggering of a landslide.
To analyze static and seismic slope stability a multitude of methods and numerical codes are nowadays available. All of them have their conditions, hypotheses, limitations, advantages and disadvantages as well as fields of suitable application. Particular care has thus to be taken when choosing the right method for a distinct problem to properly include geological and geotechnical information, soil properties, the groundwater regime and the seismicity at the site.
In this part of the thesis the focus will be on the concept of limit equilibrium for static and seismic slope stability analyses considering mainly the aspects of stratigraphy and the hydraulic state of a slope. The aspects of stress-strain behavior, volume change and time will be treated in chapters 6. and 7. later on.

5.2. Static Slope Stability

Static slope stability describes whether natural or artificial slopes (such as embankments, cuts or mining pits) are to be considered safe or unsafe under static conditions. Equilibrium is ensured when the available shear strength exceeds the shear stress. In the contrary case, the slope becomes unstable.
Comparing methods of seismic (cf. 5.3.) and static slope stability analysis, it appears that the former relies on the latter. In many cases the additional dynamic stress necessary for inducing a landslide can be even very small, especially when the difference between shear stress and shear strength is not very large. Due to this obvious importance of static slope stability, the basic concept of limit equilibrium will be presented in this section.

5.2.1. Concept of Limit Equilibrium Analysis

Limit equilibrium analyses examine the equilibrium of forces and/or moments of a mass above a failure surface. Only the weight of the mass itself and – if present – additional static loads are considered. The objective is to identify the point at which the material reaches its limit of stability considering yield criteria and stress-strain relationships.
The involved material above and below the failure surface is assumed to behave in a rigid and perfectly plastic manner without internal deformation and the process of shearing is supposed to take place only along the failure surface. Mechanically, this plane stress-strain condition means that no shear strain can occur before reaching the shear strength of the concerned material. Beyond this threshold the material deforms in a perfectly plastic manner.
The interface behavior along the sliding surface is assumed to follow the Mohr-Coulomb Failure Criterion which was first formulated by the French military engineer Charles-Augustin DE COULOMB (1776) and brought to its today's form by the German structural engineer Otto Christian MOHR (1900). It gives the relationship between shear strength and normal stress on a failure surface. The Austrian engineer and geologist Karl TERZAGHI (1950) – known as the "father of soil mechanics" – added later the principle that total stress is the sum of effective stress and pore water pressure ($\sigma = \sigma' + u$). The dimensionless friction coefficient (μ) equals the tangent of the effective internal friction angle (Φ').

$$\tau = \underbrace{\sigma'}_{\sigma - u} \cdot \underbrace{\tan(\Phi')}_{\mu} + c'$$

where	τ	...	shear strength	[Pa]
	σ'	...	effective normal stress to the sliding surface	[Pa]
	u	...	pore water pressure on the sliding surface	[Pa]
	Φ'	...	effective internal friction angle	[°]
	μ	...	friction coefficient	[-]
	c'	...	effective cohesion	[Pa]

Based on the Mohr-Coulomb Failure Criterion, slope stability can be expressed by one value – by the factor of safety (SF), which was first formulated by LOWE (1976) as the factor between holding and driving stresses (or forces; cf. Tab. 5.1) corresponding simply spoken to the factor between "what the material can hold according to the Mohr-Coulomb Failure Criterion" and the occurring shear stress (or force). Driving stresses (or forces) result from the weight of the material itself and (if present) from the weight of water and additional static loads. Resisting stresses (or forces) are caused by frictional strength and cohesion and – if present – by artificial reinforcement.

$$SF = \frac{holding}{driving} = \frac{shear\ strength}{shear\ stress}$$

	force	stress / strength / pressure
shear ...	T	τ
normal ...	N	σ
water ...	U	u
cohesion ...	C	c
unit	$N = (kg \cdot m)/s^2$	$Pa = N/m^2 = kg/(m \cdot s^2)$

Tab. 5.1. Nomenclature of forces and stresses.

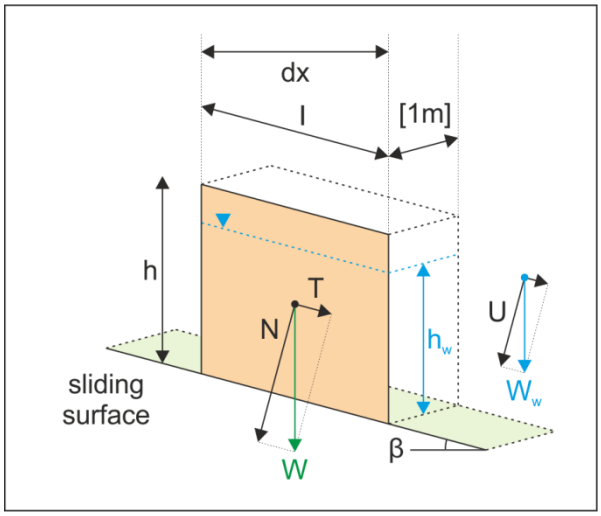

Fig. 5.1. Block on an inclined planar surface. The force vectors of the water have their origin at the gravity center of the saturated part of the mass.

The factor of safety for a block (cf. Fig. 5.1) on an inclined planar surface is obtained as shown via the following equations. It should be mentioned that the factor "1" in these equations represents the unit width; it is necessary to introduce the unit of meter to properly obtain a volume. All variables are in SI-units; "g" is the gravity constant (9.81 m/s^2), "β" is the slope angle and "γ" is the specific weight (in N/m^3).

The weight of a block is given by $W = m \cdot g = (V \cdot \rho) \cdot g = V \cdot (\rho \cdot g) = V \cdot \gamma$

with the exerting normal force $N = W \cdot \cos(\beta) = \big(\gamma \cdot (h \cdot 1 \cdot dx)\big) \cdot \cos(\beta)$

and similarly:
$$U = W_w \cdot \cos(\beta) = \big(\gamma_w \cdot (h_w \cdot 1 \cdot dx)\big) \cdot \cos(\beta) = u \cdot l \cdot 1$$
$$\gamma_w \cdot h_w \cdot 1 \cdot (l \cdot \cos(\beta)) \cdot \cos(\beta) = u \cdot l \cdot 1$$
$$\gamma_w \cdot h_w \cdot 1 \cdot l \cdot \cos^2(\beta) = u \cdot l \cdot 1$$
$$\gamma_w \cdot h_w \cdot \cos^2(\beta) = u$$

The factor of safety is defined as follows. The first equation is in forces; the result is in pressure.

$$SF = \frac{c' \cdot \frac{dx}{\cos(\beta)} \cdot 1 + \left(N - u \cdot \frac{dx}{\cos(\beta)} \cdot 1\right) \cdot \tan(\Phi')}{W \cdot \sin(\beta)} = \frac{shear\ strength}{shear\ stress}$$

$$= \frac{c' \cdot \frac{dx}{\cos(\beta)} \cdot 1}{\gamma \cdot h \cdot 1 \cdot dx \cdot \sin(\beta)} + \frac{\left(\gamma \cdot h \cdot 1 \cdot dx \cdot \cos(\beta) - \gamma_w \cdot h_w \cdot \cos^2(\beta) \cdot \frac{dx}{\cos(\beta)} \cdot 1\right) \cdot \tan(\Phi')}{\gamma \cdot h \cdot 1 \cdot dx \cdot \sin(\beta)}$$

$$= \frac{c'}{\gamma \cdot h \cdot \sin(\beta) \cdot \cos(\beta)} \cdot \frac{2}{2} + \frac{1 \cdot dx \cdot \cos(\beta) \cdot (\gamma \cdot h - \gamma_w \cdot h_w) \cdot \tan(\Phi')}{\gamma \cdot h \cdot 1 \cdot dx \cdot \sin(\beta)}$$

$$= \frac{2 \cdot c'}{\gamma \cdot h \cdot \sin(2 \cdot \beta)} + \frac{(\gamma \cdot h - \gamma_w \cdot h_w) \cdot \tan(\Phi')}{\gamma \cdot h \cdot \tan(\beta)}$$

Factors of safety less than 1 testify unstable conditions of the sliding mass, whereas values above 1 describe stable conditions. However, for civil engineering purposes only values above 1.3 are considered as reasonably safe (FAURE, 2000) and for long term stability a factor of safety of 1.5 is required (KRAMER, 1996).

One point of criticism of the concept of the factor of safety is that one value is representative for the entire rupture surface because limit equilibrium analyses assume that a rupture is a static issue and that all points along the rupture surface experience movement at the same time. However, natural materials are usually brittle or ductile and show a strain-dependent behavior. Therefore, a failure is rather likely to be progressive with points failing at different times. Hence, when studying strain-softening materials with limit equilibrium analysis, residual shear strengths must be used (cf. Tab. 4.1). Also the pore water pressure plays an important role; guidelines were published by DUNCAN (1992) on this subject.

Moreover, methods using limit equilibrium analysis only give an indication about the stability of a slope, but not about the displacement that can be expected after the rupture.

Another issue arises due to simplifications and assumptions of many methods based on limit equilibrium analyses. In principle, a complete static slope stability analysis should satisfy all three equilibrium conditions: vertical force balance, horizontal force balance and moment balance. If this is the case a method is called “rigorous”, in the contrary they are “non-rigorous”.

One major difference between methods based on the concept of limit equilibrium is the subdivision of the failure mass. Those methods that laminate the mass vertically are called “methods of slices”; by contrast, “slice-free methods” consider the failure mass as one single compound. The latter is more frequently applied to problems with very homogeneous material failing on a circular rupture surface. Here, the factor of safety is obtained by comparing the resisting and the overturning moment instead of the holding and driving stresses (or forces). If the sliding surface is known, the factor of safety can simply be obtained by one calculation. As in

the case of a practical stability proof, however, the radius and the origin of the slip circle are iteratively varied until the circle delivering the smallest factor of safety is found (cf. Fig. 5.2). The thereby defined sliding surface is not necessarily the most probable one.

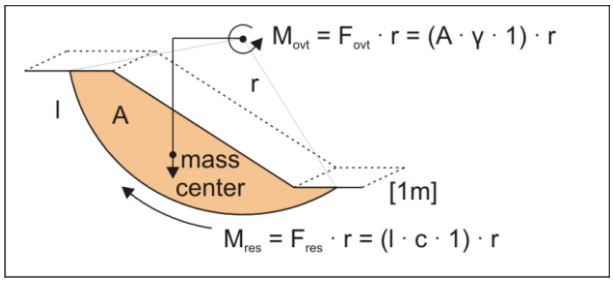

Fig. 5.2. Case of a slice-free method with a circular sliding surface.

Historically the employment of the slip circle concept dates back to 1916. The geotechnical pioneer Knut E. PETTERSON (1955) of the Swedish harbor authority calculated the stability of a quay wall in Göteborg. Shortly after, the Geotechnical Commission of the Swedish State Railways investigated a costly slope failure at an embankment (STATENS JÄRNVÄGARS GEOTEKNISKA KOMMISSION, 1922). Their method became known as the "Swedish Slip Circle Method" and was rather simple assuming the shear strength to be solely due to cohesion; i.e. friction angle was supposed to be zero.
The method was developed further by FELLENIUS (1927) and later by BISHOP (1955) both of which are non-rigorous methods; they are described in the following sections. Although these methods dispose of a lengthy history with many modifications and refinements, they still take an important place nowadays. For example the German norm for calculations of terrain failures (DIN 4084) contains guidelines based on them (DIN, 2009).

5.2.2. FELLENIUS-Method of Slices

Alternatively known as the "Ordinary Method of Slices", the FELLENIUS-Method (1927 & 1936) applies to a sliding mass on a circular rupture surface. It is divided into vertical slices of which each is considered separately (cf. Fig. 5.3, Fig. 5.1). The specific weight, the cohesion and the internal friction angle are assumed to be the same for every slice.
In terms of equilibrium conditions, the method satisfies only the vertical force balance and moment balance; it neglects the interaction of inter-slice forces (CORNFORTH, 2005). Thus, the factor of safety is obtained only on the basis of the weight of the mass and the applying stresses (or forces) along the rupture surface.

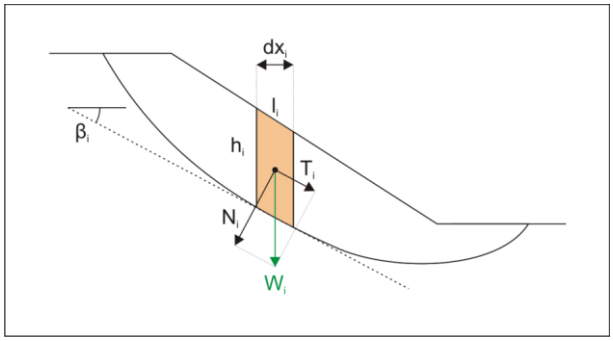

Fig. 5.3. One slice of the FELENIUS-Method (1927 & 1936) comparable to Fig. 5.1.

Depending on whether the slices are equally large or not (i.e. if all "dx_i" are equal or not) the equation of the factor of safety reads as follows; the shorter one has equally large slices.

$$SF_{FEL} = \frac{\sum (c' + (\gamma \cdot h_i \cdot \cos^2(\beta_i) - u_i) \cdot \tan(\Phi')) \cdot \frac{1}{\cos(\beta_i)}}{\sum \gamma \cdot h_i \cdot \sin(\beta_i)}$$

$$SF_{FEL} = \frac{\sum \left(c' \cdot \frac{dx_i}{\cos(\beta_i)} \cdot 1 \right) + \left(\gamma \cdot h_i \cdot dx_i \cdot 1 \cdot \cos(\beta_i) - \gamma_w \cdot h_{wi} \cdot \cos^2(\beta_i) \cdot 1 \cdot \frac{dx_i}{\cos(\beta_i)} \right) \cdot \tan(\Phi')}{\sum \gamma \cdot h_i \cdot dx_i \cdot 1 \cdot \sin(\beta_i)}$$

5.2.3. Modified (or Simplified) BISHOP-Method of Slices

Also the BISHOP-Method (1955) applies to a sliding mass on a circular rupture surface and satisfies only the equilibrium conditions of vertical force balance and moment balance. However, it takes into account the inter-slice forces (CORNFORTH, 2005).
In contrast to the FELLENIUS-Method (1927 & 1936), this method approaches the factor of safety iteratively; i.e. the obtained factor of safety must be inserted back to the equation until its value becomes stable. Indeed, the initial value for the factor of safety must be estimated with any other method. The final factor of safety differs by a few percent from the one that results from the FELLENIUS-Method (1927 & 1936).

$$SF_{BIS} = \frac{\sum \frac{c' \cdot \frac{dx_i}{\cos(\beta_i)} \cdot 1 + \frac{\gamma \cdot h_i \cdot dx_i \cdot 1 - \gamma_w \cdot h_{wi} \cdot \cos^2(\beta_i) \cdot dx_i \cdot 1}{\cos(\beta_i)} \cdot \tan(\Phi')}{1 + \frac{\tan(\Phi') \cdot \tan(\beta_i)}{SF_{BIS}}}}{\sum \gamma \cdot h_i \cdot dx_i \cdot 1 \cdot \sin(\beta_i)}$$

5.2.4. Other Methods

Over time a variety of methods for limit equilibrium analysis have been proposed. They differ not only by the material to be involved, but also by the failure geometry of the slope. Some methods are designed for translational failures, whereas others consider rotational ones. Sliding surfaces can thus be planar, multi-planar, circular, non-circular or even irregular.
Materials for which these methods are suitable range from homogeneous to strongly heterogeneous in terms of strength, cohesion, stratification and discontinuities such as joints and seams. Another difference between the methods is the extent to which static equilibrium conditions are satisfied; not all of them satisfy vertical and horizontal force balance as well as moment balance. Moreover, some methods consider the movement of an entire homogeneous volume; others divide the volume into slices.
Table 5.2 gives an overview of proposed methods. It should be noted that the list is surely not exhaustive and that some methods are further developments of others and in that sense very similar to each other.
Since this thesis does not employ any of these methods, they are mentioned but not explained in detail at this stage. Straightforward descriptions of them are to be found in a summarizing publication of SOILVISION SYSTEMS LTD. (2007) referring to ABRAMSON et al. (2002) and to the TRANSPORTATION RESEARCH BOARD (1996). Also MELOUKA (2003) gives a good introduction to static slope stability methods in his thesis; generalized delineations are to be found in KRAMER (1996) and also in the bibliography of WIKIPEDIA (2017a).

publication year	author & method name	alternative name
1866	CULMANN	
1937 & 1948	TAYLOR	
1954	CAQUOT	
1954 & 1973	JANBU	Simplified JANBU
1954 & 1973	JANBU	Generalized or Rigorous JANBU

1960	LOWE & KARAFIATH	
1960	BISHOP & MORGENSTERN	
1960 & 1965	BIAREZ	
1965	MORGENSTERN & PRICE	
1966	CAQUOT & KERISEL	
1967	SPENCER	
1968	HUNTER & SCHUSTER	
1968 & 1969	BELL	
1969	LAMBE & WHITMAN	
1970	US ARMY CORPS OF ENGINEERS	Modified Swedish Method
1973, 1975 & 1979	SARMA	
1974	RAULIN et al.	Method of Perturbations
1976	PERLOFF & BARON	
1977	FREDLUND & KRAHN	
1981	FREDLUND et al.	General Limit Equilibrium Method
1982	CHUGH	
1985	FAURE	
1992	LI	

Tab. 5.2. Methods for limit equilibrium analysis proposed in the course of the last century. It should be noted that the methods of SARMA (1973, 1975 & 1979) and CHUGH (1982) can also be used for seismic slope stability.

5.3. Seismic Slope Stability

The further complex methods to assess seismic slope stability incorporate the dynamic aspect of the earthquake. More precisely, they account for stresses induced by seismic shaking and for the entailed behavior of the slope materials.
Since the 20th century several methods are available. According to the predominant type of instability, two categories are to be distinguished (KRAMER, 1996):

- inertial instability (assuming shear strength to be relatively constant; slope deformation by temporary exceedance of shear strength)
- weakening instability (assuming the earthquake to weaken the soil so that it cannot remain stable under induced stresses; most commonly liquefaction and cyclic mobility)

The methods are based either on the concept of limit equilibrium or the stress-strain approach. As mentioned in the introduction (cf. 5.1.), the focus in this part of the thesis is on the concept of limit equilibrium. The stress-strain behavior, the dynamic response of a landslide mass and its deformability will be treated in chapters 6. and 7. later on. Thus, only the concept of inertial instability will be discussed in the section.
Inertial instability analysis can be seen as an extension of limit equilibrium analysis (cf. 5.2.1.). The sum of dynamic stress caused by the earthquake is superimposed on the static stresses what might lead to the exceedance of shear strength of the soil and a failure might be induced. Usually an earthquake causes significant horizontal and less significant vertical dynamic stresses, of which the latter are often neglected. Horizontal dynamic stresses are more significant and strongly influence the normal stress on and the shear stress along the failure surface.
Unlike limit equilibrium analyses (cf. 5.2.1.) that give only a factor of safety, at least some of the methods using inertial instability analysis also provide an estimation of the expected displacement of the landslide mass – e.g. the MAKDISI-SEED-Method (1978). In the following the Psdeudostatic Method and the thereupon based NEWMARK-Method (1965) will be presented; both of them were applied to the Diezma Landslide (cf. 5.4.) in the course of this thesis.

5.3.1. Pseudostatic Analysis

One of the first widely used approaches to assess seismic slope stability is the Pseudostatic Analysis introduced by TERZAGHI (1950) for dry materials.
In this approach the dynamic force of an earthquake is represented by pseudostatic accelerations and their respective inertial forces. However, those forces are assumed constant and static and apply to the centroid of the landslide mass (cf. Fig. 5.4) – a fact that leaves the approach to remain rather crude in terms of property characterization.

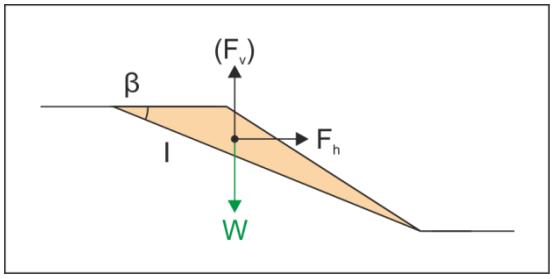

Fig. 5.4. Pseudostatic horizontal (F_h) and vertical (F_v) forces applying to the centroid of the landslide mass.
The landslide mass has a unit width of 1 m.

TERZAGHI (1950) defined the horizontal and vertical pseudostatic forces as stated below. It should be noted that the vertical pseudostatic force can have a resisting or driving effect, but since it tends to average out to zero the vertical pseudostatic force is often neglected. In theory, also the horizontal pseudostatic force could have a resisting effect, but by convention horizontal accelerations (and thus forces) are assumed to apply "away from the slope" as shown in Fig. 5.4. When superimposing the pseudostatic forces on the equation of the static factor of safety, one obtains the extended version for the pseudostatic factor of safety.

$$F_h = \frac{a_h \cdot W}{g} = k_h \cdot W \qquad F_v = \frac{a_v \cdot W}{g} = k_v \cdot W$$

$$SF_{pseu} = \frac{c \cdot l \cdot 1 + \left((W - F_v) \cdot \cos(\beta) - F_h \cdot \sin(\beta)\right) \cdot \tan(\Phi)}{(W - F_v) \cdot \sin(\beta) + F_h \cdot \cos(\beta)}$$

$$SF_{pseu} \approx \frac{c \cdot l \cdot 1 + (W \cdot \cos(\beta) - F_h \cdot \sin(\beta)) \cdot \tan(\Phi)}{W \cdot \sin(\beta) + F_h \cdot \cos(\beta)}$$

where	F_h, F_v	...	horizontal and vertical pseudostatic forces	[N]
	a_h, a_v	...	horizontal and vertical pseudostatic PGA	[m/s²]
	W	...	weight of the landslide mass	[N]
	g	...	gravity constant	[9.81 m/s²]
	k_h, k_v	...	horizontal and vertical pseudostatic coefficient	[-]
	c	...	cohesion	[Pa]
	l	...	length of the failure surface	[m]
	β	...	slope angle	[°]
	Φ	...	internal friction angle	[°]

Being a fraction of the peak ground acceleration ($a_h = k_h \cdot g$), the pseudostatic coefficient reflects to some degree the severity of the earthquake. This accounts for the fact that the peak ground accelerations are reached only very shortly in time and therefore landslides are not exposed to an additional force for a long time (JIBSON, 2011).
Due to the relation to the peak ground acceleration, the pseudostatic coefficient plays an important role at the search for the critical acceleration a landslide mass has to overcome to fail. Using the equation of the pseudostatic factor of safety the pseudostatic coefficient is iteratively

varied until the factor of safety becomes 1. In this particular case (when SF = 1) the pseudostatic coefficient (k_h) becomes the "critical coefficient" or "yield coefficient" ($k_c = k_y$) and accelerations bigger than the critical acceleration ($a_c = k_c \cdot g$) cause a failure.
For a simple pseudostatic stability analysis where the factor of safety is to be calculated, the pseudostatic coefficient must be selected. This selection is crucial and difficult at the same time because first, it should properly reflect the expected acceleration of the landslide mass and second, it significantly influences the result in terms of displacement. Empirical recommendations for the pseudostatic coefficient are provided by TERZAGHI (1950), SEED (1979), MARCUSON (1981), HYNES-GRIFFIN & FRANKLIN (1984) and the CALIFORNIA DIVISION OF MINES AND GEOLOGY (1997). Depending on what geological or geotechnical framework conditions they were calibrated (dams, embankments, natural slopes, etc.) their values are quite variable since acceptable displacements differ among the concerned sites (i.e. meters to centimeters). Only recently STEWART et al. (2003) and BRAY & TEAVASAROU (2009) proposed a procedure to calculate the pseudostatic coefficient based on the maximum horizontal peak ground acceleration, the magnitude of the earthquake, the source distance, the spectral acceleration and the permitted displacement.
Like at conventional static equilibrium analysis (cf. 5.2.1.), the pseudostatic factor of safety is a simple scalar index for the stability of the landslide mass. It does not give information on the consequences after exceedance of the critical acceleration, on the displacement or on the likelihood of failure.
Another drawback is that the approach is not applicable to every material. Soils that build up significant pore water pressure during an earthquake or those that lose more than 15% of their peak shear strength while shaking (KRAMER, 1996) cannot be examined using the pseudostatic approach. On this, SEED (1979) presents the examples of dams that failed during an earthquake although they had pseudostatic factors of safety well above 1. Also, sites likely to experience liquefaction are non-candidates for the Pseudostatic Analysis.
But yet, and due to the simplicity of the method, it serves for preliminary screening purposes of non-sensitive soil structures with planar, circular or non-circular sliding surfaces.

5.3.2. NEWMARK-Method

In 1965 NEWMARK introduced a method for analyzing the dynamic performance of slopes undergoing seismic shaking. For the first time a slope stability analysis did not only deliver a factor of safety, but also the expected displacement of the sliding mass after it experienced an acceleration bigger than the critical acceleration. The NEWMARK-Method (1965) is therefore one step ahead of the older approaches such as the Pseudostatic Analysis. Interestingly finite element modeling approaches (JIBSON, 2011; cf. 6.2.1.) date back already to the 1950s, but being still in their very early ages the NEWMARK-Method (1965) quickly became a simple and fast tool for the evaluation of co-seismic permanent displacement. It is still widely used today representing a bridge between simple limit equilibrium analysis and highly complex numerical modeling of stress-strain behavior over time.
Originally, NEWMARK (1965) proposed the method for embankments as he stated in his publication:

> *"[…] In all compacted dam-construction materials, and in many natural soil strata, the dynamic shearing resistance is about the same as the static shearing resistance […]. However, at some localities, natural soil strata […] can lose […] their shearing resistance under shock conditions, either because of increased hydrostatic pressure or owing to loss in shearing strength from even slight remolding [i.e. disturbance]." (p. 142)*

However, WILSON & KEEFER (1983) discovered reasonable results also for the dynamic behavior of sliding masses on natural slopes pointing out that the method should be applied, though, for thin and stiff landslides. These types are indeed the most common types of landslides (KEEFER, 1984; KEEFER, 2002) that can make up 90% or more per earthquake (HARP et al.,

1981; HARP & JIBSON, 1995; HARP & JIBSON, 1996; KEEFER & MANSON, 1998; JIBSON et al., 2004; JIBSON et al., 2006).
Mechanically the NEWMARK-Method (1965) is a classic rigid-block analysis approximating a landslide by a rigid block on an inclined plane (cf. Fig. 5.5). No displacement takes place until the critical (or yield) acceleration is overcome. Beyond that point the block experiences permanent displacement at constant stress along the shear surface until the velocity comes back to zero. The block does not undergo internal deformation and hence behaves in a perfectly plastic manner.

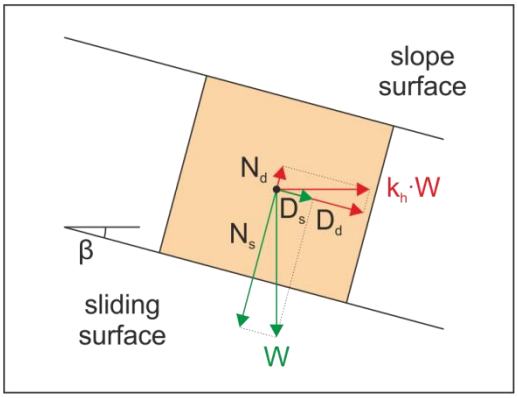

Fig. 5.5. A block on an inclined planar surface. A permanent force (red) representing the earthquake is added to the static forces (green; cf. Fig. 5.1). The abbreviations "N" and "D" stand for "normal force" and "driving force"; "s" and "d" indicate the "static" and "dynamic" character of the force.

Other limiting assumptions (that do not necessarily apply to more recent further developments of the method; cf. below) are:

- The static and the dynamic shear stress are the same.
- The critical acceleration is not strain-dependent and constant throughout the analysis; upslope displacement does not happen.
- The dynamic pore water pressure is neglected (also in further developments of the method), and thus the method is rather suitable for dry soils, compacted or over-consolidated clays and dense or dry sands.

Similar to the concept of limit equilibrium analysis employing the Mohr-Coulomb Failure criterion (cf. 5.2.1.) and to the Pseudostatic Analysis (cf. 5.3.1.) representing the earthquake by an additional body force (as $k_h \cdot W$), the NEWMARK-Method (1965) also considers the unique point where the mass comes out of equilibrium. Physically expressed this means:

$$\frac{static\ and\ dynamic\ resisting\ forces}{static\ and\ dynamic\ driving\ forces} = 1$$

In order to obtain a dynamic factor of safety, that clearly describes the critical condition, one sets:

$$SF_{NEW} = \frac{\overbrace{c' \cdot l \cdot 1}^{neglected} + \left(N - \overbrace{u \cdot l \cdot 1}^{neglected}\right) \cdot tan(\phi)}{W \cdot sin(\beta)}$$

$$= \frac{\left(N_{stat} - N_{dyn}\right) \cdot \tan(\Phi)}{D_{stat} + D_{dyn}} = \frac{(W \cdot \cos(\beta) - k_h \cdot W \cdot sin(\beta)) \cdot \tan(\Phi)}{W \cdot sin(\beta) + k_h \cdot W \cdot \cos(\beta)}$$

It should be noted that in this equation the vertical force induced by the earthquake, the water pressure (u) as well as the cohesion (c') are neglected. In this particular case the factor of safety can be also expressed as:

$$SF_{NEW} = \frac{\tan(\phi)}{\tan(\beta)}$$

Again, the critical (or yield) coefficient ($k_c = k_y$) required for a factor of safety of 1 defines the critical acceleration ($a_c = k_c \cdot g$) which the block has to overcome for instability. It is not strain-dependent and constant throughout the analysis.
As indicated in section 5.3.1., the critical acceleration can be found by iteratively varying the critical coefficient until the factor of safety becomes 1. Another option was proposed by NEWMARK (1965) assuming the seismic force to be applied parallel to the slope (and not horizontally):

$$a_c = (SF_{stat} - 1) \cdot g \cdot \sin(\beta)$$

where a_c is in g

As for the displacement, NEWMARK (1965) suggested that it must be related to the amplitude and frequency content of an earthquake, i.e. the expected displacement depends on (KRAMER, 1996):

- whether the critical acceleration is exceeded,
- how often and for how much time it is exceeded and
- by how much the critical acceleration is exceeded.

Depending on the number of pulses that a slope experiences there are two ways of displacement estimation. For single-pulse displacements NEWMARK (1965) proposed one equation for the relative and one for the maximum displacement.

$$d_{rel} = \frac{{v_{max}}^2}{2 \cdot a_c} \cdot \left(1 - \frac{a_c}{A}\right) \qquad d_{max} = \frac{{v_{max}}^2}{2 \cdot a_c} \cdot \frac{a_{max}}{a_c}$$

where	d_{rel}, d_{max}	…	relative and maximal displacement	[m]
	v_{max}	…	peak ground velocity	[m/s]
	a_{max}	…	peak ground acceleration	[g]
	a_c	…	critical acceleration	[g]
	A	…	acceleration (the time-dependent signal)	[g]

For more complex signals with many pulses exceeding the critical acceleration displacements are usually obtained by a double-integration procedure. In a first step, the acceleration time-history is reduced to only the parts above the critical acceleration (cf. Fig. 5.6); these parts are then integrated to obtain the respective velocity time-history. In a second step, this velocity time-history is again integrated to obtain the displacement time-history which is shown in its cumulative form. The highest value depicts the maximal displacement of the soil mass. This procedure is highly sensitive to the value of the critical acceleration and thus to the critical coefficient; even small differences can result in large variations of displacement.
As mentioned before, the dynamic response of the slope is not only a function of its geometry and the properties of the involved material. It also depends largely on the amplitude and frequency content of the strong-motion signal. One important detail of the NEWMARK-Method (1965) is that the hypothesis of a fully rigid behavior is only true for signals with low frequencies (cf. Fig. 5.7a). Only at long wavelengths (λ) the entire soil mass moves in phase. In case the wavelength of the arriving shear wave is too short, inertial forces inside the soil mass

might act in opposite directions (cf. Fig. 5.7b), and the resultant inertial force could be significantly smaller than that implied by NEWMARK's (1965) rigid-block assumption (KRAMER, 1996).

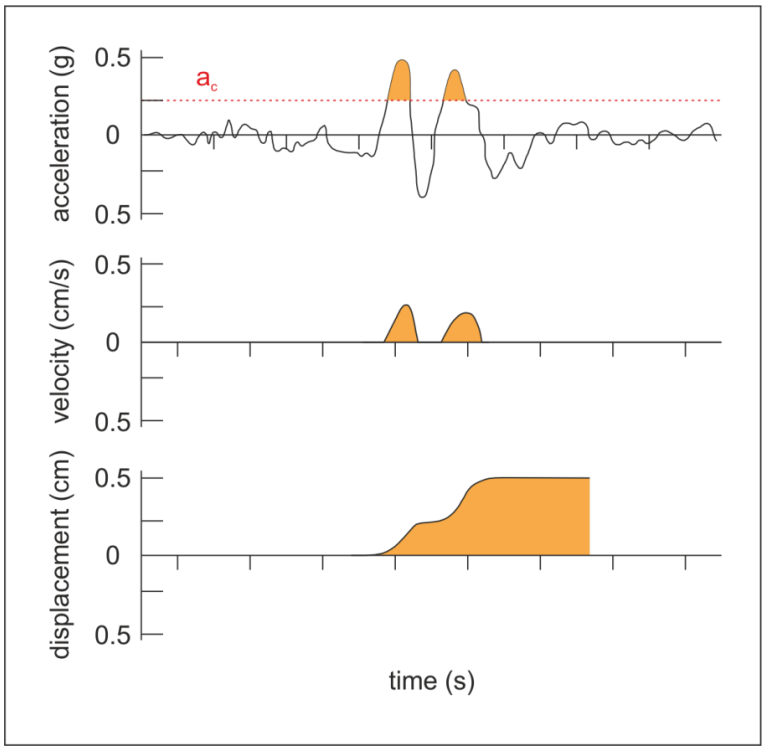

Fig. 5.6. Double-integration procedure leading from an acceleration time-history to a cumulative displacement history (after WILSON & KEEFER, 1985).

JIBSON et al. (2013) suggest the method to be satisfactory only for relatively thin landslides in stiff or brittle material having a T_s/T_m-ratio (cf. 6.4.2.) of less than 0.1, but not for thicker landslides in softer materials (RATHJE & ANTONAKOS, 2010).

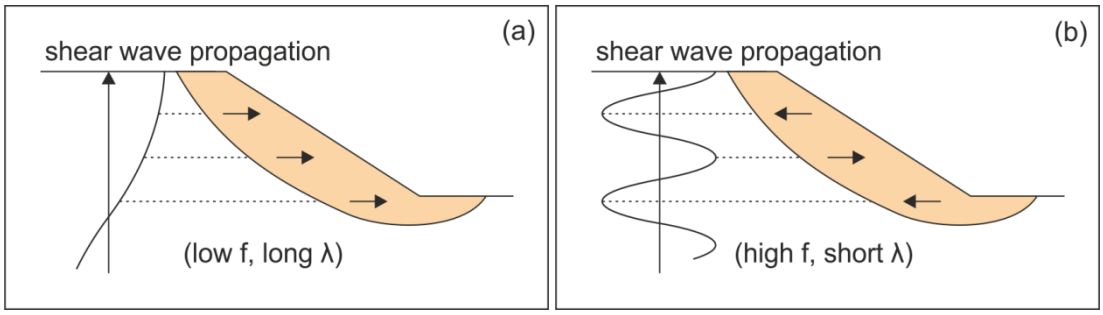

Fig. 5.7a-b. In-phase and out-of-phase movement of a landslide mass due to different wavelengths and frequencies (after KRAMER, 1996).

Subsequent modifications of the NEWMARK-Method (1965) made it applicable to a wider range of landslide types. Further developments included more complex geological and geotechnical settings, hence more diverse and realistic settings, and more specific consideration of the dynamic response of the concerned slope. Some also account for internal deformation during seismic shaking.

Widely known further developments are the so-called "De-Coupled Method" and "Coupled Method". The first one – also named "Modified NEWMARK-Method" – calculates the dynamic response independently of the permanent displacement of the landslide, whereas the Coupled Method can model both simultaneously. The latter represents the most sophisticated and time-consuming type of sliding-block analysis (JIBSON, 2011).

Over time, many authors also undertook empirical approaches to relate the displacement of rigid blocks to one or more parameters of the strong-motion signal. Closed-form solutions for permanent displacements were derived by SARMA (1975) and YEGIAN et al. (1988) for rectangular, triangular and sinusoidal periodic signals (cf. Fig. 5.8). FRANKLIN & CHANG (1977) found that displacements induced by real earthquakes are very similar to what the sinusoidal and the triangular curves predict above an a_c/a_{max}-ratio of 0.5.
Beginning in the later 1980 up to the present day, authors attempt to consider many more earthquake parameters because it was recognized that the peak ground acceleration as unique descriptive factor might not be sufficient. First, YEGIAN et al. (1991) empirically related the displacement also to frequency content and duration; his curve is shown in orange in Fig. 5.8. Later, sliding-block displacements were correlated with peak ground acceleration, peak ground velocity, Arias Intensity and moment magnitude. Usually authors conduct a number of NEWMARK-Analyses (1965) employing various single horizontal component strong-motion records that are either globally or regionally representative and finally form regression laws based on the results.

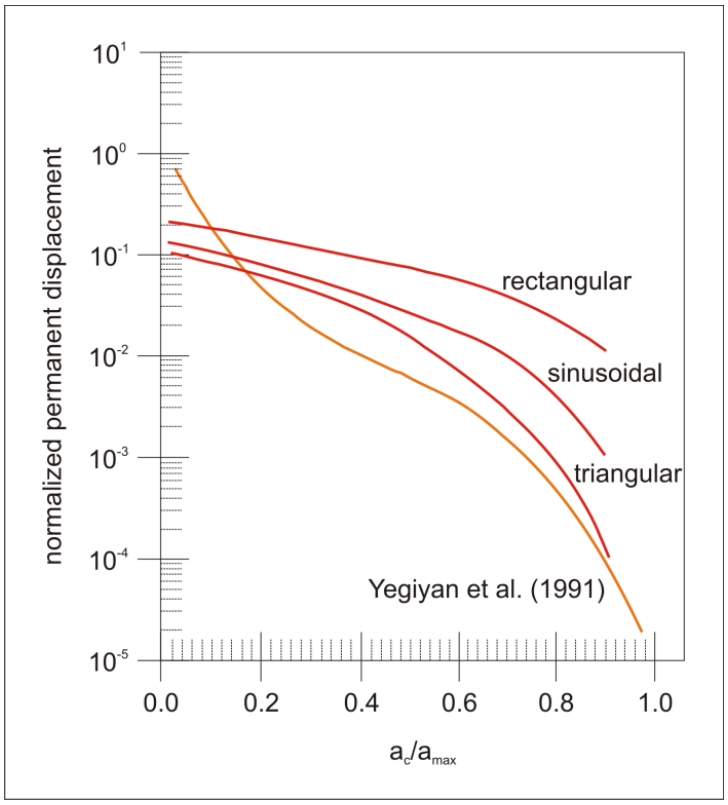

Fig. 5.8. Empirical regression laws correlating rigid-block displacement and the a_c/a_{max}-ratio (after SARMA, 1975; after YEGIAN et al. 1988; after YEGIAN et al., 1991).

Table 5.3 shows eleven recent regressions by various authors based on different combinations of correlation parameters. In the following the respective equations are given. It should be noted that "log" refers to the common logarithm (with base 10) and "ln" to the natural logarithm (with base e).

Units are:	D_n	…	displacement	[cm]
	a_c	…	critical acceleration	[g]
	a_{max}	…	peak ground acceleration	[g]
	v_{max}	…	peak ground velocity	[cm/s]
	I_a	…	Arias Intensity	[m/s]
	M_w	…	moment magnitude	[-]

RATHJE & SAYGILI (2009):

$$\ln(D_n) = 4.89 - 4.85 \cdot \left(\frac{a_c}{a_{max}}\right) - 19.64 \cdot \left(\frac{a_c}{a_{max}}\right)^2 + 42.49 \cdot \left(\frac{a_c}{a_{max}}\right)^3 - 29.06 \cdot \left(\frac{a_c}{a_{max}}\right)^4 + 0.72 \cdot \ln(a_{max}) + 0.89 \cdot (M_W - 6.00)$$

SAYGILI & RATHJE (2008①):

$$\ln(D_n) = 5.52 - 4.43 \cdot \left(\frac{a_c}{a_{max}}\right) - 20.39 \cdot \left(\frac{a_c}{a_{max}}\right)^2 + 42.61 \cdot \left(\frac{a_c}{a_{max}}\right)^3 - 28.74 \cdot \left(\frac{a_c}{a_{max}}\right)^4 + 0.72 \cdot \ln(a_{max})$$

SAYGILI & RATHJE (2008②):

$$\ln(D_n) = -1.56 - 4.58 \cdot \left(\frac{a_c}{a_{max}}\right) - 20.84 \cdot \left(\frac{a_c}{a_{max}}\right)^2 + 44.75 \cdot \left(\frac{a_c}{a_{max}}\right)^3 - 30.50 \cdot \left(\frac{a_c}{a_{max}}\right)^4 - 0.64 \cdot \ln(a_{max}) + 1.55 \cdot \ln(v_{max})$$

SAYGILI & RATHJE (2008③):

$$\ln(D_n) = -0.74 - 4.93 \cdot \left(\frac{a_c}{a_{max}}\right) - 19.91 \cdot \left(\frac{a_c}{a_{max}}\right)^2 + 43.75 \cdot \left(\frac{a_c}{a_{max}}\right)^3 - 30.12 \cdot \left(\frac{a_c}{a_{max}}\right)^4 - 1.30 \cdot \ln(a_{max}) + 1.04 \cdot \ln(v_{max}) + 0.67 \cdot \ln(I_a)$$

JIBSON (2007①):

$$\log(D_n) = 0.215 + \log\left(\left(1 - \frac{a_c}{a_{max}}\right)^{2.341} \cdot \left(\frac{a_c}{a_{max}}\right)^{-1.438}\right)$$

JIBSON (2007②):

$$\log(D_n) = -2.710 + \log\left(\left(1 - \frac{a_c}{a_{max}}\right)^{2.335} \cdot \left(\frac{a_c}{a_{max}}\right)^{-1.478}\right) + 0.424 \cdot M_W$$

JIBSON (2007③):

$$\log(D_n) = 2.401 \cdot \log(I_a) - 3.481 \cdot \log(a_c) - 3.230$$

JIBSON (2007④):

$$\log(D_n) = 0.561 \cdot \log(I_a) - 3.833 \cdot \log\left(\frac{a_c}{a_{max}}\right) - 1.474$$

JIBSON et al. (1998 & 2000):

$$\log(D_n) = 1.521 \cdot \log(I_a) - 1.993 \cdot \log(a_c) - 1.546$$

JIBSON (1993):

$$\log(D_n) = 1.460 \cdot \log(I_a) - 6.642 \cdot a_c + 1.546$$

AMBRASEYS & MENU (1988):

$$\log(D_n) = 0.90 + \log\left(\left(1 - \frac{a_c}{a_{max}}\right)^{2.53} \cdot \left(\frac{a_c}{a_{max}}\right)^{-1.09}\right)$$

authors	records	tested for	standard deviation
RATHJE & SAYGILI (2009)	> 2000 worldwide	$0.05\ g \le a_c \le 0.30\ g$	0.95
SAYGILI & RATHJE (2008①)	2383 worldwide		1.13
SAYGILI & RATHJE (2008②)			$0.41 + 0.52\ (a_c/a_{max})$
SAYGILI & RATHJE (2008③)			$0.20 + 0.79\ (a_c/a_{max})$
JIBSON (2007①)	2270 worldwide	$0.05\ g \le a_c \le 0.40\ g$	0.51
JIBSON (2007②)			0.45
JIBSON (2007③)	875 worldwide		0.66
JIBSON (2007④)			0.62
JIBSON et al. (1998 & 2000)	555 Los Angeles	$0.02\ g \le a_c \le 0.40\ g$	0.38
JIBSON (1993)	11 worldwide		0.41
AMBRASEYS & MENU (1988)	50 worldwide	$0.1 \le a_c/a_{max} \le 0.9$	0.30

Tab. 5.3. Empirical regressions for rigid-block displacements.
Numbers ① to ④ serve to distinguish those equations that are published in the same reference.

5.4. Application to the Diezma Landslide

Methods to assess the slope stability and the expected displacement of the Diezma Landslide were to some extent "customized" in order to ensure best compatibility with a few compromises. The following subsections describe the entire procedure of calculating expected displacements: from the definition of the slice geometry via the FELLENIUS- and the BISHOP-Method (1927 & 1936 and 1955 respectively) to the critical acceleration, and finally to the NEWMARK-Method (1965) and thereupon based further developments. The section finishes with a critical view on the procedure.

5.4.1. Slice Geometry of the Diezma Landslide

Section 4.2. discusses the differences between the simplified (cf. 4.2.2.) and fine (cf. 4.2.3.) geometry as well as the fact that both of them have a long and a short version (cf. 4.2.1.). Therefore, in principle, four LCS can be considered for imposing on them a slice geometry. However, it seemed to be very much sufficient to limit the slice geometry to the two LCS of the simplified geometry because of two reasons. First, the long and short LCS of the fine geometry (LCS Aal and LCS Aas; cf. Fig. 4.15o, Fig. 4.15p) are very similar to the long and short LCS of the simplified geometry (LCS Aal and LCS Aas; cf. Fig. 4.10k, Fig. 4.10l). Second, the FELLENIUS-Method (1927 & 1936) as well as the NEWMARK-Method (1965) both introduce many simplifying hypotheses and it would not be worth the effort to create a very fine and elaborate slice geometry under this circumstances. Then note in Tab. 4.9 stating that the fine geometry is "not to be divided into slices" is therefore not referring to the possibility to do so, but to the sense of purpose.
For simplicity, the already exiting sectioning of the simplified 2D-geometry (corresponding to the LCS Aa of the simplified geometry, cf. Fig. 4.8) was used for the slice geometry. The convenient advantage here is that the sections do not only have the same length (dx_i; cf. Fig. 5.3) but are also well defined in all other dimensions. A weak point is that the hereby obtained slices consist of two triangles and two trapezes instead of rhombus-shaped slices. For the FELLENIUS-Method (1927 & 1936), though, this is of minor importance since the method ascribes the point of force application to the gravity center of the slice which does not have to be located. The respective weight can be calculated therefore via the surface of the slices (cf. 5.4.2.).

5.4.2. Factor of Safety according to the FELLENIUS-Method

The NEWMARK-Method (1965) requires a factor of safety that will subsequently define the critical acceleration that the sliding mass has to overcome to start moving down slope. But since

the NEWMARK-Method (1965) does only represent one block that can experience a supplementary body force representing the earthquake, this supplementary force was introduced to the equation of FELLENIUS (1927 & 1936).

$$SF_{FEL} = \frac{\sum(c' \cdot 1 \cdot l_i) + (\gamma \cdot h_i \cdot dx_i \cdot 1 \cdot \cos(\beta_i) - k_h \cdot \gamma \cdot h_i \cdot dx_i \cdot 1 \cdot \sin(\beta_i) - u \cdot 1 \cdot l_i) \cdot \tan(\Phi')}{\sum \gamma \cdot h_i \cdot dx_i \cdot 1 \cdot \sin(\beta_i) + k_h \cdot \gamma \cdot h_i \cdot dx_i \cdot 1 \cdot \cos(\beta_i)}$$

In contrast to a simple static or pseudostatic limit equilibrium analysis (cf. 5.2.1., 5.3.1.) with one single compound mass, this equation allows for individual slice characterization in terms of dimension, soil properties and water saturation – all of which are known and well defined for the Diezma Landslide (cf. Tab. 5.4, Fig. 4.8). For comparison, the static as well as the pseudo-dynamic factor of safety can easily be calculated.
The factor of safety was assessed for the long and the short slice geometry by a simple spreadsheet calculation in Microsoft Excel which computes resisting and driving forces for each slice separately to finally put their sum in relation. The sliding mass was assumed to be entirely dry and thus the pore water pressure is 0. If the pseudostatic coefficient is kept equal to 0 as well, the factor of safety will be static and representative for the stability of the slope in times without seismic shaking. By iteratively varying the pseudostatic coefficient the factor of safety is brought to 1, i.e. to the point where the sliding mass becomes unstable.

slice	γ (N/m^3)	c' (Pa)	u (Pa)	Φ' (°)	β (°)	dx (m)	shape
1l	21400	4000	0.00	12.00	15.04	123.75	triangle
1s					16.58	68.00	triangle
2					11.09	123.75	trapeze
3					8.39	123.75	trapeze
4					6.11	123.75	triangle

Tab. 5.4. Soil properties, water saturation and shape of the slices of the Diezma Landslide. It should be noted that the first slice can either be big or small representing the long (l) or short (s) geometry respectively.

The weight of a slice is defined by "γ·h·dx·1". Attention must be paid, however, because this equation is not suitable for the "irregular" slices of the Diezma Landslide. The correct surfaces (that must be later multiplied by the unit width to get the volume) for triangles and trapezes are given in Tab. 5.5. Alternatively one also could make use of the Heron's Formula (cf. below) to calculate the surfaces of triangles (cf. Fig. 4.8), then recombine them to trapezes where needed and multiply by the unit width to obtain the volumes.

$$A = \sqrt{s \cdot (s-a) \cdot (s-b) \cdot (s-c)} \qquad \text{with} \qquad s = \frac{a+b+c}{2}$$

where a, b, and c are the sides of an arbitrary triangle

slice	shape	surface with height-equation	surface with Heron's equation	≈ … [m^2]
1l	triangle	(dx*h)/2	$A_{(triangle\ 1l)}$*1	700
1s	triangle	(dx*h)/2	$A_{(triangle\ 1s)}$*1	400
2	trapeze	(dx*(h_l+h_r))/2	$A_{(triangles\ 2+3)}$*1	1900
3	trapeze	(dx*(h_l+h_r))/2	$A_{(triangles\ 4+5)}$*1	2900
4	triangle	(dx*h)/2	$A_{(triangle\ 6)}$*1	1700

Tab. 5.5. Shape of the slices of the Diezma Landslide. It should be noted that the first slice can either be big or small representing the long or short geometry respectively (cf. Fig. 4.8). The indices "l" and "r" at the trapezes refer to the left and right margins.

Regardless of how the weight of the four slices was calculated, static factor of safety for the long and the short slice geometry appeared to be almost the same. Likewise, by bringing the factor of

safety to 1, for both slice geometries a very similar pseudostatic coefficient was obtained (cf. Tab. 5.6). The last row shows the adopted values for further calculations with other methods. They show one very important aspect for all following displacement models: the small volume difference in the crown area of the Diezma Landslide does not contribute significantly to the outcome of displacement analyses.

surface calculation	long simplified slice geometry			short simplified slice geometry		
		SF	k_h		SF	k_h
height based	static	1.3940	0	static	1.4162	0
	pseudostatic	1	0.0617	pseudostatic	1	0.0639
Heron based	static	1.3936	0	static	1.4158	0
	pseudostatic	1	0.0617	pseudostatic	1	0.0639
adopted values for further calculations			0.06			0.06

Tab. 5.6. Results for the static factor of safety and the pseudostatic coefficient of the long and the short slice geometry. Values are rounded to their fourth decimal to underline the similarity and justify the choice of k_h.

Under static conditions, thus, the landslide mass – in its initial state in 1990 before the main failure – should be very stable. As FAURE (2000) stated, values above 1.3 are considered as reasonably safe (cf. 4.2.1.). However, the fact that the Diezma Landslide was and is moving at certain intervals even in phases without seismic activity or heavy rain is to some extent discordant with the high factor of safety.
In this regard, the factor of safety proposed by RODRÍGUEZ-PECES et al. (2011) seems to fit better. The authors conducted an evaluation of effectiveness of slope stability measures in five stages using the 2D slope stability software Slide which is based on the limit equilibrium approach of MORGENSTERN & PRICE (1965). The value of 1.05 represents the state of the slope under dry conditions in 1990 after the highway A-92 was built (cf. 4.2.1., Fig. 4.7). It remains, though, unclear why the considered sliding mass is so small and does not extend until beyond the old road.

5.4.3. Factor of Safety according to the BISHOP-Method

The static factors of safety of the BISHOP-Method (1955) are very similar to those of the FELLENIUS Method (1927 & 1936). For the long and the short slice geometries the iterative height based equations even out at 1.396 and 1.419 already after the first iteration. Values are rounded to their fourth decimal to enable clear comparisons with values in Tab. 5.6.
Because of the high similarity, it might be reasonably assumed that the FELLENIUS-Method (1927 & 1936) is good enough to correctly represent the slices of the Diezma Landslide with their mechanical conditions.

5.4.4. Critical Acceleration for the Diezma Landslide

By definition (cf. 5.3.1. & 5.3.2.) the critical acceleration is obtained by multiplying the critical coefficient (the one driving the factor of safety to 1) with the gravity constant:

$$a_c = k_c \cdot g$$

where a_c is in [g] or [m/s^2]

Therefore the critical coefficients and critical accelerations of the two simplified landslide geometries (long and short version) in 2D are:

$$k_c = 0.06 \qquad a_c = 0.06\, g = 0.59\, \frac{m}{s^2}$$

5.4.5. Displacement according to the NEWMARK-Method

The classic NEWMARK-Method (1965) is suitable for permanent displacement analysis of stiff and thin landslides (cf. 5.3.2.) – a condition that the Diezma Landslide fulfills almost perfectly within its main sliding mass (cf. 4.1.). Moreover, the method neglects the pore water pressure, what in this case does not turn out to be a disadvantage since the Diezma Landslide is assumed to be dry in any model throughout the thesis.
A point that deserves a closer look is the fact that the method is designed for almost planar sliding surfaces. According to this, on the one hand, the Diezma Landslide is also a very good candidate because it is mostly described as a roto-translational or even purely translational landslide. On the other hand, one can argue that – if considered as such – the FELLENIUS-Method (1927 & 1936) might have been not suitable because it is designed for circular rupture surfaces. However, as explained in section 4.1., the exact mechanical type of the Diezma landslide varies in literature and RODRÍGUEZ-PECES et al. (2011; cf. Fig. 4.7) even depict a stability analysis with a slip circle whose radius is so large that the sliding mass becomes again comparable to a roto-translational setting.
Another critical point is that according to JIBSON et al. (2013) the method is satisfactory only for landslides having a ratio of T_s/T_m (cf. 6.4.2.) of less than 0.1. This condition is not fulfilled (cf. Tab. 5.7); for values between 0.1 and 1.0 JIBSON et al. (2013) describe the method as applicable but rather unconservative. The characteristic site period ($T_s = 4 \cdot h/v_s$) is calculated with a (middle) height of 19.50 m of the landslide mass (cf. Fig. 4.8) and a shear wave velocity of 300 m/s (cf. 4.1.). Being linked only to height and velocity it is the same for all signals (cf. Fig. 6.6) that are applied to the Diezma Landslide during the NEWMARK-Analysis (1965). For consistency, also the characteristic site period related to the (down slope) length of the landslide ($T_l = l/v_s$) and the ratio of T_l/T_m (cf. 6.4.2.) is given in Tab. 5.7. although no recommendations for suitable ranges appear in literature.

signal	ID	T_s* (s)	T_l* (s)	T_m (s)	T_s/T_m* (-)	T_l/T_m* (-)
A	000049x	0.26	1.68	0.70	0.37	2.40
B	000133x			0.66	0.39	2.54
C	000127x			0.32	0.81	5.21
D	000294x			1.08	0.24	1.55
E	000335x			0.77	0.34	2.16
F	001875x			0.58	0.45	2.87
G	006142x			1.02	0.26	1.65
H	000599x			0.38	0.68	4.37
I	000612x			1.19	0.22	1.41
J	000625x			0.49	0.54	3.46
K	005820x			0.76	0.34	2.20

Tab. 5.7. Characteristic site periods and ratios of the Diezma Landslide for v_s = 300 m/s (*)..

It should be noted that the NEWMARK-Method (1965) calculates displacements based on geotechnical and geometrical parameters other than the shear wave velocity. Therefore, the displacements are no function of the characteristic site periods (T_s and T_l). If the displacements are dependent on the characteristic periods of the signals (T_m) will be discussed below together with the eventual influence of other important parameters.
A software which is described by the developers as a tool to facilitate sliding-block analysis is the program SLAMMER (Seismic LAndslide Movement Modeled using Earthquake Records; JIBSON et al., 2013). It comprises more than 2100 strong-motion from 28 earthquakes to conduct classic NEWMARK-Analyses (1965) as well as its further developments and regression approaches. Furthermore, the user can import other strong-motion data.

SLAMMER calculates the cumulative displacement in the same way as described in section 5.3.2. via double-integration of the acceleration time-history of a strong-motion. However, this integration procedure is not only conducted for the "truncated" signal of the normal (upper) polarity, but also – and separately – for the one of the inverse (lower) polarity (cf. Fig. 5.9a-k). The reasoning behind this practice is that the permanent force representing the earthquake is indeed assumed to apply in the most unfavorable direction (red arrow in Fig. 5.10). But since the used signal is simply a horizontal component without information about its directivity, it must be considered that the biggest displacement can originate from the normal or the inverse polarity part.
Maximum (cumulative) displacements per signal calculated with SLAMMER are listed in Tab. 5.8. The cumulative curves are to be found in the appendix (cf. A.4.).

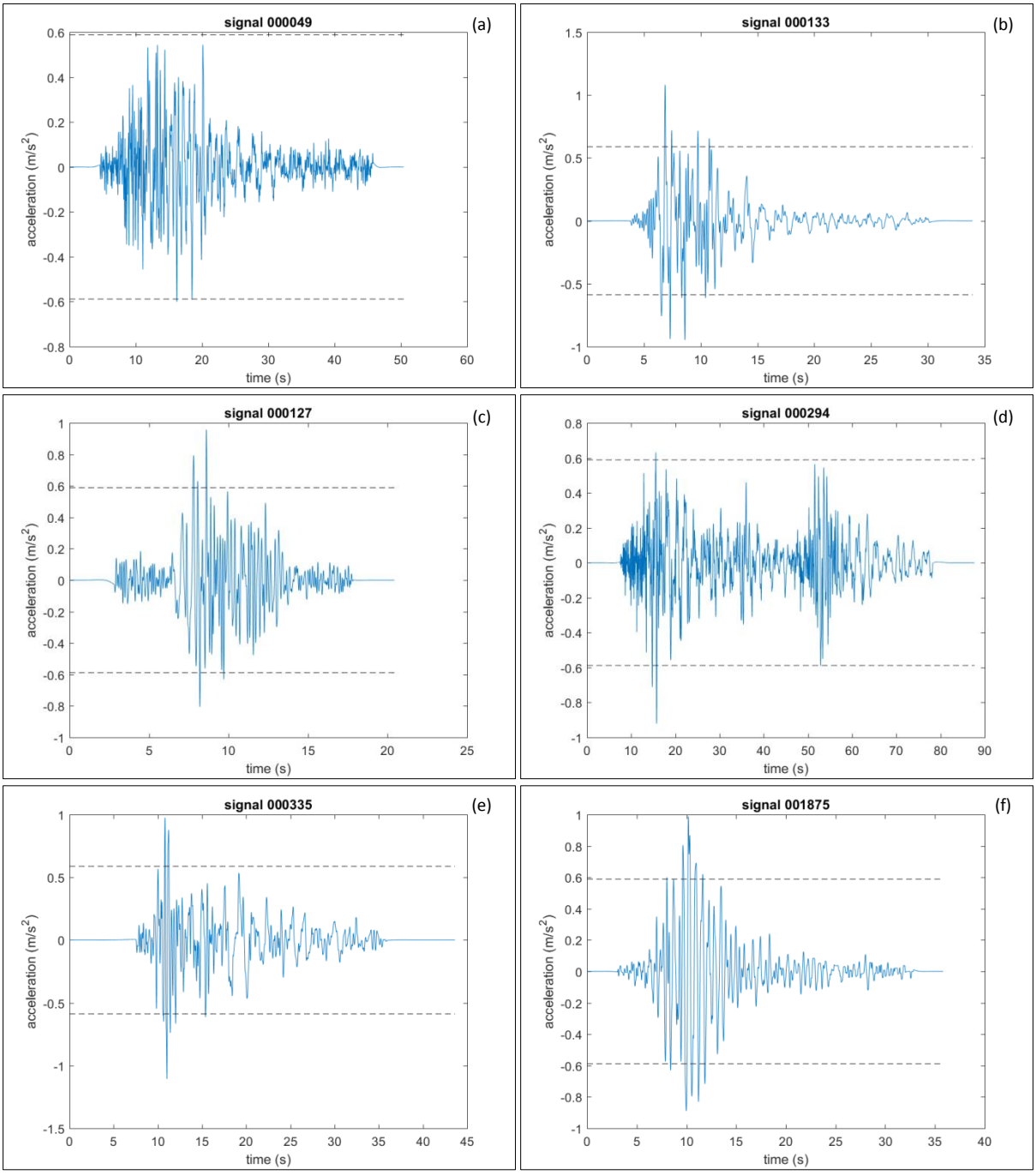

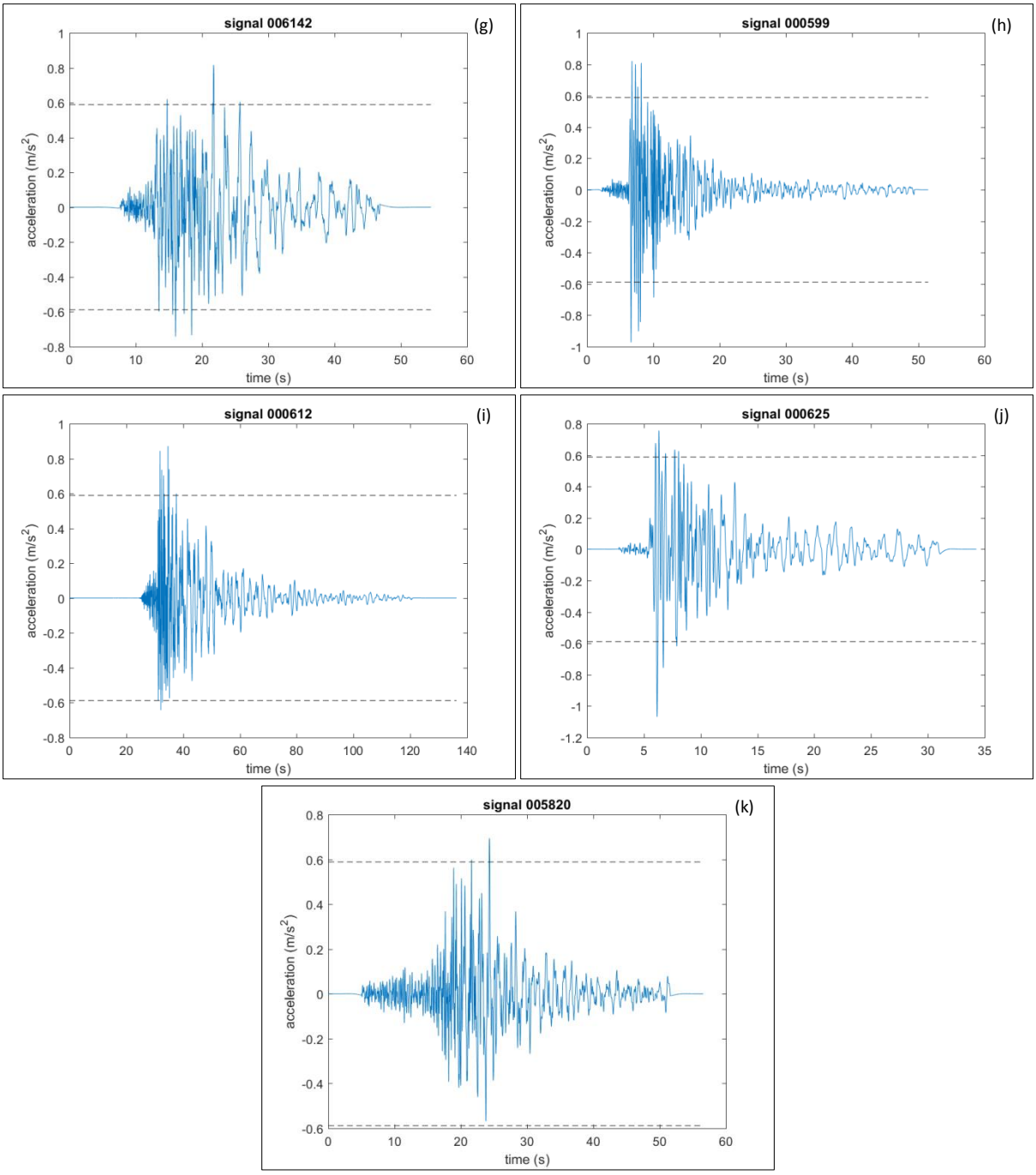

Fig. 5.9a-k. Acceleration time-histories of all filtered (cf. 4.4.) signals with "truncated" normal and inverse polarity.

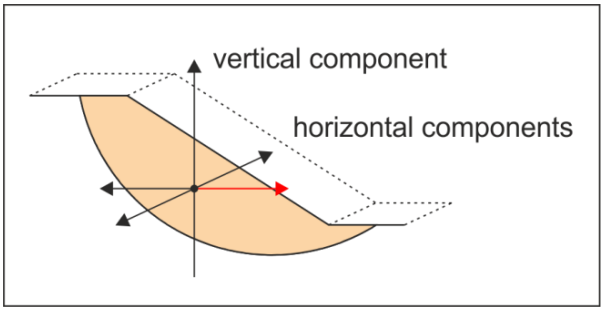

Fig. 5.10. Direction in which the permanent force representing the earthquake is assumed.

signal	ID	PGA in … polarity	d_{max} in … polarity	normal d_{max} (cm)	inverse d_{max} (cm)
A	000049x	inverse		0.0000	0.0002
B	000133x	normal		0.3840	0.3510
C	000127x	normal		0.1201	0.0323
D	000294x	inverse		0.0038	0.3254
E	000335x	inverse	normal	0.5309	0.3699
F	001875x	normal		1.4084	1.1590
G	006142x	normal		0.2138	0.0490
H	000599x	inverse		0.1284	0.3034
I	000612x	normal		0.1488	0.0020
J	000625x	inverse		0.0488	0.3534
K	005820x	normal		0.0565	0.0000

Tab. 5.8. Maximum (cumulative) displacements per signal.

Signal A (000049x) and signal K (005820x) show no displacement for the normal and the inverse polarity respectively because the amplitudes never exceed the critical acceleration.
In most of the cases the peak ground acceleration has the same polarity as the maximum displacement. Only for signal E (000335x) this is not the case. Its peak ground acceleration (1.11 m/s^2) is located in the inverse polarity whereas the maximum displacement is in the normal polarity. This fact is simply explained by the area content over which the double-integration was performed; although the peak ground acceleration is higher in the inverse polarity, the peak does not overdraw as much surface as the slightly smaller peaks in the normal polarity do together. As final results of the classic NEWMARK-Analysis (1965) the bigger value of the maximum displacement per signal was retained. The values of the normal polarity range from 0.0 cm to 1.4 cm and the ones of the inverse polarity range from 0.0 cm to 1.2 cm; both have the same average of 0.3 cm.
An interesting question is which earthquake characteristics influence the obtained displacements. The software SLAMMER only needs an acceleration time-history and a critical acceleration to perform an estimation of displacement. It does not take into account the moment magnitude of the respective earthquake. However, parameters such as characteristic period (T_m) and characteristic frequency (F_m), characteristic ratios (T_s/T_m and T_l/T_m), peak ground acceleration (PGA), peak ground velocity (PGV), peak ground displacement (PGD), Arias Intensity (AI) and the duration are easy to deduce from a given acceleration time-history. One might thus ask, if those parameters show a relation to the estimated displacements.
Figures 5.11a-i give an answer on this question. The graph relating the peak ground acceleration to the estimated displacement shows an upward-trend; and it is the only graph doing so. Nevertheless, even here conclusions have to be drawn with reservation; higher peak ground accelerations do not imply higher displacements at all points. If the correlation was that simple, the NEWMARK-Method (1965) with its approach of critical acceleration and integration would probably be meaningless, which is certainly not true.
All other graphs do not show a tendency leading to the assumption that – in plain language – every signal produces a distinct displacement which is shown in the graphs regardless of the selected earthquake parameter. Indeed, the striking downward peak always belongs to signal A (000049x), the highest peak is always caused by signal F (001875x), and similarly all other points have their particular “position” that logically varies horizontally but not vertically in the graphs.

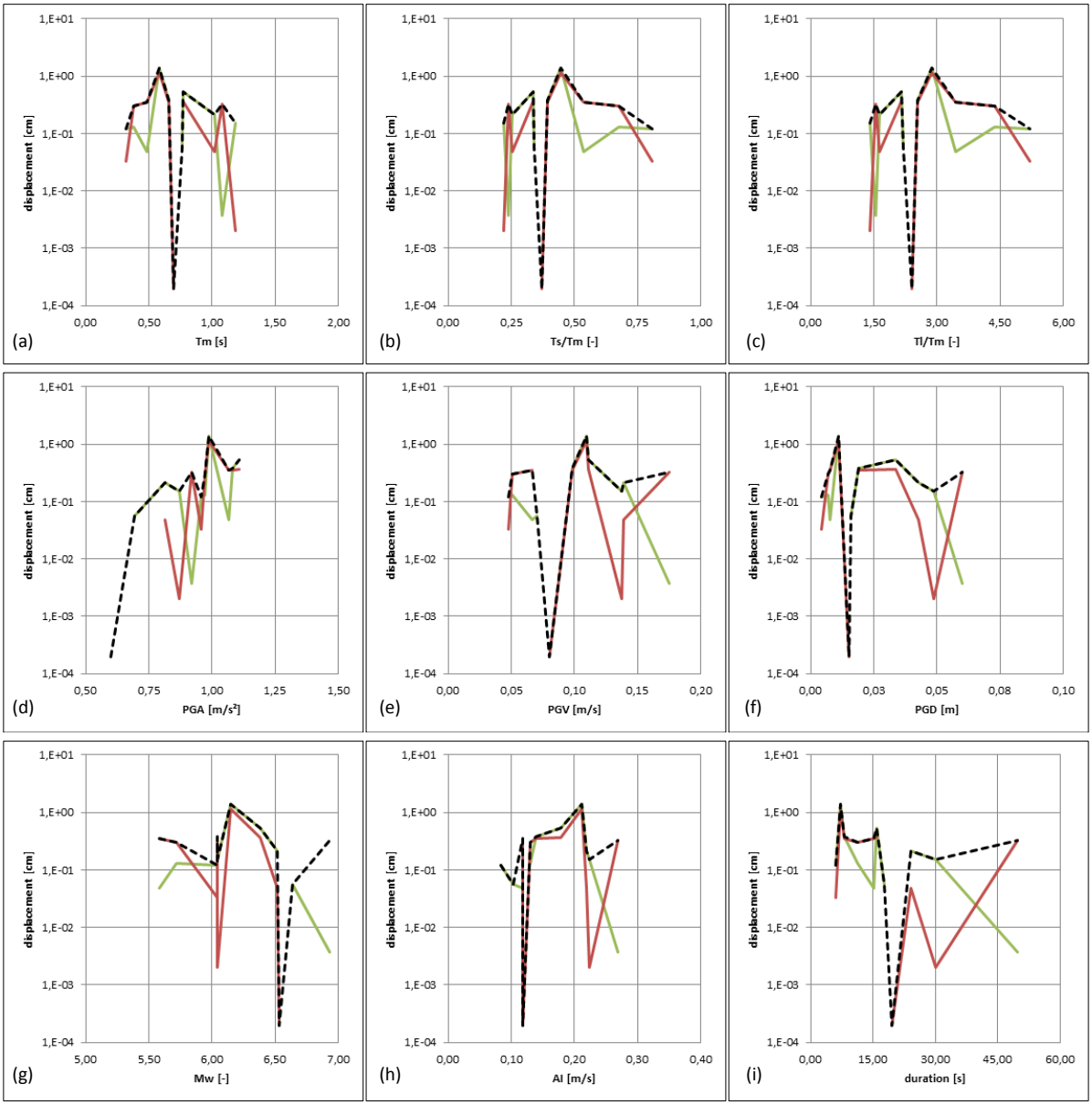

Fig. 5.11.a-i. Maximum (cumulative) displacements obtained by the NEWMARK-Method (1965) as function of different earthquake characteristics (normal polarity in green, inverse polarity in red, bigger values of either polarity in black). For better understanding, it should be mentioned that some of the red and green lines are not entirely shown. This is solely a peculiarity of Microsoft Excel where points cannot be linked to a "0-point" on a logarithmic scale. The dashed black line is always complete. The duration is the one defined by TRIFUNAC & BRADY (1975; cf. 4.4.).

5.4.6. Displacements by further Developments based on NEWMARK

The classic NEWMARK-Method (1965) applied to the Diezma Landslide with each of the 11 filtered signals revealed permanent displacements of 0.0 cm to 1.4 cm. In order to have a comparison twelve further developments of the methods were tested. NEWMARK's (1965) own maximum displacement regression and the eleven empirical regression laws are presented in Tab. 5.9. Here, an issue might be the calibration of each law.

NEWMARK's (1965) maximum displacement regression is based on several earthquake motions with an a_c/a_{max}-ratio bigger or at least equal to 0.17 (KRAMER, 1996) which is the case for all of the here employed signals.

The other eleven empirical regression laws should be suitable likewise in terms of critical acceleration ranges for which the strong-motion records were tested (cf. Tab. 5.3). The critical acceleration of the Diezma Landslide (0.06 g) lies inside all of the ranges and its a_c/a_{max}-ratios of 0.53 to 0.98 are also very acceptable for the range given by AMBRASEYS & MENU (1988).

Among all global regression laws only the one of JIBSION et al. (1998 & 2000) was calibrated with earthquake and landslide data from the Northridge Earthquake on the 17th of January 1994. However, and due to the statistically reasonable number of 555 tested strong-motion records and the fact that most of the landslides appeared to be fairly shallow and disrupted (JIBSON et al., 2003), the regression law can be applied although with reservation.
Compared to the classic NEWMARK-Method (1965), results are very similar ranging from 0.0 cm to 4.1 cm (cf. Tab. 5.8) with an average of 0.5 cm. At this stage, one can legitimately content oneself with the finding that the empirical displacements are all small in the order of a few centimeters (if at all) and that differences in the range of millimeters bring no significant change to this finding – especially when keeping in mind all simplifications and hypotheses behind the employed equations.

authors		RATHJE & SAYGILI (2009)	SAYGILI & RATHJE (2008①)	SAYGILI & RATHJE (2008②)	SAYGILI & RATHJE (2008③)	JIBSON (2007①)	JIBSON (2007②)	JIBSON (2007③)	JIBSON (2007④)	JIBSON et al. (1998 & 2000)	JIBSON (1993)	AMBRASEYS & MENU (1988)	NEWMARK (1965) – empiric
involved parameters		M_W					M_W						
					I_a			I_a	I_a	I_a	I_a		
				PGV	PGV								PGV
		a_c	a_c	a_c	a_c	a_c	a_c	a_c	a_c	a_c	a_c	a_c	a_c
		PGA	PGA	PGA	PGA	PGA	PGA		PGA			PGA	PGA
signal	ID	displacement (cm)											
A	000049x	0.00	0.00	0.00	0.00	0.00	0.00	0.10	0.00	0.30	0.60	0.00	0.56
B	000133x	0.40	0.80	0.50	0.40	0.60	0.30	0.10	0.10	0.40	0.80	2.10	1.51
C	000127x	0.20	0.50	0.10	0.10	0.40	0.20	0.00	0.10	0.20	0.40	1.20	0.31
D	000294x	0.40	0.40	0.60	0.60	0.30	0.30	0.50	0.10	1.10	2.10	1.00	4.07
E	000335x	0.70	0.90	0.60	0.50	0.70	0.40	0.20	0.10	0.60	1.10	2.30	1.96
F	001875x	0.30	0.50	0.40	0.40	0.40	0.20	0.30	0.10	0.70	1.40	1.40	1.72
G	006142x	0.10	0.20	0.20	0.20	0.10	0.10	0.30	0.00	0.80	1.50	0.40	2.28
H	000599x	0.20	0.50	0.10	0.10	0.40	0.10	0.10	0.10	0.30	0.70	1.30	0.36
I	000612x	0.10	0.30	0.30	0.30	0.20	0.10	0.30	0.10	0.80	1.60	0.70	2.37
J	000625x	0.30	0.80	0.30	0.20	0.60	0.20	0.10	0.10	0.30	0.60	2.00	0.68
K	005820x	0.00	0.00	0.00	0.00	0.00	0.00	0.00	0.00	0.20	0.50	0.10	0.50

Tab. 5.9. Displacements estimated by different empirical methods. Darker colors indicate higher values. Numbers ① to ④ serve to distinguish those equations that are published in the same reference.

If one still wants to have a closer look on the 132 individual estimated displacements, one might discover a few features in the color-coded Tab. 5.9:

1. The older the regression law, the bigger are the displacements. Assuming that more available data leads to better calibration and smaller displacement estimations, this could reflect smaller data availability back in the day. From Tab. 5.3 it can be seen that the number of tested records decreases drastically with the age of the regression law.

Of course, if good calibration does not come along with smaller displacement estimations, this assumption is wrong.

2. However, to the former assumption fits to a certain degree the fact that laws based on only two parameters appear (slightly) darker in the color-coded table. Here, especially the two recently proposed regressions by SAYGILI & RATHJE (2008) and JIBSON (2007) involving only the peak ground acceleration and the critical acceleration stand out. More involved "information" might refine the results causing them to become smaller.
3. Signals A and K figuratively break ranks as they show almost no displacements – only with the very old regression laws. Interestingly, those both are the two signals which do not reach the critical acceleration in their normal and inverse polarity respectively (cf. Fig. 5.9a & Fig. 5.9k).

The parameter certainly having the biggest influence on the estimated displacements is the critical acceleration because – at the classic NEWMARK-Method (1965) – it defines how much of the enclosed area is to be integrated (cf. Fig. 5.6). Indeed, a similar effect can be detected in connection with the color code in Tab. 5.9 – the bigger the difference between the critical acceleration and the peaks of acceleration, the bigger is the estimated displacement.

- light colors: with signals A, G and K → far from 1 m/s^2 (closer to a_c)
- intermediate colors: with signals C, F, H, and I → around 1 m/s^2
- dark colors: with signals B, D, E and J → exceeding 1 m/s^2

5.4.7. Failure Probability according to JIBSON

JIBSON et al. (2000) compared the full inventory of landslides triggered by the Northridge Earthquake on the 17th of January 1994 with the displacements that were estimated with the respective empirical regression law (cf. 5.4.6.). Afterwards, they regressed the results with a WEIBULL Probability Distribution (1951) which delivered the following equation.

$$P = 0.335 \cdot \left(1 - e^{-0.048 \cdot {D_n}^{1.565}}\right)$$

where P is the failure probability in decimals and D_n the displacement in centimeters

JIBSON (2011) states that although this equation was calibrated on a regional scale, it can be used in any ground-shaking condition to assess the failure probability of slopes as a function of rigid-block displacements according to NEWARK (1965). This emphasizes also the employment of the associated displacement equation for the Diezma Landslide refuting to some extent the argument of inappropriate calibration.

signal	ID	P
A	000049x	0.0%
B	000133x	0.4%
C	000127x	0.1%
D	000294x	0.3%
E	000335x	0.6%
F	001875x	1.9%
G	006142x	0.1%
H	000599x	0.2%
I	000612x	0.1%
J	000625x	0.3%
K	005820x	0.0%

Tab. 5.10. Failure probability (P) per signal.

Failure probabilities of the Diezma Landslide per signal are given in Tab. 5.10 and it appears that under seismic shaking the mass is very unlikely to fail. This finding is rather contrary to the opinion of authors who display favorable conditions for seismically induced failures (DELGADO et al., 2015; LENTI & MARTINO, 2016; MARTÍNEZ-SOLAREZ et al., 2013; cf. 4.1., 4.4.).

5.4.8. Critical View on the NEWMARK-Method

Despite its simplifications the NEWMARK-Method (1965) has proven to be straightforward, easy to apply and fast. It is a convenient tool and as JIBSON (2011) stated.

> *"Permanent-displacement analysis begins, in fact, exactly where pseudostatic analysis ends: at the moment the critical or yield acceleration is exceeded. The displacement thus modeled provides a quantitative measure – an index – of co-seismic slope performance." (p. 48)*

Therefore it is still a widely used standard method for geotechnical purposes and deserves well its place among other methods that might even be far more elaborate.
Nonetheless, there are aspects that deserve a close and critical view. The majority of them were brought up in the previous sections describing the method and its applications to the Diezma landslide. The so far unaddressed points of criticism will be discussed in the following.
What surely misses out at the NEWMARK-Method (1965) is the strain-dependency of the behavior of the sliding mass. Usually natural soils do not behave perfectly plastic when stresses are applied; they rather exhibit strain-softening or strain-hardening behaviors. The former causes expected displacements to be bigger and the latter smaller than predicted. Also the stress regime is likely to change over time; the bigger the rotational character of the sliding mass, the more likely it is that the slope will be flattened due to the movement itself. This would reduce the driving force and increase the critical acceleration (KRAMER, 1996).
Another important point giving food for thought is the actual concept of the critical acceleration. On the one hand it seems very logic to assume that below a certain acceleration level no displacement is induced: it is easy to imagine that every material can resist to a certain stress regime. On the other hand this concept leads to a substantial loss of information especially regarding the frequency content and the duration of the applied signal – two factors that interestingly were described by NEWMARK (1965) himself as very important for displacement analysis (cf. 5.3.2.).
Comparing, for instance, signals D (000294x) and H (000599x) in their inverse polarities it appears that the expected displacements are very similar (0.33 cm and 0.30 cm respectively) even though with signal D the mass experiences two phases of strong acceleration. According to the critical acceleration concept this second acceleration phase does not play any role for the displacement estimation, which would be more than doubtful in reality.
Another example is illustrated by the comparison of signals C (000127x) and H (00059x). It is well known that in nature many relatively smaller impacts can have a bigger effect on a structure than a few high impacts. Thus, it is important how often a certain threshold is exceeded. In the normal polarities one can see that signal C has two strong peaks whereas signal H has four slightly less strong ones. However, the estimated displacement in both cases is almost the same (0.12 cm and 0.13 cm respectively).
Unfortunately the NEWMARK-Method (1965) does not relate to the ratios of T_s/T_m and T_l/T_m (cf. 6.4.2.). In other words the method does not account for the shear wave velocity, which is indeed astonishing since it is one of (if not) the most important parameter when dealing with wave propagation through a material. Therefore a 3D-plot relating either of the ratios, the velocity and the displacement (such as in Fig. 6.9) is not possible. Only single parameters of the signals (PGA, PGV, T_m, I_a, duration, M_W, etc.) can be put in relation with the estimated displacements; however, no outstanding behavior will be revealed thereby because the integration surface remains the most influential factor.

CHAPTER 6
MODAL RECOMBINATION ANALYSIS

6.1. Introduction

The previous chapter (5.) presented the concept of limit equilibrium analyses and its application to the Diezma Landslide. The theoretical background as well as the case study itself drew a picture of advantages and drawbacks of this analytical method, of which the latter are mainly due to the fact that neither stress-strain behavior, nor the aspect of time, nor site effects can be taken into account.
Numerical methods provide remedy on this very issue at the cost of much more complex and time-consuming procedures. In this chapter the focus is on numerical modeling, and the chapter structure will follow a layout similar to the chapter on limit equilibrium analyses.
First, an overview on numerical modeling will be given. It should be noted, that this overview serves to place the employed methods to a typological and historical context. However, it does not explain in depth the mathematical, physical and computational background of the methods. A multitude of textbooks and technical literature on numerical modeling is available for this purpose, but even an abridgment would go beyond the scope of this thesis.
In the next stage the functionality of the finite element code CESAR-LCPC will be presented. Since it is one of the two software packages used in the course of this thesis it is worth to have a closer look on its mode of operation. In contrast to the introductory section, where the mathematical, physical and computational background is kept rather simple, a little more effort will be spent in this section. Principals of structural dynamics will be explained along with their equivalent procedure steps – i.e. the method of modal recombination – in CESAR-LCPC.
The biggest part of this chapter will be dedicated to the modal recombination analysis applied to the Diezma Landslide in 2D and 3D. Step by step the procedure will be followed by visualization and interpretation of data and finally results from the 2D- and the 3D-analyses will be compared.

6.2. Overview on Numerical Modeling

Unlike limit equilibrium analyses, numerical modeling treats not only the possibility of deformation but also the process of deformation itself. Considering the amount of methods with their particular fields of application as well as the advancements of technical and computing power of the last decades numerical modeling offers – theoretically – an almost endless number of options to conduct deformation analysis.
Over time, the development of numerical modeling came along with major advances in diverse fields of science such as for example continuum mechanics, rheology and computer science in the 1960s and 1970s; today numerical modeling is coupled with thermodynamics, hydraulics, seismology and many more physical sub-disciplines what makes it an enormously powerful tool for planning, monitoring and maintenance of natural and artificial structures.
In the particular case of studies on seismically induced landslides numerical modeling nowadays assumes a leading role in slope stability assessment. The more advanced the methods became and the better the dynamic aspect of earthquakes could be incorporated, the closer came numerical results to reality and, hence, the more credible and valuable became the contributions to the understanding of (potentially) unstable slopes.
Compared to analytical methods that usually comprise a multitude of simplifications and assumptions, numerical methods deal much more efficiently with many more specifications and physical conditions applying to the structure of interest:

- structural heterogeneity: layering, discontinuities, complex boundary conditions
- property heterogeneity: location- and/or time-dependent variations, anisotropy
- slope geometry: regular or irregular shapes, progressive geometry change
- material behavior: linear-elastic, (visco)-elasto-plastic, strain-softening, non-linear
- material laws: stress-strain laws and stress-deformation laws
- water saturation: ground water level, pore water pressure distribution, fluctuations
- stress state: before, during and after the deformation, static or dynamic analyses

- external solicitation: cyclic and impulsive loading
- development over time
- data uncertainties
- site effect evaluation
- coupled processes: e.g. pore water pressure increase after seismic loading
- effects of construction, excavation and overload
- soil-structure interaction

Yet from this non-exhaustive list it is evident that numerical modeling reduces the number of hypotheses by offering more room for site specific conditions. Moreover, stress- and strain-fields are constantly evaluated for different time-steps; and in contrast to limit equilibrium analyses, where (and if at all) displacements are attributed to one particular point of the concerned sliding mass, numerical modeling allows for stress-strain quantification in every point of the mass and thus draws the most accurate picture of the behavior of a slope with time.
One big issue at numerical modeling is the fact that the accuracy of the outcome is strongly dependent on the input. In other words, usually great efforts must be made for high quality and quantity data, intensive laboratory testing and material characterization, proper selection of input motion (in case of ground response analysis) and interpretation of results (JIBSON, 2011).
Also the involvement of the above listed properties, conditions and physical laws entrain highly complex calculations that can quickly become computationally intensive and time-consuming especially with high densities of data. The computations occasionally reach their borders in terms of time restrictions or hardware memory.
Due to the considerably bigger effort compared to limit equilibrium analyses numerical models are therefore rather suitable for specific case studies which require particular accuracy of assessment. JIBSON (2011) describes stress-deformation analysis as standard for single-site analysis where sufficient data exist and mentions that for critical structures the effort is generally satisfied; however it cannot be regarded as a routine application.
According to EBERHARDT (2003) numerical modeling methods can be grouped into three categories: continuum-, discontinuum- and hybrid-methods. Despite their conceptual differences which will be discussed later, they share many basic principles.
Their most fundamental and common principle is that the structure of interest is dissected into

> *"[…] a mesh in which the internal stresses and strains within elements are computed based on the applied external loads, including gravity and seismic loads." (JIBSON, 2011, p. 43)*

Moreover, the behavior of the thereby created individual points (or nodes) is described by equations of physical processes. Usually those equations are differential equations such as for example Isaac NEWTON's Second Law of Motion (1687), redefined as the Basic Law of Mechanics by Leonhard EULER (1752) relating the applied force to the mass and acceleration of a body:

$$F = m \cdot \frac{dv}{dt} = m \cdot a$$

Due to the complexity of the equation systems, solutions can only be obtained numerically which eventually led to the nomenclature of this field of analytical techniques. According to the method the solutions of the governing (physical) equations are then approximated by discrete equations (ISMAIL-ZADEH & TACKLEY, 2010). The relation to the model type is given by:

$$\text{mathematical model} \leftrightarrow \text{governing equations}$$
$$\text{numerical model} \leftrightarrow \text{discrete equations}$$

Regardless of the method, the quality of numerical models can be described by five important properties. A high accurateness implies good comparability between the predicted solutions of

the mathematical and the numerical model. Physical quantities like mass and momentum must respect the principle of conservation when approximating governing equations by discrete equations; in many cases governing equations are thus derived from conservation laws. Good consistency is achieved when the error between the governing and the discrete equations tends to zero, what usually involves a decrease of the mesh increment size. The closer the results from numerical modeling come to those of mathematical modeling, the better is the convergence. The requirement of stability is met when errors do not amplify during computation (ISMAIL-ZADEH & TACKLEY, 2010).

6.2.1. Continuum Modeling

As specified by the name, methods of continuum modeling treat the body of interest as a continuum, and hence they are mainly applied to soil slopes or massive rock masses (EBERHARDT, 2003). The two most widespread types of continuum modeling codes are finite element methods (FEM) and finite difference methods (FDM), both of which were used in this thesis:

FEM	→	CESAR-LCPC	(in the following abbreviated by CESAR)
FDM	→	FLAC	(cf. 7.)

Finite Element Methods (FEM)

Being highly sophisticated, FEM discretizes the body of interest into a finite number of non-overlapping elements by – for instance – a triangular, tetrahedral or quadrilateral mesh. Calculations hence become matrix operative and the stress-strain variability can be evaluated throughout the elements.
Initially FEM were developed for mechanical issues and more precisely for the assessment of stiffness and deformation of solid bodies with complex shapes. Based on mathematical concepts of COURANT (1943), first attempts to use FEM were made in the 1950s by the automobile and aerospace industry (TURNER & CLOUGH, 1950). The actual name involving the term "finite element" was later introduced by CLOUGH in 1960, after he developed FEM for engineering purposes. Although daunting and complex in the beginning, FEM was soon after applied to slopes of earth dams (CLOUGH & CHOPRA, 1966; CLOUGH & WOODWARD, 1967) and quickly became of great value for modeling static and dynamic slope deformation, not least on account of convenient and accurate representation of complex geometries with overall or locally modifiable mesh-sizes.
Today FEM applications to earth structures are popular; KRAMER (1996) lists a variety with associated studies. In the case of dynamic stress-deformation analysis seismically induced strains in each element of the mesh are integrated in order to obtain the permanent displacement of the slope. In this context, three approaches to assess permanent displacement are worth to mention:

- Strain Potential Approach (SEED et al., 1973)
  a laboratory based approach predicting the shear potential as shear strain per element
- Stiffness Reduction Approach (LEE, 1974; SERFF et al., 1976)
  a laboratory based approach where strain potentials are used to reduce the stiffness
- Non-linear Analysis Approach (PREVOST, 1981; GRIFFITHS & PREVOST, 1988)
  an approach using non-linear stress-strain laws to describe the behavior of the soil

Finite Difference Methods (FDM)

Like FEM also FDM discretize the modeled domain, however with a finite number of points at which stresses and strain are defined. The concept of calculation lies on the numerical solution

of differential equations at these points via approximation by difference equations; derivatives are then approximated by finite differences what explains the name of the method.
FDM is widely used in fluid dynamics and meteorology, but also in structural analysis. Earliest pioneering applications date back to the beginning of the last century where RICHARDSON (1911) tested a masonry dam.
In contrast to FEM, FDM do not use a global stiffness matrix and solutions are obtained stepwise for one point and its neighbors. FDM are in most cases faster than FEM and easier to implement. The finite difference code FLAC will be described in chapter 7.

Other Methods

Methods that are similar to FEM are Finite Volume Methods (FVM) and Spectral Element Methods (SEM). FVM are conservative methods and thus particularly suitable for problems involving differential equations based on conservation laws, i.e. where energy or impulse conservation must be ensured. In contrast to FEM, the body of interest is discretized to a finite number of volumetric elements surrounding the calculation points in their centers. SEM have the advantage of handling mathematical series such as for example Fourier- or Taylor-Series. Both method types shall only be mentioned here; they are not used in this thesis.

6.2.2. Discontinuum Modeling

Discontinuum modeling methods do not treat the body of interest as a continuum, but as an assembly of separate but interacting elements of different forms with distinct properties – hence as a discontinuum. This fundamental hypothesis makes the methods applicable to materials characterized by a large amount of discontinuities such as fractured rock.
Today, Discrete (or Distinct) Element Methods (DEM) are most popular in discontinuum modeling. Initially developed by CUNDALL (1971) for particle motion in molecular dynamics and described in detail by HART (1993), DEM quickly found their way to mechanical and geotechnical engineering.
DEM are of great importance when it comes to modeling of heavily jointed rock slopes, relative movement between blocks and the potential creation of voids within the body of interest. Equilibrium equations are solved repeatedly for each block until contact laws and boundary conditions are met (EBERHARDT, 2003; ISMAIL-ZADEH & TACKLEY, 2010).

6.2.3. Hybrid Modeling

EBERHARDT (2003) classifies coupled methodologies as hybrid modeling. The combination of continuum and discontinuum approaches allows for optimized employment and makes use of the advantages of the methods. Examples of such methodology couples are (ISMAIL-ZADEH & TACKLEY, 2010):

FEM (cf. 6.2.1.) + LEA (cf. 5.)	→ e.g. GeoStudio	(GEOSLOPE, 2018)
FDM (cf. 6.2.1.) + DEM (cf. 6.2.2.)	→ e.g. PFC	(ITASCA, 2018)
FEM (cf. 6.2.1.) + DEM (cf. 6.2.2.)	→ e.g. Elfen	(ROCKFIELD, 2018)

6.3. Functionality of CESAR

CESAR is a finite element software dedicated to stability and deformation analyses in 2D and 3D. It is widely used for geotechnical and civil engineering purposes which are addressed in the beginning of this chapter (cf. 6.2.).
Effectively, the software is an “in-house product”. Research and expertise that contribute to the constant advancement of CESAR is provided by the scientific developer Laboratoire Central des Ponts et Chaussées (LCPC) – the today’s Institut Français des Sciences et Technologies des Transports, de l'Aménagement et des Réseaux (IFSTTAR). The distribution is ensured by itech

(ITECH, IFSTTAR, 2018) who also provides user manuals and training materials for diverse applications.
A detailed description of the functionality of CESAR would go beyond the scope of the thesis, especially since detailed documentation is already available (ITECH, IFSTTAR, 2014):

CESAR 2D Version 6.0 User's Manual
CESAR 3D Version 6.0 User's Manual

However, for better understanding and reproducibility of the modal recombination analysis presented in this chapter, sections 6.3.2. and 6.4. will explain the necessary sequence of steps in CESAR-2D and -3D. It should be noted, that this particular procedure only applies to a modal recombination analysis and all other analysis types offered by CESAR are described in the respective documentation.

6.3.1. Principals of Structural Dynamics

Structural dynamics are a vast field of mechanical engineering. For that reason only the principles necessary to understand the procedure of modal recombination will be explained. The section is entirely based on the course "Dynamique des Structures et des Ouvrages" held at École des Ponts – ParisTech (PECKER, 2018); no further references will be made in the text.
Modal recombination is a method to determine the response of an oscillator of n degrees of freedom to dynamic loading in terms of displacement. In the present case the oscillator is the landslide mass and the dynamic load is the earthquake – or more precisely, one of the 11 separately tested seismic signals. The landslide mass is assumed to behave in a linear visco-elastic manner what qualifies it for modal recombination analysis.
An important detail is that the procedure does not assess the absolute displacement of the oscillator caused by the earthquake, but its relative displacement to the foundation what is of much greater interest in engineering. This difference is illustrated in Fig. 1 showing a visco-elastic oscillator with one degree of freedom only. It can be easily seen that the absolute displacement caused by the earthquake (y) refers to the inertial frame, whereas the relative displacement of the oscillator (u) is given with respect to the foundation.

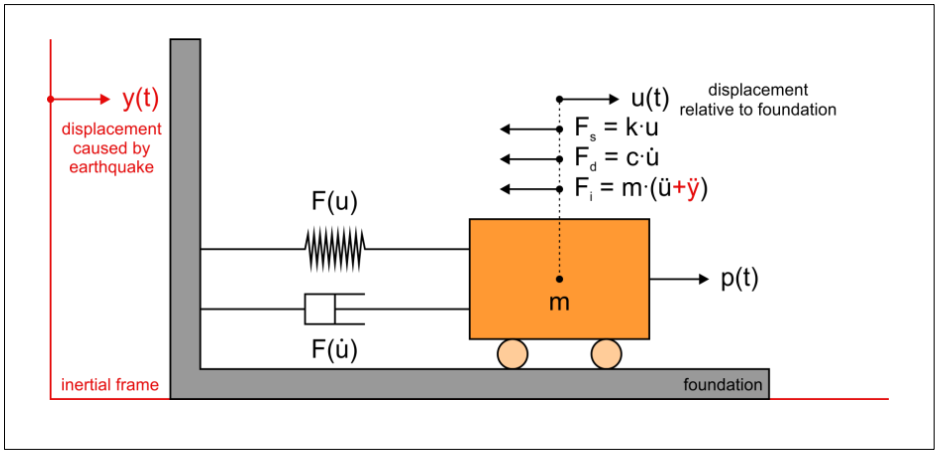

Fig. 6.1. Scheme of a linear visco-elastic oscillator with one degree of freedom.
The vibration is supposed to be free and damped if there is no external force applied, i.e. if p(t) = 0.

The setting of Fig. 6.1 can be described by the vibration equation that balances forces

$$\underbrace{m \cdot (\ddot{u} + \ddot{y})}_{F_i} + \underbrace{c \cdot \dot{u}}_{F_d} + \underbrace{k \cdot u}_{F_s} = p(t)$$

with:	m	…	mass of the oscillator	
	c	…	damping constant	
	k	…	stiffness constant	
	p	…	external force applied to the oscillator	(in this case 0)
	F_i	…	inertial force applying on the oscillator	(as function of ü and ÿ)
	F_d	…	damping force applying on the oscillator	(as function of u̇ only)
	F_s	…	elastic force applying on the oscillator	(as function of u only)

With the two physical quantities of eigenfrequency (f) and the damping ratio (ξ)

$$f = \frac{1}{T} = \frac{\omega_0}{2 \cdot \pi} = \frac{1}{2 \cdot \pi} \cdot \sqrt{\frac{k}{m}} \qquad \xi = \frac{c}{2 \cdot \sqrt{k \cdot m}} = \frac{c}{2 \cdot m \cdot \omega_0} = \frac{c}{c_c}$$

the equation can be rewritten as one of a free and damped vibration without external force:

$$\ddot{u} + 2 \cdot \xi \cdot \omega_0 \cdot \dot{u} + {\omega_0}^2 \cdot u = -\ddot{y}(t)$$

The interest on the solution for a time-history of the displacement (u) which is obtained by:

- an analysis in the frequency domain

$$u(t) = \sum_{k=-\infty}^{\infty} c_k \cdot H \cdot \left(\frac{2 \cdot \pi \cdot k}{T_p} \right) \cdot e^{\frac{2 \cdot i \cdot \pi \cdot k}{T_p} \cdot t}$$

- or Duhamel's Integral in the time domain

$$u(t) = -\frac{1}{\omega_d} \cdot \int_0^t \ddot{y}(\tau) \cdot e^{-\xi \cdot \omega_0 \cdot (t-\tau)} \cdot \sin\left(\omega_d \cdot (t-\tau)\right) d\tau$$

In many cases it is rather the maximum value of the displacement-time-history that is of particular importance; it is usually given in form of the response spectrum (S_D) of the relative displacement. Also a response spectrum of the pseudo-acceleration (S_A) is frequently used. The prefix "pseudo-" refers to the fact, that it designates the acceleration relative to the foundation (cf. Fig. 6.1).

$$S_D(T, \xi) = \max_t u(T, \xi, t)$$

$$S_A(T, \xi) = {\omega_0}^2 \cdot S_D(T, \xi)$$

In case T and ξ are not variable – i.e. if there is only one oscillator with one signal to test – the result will not be a spectrum but one single maximum displacement value as in CESAR.
Although the background principles are the same, a system with n degrees of freedom is more complex to deal with. Here, the method of modal recombination is necessary to obtain a displacement time-history or a response spectrum.
In contrast to the previous case (cf. Fig. 6.1) where a mass is concentrated in only one point, a model usually contains a multitude of points – the finite number of nodes of the imposed mesh – in which the displacement should be evaluated. By only considering points (and not elements), every distinct one can experience translational motion in three directions. The degree of freedom (n) of a system is hence:

$$n = p \cdot 3 \qquad \text{with p being the number of points}$$

Accordingly, a system has also n eigenfrequencies and n eigenmodes. Following the direct method of setting up an equilibrium equation, the resulting force in every point must be 0. In analogy to the previous equation the applying inertial, damping, elastic and external forces are:

$$\underbrace{\underline{\underline{M}} \cdot \underline{\ddot{U}}}_{\underline{F_i}} + \underbrace{\underline{\underline{C}} \cdot \underline{\dot{U}}}_{\underline{F_d}} + \underbrace{\underline{\underline{K}} \cdot \underline{U}}_{\underline{F_s}} = \underline{P}(t)$$

In this equation for a forced and damped vibration, $\underline{\underline{M}}$, $\underline{\underline{C}}$ and $\underline{\underline{K}}$ are matrices; $\underline{\ddot{U}}$, $\underline{\dot{U}}$, $\underline{U}$, $\underline{F_i}$, $\underline{F_d}$, $\underline{F_s}$ and $\underline{P}$ are vectors.
The preceding step for the modal recombination is the evaluation of the eigenfrequencies and the eigenmodes of the system. Logically, they depend only on the oscillator itself and therefore the evaluation is carried out for an equation of a free and undamped vibration:

$$\underline{\underline{M}} \cdot \underline{\ddot{U}} + \underline{\underline{K}} \cdot \underline{U} = \underline{0}$$

After several mathematical shifts the equation has the general solution $\underline{U}$ in which ω_i are the eigenvalues, $\underline{D_i}$ the associated eigenvectors (or eigenmodes) and f_i the eigenfrequencies.

$$\left(\underline{\underline{K}} - {\omega_i}^2 \cdot \underline{\underline{M}}\right) \cdot \underline{D_i} = \underline{0} \qquad f_i = \frac{\omega_i}{2 \cdot \pi}$$

$$\underline{U} = \sum_{i=1}^{n} \underline{D_i} \cdot \underbrace{\sin(\omega_i \cdot t + \theta_i)}_{below\ called\ b_j(t)}$$

Once the matrices $\underline{\underline{M}}$ and $\underline{\underline{K}}$ are known, the eigenvalues (ω_i) can be calculated via the equation below; this is possible due to the orthogonality of the eigenvalues to the matrices $\underline{\underline{M}}$ and $\underline{\underline{K}}$.

$${\omega_i}^2 = \frac{\underline{D_i}^T \cdot \underline{\underline{K}} \cdot \underline{D_i}}{\underline{D_i}^T \cdot \underline{\underline{M}} \cdot \underline{D_i}}$$

Having such an expression for the displacement ($\underline{U}$) with the eigenmodes $\underline{D_i}$ and their particular orthogonal properties is a great advantage for further computations – e.g. at the solution of an equation of a forced and damped vibration. By making use of the quantities of generalized mass (m_j), stiffness (k_j), damping (c_j) and external load (p_j), the equation takes a well familiar shape:

- $m_j = \underline{D_j}^T \cdot \underline{\underline{M}} \cdot \underline{D_j}$
- $k_j = \underline{D_j}^T \cdot \underline{\underline{K}} \cdot \underline{D_j}$
- $c_j = \underline{D_j}^T \cdot \underline{\underline{C}} \cdot \underline{D_j}$
- $p_j = \underline{D_j}^T \cdot \underline{P}$

$$\ddot{b}_j(t) + 2 \cdot \xi_j \cdot \omega_j \cdot \dot{b}_j(t) + {\omega_j}^2 \cdot b_j(t) = \frac{p_j(t)}{m_j}$$

for j = 1, … , n

As for the damping, ξ_j is the percentage of damping for each mode and alternatively called "modal damping". The damping matrix $\underline{\underline{C}}$ is in general very difficult to build; among other forms of damping, CESAR uses Rayleigh-Damping which conveniently expressed as function of the matrices $\underline{\underline{M}}$ and $\underline{\underline{K}}$.

$$\xi_j = \frac{c_j}{2 \cdot m_j \cdot \omega_j} \qquad \underline{\underline{C}} = \alpha \cdot \underline{\underline{M}} + \beta \cdot \underline{\underline{K}}$$

In conformity to the setting in Fig. 6.1 and considering the effect of an earthquake, one can now define an equation for a free and damped vibration with n degrees of freedom as well as its solution:

$$\underline{\underline{M}} \cdot \ddot{\underline{U}} + \underline{\underline{C}} \cdot \dot{\underline{U}} + \underline{\underline{K}} \cdot \underline{U} = -\underline{\underline{M}} \cdot \ddot{\underline{Y}}$$

$$\underline{U} = \underline{\underline{\Phi}} \cdot \underline{B} = \sum_{i=1}^{n} \underline{D_i} \cdot b_j(t)$$

Making again use of the generalized quantities (m_j, k_j, c_j and p_j), the orthogonality of the eigenvalues to the matrices $\underline{\underline{M}}$ and $\underline{\underline{K}}$, the vector $\underline{\Delta}$ giving the direction of loading and the participation factors a_j, the equation becomes:

$$a_j = \frac{\underline{D_j}^T \cdot \underline{\underline{M}} \cdot \underline{\Delta}}{\underline{D_j}^T \cdot \underline{\underline{M}} \cdot \underline{D_j}} = \frac{b_j}{q_j}$$

$$\underline{U} = \sum_{i=1}^{n} \underline{U_i} = \sum_{i=1}^{n} a_j \cdot \underline{D_i} \cdot q_j(t)$$

The total displacement is hence a summation over (or a "superposition" of) all the modes. Again, the variation of the displacement ($\underline{U}$) can be computed with Duhamel's Integral. Maximum values are to be represented in a response spectrum of the relative displacement (S_D) or in a response spectrum of the pseudo-acceleration (S_A). In this thesis, the interest is on the recovery of maximum displacements; the necessary procedure is referred to as "modal recombination".

$$q_j(t) = -\frac{1}{\omega_{dj}} \cdot \int_0^t \ddot{Y}(\tau) \cdot e^{-\xi_j \cdot \omega_j \cdot (t-\tau)} \cdot \sin\left(\omega_{dj} \cdot (t-\tau)\right) d\tau$$

$$S_D(\omega_j, \xi_j) = \max_t q(\omega_j, \xi_j, t) \qquad S_A(\omega_j, \xi_j) = {\omega_j}^2 \cdot S_D(\omega_j, \xi_j)$$

6.3.2. Equivalent Steps in CESAR

For a modal recombination analysis in CESAR there are two computational modes to be applied one after the other; both modes belong to the mode types "dynamic mechanics" in CESAR:

- MODE: referring in French to "analyse modale"
- SUMO: referring in French to "superposition modale" – i.e. here modal recombination

Based on the structure of interest itself, a MODE-computation determines the first n eigenvalues ω_i and n associated eigenvectors Φ_i that satisfy the following relation (ITECH, IFSTTAR, 2014). For the Diezma Landslide the first 20 eigenvalues and eigenvectors were calculated.

$$\underline{\underline{K}} \cdot \underline{\underline{\Phi_i}} = \omega_i \cdot \underline{\underline{M}} \cdot \underline{\underline{\Phi_i}} \qquad \text{for i = 1, … , n (here 20)}$$

Every SUMO-computation is preceded by a MODE-computation since the procedure of modal recombination incorporates the eigenmodes of the structure itself. Thereupon based, a SUMO-computation determines the response of a structure subjected to dynamic loading in terms of nodal displacements. Out of two options, which are either a computation of the full response, or an estimation of solely the maximum response using spectral computation, the latter was chosen.

6.4. Application to the Diezma Landslide

For the Diezma Landslide there are a simplified 2D- and a simplified 3D-geometry (cf. 4.2.2., 4.2.3.), both of which were analyzed with CESAR – however with a different number of separate sub-models. In the following, the model outlines (cf. A.12.) in 2D and 3D are specified according to the input procedure within CESAR.

Geometry

The model dimensions in 2D and 3D correspond exactly to the simplified 2D- and 3D-geometries (cf. Fig. 4.12, Fig. 4.17). It should be noted that the longitudinal cross section (2D) fits into the 3D-model without compromise and lies in its first axis.
The 2D-geometry is subdivided into five adjacent surfaces. The 3D-geometry is delimited by 34 triangular planes across the ground surface and the sliding surface; the total of 68 planes encloses one single volume without subdivisions.

Mesh

Mesh-sizes differ for both models. The 2D- and the 3D-model have respectively a triangular mesh with an increment size of 0.5 m and a tetrahedral mesh with an increment size of 1.1 m. As a result, the point numbers in each of them vary considerably. Considering the necessary relation for appropriate mesh creation (cf. 4.4.) with respect to increment size, frequency content and wave velocity, one can see that 1.1 m is just enough to properly represent the Diezma Landslide with its shear wave velocity of 300 m/s.

$$\frac{v_{min}}{f_{max}} = \lambda_{min} \qquad \text{and} \qquad \frac{\lambda_{min}}{10} = \Delta x$$

In 2D and 3D, the models have approximately 40,000 and 450,000 mesh-points respectively.

Properties

When attributing properties to surfaces or volumes, CESAR asks for the density (ρ in kg/m^3), the Young's Modulus (or elasticity modulus; E in MN/m^2) and the Poisson's Ratio (υ without dimension). The shear wave velocity (v_s in m/s) influences the Young's Modulus (E) inasmuch as the latter includes the shear modulus (G in Pa).

$$\rho \cdot g = \gamma \qquad v_s = \sqrt{\frac{G}{\rho}} \qquad G = \frac{E}{2 \cdot (1+\nu)}$$

Constant parameters throughout the 2D- and 3D-models are thus:

- ρ = 2181.45 kg/m^3 (γ = 21400 N/m^2; DELGADO et al., 2015)
- υ = 0.25 (-) (MARTINO et al., 2016)

Parameters dependent on the shear wave velocity must be calculated, e.g. via a simple Excel-spreadsheet. Shear wave velocities ranges are:

- 2D: 100-1000 m/s (in steps of 50 m/s)
- 3D: 300 m/s (only)

The response spectra – which allowed maximum displacement estimations for each eigenmode – were calculated assuming a damping ratio of 5%.

Boundary conditions

In 2D, boundary conditions of "zero-displacement" were applied to all edges along the sliding surface meaning that in all concerned points (including point 0 and E; cf. Fig. 4.8) the expected displacements are 0. In analogy for the 3D-case, the same boundary condition was imposed to all triangular planes and edges delimiting the sliding surface. Hence, the edges that the sliding surface and the ground surface have in common show zero displacements in all directions.

Loading

In CESAR, dynamic loading is applied to the lower model base as displacement time-history in meters, which are then transformed into body forces, and a so-called "load-case-factor" multiplies the signal before application. In the present case, the shear wave signal is supposed to arrive vertically and taking effect on the landslide mass by horizontal particle motion only. Therefore factors for body forces are 1-0 for (u-v) in 2D and 1-0-0 (for u-v-w) in 3D (cf. blue letters in Fig. 6.16).

The exact procedure for conducting MODE- and SUMO-computations in 2D and 3D for the Diezma Landslide can be found in the appendix. Two expandable workflow charts describe all steps; additional comments and code notes are to be found in section A.5. with its subsections.

6.4.1. Step MODE in 2D

As a first step, eigenfrequencies resulting from the MODE-computation were recovered from the output files. For every shear wave velocity there is a series of the twenty first eigenfrequencies; f_0 is the fundamental one and f_1-f_{19} represent the following ones (cf. Fig. 6.2). Strikingly, frequencies of the same rank form a straight line on the plot, and the higher the rank, the closer – and flatter – is the gradient of the line. It appears therefrom that the frequencies are mainly influenced by the shear wave velocity, since neither the geometry nor the site-specific parameters (cf. 6.4.) changed during the computation of the 19x20 values and in contrast to the following SUMO-computation (cf. 6.4.2.) there is no seismic signal involved yet.
The dashed line in Fig. 6.2 shows the real resonance frequency of the Diezma Landslide indicated by DELGADO et al. (2015). Considering the fact that the here presented data is based on the simplified geometry, which does not feature all the details of the original landslide mass, the real and calculated fundamental eigenfrequency at the shear wave velocity of 300 m/s are in very good correspondence.

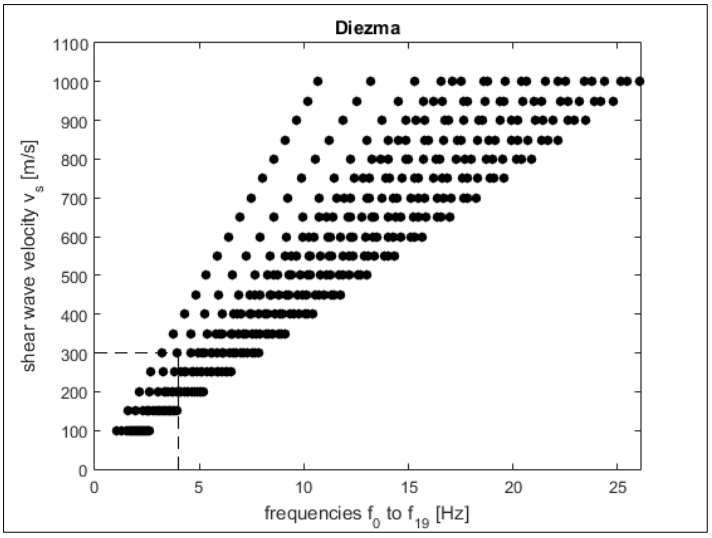

Fig. 6.2. First twenty resonance frequencies per shear wave velocity.
The fundamental frequency (f_0) is always the leftmost; dashed lines show the real values of the Diezma Landslide.

6.4.2. Step SUMO in 2D

To get a global idea of maximum displacements along the slope surface of the Diezma Landslide the three points 1, 2 and 3 having the identification numbers 3831, 13756 and 29374 were examined (cf. Fig. 4.8, Fig. A.1.) before processing the entirety of all 1011 surface points. Per signal, maximum horizontal and vertical displacements were calculated for each shear wave velocity to represent them in two double logarithmic plots respectively (cf. Fig. 6.3). The fact that labels are too small to be legible is of minor importance since interpretations in these section focus on the behavior of the curves only. The legend in the right lower corner indicates the labels of all plots.
Compared to the plots shown in Fig. 6.8, the representation of Fig. 6.3 can be seen as sections in the plane defined by the second and the third axes (i.e. by displacement versus shear wave velocity). Nevertheless, it must be noted that although the displacement curves in both plots have similar decreasing tendencies, the plots do not show the same type of displacements. Figure 6.3 shows displacements of three particular points, whereas displacements in Fig. 6.8 are averaged on certain percentages – a concept that will be explained alongside the Characteristic Period Based Approach (MARTINO et al., 2016).
What is clearly evident from Fig. 6.3 is that both the horizontal as well as the vertical displacements become bigger with decreasing shear wave velocity what corresponds to the concept of site effects and impedance contrast (cf. Fig. 1.3). If the usually high shear wave velocity of the underlying bedrock is similar to the one of the landslide mass, the impedance contrast and expected displacements are low.
The comparisons of horizontal and vertical displacements throughout the signals reveal that generally the former is bigger than the latter. Roughly speaking, it seems on a first glance that vertical displacements in points 2 and 3 are smaller by one order of magnitude than their horizontal counterparts; vertical displacements in point 1 are also smaller but remain of the same order of magnitude.
The comparison of horizontal and vertical displacements per individual signal shows that point 3 is the most prone to offset, followed by point 2 in the same range and finally by point 1 with a significant difference.
Both findings – regardless of the exact influence of the distinct seismic signals – emphasize several preliminary conclusions:

- one main zone of displacement located around point 3 where the landslide is thickest
- almost negligible displacements around point 1 where the landslide is thinnest
- biggest contributions to displacement by horizontal components

Actually, the last finding is also typical for landslides controlled by static loads – not only for those undergoing dynamic loading.
In some respects peculiar are also the curve shapes of points 1, 2 and 3 in Fig. 3. Some of the curves appear almost straight in the double-logarithmic plot whereas some clearly show a hunch. One attempt to explain this behavior consists in cross-checking with the respective Fourier Amplitude Spectra (FAS; cf. Fig. 4.20a-k) and listing if the curves show hunches or if the FAS includes two peak zones. FAS with two peak zones are such having one high peak at a very low frequency followed by two or three more almost equally high peaks “shortly afterwards” as for example in the FAS of signal D (cf. Fig. 4.20d). Here, the conjecture is that signals with two FAS zones cause hunches, whereas one FAS zone entails only a straight line. According to Tab. 6.1 the conjecture is confirmed in most but not all of the cases.
Signal F represents the “unexplainable artifact”. In no other plot (cf. Fig. 6.3) the displacements at 100 m/s are smaller than the ones at 150 m/s. Interestingly, only point 3 is affected by this unusual behavior, which is also visibly – but not explicable – in Fig. 6.8 and Fig. 6.9 depicting displacements averaged on certain percentages.

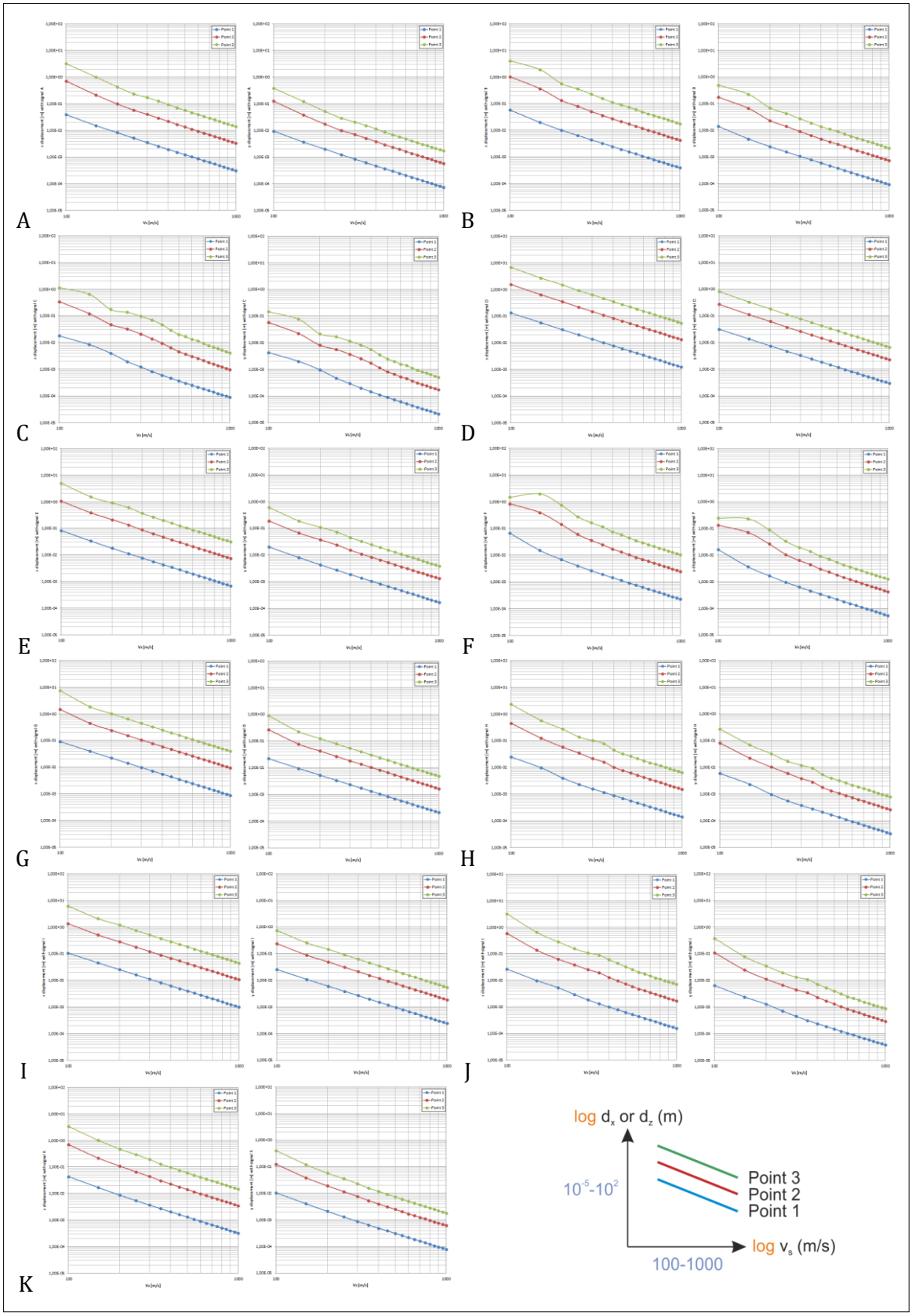

Fig. 6.3. Horizontal (left) and vertical (right) displacements for points 1, 2 and 3 (cf. Fig. 4.8) per signal. For easy comparability all plots have the same format which is exemplarily shown by the legend in the right lower corner. Horizontal and vertical displacement are abbreviated with "d_x" and "d_z" respectively.

signal	line/hunch	FAS zones	conjecture confirmed
A	L	1	✓
B	H	2	✓
C	H	2	✓
D	L	1	✓
E	H & L	2	2 pronounced zones and almost no hunch
F	H	1	1 pronounced zone and an extreme hunch
G	L	1	✓
H	H	2	✓
I	L	1	✓
J	H	2	2 pronounced zones and almost no hunch
K	L	1	✓

Tab. 6.1. Correlation between curve behavior (cf. Fig. 6.3) and respective FAS (cf. Fig. 4.20a-k).

In a second stage, tests for 100 m/s, 300 m/s and 1000 m/s examined if there is a relation between horizontal and vertical displacements and the highest reached FAS amplitude per signal. Unfortunately one can recognize from Tab. 2 that the signals with the highest FAS peaks do not induce the greatest displacements. Although tested for the above mentioned shear wave velocities and for horizontal and vertical displacements, Tab. 6.2 only lists values for the horizontal displacements at 100 m/s. However, the general qualitative behavior appearing via the gray shading is the same for all combinations.

Also questionable and maybe even more promising is the correlation to the filtered characteristic mean periods of the earthquakes (T_m) and the ratios of the characteristic site periods (T_s/T_m and T_l/T_m) both of which will be explained alongside the Characteristic Period Based Approach (MARTINO et al., 2016).

Clearly, signals D, E, G and I have the greatest displacements at the points 1, 2 and 3. Surprisingly they share not only a spectrum starting out with two to three very high peaks, but also the highest T_m-values. Signals D, I and G exceed 1 and signal E reaches still 0.77. This finding thus leads to assumption that the characteristic earthquake period (T_m) might have a considerable influence on seismically induced displacements.

The ratios of the characteristic site periods (T_s/T_m and T_l/T_m) seem to be inversely orientated towards the greatest displacements. Here, it should be considered, though, that the characteristic earthquake period (T_m) – which is the denominator in both ratios – correlates well and that therefore an inverse correlation with the characteristic site periods is not surprising. The fact rather underlines the assumption of a T_m-correlation.

signal	max FAS (m/s)	filtered T_m (s)	T_s/T_m* (-)	T_l/T_m* (-)	dx_1* (m)	dx_2* (m)	dx_3* (m)
A	> 0.01	0.70	1.12	7.20	0.04	0.71	3.20
B	> 0.02	0.66	1.18	7.61	0.06	1.03	4.07
C	> 0.02	0.32	2.43	15.64	0.02	0.34	1.15
D	> 0.02	1.08	0.72	4.66	0.13	1.55	6.81
E	> 0.02	0.77	1.01	6.49	0.08	1.06	5.04
F	> 0.04	0.58	1.34	8.62	0.07	0.84	1.47
G	> 0.02	1.02	0.77	4.94	0.09	1.48	7.56
H	> 0.01	0.38	2.03	13.11	0.02	0.45	2.32
I	> 0.01	1.19	0.66	4.24	0.11	1.36	6.21
J	> 0.02	0.49	1.61	10.37	0.03	0.60	3.24
K	> 0.02	0.76	1.02	6.60	0.04	0.70	3.40

Tab. 6.2. Comparison of different signal properties and horizontal displacement values for v_s = 100 m/s (*).

After this first overview with focus on three points along the slope surface, further examinations were carried out for all of the 1011 surface points.
For each of the 209 combinations – 11 signals with 19 shear wave velocities – there is one longitudinal cross section showing the horizontal, the vertical and the resultant displacement of every point in green, blue and red respectively (cf. Fig. 6.4a-b). It should be noted that the resultant displacement is simply calculated by the Pythagorean Theorem:

$$d_r = \sqrt{{d_x}^2 + {d_z}^2}$$

For better visualization all displacements in those plots are factorized by 50. Scientifically this is surely an uncomfortable number since it does not allow for easy reading of values, but unfortunately the factor 10 appeared to be by far too small because the biggest displacements reach values in the centimeter range. The factor 100, in contrast, would have caused the colored curves to exceed the image frames.
A second type of graphic representation shows the curves of horizontal, vertical and resultant displacement per x-coordinate-position (cf. Fig. 6.4c-d) per combination. The advantage of this representation is that it avoids the factor issue by automatically scaling the second axis according to the reached maxima. Nevertheless, one should pay attention to the orientation of those plots since the x-coordinate-position is similar but not identical to the real point position on the slope surface. Also, the three types of displacement are plotted "vertically upwards"; i.e. one should not interpret the horizontal and resultant displacements in Fig. 6.4c-d as topographic heaves.

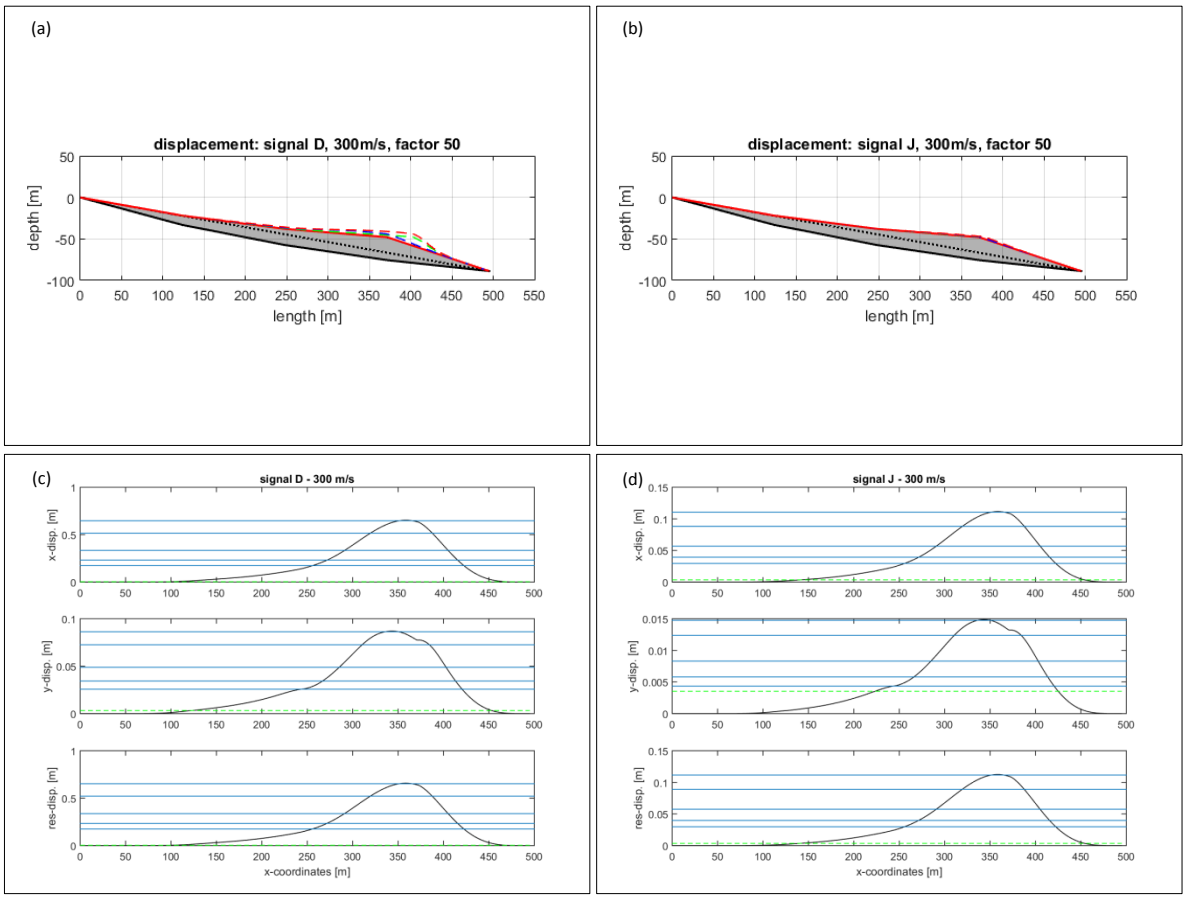

Fig. 6.4a-d. Horizontal (green dashed & 1st subplot), vertical (blue dashed & 2nd subplot) and resultant (red dashed & 3rd subplot) displacements for signals D and J at shear wave velocities of 300 m/s. Both signals represent cases with high and low entrained displacements respectively. The green dashed lines in c) and d) mark the Newmark-displacement (1965) which is constant per signal. The blue lines in c) and d) mark the average of the biggest 5%, 25%, 50%, 75% and 100% (cf. Excursus – 6.4.2.).

Comparing the 209 graphics of each representation type, several qualitative and quantitative features can be recognized:

- displacements appear to be of the same pattern regardless of the signal, and generally d_x are considerably bigger than d_z, thus d_r are slightly smaller than d_x
- displacements rapidly decrease with increasing shear wave velocity, and even at factor 50 displacements are invisible at 250-350 m/s (cf. Fig. 6.4a-b)
- per signal displacements decrease most significantly between 100 m/s and 150 m/s, and at signals D, E, G and I displacements stay visible up to 600-750 m/s (cf. Tab. 6.3)

signal	d_r invisible at	F	~ 400 m/s
A	~ 450 m/s	G	~ 600 m/s
B	~ 450 m/s	H	~ 350 m/s
C	~ 350 m/s	I	~ 700 m/s
D	~ 750 m/s	J	~ 350 m/s
E	~ 600 m/s	K	~ 400 m/s

Tab. 6.3. Visibility of the resultant displacement (d_r) up to certain shear wave velocities.

Taking up again the hypothesis of hunches addressed in the beginning of this section, the second graphic type (cf. Fig. 6.4c-d) sheds light on some more details. Overall, horizontal, vertical and resultant displacements all show the expected behavior of a landslide with one main mobility zone. In this case this zone is located asymmetrically around point 3 where the slope angle changes from around 4° to around 18° (cf. Fig. 10). The fact that the vertical displacements are much smaller than the horizontal and the resultant ones lets the curves of the vertical displacements appear hunched and notches at zone limits (cf. Fig. 6.10). Therefore, one should not falsely interpret these features as real hunches. Slight hunches are though observable at the horizontal and resultant displacements at combinations B-100 m/s and C-100 m/s; at signal F appears again the conspicuous "unexplainable artifact" at 100 m/s (cf. Fig. 6.5a-c).

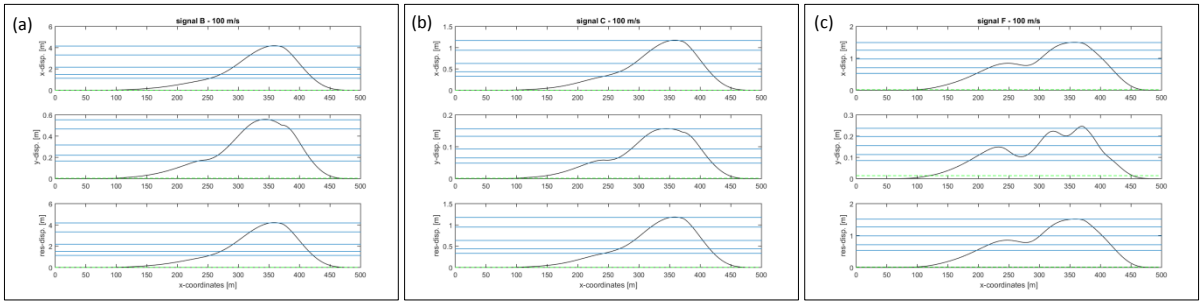

Fig. 6.5a-c. Horizontal, vertical and resultant displacements for combinations B-100 m/s, C-100 m/s and F-100 m/s. Axis labels and marking correspond to the ones in Fig. 6.4c-d.

The second graphic type (cf. Fig. 6.4c-d, Fig. 6.5a-c) also contains a dashed green line representing the respective Newmark-displacement (1965); it only varies per signal but it is constant throughout the shear wave velocities. It is therefore not surprising that the Newmark-displacement (1965) "grows" and even exceeds the displacements calculated by modal recombination with increasing shear wave velocity. Especially the vertical displacements are prone to exceedance due to their generally small values.
Table 6.4 displays in percent how many of the 1011 resultant displacements along the surface are bigger than the Newmark-displacement (d_n; 1965). It can be seen that – with one exception – the displacements calculated by modal recombination exceed the Newmark-displacement (1965) by 24-85% even at the highest shear wave velocity. Only at signal F, which has the highest Newmark-displacement (1965), there is no exceedance beyond 900 m/s. Tables for the resultant and the horizontal displacement are almost identical; in the table for the vertical displacement the exceedance levels are naturally much lower. Considering percentages at 300

m/s, it can be seen that 63-89% of the resultant displacements in every point along the slope surface are greater than the Newmark-displacement (1965) suggesting that particular care must be taken when using one of the two methods only. Table 6.4 shows also the maximum resultant displacements at 300 m/s; they exceed the respective d_n-values by up to 65.5 cm.

v_s	A	B	C	D	E	F	G	H	I	J	K
100	91	79	79	82	80	75	82	78	83	78	83
150	90	76	77	80	76	69	80	74	81	74	81
200	90	73	74	78	74	64	78	70	80	70	79
250	89	71	71	76	72	57	77	66	78	67	78
300	89	69	68	75	70	51	75	63	77	63	77
350	88	67	66	74	68	45	74	60	76	60	75
400	88	64	63	72	66	39	73	55	75	56	74
450	87	62	60	71	64	35	72	52	74	52	73
500	87	60	57	70	63	31	71	48	73	48	72
550	87	57	54	69	60	28	69	45	72	45	71
600	86	55	51	68	58	25	68	42	71	41	70
650	86	52	49	67	56	22	67	39	70	38	70
700	86	50	46	66	54	19	66	36	70	36	69
750	86	48	43	65	52	16	65	34	69	33	68
800	85	46	41	64	50	12	64	32	68	31	67
850	85	44	39	63	48	7	63	30	67	29	66
900	85	42	36	61	46	0	62	28	66	27	65
950	85	40	35	60	44	0	61	26	65	26	64
1000	85	38	33	59	42	0	60	25	65	24	63
T_m (s)	0.70	0.66	0.32	1.08	0.77	0.58	1.02	0.38	1.19	0.49	0.76
d_N (cm)	0.00	0.38	0.12	0.33	0.53	1.41	0.21	0.30	0.15	0.35	0.06
$d_{\_res\_max\_300}$ (cm)	17.8	23.6	10.0	65.8	38.4	16.9	45.5	10.5	53.1	11.3	19.9
diff. to d_N (cm)	17.8	23.2	9.9	65.5	37.8	15.4	45.3	10.2	53.0	10.9	19.9

Tab. 6.4. Percentage points (of 1011 in total) for which the resultant displacements are bigger than the d_n-values per signal. There is no obvious relation to T_m-values. The last two rows give the maximum resultant displacements at 300 m/s per signal and the maximum differences to the respective d_n-values.

There is no obvious relation to characteristic periods nor to their ratios. In some degree this could be expected, because a comparison implies the line-up of T_m, Ts/T_m or T_l/T_m (which are based on the shear wave velocity) and the exceedance of the Newmark-displacement (1965) in percent (which clearly does not include the velocity concept).
From the previous paragraphs it is thus clear how difficult displacement comparisons are since they do not base on the same input and give a different quantitative output (cf. Tab. 6.5):

method	input	output
NEWMARK (1965)	W, l, c', Φ', β', signals	1 d_n for entire slope per signal
modal recombination	v_s, γ, ρ, υ, G, E, signals	1 d_x, 1 d_z and 1 d_r for each point along slope per signal

Tab. 6.5. Input dependency of d_n-values; it should be noted that in 3D modal recombination analysis also gives a second horizontal displacement (d_y).

Ideally one method would deliver one value, and in the best case the obtained displacement would be in the same direction. Simply by checking the third column of Tab. 6.5, one can see that this is not the case for both concerned methods. In order to avoid this discrepancy MARTINO et al. (2016) proposed the Characteristic Period Based Approach which derives from all horizontal displacement values (i.e. in the direction of d_x) only one value that should be representative for

the entire slope. In this thesis, attempts for usage of this approach were made; prior to the description of the procedure, though, an excursus presents the background and concept of the approach.

Excursus – The Characteristic Period Based Approach and its Application in two Examples

The Characteristic Period Based Approach (MARTINO et al., 2016; in the following abbreviated by CPB-Approach) estimates seismically induced landslide displacements and gives results in relation to the characteristic period ratios T_s/T_m and T_l/T_m. The components of these ratios are:

characteristic earthquake period	$T_m = \frac{\sum A_i^2 \cdot T_i}{\sum A_i^2}$	(RATHJE et al., 2004; cf. equation in 4.4.)
characteristic site period	$T_s = \frac{4 \cdot h}{v_s}$	(RATHJE & BRAY, 2000; cf. Fig. 6.6)
characteristic site period	$T_l = \frac{l}{v_s}$	(HUTCHINSON, 1978; cf. Fig. 6.6)

The authors suggest that the expected horizontal displacements depend on a combination of 1D- and 2D-effects – more precisely on the interplay of the resonance of the landslide and the interaction between the earthquake and the landslide. Maximum horizontal displacements are expected for:

$$\frac{T_s}{T_m} \approx 1.0 \quad \text{and} \quad \frac{T_l}{T_m} \approx 0.5$$

As for T_s, it is obvious that when $T_s \approx T_m$, then also $f_s \approx f_m$, and the more similar two frequencies are, the more likely is the phenomenon of resonance and constructive interference. For T_l however, maximum displacements are expected when $T_l \approx l$ and $T_m \approx 2 \cdot l$. Under that condition, and especially when the landslide is rather flat, its entire mass is subjected to movement in one direction only (cf. Fig. 6.6).

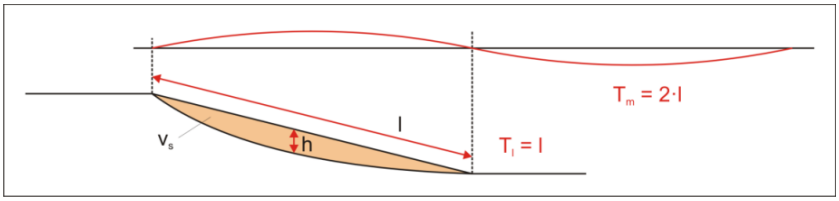

Fig. 6.6. Setting assumed to cause maximum displacement.

After the application of different seismic signals (T_m) to one particular slope geometry (T_s and T_l), the CPB-Approach retrieves one horizontal displacement per combination by:

- sorting all d_x-values from the biggest to the smallest,
- keeping the biggest 5% of them,
- and plotting the mean value of those remaining 5%.

In their publication the authors tested the approach at two well studied landslide sites. The Güevéjar Landslide is known not to have any particular resonance. It was activated by the Lisbon 1755 Earthquake (1st of November 1755; M_W = 8.5) and reactivated by the Arenas del Rey Earthquake (25th of December 1884; M_W = 6.3); for this reason it is listed with numbers 040.01 and 040.02 in the database. The Diezma Landslide (001.00) does not have a seismic trigger but clear signs of resonance within its body. The application of the CPB-Approach to both landslides revealed a coherent picture which is schematically shown in Fig. 6.7 and explained in Tab. 6.6.

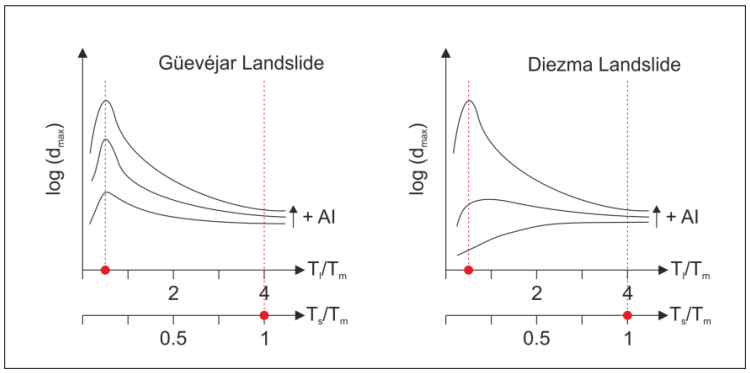

Fig. 6.7. Schematic semi-logarithmic plots relating the maximum horizontal displacement to the characteristic period ratios (cases of the Güevéjar Landslide and the Diezma Landslide).

landslide	1D-effect	2D-effect
Güevéjar	no particular resonance effect (no max. d_x at $T_s/T_m \approx 1.0$)	more significant with increase of Arias Intensity (max. d_x at $T_l/T_m \approx 0.5$)
Diezma	resonance effect visible at low Arias Intensity (max. d_x at $T_s/T_m \approx 1.0$)	

Tab. 6.6. Differences of 1D- and 2D- effects of the Güevéjar and the Diezma Landslides.

The findings are in good accordance with LENTI & MARTINO (2013) who suggested that 1D-effects are usually more significant at slopes with low inclinations, and rather to be seen at low energy input. With increasing Arias Intensities the 2D-effects seem to overshadow the 1D-effects.
In this thesis the CPB-Approach was again applied to the Diezma Landslide but with one major difference: MARTINO et al. (2016) used LEMA_DES-signals (cf. 4.4.), whereas here real filtered signals were applied to the slope in order to test the functionality of the approach with unprocessed signals. It should be noted that the LEMA_DES-series used by MARTINO et al. (2016) in fact consist of 11 signals just as well as the here employed series (signals A-K). However, the signals in the two series are not identical although they both were filtered from the ESMD (cf. 4.4.). In the two series the filtering criteria are different.
Furthermore, in the present case the analysis also deals with a variation of the shear wave velocity from 100 m/s to 1000 m/s. Thus, a third axis is added to the plots. In Fig. 6.8 and Fig. 6.9 one can see the horizontal displacements according to the CPB-Approach in relation to T_s/T_m and T_l/T_m respectively. Red and blue lines link values based on the same shear wave velocity and black lines link values obtained by the same signal; the order of the signals is indicated in the captions. The three small sub-figures show the main plot from the top, the front and the side which facilitates the interpretation:

top view ($1^{st}/2^{nd}$ axis) → smaller v_s with increase of characteristic period ratio
side view ($2^{nd}/3^{rd}$ axis) → smaller d_x with increase of v_s (signal F showing its hunch)
front view ($1^{st}/3^{rd}$ axis) → distorted two-notched d_x-pattern with increase of v_s

The appearances of the top and the side view were very coherent with the so far described principles. The front view, though, was rather surprising and even in some ways unsatisfactory since it was expected to reflect the principles of the CPB-Approach. Unlike in Fig. 6.7, the horizontal displacements are quite variable throughout the characteristic period ratios and there is no obvious tendency to be recognized – not for a T_s/T_m-ratio around 1.0 neither for T_l/T_m-ratio around 0.5.
Only at very high shear wave velocities the curves tend towards displacement maxima. Nevertheless, those shear wave velocities are by far too big to correspond to the real site conditions (300 m/s) and from the distorting behavior of the curves it is not clear if maxima are to be found around 0.5 or at even smaller T_l/T_m-values.

Incidentally, the appearance of the curves in the two plots does not change because of the fact that T_s/T_m and T_l/T_m are related by the factor $l/(4 \cdot h)$ (cf. Fig. 6.6), and so the representation is a question of the right scaling of the first axis (cf. Fig. 6.7).

$$\text{from} \quad T_s = \frac{4 \cdot h}{v_s} \quad \text{follows} \quad v_s = \frac{4 \cdot h}{T_s} \quad \text{and so} \quad T_l = \frac{l}{v_s} = \frac{l}{\frac{4 \cdot h}{T_s}} \quad \text{and thus} \quad \frac{T_l}{T_s} = \frac{l}{4 \cdot h} \cdot \frac{T_s}{T_m}$$

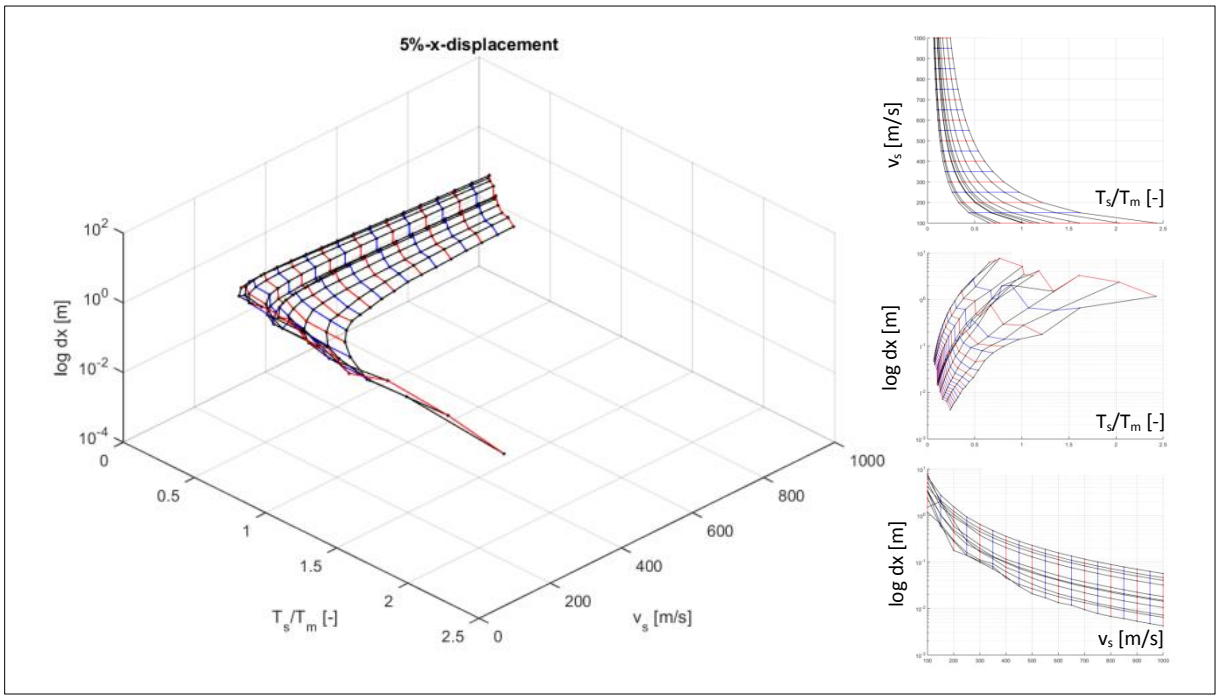

Fig. 6.8. Expected horizontal displacement according to the CPB-Approach in relation to T_s/T_m.
The sub-figures show the top, the front and the side views (from top to bottom).
For the top view, signals from left to right are I, D, G, E, K, A, B, F, J, H and C.

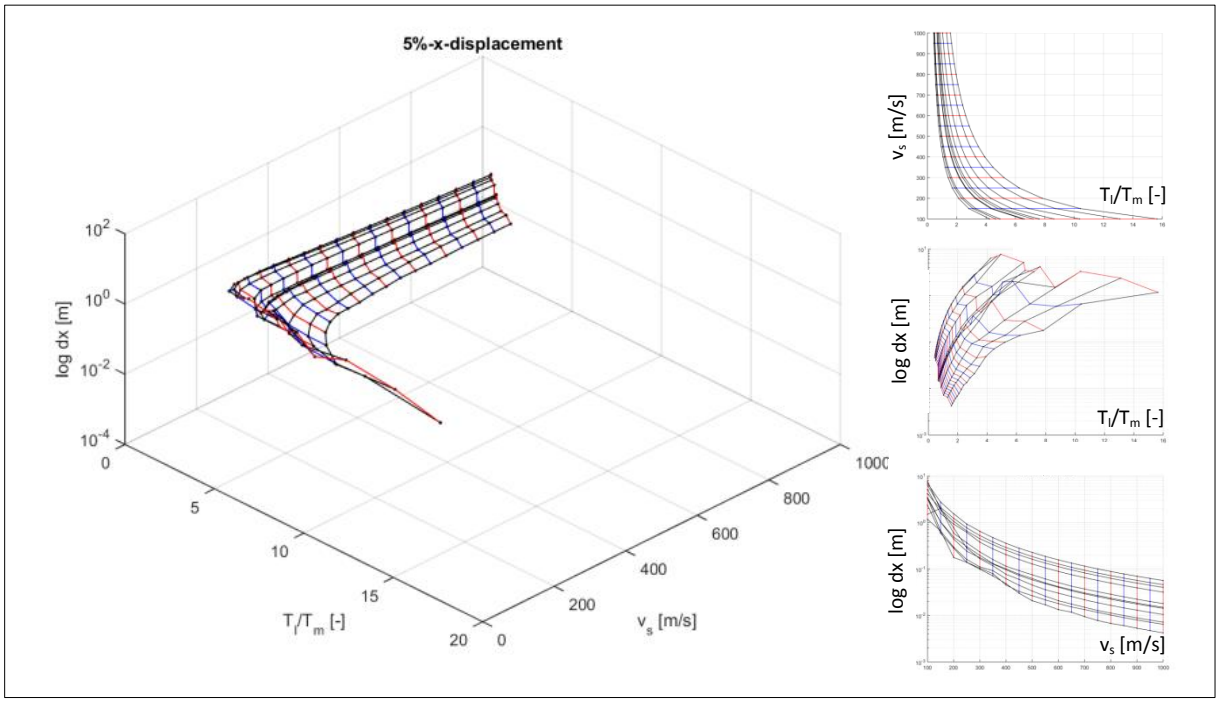

Fig. 6.9. Expected horizontal displacement according to the CPB-Approach in relation to T_l/T_m.
The sub-figures show the top, the front and the side views (from top to bottom).
For the top view, signals from left to right are I, D, G, E, K, A, B, F, J, H and C.

Due to that non-specific outcome of the analysis, the entire CPB-Approach was subsequently tested for the vertical and resultant displacements (with 5%) and also for the three displacements (horizontal, vertical and resultant) for 25%, 50%, 75% and 100% – of which the latter corresponds to the average of all displacements at the 1011 considered surface points.
Unfortunately all plots look almost identically and show the same distorted two-notched pattern. The overall expected principles (cf. previous paragraphs) could be confirmed:

- d_x being slightly bigger than d_r
- d_z being roughly one order of magnitude smaller than d_x
- displacements decreasing with increase in percentage (cf. Fig. 6.4c-d, Fig. 6.5a-c)

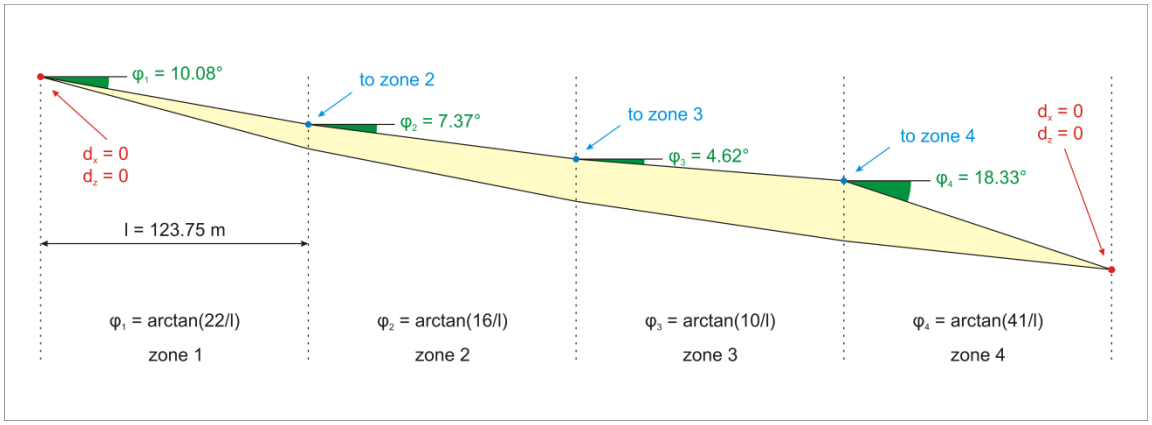

Fig. 6.10. The simplified geometry of the Diezma Landslide divided into 4 zones for projection of displacement components. Due to the boundary condition definition the first and the last point (red) have no displacement and hence their projections are 0 as well. Points 1, 2, and 3 (blue; cf. Fig. 4.8) are projected with φ_1, φ_2 and φ_3 respectively.

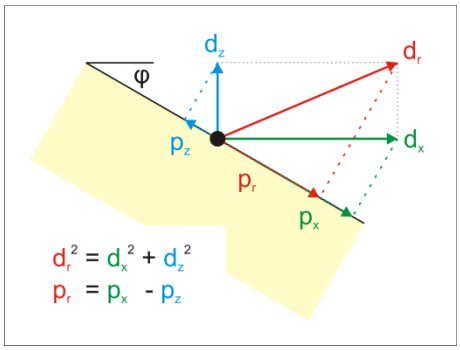

Fig. 11. Principle of projection.

In another attempt to verify the findings of MARTINO et al. (2016) and LENTI & MARTINO (2013) the entire analysis was repeated for projected displacements – starting out from graph plotting of type 1 and 2 (cf. Fig. 6.4a-d) and comparison of the 209 signal-v_s-combinations, via the line-up with Newmark-displacements (1965), to the CPB-Approach for all three types of displacement with the same steps of percentages.
The term "projected displacements" refers here to those displacement values that result from projection to the slope surface. Since the simplified geometry has four zones with different surface inclinations (cf. Fig. 6.10), horizontal and vertical components were projected according to the local slope angle. The resultant displacement is in this case defined by:

$$p_r = px - pz$$

Without long circumlocution, the results are almost equal. The same zonal behavior around point 3 (cf. Fig. 6.4a-d) as well as the "unexplainable artifact" at combination F-100 m/s reappears. Although the projected vertical displacements became considerably smaller than the

projected horizontal ones, the overall relation between the three types of displacement remains the same. The line-up with the Newmark-displacement (1965) is in good accordance with the results from the "non-projected" analysis; only the projected vertical displacements lie closer to the Newmark-displacement (1965). Finally, the application of the CPB-Approach in all combinations (p_x, p_z and p_r with 5%, 25%, 50%, 75% and 100%) could not clearly reproduce the schematic plots of Fig. 6.7 either. For this very reason, the CPB-Approach was not applied to the data resulting from modal recombination analysis in 3D.
Questionable remain the exact causes that lead to such diverging results. Some might be:

- the use of filtered but non-processed signals
  (In contrast to the here presented study, MARTINO et al. (2016) used signals that had undergone the LEMA_DES procedure (cf. 4.4.). The CPB-Approach was not tested for non-processed signals so far.)
- the unfavorable data coverage of the plots
  (It turned out that the zones of interest – i.e. around $T_s/T_m \approx 1.0$ and $T_l/T_m \approx 0.5$ – are only covered by displacement values that result from high shear wave velocities. The Diezma Landslide, however, has a shear wave velocity of 300 m/s. Therefore it is suggested that for future studies using the CPB-Approach, the coverage range should be taken into account while filtering seismic records from a database.)
- the less significant variation of the Arias Intensity
  (The main interpretation of the CPB-Approach is actually dependent on an energy increase – hence on a significant variation of the Arias Intensity. In this study, signals were filtered from the ESMD (cf. 4.4.) with the criterion of the Arias Intensity ranging from 0.1-1 m/s. Together with the three other filtering criteria the range of available Arias Intensities is only 0.08-0.27 m/s.
- the difference of the considered geometry
  (This study considers a simplified geometry which deviates from the original landslide mass. It remains doubtful, though, that the simplified geometry has such a strong influence on the applicability of CPB-Approach; effectively, conventional displacement evaluations without the CPB-Approach gave a very conclusive image of the expected behavior.)
- the choice of the h-value
  (By need of one single height value for almost any involved equation a choice had to be made in the very beginning of all subsequent studies. In this case h was set to 19.5 m which corresponds to the thickness of the landslide at point 2 (cf. Fig. 4.8). As Fig. 6.12 shows the thickness is very variable throughout the landslide body and so is the characteristic site period T_s.)

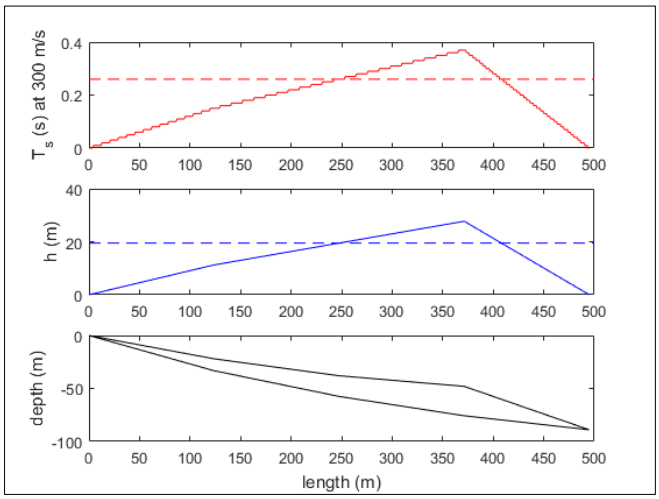

Fig. 6.12. Variation of the thickness (here called h) and the thereby linked characteristic site period (T_s). Adopted values are marked as dashed lines.

6.4.3. Step MODE in 3D

In analogy to the MODE-computation in 2D also the first twenty eigenfrequencies (f_0-f_{19}) in 3D were recovered. The frequency series per shear wave velocity are shown in Fig. 6.13 as red dots. Since the 2D-MODE-computation (cf. 6.4.1.) had shown that all dots align straightly with different inclinations, only frequency series for 100 m/s, 300 m/s and 1000 m/s were calculated to connect the dots by lines. For comparison the black dots represent the resonance frequencies in 2D.
Again, the real fundamental frequency revealed by the 3D-MODE-computation comes very close to what DELGADO et al. (2015) indicated.
Of particular note is the fact that the straight lines connecting frequencies of each rank lie much closer to each other. In other words, the inclinations of the straights do not become as low as in 2D. However, the inclination of the line connecting the fundamental frequencies has almost the same inclination and – as in 2D – the higher the rank of the frequencies, the closer come the connecting straights. It is thus quite possible that this striking difference of eigenfrequencies also has a considerable effect on the outcome of the 3D-SUMO-computation (cf. 6.4.4.) whose values are generally bigger than those of the 2D-SUMO-computation.

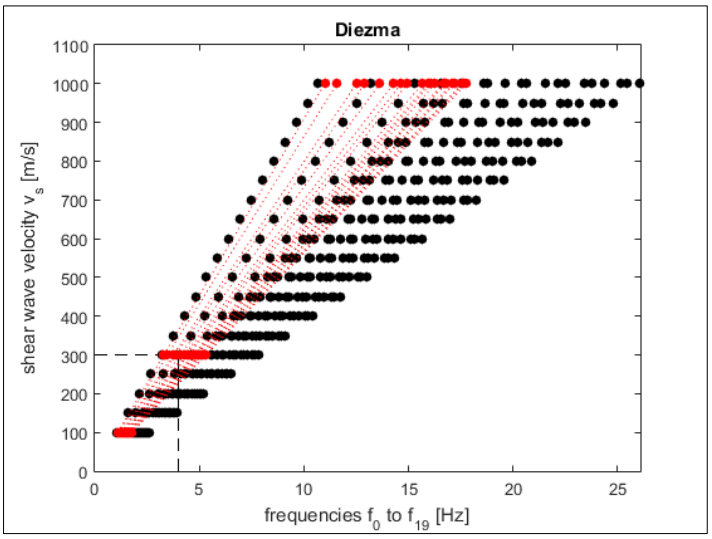

Fig. 6.13. First twenty eigenfrequencies per shear wave velocity (red dots for 3D, black dots for 2D)
The fundamental frequency (f_0) is always the leftmost; dashed lines show the real values of the Diezma Landslide.

6.4.4. Step SUMO in 3D

The displacement analysis in 3D was carried out in two versions and only for 11 combinations each (11 signals at 300 m/s):
One version only deals with points along the slope surface of the longitudinal cross section which corresponds to the one of the analysis in 2D. Here, the objective was to allow for easy comparison of 2D- and 3D-displacements. It is worth to note that in 3D there are only 479 points located along the slope surface of the concerned cross section – a fact that results from different mesh-sizes in the CESAR-Models (cf. 6.4.).
The other version includes all points on the slope surface making up a total of 61,594 points and enabling the exact localization of deformation zones by taking into account the second horizontal dimension.
To distinguish the two versions, the first one is called “LCS” and the second one “plane” although both terms are not ideal. According to the previous employment of the term “LCS” it refers to simply a whole longitudinal cross section (cf. 2.4.2.); as for the term “plane”, it refers to the fact that in the 3D-CESAR-Model the landslide mass is entirely covered by triangular plane tiles.
For all 11 signal-v_s-combinations of the LCS-version there is one quadripartite plot similar to the second graphic type (cf. Fig. 6.4c-d) showing the two horizontal displacements (red and blue),

the vertical (blue) and the resultant displacements (black) as function of the x-coordinate of the point (Fig. 6.14a-b.). The deducible behavior is corresponding well to the one observed in 2D:

- one main zone of displacement around point 3 (cf. Fig. 4.8)
- d_x significantly bigger than d_z (with d_y in between)
- d_x only slightly bigger than d_r
- visible zone limits (cf. Fig. 6.10) at d_y and d_z due to their small values and thus sensitivity

The resultant displacement is again defined by the root of the squared components as in 2D:

$$d_r = \sqrt{{d_x}^2 + {d_y}^2 + {d_z}^2}$$

Strikingly, all horizontal displacements in d_y-direction are positive, i.e. in the "inwards" direction if one considers the whole landslide mass as a curve-shaped object (cf. Fig. 6.20). This is inasmuch surprising as one might imagine rather the opposite. One explanation could be that the landslide mass is – lengthwise – unevenly thick; its western upper part is thinning out and gradually mixing with another geological formation (cf. 4.1., Fig. 4.3) whereas its middle and eastern parts reach much bigger depths leaving more mass to be excited.

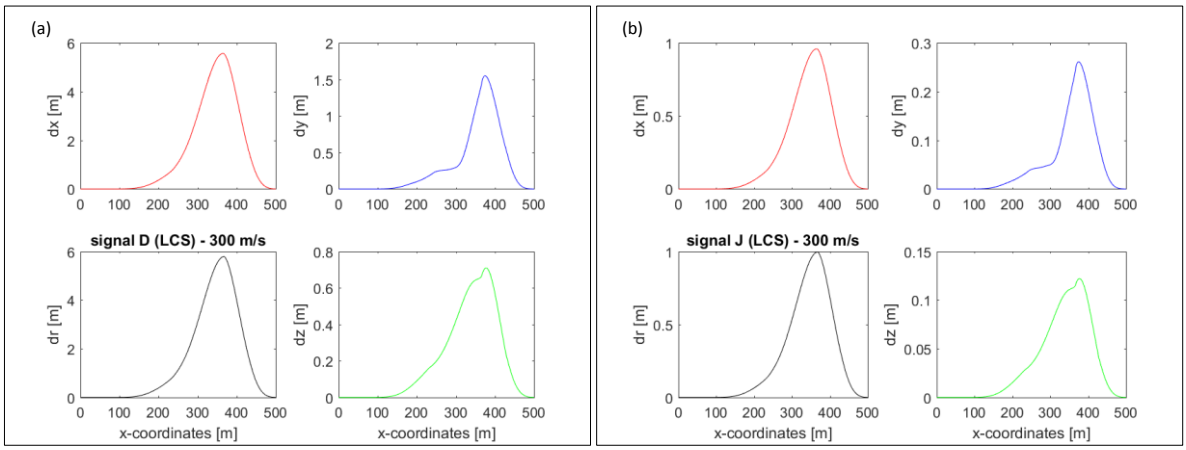

Fig. 6.14a-b. Horizontal (red and blue), vertical (green) and resultant (black) displacements for signals D and J at a shear wave velocity of 300 m/s. Both signals represent cases with high and low entrained displacements respectively.

Figure 6.15a-d show the same graphic type for the "plane" version with the same color codes and arrangements. Here, displacements are plotted as function of the x- and y-coordinates.
The lower two quadripartite plots (cf. Fig. 6.15c-d) are front views of their upper counterparts. Although they also represent a sort of longitudinal cross sections similar to those of Fig. 6.14a-b, it appears on a closer look that they reach slightly different values in all components as well as in the resultant displacement. The reason for this difference is that even though the simplified 3D-geometry does contain the simplified 2D-geometry without compromise, this simplified 2D-geometry does not constitute the relative topographical maximum of the landslide. The latter is defined by the middle point of the TCS C (cf. Fig. 4.10i) and in the following termed "nose (of the landslide)" to distinguish it from point 3, which is the relative topographical maximum of the simplified 2D-geometry (cf. Fig. 4.8).

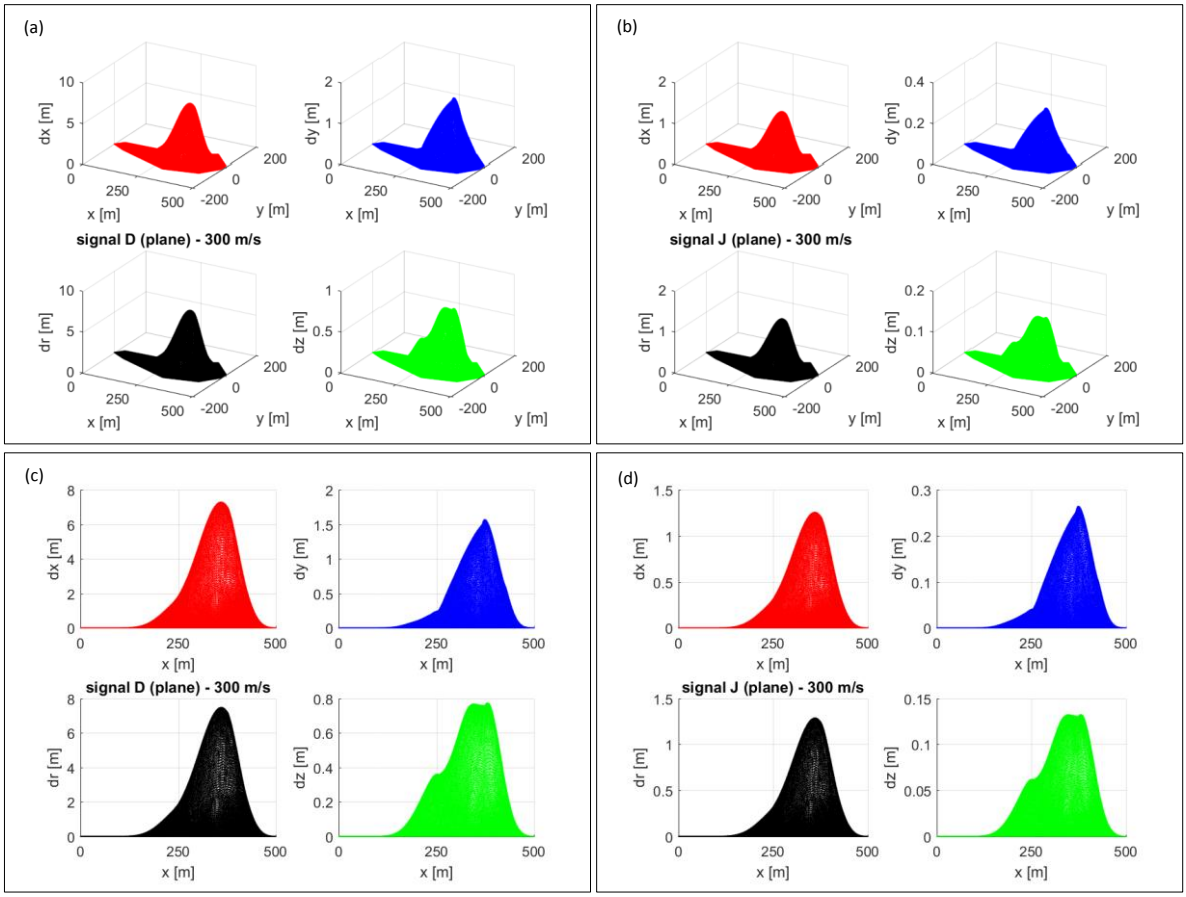

Fig. 6.15a-d. Horizontal (red and blue), vertical (green) and resultant (black) displacements for signals D and J at a shear wave velocity of 300 m/s. Both signals represent cases with high and low entrained displacements respectively. The lower series are front views of the upper series.

6.4.5. Comparison of CESAR-Models

The biggest interest after the 2D- and 3D-analyses of the Diezma Landslide in CESAR is the comparison of results. Throughout the last sections it became clear that a multitude of data in numerous combinations is available, and that per combination displacement data is variable and even to be distinguished according to its directivity. Thus, comparisons must be reduced such that they are simple enough to synthetize the entirety of the data, but still detailed enough to point out important differences.

One restriction to comparisons is the fact that the entire 3D-analysis exists only for the shear wave velocity of 300 m/s; hence one only can make use of those 11 combinations in 2D that cover the same shear wave velocity. A second confinement is that only one value has to be attributed to one combination in order to make straightforward comparisons without drifting off in too many details.

This second point is of course tricky because of the question of representativeness. Finally the maximum displacement of all points in the entire mesh was selected for two reasons:

First, if being interested only in the difference of slope behavior in 2D and 3D, this is a meaningful value. However, it must be kept in mind that the point experiencing the biggest displacement is not necessarily a point on the slope surface. Indeed, it turned out, that usually concerned points are situated just below the slope surface.

Second, the maximum values of all points are displayed right away in CESAR after visualizing the results and statistical testing revealed that the maximum displacements at the surface are almost equal to their “mesh-wide” counterparts (cf. Tab. 6.7).

dimension	d_{x_surf}/d_{x_all}	d_{y_surf}/d_{y_all}	d_{z_surf}/d_{z_all}	d_{r_surf}/d_{r_all}
2D	1.3	-	1.3	1.3
LCS (3D)	0.9	1.2	1.1	0.9
plane (3D)	1.2	1.2	1.2	1.1

Tab. 6.7. Average differences between maximum displacements of all points on the surface and of the entire mesh.

With respect to the above mentioned conditions and necessities comparisons between 2D- and 3D- analyses can be made for:

① LCS (3D) ↔ 2D (cf. Tab. 6.8)
② plane (3D) ↔ LCS (3D) (cf. Tab. 6.8)
③ relations of displacement types among each other for 2D, LCS and plane (cf. Tab. 6.9)

In contrast to all other comparisons, the second one relies on maximum displacements of all points on the surface because both 3D-analyses (LCS and plane) have the same maximum displacements of the entire mesh.

①	d_{x_LCS}/d_{x_2D}	d_{y_LCS}/d_{y_2D}	d_{z_LCS}/d_{z_2D}	d_{r_LCS}/d_{r_2D}
LCS (3D) ↔ 2D	11.2	-	9.0	11.4
②	d_{x_plane}/d_{x_LCS}	d_{y_plane}/d_{y_LCS}	d_{z_plane}/d_{z_LCS}	d_{r_plane}/d_{r_LCS}
plane (3D) ↔ LCS (3D)	1.3	1.0	1.1	1.3

Tab. 6.8. Average differences between maximum displacements of 2D and LCS.

③	d_x/d_y	d_x/d_z	d_x/d_r
2D	-	7.5	1.0
LCS (3D)	4.7	9.4	1.0
plane (3D)			

Tab. 6.9. Average relations of displacement types among each other.
The two 3D-versions (LCS and plane) share the same values because they have the same maximum displacements of the entire mesh.

In words, one can derive from these three comparisons that:

① ⇒ horizontal displacements in 3D are on average 11.2-times bigger than in 2D
⇒ vertical displacements in 3D are on average 9.0-times bigger than in 2D
⇒ resultant displacements in 3D are on average 11.4-times bigger than in 2D

② ⇒ horizontal, vertical and resultant displacements of the two 3D-versions are almost equal

③ ⇒ there is a comparable factor between horizontal and vertical displacements (in 2D & 3D)
⇒ horizontal and resultant displacements are almost equal (in 2D & 3D)
⇒ both horizontal displacements differ by a factor of 4.7 on average (in 3D only)

Especially the factors that appear between the 2D- and the 3D-analysis are striking and must be considered with particular care. It becomes clear what these factors can imply when comparing Fig. 6.4c-d and Fig. 6.14a-b. Signal J is a weak one; in 2D its maximum horizontal displacement close to point 3 reaches roughly speaking 10 cm but in 3D almost 1 m close to the nose. Signal D – being one of the strongest – causes exorbitant horizontal displacements: they jump from about 60 cm in 2D to 6 m in 3D. One can only imagine the difference when comparing sets based on 100 m/s.
Although examples of 3D-FEM-modeling with CESAR are not yet numerous, literature on available case studies confirms a significant difference between displacements in 2D and 3D. For

example, seismic analysis of the Salanfe Hydropower Dam (Switzerland) revealed a factor of around 5 (LENTI & SEMBLAT, 2011; DESPREZ & LENTI, 2013).
Due to this obvious difference a simple test was conducted in CESAR for a square and a cube with edge lengths of 10 m. More precisely, the square corresponds exactly to the x-z-plane inside the cube. This setting should resemble the position of the simplified geometry of the Diezma Landslide in 2D inside the one in 3D (cf. Fig. 6.16). Both the square and the cube have the same orientation, the same origin and a triangular mesh – also in analogy to the setting of the Diezma Landslide. Different are the increment size of the mesh (1 m) and the employed soil parameters ρ (2000 kg/m^3), γ (54 MN/m^2) and υ (0.35). Testing was only carried out with a shear wave velocity of 100 m/s – what was assumed to cause the biggest displacements – and with signal A. Similar to the Diezma Landslide, boundary conditions were applied on all enveloping surfaces and edges with exception of the covering surface or edge (cf. red lines and shaded surfaces in Fig. 6.16) and displacement analysis was focused on the 11 nodal points that the cube and the square have in common (cf. Fig. 6.17a-b).

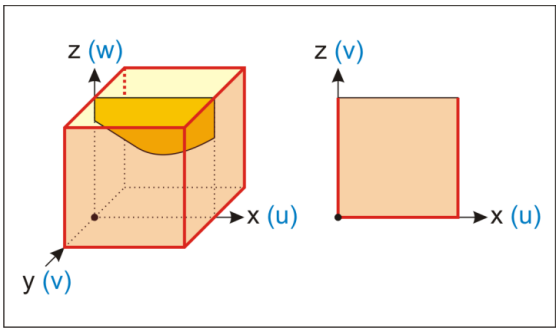

Fig. 6.16. Setting for the factor test between a 3D- and a 2D-object in CESAR.
The blue axis labels are those used by CESAR in the respective dimension mode.

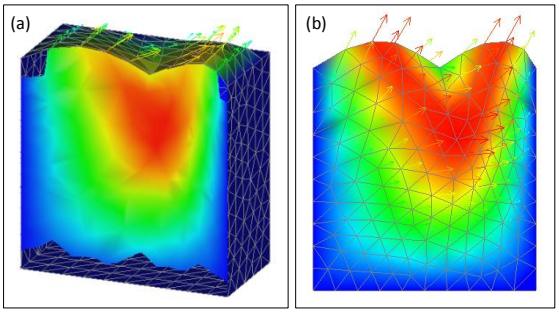

Fig. 6.17a-b. Outcome of the factor test between a 3D- and a 2D-object in CESAR.
Arrows represent displacement vectors; colors from blue (low) to red (high) show the amount of displacement.

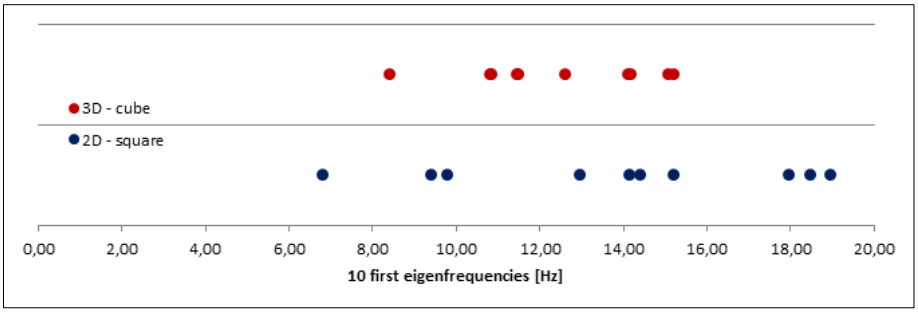

Fig. 6.18. MODE-computations for the 3D- and a 2D-object in CESAR.

The MODE-computations show two interesting features for the first 10 eigenfrequencies (cf. Fig. 6.18): First, when representing values in a plot like Fig. 6.13 the relative position of the values towards each other are equal in 2D and 3D but differently spaced than in the case of the Diezma

Landslide. Second, values lie again closer to each other in 3D. Both findings emphasize the assumption that:

⇒ Eigenfrequencies and eigenmodes depend strongly on the geometry and boundary confinement of the object.

Adding a lateral confinement by introducing the third dimension is therefore supposed to have a great influence on the excitation of the structure of interest.
The SUMO-computations revealed that for those 9 points on the surface, which can experience displacements, horizontal, vertical and resultant displacements are on average 4.3-, 2.6- and 3.4-times bigger in 3D.
More attention deserves also the relation of displacement types among each other. As mentioned before there are comparable factors between them and these factors are more or less constant throughout the 209 signal-v_s-combinations in 2D and the 2x11 signal-v_s-combinations in 3D. Table 6.10 shows the factor relationships in a gray-shaded color code.

signal	2D				3D			
	d_x (mm)	d_y (mm)	d_z (mm)	d_r (mm)	d_x (mm)	d_y (mm)	d_z (mm)	d_r (mm)
A	176.4		23.5	177.8	1939.6	0417.2	207.7	1987.3
B	234.4		31.2	236.3	2473.3	0533.9	264.6	2534.5
C	99.5		13.3	100.3	1083.9	0233.1	114.1	1110.5
D	652.6		87.0	658.0	7290.8	1569.8	782.2	7470.2
E	380.4		50.7	383.5	4252.4	0917.9	455.6	4357.6
F	167.1	-	22.3	168.5	1859.4	0400.5	196.7	1905.2
G	451.7		60.2	455.5	5063.0	1089.6	544.6	5187.5
H	104.4		13.9	105.2	1301.7	0277.0	136.2	1332.9
I	526.7		70.2	531.0	5824.8	1255.4	626.5	5968.5
J	111.6		14.9	112.5	1256.3	0264.2	134.0	1285.9
K	197.6		26.3	199.2	2230.8	0481.3	237.7	2286.0

Tab. 6.10. Maximum displacements of all points of the entire mesh for v_s = 300 m/s.

After cross-checking displacement plots and visual interpretation of result plots from CESAR it became clear that:

⇒ The general (qualitative) behavior of the slope in terms of horizontal, vertical and resultant displacement is the same for all signals featuring one zone of major deformation.
⇒ According to the signal as well as to the respective shear wave velocity, these displacements are greater or smaller – hence, they differ quantitatively.

The first point is illustrated by the figure series in the appendix (cf. A.6.) which shows all color-coded figure exports from CESAR for 300 m/s and signals A-K. Series are available in:

→ 2D for d_x, d_z, d_r in side view
→ 3D for d_x, d_y, d_z, d_r in front, top and side view

The side views in 3D give insights to the interior of the models after imaginarily cutting along the 1st and 2nd axis. Thus these views do not include the nose of the landslide but are situated at the exact position of the simplified 2D-geometry allowing for direct comparison.
Figure 6.19 is a qualitative summary of the general displacement patterns which are almost identical in 2D and in 3D. It appears that:

⇒ for d_x, the maximum zone is situated just upslope of point 3
⇒ for d_y, the maximum zone is situated just downslope of point 3
⇒ for d_z, the maximum zone is situated just upslope of point 3 and looping beneath it
⇒ for d_r, the maximum zone is situated just upslope of point 3

Comparisons of the qualitative summary displacement patterns in their front view (Fig. 6.20) with their counterparts in the side view (Fig. 6.19) give a conclusive result:

⇒ for d_x, the maximum zone is situated just upslope of the nose of the landslide
⇒ for d_y, the maximum zone is situated just downslope of the nose of the landslide
⇒ for d_z, the maximum zone is situated just upslope of the nose of the l. (loop invisible)
⇒ for d_r, the maximum zone is situated just upslope of the nose of the landslide

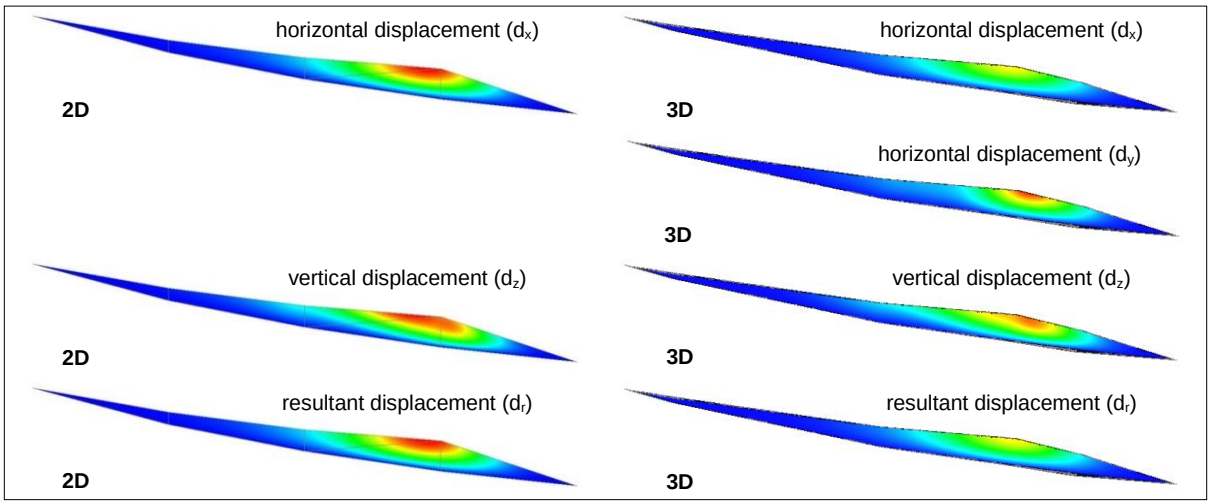

Fig. 6.19. Qualitative summary of the general displacement patterns in side view.
Colors from blue (low) to red (high) show the amount of displacement.

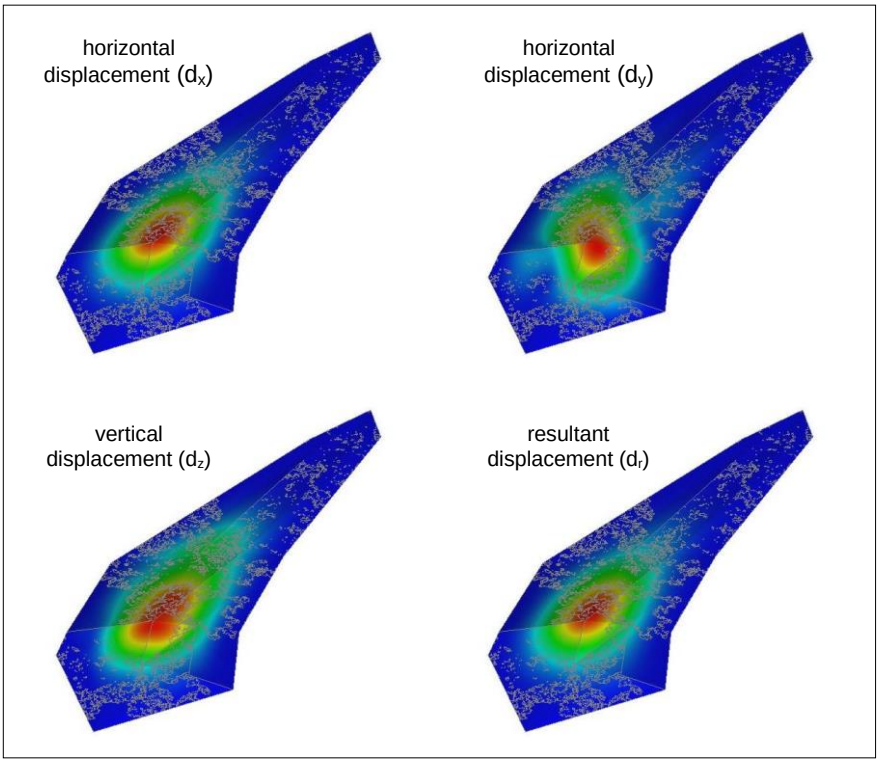

Fig. 6.20. Qualitative summary of the general displacement patterns in front view.
Colors from blue (low) to red (high) show the amount of displacement.

CHAPTER 7
FINITE DIFFERENCE ANALYSIS

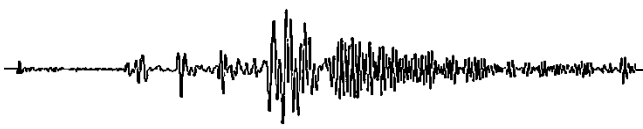

7.1. Introduction

The two preceding chapters 5. and 6. presented respectively the concepts of limit equilibrium analysis and modal recombination analysis as well as their applications to the Diezma Landslide. This chapter is dedicated to the third employed method to analyze seismically induced displacements across the slope of the Diezma Landslide, i.e. to the finite difference analysis with the numerical modeling software FLAC 2D and FLAC 3D (both abbreviated in the following as FLAC).
As described in sections 6.1. and 6.2. finite difference methods belong to the field of continuum modeling; for further information on categorical and historical emplacement of these methods one may refer to the mentioned sections.
Again, this chapter follows the structure of the previous ones by passing from theory to practice. First, an overview on the software FLAC will be given, which covers likewise its 2D- and its 3D-version. A closer look will be taken on the required procedures for the analysis of seismically induced displacements as well as on the assessment of site effects. The evaluation of site effects will be presented in more detail in a short excursus (cf. Excursus – 7.3.3.).
The second part describes the application of these procedures to the Diezma Landslide. Similar to the order of chapter 6., the procedures will be followed step by step with visualizations of results and appendant interpretations. The last section comprises a comparison of the 2D- and 3D-FLAC-Models.
One important fact to note is that throughout the thesis, only the analysis with the code FLAC was carried out for the simplified and the fine geometry in 2D and 3D. Both the NEWMARK-Method (1965; cf. 5.) as well as the analysis with modal recombination (cf. 6.) were based only on the simplified geometry of the Diezma Landslide (cf. Fig. 4.12).

7.2. Functionality of FLAC

The software FLAC is very comprehensive and disposes also of extensive documentation:

FLAC 2D Version 7.0 User's Manual (15 volumes; ITASCA, 2011)
FLAC 3D Version 5.0 User's Manual (13 volumes; ITASCA, 2012)

In order to give an overview on the software, basic concepts are summarized in the next sections (cf. 7.2.1., 7.2.2.) instead of rewriting the user manuals, what would miss the target of the thesis. In terms of references, both following sections refer exclusively to ITASCA (2011) and ITASCA (2012); no further references will be made in the text.

7.2.1. Overview on the Software

One of the most powerful numerical codes for geotechnical analysis is the commercial software FLAC which is a product of the American consulting group ITASCA on the market since 1986. Due to its multitude of possibilities to solve complicated mechanical problems involving geological materials, it is widely used in the fields of civil and mining engineering to model complex ground behavior.
In this regard, the software is equally suitable for designing as well as for testing objectives. On the one hand, when exact data is available, the code creates a numerical image of the location of interest allowing for surveillance, analysis, design of construction measures and the prediction of effects caused by the latter. On the other hand, the code can also be used as testing environment, when data is not or not entirely available; in this case it becomes a convenient tool to conduct research offering an almost endless number of ways to analyze the setting of interest. In the case of the Diezma Landslide, FLAC is used in both ways: There is enough data available to build a detailed numerical image of the site which is used for the analysis of the ground response after having tested different seismic scenarios.

Shortly spoken, FLAC is an explicit finite difference code and named without abbreviation "Fast Lagrangian Analysis of Continua". One might thus ask what these terms represent.
Generally, involved materials are represented by elements. Each element can have its particular properties and behaves according to assigned material laws when subjected to forces and boundary conditions. Version 7.0 of FLAC offers fourteen built-in linear and non-linear material models (cf. 1.1.) of three categories: the null model for voids, elastic and plastic models. In the next section (cf. 7.2.2.) it will be explained why for this thesis only the isotropic elastic and the Mohr-Coulomb-Model (from the plastic "family") are relevant. The totality of all elements form a grid which is preferably of – but not restricted to – a rectangular appearance, since FLAC uses the finite volume method (WILKINS, 1964) that allows elements to take any shape.
The creation of a grid (or mesh) is thus a discretization of the domain of interest (cf. 6.2.1.). In contrast to finite element methods (FEM), the discretization of finite difference methods (FDM) does not result in a finite number of elements but in a finite number of grid points (or nodes) that define zones to which stresses and strains apply. Another difference between FEM and FDM is, that FEM have a matrix-based way of operation with matrix contents being constantly updated, whereas the principle of FDM is to regenerate the finite difference equations applying to the grid points with each computation cycle (or step).
Figure 7.1 illustrates such a computation cycle. To start the first cycle the code makes use of the initial equilibrium equation and stress/strain-state to calculate velocities and displacements for all grid points. These velocities are then used by the constitutive equations (or material laws) to derive strain rates and stresses. In return, these latter ones are re-used by the equilibrium equation to launch the next cycle. This way of stepwise state calculation, in which the new state is only a function of the previous one, is called explicit.
An important detail of the cycles is, that when one of the equations operates, the updated input is kept constant. This appears questionable, since – for example – one might expect a stress change in one point to cause a stress change at its neighboring points. If the time-step, however, is very small, neighbors figuratively "do not have time to come into conflict". Small time-stepping, though, is the major drawback of FDM since it leads to time-consuming procedures.

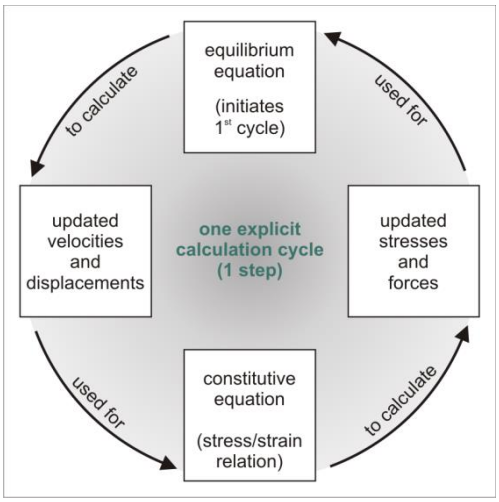

Fig. 7.1. One calculation cycle of FDM.

The definition of a Lagrangian Analysis is linked to the way the grid deforms. In fact, in this type of formulation it is the grid itself that deforms with the material it represents and incremental displacements are added to the coordinates of the grid points. With an Eulerian formulation, in contrast, only the material deforms with respect to a stationary grid.

7.2.2. Required Procedure for Displacement and Site Effect Analysis

The two main steps of analysis in this thesis are the static and the dynamic computation of the behavior of the slope (cf. Fig. 7.2).

The static phase includes the generation of the geometry of the slope and the creation of a mesh, on whose points displacements are to be assessed. Also interfaces, material zones, respective mechanical properties and boundary conditions are defined here. The purpose of the static computation is the assessment of slope deformation due to settlement by gravity.
Based on this state of settlement, a dynamic computation can follow assessing the response of the slope to a seismic scenario under distinct damping characteristics that must be defined.
One important point to memorize is, that for the assessment of slope deformation the entire procedure (i.e. both phases) must be run under conditions according to Mohr-Coulomb, whereas for the evaluation of site effects the model must behave in a purely elastic manner (cf. Fig. 7.2). Also for a computation of the factor of safety based on the static phase, a Mohr-Coulomb-Model is necessary.

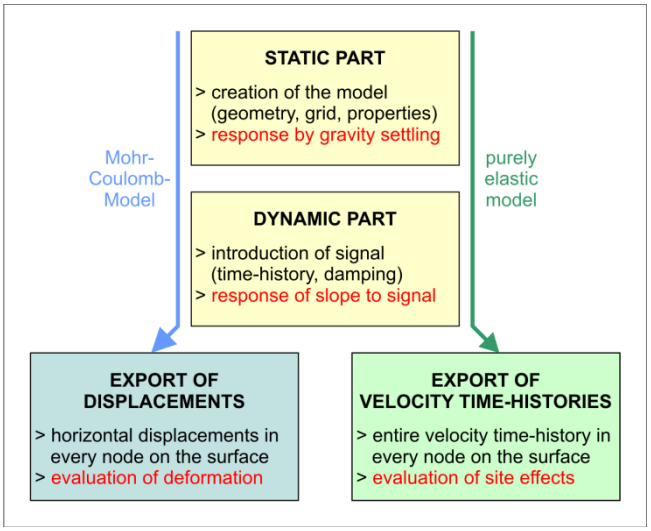

Fig. 7.2. Required procedures for displacement and site effect analysis in FLAC 2D and 3D.

The Mohr-Coulomb Model that is assumed for the involved material describes an elasto-perfectly-plastic behavior (cf. Fig. 7.3a); in literature, it is also known as Prandtl Model. The basic hypothesis is that a material is responding instantly and in a purely elastic manner until the yield strain is reached. After that, the deformation becomes purely plastic at constant stress. This particular behavior is easily illustrated by a mass-spring-system such as shown in Fig. 7.3a. The spring is tensioned and the strain-response remains elastic and thus reversible as long as the yield stress is not reached; once the yield stress is overcome, the mass is torn across the surface and plastic – i.e. irreversible – deformation takes place. If at a later stage of time, the applying force is suspended, only the amount of reversible deformation drops off, whereas the irreversible deformation remains. A detail to note is that, because of to the involvement of Rayleigh-Damping, the material behavior includes also a small viscous part; thus, the most accurate term to describe the model is “visco-elasto-perfectly-plastic”.
Rayleigh-Damping is a form of viscous damping. Due to its convenience of being defined as linear combination ($\underline{C} = \alpha \cdot \underline{M} + \beta \cdot \underline{K}$) of the mass matrix ($\underline{M}$) and the stiffness matrix ($\underline{K}$) it is frequently used to numerically model internal structural damping (cf. 6.3.1.). The Rayleigh-Damping function as well as its two components – the mass-proportional part ($\alpha \cdot \underline{M}$) and the stiffness-proportional part ($\beta \cdot \underline{K}$) – are shown in Fig. 7.3b. One less convenient characteristic of Rayleigh-Damping is the fact that the function is very variable over frequency, and thus only the very small section around the lowest damping ratio (ξ_{min}) at its associated damping frequency (f_{damp}) can be considered as constant. In theory, the total amount of damping a vibration experiences by traveling over a given distance depends on its frequency since damping affects the amplitude per cycle and therefore:

- A wave with a high f (i.e. a low λ) experiences a higher total damping over distance x.
- A wave with a low f (i.e. a high λ) experiences a lower total damping over distance x.

Indeed, frequency-dependent damping is rather disadvantageous for models (cf. 1.1) in which the damping ratio (ξ) should be constant over a large frequency range. In order to stretch down the Rayleigh-Damping function the lowest damping ratio (ξ_{min}) and its associated damping frequency (f_{damp}) are manipulated. Usually a value is first accorded to ξ_{min} at which the function should flatten out; it is important to note that this value normally ranges in the single-digit percentage and it appears in the equation in decimal format (cf. Fig. 7.4). Then a rather high frequency is assigned to f_{damp} to enforce a low gradient on the stiffness-proportional asymptote. With experience, literature and trial-and-error approximation the two values can be defined without major difficulties. In a second stage, the system of differential equations consisting of the Rayleigh-Damping function (ξ(f)) and its first derivative is solved for the minimum point (ξ_{min}/f_{damp}). With the resulting parameters α and β the damping matrix $\underline{\underline{C}}$ is finally defined since the mass matrix ($\underline{\underline{M}}$) and the stiffness matrix ($\underline{\underline{K}}$) are known.

$$\xi(f) = \frac{1}{2} \cdot \left(\frac{\alpha}{2 \cdot \pi \cdot f} + \beta \cdot 2 \cdot \pi \cdot f \right)$$

$$\frac{d\xi(f)}{df} = \frac{1}{2} \cdot \left(\frac{-\alpha}{2 \cdot \pi \cdot f^2} + \beta \cdot 2 \cdot \pi \right)$$

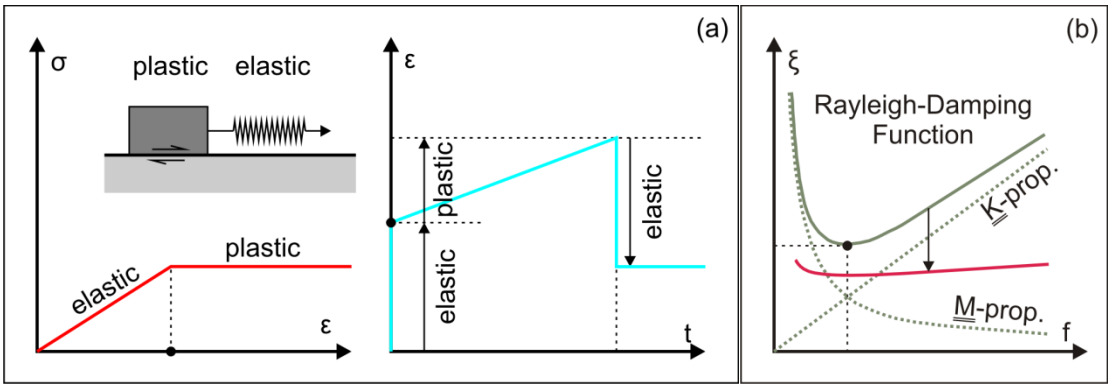

Fig. 7.3a-b. Perfect elasto-plastic behavior and Rayleigh-Damping.

Similar to the numerical code CESAR (cf. 6.3., A.5.), FLAC has a command driven way of operation as well as a graphical user interface, but for purposes of automatization, it is more efficient to use so-called "FISH-commands". "FISH" is the abbreviation of the scripting language "FLACish" that allows the user to write command sequences, manage variables and customize analyses. Also for pre- and post-processing the FISH-language offers many advantages.
As a matter of fact, there are no workflow charts at the end of the appendix describing the "clicking order" as for the graphical interface of CESAR. The used FISH-commands for the static and the dynamic computations as well as for the exports of displacements and velocity time-histories were developed over the last years by one of the thesis supervisors. For reasons of authorship, they are not displayed in the appendix. However, the MATLAB-code for the evaluation of site effects is available (cf. A.9., A.10.).

7.3. Application to the Diezma Landslide

In this section, model outlines for both dimensions will be discussed before passing on to detailed descriptions of the static and dynamic phases. In the following, the basic points of geometries, meshes, properties, boundary conditions and loading will be addressed (cf. A.12.). It is important to note that – for better comparison – the order of these basic points corresponds to the one in section 6.4.; however the arrangement does not reflect the structure of the FISH-commands for FLAC.

Geometry

As mentioned before, only the analysis with FLAC was carried out for the simplified and the fine geometry. There are thus two sets of models in 2D as well as in 3D. The procedure per dimension is, however, the same since it only reads different geometry inputs. In analogy to the analysis with CESAR, the longitudinal cross section of the simplified geometry fits into the simplified 3D-geometry (cf. Fig. 4.8, Fig. 4.12); the longitudinal cross section of the fine geometry fits into the fine 3D-geometry (cf. Fig. 4.15o, Fig. 4.16). Both the simplified and the fine longitudinal cross sections lie in the xz-plane of their respective 3D-geometries; the fine geometry was therefore rotated. Sections 7.3.1. and 7.3.4. describe the geometric setups defined by the FISH-commands.

Mesh

Being linked to the geometrical setups and the grids of the models, also the meshes are described in these sections (cf. 7.3.1., 7.3.4.). To summarize, the mesh-size of the 2D-geometry is 1 m (resulting in ca. 250,000 zones surrounded by four mesh-points), whereas the one for the 3D-geometry is 3 m (resulting in ca. 4,000,000 zones surrounded by four mesh-points).

Properties

Required properties for the landslide mass, the underlying bedrock and the sliding surface are the shear wave velocity (v_s in m/s), the density (ρ in kg/m^3), the Poisson's Ratio (υ without dimension), the cohesion (c in Pa) and the friction angle (Φ in degrees). In addition to those five properties, the code also needs the shear modulus (G in Pa) and the bulk modulus (K in Pa) which can be calculated via the compressional wave velocity (v_p in m/s) and the longitudinal module (M in Pa).

$$G = \rho \cdot {v_s}^2 \qquad v_p = v_s \cdot \sqrt{\frac{2\cdot(\nu-1)}{2\cdot\nu-1}} \qquad M = \rho \cdot {v_p}^2 \qquad K = M - \left(\frac{4}{3}\right) \cdot G$$

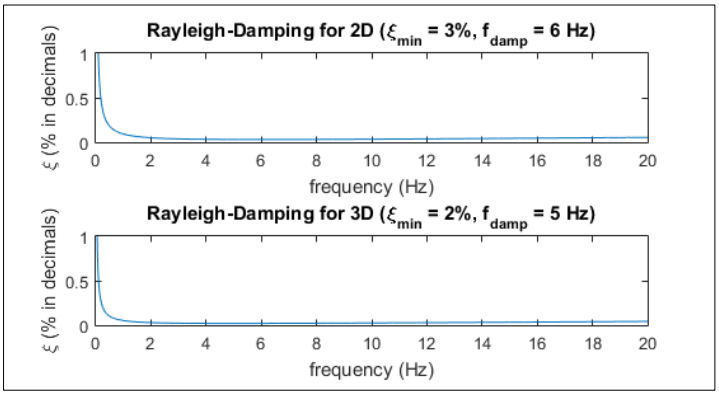

Fig. 7.4. Rayleigh-Damping functions for the 2D- and 3D-models.

Table 7.1 shows the values of the respective properties. The density and the Poisson's Ratio are taken from literature (DELGADO et al., 2015; MARTINO et al., 2016; cf. Tab. 4.1); the landslide mass adopts the peak values, whereas the sliding surface reflects the residual counterparts. To have a distinct contrast the shear wave velocity of the bedrock was assumed to be 1000 m/s, although MARTINO et al. (2016) estimate only 750 m/s. The other values related to the bedrock are also reasonable assumptions. Rayleigh-Damping is assumed for the involved material; values differ slightly for the 2D- and the 3D analysis with no significant effect (cf. Fig. 7.4).
All models in this chapter are computed with a shear wave velocity of 300 m/s for two reasons: First, this is the true value as indicated in literature (DELGADO et al., 2015), and second, most of the modal recombination analysis with CESAR (cf. 6.) is based only on this value.

Boundary conditions

In order to correctly deal with artificial boundaries – i.e. such that are no real physical boundaries – conditions have to be applied to them. For static analyses boundary conditions might be fixed or elastic. For dynamic analyses, though, such boundary conditions cause reflections of propagating waves back into the model. Energy is thus accumulated in the model what does not correspond to wave propagation patterns in reality. To avoid such reflection phenomena the model can either be very large so that most of the reflected wave energy will be absorbed by the material damping when "coming back", or quiet (absorbing) boundaries and free field boundaries must be applied in order to ensure energy absorption.
For displaying boundary conditions of the models, it helps to imagine a rectangle and a cuboid corresponding to the respective model geometries in FLAC. Boundary conditions for the static and dynamic phases then are:

- static 2D: no d_x on sides, no d_z on the model basis
- static 3D: no d_x on yz-sides, no d_y on xz-sides, no d_z on the model basis
- dynamic 2D: free field on lateral sides, quiet boundaries on the model basis
- dynamic 3D: free field on lateral sides, quiet boundaries on the model basis

Loading

Dynamic loading is inserted to FLAC via a velocity time-history in meters per second. Similar to the way of signal application in CESAR (cf. 6.4.), the shear wave signal is supposed to originate from a sufficiently far hypocenter in order to arrive vertically and taking effect on the model by horizontal shaking (cf. Fig. 1.3). The difference is that in FLAC the signal is applied to the bottom of the model, and not on the sliding surface as in CESAR.
One major point of discussion was the choice of signals to apply to the Diezma Landslide due to very time-consuming computations. Depending on the signal duration (Fig. 7.22) and the time-stepping (cf. Fig. 7.1) dynamic phases in 2D needed up to three days of processing time. Also the preceding static phase – that is the same for all dynamic computations – took around two days to run. Being still in the realms of possibility, all 11 signals were tested on the simplified as well as on the fine 2D-geometry. For the simplified and the fine 3D-geometry, though, a selection was necessary since one second needs around one day of processing time. Finally, the decision was made for signals E and B because of the following consideration: Figure 7.22 shows the maximum displacements per signal and the methods other than FLAC 3D. Intriguingly, signals E, B and C are always among the highly, medium- and less provocative signals in terms of respective caused displacements. Luckily, the three signals are also among the shortest in duration. There are thus four 3D-models: two with the simplified and two with the fine geometry representing pairwise scenarios with high and medium expected displacements (i.e. with signal E and B respectively).

property	landslide mass	sliding surface	underlying bedrock
v_s	300 m/s	300 m/s	1000 m/s
ρ	2181.4 kg/m^3	2181.4 kg/m^3	2500 kg/m^3
υ	0.25	0.25	0.35
c'	46e3 Pa	4e3 Pa	4e9 Pa
Φ'	26°	12°	30°
ξ_{min} (2D / 3D)	0.03 / 0.02	-	0.01 / 0.005
f_{damp} (2D / 3D)	6 Hz / 5 Hz	-	6 Hz / 5 Hz

Tab. 7.1. Properties of the landslide mass, the sliding surface and the underlying bedrock.

7.3.1. Geometry of the Models in 2D

For both the simplified and the fine 2D-geometry the layout of the model is very similar. It consists of a rectangular block with the dimensions listed below and it has the uppermost point of the landslide crown at 0 m on the x-axis and at 0 m on the z-axis.

- x-axis (called x-axis in FLAC): from -250 m to 700 m → 950 m in total
- z-axis (called y-axis in FLAC): from -300 m to 0 m → 300 m in total

The model geometries differ of course in those parts that represent the landslide mass. As explained in section 4.2.2., the simplified and the fine geometry do not have the same length (cf. Tab. 4.4). As a result, the longer fine geometry occupies more space in the model; it also has a few more grid points along the slope surface where displacements can be evaluated.
The imposed grid is equal for all 2D-models. It has a mesh-size of 1 m by 1 m, what theoretically allows for correct propagation of waves that include frequencies up to 30 Hz (cf. 4.4). This value is well above the frequency content of the signals after they had undergone the 4th-order low-pass Butterwoth Filter with a cut-off frequency of 10 Hz (cf. 4.4.). The grid consists predominantly of a square mesh; only at parts close to the slope surface elements have different shapes (cf. 7.2.2.).

7.3.2. Static Analysis in 2D

The static phase of the analysis is necessary to bring the model to equilibrium after the settlement due to gravity (g = 9.81 m/s^2). The result shows – so to speak – the stability of the slope without the influence of a seismic scenario but taking into account the previously defined model geometry and mechanical properties of the involved material.

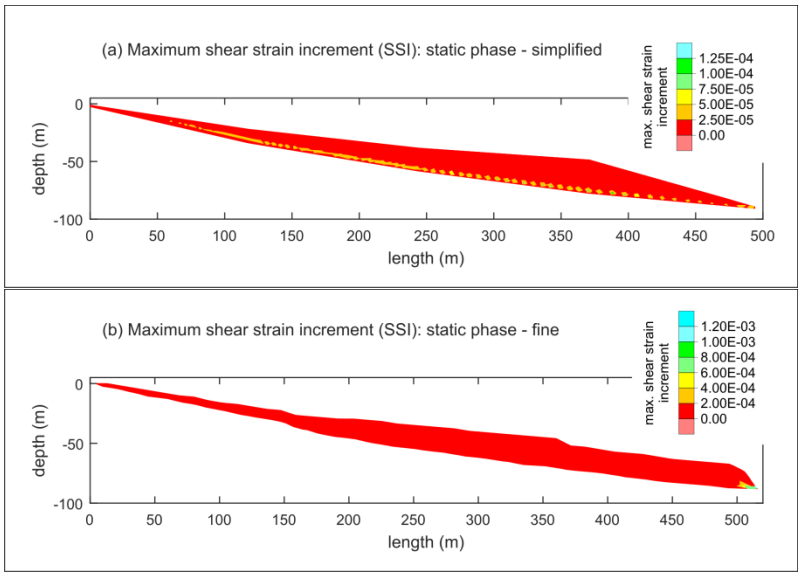

Fig. 7.5a-b. SSI localization after the static phase for the simplified and the fine 2D-geometry.
It should be noted that that in contrast to most of the other color-coded figures in this thesis the red-to-blue-sequence is here opposite. The SSI is dimensionless.

One way in FLAC to represent the final state of the static analysis is to color-code the model according to strain patterns. Strains, however, can be computed only at nodes via their displacements. By attributing the average of all maximum nodal strains around one element to the element itself, one obtains the maximum shear strain increment (in the following called "SSI") of that element which in turn is easily color-coded. Being an average value, the SSI is still dimensionless. In the case of landslides, it seems very likely that regions with high SSI values tend to accumulate close to the sliding surface, and CHENG et al. (2013) go even further by

proposing a procedure to localize sliding surfaces via SSI patterns. Nevertheless, one has to keep in mind that SSI can also show high values elsewhere in the model and that they do not obligatorily accumulate along the entire sliding surface (cf. Fig. 7.5a-b). If SSI form a continuous "chain" segregating one part or the entire landslide mass from its surrounding material, it would be an indication for static instability of the model; it would not come to equilibrium after the static phase and a failure would be likely.
The two figures (cf. Fig. 7.5a-b) show the SSI for the simplified and the fine geometry covering only the landslide mass but not the underlying bedrock. It is easy to see that the pattern is quite different with respect to the geometry and the reached values. In the simplified geometry (cf. Fig. 7.5a) the SSI tend to accumulate along the sliding surface; they are smaller than the ones of the fine geometry by roughly one order of magnitude. SSI in the fine geometry (cf. Fig. 7.5b) concentrate around the toe of the landslide, and in contrast to the simplified geometry the pattern seems more similar to the one obtained by the respective computation of the factor of safety (cf. Fig. 7.6b). One major factor explaining the unequal patterns is the effect of gravity on a diverging mass distribution in both cases. Especially the fine geometry shows a SSI pattern that is very typical for gravity-controlled slopes with a steep toe and an almost constant or gradually increasing thickness. If this is considered the predominant static state of the slope, it might not be surprising that although RODRÍGUEZ-PECES et al. (2011) concluded a factor of safety of 2.12 for the slope in 2000, such a tremendous slip-off could occur on the 18th of March 2001 (cf. Fig. 7.7a-b); the landslide mass became quickly saturated and much heavier than usual after a period of intense rainfall.
This apparent dependency of the SSI pattern on the geometry is of particular importance and confirms one major relationship: As the static behavior of a slope strongly depends on its geometry, so should do the dynamic behavior – an expectancy that will be tested in the next section (cf. 7.3.3.).
Based on the static analysis, FLAC can compute the factor of safety (cf. 5.2.1.). Here, the software does not consider the actual sliding surface, but it tests many possible sliding surfaces dissecting the numerical model. It returns at the end the sliding surface with the lowest factor of safety, i.e. the most critical one. Plots of the SSI for the two geometries (Fig. 7.6a-b) show the strain pattern after the calculation of the factors of safety. The two obtained factors of safety are:

- simplified geometry: SF = 1.70 (critical slip surface roughly shown in Fig. 7.6a)
- fine geometry: SF = 1.16 (critical slip surface roughly shown in Fig. 7.6b)

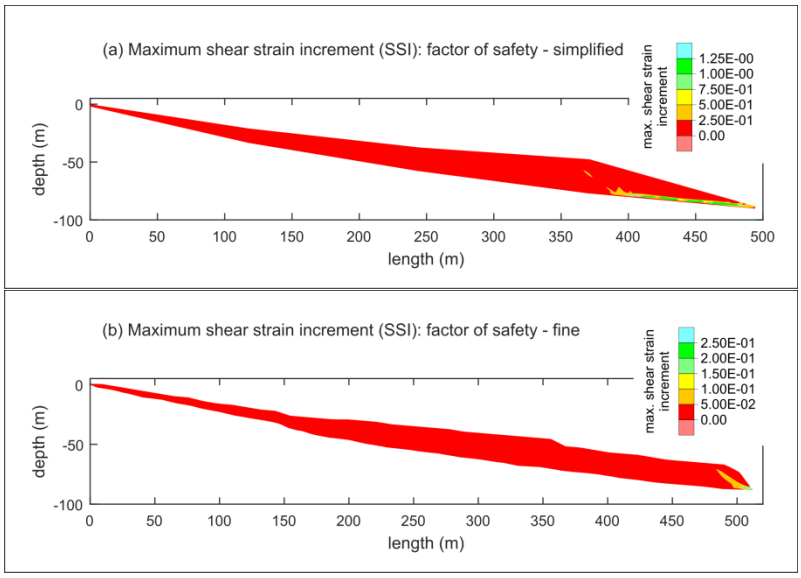

Fig. 7.6a-b. SSI localization after the calculation of the factor of safety for the simplified and the fine 2D-geometry. It should be noted that that in contrast to most of the other color-coded figures in this thesis the red-to-blue-sequence is here opposite. The SSI is dimensionless.

Both values lie above 1 implying that the slopes are stable. However, this hypothesis seems only reassuring for the simplified geometry. The factor of safety for the fine geometry is actually very close to 1 and thus holding and driving forces must have very similar values. With a slight change of properties for example, the slope could easily fail.

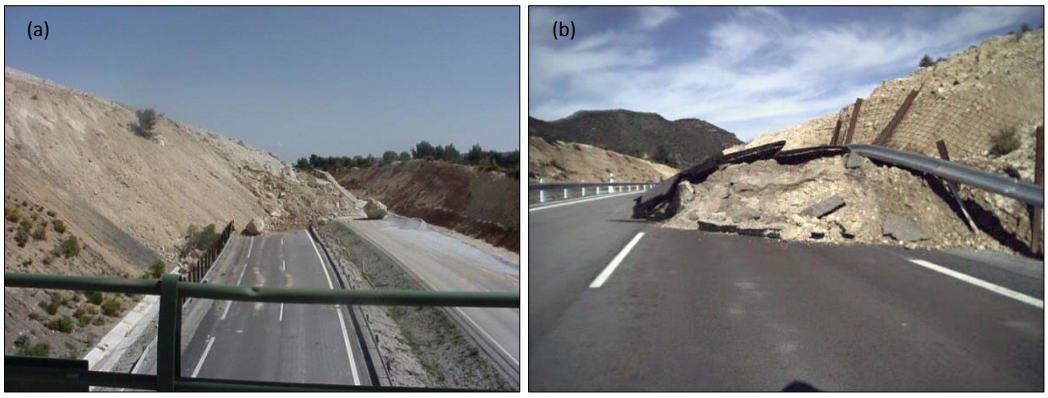

Fig. 7.7a-b. Major slip-off of the Diezma Landslide on the 18th of March 2001
(photos by courtesy of: JUNTA DE ANDALUCÍA, CONSEJERÍA DE OBRAS PÚBLICAS).

Results from the static analysis and the calculation of the factors of safety suggest that the models of both geometries come to equilibrium after the static phase. From Fig. 7.5a-b it is obvious that no continuous shear strain increment pattern could form in neither geometry. Referring to Fig. 7.6a-b one can reason in the following way: If the most critical sliding surfaces have factors of safety above 1, they testify to stability; any other sliding surfaces elsewhere in the models – including the actual ones – must then have even higher factors of safety and the respective landslide mass is stable under static conditions.

7.3.3. Dynamic Analysis in 2D

Once the two models – the one for the simplified and the one for the fine geometry – are brought to equilibrium during the static phase of the analysis, a dynamic phase can follow (cf. Fig. 7.2). Since the static phase does not depend on the seismic scenario, it is the base for all 11 signals that are to be applied. Dealing though with two geometries and thus two different static results, there will be in total 22 dynamic results – i.e. eleven displacement predictions from either geometry and hence the double amount as with the NEWMARK-method (1965; cf. 5.) and the method of modal recombination (cf. 6.) which both used only the simplified geometries in 2D and 3D. Compared to section 6.4.2., this section is structured in a similar way in order to facilitate the comparison.
From the previous section (cf. 7.3.2.) it is obvious that both geometries dispose of a different mass distribution and that under static conditions the stress patterns show significant differences (cf. Fig. 7.5a-b, Fig. 7.6a-b). This observation leads to two main preliminary hypotheses that are to be examined in the course of this section:

- The slope response to seismic scenarios should depend on the geometry.
- According to the applied signal, the intensity of the response should differ.

The second hypothesis is consistent with what the NEWMARK-method (1965; cf. 5.) and the method of modal recombination (cf. 6.) revealed. A particular behavior that – although expected – did not present itself so far throughout the thesis, is the qualitative dependency of the slope response on the signals. One of the most stunning conclusions after the modal recombination analysis (cf. 6.4.5.) was that qualitative displacement patterns per component appeared to be the same for all signals, but the reached values are dependent on the signals (cf. 6.4.5.). The third hypothesis that

- the behavior of the slope should be different according to the applied signal

is finally expected to appear in the predicted displacement patterns after the dynamic phases for both geometries.
The term "predicted displacement pattern" needs more clarification inasmuch as in this section displacements are specified in many ways: horizontal (or x-) displacements, relative displacements (cf. Fig. 7.10a-f) and residual displacements. Much to the discomfort of the reader, all terms are related to each other – not to say "almost the same" as the next paragraphs will explain.
Compared to the CESAR-Models, in which the sliding surface corresponded in fact to the stationary boundaries, the model boundaries in FLAC lie further away from the landslide body. As a result, when evaluating surface displacements, one needs to consider the displacements of all nodes along the ground surface with respect to the displacements of all nodes along the sliding surface. Since FLAC preferably imposes a square grid on the model, each node bears an index with "i" designing the horizontal and "j" the vertical position; via these indices nodes whose displacements are to be set in relation can be easily located. An example for the calculation of such a relative displacement based on only one pair of points might be:

- x-displacement at ground surface: 1.5 cm
- x-displacement at sliding surface: 0.5 cm
- relative displacement between the ground and the sliding surface: 1.0 cm

Theoretically, there are many more combinations of how two respective points can move relatively to each other (cf. Fig. 7.8). A point at the ground surface can experience a positive, a negative or no displacement and so does the respective underlying point on the sliding surface. In addition, the underlying point can experience equal, smaller or greater absolute displacements than the point on the ground surface. Practically though, exact zero-displacements usually do not result from numerical models, and thus combinations involving zero-displacements are not considered. Furthermore, all combinations resulting in a negative relative displacement are not to be considered either since they imply a displacement "towards the interior" of the landslide. After discarding the mentioned combinations as well as the combination-doubles that Fig. 7.8 generated, only seven combinations remained for positive (or zero-) relative displacements. A MATLAB-procedure (cf. A.7.) helps to retrieve the relative displacements from the FLAC-outputs. It calculates the value if one of the seven combinations is met and in any other case it attributes a zero-displacement to the point on the ground surface.

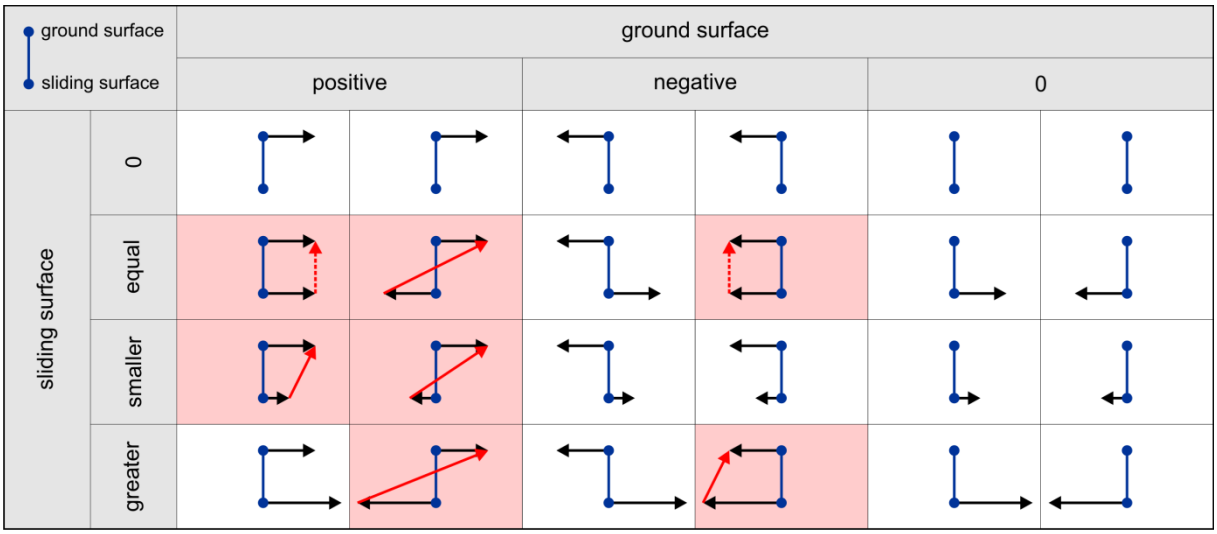

Fig. 7.8. Combinations showing the possible behaviors between points on the ground and on the sliding surface. Combinations shed in red are the only ones resulting in a positive or (zero-) relative displacement.

The term "residual displacement" originates from the fact that FLAC returns the "left-over displacement" (visible in the displacement time-history of the ground response per point; cf. Fig. 8.1c) once the entire computation has finished. CESAR in contrast, returns the maximum value that was reached in the displacement time-history of the ground response per point (cf. Fig. 8.1b). For simplicity, the final displacements obtained via finite difference modeling in FLAC will be referred to as "residual" in chapter 8., although they are in fact "relative from residual".
The designation "residual" should neither be confounded with "resultant". Within the frames of the analysis with FLAC this is though unlikely because here only displacements in x-direction are considered.
For each of the 22 signal-geometry-combinations there is a comparative plot with three sections (cf. Fig. 7.10a-f). The first subplot shows the applied signal as velocity time-history, and logically each velocity time-history appears twice – i.e. for each "geometry-pair". The second subplot contains the longitudinal cross section of either the simplified or the fine geometry without the underlying bedrock. They are filled with a color-coded pattern that represents the residual x-displacement in every grid point of the model. It should be noted that the legends to the color-codes are consistent only per geometry; i.e. the legend for the simplified geometry is differently scaled than the one for the fine geometry. This might seem impractical, but due to a significant factor of up to 24 (cf. Tab. 7.3) between the maximum horizontal displacements obtained with the simplified and the fine geometry it became necessary to opt for a differently scaled legend. In this way displacement variations could be properly visualized at least within the respective geometry-group. The ranges of the two legends are:

- simplified 2D-geometry: 0.00 m – 0.03 m in steps of 0.005 m
- fine 2D-geometry: 0.00 m – 0.20 m in steps of 0.025 m

The third subplot displays the actual relative displacement of the grid points along the ground surface. The second axis of these subplots is auto-scaled in order to visualize the slope response as clearly as possible.
Even though for the geometries all 22 FLAC-Models are available, only the pairs for signals E, B and C are kept in the text body of the thesis, whereas the ones for the other signals are to be found in the appendix (cf. A.8.). The reason is linked to the choice of signals for the analysis in 3D (cf. 7.3., Fig. 7.22); here, the argumentation is that due to time restrictions only two of these signals (E and B) are used representing respectively a highly and medium-provocative scenario in terms of caused displacements. If, thus, only plots for signals E, B and C are shown in this section, it is on the account of comparison to Fig. 7.23a-d.
Comparing all 22 graphics, the following qualitative and quantitative features can be recognized; they will be discussed in detail in the next paragraphs.

- Internal displacement patterns are roughly similar for the simplified geometry and so are patterns for the fine geometry; however both pattern groups differ significantly among each other.
- Superficial displacement patterns are rather variable for the simplified geometry, but patterns for the fine geometry behave in a very similar manner.
- Different signals clearly cause different slope responses and the divergence is more apparent within the simplified geometry group.
- Displacements of the fine geometry group reach higher values and within the groups the same signals cause the highest displacements.

Concerning the internal displacements at every grid point, a great variability is apparent when comparing the effects of different seismic scenarios per geometry group.
Within the simplified geometry group, four signals (A, C, I and K) cause almost no displacements and the color-coded longitudinal cross sections are comparable to Fig. 7.10c. The majority of signals (B, D, F, G, H and J) display a concentration of high displacement values below point 3 (cf. Fig. 4.8) comparable to Fig. 7.10b; extending patterns of these concentrations often reach zones

above point 3. Particular is the displacement pattern caused by signal E (cf. Fig. 7.10a); it is the only case where the main concentration of high displacement values is located above point 3, and where extending patterns loop forward and back beneath point 3 (cf. Fig. 4.8).
The "fine geometry group" seems much less variable. All displacement patterns cover at maximum the last 30 m measured backwards from the landslide toe. Depending on the signal the patterns extend further backwards and curve up as did the most critical sliding surface obtained from the static calculation of the factor of safety (cf. Fig. 7.6b). Only signals A and K seem not strong enough to cause up-curving patterns over the whole toe zone; in those two cases the zone of maximum displacements is limited to the last 10 m of the model where the inclination of the slope is greatest. Generally, even with the less provocative scenarios, the slope always experiences displacements, what could lead to the assumption that the Diezma Landslide – here represented with the fine geometry – is actually quite easily affected at its toe zone by any disturbance.
In terms of superficial displacements, one also perceives a significant difference not only between the two geometry groups, but also between the eleven scenarios within the simplified geometry group. The third subplots for this latter group (cf. Fig. 7.10a-c) reveal two main behaviors of superficial displacements. One could be characterized by a very slow build-up over about the first half of the model followed by a rather fast increase that finds its maximum in the last fourth of the model before an abrupt decrease; it is referred to as "hunch" and comparable to Fig. 7.10b. The other type is – in spite of all the scientific serenity of the thesis – best described by one very non-scientific worldwide well-known drawing of Antoine DE SAINT-EXUPÉRY: the boa constrictor digesting an elephant (cf. Fig. 7.9).

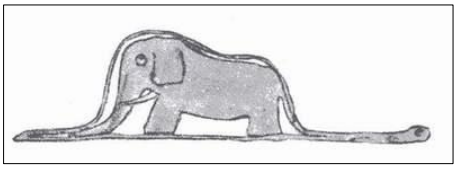

Tab. 7.9. Boa constrictor digesting an elephant (SAINT-EXUPÉRY, 1943[1]).

These "elephant-type" curves of superficial displacements describe a more or less gradual build-up over the first half of the model followed by an explicit plateau with an equally abrupt decrease (cf. Fig. 7.10a). The peak values are reached always around 300 m. Only with signal C, there appears a notch just between 250 m and 300 m (cf. Fig. 7.10c).
As for the superficial displacements within the fine geometry group, the behavior is again much more similar comparing the eleven scenarios; the curves in the third subplots show a short double-step feature which starts without exception pretty precisely at 425 m and 500 m. Only the second location (500 m) corresponds to a prominent geometric change: the change of the slope angle above the toe zone of the landslide. Also just before 150 m and right after 300 m there are two prominent geometric changes throughout the geometry. However, they are not accompanied by particular step-like (or other) features in the respective curves. One reason therefore might be that the fine geometry is of constant thickness over large parts and that the significant build-up in the displacement curves seems to come along with much more pronounced geometry changes as in the toe zone.
Superficial displacement curves of both geometry types do not reach 0 at their ends; i.e. the toe of the Diezma Landslide is always supposed to experience displacements – but depending on the considered geometry and scenario with different intensities.
Similarly to section 6.4.2., there arises again the question why the displacement pattern is so variable and if it can be linked to a seismic scenario. Of course it is essential to keep in mind that it is not one single seismic parameter that has an influence on slope response; the latter is more likely a result of a – probably weighted – multi-factorial combination of parameters. If the following attempts to correlate FAS- and velocity-zones (for the definition of "zone" cf. Tab. 7.2)

[1] The drawing originates from the book "The Little Prince" by SAINT-EXUPÉRY (1943); its English version is in public domain since the 1st of January 2015.

are hence only uni-factorial, it is simply to show which seismic parameters could be influential in combination with others. It should be noted that the here presented attempt of linkage concerns only the simplified geometry group as the obtained displacement patterns are much more variable that the ones from the fine geometry group, for which the dynamic behavior seems mostly controlled by the static stability of the slope.
Interestingly, there seems to be not only a correlation between the Fourier Amplitude Spectra (FAS; Fig. 4.20a-k), but also with the velocity time-histories (cf. Fig. 7.10a-f; A.8.). The conjecture with respect to the FAS is that those with one zone are more likely to cause hunches in the curve showing the superficial displacement pattern, whereas the FAS with two zones rather result in "elephant-type" curves. Here, the term "zones" designs frequency ranges of the FAS that host more amplitude peaks than other ranges. Likewise, velocity time-histories have such zones – however with more or fewer velocity peaks over certain time ranges. The second conjecture is that velocity time-histories with two zones, or those for which it is difficult to identify one or two zones, cause internal displacement patterns, that are either located around point 3 (cf. Fig. 4.8) or in the last fourth of the landslide mass. Velocity time-histories with only one zone do not show internal displacement patterns what is an effect of the uniformly color-coded legend per geometry group. Surely the concerned cases have an internal displacement pattern as they have an – allowedly very small – superficial displacement pattern. By letting the internal displacement patterns of signals A, C, I and K auto-scale their respective color-coded legend it becomes apparent that three of them actually belong to the group of velocity time-histories with (one to) two zones causing internal displacement patterns around point 3 or in the last fourth of the landslide mass.
According to Tab. 7.2. both conjectures could be confirmed in most of the cases. Moreover, there seems to be a relation between the two conjectures. Strikingly this appears however to be a "one-way-relation". One finds that all hunches appearing in the curves of the superficial displacement patterns have an underlying internal displacement pattern that concentrates around point 3 or in the last fourth of the landslide mass – including the two "mixed hunches" of signals B and I. But not all cases with internal displacement patterns around point 3 or in the last fourth of the landslide mass are restricted to hunched superficial displacement patterns; in fact, signals E, H and J result in "elephant-type" curves.
An issue that might be addressed in future is the covered frequency range by FAS-zones with high amplitudes. Later on in the section it will be shown, that the Diezma Landslide has a strong resonant response in the range of 3 Hz to 6 Hz; it could therefore be of further interest, if and how many FAS-zones are located in this highly responsive frequency range.

signal	velocity zones	internal pattern	conjecture confirmed	FAS zones	superficial pattern	conjecture confirmed
A	1-2	(~ P3)	✓	1	∩	✓
B	1-2	~ P3	✓	2	∩ & E	✓ (if rather as E)
C	1	(2 regions)	clearly 2 patterns	2	E	✓
D	2	~ P3	✓	1	∩	✓
E	2	loop	✓ (if loop = ~ P3)	2	E	✓
F	1	~ P3	clearly 1 vel. zone	1	∩	✓
G	1-2	~ P3	✓	1	∩	✓
H	1-2	~ P3	✓	2	E	✓
I	1-2	(~ P3)	✓	1	∩ & E	✓(if rather as ∩)
J	1-2	~ P3	✓	2	E	✓
K	1-2	(~ P3)	✓	1	∩	✓

Tab. 7.2. Correlations between internal displacement patterns (cf. Fig. 7.10a-f) and respective velocity time-histories and between superficial displacement patterns and respective FAS (cf. Fig. 4.20a-k, Tab. 6.1). The table refers only to the simplified geometry. Abbreviations are: "~ P3" for "around point 3", "∩" for "hunch" and "E" for "elephant-type". A "zone" is assumed to be an accumulation of comparably high amplitudes which is either present once in a velocity time-history or a FAS, or which is separated from another zone by smaller amplitudes in between.

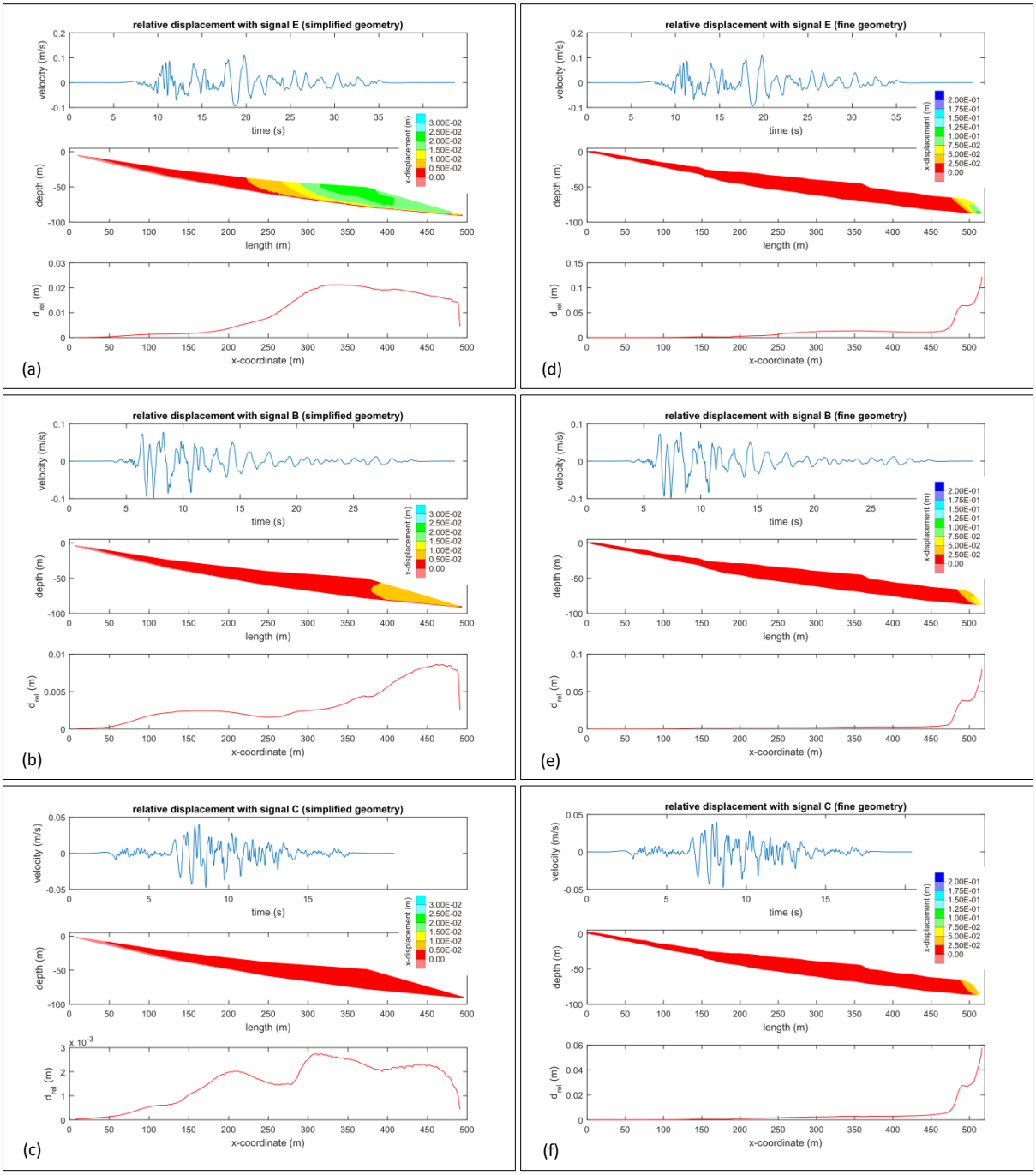

Fig. 7.10a-f. Relative horizontal displacements for signals E, B and C and the simplified (left) and fine (right) 2D-geometry. The three signals represent cases with high, medium and small entrained displacements respectively. The three subplots represent the signal, the internal displacement pattern and the displacements at the surface. It should be noted that signals A, D, F, G, H, I, J and K are shown in the appendix (cf. A.8.), and that in contrast to most of the other color-coded figures in this thesis the red-to-blue-sequence is here opposite.

After the qualitative discussion of the first three mentioned points, also the fourth – which is of rather quantitative nature – deserves a closer look. From Tab. 7.3 it can be seen that residual displacements reach higher values within the fine geometry group; their maximum values are between 6 and 24 times bigger than their counterparts of the simplified geometry group. By using the term "counterpart" one should pay attention to the fact that the maximum displacements are not to be attributed to the same point as one can conclude from the qualitative pattern analysis. It is interesting, that factors between counterparts are highest for the signals causing the lowest displacements (A, C, I and K) smallest for the signals causing the highest displacements (E and F). Furthermore, the ranking of entrained displacement by signal

is identical per geometry group; the average maximum displacements for the simplified and the fine geometry group are 0.9 cm and 8.3 cm respectively.
As in section 6.4.2. one important question was, if there is an obvious relationship between the intensity of the predicted response of the slope and the characteristic mean earthquake period (T_m) and/or the ratios of the characteristic site periods (T_s/T_m and T_l/T_m; cf. Excursus – 6.4.2.). Unfortunately there appears no striking correspondence via the gray-scale color-code in Tab. 7.3; the shading of neither parameter involving T_m is directly or inversely harmonized with the predicted maximum displacements. Uniquely, the highest obtained FAS peak with signal F coincides with the highest reached maximum displacements. It remains however questionable, if one can deduce a relationship from this eventuality; especially the fact that the smallest FAS peaks do not align with the smallest maximum displacements debilitates to some extent the hypothesis of a possible correlation.

signal	max FAS (m/s)	filtered T_m (s)	T_s/T_m* (-)	T_l/T_m* (-)	$dx_{simpl.}$* (cm)	dx_{fine}* (cm)	factor between dx_{fine} & $dx_{simpl.}$
A	> 0.01	0.70	0.37	2.40	0.18	4.25	~ 24
B	> 0.02	0.66	0.39	2.54	0.86	7.99	~ 9
C	> 0.02	0.32	0.81	5.21	0.28	5.76	~ 21
D	> 0.02	1.08	0.24	1.55	0.98	8.64	~ 9
E	> 0.02	0.77	0.34	2.16	2.12	12.20	~ 6
F	> 0.04	0.58	0.45	2.87	2.85	17.06	~ 6
G	>0.02	1.02	0.26	1.65	0.52	6.15	~ 12
H	> 0.01	0.38	0.68	4.37	0.69	9.35	~ 13
I	> 0.01	1.19	0.22	1.41	0.30	7.08	~ 23
J	> 0.02	0.49	0.54	3.46	0.91	9.58	~ 10
K	> 0.02	0.76	0.34	2.20	0.17	3.64	~ 21

Tab. 7.3. Comparison of different signal properties and horizontal displacement values for v_s = 300 m/s (*).

The dynamic analysis of all 22 signal-geometry-combinations has finally proven the hypothesis that – at least via finite difference modeling – the predicted behavior of the slope is dependent on the input geometry as well as on the applied seismic scenario. Since neither of the two factors alone was fully explicative, another approach incorporating both factors at the same time turned out to be highly promising: the analysis of site effects.
Before discussing results from the site effect study for both the simplified and the fine geometry, a short excursus will present the theoretical background of site effect analysis.

Excursus – The Evaluation of Site Effects

Section 1.2. explained the conditions for site effects and their consequences; another question is how to evaluate and quantify them. A widely used type of visual quantification is the transfer function map (TFM) illustrating the amplification pattern (cf. Fig. 7.12). It is obtained by the following steps:

1. Time-histories – usually of the acceleration or velocity – are registered at different locations on the ground surface.
2. One point that is situated on a bedrock outcrop is chosen as reference location.
3. With the Fast Fourier Transform (FFT) a Fourier Amplitude Spectrum (FAS) is computed for every location including the one of the reference.
4. Every FAS is divided by the reference FAS in order to obtain a transfer function representing the amplification for each location; when the FAS of the reference location is divided by itself, it will result in a "1-function".

5. Finally all transfer functions are arranged "sheet wise" according to their respective location showing the frequency at which amplifications occur on the second axis and the amount of amplification as color code to replace the third axis; for better visualization the entire plot surface is usually filled via interpolation resulting in a TFM.

Attention has to be paid when evaluating TFM based on time-histories from models rather than from real records. An oversimplified example of 1D-resonance shows why (cf. Fig. 7.11a):
If one models a 25 m thick sand lens (with v_s = 400 m/s) on a more compacted material (with v_s = 700 m/s) in a numerical model that is 175 m deep in total, one would see amplifications due to the sand lens (at 4 Hz) as well as to the model itself (at around 1 Hz). However, due to the sophisticated numerical methods, deep model bases with respect to the zone of interest and the use of quiet boundary conditions such model-induced artifacts are not too pertinent.

$$f_{res} = \frac{v_s}{4 \cdot h} \qquad f_{res} = \frac{400}{4 \cdot 25} = 4\ Hz \qquad f_{res} = \frac{700}{4 \cdot 175} = 1\ Hz$$

Although it seems quite oversimplified, the principle of 1D-resonance plays an important role for amplification patterns. It explains why a site with variable sediment thickness might experience different amplifications at distinct locations; i.e. why different frequencies contained in a signal cause resonance preferably at those locations where the sediment depth (h) comes close to a fourth of the shear wave velocity divided by the respective frequencies ($v_s/(4 \cdot f_{res})$; cf. Fig. 7.11b).

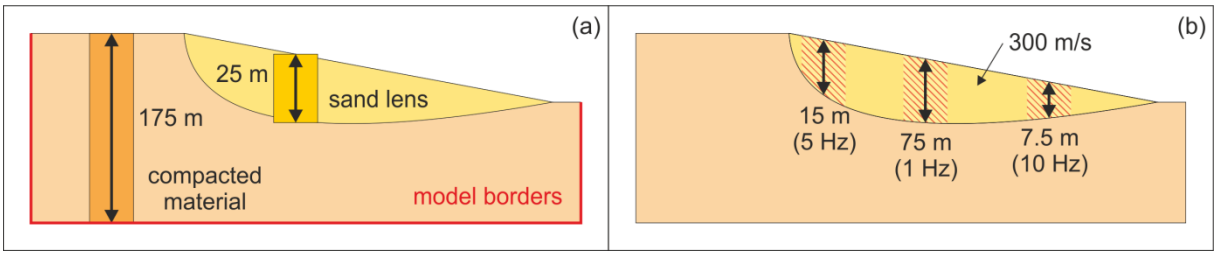

Fig. 7.11. Example of two 1D-resonance-colums in a model with a shallow base (a) and frequency-dependent locations experiencing resonance phenomena (b). Both figures are not proportional in length and width.

The evaluation of site effects requires a full computation of the static and the dynamic phase of a purely elastic model (cf. Fig. 7.2), but it is possible to apply a much simpler signal, such as for example a Ricker Wavelet which is expressed in the time-domain by:

$$v_R(t) = A \cdot \left(1 - 2 \cdot \pi^2 \cdot {f_{dom}}^2 \cdot (t-1)^2\right) \cdot e^{-\pi^2 \cdot {f_{dom}}^2 \cdot (t-1)^2}$$

where A is the amplitude and f_{dom} the dominant frequency

Since Ricker Wavelets are common for eigenmodes vibration studies due to their well-defined spectral frequency content around the dominant frequency and their short duration (GISCHIG et al. 2015), one of its kind was used in this thesis to compute TFM for the simplified and the fine 2D-geometry (cf. Fig. 7.5a-b). The wavelet is shown in the lowest subplots of Fig. 7.13 and Fig. 7.14; its amplitude and dominant frequency are 0.15 m/s and 6 Hz respectively. Counting from the left model margin, the reference FAS for the simplified geometry is the 50th FAS and the one for the fine geometry is the first FAS.
Simply spoken, the two uppermost subplots of Fig. 7.13 and Fig. 7.14 indicate the degree of amplification for a particular position and frequency via the color-code. The following paragraphs discuss the characteristics and differences of both TFM; interpretations and explicative presumptions are given for the detected features. Where possible, parallels are drawn to results from the static and the dynamic analysis of the 22 signal-geometry-combinations.

At a first view, it is clearly apparent that the amplification pattern covers only the landslide mass but not the bedrock. Despite this obvious similarity, the patterns are though quite different in many details. The TFM of the simplified geometry seems more symmetric over the landslide mass; the TFM of the fine geometry, in contrast, includes a strong toe-oriented behavior. Surely one could argue that in fact the amplification pattern of the simplified geometry is not perfectly symmetric either; however, it is more equally distributed what originates probably from a more gradual thickness in- and decrease of the landslide mass. In comparison to this, the fine geometry is by far more sectional what is reflected in the amplification pattern of the fine geometry. Here, the two abrupt thickness changes at 150 m and 350 m appear as vertical blue strip in the TFM. These two vertical lines separate the amplification pattern in three zones of which the first two (covering the upper landslide mass) bear a strong resemblance to the respective parts of the amplification pattern of the simplified geometry. The third zone, though, is very different and ends with an even more pronounced vertical blue line that sharply confines the amplification pattern. This end is the only one of its kind as all other ends "fade-out". Comparing these particularities with the shape of the landslide mass, it becomes obvious that the amplification pattern is strongly dependent on the geometry:

- Gradually decreasing thickness appears as "fade-out" pattern, whereas abrupt thickness changes cause "amplification gaps".
- Depending on the thickness gradient, the "fade-out" pattern is more or less curved.

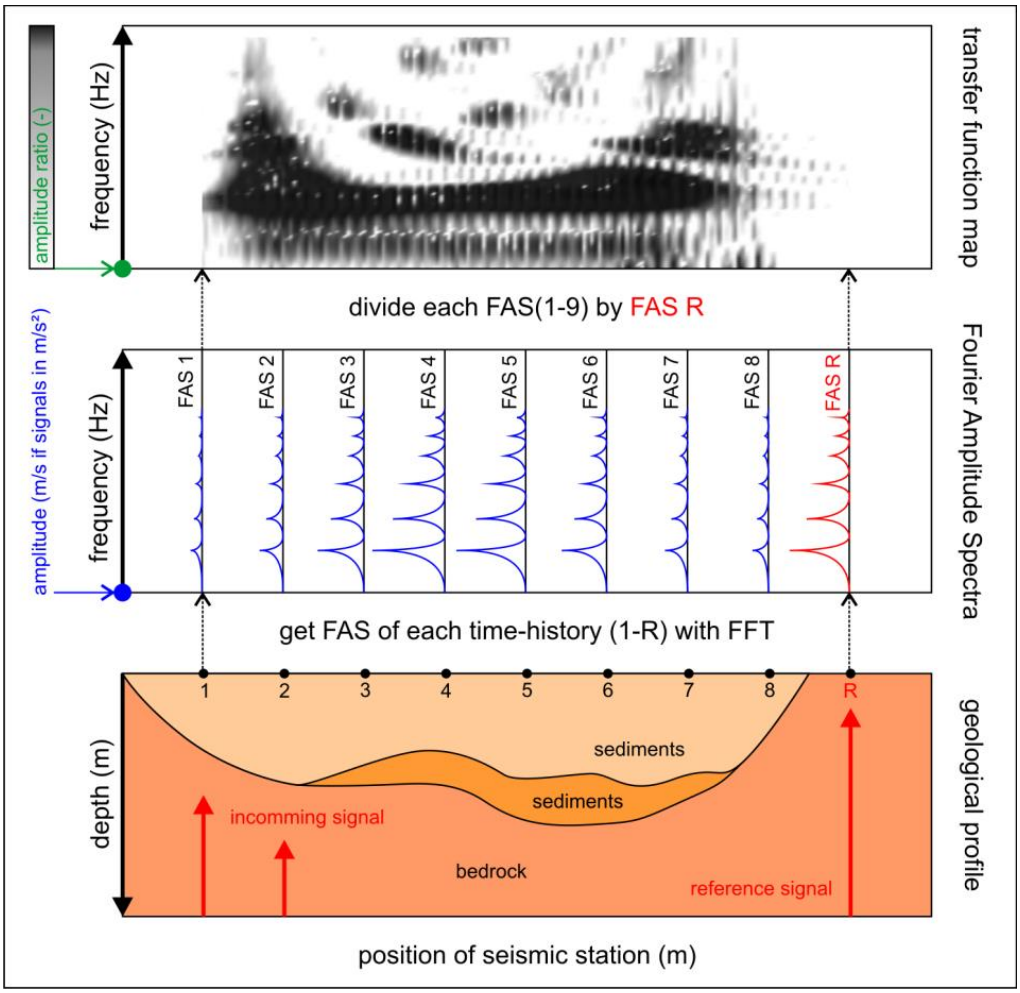

Fig. 7.12. Principle of the evaluation of site effects.

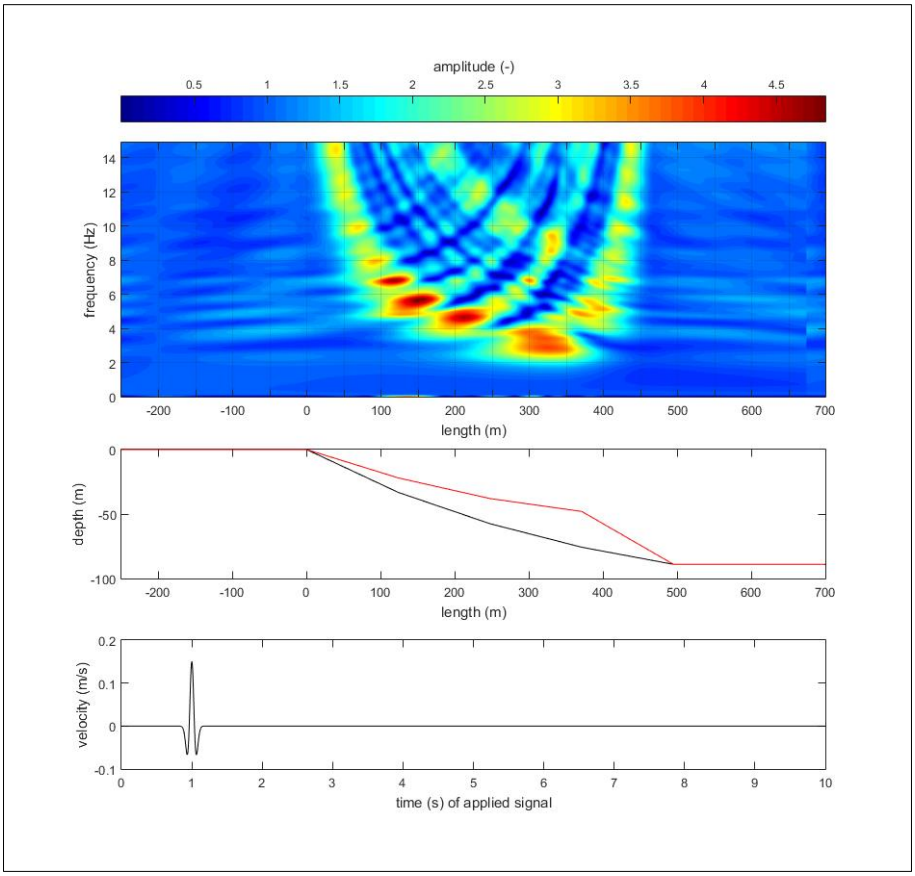

Fig. 7.13. Site effect evaluation for the simplified 2D-geometry in the form of a TFM.

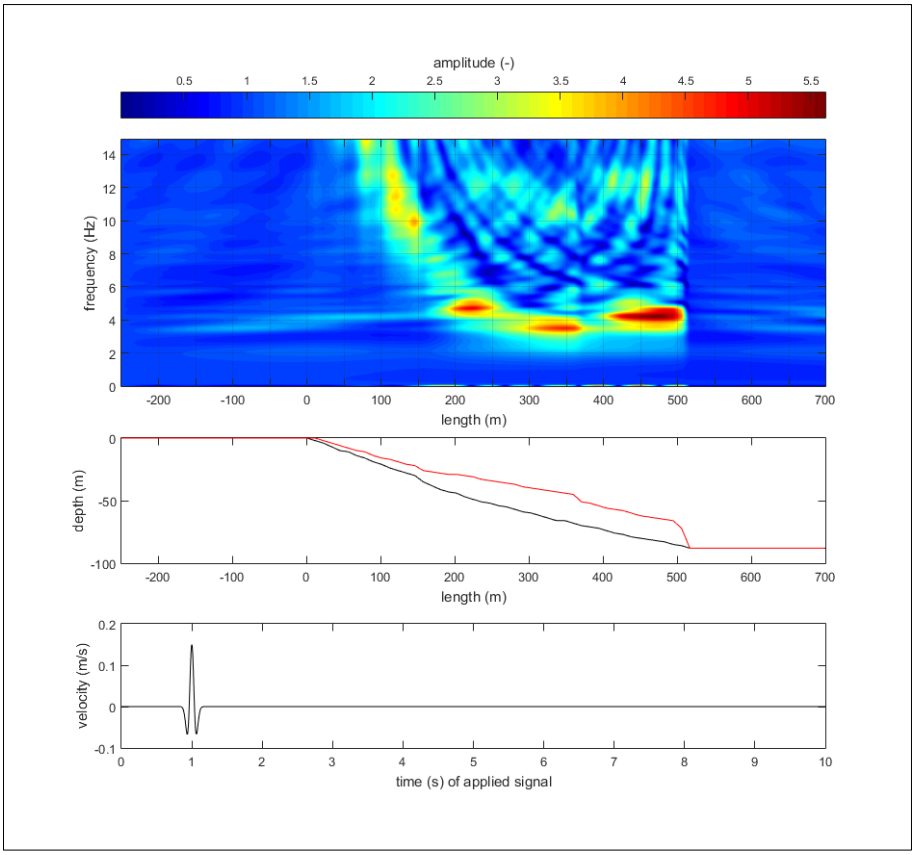

Fig. 7.14. Site effect evaluation for the fine 2D-geometry in the form of a TFM.

In a next step the amplification patterns with respect to the covered frequency ranges were examined. In both TFM it is primarily the before mentioned curved pattern in yellow and red colors that attracts attention. From the examination with respect to the landslide mass, it is already obvious that the thickness considerably influences the curvature – i.e. the resonance at which the mass responds to a vibratory motion. The equation for 1D-resonance relates thickness and resonance frequency (cf. Excursus – 7.3.3.):

- Smaller thicknesses cause resonance frequencies to be high; and vice versa.

As a result, the amplification patterns of the crown and the toe areas of both TFM cover the highest frequency ranges, and the lowest covered frequency ranges are located at the thickest parts of the two geometries.
The amplitude per frequency is not as easily explained since amplification processes do not only depend on simplified concepts such as 1D-resonance. For this very reason red colors tend to occur in similar zones of the two landslide masses, but the highest amplifications (i.e. the reddest spots) are not located in similar zones.
A rough measure for an average amplitude representative for a hypothetical layered setting in 1D is the ratio (I) between the seismic impedance of the landslide mass and the one of the bedrock (cf. 1.2.; SEMBLAT & PECKER, 2009).

$$I = \frac{Z_{BR}}{Z_{LS}} = \frac{\rho_{BR} \cdot v_{BR}}{\rho_{LS} \cdot v_{LS}} = \frac{2500 \cdot 1000}{2181.4 \cdot 300} = 3.82$$

Indeed, for those zones that experience strong amplifications an impedance ratio of 3.82 is quite representative for both TFM.
Combining the aspects of thickness, frequency and amplification, one more obvious feature comes to the fore. The patterns of the highest amplifications of both geometries cover a frequency range between roughly 3 Hz and 6 Hz; DELGADO et al. (2015) cite relating thereto a resonance frequency of the Diezma Landslide of 4 Hz, which fits very well to the obtained results and especially to the TFM of the fine geometry. In terms of resonance, the landslide mass is thus strongly responsive to vibrations in this particular frequency range which is usually largely present in the frequency contents of seismic signals. By comparing the distinct zones that are prone to particular resonance, it appears that the amplification pattern conforms – not perfectly, but still by and large – to the displacement patterns obtained from the dynamic finite difference analysis (cf. Fig. 7.10a-f). The pattern of the highest amplifications of the simplified geometry covers a wider span of the landslide mass and it is rather orientated around point 3 (cf. Fig. 4.8). The pattern of the highest amplifications of the fine geometry is much more geared towards the landslide toe.
With consideration of the finding that the Diezma Landslide shows a strong resonant response in the range of 3 Hz to 6 Hz, there arises the question if the distinct predicted slope deformations relate in some way to this frequency range. Interestingly, and with exception of signal C, the predicted maximum displacements per signal do correlate roughly with the peak amplitude as well as with the mean amplitude of the Fourier Amplitude Spectrum (FAS) between 3 Hz and 6 Hz of the respective signal – though not perfectly in the same ranking. From Tab. 7.4 and Fig. 7.15 one very obvious characteristic is visible:

- Signals causing great displacements have high FAS peaks and FAS means in the range between 3 Hz and 6 Hz. (Signals B, D, E, F, H and J)
- Signals causing small displacements have low FAS peaks and FAS means in the range between 3 Hz and 6 Hz. (Signals A, H, I and K)
- Signal C is the only one that does not satisfy this relationship; it is also the only one with an internal deformation pattern revealing two regions of high values (cf. Tab. 7.2).

signal	FAS peak (3-6 Hz)	FAS mean (3-6 Hz)	$dx_{simpl.}$* (cm)	dx_{fine}* (cm)
A	0.008	0.003	0.18	4.25
B	0.014	0.005	0.86	7.99
C	[0.024]	[0.009]	0.28	5.76
D	0.006	0.002	0.98	8.64
E	0.013	0.003	2.12	12.20
F	0.011	0.003	2.85	17.06
G	0.005	0.002	0.52	6.15
H	0.015	0.004	0.69	9.35
I	0.004	0.001	0.30	7.08
J	0.020	0.005	0.91	9.58
K	0.006	0.002	0.17	3.64

Tab. 7.4. Peak and mean amplitudes of the FAS per signal in relation to maximum displacements for v_s = 300 m/s (*). The columns containing the FAS peaks and means are color-coded wit exception of signal C.

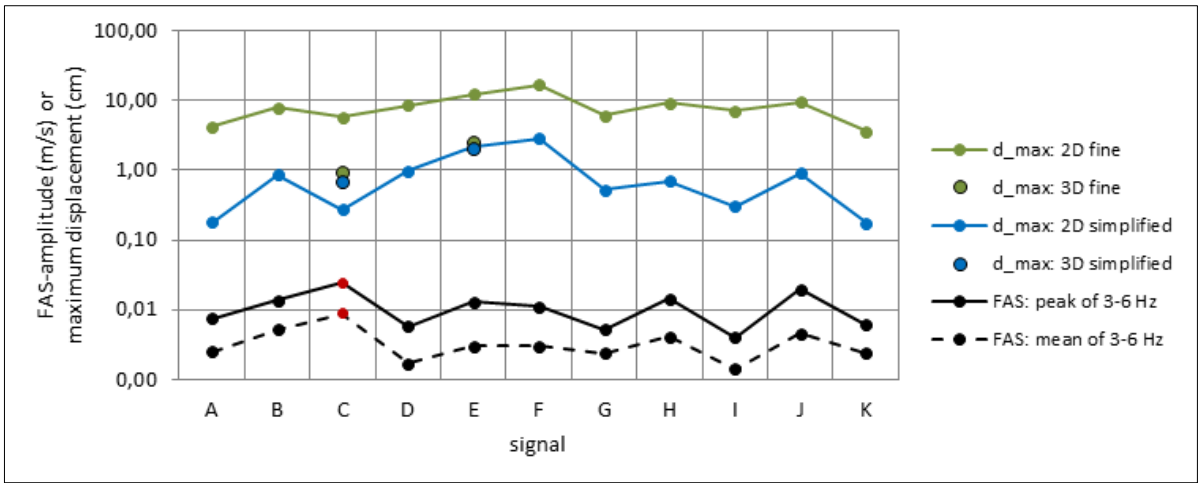

Fig. 7.15. Peak and mean amplitudes of the FAS per signal in relation to maximum displacements. The two red points of signal correspond to the FAS peak and mean marked in Tab. 7.4. Blue and green points indicate the displacement values for signals E and B in 3D (cf. 7.3.6.).

Since this relation has one non-satisfying element, the finding has to be taken with care. Nonetheless, the approach seems reasonable; it appears logic that the characteristics of the FAS parts in the range of 3 Hz to 6 Hz have a stronger influence on the slope response than the characteristics of the entire FAS. A question for future research might be, if these FAS characteristics can be combined with other influencing factors – such as for example macro-seismic parameters – to better explain the quantitative aspect of entrained displacements per signal.

The theoretical excursus on site effect evaluation (cf. Excursus – 7.3.3.) has shown that either acceleration or velocity time-histories can be used to compute FAS and their ratios with the reference FAS. In order to obtain a simplified displacement evaluation, one must simply skip the FFT-processing and integrate the recorded time-histories once or twice depending on the recording type. Displacement time-histories are then drawn – as the name suggests – over time in contrast to TFM which are represented in the frequency domain.

By simple integration of the velocity time-histories that resulted from the purely elastic computation (cf. Fig. 7.2) using the above mentioned Ricker Wavelet (cf. Fig. 7.13, Fig. 7.14), two very conclusive wave propagation maps (cf. Fig. 7.16, Fig. 7.17) emerge for the simplified and the fine geometry. Traces caused by first-arrival wave fronts and those generated by reflected waves localize deformation patterns in very similar zones as in the respective TFM. Again, the pattern with the highest values of the simplified geometry covers a wider span of the landslide

mass and it is rather orientated around point 3 (cf. Fig. 4.8). The pattern of the highest deformations of the fine geometry is geared towards the landslide toe.

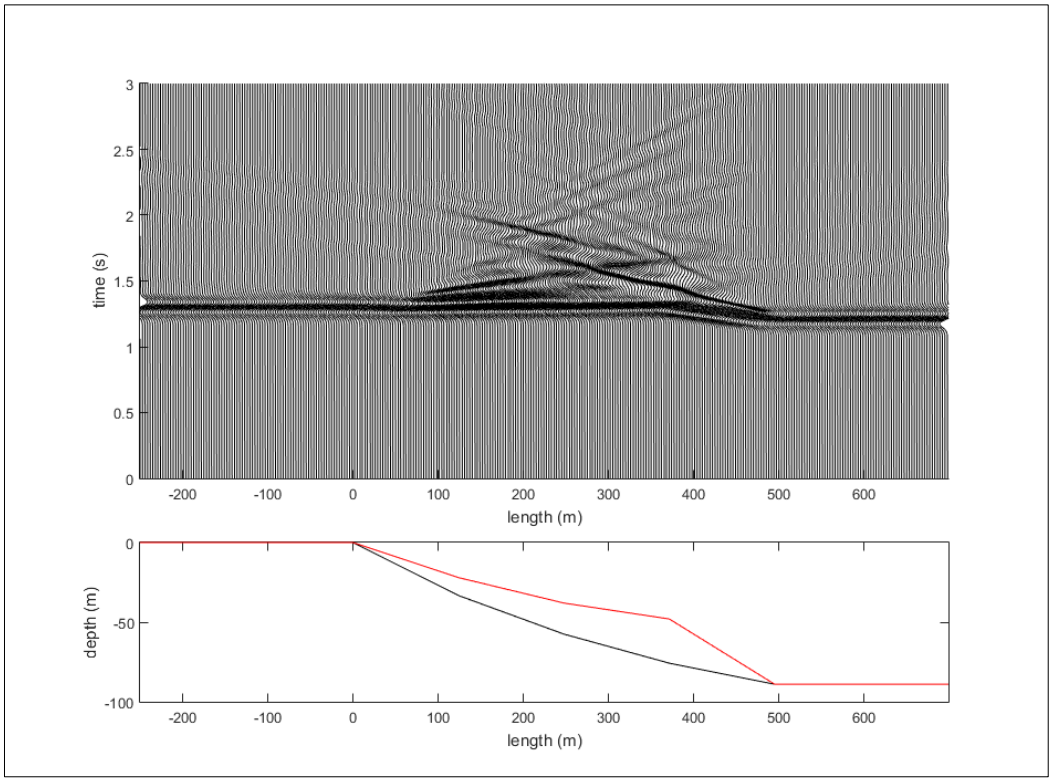

Fig. 7.16. Wave propagation map obtained from the site effect evaluation for the simplified 2D-geometry. Every third displacement time-history is shown with a multiplicative factor of 1500.

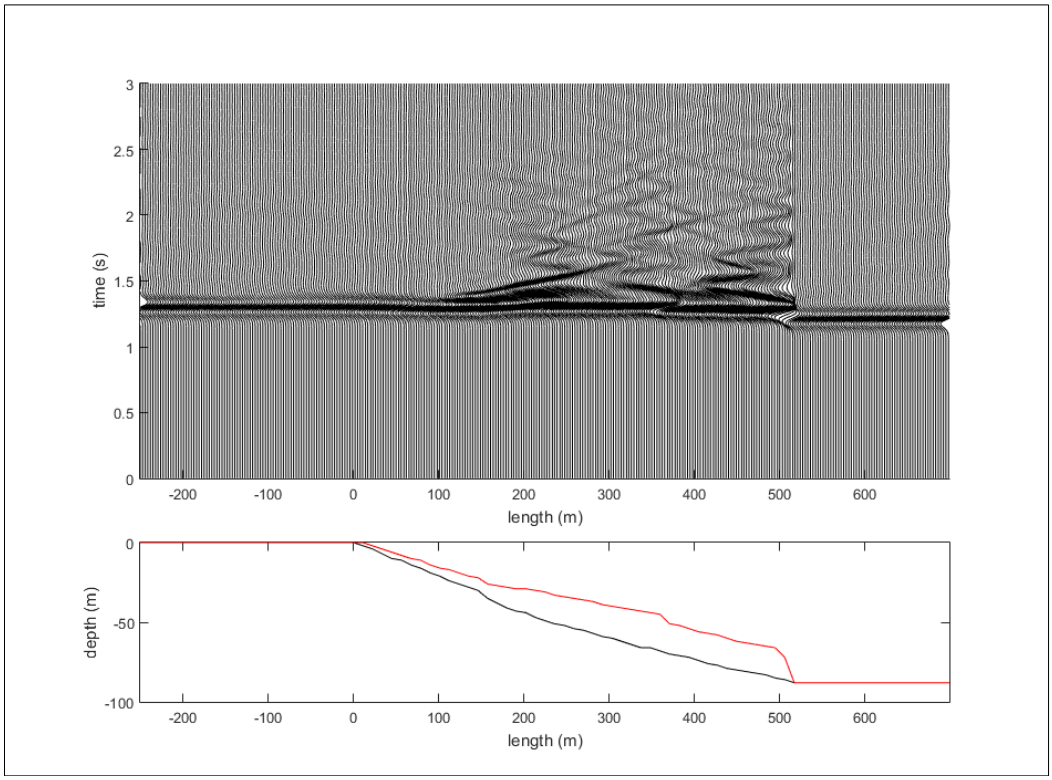

Fig. 7.17. Wave propagation map obtained from the site effect evaluation for the fine 2D-geometry. Every third displacement time-history is shown with a multiplicative factor of 1500.

7.3.4. Geometry of the Models in 3D

In analogy to the model layout in 2D, also the layout should be similar for the simplified and the fine 3D-geometry consisting of a cuboid in which the two landslide masses occupy a different amount of space. The uppermost point of the landslide crown should lie at 0 m on the x-axis, at 0 m on the y-axis and at the respective altimetric level on the z-axis.
Unlike in FLAC 2D, in which the landslide mass is simply defined by the points enveloping the LCS Aa, FLAC 3D needs more points than those enveloping the two LCS (As and Aal), the four TCS (N, B, C, and M) and the trace Ql (cf. Tab. 4.8) in order to define the ground surface and the sliding surface of the landslide.
At this point the geological modeling software GDM came into play. Using the geostatistical technique of Kriging, the software interpolates z-values for places without available z-information taking into account the existing coordinates – i.e. those of the existing cross sections and the trace Ql. Effectively, the places at which z-data is to be interpolated must be defined in advance; in this case all concerned points lie on a xy-grid with a mesh-size of 10 m by 10 m and the following dimensions:

- x-axis: from -50 m to 640 m → 690 m in total
- y-axis: from -250 m to 190 m → 440 m in total

While creating continuous surfaces with Kriging it is important to treat the ground and the sliding surface separately to avoid interpolations including both altimetric sets at the same time. Once both surfaces are complete, there must be a careful inspection on whether all created ground surface points lie above their counterparts of the sliding surface. If not, their coordinates must be adjusted manually.
The thereby obtained volumes for the simplified and the fine geometries amount to 791,000 m^3 and 720,000 m^3 respectively. Certainly, these volumes differ from the volume estimation of 1.2 million m^3 for the Diezma Landslide by DELGADO et al. (2015). However, it must be kept in mind that every sort of modeling will always draw a more or less altered image of the reality. To verify the obtained volume of the fine geometry, a similar procedure was carried out in MATLAB. For grids with mesh-sizes ranging from 5 m to 15 m and for three triangulation-based interpolation methods (namely the natural neighbor, linear and cubic methods) volumes resulted in 708,000 m^3 on average. The mesh-size of 10 m by 10 m – which reflects somehow the spacing between coordinate points on the cross sections and the trace Ql – delivered the best results in terms of "geological appearance"(cf. Fig. 7.18a-b). The terrain does not look as blurred as with a mesh-size of 15 m by 15 m, and it does not include artificial ditches and notches as with a mesh-size of 5 m by 5 m. Therefore the mesh-size in GDM was chosen to be 10 m by 10 m. Figure 7.19 and Figure 7.20 show the final thickness plots for both geometries as they appear in GDM. The white points refer to existing coordinate points of the cross sections and the trace. The pink points in Fig. 7.19 had to be added in order to avoid a creation of two separate volumes (one close to the landslide crown and one covering the lower two thirds of the landslide mass); during the interpolation process they were manually retrieved from the triangular planes that cover the simplified 3D-model in CESAR (cf. 6.4.) so that they would not modify the shape of the simplified geometry.
From GDM data is exported in the form of CSV-files and imported to FLAC via a FISH-command. The initial cube grid with the below listed dimensions then conforms itself to the introduced data such that the surface of the FLAC-model corresponds to the ground surface defined in GDM.

- x-axis: from -50 m to 640 m → 690 m in total
- y-axis: from -250 m to 190 m → 440 m in total
- z-axis: from 900 m to 1310 m → 410 m in total

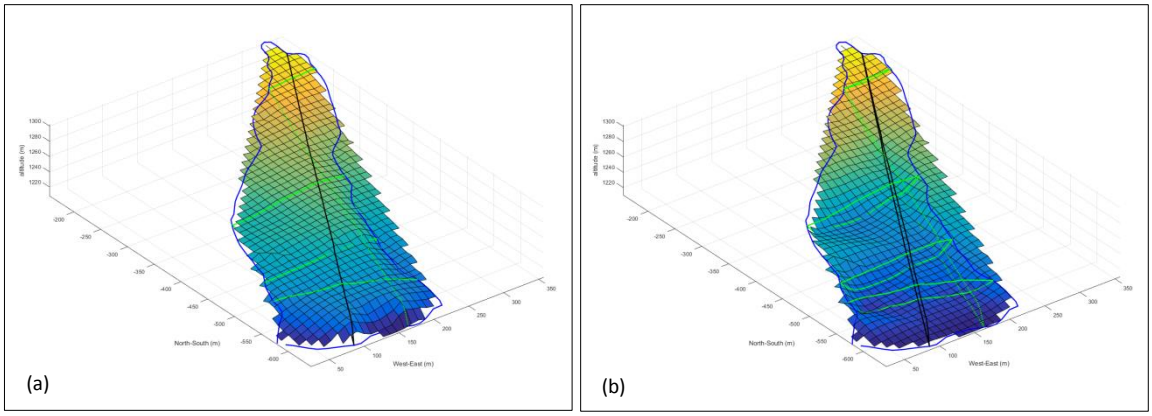

Fig. 7.18a-b. Interpolations for the ground surface (left) and the sliding surface (right) of the fine 3D-geometry with MATLAB using the cubic triangulation based method and a grid with a mesh-size of 10 m by 10 m (black: LCA Aal; green: LCA As, TCS N, TCS B, TCS C, TCS M; blue: Ql; cf. Tab. 4.8).

In a next step, the altimetric information of every created zone is checked on whether it lies between the ground and the sliding surface defined in GDM; if this is the case, the zone belongs to the landslide mass, if not it becomes a bedrock zone.
The imposed grid is equal for all 3D-models, but in contrast to the 2D-models (cf. 7.3.1.) it has a mesh-size of 3 m by 3 m what actually allows for correct propagation of waves that include frequencies up to 8 Hz (cf. 4.4) only. This value is, however, below the frequency content of the signals after they had undergone the 4th-order low-pass Butterwoth Filter with a cut-off frequency of 10 Hz (cf. 4.4.). Nonetheless, the choice of 8 Hz has its legitimacy; the smaller the mesh-size, the more time-consuming becomes the computation. A maximum frequency of 8 Hz is therefore a compromise between computation time and the frequency content of the signals that should be properly propagated through the model.

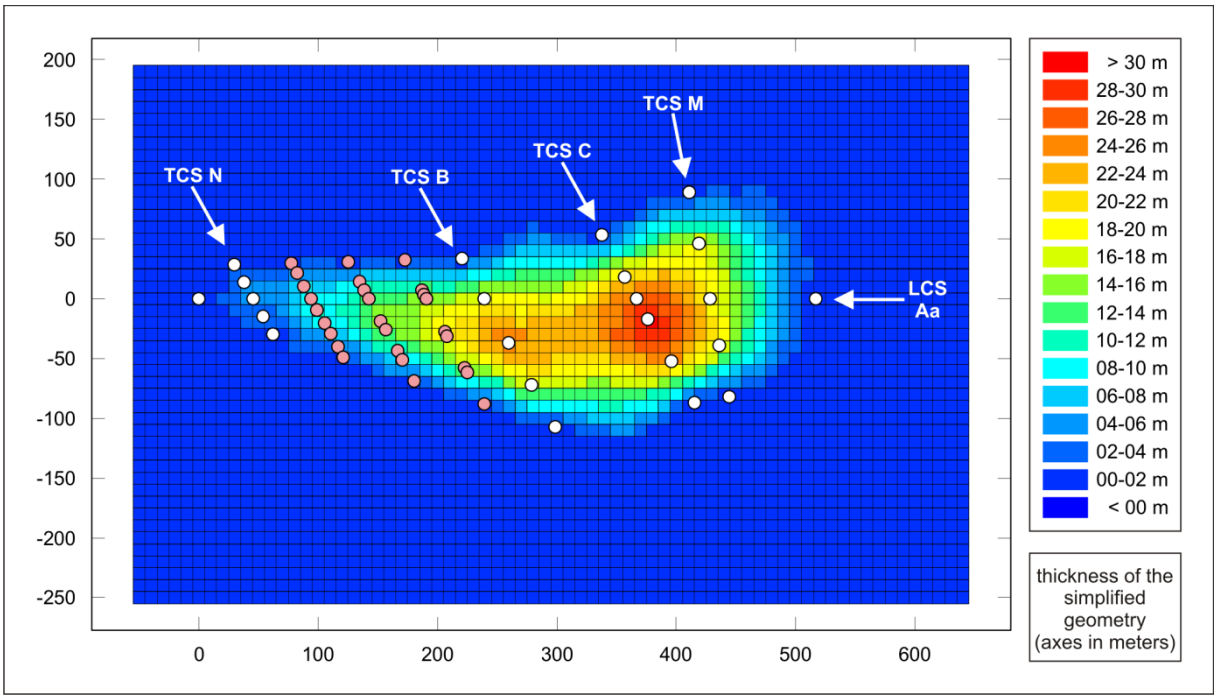

Fig.7.19. Thickness plot of the simplified 3D-geometry in GDM
(white points: existing coordinates; pink points: additional coordinates; for abbreviations cf. Tab. 4.8).

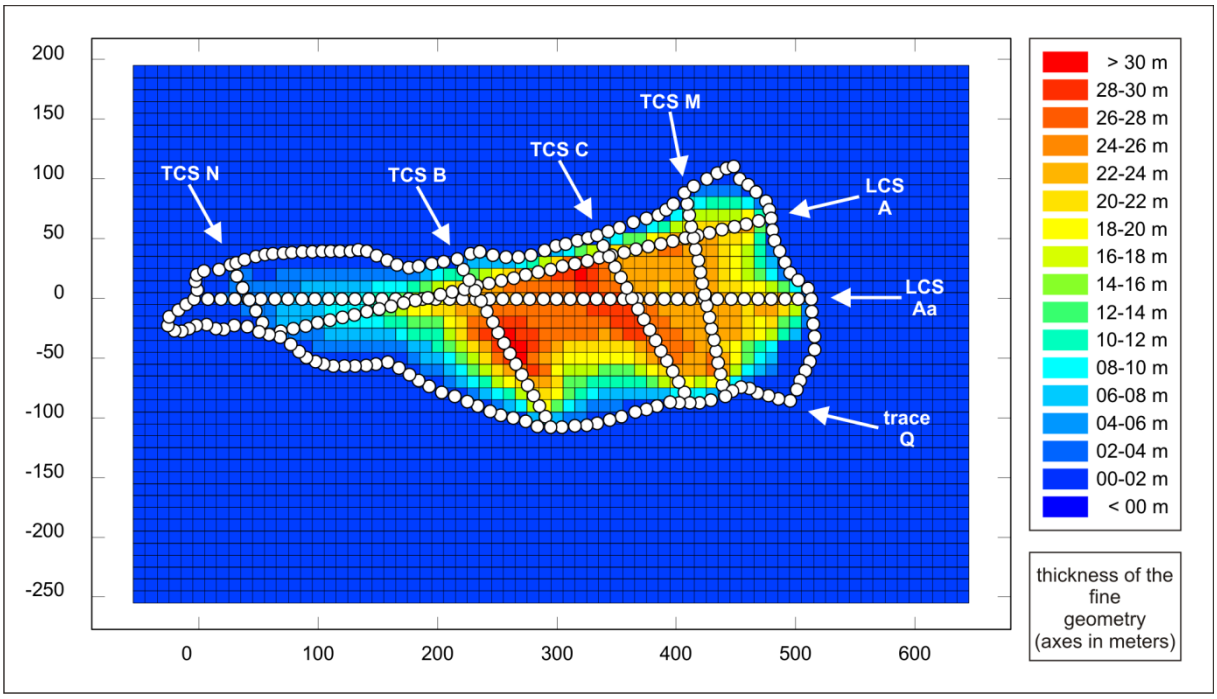

Fig. 7.20. Thickness plot of the fine 3D-geometry in GDM
(white points: existing coordinates; for abbreviations cf. Tab. 4.8).

7.3.5. Static Analysis in 3D

Although FLAC 3D is different to handle in comparison to its 2D-version, the procedure of a static analysis remains the same. The objective is to bring the model to equilibrium after the settlement due to gravity (9.81 m/s^2) in order to represent the stability of the slope without the influence of a seismic scenario.

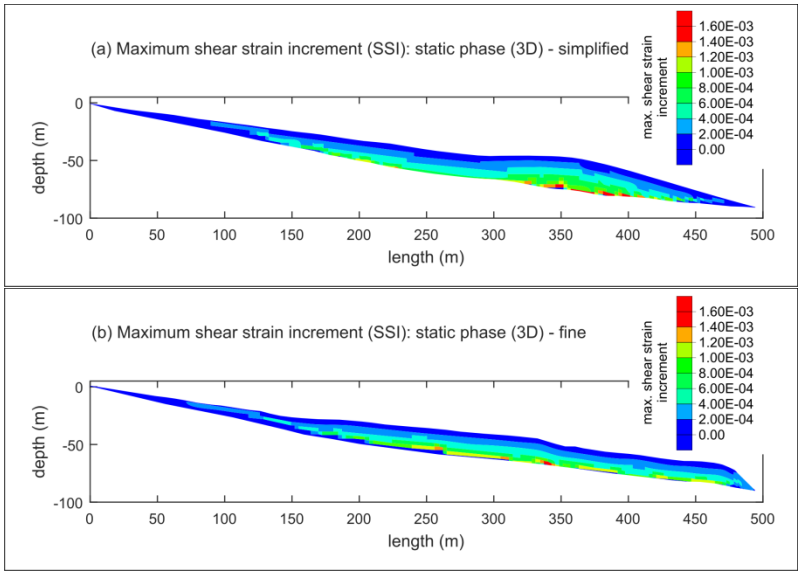

Fig. 7.21-b. SSI localization after the static phase for the simplified and the fine 3D-geometry.
The SSI is dimensionless.

Therefore the focus in this section will be on the obtained results, rather than on the necessary procedures and theory which both are described already in section of the static analysis in 2D (cf. 7.3.2.). Two important points should be noted. First, due to time restrictions there is no computation of the factor of safety available neither for the simplified nor for the fine 3D-geometry. Second, the evaluation of the static phase is based on virtual cuts through the 3D-

models along LCS Aa (cf. Fig. 7.19, Fig. 7.20) for both geometries. Also the dynamic analysis will only show virtual cuts. In contrast thereto, the modal recombination analysis with CESAR 3D resulted in virtual cuts as well as in superficial representations of the models along and across which displacements were recovered (cf. Fig. 6.19, Fig. 6.20).
Again, the static state of each model can be conveniently represented via shear strain patterns in the form of color-coded shear strain increments (SSI; cf. 7.3.2.). In contrast to the 2D-geometries, the SSI tend to accumulate along the sliding surface in both geometries. Their patterns are in fact quite comparable unlike as in 2D (cf. Fig. 7.5b) where the fine geometry appears to be decidedly "statically inspired". This typical static stress pattern of stress concentration towards the landslide toe could not be confirmed for the fine geometry in 3D. Instead, both 3D-models reach comparable values of SSI and high SSI values cover similar ranges along the sliding surfaces.
As it appeared in sections 7.3.2. and 7.3.3., the static behavior of the models strongly depends on its geometry and so does the dynamic behavior. By reason thereof, the expected displacement patterns should relate to the respective SSI patterns.

7.3.6. Dynamic Analysis in 3D

Likewise, there is no particular difference between the dynamic phase in 3D in comparison to the one in 2D. Nevertheless, one detail is unmissable: the limitation to the two signals E and B due to computation time restrictions. Section 7.3. already mentioned shortly why these two signals were chosen. A little more effort is spent in this section in order to explain the reasoning behind this choice.
Figure 7.22. shows rankings of maximum displacements caused by the eleven seismic scenarios with respect to method, dimension and geometry. It is very obvious that each method entrains another ranking; both "CESAR-siblings" (2D and 3D), though, are very similar and so are both "FLAC-siblings" (simplified and fine in 2D) – a fact that will be discussed further in the overall conclusions (cf. 8.3.). Another very apparent, yet stunning, detail is that some of the signals tend to cause rather small or high displacements, whereas others do not show such a tendency. Most surprisingly, three signals (C, B and E) remain without exception in the small, medium and high displacement groups regardless of the applied method.

- tending to cause small displacements: A, K
- tending to cause high displacements: D, I
- no tendency: F, G, H, K
- group restrictive: C, B, E

With respect to the finding that three of the eleven signals are group-restrictive, and having learned from this comparative line-up that rankings are very similar per "method siblings", it was assumed that these three signals would also cause small, medium and high displacements for the simplified and the fine geometry in 3D. Ideally, all three signals should have been tested for the two geometries, but even though their durations are among the shorter ones of all signals, the time frame of this thesis allowed only for two signals to be entirely processed. Because of this limitation signals E and B were chosen in the attempt to represent high and medium displacements. Signal C also would have been an option since it represents the lower extreme, but due to its "outlier" characteristics (cf. Tab. 7.4, Fig. 7.15) it was considered as unfavorable.
Like in section 7.3.5. describing the static analysis in 3D, the focus is here also on the obtained results rather than on the required procedures. This section likewise follows up the three main hypotheses that were already set for the analysis in 2D:

- slope response as function of geometry
- slope response as function of seismic signal
- response intensity as function of seismic signal

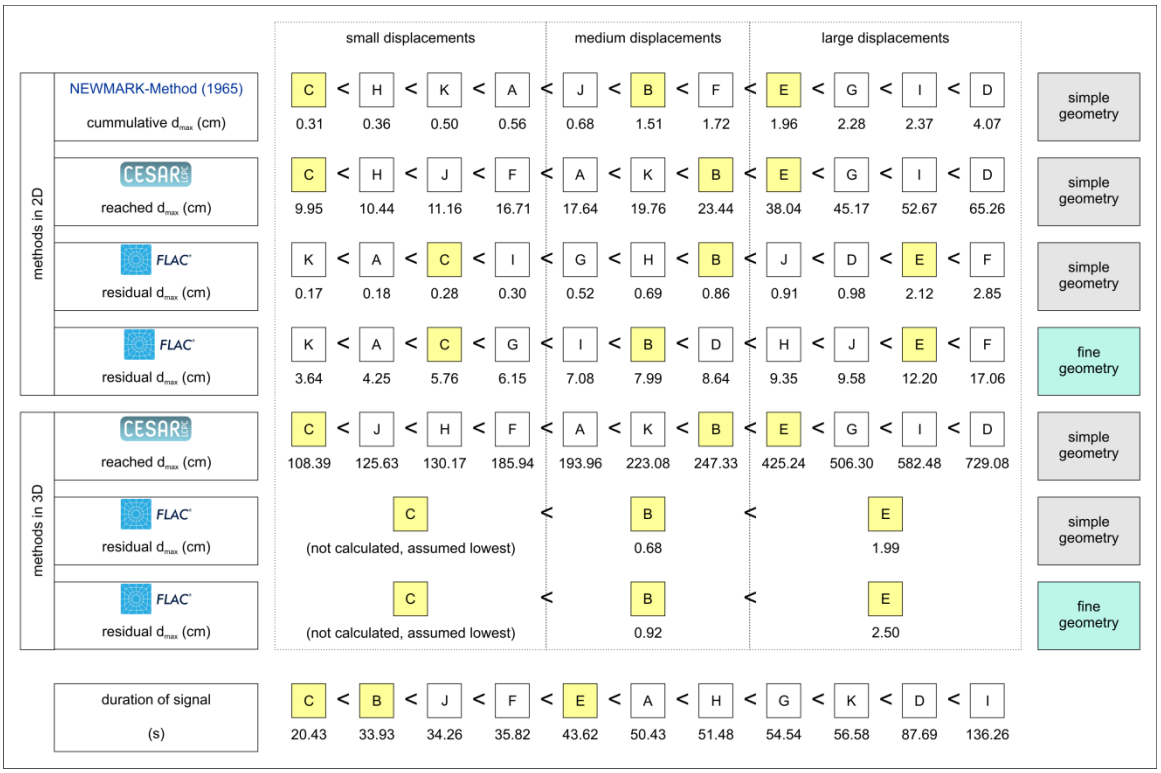

Fig. 7.22. Maximum displacements (cm) per method, dimension and geometry.
Signals E, B and C are marked in yellow; their ranking is variable, however they do not leave the ranking group.

Light on these hypotheses is shed by Fig. 7.23a-d which appear in the same format as their counterparts in 2D; they consist of three subplots of which the first shows the applied signal as velocity time-history, the second contains the color-coded virtually cut as longitudinal cross section representing the residual x-displacement, and the third one displays the x-displacement of the grid points along the ground surface. The ranges of the two legends are:

- simplified 3D-geometry: 0.000 m – 0.020 m in steps of 0.0020 m
- fine 3D-geometry: 0.000 m – 0.025 m in steps of 0.0025 m

As mentioned above, the time limit for this thesis did not allow for processing more than two signals in both geometries. Hence, a total of four signal-geometry-combinations is somewhat lean when it comes to comparative discussions.
Nonetheless, there are very interesting observations to be made even from this small number of models. Some of them are in good accordance with the findings of the dynamic analysis in 2D; some others, though, differ considerably what will later question the reasonableness of model dimensions at least in the case of the Diezma Landslide (cf. 7.3.7.).
In analogy to the four major qualitative and quantitative features of section 7.3.3., one recognizes the following characteristics, which will be discussed in the paragraphs thereafter.

- Internal displacement patterns of the simplified geometry group and the ones of the fine geometry group differ among each other, but not as much as in 2D; internal displacement patterns within one group are roughly similar.
- Superficial displacement patterns of both geometry groups show a similar behavior inasmuch as neither of them finds its maximum in the toe zone of the landslide.
- Different signals cause different slope responses; the divergence is more apparent within the fine geometry group.
- Within the groups signal E causes higher displacements than signal B.

Comparing the internal displacement patterns of both geometry groups, it appears that these patterns are much less distinct in 3D than in 2D. The simplified geometry group displays a concentration of high displacement values around point 3 (cf. Fig. 4.8) and the concentration extends deeply into the landslide mass reaching the sliding surface at some points. The concentration of high displacement values within the fine geometry group is located some 50 m further upslope; it does not reach as deeply as necessary to encounter the sliding surface. Despite this difference, both internal pattern structures are similar as they level out to zero-displacements in the zones around the crown and the toe; the zones of high displacements also correspond well to the zones covered by high values of SSI in the static analysis.
As for the superficial displacements, it is also obvious from the third subplots (cf. Fig. 7.23a-d) that the slope behaviors within the two geometry groups are reasonably comparable. Curves of both geometry groups reach their maximum in the range of 300 m to 350 m measured from the crown downslope. Furthermore, curves display a rather slow build-up over about the first third of the model followed by an increase towards the maximum. The decrease is characterized by a higher absolute average gradient than the build-up in the curves of both geometry groups. Interestingly, curves of the superficial displacements resemble thus the "elephant-type" curves of the simplified geometry group in 2D (cf. Fig. 7.9, 7.10a, 7.3.3.) and the typical statically conditioned behavior of the curve did not present itself in the fine geometry group.

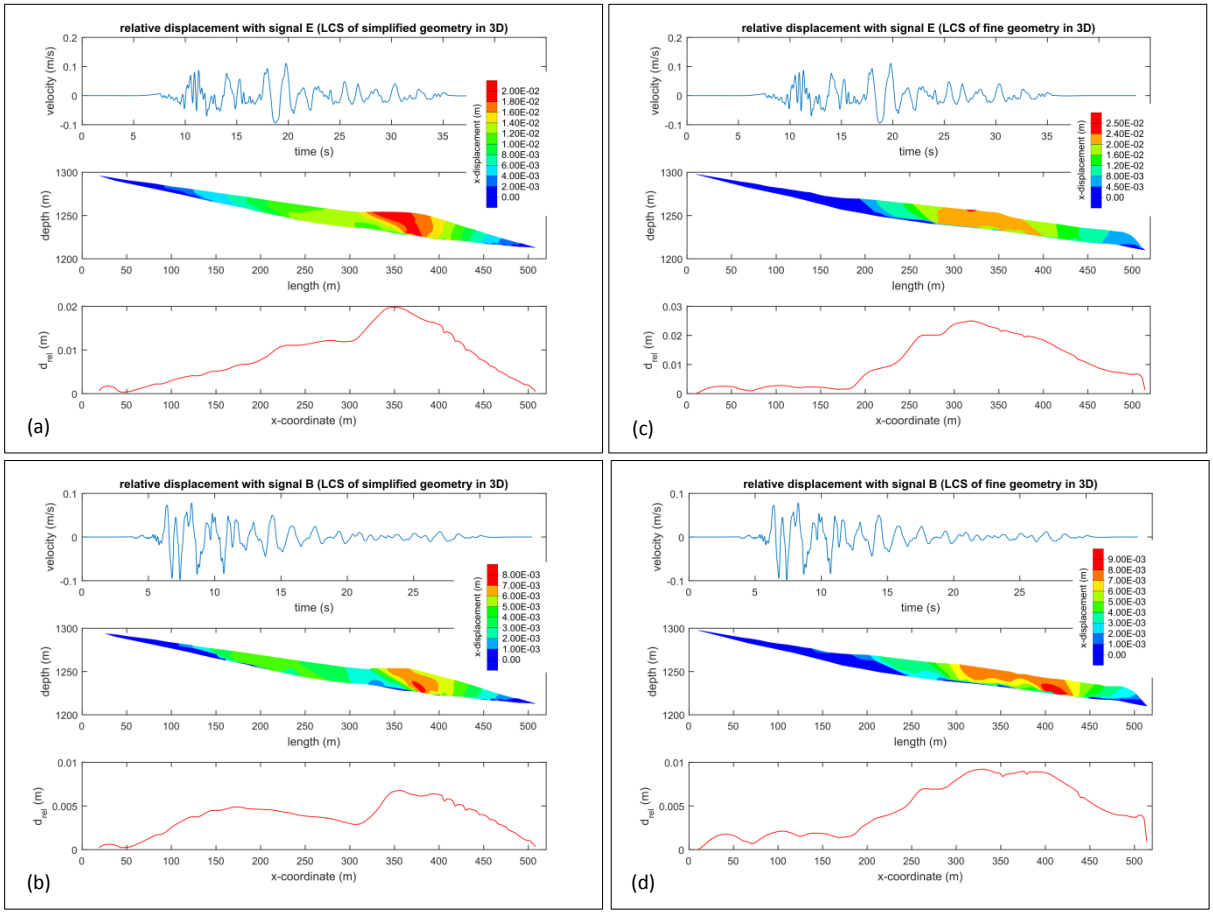

Fig. 7.23a-d. Relative horizontal displacements for signals E and B and the simplified (left) and fine (right) 3D-geometry. The two signals represent cases with high and medium entrained displacements respectively. The three subplots represent the signal, the internal displacement pattern and the displacements at the surface. It should be noted that the legends are not yet scaled in the same way since signal B is still being processed.

One differing detail between curves of both geometry groups in 3D is, that the abrupt end of the superficial displacement curves within the fine geometry group seems to reflect the steep toe zone that exists only in the fine geometry. In contrast, the superficial displacement curves within the simplified geometry group do not show such abrupt features. As stated in section 7.3.3., it is

probably the variability of thickness of the landslide – and hence the varying resonance frequencies – that influences the curves appearance. For the simplified geometry the thickness of the considered longitudinal cross section in- and decreases gradually without major steps and so do the curves of the superficial displacements; also the section between 250 m and 300 m, which is of rather constant thickness, emerges as local plateau in the curves. For the fine geometry the thickness of the longitudinal cross section is very thin at the beginning, and at around 200 m a significant increase is to be observed what comes along with the build-up of the curves; once the thickness declines in the toe zone, also the curve drops abruptly.
From Fig. 7.23a-d two other important points can be retrieved. First, within both geometry groups zero-displacements are reached at the end, so the Diezma Landslide is not supposed to experience displacements at its toe according to the model. However it should be considered, that this particular longitudinal cross section does not represent the entire toe area in either geometry; it corresponds only to the location of LCS Aa (cf. Fig. 7.19, Fig. 7.20). At another position the displacement of the toe zone might take up other values than zero. The second point is simply the fact, that slope responses are different according to the seismic scenario.
Comparisons of displacement patterns and reached values as well as their possible link to a distinct seismic scenario are generally difficult. Especially in this case, where only four models are available, attempts of testing and establishing relationships between signal characteristics and obtained displacements are not very promising. For this very reason, predicted displacements will only be presented at this stage (cf. Tab. 7.5); graphically these maximum horizontal displacements per model are marked as separate points in Fig. 7.15.

signal	$dx_{simplified}$ (cm)	dx_{fine} (cm)
E	1.99	2.50
B	0.68	0.92

Tab. 7.5. Maximum horizontal displacements for the simplified and the fine 3D-geometry.

Interestingly, the maximum displacements obtained from both the simplified as well as from the fine 3D-geometry come close to the values resulting from the simplified geometry in 2D:

- simplified 2D-geometry (signal E): 2.12 cm (cf. Tab. 7.3)
- simplified 2D-geometry (signal B): 0.86 cm (cf. Tab. 7.3)

What this finding implies for the overall study of the Diezma Landslide via finite difference modeling, will be discussed together with the results of the analysis in 2D in the following comparative section (cf. 7.3.7.).

7.3.7. Comparison of FLAC-Models

As it proved helpful already in section 6.4.5. to summarize and compare the most important findings after the application of one method, the example is followed also for the results after finite difference modeling with FLAC. Thereby, the last chapter of the thesis (cf. 8.) is prevented from being overloaded since this latter one focuses in fact on the comparison of the methods rather than on their detailed results.
Upon a first thought one might assume that a general comparison of results from the 2D- and 3D-FLAC-Models would become more complex and figuratively voluminous since with finite difference modeling the simplified as well as the fine geometry were used in both dimensions. However – and in contrast to the 2D- and 3D-CESAR-Models (cf. 6.4.) – several alleviating conditions apply within the frame of FLAC-Modeling due to reasons that were extensively discussed in the previous sections:

- no variation of v_s from 100 m/s to 1000 m/s → only 300 m/s
- no displacement components d_y, d_z and d_r → only d_x
- no surficial displacement evaluation in 3D → only virtually cut LCS
- no complete set of 11 scenarios in 3D → only signals E and B

One issue that previously crossed the way at several occasions is the necessity to attribute one value to each of the distinct scenario-responses to make them comparable without a drift-off into details. Here, this "one-value-policy" is even more questionable than for the CESAR-Models (cf. 6.4.5.) since finite difference modeling revealed not only a geometry-dependent behavior of the Diezma Landslide, but also a significant dependency on the applied signals.
With the above mentioned conditions, alleviations and necessities maximum displacement comparisons are thus restricted to the following line-ups:

- simplified geometry ↔ fine geometry in 2D (cf. Tab. 7.4)
- simplified geometry ↔ fine geometry in 3D (cf. Tab. 7.5)
- 2D v_s. 3D between simplified geometries (cf. Tab. 7.6)
- 2D v_s. 3D between fine geometries (cf. Tab. 7.6)

signal	simplified geometry		fine geometry	
	dx_{2D} (cm)	dx_{3D} (cm)	dx_{2D} (cm)	dx_{3D} (cm)
E	2.12	1.99	12.20	2.50
B	0.86	0.68	7.99	0.92

Fig. 7.6. Maximum horizontal displacements for the simplified and the fine 2D- and 3D-geometries.

With respect to the quantitative behavior, one can derive from these four comparisons that:

⇒ All model groups (simplified geometry in 2D, simplified geometry in 3D, fine geometry in 3D) predict displacements of the same order of magnitude, except of the model group of the fine geometry in 2D whose displacements are greater by one order of magnitude.
⇒ In 2D, the displacements predicted by the simplified geometry group are between 6 and 24 times smaller than those predicted by the fine geometry group.
⇒ In 3D, the displacements predicted by the simplified geometry group and the fine geometry group differ insignificantly. (Comparisons can be made only with signals E and B here.)

By cross-checking displacement evaluations and visual interpretation of results from finite difference modeling two major points became apparent:

⇒ The overall qualitative slope response to a seismic scenario is influenced by the static slope stability, which itself is dependent on the geometry of the slope.
⇒ The applied seismic scenario does not only alter the slope response but also its intensity.

The most unexpected finding from the finite difference analysis in 2D and 3D is that in terms of seismically induced displacements three of the four model groups show similar results, whereas one model group does not keep in line with these results:

- simplified geometry group (2D)
- simplified geometry group (3D) ≠ fine geometry group (2D)
- fine geometry group (3D)

From the obtained superficial displacement curves and internal displacement patterns it is very obvious that the triplet of groups with similar results reveal slope responses related to the applied signals. By contrast, the group of the fine geometry in 2D is predominantly influenced by

the respective static slope stability. One might therefore ask what the groups forming the triplet have in common compared to the outlier group.
One consideration towards an explanation of this discrepancy might be the dimensional concept in finite difference modeling itself. In 2D the lateral expansion of a model is considered infinite and thus the landslide mass is assumed to have no lateral borders (i.e. in y-direction; cf. Fig. 7.24). In 3D however, the landslide mass is laterally well confined. It could be presumed, thus, that with the simplified 2D-geometry results simply came much closer to the ones of both 3D-geometries. Indeed, this presumption seems vague at a first view. Nonetheless, a closer look on the landslide thicknesses per model group – which in turn influence the resonance and predicted displacements – might give emphasize on this consideration. From Fig. 7.24, Fig. 7.19 and Fig. 7.20 it can be seen that the respective models are thickest from around 300 m to 400 m measured from the crown downslope and the thicknesses are gradually decreasing towards the crown and the toe zones. The simplified 2D-geometry might therefore be considered as tolerably representative for virtual longitudinal cuts through the Diezma Landslide even with an angular offset from the position of LCS Aa. As for the fine 2D-geometry, this representativeness is rather questionable, since its thickness is more or less constant over the lower three fourths of the landslide length; moreover the landslide mass is characterized by an abrupt step at its toe. As one recognizes from Fig. 7.20 the fine 2D-geometry certainly fits into its counterpart in 3D, but the location of LCS Al does not seem to be representative for the entire landslide mass. The fine 2D-geometry (at the position of LCS Aa) passes next to one thickness maximum close to the intersection with TCS B and in between two thickness maxima before the intersection with TCS C. Especially by imagining an angular offset from LCS Aa, it is obvious that the fine 2D-geometry would be much thicker in the region from about 300 m to 400 m and also the toe area would be much smoother.

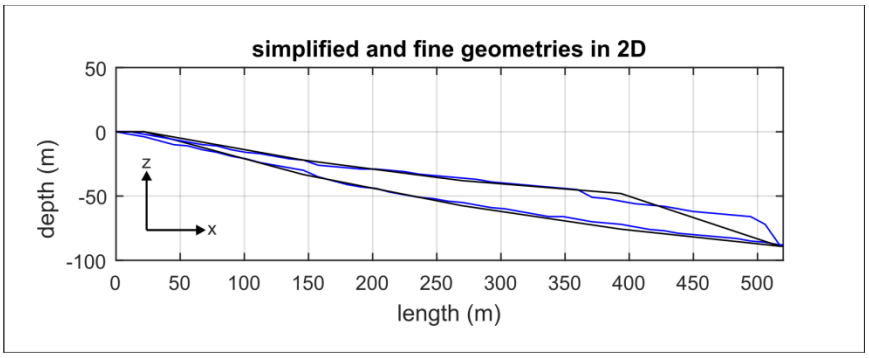

Fig. 7.24. Superposition of the simplified (black) and the fine (blue) geometry in 2D.

CHAPTER 8
DISCUSSION, CONCLUSION & PERSPECTIVES

8.1. Scope of the Thesis – Revisited

To come full circle, this chapter is dedicated to comparative discussions, conclusions and perspectives. It revisits in a first place the scope of the thesis (cf. 1.1.) to answer the question if the overall objective of research was achieved.
On the aim of contribution to better understanding of seismically induced landsliding, three different methods were applied to the Diezma Landslide resulting in many interesting analyses and interpretations. Each method is described in detail in its respective chapter (cf. 5., 6., 7.), whereas room for cross-comparisons is given in sections 8.2., 8.3. and 8.4. of this chapter.
Having followed the structure of the thesis up to this point, one might perceive it as bipartite with one part focusing on the landslide database and its statistical exploration (cf. 2., 3.), and with the other one assessing the behavior of the Diezma Landslide. Admittedly, both parts seem at a first view rather less connected to each other, all the more as the extensive analyses of the Diezma Landslide would surely have been "frame-filling" by themselves for an entire thesis. Effectively, such a case study – even though very sophisticated – could have been made with the same qualitative outcome without the construction of a landslide database beforehand. Likewise, the database with its statistical exploration can be seen as an elaborate stand-alone work whose legitimacy is defined amongst other things by its recency and independent global coverage. Nonetheless, both parts figuratively reach out towards each other what makes them at least partially complementary as the following considerations will show.
As explained in section 4.1., the Diezma Landslide was chosen from the database not only on the purpose of a case study, but also in order to develop an exemplarily procedure to assess seismically induced displacements that would be applicable to other real or theoretically created landslide sites. In this thesis the nine mean geometries (cf. Fig. 3.10a-i) belong to this latter category, and the Diezma Landslide reasonably compares to an intermediate geometry between Fig. 3.10d and 3.10e.
In return, there is also a clear outreach from the database and its statistical exploration towards the "case study part". The most stunning result after the exploration of the database is probably the fact that – statistically and by considering only the source zone of a landslide – dimensions and shapes of landslide masses do not behave in the same way; dimension-related parameters increase significantly with larger landslide masses, whereas shape-related parameters are remarkably constant (cf. Averaging Parameters – 3.3.3., Fig. 3.9a-e). This finding is of great importance for numerical modeling since the shape of a landslide mass governs the seismic interaction with the underlying bedrock – and hence site effects –, but the dimension controls the intensity of the phenomenon (LENTI & MARTINO, 2013). Especially the latter aspect becomes a major interest when thinking one step further and passing over from numerical modeling to actual hazard assessment in endangered areas.
Another detail related to the constancy of shapes of landslide masses is, that also ratios between dimension-related parameters revealed to be remarkably constant for different landslide volumes – i.e. the ratios of:

- height/length (H_{0E}/L_h)
- width/length (w_{av}/L_h)
- depth/length (d_{av}/L)
- depth/width (d_{av}/w_{av})

These relationships could be of particular use when only one of the ratio-parameters is known and the second one should be recovered. Stable ratios could also find an application for rough volume estimations in inaccessible terrain or when tracing back the source zone of a landslide from which it was initiated. As a matter of fact, this field of application deserves a closer look not to say further developments; for this reason it could actually be listed rather in the section of perspectives (cf. 8.5.). However, it fitted well to the topic of shape consistency and was therefore mentioned at this occasion.

8.2. Comparative Discussion of Methods

The three applied methods to assess seismically induced displacements of the Diezma Landslide under particular seismic scenarios were described extensively in the respective chapters; each chapter emplaced the method with respect to its technical and historical background. At many stages throughout the thesis questions towards the general comparability of these methods arose; so – without drifting off in too much details – this section recapitulates in a few words each of the three methods in order to provide a straightforward comparison and to allow for easy distinction of their principal characteristics (cf. Fig. 8.1, Tab. 8.1, Tab. 8.2).

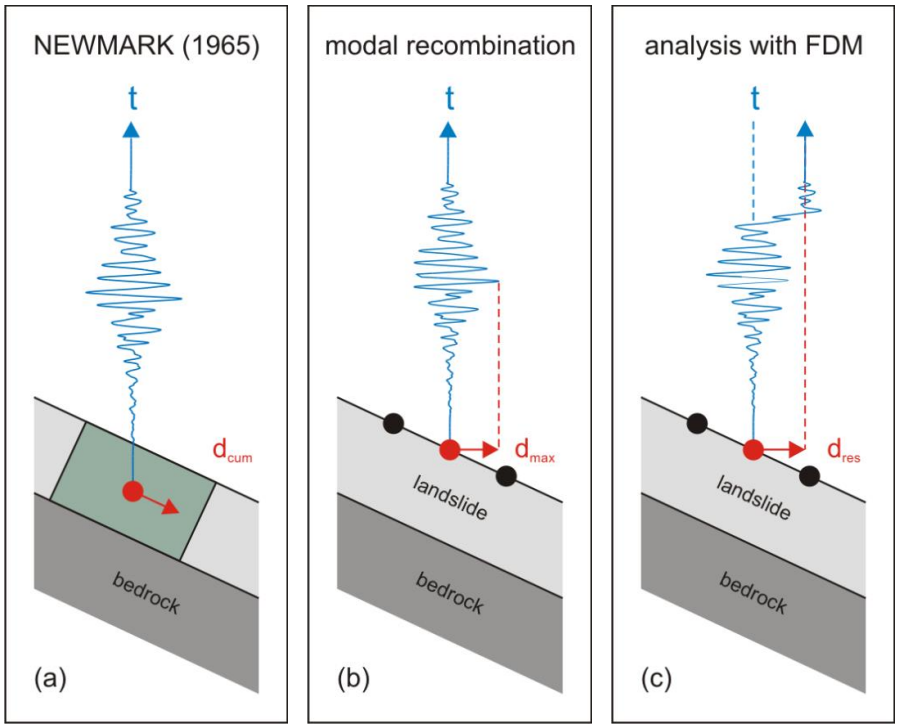

Fig. 8.1a-c. Types of displacements and their orientations obtained by the three methods: Cumulative (NEWMARK, 1965), maximal (modal recombination analysis) and residual displacements (FDM). The blue oscillation represents the horizontal displacement time-history of the ground response of the considered point over time (i.e. it does not represent the incoming signal). It should be noted that there is no red dashed line in the first figure because the cumulative displacement does not directly relate to the displacement time-history of the ground response (cf. Fig. 5.6).

Although assisted by the software SLAMMER, the NEWMARK-Method (1965; cf. 5.) is the only analog method and based on the concept of limit equilibrium (cf. 5.2.). Two peculiarities are that a landslide is approximated by a single compound material block, and that the dynamic aspect of an earthquake is represented by an additional force imposed on the mass center of the block what appoints the method as pseudostatic. It is assumed that displacements can only occur once the block experiences a certain critical acceleration.
From section 5.3.2. it can easily be seen that the NEWMARK-Method (1965) assumes the involved material to behave in an elasto-plastic manner as the actual equation of the factor of safety incorporates the Mohr-Coulomb Failure Criterion (cf. Tab. 8.2). Since the method is not numeric it cannot be classified as computation in the time- or the frequency-domain; however, a predicted displacement refers to the point of time when the block is supposed to have come to rest after the earthquake has passed (cf. Fig. 5.6).
In terms of necessary input and obtained output, the method differs significantly from its numeric counterparts. It is the only employed method exclusively designed for analysis in 2D. Furthermore, input parameters target the classical geotechnical soil properties (weight of the mass (W), length of the failure surface (l), effective cohesion (c'), effective internal friction angle (Φ'), slope angle (β')) but material properties with respect to deformation and wave propagation

are not represented. The NEWMARK-Method (1965) is the only one reading acceleration time-histories and returning one single value of displacement. This latter displacement is cumulative (i.e. the final value after the block has come to rest again; cf. Fig. 8.1a), its direction is parallel to the sliding surface and it is assumed to be representative for the entire block (i.e. in the broader sense to the landslide).

method	geometry	input	signal	output
NEWMARK (1965)	2D (simplified in slices)	W, l, c, Φ, β	acceleration time-histories	d_{cum} (1 value for 1 point)
modal recombination analysis	2D & 3D (simplified)	v_s, γ, υ and as function thereof ρ, G, E	displacement time-histories	d_{max} (1 value per point)
finite difference analysis	2D & 3D (simplified & fine)	v_s, ρ, υ, c', Φ' and as function thereof G, K	velocity time-histories	d_{res} (1 value per point)

Tab. 8.1. Comparison of methods with respect to their input and output information.

The method of modal recombination (cf. 6.) was applied to the Diezma Landslide by means of the software CESAR. Being a numeric finite element code, the software belongs to the group of continuum modeling codes. As the name suggests, the method of modal recombination is based on the assessment and subsequent superposition of eigenfrequencies and eigenmodes of the structure of interest (i.e. the landslide mass) during a vibratory motion (cf. 6.3.1.).
The method of modal recombination is the only one operating in the frequency domain and assumes a visco-elastic behavior for the involved material (cf. Tab. 8.2).
The software CESAR is designed for 2D- and 3D-analysis, and in comparison to the NEWMARK-Method (1965) it requires material properties with respect to deformation and wave propagation (shear wave velocity (v_s), Poisson's Ratio (υ), specific weight (γ), density (ρ), shear modulus (G), Young's Modulus (E)). Seismic scenarios are read as displacement time-histories and predicted slope displacements are returned in the form of maximum displacement in x-direction (cf. Fig. 8.1b). In contrast to the analog NEWMARK-Method (1965), numeric models dispose of a mesh and displacement time-histories of the ground response are available in every node; a maximum entrained displacement can therefore be computed in every point on the surface (and elsewhere in the model).
The finite difference software FLAC also belongs to the group of continuum modeling codes. Computations in FLAC mainly differ from modal recombination analysis by the fact that they operate in the time domain. It should be noted that comparison is made here intentionally to modal recombination analysis – and not to CESAR – as the software offers a multitude of methods with different ways of operation.
In other aspects, characteristics of finite difference analysis with FLAC is similar to modal recombination analysis; it is likewise designed for 2D and 3D and requires material properties with respect to deformation and wave propagation (shear wave velocity (v_s), density (ρ), Poisson's Ratio (υ), shear modulus (G), bulk modulus (K)). Also two of the classical geotechnical soil properties (effective cohesion (c'), effective internal friction angle (Φ')) are taken into account. However, the assumed material behavior is assumed to be visco-elasto-perfectly-plastic (cf. Tab. 8.2).
FLAC reads the seismic scenarios in the form of velocity time-histories when absorbing boundaries are applied in order to simulate an infinite extension of the model. Again, displacement time-histories of the ground response are available in every point and evaluated in x-direction. Compared to the modal recombination analysis, displacements are though residual (cf. Fig. 8.1c; 7.3.3.).

method	simplified geometry	fine geometry	material behavior	operating domain
NEWMARK (1965)	2D: 11		elasto-perfectly-plastic	(time-related)
modal recombination analysis	2D: 209 3D: 11		visco-elastic	frequency domain
finite difference analysis	2D: 11 3D: 2	2D: 11 3D: 2	visco-elasto-perfectly-plastic	time domain

Tab. 8.2. Number of individual models per method, material behavior and operating domain.
The number of finite difference models in 3D could increase to 3,
if the first point mentioned under the perspectives (cf. 8.5) is realized.

From this recapitulation the two numerical methods seem more comparable to each other; both of them account for material properties with respect to deformation and wave propagation (several moduli, shear wave velocity, specific weight and/or density) and both compute displacement time-histories of the ground response in every point of the 2D- and 3D-mesh. But before hasty jumping to conclusions on the comparability and adequacy of the three methods, it is worth to have a closer look also on the obtained displacements. In the next section (cf. 8.3.) it will be discussed that the modal recombination analysis with CESAR is – eventually – not as comparable to the finite difference analysis with FLAC.
A final balance on the advantages, disadvantages and suitability of the three methods will therefore be drawn in the last comparative section (cf. 8.4.).

8.3. Comparative Discussion of Obtained Displacements

For the comparison of obtained displacements by the three types of analysis there are two targets: a line-up of qualitative as well as of quantitative behavior of the landslide mass under seismic shaking, which will also be discussed in this order.
Because of the different options of model-setup concerning geometry, dimension and time-restrictions within the framework of each of the three types of analysis, a distinct number of "sub-model-groups" are available. These latter are (cf. Tab. 8.1, Fig. 8.2, Fig. 7.22):

- for the NEWMARK-Method (1965): group of simplified 2D-geometry
- for the modal recombination analysis: group of simplified 2D-geometry
  group of simplified 3D-geometry
- for the finite difference analysis: group of simplified 2D-geometry
  group of simplified 3D-geometry
  group of fine 2D-geometry
  group of fine 3D-geometry

Particular differences in qualitative behavior of models are mainly to be observed within the two numerical methods. The following key points sum up the respective comparative sections of the chapters on modal recombination analysis and finite difference analysis (cf. 6.4.5., 7.3.7.). It should be kept in mind, that the here presented characteristics serve as broad conclusive results; for further details one should refer to chapters 6. and 7. and the final comparisons in there.

⇒ Within the modal recombination analysis, the general qualitative slope behavior can be analyzed with respect to its displacement components (d_x, d_y, d_z) and its resultant displacement (d_r); it appears that displacement patterns are the same for all signals.
⇒ Patterns (per displacement component or resultant displacement) always feature one zone of major displacement however with different orientations and intensities.
⇒ The pattern within the group of the simplified 2D-geometry is roughly concentrated around point 3 (cf. Fig. 4.8).

⇒ The pattern within the group of the simplified 3D-geometry is roughly concentrated around the landslide nose (cf. Fig. 4.10i).
⇒ The signal-dependency manifests itself only in the intensity of the qualitative displacement patterns.

⇒ Within the finite difference analysis, the general qualitative slope behavior was only analyzed with respect to its resultant displacement; it appears that displacement patterns are different for all signals.
⇒ Displacement patterns (for resultant displacements) are strongly influenced by the static slope stability, which is in turn dependent on the model-geometry; featured zones of major displacement per model-geometry are similar to a greater or lesser extent and differ in their intensities.
⇒ The patterns within the groups of the simplified 2D-geometry, the simplified 3D-geometry and the fine 3D-geometry roughly cover the last two thirds of the landslide mass.
⇒ The pattern within the group of the fine 2D-geometries covers only the toe zone of the landslide mass.
⇒ The signal-dependency manifests itself in the intensity of the qualitative displacement patterns as well as in distinct slope responses per model.

It is difficult to contrast those two numerical methods with the analogue NEWMARK-Method (1965), which returns one displacement value per model and signal and thus does not allow for displacement variations inside the considered landslide mass or at its surface. The obtained results are therefore more than uniform in terms of qualitative behavior and – naturally – the signal-dependency manifests itself in the intensity of displacements, although in the case of the NEWMARK-Method (1965) it is the acceleration time-history of a seismic scenario that is crucial for the outcome rather than any macro-seismic parameters.
In a second stage displacements obtained by the three methods can also be compared with respect to their quantitative behavior. As mentioned at many points throughout the thesis, these comparisons refer to the concept of how provocative influencing parameters are on the slope response – i.e. how pronounced the predicted displacements are per computed model. Likewise it has already been pointed out that line-ups of quantitative displacements can only follow the "one-value-policy" (cf. 6.4.5., 7.3.7.) because the NEWMARK-Method (1965; cf. 5.) provides only one displacement value per model, and so the two numerical methods figuratively have to take a compromise to be comparable to the analogue method.
The following considerations on the quantitative behavior of displacements per model and method types refer to cumulative, maximum and residual displacements as indicated in Fig. 8.1a-c; in this section all three types of displacements will be referred to as "maximum" displacements for simplicity. The first part is dedicated to the performance of the models themselves and their proportionality among each other, whereas the second part takes a closer look on macro-seismic parameters that could possibly have an influence to a smaller or greater extent on the obtained displacements per method.
In Tab. 8.3 and Fig. 8.2 all maximum displacements per method, geometry, dimension and signal are listed; from the table as well as from the figure several interesting features are to be recognized:

⇒ The ranking of displacements entrained by distinct signals is very similar for the NEWMARK-Method (1965) and for finite difference analyses, but not for the modal recombination analyses (Tab. 8.3).
⇒ Rankings within one method type are consistent among each other (cf. Tab. 8.3).
⇒ To allow for a reliable statement with respect to the finite difference analysis in 3D, more than the two signals E and B would have to be processed.

⇒ Tendencies resulting from these rankings show a very similar relationship between maximum displacements: tendency curves for the NEWMARK-Method (1965) and the finite difference analyses are almost congruent, whereas the tendency curves for the modal recombination analyses are different but congruent among themselves only (cf. Fig. 8.2).

signal	NEWMARK (1965)	modal recomb.		finite difference analysis				$dur_{TRIFUNAC}$ (s)
		2D (simplified geometry)	3D (simplified geometry)	2D (simplified geometry)	2D (fine geometry)	3D (simplified geometry)	3D (fine geometry)	
A	0.00	17.64	193.96	0.18	4.25			19.91
B	0.38	23.44	247.33	0.86	7.99	0.68	0.92	10.24
C	0.12	9.95	108.39	0.28	5.76			5.76
D	0.33	65.26	729.08	0.98	8.64			49.93
E	0.53	38.04	425.24	2.12	12.20	1.99	2.50	15.62
F	1.15	16.71	185.94	2.85	17.06			7.75
G	0.21	45.17	506.30	0.52	6.15			23.27
H	0.30	10.44	130.17	0.69	9.35			11.37
I	0.15	52.67	582.48	0.30	7.08			29.70
J	0.35	11.16	125.63	0.91	9.58			15.29
K	0.06	19.76	223.08	0.17	3.64			16.43
average	0.33	28.20	314.33	0.90	8.34	1.33	1.71	-

Tab. 8.3. Rankings (in gray-shading) for different methods, geometries and dimensions.
The last column shows the ranking of one possibly influential factor on predicted displacements (cm).

Furthermore, from Tab. 8.3 and Fig. 8.2 it becomes obvious that the (highest) predicted displacements values per method differ by about one order of magnitude. The last row of Tab. 8.3 includes the mean displacement value per method, geometry and dimension; together with the tendency curves (cf. Fig. 8.2) this information leads to the conclusions that:

⇒ A difference of roughly one order of magnitude manifests itself between the simplified and the fine 2D-geometry within the finite difference analysis as well as between the 2D- and the 3D-geometry within the modal recombination analysis.
⇒ In terms of orders of magnitude, results of the simplified 2D-geometry within the modal recombination analysis and the fine 2D-geometry within the finite difference analysis resemble each other, and so do results of the simplified 2D-geometry within the finite difference analysis and the NEWMARK-Method (1965).
⇒ Results from all methods, geometries and dimensions seem more or less conceivable with exception of the tremendous maximum displacements obtained with the simplified 3D-geometry within the modal recombination analysis.

One possible explanation for such tremendous displacement values might be – in simple words – an unfavorable combination of geometry and applied signals. From section 6.4.4. it became clear that eigenfrequencies of the object of interest – hence the landslide mass – strongly depend on

its geometry and boundary confinement. In the case of the modal recombination analysis in 3D the eigenfrequencies of the landslide mass experienced a significant shift towards lower frequencies compared to the ones obtained from the analysis in 2D (cf. Fig. 6.13). Especially for shear wave velocities around 300 m/s eigenfrequencies coincide there exactly with the frequency range, which was found by the site effect evaluation (cf. 7.3.3.) to have a particular resonant response.

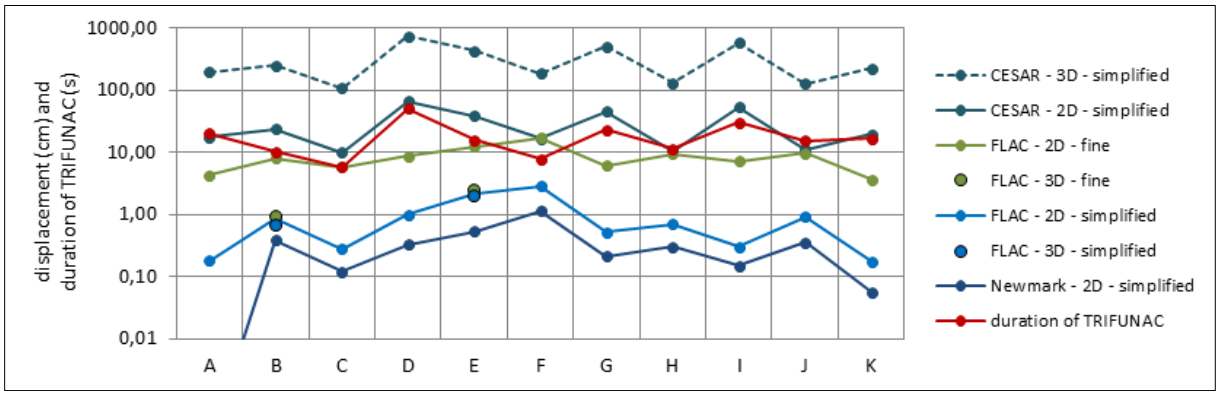

Fig. 8.2. Tendency curves for different methods, geometries and dimensions.
The red curve shows the tendency of one possibly influential factor on predicted displacements.
The value for signal A from the NEWMARK-Analysis (1965) cannot be shown on a logarithmic scale since it is true value of 0.0002 rounds to 0.00; it appears however in the plot of the mean FAS in the appendix (cf. A.11.).

The second part of comparisons of quantitative behaviors pays closer attention to the value rankings and tendency curves of macro-seismic parameters and their similarities to the before discussed rankings and tendencies of maximum displacements per method, geometry and dimension. Throughout the thesis, at many stages of presented results the question arose whether or not particular earthquake parameters can be linked to predicted displacements. One indication therefore could be a similar (or similarly inverse) ranking or tendency-curve of the considered parameter to one or several "method-curves". Throughout the thesis a total of 17 recurrent parameters are to be found that are worth to be considered as possibly influential (cf. first column of Tab. 8.4). Even though some of them – namely those that are shaded in gray in Tab. 8.4 and Tab. 8.5. – have already been tested for coherences in the respective chapters, a full summary is given here. It should be noted that, first, tables are split in order to represent rankings and tendencies separately because the former does not necessarily come along with the latter, and second, that exemplarily Tab. 8.3. and Fig. 8.2 show only the duration of TRIFUNAC & BRADY (1975) as parameter to be tested. Tendency-graphs of the other 16 parameters are to be found in the appendix (cf. A.11.) and associated rankings appear throughout the thesis. For the interpretation the following abbreviations are used:

- for Tab. 8.4:
  - ≈ / (≈) — similar / less similar
  - inv / (inv) — inversely similar / less inversely similar
  - x — no similarity
- for Tab. 8.5:
  - ✓ / (✓) — similar / less similar
  - inv — inversely similar
  - x — no similarity

From the two tables several interesting details could be detected:

⇒ Similarities of rankings and tendencies seem to appear more frequently with displacements obtained by the NEWMARK-Method (1965) and the finite difference analysis modal than by the modal recombination analysis.

⇒ Rankings of the the modal recombination analysis seem to be more or less sensitive to six parameters ($dur_{TRIFUNAC}$, dur_{signal}, AI, PGV, PGD, T_m) and inversely sensitive to five

parameters (F_m, T_s/T_m, T_l/T_m, $FAS_{max\_3\text{-}6Hz}$, $FAS_{mean\_3\text{-}6Hz}$). The tendencies let also assume a similarity to the seismic moment (M_0) and the two magnitudes (M_W, M_S).

⇒ Rankings of the NEWMARK-Analysis (1965) and thefinite difference analysis do not seem to be sensitive to any parameter. However, tendencies show similarities to three parameters (PGA, $FAS_{max\_3\text{-}6Hz}$, $FAS_{mean\_3\text{-}6Hz}$).

As mentioned in section 7.3.3., slope response is in general doubtlessly a result of a multi-factorial combination of parameters. Thus the here presented reductive approach of comparing one single parameter at the time to predicted maximum displacement per method, geometry and dimension simply serves to show which parameter might play a role for a particular method. It likewise underlines the difficulty that arises from the use of real instead of more easily controllable synthetic signals. Finally, the approach also justifies the effort that could be spent in future (cf. 8.5.) when it comes to "back-tracing" of caused displacements by sophisticated statistical tools that would allow for detailed testing and weighting of influencing parameters.

similarities of rankings		NEWMARK (1965)	modal recombination		finite difference analysis	
			2D (simplified geometry)	3D (simplified geometry)	2D (simplified geometry)	2D (fine geometry)
$dur_{TRIFUNAC}$	(s)	x	≈	≈	x	x
dur_{total_signal}	(s)	x	(≈)	(≈)	x	x
M_0	(-)	x	x	x	x	x
M_W	(-)	x	x	x	x	x
M_S	(-)	x	x	x	x	x
AI	(m/s)	x	(≈)	(≈)	x	x
PGA	(m/s^2)	x	x	x	x	x
PGV	(m/s)	x	≈	≈	x	x
PGD	(m)	x	≈	≈	x	x
T_m	(s)	x	(≈)	(≈)	x	x
F_m	(Hz)	x	(inv)	(inv)	x	x
T_s/T_m*	(-)	x	(inv)	(inv)	x	x
T_l/T_m*	(-)	x	(inv)	(inv)	x	x
FAS_{max}	(m/s)	x	x	x	x	x
FAS_{mean}	(m/s)	x	x	x	x	x
$FAS_{max\_3\text{-}6Hz}$	(m/s)	x	(inv)	(inv)	x	x
$FAS_{mean\_3\text{-}6Hz}$	(m/s)	x	(inv)	(inv)	x	x

Tab. 8.4. Similarities between rankings of macro-seismic parameters and those of different methods, geometries and dimensions (cf. Tab. 8.3). Ratios of characteristic site periods are for v_s = 300 m/s (*). Gray-shading refers to already tested similarities in the respective chapters.

In good agreement with the results of this thesis – and particularly with the detected difficulty to link macro-seismic parameters with expected displacements – is a recent study by GISCHIG et al. (2015) who assessed the seismic response of rock slope instabilities via distinct element

modeling in 2D to evaluate the role of amplification on expected deformations. By applying real seismic signals and varying relevant parameters no clear link was to be established between predicted displacements and frequency contents of the applied signals, but – in general – amplification patterns are mentioned to be of great use for seismic slope stability analysis as they help to identify zones in which displacements are expected to be large (GISCHIG et al., 2015).

similarities of tendencies		NEWMARK (1965)	modal recombination		finite difference analysis	
			2D (simplified geometry)	3D (simplified geometry)	2D (simplified geometry)	2D (fine geometry)
$dur_{TRIFUNAC}$	(s)	x	✓(A)	✓(A)	x	x
dur_{total_signal}	(s)	x	✓(A)	✓(A)	x	x
M_0	(-)	x	(✓) (A)	(✓) (A)	x	x
M_W	(-)	x	(✓) (A)	(✓) (A)	x	x
M_S	(-)	x	(✓) (A)	(✓) (A)	x	x
AI	(m/s)	x	✓ (F, K)	✓ (F, K)	x	x
PGA	(m/s^2)	✓ (C, F)	x	x	✓ (C, F)	✓ (C, F)
PGV	(m/s)	x	✓	✓	x	x
PGD	(m)	x	✓	✓	x	x
T_m	(s)	x	✓ (A)	✓ (A)	x	x
F_m	(Hz)	x	inv (A)	inv (A)	x	x
T_s/T_m*	(-)	x	inv (A)	inv (A)	x	x
T_l/T_m*	(-)	x	inv (A)	inv (A)	x	x
FAS_{max}	(m/s)	x	x	x	x	x
FAS_{mean}	(m/s)	x	x	x	x	x
$FAS_{max\_3\text{-}6Hz}$	(m/s)	✓ (C, F)	inv (A)	inv (A)	✓ (C, F)	✓ (C, F)
$FAS_{mean\_3\text{-}6Hz}$	(m/s)	✓ (C, F)	inv (A)	inv (A)	✓ (C, F)	✓ (C, F)

Tab. 8.5. Similarities between tendencies of macro-seismic parameters and those of different methods, geometries and dimensions (cf. Fig. 8.2). Ratios of characteristic site periods are for v_s = 300 m/s (*). Gray-shading refers to already tested similarities in the respective chapters. Notes in brackets refer to signals that "disturb" the tendency-curves.

8.4. Consideration on the Suitability of Methods & Conclusions

The three employed methods of assessing seismic slope stability were presented in detail in the respective sections (cf. 5.3.2., 6.3.1., 7.2.1.) followed by the processes of analyses as well as by the obtained results. The remaining question is, therefore, which of the methods is the most suitable for landslide studies. In short, the question is not to be answered – at least not by naming one of them.

All methods – if simple or sophisticated – have their advantages and disadvantages which must be weighed against each other; hence, the choice of one or several methods depends on the purpose of the study and it is made according to requirements and constraints of data availability, desired outcome, time and budget.

Usually, a widespread common conception is that a greater richness of detail, the use of numerical methods and the introduction of third dimension draw more accurate images of real site conditions. Undoubtedly this is true as numerical methods offer a mere unlimited number of options to model and analyze a particular site of interest, and the more data of all types is available, the better a model can be adjusted before running the process of calculation. However, this thesis has shown that – at least in the case of the Diezma Landslide – it is not as trivial as it seems to explain the most satisfying outcome by use of the three above mentioned criteria for greater accurateness. By comparing displacement patterns of 2D- and 3D-models, it appeared that:

- ⇒ Slope responses are similar for the simplified geometries (with FDM).
- ⇒ Slope responses are different for the fine geometries (with FDM).
- ⇒ Slope responses are similar for the simplified geometries (with modal recombination).

In terms of expected displacements, however, it was discovered that the introduction of the third dimension results in:

- ⇒ the same order of magnitude for the simplified and the fine geometries (with FDM),
- ⇒ and exorbitantly high values (with modal recombination).

It is thus obvious that numerical models allow for detailed analysis but do not necessarily become more realistic by switching from 2D to 3D or by a finer input geometry.
Opposite to these two powerful numerical methods stands the NEWMARK-Method (1965), which – although frequently criticized – is still in use nowadays for quick estimations and screening purposes. One could argue that both purposes were not intended in this thesis since an abundance of data is available for the Diezma Landslide and analyses do not demand for long calculation times. Furthermore, the landslide consists in fact of highly deformable materials what makes the approximation by a rigid block on a planar sliding surface rather questionable. Nonetheless, one of the goals of the thesis was to compare results from numerical methods to those of the NEWMARK-Method (1965) as many other authors do and the reliability of calculated displacements and probabilities of failure are often questioned. LENTI & MARTINO (2013) report over- as well as under-estimations of displacements with respect to results from finite difference modeling what – simply spoken – means that the method could predict safety where slopes are unsafe and vice versa. Also GISCHIG et al. (2015) detected underestimations. In the course of this thesis displacements obtained from the NEWMARK-Analysis (1965) are also rather small; however their values range in the same order of magnitude as those of the finite difference analysis of the simplified 2D-geometry, the simplified 3D-geometry and the fine 3D-geometry (cf. Fig. 8.2).
Returning back to the question of suitability it can be concluded that after considering purposes, outcomes, advantages, disadvantages and reliability, the most accurate and realistic way to assess seismically induced slope displacements seems to be finite difference modeling although computation time remains a considerable issue. Analysis by modal recombination has to be conducted with care as the method is rather applicable for engineering purposes involving well defined materials; especially the not (yet) fully explicable jump of displacement values by one order of magnitude when switching from 2D to 3D makes the method somewhat debatable and thus probably less suitable. The NEWMARK-Method (1965) retakes its traditional non-competitive status as easy-to-apply tool for quick estimations of seismically induced slope displacements that would be followed by more sophisticated numerical methods if considered necessary. Efforts to conduct these numerical analyses also in 3D remain after all questionable, as they demand for time-consuming model construction and longer computation times than in 2D. Moreover, as this thesis has shown, 3D-models can be misleading under certain circumstances and even for the exceptionally well-studied Diezma Landslide more geometric information on the landslide mass might probably be necessary for reproducing an image of reality that can be reliably numerically modeled.

8.5. Perspectives

Like with almost every thesis, three years is a short time to treat a complex topic and even if the initially set goal is achieved, there will always arise more questions and possibilities to drive research to a next level. In the case of this thesis there several perspectives for future work on the phenomenon of seismically induced landslides and in particular on the site of the Diezma Landslide.
Some steps of work could not be conducted due to time restrictions. Their absence surely does not contest the results obtained in the course of three years; however, they would constitute further interesting information and complete the here presented work. In specific terms, supplementary steps are:

- the application of signal C in 3D
  (The argumentation in section 7.3.6. has shown that finite difference modeling with FLAC 3D had to be limited to two signals, and the choice fell on signals E and B. In order to represent the full range from small to medium and to high expected displacements signal C should be applied as well to the simplified and the fine 3D-geometry.
  The ideal solution of applying all remaining signals other than E and B is unfortunately a rather protracted process since it would probably take up to one and a half year of computing time counting from the defense date of this thesis.)

- the evaluation of the factor of safety in 3D
  (In analogy to the computation of the factors of safety for the simplified and the fine 2D-geometries (cf. 7.3.2.) also the counterparts in 3D should be computed in order to complete the discussion about the static behavior of the slope, since it appeared – at least in 2D – that this latter one has a major influence on the dynamic behavior.
  Although still time-consuming, this is a more realistic intention as a calculation of a factor of safety is carried out on the existing respective static phase.)

- the evaluation of site effects in 3D
  (Also the evaluation of site effects for the simplified and the fine 3D-geometry would be of great interest to allow for better explanation of entrained displacements; simply by comparing Fig. 7.19 and Fig. 7.20 it is very obvious that thickness-dependent resonance-patterns must be very different for the two geometries and, hence, signal amplification is expected to differ as well.
  In terms of computation time, site effect evaluations remain in the limits of possibility and as in section 7.3.3. a simple Ricker Wavelet can be used for the dynamic phase. Since the entire model must be calculated, though, in a purely elastic mode, the time-consuming static phase would have to be repeated.
  It should be noted that a site effect evaluation in 3D can only result in a pseudo-3D-representation via intersecting transfer function maps (TFM; cf. Fig. 7.13, Fig. 7.14) because – simply spoken – the 2D-TFM already have three axes and by switching to 3D one would miss one axis.)

The three mentioned points would enrich the so far presented results in this thesis and allow for another solidly argued scientific publication. Ambitions thereupon are set for the months following the defense of this thesis.
Another interesting question might be, whether and to what extent distinct landslide and earthquake parameters influence each other while causing displacements. Throughout the thesis it regularly turned out that some parameters are more prone than others to entrain displacements. Taking into account the established hypotheses, the topic would deserve more effort of examination in order to test, if predicted displacements could be linked to parameter combinations. Maybe professional statistical testing might be an adequate way of examination.

In a more general prospect, there is no lack of further ideas for research based on this thesis. To mention only a few of them, there might be tests on:

- the directivity of incoming seismic signals
- shaking in more than one direction
- a more complex material structure
- the involvement of water-saturated or submerged materials

One point of consideration could also be the usage of simpler input-signals. As mentioned above, it is far from trivial to link landslide and earthquake parameters to the entrained displacements when using real signals and when assuming that they influence each other. Parametric studies with signals having undergone the LEMA_DES procedure (cf. 6.4.2.) or even with synthetic signals such as the Ricker Wavelet (cf. 7.3.3.) might be much easier to control in terms of properties and effects.
A very practically-orientated idea could be the application of the three presented methodical procedures to another landslide site to test their performances. If results are satisfactory, one could think one step further and develop recommendations on the appropriate employment of methods according to the required level of detail. This latter was one of the key questions that the thesis aimed to answer (cf. Fig. 4.1).
Finally, a quite ambitious topic might be the difference between the here presented linear models and non-linear ground response (cf. 1.1.). It stands however in sharp contrast to previously suggested possible attempts to reduce factors which strongly contribute to the outcome of a model, but which are at the same time difficult to control.

CHAPTER R
REFERENCES

R.1. References

References are in English and French except where indicated in parenthesis.

A

ABRAMSON L. W. et al., 2002. Slope Stability and Stabilization Methods. John Wiley & Sons, ed. ?, 736 p.

AHEAD, 2016. Catalog of the European archive of historical earthquake data. Download from http://www.emidius.eu/AHEAD on the 5th of March 2016.

ALFARO P. et al., 2012. The role of near-field interaction between seismic waves and slope on the triggering of a rockslide at Lorca (SE Spain). Natural Hazards and Earth System Sciences, vol. 12, p. 3631-3643.

AMBRASEYS N. N., BILHAM R., 2012. The Sarez-Pamir earthquake and landslide of 18 February 1911. Seismological Research Letters, vol. 83, p. 294-314.

AMBRASEYS N. N., MENU J. M., 1988. Earthquake-induced ground displacements. Earthquake Engineering and Structural Dynamics, vol. 16, p. 985-1006.

AMBRASEYS N. N. et al., 2004. Dissemination of European Strong-Motion Data. Engineering and Physical Sciences Research Council of the United Kingdom, vol. 2, CD ROM collection.

AVERSA S. et al., 2016. Landslides and Engineered Slopes. Experience, Theory and Practice. Proceedings of the 12th International Symposium on Landslides, Naples, Italy, vol. 1-3, 2224 p.

AZAÑON J. M. et al., 2010. Regional-scale high-plasticity clay-bearing formation as controlling factor on landslides in Southeast Spain. Geomorphology, vol. 120, p. 26-37.

B

BENITO M. B. et al., 2010. A new seismic hazard assessment in the region of Andalusia (Southern Spain). Bulletin of Earthquake Engineering, vol. 8, p. 739-766.

BELL J. M., 1968. General Slope Stability Analysis. Journal of the Soil Mechanics and Foundations Division, vol. 94, p. 1233-1270.

BELL J. M., 1969. Non circular sliding surfaces. Journal of Soil Mechanics and Foundation Division, vol. 3, p. 829-844.

BIAREZ J., 1960. Remarques sur la stabilité des talus ; influence de la loi de répartition des contraintes. Archiwum hydrotechniki, Polska Akademia Nauk, no. 7, p. ?. (in Polish)

BIAREZ J., 1965. Equilibre Limite des Talus et Barrages en terre. Annales de l'Institut Technique du Bâtiment et des Travaux Publics. Sols et Fondations, vol. 51, p. ?.

BISHOP A. W., 1955. The Use of the Slip Circle in the Stability Analysis of Slopes. Géotechnique, vol. 5, p. 7-17.

BISHOP A. W., MORGENSTERN N. R., 1960. Stability Coefficients for Earth Slopes. Géotechnique, vol. 10, p. 129-14.

BIRD J. F., BOMMER J. J., 2004. Earthquake losses due to ground failure. Engineering Geology, vol. 75, p. 147-179.

BLANC A. et al., 1987. Méthodes de surveillance d'un glissement de terrain de très grande ampleur : La Clapière, Alpes Maritimes, France. Bulletin of the International Association of Engineering Geology, vol. 35, p. 37-46.

BOMMER J. J., RODRÍGUEZ C., 2002. Earthquakeinduced landslides in Central America. Engineering Geology, vol. 63, p. 189-220.

BOURDEAU C., HAVENITH H. B., 2008. Site effects modelling applied to the slope affected by the Suusamyr earthquake (Kyrgyzstan,1992). Engineering Geology, vol. 97, pp. 126-145.

BOURGOIS J. et al., 1974. La formation d'argiles a blocs dans la province de Cadix, Cordilleras Betiques, Espagne. 2ème Réunion Annuelle des Sciences de la Terre, vol ?, 79 p.

BOURGOIS J. et al., 1978. La transversale de Ronda, Cordillères Bétiques, Espagne. Données géologiques pour un modèle d'évolution de l'Arc de Gibraltar. Doctoral thesis, Université de Besançon, 445 p.

BOZZANO F. et al., 2011. Earthquake triggering in highly jointed rock masses: reconstruction of the 1783 Scilla rock avalanche (Italy). Geomorphology, vol. 129, p. 294-308.

BRAY J. D., RATHJE E. M., 1998. Earthquake-induced displacements of solid-waste landfills. Journal of Geotechnical and Geoenvironmental Engineering of the American Society of Civil Engineers, vol. 124, p. 242-253.

BRAY J. D., TRAVASAROU T., 2009. Pseudostatic Coefficient for Use in Simplified Seismic Slope Stability Evaluation. Journal of Geotechnical and Geoenvironmental Engineering, vol. 135, p. 1336-1340.

C

CALIFORN. DIV. OF MINES AND GEOL., 1997. Guidelines for Evaluating and Mitigating Seismic Hazards in California. California Division of Mines and Geology, Special Report no. 117, 74 p.

CAQUOT A., 1954. Méthode exacte pour le calcul de la rupture d'un massif par glissement cylindrique. Annales des Ponts et Chaussées, vol. 3, p. 345-355.

CAQUOT A., KERISEL J., 1966. Traité de mécanique des sols. Gauthier-Villars, ed. ?, p. ?.

CASSON B. et al., 2003. Seventeen years of the "La Clapière" landslide evolution analysed from ortho-rectified aerial photographs. Engineering Geology, vol. 68, p. 123-139.

CARSON M. A., KIRKBY M. J., 1972. Hillslope form and process. Cambridge Geographical Studies No. 3, Cambridge University Press, New York, ed. ?, p. viii+475.

CHENG L. Y. et al., 2013. An Application of the Maximum Shear Strain Increment in Searching Sliding Surfaces. Applied Mechanics and Materials, vol. 423-426, p. 1618-1622.

CHUGH A. K., 1982. Slope stability analysis for earthquakes. International Journal for Numerical and Analytical Methods in Geomechanics, vol. 6, p. 307-322.

CLAGUE J. J., STEAD D., 2014. Landslides: Types, Mechanisms and Modeling. Cambridge University Press, ed. ?, 436 p.

CLAUSER C., 2014. Einführung in die Geophysik. Springer Berlin-Heidelberg, ed. 1, p. XV+409.

CLOUGH R. W., 1960. The Finite Element Method in Plane Stress Analysis. Proceedings of the 2nd Conference on Electronic Computation, Pittsburgh, USA, vol. ?, p. 345-378.

CLOUGH R. W., CHOPRA A. K., 1966. Earthquake Stress Analysis in Earth Dams. Journal of Geotechnical Engineering of the American Society of Civil Engineers, vol. 92, p. 197-212.

CLOUGH R. W., WOODWARD R. J., 1967. Analysis of Embankment Stresses and Deformations. Journal of the Soil Mechanics and Foundations Division, vol. 93, p. 529-549.

COBELDICK S., 2012. Customizable Natural-Order Sort. MATLAB-function download from https://fr.mathworks.com/matlabcentral/fileexchange/34464-customizable-natural-order-sort?focused=d73df16e-784f-4479-b22f-e1d9885d2bdd&tab=function on the 16th of July 2018.

COBELDICK S. 2012. Natural-Order Filename Sort. MATLAB-function download from https://fr.mathworks.com/matlabcentral/fileexchange/47434-natural-order-filename-sort?focused=4dde5af4-2114-f9f5-8d72-50000b7f68a0&tab=function on the 16th of July 2018.

COLTORTI M. et al., 1984. The December 1982 Ancona landslide: a case of deep-seated gravitational slope deformation evolving at unsteady rate. Zeitschrift für Geomorphologie, vol. 29, p. 335-345.

CORNFORTH D., 2005. Landslides in Practice: Investigation, Analysis, and Remedial/Preventative Options in Soils. John Wiley & Sons, ed. ?, 624 p.

COURANT R., 1943. Variational methods for the solution of problems of equilibrium and vibrations. Bulletin of the American Mathematical Society, vol. 49, p. 1-23.

CRUDEN D. M., VARNES D. J.,1996. Landslide types and processes. In: Turner A. K., Schuster R. L. (Eds.). Landslides: Investigation and Mitigation. National Research Council, Washington D. C., Transportation Research Board, Special Report no. 247, p. 36-75.

CULMANN K., 1866. Die graphische Statik. Meyer & Zeller, ed. ?, p. ?.

CUNDALL P. A., 1971. A Computer Model for Simulating Progressive Large Scale Movements in Blocky Rock Systems. Proceedings of the Symposium of the International Society for Rock Mechanics, Nancy, France, vol. II-8, p. ?.

D

DANNEELS G. et al., 2008. Geophysical investigation and dynamic modelling of unstable slopes: case-study of Kainama (Kyrgyzstan). Geophysical Journal International, vol. 175, p. 17-34.

DE COULOMB C. A., 1776. Essai sur une application des règles de maximis & minimis à quelques problèmes de statique, relatifs à l'architecture. Imprimerie Royale de Paris, ed. ?, p. ?.

DE SAINT-EXUPÉRY, A., 1943. The Little Prince. Reynal & Hitchcock, ed. 1, p. ?.

DELGADO J. et al., 2011. On far field occurrence of seismically induced landslides. Engineering Geology, vol. 123, p. 204-213.

DELGADO J. et al., 2011. Seismically-induced landslides in the Betic Cordillera (S Spain). Soil Dynamics and Earthquake Engineering, vol. 31, p. 1203-1211.

DELGADO J. et al., 2015. Unconventional pseudostatic stability analysis of the Diezma landslide (Granada, Spain) based on a high-resolution engineering-geological model. Engineering Geology, vol. 184, p. 81-95.

DELLA SETA M. et al., 2013. The Vasto Landslide (Adriatic coast, central Italy): geomorphological constraints and numerical modelling to reconstruct the evolution of a large instability affecting a coastal slope. Geomorphology, vol. 201, p. 462-478.

DESPREZ C., LENTI L., 2013. Barrage de Salanfe – Analyse sismique – Modélisation numérique du comportement dynamique sous sollicitation sismique : Analyse avant et après sciage. Nomenclature d'activité 33R11P32 – rapport interne de l'IFSTTAR.

DEWITTE O., DEMOULIN A., 2005. Morphometry and kinematics of landslides inferred from precise DTMs in West Belgium. Natural Hazards and Earth System Sciences, vol. 5, p. 259–265.

DIN, 2009. DIN 4084 Baugrund – Geländebruchberechnungen. Normenausschuss Bauwesen des Deutschen Instituts für Normungen, ed. ?, p. ?. (in German)

DOBRY R., VUCETIC M., 1987. Dynamic properties and seismic response of soft clay deposits. Proceedings of the International Symposium on Geotechnical Engineering of Soft Soils, Mexico City, Mexico, vol. 2, p. 51-87.

DOMEJ G., 2012. Geophysical investigations on a system of active landslides in the village of Tusion (Pamir, Tajikistan). Master thesis, University of Natural Resources and Life Sciences Vienna, 128 p.

DOMEJ G. et al., 2017. A global database of seismically and non-seismically triggered landslides for 2D/3D numerical modeling. Geophysical Research Abstracts, vol. 19, EGU2017-5286.

DOMEJ G. et al., 2017. Mean landslide geometries inferred from a global database of earthquake- and non-earthquake-triggered landslides. Italian Journal of Engineering Geology and the Environment, vol. 17/2, p. 87-107.

DOMEJ G. et al., 2018. Statistical analyses of landslide geometries inferred from a global database of seismically and non-seismically triggered landslides. Geophysical Research Abstracts, vol. 20, EGU2018-6219.

DUNCAN J. M., 1992. State of the Art: Static Stability and Deformation Analysis. American Society of Civil Engineers Geotechnical, Special Publication no. 1, p. 222-266.

DUNNING S. A. et al., 2007. The Hattian Bala rock avalanche and associated landslides triggered by the Kashmir Earthquake of 8 October 2005. Engineering Geology, vol. 93, p. 130-144.

E

EBERHARDT E., 2003. Rock Slope Stability Analysis - Utilization of Advanced Numerical Techniques. University of British Columbia Vancouver, Department of Earth and Ocean Sciences, ed. ?., 41 p.

EULER L., 1752. Découverte d'un nouveau principe de Mecanique. Mémoires de l'Académie des Sciences de Berlin, vol. 6, p. 185-217.

EVANS S. G. et al., 2009. Landslides triggered by the 1949 Khait earthquake, Tajikistan, and associated loss of life. Engineering Geology, vol. 109, p. 195-212.

EVANS S. G., BENT A. L., 2004. The Las Colinas landslide, Santa Tecla: a highly destructive flowslide triggered by the January 13, 2001, El Salvador earthquake. Geological Society of America, Special Papers no. 375, p. 25-38.

F

FAURE R. M., 1985. Analyse des contraintes dans un talus par la méthode des perturbations. Revue Française de Géotechnique, vol. 33, p. 49-59.

FAURE R. M., 2000. L'évolution des méthodes de calcul en stabilité de pentes. Partie I : Méthodes à la rupture. Revue Française de Géotechnique, vol. 92, p. 3-16.

FELLENIUS W. K. A., 1927. Erdstatische Berechnungen mit Reibung und Kohäsion (Adhäsion) und unter Annahme kreiszylindrischer Gleitflächen. Wilhelm Ernst & Sohn, Berlin, Germany, ed. ?, 40 p. (in German)

FELLENIUS W. K. A., 1936. Calculations of the stability of earth dams. Transactions of the 2nd Congress on Large Dams, Washington D. C., USA, vol. 4, p. 445-463.

FRANKLIN A. G., CHANG F. K., 1977. Earthquake resistance of earth and rock-fill dams. Permanent displacements of earth embankments by Newark sliding block analysis. United States Army Engineer Waterways Experiment Station Vicksburg, report no. 5/S-71-17, p. ?.

FREDLUND D. G., KRAHN J., 1977. Comparison of slope stability methods of analysis. Canadian Geotechnical Journal, vol. 14, p. 429-439.

FREDLUND D. G. et al., 1981. The relationship between limit equilibrium slope stability methods. Proceedings of the 10th International Conference on Soil Mechanics and Foundation Engineering, Stockholm, Sweden, vol. 3, p. 409-416.

G

GAFFET S. et al., 2010. Use of the simultaneous seismic, GPS and meteorological monitoring for the characterization of a large unstable mountain slope in the southern French Alps. Geophysical Journal International, vol. 182, p. 1395-1410.

GEOSLOPE, 2018. GeoStudio - The modeling software for geo-engineers and earth scientists. Download from https://www.geoslope.com/products/geostudio on the 22nd of April 2018.

GIARDINI D. et al., 2003. The GSHAP Global Seismic Hazard Map. In: Lee W. et al. (Eds.). International Handbook of Earthquake & Engineering Seismology. International Geophysics Series 81 B, Academic Press Amsterdam, ed. ?, p. 1233-1239.

GISCHIG V. S. et al., 2015. On the seismic response of deep-seated rock slope instabilities — Insights from numerical modeling. Engineering Geology, vol. 193, p. 1-18.

GOOGLE EARTH, 2016. Images. Retrieved from Google Earth in December 2016.

GOOGLE EARTH PRO, 2015-2017. Images. Retrieved from Google Earth Pro from 2015-2017.

GRIFFITHS D. V., PRÉVOST J. H., 1988. Two and three-dimensional dynamic finite element analyses of the Long Valley Dam. Géotechnique, vol. 38, p. 367-388.

GUTENBERG B., 1927. Grundlagen der Erdbebenkunde. Gebrüder Bornträger Berlin, ed. 12, 189 p. (in German)

GUTENBERG B., RICHTER C. F., 1956. Magnitude and energy of earthquakes. Annals of Geophysics, vol. 9, p. 1-15.

GUZZETTI F. et al., 2009. Landslide volumes and landslide mobilization rates in Umbria, central Italy. Earth and Planetary Science Letters, vol. 279, p. 222-229.

H

HALLIDAY G. S., 2016. Evidence of a post-glacial rock avalanche impact on Lake Wanaka, New Zealand. In: Aversa S. et al. (Eds.). Landslides and Engineered Slopes. Experience, Theory and Practice. Proceedings of the 12th International Symposium on Landslides, Napoli, Italy, vol. 1-3, p. 1049-1054.

HANKS T. C., KANAMORI H., 1979. A Moment Magnitude Scale. Journal of Geophysical Research, vol. 84-B5, p. 2348-2350.

HARP E. L., JIBSON R. W., 1995. Inventory of landslides triggered by the 1994 Northridge, California earthquake. United States Geological Survey, Open File Report no. 95-213, 17 p.

HARP E. L., JIBSON R. W., 1996. Landslides triggered by the 1994 Northridge, California earthquake. Bulletin of the Seismological Society of America, vol. 86, p. 319-332.

HARP E. L. et al., 1981. Landslides from the February 4, 1976, Guatemala earthquake. United States Geological Survey, Professional Paper no. 1204-A, 35 p.

HART R. D., 1993. An Introduction to Distinct Element Modeling for Rock Engineering. In: Fairhurst C. (Ed.). Analysis and Design Methods: Principles, Practice and Projects. Pergamon Press Oxford, ed. ?, p. 245-261.

HUNGR O. et al., 2014. The Varnes classification of landslide types, an update. Landslides, vol. 11, p. 167-194.

HUNTER J. H., SCHUSTER R. L., 1968. Stability of Simple Cuttings in Normally Consolidated Clays. Géotechnique, vol. 18, p. 372-378.

HUTCHINSON J. N., 1987. Mechanism producing large displacements in landslides on pre-existing shears. Memoir of the Geological Survey of China. 1st Sino-British Geological Conference, Tapei, Taiwan, vol. 9, p. 175-200.

HUTCHINSON J. N., 1994. Some aspects of the morphological and geotechnical parameters of landslides with examples drawn from Italy and elsewhere. Geologica Romana, vol. 30, p. 1-14.

HYNES-GRIFFIN M. E., FRANKLIN A. G., 1984. Rationalizing the Seismic Coefficient Method. United States Army Engineer Waterways Experiment Station Vicksburg, report no. GL-84-13, 37 p.

I

IAEG, 1990. Suggested Nomenclature for Landslides. Bulletin of the International Association of Engineering Geology, no. 41, p. 13-16.

ISMAIL-ZADEH A., TACKLEY P., 2010. Computational methods for geodynamics. Cambridge University Press, ed. 1, 332 p.

ISC, 2016. Bulletin of the International Seismological Centre. Download from http://www.isc.ac.uk/iscbulletin on the 5th of March 2016.

ITASCA, 2016. Numerical Analysis in Geomechanics using FLAC and FLAC3D. Download from http://www.itasca.com.au/training-events/training/numerical-analysis-in-geomechanics-using-flac-and-flac3d-1 on the 29th of December 2016.

ITASCA, 2018. PFC - General Purpose Distinct-Element Modeling Framework. Download from https://www.itascacg.com/software/pfc on the 22nd of April 2018.

ITASCA, 2011. Manual of FLAC 2D Version 7.0 (15 volumes). ITASCA, ed. ?, p. ?.

ITASCA, 2012. Manual of FLAC 3D Version 5.0 (13 volumes). ITASCA, ed. ?, p. ?.

ITECH, IFSTTAR, 2014. CESAR 2D Version 6.0 User's Manual. iTech, ed. ?, 180 p.

ITECH, IFSTTAR, 2014. CESAR 3D Version 6.0 User's Manual. iTech, ed. ?, 204 p.

ITECH, IFSTTAR, 2016. FEA Software for Civil, Tunnel and Geotechnical Engineering. Download from http://www.cesar-lcpc.com/ on the 29th of December 2016.

ITECH, IFSTTAR, 2018. CESAR-LCPC. Download from www.cesar-lcpc.com on the 23rd of April 2018.

J

JANBU N., 1954. Stability analysis of slopes with dimensionless parameters. Harvard Soil Mechanics Series. Cambridge University Press New York, ed. 46, 81 p.

JANBU N., 1973. Slope stability computation. In: Hirschfeld R. C., Poulos S. J. (Eds.). Embankment Dam Engineering. John Wiley and Sons New York, ed. ?, p. 47-86.

JIAN W. X. et al., 2009. Mechanism of the Anlesi landslide in the Three Gorges Reservoir, China. Engineering Geology, vol. 108, p. 86-95.

JIBSON R. W., 2007. Regression models for estimating coseismic landslide displacement. Engineering Geology, vol. 91, p. 209-218.

JIBSON R. W., 2011. Methods for assessing the stability of slopes during earthquakes - A retrospective. Engineering Geology, vol. 122, p. 43-50.

JIBSON R. W., 1993. Predicting Earthquake-Induced Landslide Displacements Using Newmark's Sliding Block Analysis. Transportation Research Record, no. 1411, p. 9-17.

JIBSON, R. W., KEEFER D. K., 1994. Analysis of the Origin of Landslides in the New Madrid Seismic Zone. United States Geological Survey, Professional Paper no. 1538-D, 23 p.

JIBSON R. W. et al., 1998. A Method for Producing Digital Probabilistic Seismic Landslide Hazard Maps: An Example from the Los Angeles, California, Area. United States Geological Survey, Open File Report no. 98-113, 17 p.

JIBSON R. W. et al., 2000. A Method for Producing Digital Probabilistic Seismic Landslide Hazard Maps. Engineering Geology, vol. 58, p. 271-289.

JIBSON R. W. et al., 2004. Landslides triggered by the 2002 M-7.9 Denali Fault, Alaska, earthquake and the inferred nature of strong shaking. Earthquake Spectra, vol. 20. p. 669-691.

JIBSON R. W. et al., 2006. Large rock avalanches triggered by the M 7.9 Denali Fault, Alaska, earthquake of 3 November 2002. Engineering Geology, vol. 83, p. 144-160.

JIBSON R. W. et al., 2013. SLAMMER—Seismic LAndslide Movement Modeled using Earthquake Records. United States Geological Survey Techniques and Methods, vol. 12/B1, version 1.1 - Nov. 2014, p. ?.

K

KAHIL S. N., 2015. Modélisation des glissements de terrain générés par les sésimes. Rapport du projet d'initiation à la recherche du Master, École Centrale de Paris, 21 p.

KANAMORI H., 1977. The Energy Release in Great Earthquakes. Journal of Geophysical Research, vol. 82, p. 2981-2987.

KEEFER D. K., 1984. Landslides caused by earthquakes. Geological Society of America Bulletin, vol. 95, p. 406-421.

KEEFER D. K., 1994. The importance of earthquake-induced landslides to long-term slope erosion and slope-failure hazards in seismically active regions. Geomorphology, vol. 10, p. 265-284.

KEEFER D. K., 2002. Investigating Landslides Caused by Earthquakes - A Historical Review. Surveys in Geophysics, vol. 23, p. 473-510.

KEEFER D. K., MANSON M. W., 1998. Regional distribution and characteristics of landslides generated by the earthquake. In: Keefer D. K. (Ed.). The Loma Prieta, California, Earthquake of October 17, 1989 - Landslides. United States Geological Survey, Professional Paper no. 1551-C, p. 4-32.

KRAMER S. L., 1996. Geotechnical Earthquake Engineering. Prentice Hall, ed. ?, 653 p.

KUROIWA J. et al., 1970. Investigations of the Peruvian earthquake of May 31, 1970. Proceedings of the 5th World Conference on Earthquake Engineering, Rome, Italy, vol. 1, p. 447-457.

L

LAMBE T. W., WHITMAN R. V., 1969. Soil Mechanics. Wiley Series in Geotechnical Engineering. John Wiley & Sons, ed. 10, 553 p.

LEE K. L., 1974. Seismic permanent deformations in earth dams. University of California, School of Engineering and Applied Science, report no. UCLA-ENG-7497, 39 p.

LENTI L., MARTINO S., 2010. New procedure for deriving multifrequential dynamic equivalent signals (LEMA_DES): a test-study based on Italian accelerometric records. Bulletin of Earthquake Engineering, vol. 8, p. 813-846.

LENTI L., MARTINO S., 2012. The interaction of seismic waves with step-like slopes and its influence on landslide movements. Engineering Geology, vol. 126, p. 19-36.

LENTI L., MARTINO S., 2013. A parametric numerical study of the interaction between seismic waves and landslides for the evaluation of the susceptibility to seismically induced displacements. Bulletin of the Seismological Society of America, vol. 103, p. 33-56.

LENTI L., SEMBLAT J. F., 2011. Analyse sismique du barrage de Salanfe (Suisse) : dimensionnement du modèle aux éléments finis et choix des paramètres. Nomenclature d'activité 33R11P32 – rapport interne de l'IFSTTAR.

LEWIS J., 1989. Image named "Nimitz Freeway Loma Prieta Quake". Download from https://commons.wikimedia.org/wiki/File:NimitzFreewayLomaPrieta Quake.jpg on the 26th of June 2018.

LI K. S., 1992. A unified solution scheme for slope stability analysis. Proceedings of the 6th International Symposium on Landslides, Christchurch, New Zealand, vol. ?, p. 481-486.

LOMNITZ C., 1970. The Peru Earthquake of May 31, 1970. Bulletin of the Seismological Society of America, vol. 60, p. 1413-1416.

LOWE J., 1967. Stability analysis of embankments. Journal of Soil Mechanics and Foundation Division, vol. 93, p. 1-33.

LOWE J., KARAFIATH L., 1960. Stability of earth dams upon drawdown. Proceedings of the 1st Pan-American Conference on Soil Mechanics and Foundation Engineering, Mexico City, Mexico, vol. 2, p. 537-552.

M

MACMURDO J., 1824. Papers relating to the earthquake which occurred in India in 1819. Philosophical Magazine, vol. 63, p. 105-177.

MAKDISI F. I., SEED H. B., 1987. Simplified Procedure for Estimating Dam and Embankment Earthquake Induced Deformations. Journal of the Geotechnical Engineering Division of the American Society of Civil Engineers, vol. 104, p. 849-867.

MALAMUD B. D. et al., 2004. Landslide inventories and their statistical properties. Earth Surface Processes and Landforms, vol. 29, p. 687-711.

MARCUSON W. F., 1981. Moderator's report for session on 'Earth dams and stability of slopes under dynamic loads'. Proceedings of the International Conference on Recent Advances in Geotechnical Earthquake Engineering and Soil Dynamics, St. Louis, USA, vol. 3, p. 1175-1175.

MARTÍNEZ-SOLARES J. M. et al., 2013. Actualización de mapas de peligrosidad sísmica de España 2012. Gobierno de España. Ministerio de Fomento, ed. ?, 267p. (in Spanish)

MARTINO S. et al., 2014. Earthquake-induced ground failures in Italy from a reviewed database. Natural Hazards and Earth System Sciences, vol. 14, p. 799-814.

MARTINO S. et al., 2016. Application of a characteristic periods-based (CPB) approach to estimate earthquake-induced displacements of landslides through dynamic numerical modelling. Geophysical Journal International, vol. 206, p. 85-102.

MELOUKA S., 2003. Au sujet de l'analyse de la stabilité des pentes en terrains meubles. Application du code de calcul "FLAC". Master thesis, Université Abou-Bekr Belkaid de Tlemcen, 122 p.

MOHR O. C., 1900. Welche Umstände bedingen die Elastizitätsgrenze und den Bruch eines Materials? Zeitschrift des Vereins Deutscher Ingenieure, vol. 24, p. 1524-1530. (in German)

MORGENSTERN N. R., PRICE V. E., 1965. The analysis of the stability of general slip surfaces. Géotechnique, vol. 15, p. 79-93.

N

NEWMARK N. M., 1965. Effects of earthquakes on dams and embankments. Géotechnique, vol. 15, p. 139-160.

NEWTON I., 1687. Philosophiae Naturalis Principia Mathematica. Royal Society, ed. 1, p. ?.. (in Latin)

O

OLIVIER P., 1984. Evolution de la limite entre Zones Internes et Zones Externes dans l'arc de Gibraltar (Maroc-Espagne). Doctoral thesis, Université de Toulouse Paul Sabatier, 229 p.

OMIV, 2016. Publications sur Séchilienne. Download from https://omiv.osug.fr/SECHILIENNE/publi.html on the 16th of April 2016.

P

PALMER H. S., 1919. New graphic methods for determining the depth and thickness of strata and the projection of dip. United States Geological Survey, Professional Paper no. 120-G, p. 123-128.

PECKER A., 2018. Dynamique des structures et des ouvrages. École des Ponts - ParisTech, ed. ?, 227 p.

PERLOFF W. H., BARON W., 1976. Soil mechanics: principles and applications. Ronald Press Co., University of Minnesota, ed. ?, 745 p.

PETLEY D. N., 2012. Global patterns of loss of life from landslides. Geology, vol. 40. p. 927-930.

PETTERSON K. E., 1955. The Early History of Circular Sliding Surfaces. Géotechnique, vol. 5, p. 275-296.

PREOBRAZHENSKY J., 1920. The Usoi Landslide. Materials on general and applied geology of the Geologic Committee, vol. 14, 21 p. (in Russian)

PRÉVOST J. H., 1981. DYNA-FLOW: A Nonlinear Transient Finite Element Analysis Program. Princeton University, School of Engineering and Applied Science, report no. ?, p. ?.

R

RATHJE E. M., ANTONAKOS G., 2010. A unified model for predicting earthquake-induced sliding displacements of rigid and flexible slopes. Engineering Geology, vol. 122, p. 51-60.

RATHJE E. M., BRAY J. D., 2000. Nonlinear coupled seismic sliding analysis of earth structures. Journal of Geotechnical and Geoenvironmental Engineering, vol. 126, p. 1002-1014.

RATHJE E. M., SAYGILI G., 2009. Probabilistic assessment of earthquake induced sliding displacements of natural slopes. Bulletin of the New Zealand Society for Earthquake Engineering, vol. 41, p. 18-27.

RATHJE E. M. et al., 1998. Simplified frequency content estimates of earthquake ground motions. Journal of Geotechnical and Geoenvironmental Engineering, vol. 124, p. 150-159.

RATHJE E. M. et al., 2004. Empirical Relationships for Frequency Content Parameters of Earthquake Ground Motions. Earthquake Spectra, vol. 20, p. 119-144.

RAULIN P. et al., 1974. Calcul de la stabilité des pentes en rupture non circulaire. Rapport de Recherches Laboratoire des Ponts et Chaussées, no. 36, 106 p.

RICHARDSON L. F., 1911. The approximate arithmetical solution by finite differences of physical problems involving differential equations, with an application to the stresses in a masonry dam. Philosophical Transactions of the Royal Society of London, vol. 210, p. 307-357.

ROCKFIELD, 2018. Elfen – Forward Modelling. Download from http://www.rockfieldglobal.com/software/geomechanical/elfen-fm/ on the 22nd of April 2018.

RODRÍGUEZ C. E. et al., 1999. Earthquake-induced landslides: 1980–1997. Soil Dynamics and Earthquake Engineering, vol. 18, p. 325-346.

RODRÍGUEZ-PECES M. J. et al., 2011. The Diezma landslide (A-92 motorway, Southern Spain): history and potential for future reactivation. Bulletin of Engineering Geology and the Environment, vol. 70, p. 681-689.

S

SARMA K. S., 1973. Stability Analysis of Embankments and Slopes. Géotechnique, vol. 23, p. 423-433.

SARMA K. S., 1975. Seismic stability of earth dams and embankments. Géotechnique, vol. 25, p. 743-761.

SARMA K. S., 1979. Stability analysis of Embankments and Slopes. Journal of the Geotechnical Engineering Division of the American Society of Civil Engineers, vol. 152, p. 1511-1524.

SASSA K., 1999. Landslides of the World. Kyoto University Press, ed. ?, 413 p.

SAYGILI G., RATHJE E. M., 2008. Empirical Predictive Models for Earthquake-Induced Sliding Displacements of Slopes. Journal of Geotechnical and Geoenvironmental Engineering, vol. 134, p. 790-803.

SCHUSTER R. L., 1996. The 25 most catastrophic landslides of the 20th century. In: Chacon J. et al. (Eds.). Landslides. Proceedings of the 8th International Conference & Field Trip on Landslides, Granada, Spain, vol. ?, 10 p.

SCHUSTER R. L., ALFORD D., 2004. Usoi landslide dam and lake Sarez, Pamir Mountains, Tajikistan. Environmental and Engineering Geosciences, vol. 10, p. 151-168.

SCHNABEL P. B., 1973. Effects on local geology and distance from source on earthquake ground motions. Doctoral thesis, University of California, p. ?.

SEED H. B., 1979. Considerations in the earthquake-resistant design of earth and rockfill dams. Géotechnique, vol. 29, p. 215-263.

SEED H. B. et al., 1973. Analysis of the slides in the San Fernando dams during the earthquake of Feb. 9. 1971. Earthquake Engineering Research Center, University of California, report no. EERC 73-2, 150 p.

SEED H. B. et al., 1990. Preliminary report on the principal geotechnical aspects of the October 17, 1989 Loma Prieta earthquake. University of California, Earthquake Engineering Research Center, report no. UCB/EERC-90/05, 137 p.

SEMBLAT J. F., PECKER A., 2009. Waves and Vibrations in Soils: Earthquakes, Traffic, Shocks Construction works. IUSS Press, ed. 1, 499 p.

SERFF N. et al., 1976. Earthquake induced deformations of earth dams. Earthquake Engineering Research Center, University of California, report no. EERC 76-4, 140 p.

SOILVISION SYSTEMS LTD., 2007. Slope Stability Overview. Download from https://www.soilvision.com/downloads/docs/pdf/research/SLOPE%20STABILITY%20OVERVIEW.pdf on the 12th of December 2017.

SPENCER E., 1967. A method for analysis of the stability of embankments assuming parallel interslice forces. Géotechnique, vol. 17, p. 11-26.

STATENS JÄRNVÄGARS GEOT. KOMM., 1922. Slutbetänkande. Geotekniska Kommission, meddelanden no. 2, p. ?. (in Swedish)

STEWART J. P. et al., 2003. A Screen Analysis Procedure for Seismic Slope Stability. Earthquake Spectra, vol. 19, p. 697-712.

STONE W. C. et al., 1987. Engineering aspects of the September 19, 1985 Mexico earthquake. Building Science Series of the National Bureau of Standards, report no. 165, 207 p.

T

TAYLOR D. W., 1948. Fundamentals of Soil Mechanics. John Wiley & Sons, ed. ?, p. ?.

TAYLOR D. W., 1937. The stability of earth slopes. Journal of the Boston Society of Civil Engineering, vol. 24, p. 197-246.

TAYLOR F. E. et al., 2015. What Shape is a Landslide? Statistical Patterns in Landslide Length to Width Ratio. Geophysical Research Abstracts, vol. 17, EGU2015-10191.

TERZAGHI K., 1950. Mechanism of Landslides. Geological Society of America, Harvard University Press, ed. ?, 41 p.

TOBYÁŠ V., MITTAG R., 1991. Local magnitude, surface wave magnitude and seismic energy. Studia Geophysica et Geodaetica, vol. 35, p. 354-357.

TRANSPORTATION RESEARCH BOARD, 1996. Landslides: Investigation and Mitigation. Transportation Research Board, Special Report no. 247, 673 p.

TRIFUNAC M. D., BRADY A. G., 1975. A study on the duration of strong earthquake ground motion. Bulletin of the Seismological Society of America, vol. 65, p. 581-626.

TURNER M. J. et al., 1956. Stiffness and Deflection Analysis of Complex Structures. Journal of the Aeronautical Sciences, vol. 23, p. 805-823.

U

UNESCO, 1990. A suggested method for reporting a landslide. Bulletin of the International Association of Engineering Geology, no. 41, p. 5-12.

UNESCO, 1991. A suggested method for a landslide summary. Bulletin of the International Association of Engineering Geology, no. 43, p. 101-110.

UNESCO, 1993. A suggested method for describing the activity of a landslide. Bulletin of the International Association of Engineering Geology, no. 47, p. 53-57.

UNESCO, 1994. A suggested method for reporting landslide causes. Bulletin of the International Association of Engineering Geology, no. 50, p. 71-74.

UNESCO, 1995. A suggested method for describing the rate of movement of a landslide. Bulletin of the International Association of Engineering Geology, no. 52, p. 75-78.

US ARMY CORPS OF ENGINEERS, 1970. Stability of Earth and Rock-Fill Dams. United States Army Engineer Waterways Experiment Station Vicksburg, no. EM 1110-2-1902, p. ?.

USGS (several authors), 1964-1970. Series on the Alaska 1964 Earthquake. United States Geological Survey, Professional Papers, no. 541-546 (with subdivisions), 1290 p.

USGS, 2004. Landslide Types and processes. USGS Fact Sheet, no. 2004-3072, 4 p.

USGS, 2016. Catastrophic Landslides of the 20th Century - Worldwide. Download from http://landslides.usgs.gov/learn/majorls.php on the 10th of April 2016.

V

VARNES D. J., 1958. Landslide types and processes. In: Eckel E. B. (Ed.). Landslides and engineering practice. National Research Council, Washington D. C., Highway Research Board, Special Report, vol. 29, p. 20-47. (Attention: Sometimes cited in literature as vol. 28 of the year 1954!)

VARNES D. J., 1978. Slope movement types and processes. In: Schuster R. L., Krizek R. J. (Eds.). Landslides—Analysis and control. National Research Council, Washington D. C., Transportation Research Board, Special Report no. 176, p. 11-33.

W

WEIBULL W., 1951. A Statistical Distribution Function of Wide Applicability. Journal of Applied Mechanics, vol. 18, p. 293-297.

WIKIPEDIA, 2016a. Löss. Download from https://de.wikipedia.org/wiki/L%C3%B6ss on the 16th of December 2016. (in German)

WIKIPEDIA, 2016b. ISO 3166-1 alpha-2. Download from https://en.wikipedia.org/wiki/ISO_3166-1_alpha-2 on the 22nd of October 2016.

WIKIPEDIA, 2016c. Restrictions on geographic data in China. Download from https://en.wikipedia.org/wiki/Restrictions_on_geographic_data_in_China#GCJ-02 on the 22nd of November 2016.

WIKIPEDIA, 2016d. Magnitude (Erdbeben). Download from https://de.wikipedia.org/wiki/Magnitude_(Erdbeben) on the 25th of November 2016. (in German)

WIKIPEDIA, 2016e. Microsoft Access. Download from https://de.wikipedia.org/wiki/Microsoft_Access on the 30th of December 2016. (in German)

WIKIPEDIA, 2016f. 1679 Armenia earthquake. Download from https://en.wikipedia.org/wiki/1679_Armenia_earthquake on the 30th of December 2016.

WIKIPEDIA, 2016g. 1786 Kangding-Luding earthquake. Download from https://en.wikipedia.org/wiki/1786_Kangding-Luding_earthquake on the 30th of December 2016.

WIKIPEDIA, 2016h. 1811–12 New Madrid earthquakes. Download from https://en.wikipedia.org/wiki/1811–12_New_Madrid_earthquakes on the 30th of December 2016.

WIKIPEDIA, 2017a. Slope stability analysis. Download from https://en.wikipedia.org/wiki/Slope_stability_analysis on the 1st of December 2017.

WILKINS M. L., 1964. Fundamental Methods in Hydrodynamics. In: Alder B. et al. (Eds.). Methods in Computational Physics. Academic Press, New York, ed. ?, 386 p.

WILSON R. C., KEEFER D. K., 1983. Dynamic analysis of a slope failure from the 6 August 1979 Coyote Lake, California, earthquake. Bulletin of the Seismological Society of America, vol. 73, p. 863-877.

WILSON R. C., KEEFER D. K., 1985. Predicting areal limits of earthquake-induced landsliding. In: Ziony J. I. (Ed.). Evaluating Earthquake Hazards in the Los Angeles Region. United States Geological Survey, Professional Paper no. 1360, p. 317-345.

X

XU C. et al., 2014. Landslides triggered by the 12 January 2010 Port-au-Prince, Haiti, Mw = 7.0 earthquake: visual interpretation, inventory compiling, and spatial distribution statistical analysis. Natural Hazards and Earth System Sciences, vol. 14, p. 1789-1818.

XU C. et al., 2016. Optimized volume models of earthquake-triggered landslides. Scientific Reports, vol. 6, p. 1-9.

Y

YIN Y. P. et al., 2009. Landslide hazards triggered by the 2008 Wenchuan earthquake, Sichuan, China. Landslides, vol. 6, p. 139-151.

YEGIAN M. K. et al., 1988. Integrated seismic risk analysis for earth dams. University of Boston, Department of Civil Engineering, ed. 88-15, 147 p.

YEGIAN M. K. et al., 1991. Earthquake-induced permanent deformations: probabilistic approach. Journal of Geotechnical Engineering of the American Society of Civil Engineers, vol. 117, p. 35-50

Z

ZACEK M., 1996. Construire Parasismique - Risque sismique, conception parasismique des bâtiments. Parenthèses, Marseille France, ed. ?, 341 p.

ZHANG Z. Z., WANG L. M., 1995. Geological Disasters in loess areas during the 1920 Haiyuan earthquake, China. GeoJournal, vol. 36, p. 269-274.

R.2. Used Programs and Online Resources

CESAR-LCPC 2D	6.0.8 & 6.2.4 (solver 6.0.x rev. J07)
CESAR-LCPC 3D	6.0.8 & 6.2.4 (solver 6.0.x rev. J07)
CorelDRAW	X4, X7 & X8
ESMD	v.2 (cf. AMBRASEYS et al., 2004)
FLAC 2D	7.00.424
FLAC 3D	5.00.121
GDM	v.7
Google Earth	7.1.7
Google Earth Pro	7.3.0
MATLAB	R2014a, R2015a & R2016b
Microsoft Office	2007 & 2010
SLAMMER	v.1.1 (cf. JIBSON et al., 2013)

AGU Publications	https://publications.agu.org/
AHEAD	http://www.emidius.eu/ahead/
Bing Maps	https://www.bing.com/maps/
EGU Publications	http://www.egu.eu/publications/
Google	https://www.google.com/
Google Maps	https://maps.google.com/
Google Scholar	https://scholar.google.com/
ISC Bulletin	http://www.isc.ac.uk/iscbulletin/
Oxford Journals	https://www.oxfordjournals.org/
Researchgate	https://www.researchgate.net/
Science Direct	http://www.sciencedirect.com/
Springer Link	http://link.springer.com/
USGS	https://www.usgs.gov/products/publications/
WikipediA	https://www.wikipedia.org/
Wiley Online Library	http://onlinelibrary.wiley.com/

CHAPTER A
APPENDIX

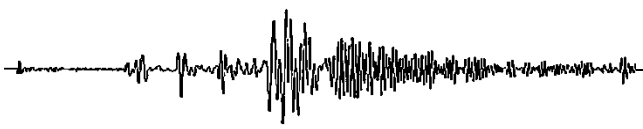

A.1. Survey Chart for the Diezma Landslide

LANDSLIDE ID						
Name	Diezma		MM Type	LS	001.00	
Earthquake	no EQ		MM ⇆ EQ	no EQ		
Date (precise or other indication)	since 1990		2001/3/18			
Fatalities						
Damage	A-92					
Location (km, direct., city, country)	25,0	NE	Grenada	ES		

Location (Google Earth)			Dynamics		
	latitude	037°18'34.00"N		active - constant / slow	x
	longitude	003°22'08.70"W		active - sudden / fast	x
	m.a.s.l.	1.250		no activity	

Material Classification			Sliding Direction	
	soil	x		
	rock		wind direction	degrees
	debris	x	SSW	202,5

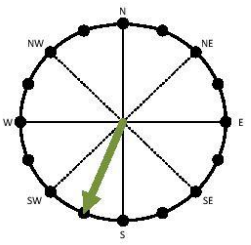

φ
11
Geometrical Correction
no

LANDSLIDE IMAGERY			
(this section refers to all related papers*)			
Map	LCS	3D	Photo
yes	yes	yes	yes

LANDSLIDE CAUSE					
Earthquake			Other		Unknown
Magnitude	Time Lag	General Seismic Area	water	wrong drainage, GW and PWP, rain	
			wind		
	no EQ	currently seismic	else	wrong safety measures	
			suspicion	motorway, f < 1 Hz	

NOTES				
assumption for map	4	LCS	knickpoints	n
assumption for LCS	6 (A-A')		XZ-scales	same scale
location problem	n		rupture zone	clear
slope modification	slope reshaped		pre-LS surface	surface
MM became / includes	LS		self-placed	n
other notes				

RELATED PAPERS* (MM, EQ, Region, etc.)	
(this section contains names as they appear in the paper collection: Name A. B., Name A. B. or et al., year)	availability
Delgado J., et al., 2015	digital
Rodríguez-Peces M. J., et al., 2011	digital
Martino S., et al., 2016	digital
Rodríguez-Peces M. J., et al., 2013	no paper

Page 1

LANDSLIDE GEOMETRY

Principal Geometry		Volume		Ratios	
(3 options: rot, trans, rototrans)	trans	according to literature	1.200.000	D/L	0,05
		according to equation (only if rotation.) V = (1/6).π.L.D.W	1.191.338	w_{av}/L_h	0,22
				H_{max}/L_h	0,18

Longitudinal Cross Section (LCS)							
Length	L	503	slope angle α	according to literature			9
	$l_1 = ... = l_4$	126		according to equation		α = atan(H_{0E}/L_h)	10
Depth	D	26	depth parts	above line	below line	angles along rupture surface	
	d_0	0	$d_{0\text{-ab}}$ & $d_{0\text{-bel}}$	0	0	δ_0	12
	d_1	11	$d_{1\text{-ab}}$ & $d_{1\text{-bel}}$	0	11	δ_1	20
	d_2	20	$d_{2\text{-ab}}$ & $d_{2\text{-bel}}$	7	13	δ_2	9
	d_3	28	$d_{3\text{-ab}}$ & $d_{3\text{-bel}}$	19	9	δ_3	7
	d_E	0	$d_{E\text{-ab}}$ & $d_{E\text{-bel}}$	0	0	δ_E	0
	d_{av}	12					
Height	H_{0E}	89					
	H_{max}	89					

cos(α) = L_h/L	Area	A	60.000
		A_h	59.053

Map		
Length	L_h	495
	$l_{h1} = ... = l_{h4}$	124
Width	W	174
	w_0	42
	w_1	95
	w_2	137
	w_3	150
	w_E	116
	w_{av}	108

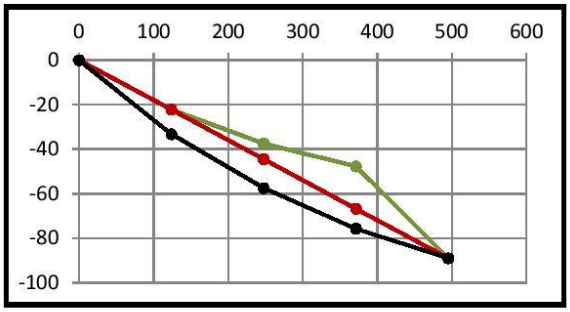

Transversal Cross Section I (TCS I)			Transversal Cross Section II (TCS II)			Tr. Cross Section III (TCS III)	
Width	w_1	95	Width	w_2	137	w_3	150
Depth	d_1	11	Depth	d_2	20	d_3	28
	d_{1t}			d_{2t}		d_{3t}	
Flank Angles	γ_{1L}		Flank Angles	γ_{2L}		γ_{3L}	
	γ_{1R}			γ_{2R}		γ_{3R}	
Rough Width Shape	V	(	Rough Width Shape	V	(	V	(
	[	U		[	U	[	U
		x			x		x

#LS	name of LS	#EQ	name of EQ	relation MM ⇆ EQ	MW	source	MS	source	mB	source	lat EQ	lon EQ	depth EQ	lat LS	lon LS	dist (m)	dist (km)
002.00	Khait	EQ.104.00	Khait	sure	7,6	P&S	7,3	ISC	7,4	ABE1	39,174	70,892	20,000	39,191	70,928	3686,1	3,7
005.01	Chengxi	EQ.164.00	Sichuan	sure	7,9	NEIC	8,1	NEIC	6,9	NEIC	31,064	103,372	7,600	31,826	104,449	132787,7	132,8
005.02	Xinbei Middle-School	EQ.164.00	Sichuan	sure	7,9	NEIC	8,1	NEIC	6,9	NEIC	31,064	103,372	7,600	31,830	104,460	133841,6	133,8
005.03	Tangjiashan	EQ.164.00	Sichuan	sure	7,9	NEIC	8,1	NEIC	6,9	NEIC	31,064	103,372	7,600	31,840	104,433	132639,6	132,6
005.04	Daguangbao	EQ.164.00	Sichuan	sure	7,9	NEIC	8,1	NEIC	6,9	NEIC	31,064	103,372	7,600	31,642	104,114	95386,3	95,4
009.01	Stewart	EQ.140.01	New Madrid Seq. 1	sure	7,5	?	7,5	?	7,5	?	35,800	-90,400	x	36,142	-89,529	87291,5	87,3
009.02	Campbell	EQ.140.01	New Madrid Seq. 1	sure	7,5	?	7,5	?	7,5	?	35,800	-90,400	x	36,064	-89,497	86597,7	86,6
012.00	Las Colinas	EQ.074.00	El Salvador	sure	7,6	NEIC	7,8	NEIC	6,4	NEIC	12,997	-88,729	82,900	13,663	-89,286	95256,5	95,3
015.00	Calitri	EQ.094.06	Irpinia 1980	sure	6,7	NEIC	6,9	NEIC	6,0	NEIC	40,862	15,327	0,000	40,899	15,436	10053,2	10,1
016.01	Tsaoling	EQ.057.00	Chi Chi	sure	7,5	NEIC	7,7	NEIC	6,5	NEIC	23,850	120,870	13,200	23,610	120,756	29046,4	29,0
016.02	Jiufenershan	EQ.057.00	Chi Chi	sure	7,5	NEIC	7,7	NEIC	6,5	NEIC	23,850	120,870	13,200	23,958	120,843	12250,1	12,3
016.03	Hungcaiping	EQ.057.00	Chi Chi	sure	7,5	NEIC	7,7	NEIC	6,5	NEIC	23,850	120,870	13,200	23,957	120,816	13037,6	13,0
020.01	Potter Hill	EQ.031.02	Alaska 1964	sure	9,2	P&S	8,4	P&S	6,7	ISC	61,050	-147,480	23,000	61,087	-149,840	127488,3	127,5
020.02	Bluff Road	EQ.031.02	Alaska 1964	sure	9,2	P&S	8,4	P&S	6,7	ISC	61,050	-147,480	23,000	61,234	-149,825	127969,9	128,0
020.03	Turnagain Heights	EQ.031.02	Alaska 1964	sure	9,2	P&S	8,4	P&S	6,7	ISC	61,050	-147,480	23,000	61,199	-149,962	134798,2	134,8
020.04	Point Campbell	EQ.031.02	Alaska 1964	sure	9,2	P&S	8,4	P&S	6,7	ISC	61,050	-147,480	23,000	61,141	-150,014	137080,4	137,1
020.05	Point Woronzof	EQ.031.02	Alaska 1964	sure	9,2	P&S	8,4	P&S	6,7	ISC	61,050	-147,480	23,000	61,203	-150,009	137351,6	137,4
020.06	L Street	EQ.031.02	Alaska 1964	sure	9,2	P&S	8,4	P&S	6,7	ISC	61,050	-147,480	23,000	61,216	-149,909	132156,3	132,2
020.07	4th Avenue	EQ.031.02	Alaska 1964	sure	9,2	P&S	8,4	P&S	6,7	ISC	61,050	-147,480	23,000	61,220	-149,885	130941,9	130,9
020.08	Government Hill	EQ.031.02	Alaska 1964	sure	9,2	P&S	8,4	P&S	6,7	ISC	61,050	-147,480	23,000	61,228	-149,873	130432,5	130,4
020.09	Native Hospital	EQ.031.02	Alaska 1964	sure	9,2	P&S	8,4	P&S	6,7	ISC	61,050	-147,480	23,000	61,221	-149,869	130109,9	130,1
021.00	Calabasas	EQ.143.00	Northridge	sure	6,7	NEIC	6,9	ISC	6,4	NEIC	34,136	-118,583	15,900	34,127	-118,650	6292,4	6,3
022.00	Degirmendere (offshore)	EQ.096.00	Izmit	sure	7,4	NEIC	7,8	NEIC	6,3	NEIC	40,756	29,955	17,000	40,722	29,782	15062,8	15,1
024.00	Mt. Saint Helens	EQ.182.00	volcanic eruption	sure	v	v	v	v	v	v	v	v	v	v	v	v	v
033.04	Casali d'Aschi	EQ.040.00	Avezzano	sure	x	x	6,6	ISC	7,1	ABE1	42,179	13,585	15,000	41,968	13,682	24779,9	24,8
033.05	Gioia dei Marsi	EQ.040.00	Avezzano	sure	x	x	6,6	ISC	7,1	ABE1	42,179	13,585	15,000	41,953	13,708	27109,4	27,1
033.06	Mt. Alvagnano	EQ.141.01	Norcia 1703	sure	6,7	AHEAD	x	x	x	x	42,708	13,071	x	42,672	13,145	7236,4	7,2
037.00	Laalam	EQ.105.00	Kherrata	sure	5,2	HRVD	4,9	NEIC	5,0	NEIC	36,710	5,323	10,000	36,581	5,457	18671,3	18,7
040.01	Güevéjar I	EQ.118.02	Lisbon 1755	sure	8,5	AHEAD	x	x	x	x	36,500	-10,000	x	37,263	-3,580	578403,1	578,4
040.02	Güevéjar II	EQ.036.00	Arenas del Rey	sure	6,3	AHEAD	x	x	x	x	36,957	-3,971	x	37,263	-3,580	48521,7	48,5
044.00	Salcito	EQ.131.02	Molise 2002	sure	5,9	NEIC	5,6	NEIC	5,3	NEIC	41,771	14,869	10,000	41,738	14,532	28226,5	28,2
045.01	Belbek	EQ.013.00	[name]	unsure	unsure	unsure	unsure	unsure	unsure	unsure	unsure	unsure	unsure	unsure	unsure	unsure	unsure
045.02	Frontovoye	EQ.014.00	[name]	unsure	unsure	unsure	unsure	unsure	unsure	unsure	unsure	unsure	unsure	unsure	unsure	unsure	unsure
045.03	Kacha 1	EQ.015.00	[name]	unsure	unsure	unsure	unsure	unsure	unsure	unsure	unsure	unsure	unsure	unsure	unsure	unsure	unsure
045.04	Kacha 2	EQ.016.00	[name]	unsure	unsure	unsure	unsure	unsure	unsure	unsure	unsure	unsure	unsure	unsure	unsure	unsure	unsure
045.05	Alma	EQ.017.00	[name]	unsure	unsure	unsure	unsure	unsure	unsure	unsure	unsure	unsure	unsure	unsure	unsure	unsure	unsure
045.06	Vishennoye	EQ.018.00	[name]	unsure	unsure	unsure	unsure	unsure	unsure	unsure	unsure	unsure	unsure	unsure	unsure	unsure	unsure
046.01	Battice 1	EQ.180.00	Verviers	sure	5,8	AHEAD	x	x	x	x	50,623	5,873	x	50,647	5,856	2961,1	3,0
046.02	Battice 2	EQ.180.00	Verviers	sure	5,8	AHEAD	x	x	x	x	50,623	5,873	x	50,647	5,856	2961,1	3,0
046.03	Battice 3	EQ.180.00	Verviers	sure	5,8	AHEAD	x	x	x	x	50,623	5,873	x	50,647	5,856	2961,1	3,0
046.04	Battice 4	EQ.180.00	Verviers	sure	5,8	AHEAD	x	x	x	x	50,623	5,873	x	50,647	5,856	2961,1	3,0
046.05	Battice 5	EQ.180.00	Verviers	sure	5,8	AHEAD	x	x	x	x	50,623	5,873	x	50,647	5,856	2961,1	3,0
046.06	Battice 6	EQ.180.00	Verviers	sure	5,8	AHEAD	x	x	x	x	50,623	5,873	x	50,647	5,856	2961,1	3,0
046.07	Battice 7	EQ.180.00	Verviers	sure	5,8	AHEAD	x	x	x	x	50,623	5,873	x	50,647	5,856	2961,1	3,0
046.08	Battice 8	EQ.180.00	Verviers	sure	5,8	AHEAD	x	x	x	x	50,623	5,873	x	50,634	5,855	1791,7	1,8
046.09	Battice 9	EQ.180.00	Verviers	sure	5,8	AHEAD	x	x	x	x	50,623	5,873	x	50,634	5,855	1791,7	1,8
046.10	Battice 10	EQ.180.00	Verviers	sure	5,8	AHEAD	x	x	x	x	50,623	5,873	x	50,634	5,855	1791,7	1,8
046.11	Battice 11	EQ.180.00	Verviers	sure	5,8	AHEAD	x	x	x	x	50,623	5,873	x	50,627	5,826	3326,1	3,3
046.12	Battice 12	EQ.180.00	Verviers	sure	5,8	AHEAD	x	x	x	x	50,623	5,873	x	50,627	5,826	3326,1	3,3
046.13	Battice 13 (Manaihan)	EQ.180.00	Verviers	sure	5,8	AHEAD	x	x	x	x	50,623	5,873	x	50,627	5,826	3326,1	3,3

#LS	name of LS	#EQ	name of EQ	relation MM ⇆ EQ	MW	source	MS	source	mB	source	lat EQ	lon EQ	depth EQ	lat LS	lon LS	dist (m)	dist (km)
047.01	Acantilada Bay	EQ.041.00	Aysén	sure	6,2	NEIC	6,3	NEIC	6,1	NEIC	-45,229	-72,488	23,800	-45,397	-72,886	36368,6	36,4
047.02	Punta Cola	EQ.041.00	Aysén	sure	6,2	NEIC	6,3	NEIC	6,1	NEIC	-45,229	-72,488	23,800	-45,380	-72,998	43391,8	43,4
047.03	Mentirosa Island	EQ.041.00	Aysén	sure	6,2	NEIC	6,3	NEIC	6,1	NEIC	-45,229	-72,488	23,800	-45,401	-72,968	42221,7	42,2
047.04	Frío Creek	EQ.041.00	Aysén	sure	6,2	NEIC	6,3	NEIC	6,1	NEIC	-45,229	-72,488	23,800	-45,399	-72,945	40462,7	40,5
047.05	Marta River 1	EQ.041.00	Aysén	sure	6,2	NEIC	6,3	NEIC	6,1	NEIC	-45,229	-72,488	23,800	-45,339	-73,004	42317,2	42,3
047.06	Fernández Creek	EQ.041.00	Aysén	sure	6,2	NEIC	6,3	NEIC	6,1	NEIC	-45,229	-72,488	23,800	-45,390	-72,905	37286,0	37,3
047.07	Marta River 2	EQ.041.00	Aysén	sure	6,2	NEIC	6,3	NEIC	6,1	NEIC	-45,229	-72,488	23,800	-45,349	-72,981	40930,3	40,9
047.08	Pescado River	EQ.041.00	Aysén	sure	6,2	NEIC	6,3	NEIC	6,1	NEIC	-45,229	-72,488	23,800	-45,424	-73,102	52759,0	52,8
048.00	Salado	EQ.070.00	Ecuador	sure	7,0	NEIC	6,9	NEIC	6,5	NEIC	0,123	-77,805	10,000	-0,201	-77,691	37970,1	38,0
049.00	Vokhchaberd	EQ.038.01	Armenian 1679	sure	x	x	6,4	Wiki	x	x	40,200	44,700	x	40,167	44,638	6444,8	6,4
050.00	Castel Frentano	EQ.113.00	Lanciano	sure	5,6	AHEAD	x	x	x	x	42,232	14,284	x	42,199	14,360	7269,4	7,3
052.01	Galdian	EQ.127.00	Manjil-Rudbar	sure	7,3	NEIC	7,4	NEIC	6,4	NEIC	36,989	49,346	18,500	36,801	49,427	22149,7	22,1
052.02	Fatalak	EQ.127.00	Manjil-Rudbar	sure	7,3	NEIC	7,4	NEIC	6,4	NEIC	36,989	49,346	18,500	36,841	49,487	20629,5	20,6
057.00	Suusamyr	EQ.168.00	Suusamyr	sure	7,3	NEIC	7,4	NEIC	6,6	NEIC	42,123	73,596	27,400	42,208	73,609	9516,2	9,5
058.01	Kokomeren	EQ.019.00	[name]	unsure	unsure	unsure	unsure	unsure	unsure	unsure	unsure	unsure	unsure	unsure	unsure	unsure	unsure
058.02	Aksu	EQ.045.00	Belovodsk	unsure	unsure	unsure	unsure	unsure	unsure	unsure	unsure	unsure	unsure	unsure	unsure	unsure	unsure
058.03	Beshkiol	EQ.020.00	[name]	unsure	unsure	unsure	unsure	unsure	unsure	unsure	unsure	unsure	unsure	unsure	unsure	unsure	unsure
058.04	Karakudjur	EQ.021.00	[name]	unsure	unsure	unsure	unsure	unsure	unsure	unsure	unsure	unsure	unsure	unsure	unsure	unsure	unsure
058.05	Sarychelek	EQ.056.00	Chatkal	unsure	unsure	unsure	unsure	unsure	unsure	unsure	unsure	unsure	unsure	unsure	unsure	unsure	unsure
058.06	Kugart	EQ.022.00	[name]	unsure	unsure	unsure	unsure	unsure	unsure	unsure	unsure	unsure	unsure	unsure	unsure	unsure	unsure
061.00	Usoi	EQ.163.00	Sarez	sure	7,2	P&S	7,3	ISC	7,3	ABE1	38,331	72,628	15,000	38,306	72,613	3100,1	3,1
062.01	Okuli	EQ.081.00	Gissar	sure	x	x	5,5	ISC	5,3	NEIC	38,460	68,692	10,000	38,485	68,632	5975,7	6,0
062.02	May 1	EQ.081.00	Gissar	sure	x	x	5,5	ISC	5,3	NEIC	38,460	68,692	10,000	38,488	68,623	6838,1	6,8
062.03	Firma	EQ.081.00	Gissar	sure	x	x	5,5	ISC	5,3	NEIC	38,460	68,692	10,000	38,490	68,636	5985,3	6,0
062.04	Sharara	EQ.081.00	Gissar	sure	x	x	5,5	ISC	5,3	NEIC	38,460	68,692	10,000	38,488	68,651	4784,7	4,8
069.00	Hope	EQ.002.00	[name]	unsure	unsure	unsure	unsure	unsure	unsure	unsure	unsure	unsure	unsure	unsure	unsure	unsure	unsure
072.00	Kahrod	EQ.128.00	Mazandaran	sure	7,1	P&S	6,7	ISC	7,1	ABE1	36,277	52,778	15,000	36,067	52,243	53477,6	53,5
078.00	Tortum	EQ.012.00	[name]	unsure	unsure	unsure	unsure	unsure	unsure	unsure	unsure	unsure	unsure	unsure	unsure	unsure	unsure
091.00	Bakacak	EQ.069.00	Düzce	sure	7,1	NEIC	7,5	NEIC	6,3	NEIC	40,806	31,187	10,400	40,755	31,372	16587,6	16,6
093.00	Scilla	EQ.051.02	Calabria Seq. 2	sure	6,2	AHEAD	x	x	x	x	38,220	15,633	x	38,248	15,702	6767,2	6,8
097.00	Uspenskoye	EQ.005.00	[name]	unsure	unsure	unsure	unsure	unsure	unsure	unsure	unsure	unsure	unsure	unsure	unsure	unsure	unsure
098.00	Nikawa	EQ.110.00	Kobe	sure	6,8	NEIC	6,5	NEIC	6,3	NEIC	34,554	135,041	19,000	34,773	135,342	36755,1	36,8
099.00	Dúdar	EQ.004.00	[name]	unsure	unsure	unsure	unsure	unsure	unsure	unsure	unsure	unsure	unsure	unsure	unsure	unsure	unsure
102.00	Vasto	EQ.080.00	Gargano	unsure	unsure	unsure	unsure	unsure	unsure	unsure	unsure	unsure	unsure	unsure	unsure	unsure	unsure
111.00	Zentoku	EQ.173.00	Tokai	unsure	unsure	unsure	unsure	unsure	unsure	unsure	unsure	unsure	unsure	unsure	unsure	unsure	unsure
112.00	Tsukidate	EQ.161.00	Sanriku-Minami	sure	7,0	NEIC	6,9	MOS	6,7	NEIC	38,869	141,525	71,200	38,728	141,010	47375,5	47,4
126.00	Dadu River	EQ.100.00	Kangding-Luding	sure	7,8	Wiki	x	x	x	x	29,900	102,000	x	29,631	102,158	33476,0	33,5
127.00	Fogo	EQ.183.00	volcanic eruption	sure	v	v	v	v	v	v	v	v	v	v	v	v	v
133.00	Latagualla	EQ.023.00	[name]	unsure	unsure	unsure	unsure	unsure	unsure	unsure	unsure	unsure	unsure	unsure	unsure	unsure	unsure
134.00	Huihuichuan	EQ.079.00	Gansu	sure	8,0	DENG	8,7	ISC	7,9	ABE1	36,888	105,606	15,000	35,952	105,670	104024,3	104,0
139.00	Cerda	EQ.053.00	Cerda	sure	5,9	NEIC	5,5	NEIC	5,8	NEIC	38,364	13,687	9,600	37,934	13,836	49463,3	49,5
144.00	Lituya Bay	EQ.031.01	Alaska 1958	sure	7,8	P&S	7,8	ISC	7,4	ABE1	58,230	-136,712	10,000	58,682	-137,486	67629,0	67,6
145.00	Mt. Boscatz	EQ.077.02	Friuli 1976	sure	x	x	6,5	NEIC	6,0	NEIC	46,352	13,260	11,700	46,289	13,077	15700,5	15,7
166.00	Lake Wanaka	EQ.190.00	[name]	unsure	unsure	unsure	unsure	unsure	unsure	unsure	unsure	unsure	unsure	unsure	unsure	unsure	unsure
177.01	Hawkesbury	EQ.191.00	blast	unsure	unsure	unsure	unsure	unsure	unsure	unsure	unsure	unsure	unsure	unsure	unsure	unsure	unsure
177.02	Toulnustouc	EQ.192.00	blast	unsure	unsure	unsure	unsure	unsure	unsure	unsure	unsure	unsure	unsure	unsure	unsure	unsure	unsure
177.03	Finneidfjord (offshore)	EQ.193.00	blast	unsure	unsure	unsure	unsure	unsure	unsure	unsure	unsure	unsure	unsure	unsure	unsure	unsure	unsure
177.04	Kattmarka	EQ.194.00	blast	unsure	unsure	unsure	unsure	unsure	unsure	unsure	unsure	unsure	unsure	unsure	unsure	unsure	unsure
177.05	La Romaine	EQ.195.00	blast	unsure	unsure	unsure	unsure	unsure	unsure	unsure	unsure	unsure	unsure	unsure	unsure	unsure	unsure

A.3. List of Landslides in the Database

no.	date*	landslide	country	earthquake	region	trigger
001.00	2001-03-18	Diezma	Spain	-	current seis.	-
002.00	1949-07-10	Khait	Tajikistan	Khait	current seis.	confirmed
003.01	paleo	Leupegem Hill 1	Belgium	-	low / no seis.	-
003.02	paleo	Leupegem Hill 2	Belgium	-	low / no seis.	-
003.03	paleo	Leupegem Hill 3	Belgium	-	low / no seis.	-
003.04	paleo	Rotelenberg Hill 4	Belgium	-	low / no seis.	-
003.05	paleo	Rotelenberg Hill 5	Belgium	-	low / no seis.	-
003.06	paleo	Rotelenberg Hill 6	Belgium	-	low / no seis.	-
003.07	paleo	Rotelenberg Hill 7	Belgium	-	low / no seis.	-
003.08	paleo	Rotelenberg Hill 8	Belgium	-	low / no seis.	-
003.09	paleo	Rotelenberg Hill 9	Belgium	-	low / no seis.	-
003.10	paleo	Rotelenberg Hill 10	Belgium	-	low / no seis.	-
003.11	paleo	Rotelenberg Hill 11	Belgium	-	low / no seis.	-
003.12	paleo	Rotelenberg Hill 12	Belgium	-	low / no seis.	-
003.13	paleo	Rotelenberg Hill 13	Belgium	-	low / no seis.	-
004.00	?	Büyükçekmece	Turkey	-	current seis.	-
005.01	2008-05-12	Chengxi	China	Sichuan	current seis.	confirmed
005.02	2008-05-12	Xinbei Middle-School	China	Sichuan	current seis.	confirmed
005.03	2008-05-12	Tangjiashan	China	Sichuan	current seis.	confirmed
005.04	2008-05-12	Daguangbao	China	Sichuan	current seis.	confirmed
006.00	?	Lushan Hot Spring	Taiwan	-	current seis.	-
007.01	1969	Ain El Hammam	Algeria	-	current seis.	-
007.02	1970	Tigzirt City	Algeria	-	current seis.	-
007.03	2009	Tigzirt Port	Algeria	-	current seis.	-
007.04	1952	Azazga	Algeria	-	current seis.	-
008.00	2014-03-22	Oso-Steelhead	USA	-	current seis.	-
009.01	1811-12-16	Stewart	USA	New Madrid Seq. (#1)	current seis.	confirmed
009.02	1811-12-16	Campbell	USA	New Madrid Seq. (#1)	current seis.	confirmed
010.00	1981-03	Avignonet	France	-	current seis.	-
011.00	paleo	Braemore	New Zealand	-	current seis.	-
012.00	2001-01-13	Las Colinas	El Salvador	El Salvador	current seis.	confirmed
013.00	1994-01-08	La Salle en Beaumont	France	-	current seis.	-
014.00	1978	Harmalière	France	-	current seis.	-
015.00	1980-11-23	Calitri	Italy	Irpinia 1980	current seis.	confirmed
016.01	1999-09-20	Tsaoling	Taiwan	Chi Chi	current seis.	confirmed
016.02	1999-09-20	Jiufenershan	Taiwan	Chi Chi	current seis.	confirmed
016.03	1999-09-20	Hungcaiping	Taiwan	Chi Chi	current seis.	confirmed
017.00	2009-08-09	Shiaolin	Taiwan	-	current seis.	-
018.01	?	Lesachriegel	Austria	-	current seis.	-
018.02	?	Gradenbach	Austria	-	current seis.	-
019.00	1903-04-29	Frank	Canada	-	current seis.	-
020.01	1964-03-28	Potter Hill	USA	Alaska 1964	current seis.	confirmed
020.02	1964-03-28	Bluff Road	USA	Alaska 1964	current seis.	confirmed
020.03	1964-03-28	Turnagain Heights	USA	Alaska 1964	current seis.	confirmed
020.04	1964-03-28	Point Campbell	USA	Alaska 1964	current seis.	confirmed
020.05	1964-03-28	Point Woronzof	USA	Alaska 1964	current seis.	confirmed
020.06	1964-03-28	L Street	USA	Alaska 1964	current seis.	confirmed
020.07	1964-03-28	4th Avenue	USA	Alaska 1964	current seis.	confirmed
020.08	1964-03-28	Government Hill	USA	Alaska 1964	current seis.	confirmed
020.09	1964-03-28	Native Hospital	USA	Alaska 1964	current seis.	confirmed
021.00	1994-01-17	Calabasas	USA	Northridge	current seis.	confirmed
022.00	1999-08-17	Degirmendere (offshore)	Turkey	Izmit	current seis.	confirmed
023.01	?	Vaculov-Sedlo	Czech Republic	-	low / no seis.	-
023.02	?	Kobylska	Czech Republic	-	low / no seis.	-
023.03	?	Kopce	Czech Republic	-	low / no seis.	-
024.00	1980-05-18	Mt. Saint Helens	USA	with volcanic eruption	current seis.	confirmed
025.00	paleo	Lluta	Chile	-	current seis.	-
026.00	postglacial	Columbia Mountain	USA	-	current seis.	-
027.00	1990-06	Eureka River	Canada	-	low / no seis.	-
028.00	1939-04	Montagneuse River	Canada	-	low / no seis.	-
029.00	1959-05-19	Dunvegan	Canada	-	low / no seis.	-
030.01	2007-05-05	Fox Creek East	Canada	-	low / no seis.	-
030.02	2007-05-05	Fox Creek West	Canada	-	low / no seis.	-
031.01	1897	CN50.9	Canada	-	current seis.	-
031.02	1886	Goddart	Canada	-	current seis.	-
032.00	1883-10-12	Beaver Creek	Canada	-	low / no seis.	-
033.01	?	Mt. Cefalone	Italy	-	current seis.	-
033.02	?	Cima della Fossa	Italy	-	current seis.	-
033.03	?	Villavallelonga	Italy	-	current seis.	-
033.04	1915-01-13	Casali d'Aschi	Italy	Avezzano	current seis.	confirmed
033.05	1915-01-13	Gioia dei Marsi	Italy	Avezzano	current seis.	confirmed
033.06	1703-01-14	Mt. Alvagnano	Italy	Norcia 1703	current seis.	confirmed
033.07	?	Fiamignano	Italy	-	current seis.	-
033.08	?	Pescasseroli	Italy	-	current seis.	-
034.00	1780	Campo Vallemaggia	Switzerland	-	current seis.	-
035.01	?	Longobardi	Italy	-	current seis.	-

035.02	1982-12-13	Ancona	Italy	-	current seis.	-
036.00	1984-04	La Clapière	France	-	current seis.	-
037.00	2006-03-21	Laalam	Algeria	Kherrata	current seis.	confirmed
038.00	1806-09-02	Goldau	Switzerland	-	current seis.	-
039.01	1980	Cerentino	Switzerland	-	current seis.	-
039.02	1834	Peccia	Switzerland	-	current seis.	-
039.03	1846	Val Canaria	Switzerland	-	current seis.	-
039.04	1896-10	Val Colla	Switzerland	-	current seis.	-
040.01	1755-11-01	Güevéjar I	Spain	Lisbon 1755	current seis.	confirmed
040.02	1884-12-25	Güevéjar II	Spain	Arenas del Rey	current seis.	confirmed
041.00	1683	Montelparo	Italy	-	current seis.	-
042.00	1933-10	Sesa	Italy	-	current seis.	-
043.01	?	Ráztoka	Slovakia	-	low / no seis.	-
043.02	?	Polská Tomanová	Slovakia	-	low / no seis.	-
044.00	2002-10-31	Salcito	Slovakia	Molise 2002	current seis.	confirmed
045.01	paleo	Belbek	Ukraine	[name]	past seis.	uncertain
045.02	paleo	Frontovoye	Ukraine	[name]	past seis.	uncertain
045.03	paleo	Kacha 1	Ukraine	[name]	past seis.	uncertain
045.04	paleo	Kacha 2	Ukraine	[name]	past seis.	uncertain
045.05	paleo	Alma	Ukraine	[name]	past seis.	uncertain
045.06	paleo	Vishennoye	Ukraine	[name]	past seis.	uncertain
046.01	1692-09-18	Battice 1	Belgium	Verviers	current seis.	confirmed
046.02	1692-09-18	Battice 2	Belgium	Verviers	current seis.	confirmed
046.03	1692-09-18	Battice 3	Belgium	Verviers	current seis.	confirmed
046.04	1692-09-18	Battice 4	Belgium	Verviers	current seis.	confirmed
046.05	1692-09-18	Battice 5	Belgium	Verviers	current seis.	confirmed
046.06	1692-09-18	Battice 6	Belgium	Verviers	current seis.	confirmed
046.07	1692-09-18	Battice 7	Belgium	Verviers	current seis.	confirmed
046.08	1692-09-18	Battice 8	Belgium	Verviers	current seis.	confirmed
046.09	1692-09-18	Battice 9	Belgium	Verviers	current seis.	confirmed
046.10	1692-09-18	Battice 10	Belgium	Verviers	current seis.	confirmed
046.11	1692-09-18	Battice 11	Belgium	Verviers	current seis.	confirmed
046.12	1692-09-18	Battice 12	Belgium	Verviers	current seis.	confirmed
046.13	1692-09-18	Battice 13 (Manaihan)	Belgium	Verviers	current seis.	confirmed
047.01	2007-04-21	Acantilada Bay	Chile	Aysén	current seis.	confirmed
047.02	2007-04-21	Punta Cola	Chile	Aysén	current seis.	confirmed
047.03	2007-04-21	Mentirosa Island	Chile	Aysén	current seis.	confirmed
047.04	2007-04-21	Frío Creek	Chile	Aysén	current seis.	confirmed
047.05	2007-04-21	Marta River 1	Chile	Aysén	current seis.	confirmed
047.06	2007-04-21	Fernández Creek	Chile	Aysén	current seis.	confirmed
047.07	2007-04-21	Marta River 2	Chile	Aysén	current seis.	confirmed
047.08	2007-04-21	Pescado River	Chile	Aysén	current seis.	confirmed
048.00	1987-03-05	Salado	Ecuador	Ecuador	current seis.	confirmed
049.00	1679-06-04	Vokhchaberd	Armenia	Armenian 1679	current seis.	confirmed
050.00	1881-09-10	Castel Frentano	Italy	Lanciano	current seis.	confirmed
051.00	1997-10-11	Mt. Nuria	Italy	-	current seis.	-
052.01	1990-06-20	Galdian	Iran	Manjil-Rudbar	current seis.	confirmed
052.02	1990-06-20	Fatalak	Iran	Manjil-Rudbar	current seis.	confirmed
053.00	1963-10-09	Vajont	Italy	-	current seis.	-
054.00	2003-09-10	Tsaitichhu	Bhutan	-	current seis.	-
055.00	2007-03-01	S. Giovanni	Italy	-	current seis.	-
056.00	1950	Rasdeglia	Italy	-	current seis.	-
057.00	1992-08-19	Suusamyr	Kyrgyzstan	Suusamyr	current seis.	confirmed
058.01	paleo	Kokomeren	Kyrgyzstan	[name]	current seis.	uncertain
058.02	1885	Aksu	Kyrgyzstan	Belovodsk	current seis.	uncertain
058.03	paleo	Beshkiol	Kyrgyzstan	[name]	current seis.	uncertain
058.04	paleo	Karakudjur	Kyrgyzstan	[name]	current seis.	uncertain
058.05	1946	Sarychelek	Kyrgyzstan	Chatkal	current seis.	uncertain
058.06	paleo	Kugart	Kyrgyzstan	[name]	current seis.	uncertain
059.00	?	Rosone	Italy	-	current seis.	-
060.00	2000-04-09	Yigong	China	-	current seis.	-
061.00	1911-02-18	Usoi	Tajikistan	Sarez	current seis.	confirmed
062.01	1989-01-22	Okuli	Tajikistan	Gissar	current seis.	confirmed
062.02	1989-01-22	May 1	Tajikistan	Gissar	current seis.	confirmed
062.03	1989-01-22	Firma	Tajikistan	Gissar	current seis.	confirmed
062.04	1989-01-22	Sharara	Tajikistan	Gissar	current seis.	confirmed
063.00	1984	Klasgarten	Austria	-	current seis.	-
064.00	1975	Niedergallmigg	Austria	-	current seis.	-
065.01	1992	Huayuanyangjichang	China	-	current seis.	-
065.02	1996	Jinjinzi	China	-	current seis.	-
065.03	1999	Yangjiaba	China	-	current seis.	-
066.00	postglacial	Atemkopf	Austria	-	current seis.	-
067.00	2002-10	La Mania	Italy	-	current seis.	-
068.00	1960	Beauregard	Italy	-	current seis.	-
069.00	1965-01-09	Hope	Canada	[name]	current seis.	uncertain
070.00	?	Anlesi	China	-	current seis.	-
071.01	1914-05-30	Cà di Malta	Italy	-	current seis.	-
071.02	1934-03-06	Rocca Pitigliana	Italy	-	current seis.	-
072.00	1957-07-02	Kahrod	Iran	Mazandaran	current seis.	confirmed
073.00	2008-09	Cerca del Cielo	USA	-	current seis.	-

074.00	?	Kutlugün	Turkey	-	current seis.	-
075.00	1987-07-28	Val Pola	Italy	-	current seis.	-
076.01	?	Varco d'Izzo	Italy	-	current seis.	-
076.02	?	Costa della Gaveta	Italy	-	current seis.	-
077.00	1979-08-08	Abbotsford	New Zealand	-	current seis.	-
078.00	17th cent.	Tortum	Turkey	[name]	current seis.	uncertain
079.00	-300	Slumgullion	USA	-	current seis.	-
080.00	1999-05-13	Rufi	Switzerland	-	current seis.	-
081.00	2007	Zhujiadian	China	-	current seis.	-
082.00	1982	Minor Creek	USA	-	current seis.	-
083.00	2005-03-17	Kuzulu	Turkey	-	current seis.	-
084.00	1995	Huangtupo	China	-	current seis.	-
085.00	1998	Fosso Spineto	Italy	-	current seis.	-
086.00	-500000	Marcus	USA	-	current seis.	-
087.00	2003-11-09	Afternoon Creek	USA	-	current seis.	-
088.00	2009-04-26	Valgrisenche	Italy	-	current seis.	-
089.00	?	Aka-Kuzure	Japan	-	current seis.	-
090.00	?	Ivancich	Italy	-	current seis.	-
091.00	1999-11-12	Bakacak	Turkey	Düzce	current seis.	confirmed
092.00	postglacial	Triesenberg	Liechtenstein	-	current seis.	-
093.00	1783-02-06	Scilla	Italy	Calabria Seq. 2	current seis.	confirmed
094.00	1972	San Donato	Italy	-	current seis.	-
095.00	?	La Salsa	Italy	-	current seis.	-
096.00	1996	Grohovo	Croatia	-	current seis.	-
097.00	-35000	Uspenskoye	Russia	[name]	current seis.	uncertain
098.00	1995-01-16	Nikawa	Japan	Kobe	current seis.	confirmed
099.00	paleo	Dúdar	Spain	[name]	current seis.	uncertain
100.01	?	Machu Picchu A	Peru	-	current seis.	-
100.02	?	Machu Picchu B	Peru	-	current seis.	-
101.01	2002	Keillor Road	Canada	-	low / no seis.	-
101.02	1999-10-23	Whitemud Road	Canada	-	low / no seis.	-
102.00	1627-07-30	Vasto	Italy	Gargano	current seis.	uncertain
103.00	1963	Kostanjek	Croatia	-	current seis.	-
104.00	1997-07	Mt. Munday	Canada	-	current seis.	-
105.00	2010-08-06	Mt. Meager	Canada	-	current seis.	-
106.00	-10000	Downie	Canada	-	current seis.	-
107.00	2005-01-10	La Conchita	USA	-	current seis.	-
108.00	postglacial	Séchilienne	France	-	current seis.	-
109.00	2004	Ogoto	Japan	-	current seis.	-
110.00	2003	Kuchi-Otani	Japan	-	current seis.	-
111.00	1854-12-23	Zentoku	Japan	Tokai	current seis.	uncertain
112.00	2003-05-26	Tsukidate	Japan	Sanriku-Minami	current seis.	confirmed
113.01	1997-01	Slesse Park	Canada	-	current seis.	-
113.02	1973-05-26	Attachie	Canada	-	low / no seis.	-
114.00	1963-09-03	Lesueur	Canada	-	low / no seis.	-
115.00	1933-07	Brazeau	Canada	-	current seis.	-
116.00	1990-06-17	Saddle River	Canada	-	low / no seis.	-
117.00	2010-01	Cenes de la Vega	Spain	-	current seis.	-
118.00	1993-12-29	Acquara-Vadoncello	Italy	-	current seis.	-
119.00	1901-10-01	Boscobel	Barbados	-	current seis.	-
120.00	paleo	Mt. Nuovo	Italy	-	current seis.	-
121.00	-140000	Baga Bogd	Mongolia	-	past seis.	-
122.00	1974-04-25	Mayunmarca	Peru	-	current seis.	-
123.00	1612	Corniglio	Italy	-	current seis.	-
124.00	?	Vallcebre	Spain	-	current seis.	-
125.00	-10000	Corvara	Italy	-	current seis.	-
126.00	1786-06-01	Dadu River	China	Kangding-Luding	current seis.	confirmed
127.00	-10000	Fogo	Cabo Verde	with volcanic eruption	current seis.	confirmed
128.00	1906	Petacciato	Italy	-	current seis.	-
129.01	-20000	El Petruso	Spain	-	current seis.	-
129.02	-20000	Sextas	Spain	-	current seis.	-
129.03	-20000	La Selva	Spain	-	current seis.	-
130.00	1996	Halden Creek	Canada	-	low / no seis.	-
131.00	-10000	Åknes	Norway	-	low / no seis.	-
132.00	-10000	Kykula	Slovakia	-	low / no seis.	-
133.00	paleo	Latagualla	Chile	[name]	current seis.	uncertain
134.00	1920-12-16	Huihuichuan	China	Gansu	current seis.	confirmed
135.00	1980	Amloke Nakka	Pakistan	-	current seis.	-
136.00	1960-10	Tessina	Italy	-	current seis.	-
137.00	paleo	Krynica	Poland	-	low / no seis.	-
138.00	paleo	Collinabos	Belgium	-	low / no seis.	-
139.00	2002-09-06	Cerda	Italy	Cerda	current seis.	confirmed
140.00	2011-09-16	Shibangou	China	-	current seis.	-
141.00	1996-04-28	Quesnel Forks	Canada	-	current seis.	-
142.00	?	Riou-Bourdoux Valley	France	-	current seis.	-
143.00	2000-11-18	Slano Blato	Slovenia	-	current seis.	-
144.00	1958-07-10	Lituya Bay	USA	Alaska 1958	current seis.	confirmed
145.00	1976-05-06	Mt. Boscatz	Italy	Friuli 1976	current seis.	confirmed
146.00	1949	Kualiangzi	China	-	current seis.	-
147.00	-1500	Ropice	Czech Republic	-	low / no seis.	-

148.00	1982	La Valette	France	-	current seis.	-
149.00	postglacial	Heather Hill	Canada	-	current seis.	-
150.00	2008-11-23	Gongjiafang	China	-	current seis.	-
151.00	paleo	Utiku	New Zealand	-	current seis.	-
152.00	paleo	Taihape	New Zealand	-	current seis.	-
153.01	paleo	Stromboli	Italy	-	current seis.	-
153.02	paleo	La Fossa	Italy	-	current seis.	-
154.00	1909-11	East Lirio	Panama	-	current seis.	-
155.01	2010-11	Cischele	Italy	-	current seis.	-
155.02	?	Ochojno	Poland	-	low / no seis.	-
156.00	postglacial	Gammajunni 3	Norway	-	low / no seis.	-
157.00	postglacial	La Frasse	Switzerland	-	current seis.	-
158.00	1953-01-31	Miramar	United Kingdom	-	low / no seis.	-
159.00	?	Mahouane Dam	Algeria	-	current seis.	-
160.00	paleo	Pianello	Italy	-	current seis.	-
161.00	2011	Santa Maria Maddalena	Italy	-	current seis.	-
162.00	?	Zhaoshuling	China	-	current seis.	-
163.00	?	Dúrcal	Spain	-	current seis.	-
164.00	1935	Aggenalm	Germany	-	low / no seis.	-
165.00	?	Huangshipan	China	-	current seis.	-
166.00	postglacial	Lake Wanaka	New Zealand	[name]	current seis.	uncertain
167.00	2015-02-02	Mofjellbekken	Norway	-	low / no seis.	-
168.00	?	Badu	China	-	current seis.	-
169.01	paleo	Number 1	China	-	current seis.	-
169.02	paleo	Number 2	China	-	current seis.	-
170.01	2005-12-10	Saint Barnabé	Canada	-	low / no seis.	-
170.02	2010-05-10	Saint Jude	Canada	-	low / no seis.	-
170.03	1994-04-21	Sainte Monique	Canada	-	low / no seis.	-
171.00	1970	Bird	New Zealand	-	current seis.	-
172.00	2013-12-03	Montescaglioso	Italy	-	current seis.	-
173.00	19th cent.	Spriana	Italy	-	current seis.	-
174.00	?	Piscopio I Tunnel	Italy	-	current seis.	-
175.00	?	La Saxe	Italy	-	current seis.	-
176.00	?	Erguxi	China	-	current seis.	-
177.01	1955-12-07	Hawkesbury	Canada	blast	low / no seis.	uncertain
177.02	1962-05-23	Toulnustouc	Canada	blast	low / no seis.	uncertain
177.03	1996-06-20	Finneidfjord (offshore)	Norway	blast	low / no seis.	uncertain
177.04	2009-03-13	Kattmarka	Norway	blast	low / no seis.	uncertain
177.05	2009-08-01	La Romaine	Canada	blast	low / no seis.	uncertain
178.01	1960	Bumper	Australia	-	low / no seis.	-
178.02	1960	Siphon Gully	Australia	-	low / no seis.	-

(*) either the time of major failure
or the time since when sliding is reported (for active landslides)

A.4. Displacement Time-histories with SLAMMER per Signal

signal A (000049x)

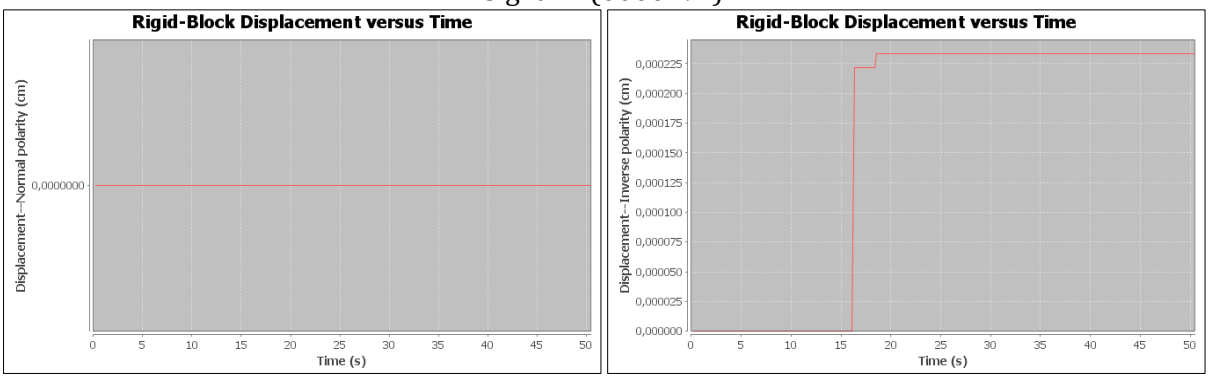

signal B (000133x)

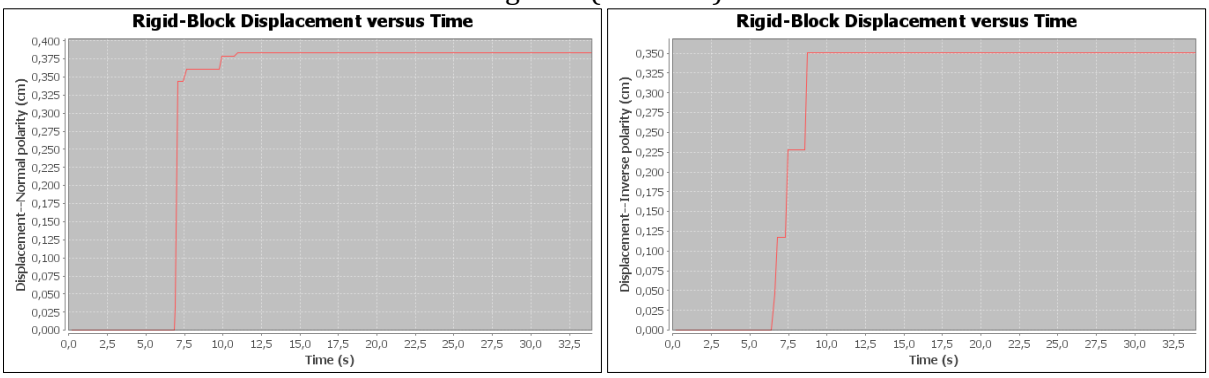

signal C (000127x)

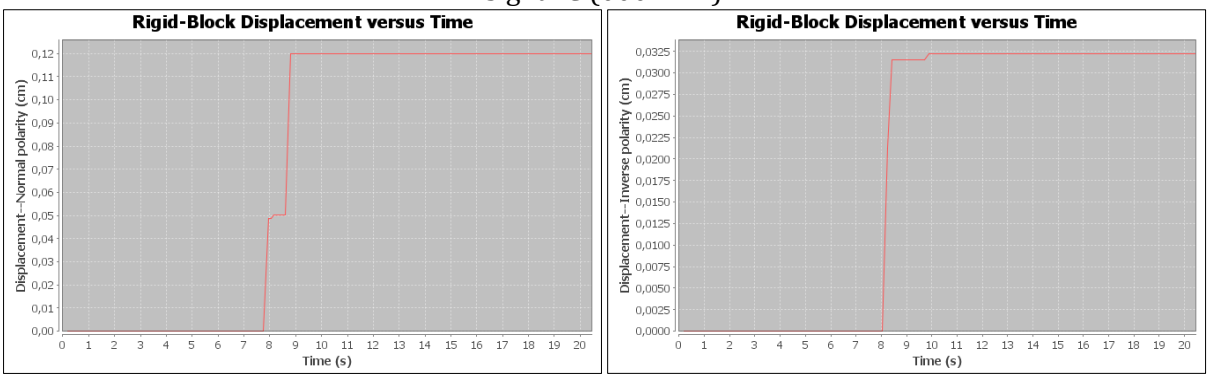

signal D (000294x)

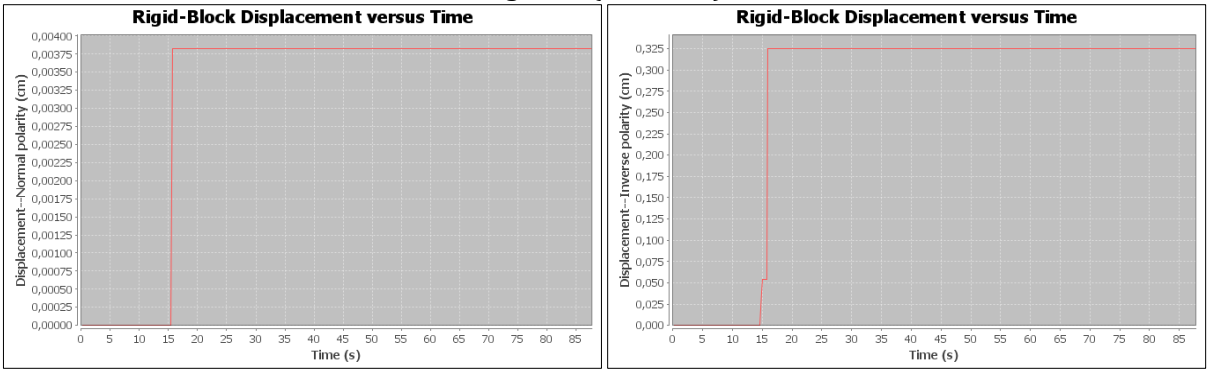

signal E (000335x)

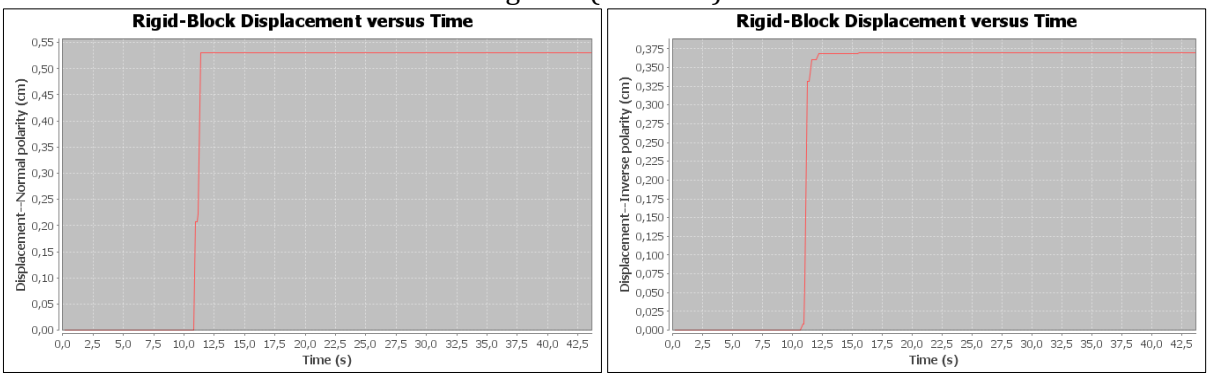

signal F (001875x)

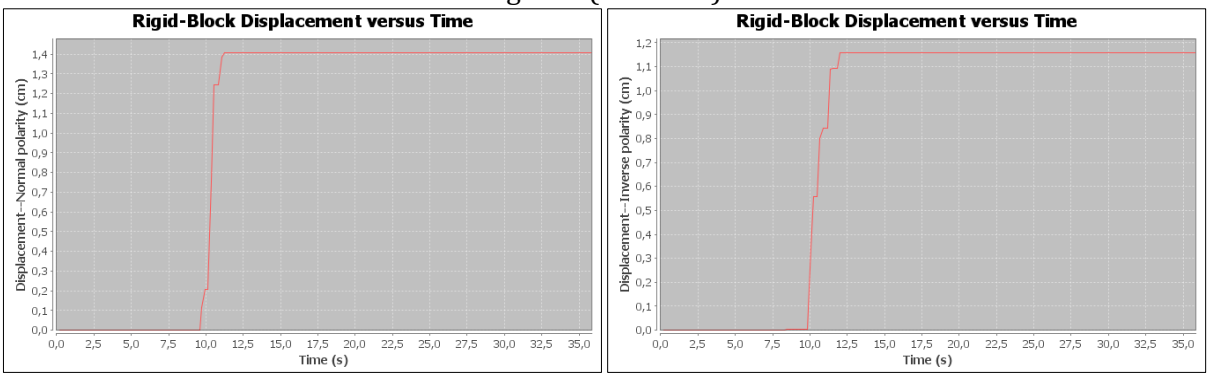

signal G (006142x)

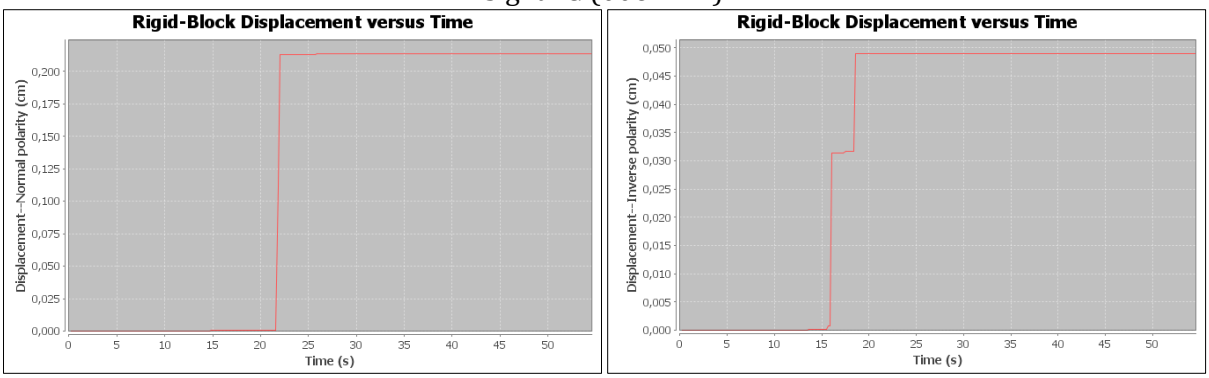

signal H (000599x)

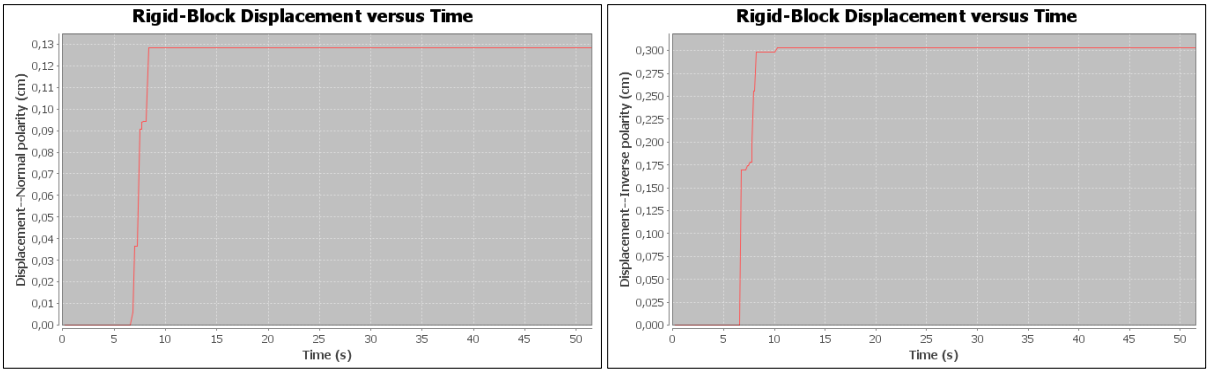

signal I (000612x)

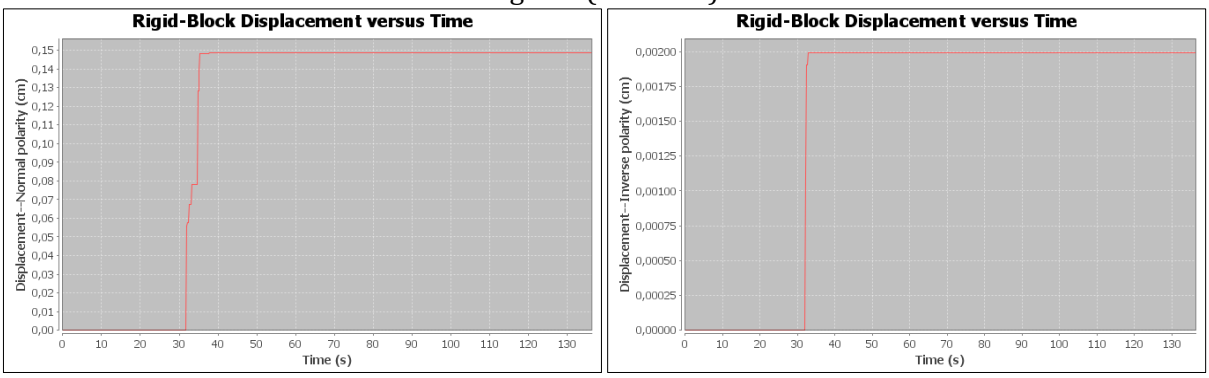

signal J (000625x)

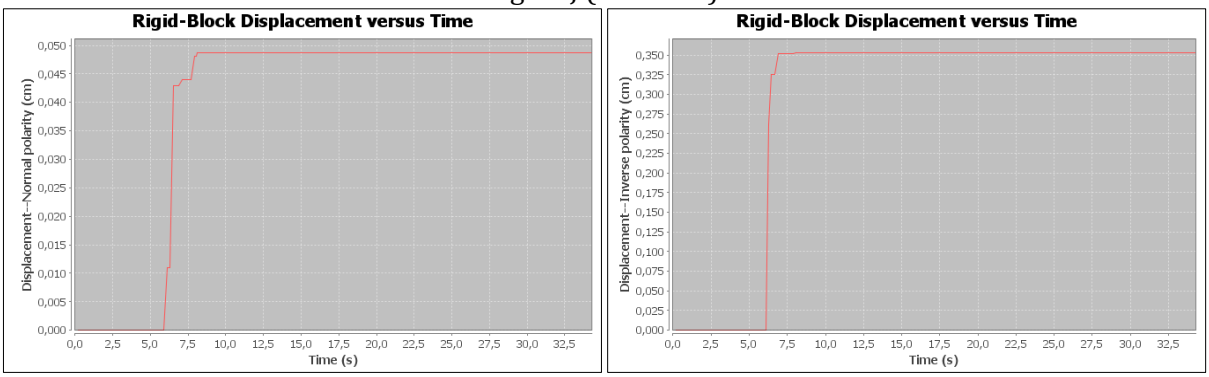

signal K (005820x)

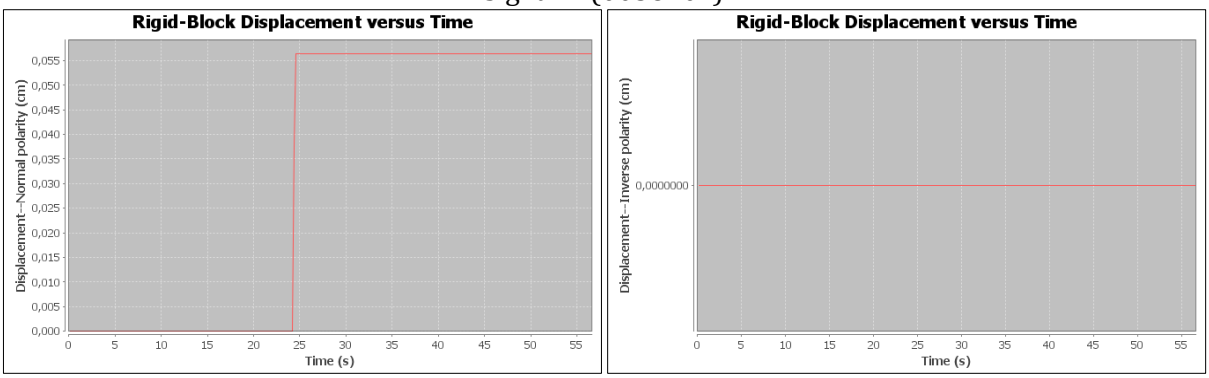

A.5. Notes for Data-Sheet Preparation in CESAR

A.5.a. Modifying a 'data' (MODE) to solve for 'rst' and 'list'

```
...
MODE                                  → search for keyword
1
2
0.00000e+00
20                                    → makes first 20 eigenvalues and eigenfrequencies
0
0.00000e+00
30                                    → "0": 15 iterations; "30": 30 iterations (convergence!)
1
1
directory\"…".rst                     → name corresponds to name of 'cleo26' or 'cleo36'
MUL                                   → especially for 3D (needed for recalling data-file)
1  0                                  → especially for 3D (needed for recalling data-file)
[ ]                                   → leave one empty line at the end
```

A.5.b. Reading ID points of boundary definition from a 'data'

```
...
COND                                  → search for keyword
2
NUL
2
___                                   → number of ID points (of boundary definition)
⌈ ⌉                                     (2D: 1011 SURF; 3D: 479 SURFlcs, 61594 SURFplane)
⌊ ⌋                                   → all ID points (of boundary definition)
1   1
0
CHAR
...
```

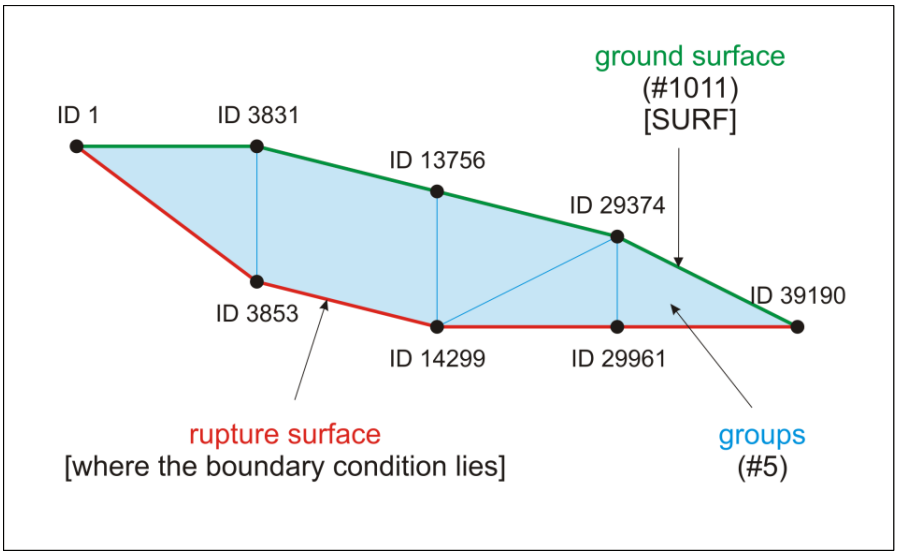

Fig. A.1: Scheme showing the long version of the 2D simplified geometry with ID points. The scheme does not show the real proportions.

A.5.c. Modifying a 'data' (SUMO) to solve for 'list'

```
...
CHAR                                  → search for keyword
2
POI
1                                     → number of charge directions (1 in x-direction)
                                      → number of groups (for charge application)
[ ]                                     (2D: 5 ⌟1 2 3 4 5; 3D: 1 ⌟1)
[ ]                                   → all groups (for charge application)
1.00000 0.00000 (0.00000)             → factors for charge (1 in x-, 0 in y- and 0 in z-direction)
IMPR
1 0
[ ]      same for all signals         → leave one empty line
2        (depends only on LCS)
                                      → number of ID points (for displacements; cf. Fig. A.1)
[ ]                                     (2D: 1011 SURF; 3D: 479 SURFlcs, 61594 SURFplane)
[ ]                                   → all ID points (for displacements; as SURF/-lcs/-plane)
[ ]                                   → leave one empty line
[ ]                                   → leave one empty line
0
SUMO     different for all velocities
2
directory\"…".rst                     → reading 'rst' even if not in SUMO-directory (cf. Tab. A.1)
1 1 1 1 … [write 20x]                 → uses first 20 resonance frequencies
3
0
                                      → exact number of entries of signal (e.g. 2D-A: 10086)
0                                     → time increment between entries (e.g. 2D-A: 0.005)
CFT
0
[ ]      different for all signals
[ ]                                   → all entries of signal
AMO
5.00000e-02 … [write 20x]             → damping for first 20 eigenfrequencies
[ ]                                   → leave one empty line at the end
```

2D	reads	3D	reads
Diezma100□.cleo26	ADiezma_M1.rst	Diezma3DlcsA.cleo36	
Diezma150□.cleo26	ADiezma_M2.rst	Diezma3DlcsB.cleo36	
Diezma200□.cleo26	ADiezma_M3.rst	Diezma3DlcsC.cleo36	
Diezma250□.cleo26	ADiezma_M4.rst	Diezma3DlcsD.cleo36	
Diezma300□.cleo26	ADiezma_M5.rst	Diezma3DlcsE.cleo36	
Diezma350□.cleo26	ADiezma_M6.rst	Diezma3DlcsF.cleo36	
Diezma400□.cleo26	ADiezma_M7.rst	Diezma3DlcsG.cleo36	
Diezma450□.cleo26	BDiezma_M1.rst	Diezma3DlcsH.cleo36	
Diezma500□.cleo26	BDiezma_M2.rst	Diezma3DlcsI.cleo36	
Diezma550□.cleo26	BDiezma_M3.rst	Diezma3DlcsJ.cleo36	Diezma3D_M1.rst
Diezma600□.cleo26	BDiezma_M4.rst	Diezma3DlcsK.cleo36	
Diezma650□.cleo26	BDiezma_M5.rst		
Diezma700□.cleo26	BDiezma_M6.rst		
Diezma750□.cleo26	BDiezma_M7.rst	same for	
Diezma800□.cleo26	CDiezma_M1.rst		
Diezma850□.cleo26	CDiezma_M2.rst	Diezma3Dplane□.cleo36	
Diezma900□.cleo26	CDiezma_M3.rst		
Diezma950□.cleo26	CDiezma_M4.rst		
Diezma1000□.cleo26	CDiezma_M5.rst		

Tab. A.1: cleo26- and cleo36-files reading the respective rst-file; (□ = signal A-K).

In the course of work with CESAR the usage of terms as well as the nomenclature of files is constantly adding up. Sometimes misleading nomenclature is the result. The following overview casts light on the matter.

2D:

The simplified geometry distinguishes:

- ground surface (= SURF) 1011 points (all kept for displacement evaluation)

Therefore, those points are identified in step 2 of the flowchart for the 2D procedure by:

- "lines to ground surface" i.e. CESAR marks lines along the ground surface

Displacements can then be identified with their ID:

- 1011 for SURF giving the displacements on the ground surface

3D:

The simplified geometry distinguishes:

- LCS (= SURFlcs) 479 points (all kept for displacement evaluation)
- topography (= SURFplane) 61594 points (all kept for displacement evaluation)

Therefore, those points are identified in step 2 of the flowchart for the 3D procedure by:

- "lines to LCS" i.e. CESAR marks lines along the same LCS used in 2D
- "tiles to topography" i.e. CESAR marks planes on the full covering topography

Displacements can then be identified with their ID:

- 479 for SURFlcs giving the displacements along the same LCS used in 2D
- 61594 for SURFplane giving the displacements on the full covering topography

→ The expandable workflow charts are to be found the very end of the thesis.

A.6. Maximum Displacements with CESAR per Signal

2D	d_x (300 m/s) called u in CESAR	d_z (300 m/s) called v in CESAR	d_r (300 m/s) called total in CESAR
A			
B			
C			
D	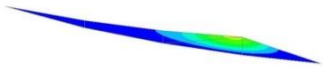	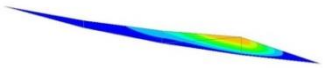	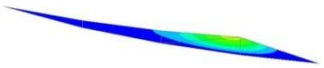
E		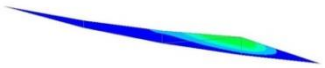	
F			
G		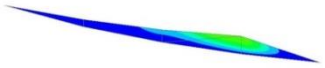	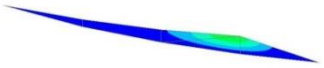
H			
I		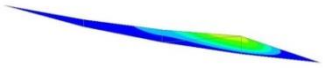	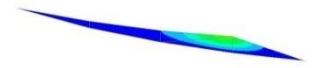
J			
K			

legend for d_x and d_r
→ 10 bin grouping
→ 0-1000 mm

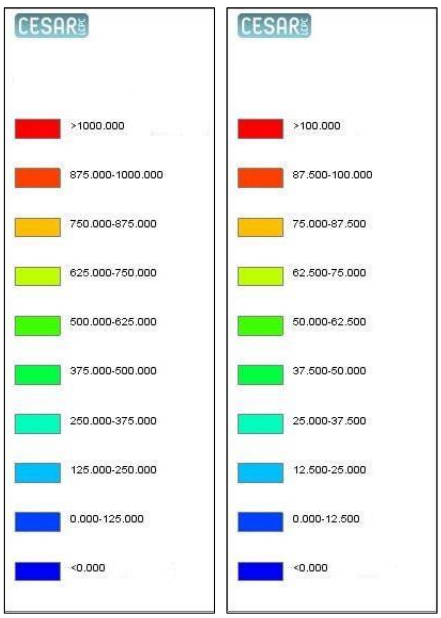

legend for d_z
→ 10 bin grouping
→ 0-100 mm

3D	d_x (300 m/s) - front called u in CESAR	d_x (300 m/s) - top called u in CESAR	d_x (300 m/s) - LCS called u in CESAR
A	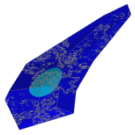	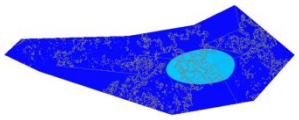	
B	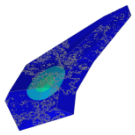	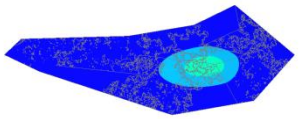	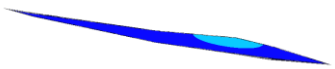
C	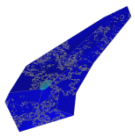	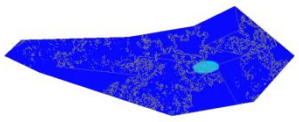	
D	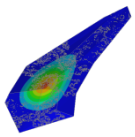	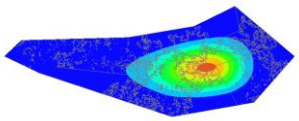	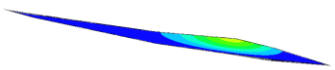
E	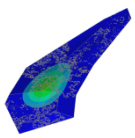	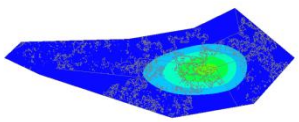	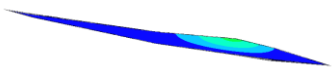
F	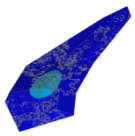	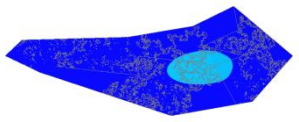	
G	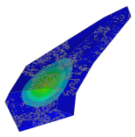	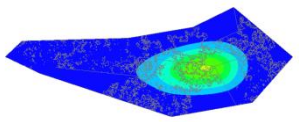	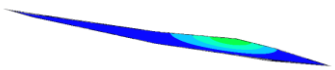
H	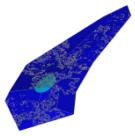	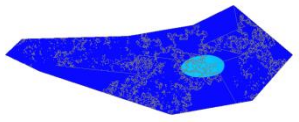	
I	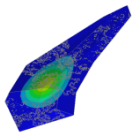	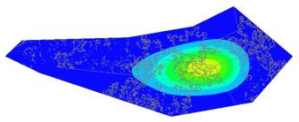	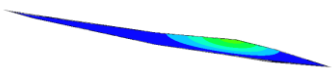
J	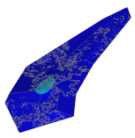	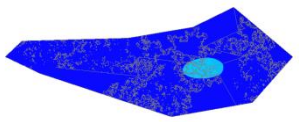	
K	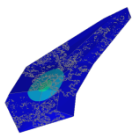	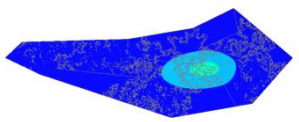	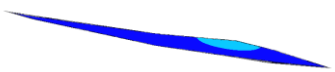

3D	d_y (300 m/s) - front called v in CESAR	d_y (300 m/s) - top called v in CESAR	d_y (300 m/s) - LCS called v in CESAR
A	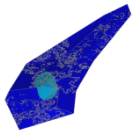	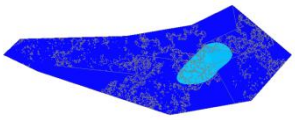	
B	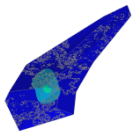	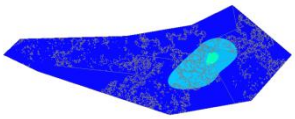	
C	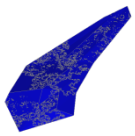	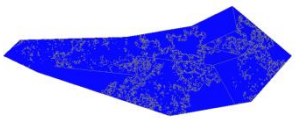	
D	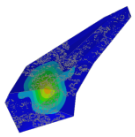	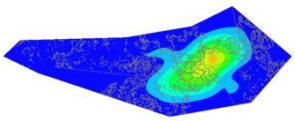	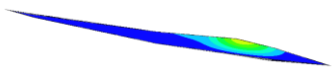
E	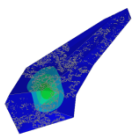	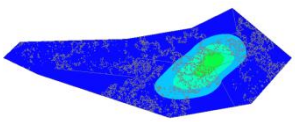	
F	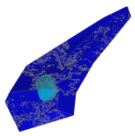	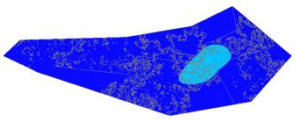	
G	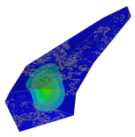	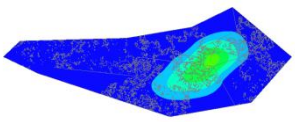	
H	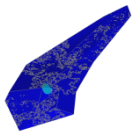	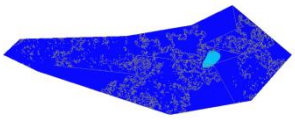	
I	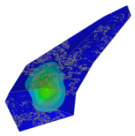	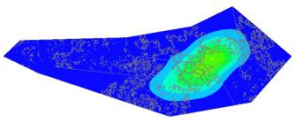	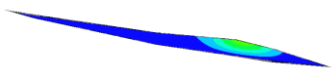
J	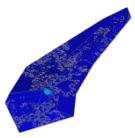	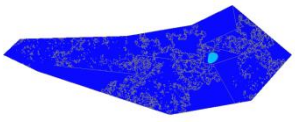	
K	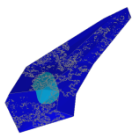	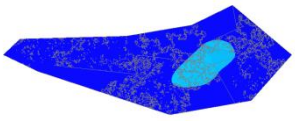	

3D	d_z (300 m/s) - front called w in CESAR	d_z (300 m/s) - top called w in CESAR	d_z (300 m/s) - LCS called w in CESAR
A	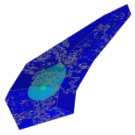	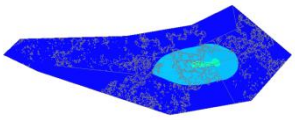	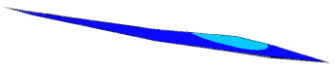
B	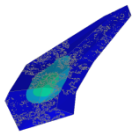	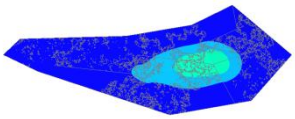	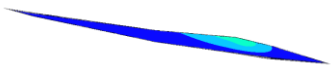
C	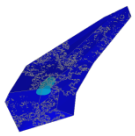	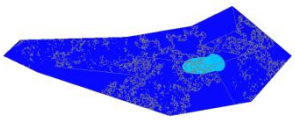	
D	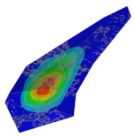	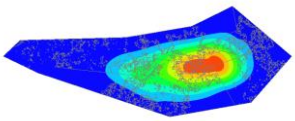	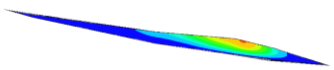
E	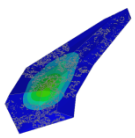	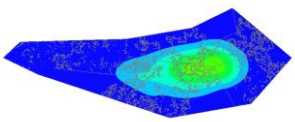	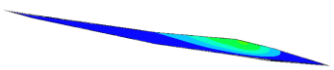
F	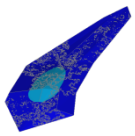	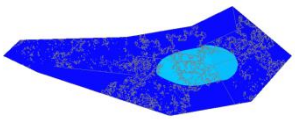	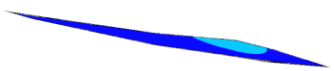
G	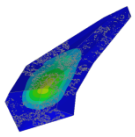	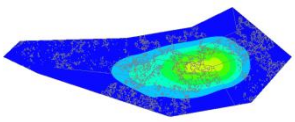	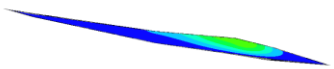
H	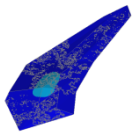	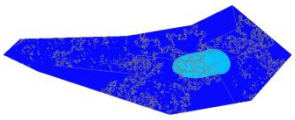	
I	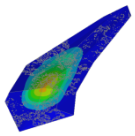	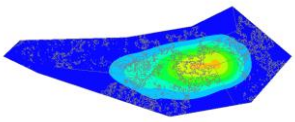	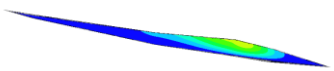
J	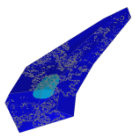	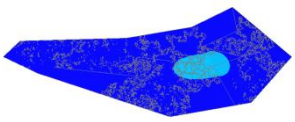	
K	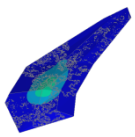	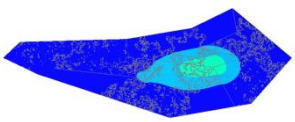	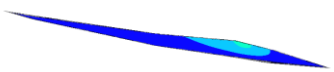

3D	d_r (300 m/s) - front called total in CESAR	d_r (300 m/s) - top called total in CESAR	d_r (300 m/s) - LCS called total in CESAR
A	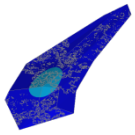	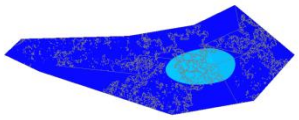	
B	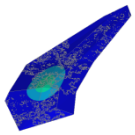	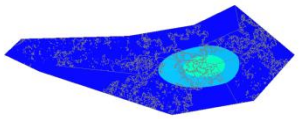	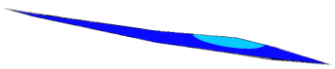
C	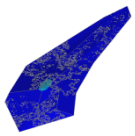	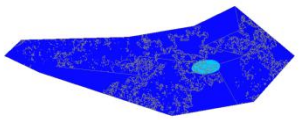	
D	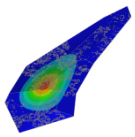	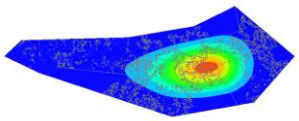	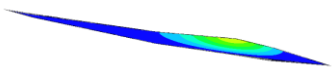
E	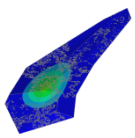	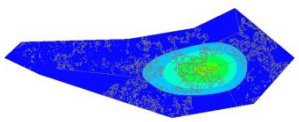	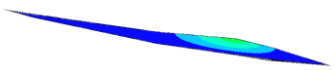
F	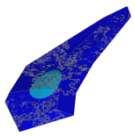	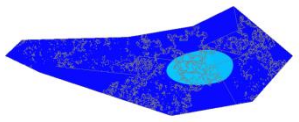	
G	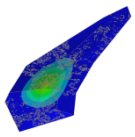	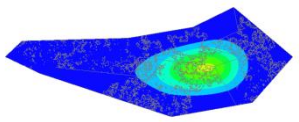	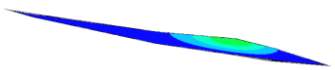
H	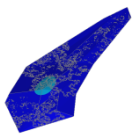	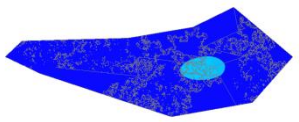	
I	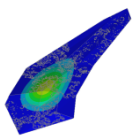	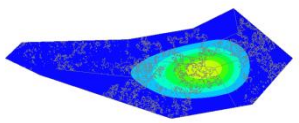	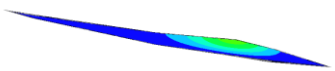
J	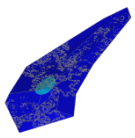	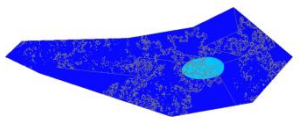	
K	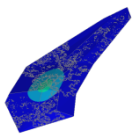	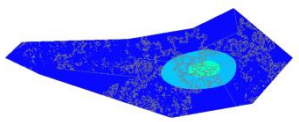	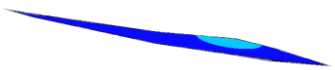

legend for d_x
→ 10 bin grouping
→ 0-8000 mm

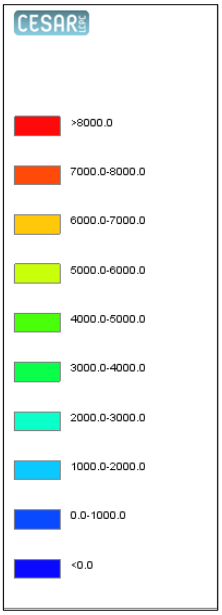

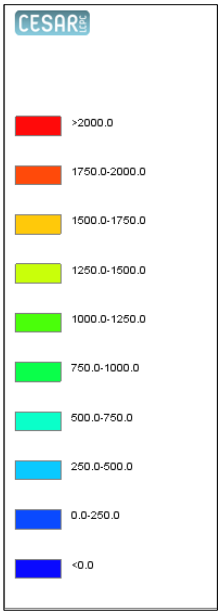

legend for d_y
→ 10 bin grouping
→ 0-2000 mm

legend for d_z
→ 10 bin grouping
→ 0-800 mm

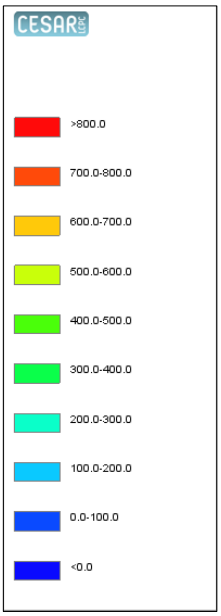

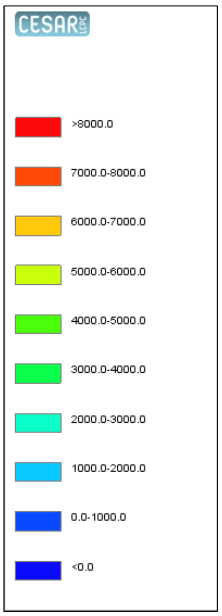

legend for d_r
→ 10 bin grouping
→ 0-8000 mm

```
% -> Vectors must have the same length and order ("crown to toe").
% -> dxGS: vector with all x-displacements along the ground surface
% -> dxSS: vector with all x-displacements along the sliding surface
% -> drel: vector with all relative displacements in x-direction

drel=zeros(length(dxGS),1);      % to be filled while looping

for i = 1:length(dxGS)

      if          dxGS(i)>0 && dxSS(i)>0 && abs(dxGS(i))==abs(dxSS(i))
                  drel(i)=dxGS(i)-dxSS(i);          % |+dxGS| = |+dxSS|

      elseif      dxGS(i)>0 && dxSS(i)<0 && abs(dxGS(i))==abs(dxSS(i))
                  drel(i)=dxGS(i)-dxSS(i);          % |+dxGS| = |-dxSS|

      elseif      dxGS(i)<0 && dxSS(i)<0 && abs(dxGS(i))==abs(dxSS(i))
                  drel(i)=dxGS(i)-dxSS(i);          % |-dxGS| = |-dxSS|

      elseif      dxGS(i)>0 && dxSS(i)>0 && abs(dxGS(i))>abs(dxSS(i))
                  drel(i)=dxGS(i)-dxSS(i);          % |+dxGS| > |+dxSS|

      elseif      dxGS(i)<0 && dxSS(i)<0 && abs(dxGS(i))<abs(dxSS(i))
                  drel(i)=dxGS(i)-dxSS(i);          % |-dxGS| < |-dxSS|

      elseif      dxGS(i)>0 && dxSS(i)<0 && abs(dxGS(i))>abs(dxSS(i))
                  drel(i)=dxGS(i)-dxSS(i);          % |+dxGS| > |-dxSS|

      elseif      dxGS(i)>0 && dxSS(i)<0 && abs(dxGS(i))<abs(dxSS(i))
                  drel(i)=dxGS(i)-dxSS(i);          % |+dxGS| < |-dxSS|

      else
                  drel(i)=0;        % no displacement in all other cases

      end
end
```

If one needs to adapt this code for other purposes a quick (counter-)test can be performed with:

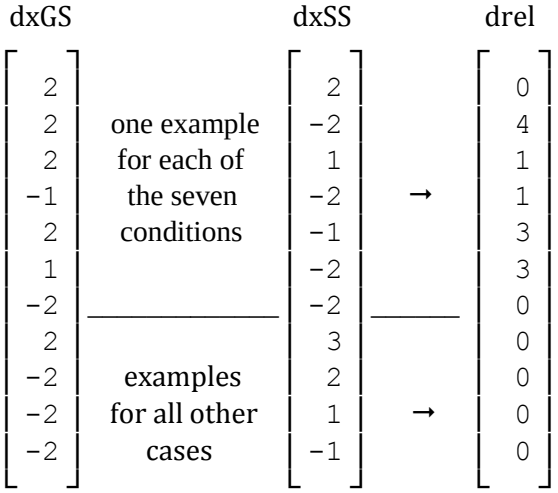

A.8. Relative Displacements Obtained from the FLAC-Models in 2D

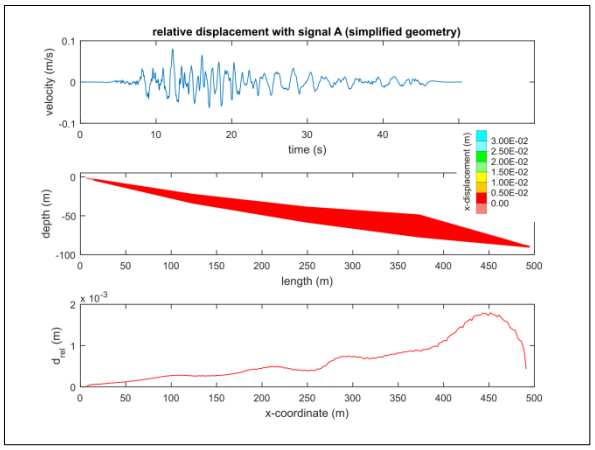

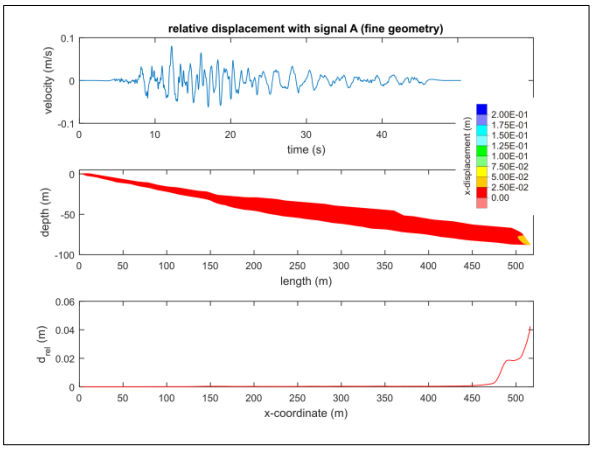

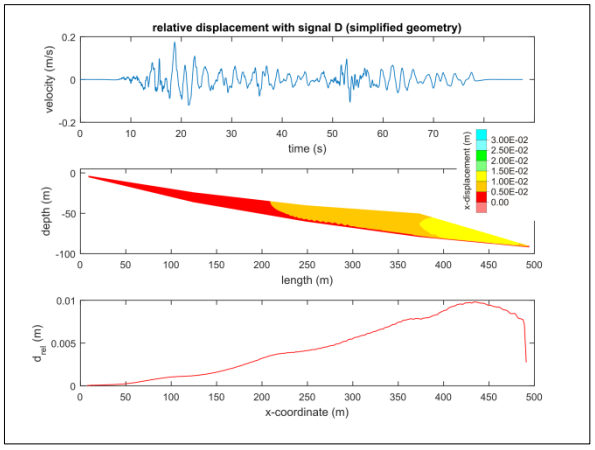

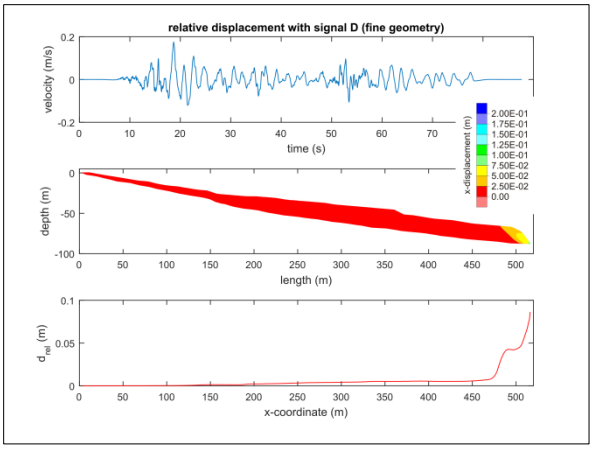

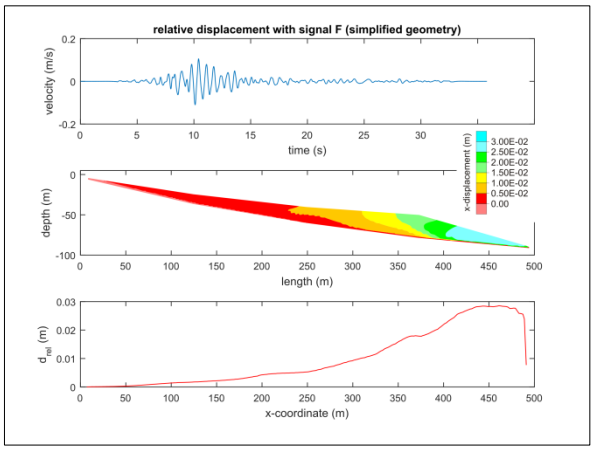

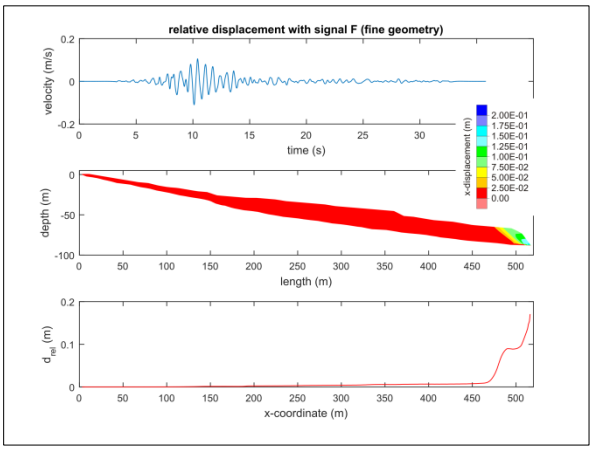

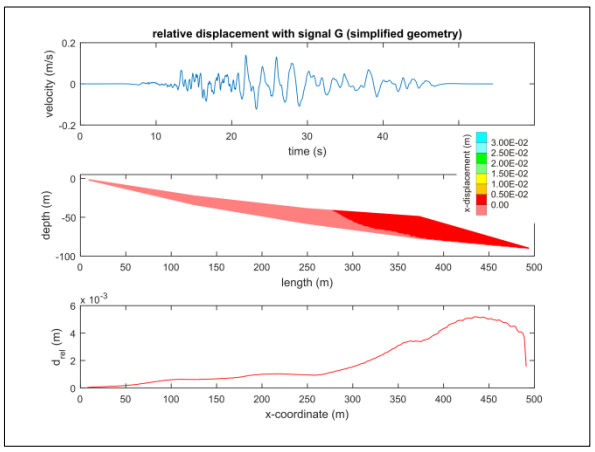

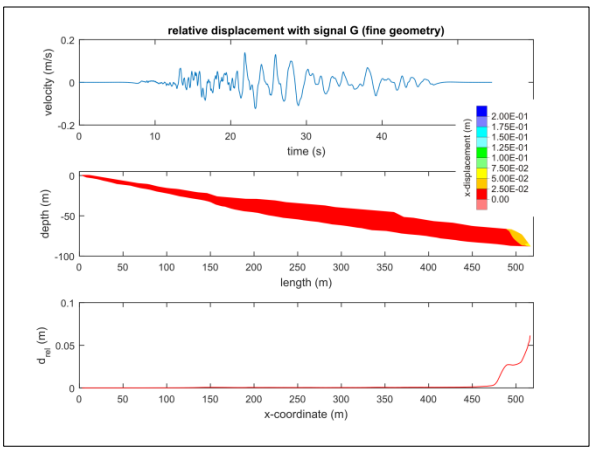

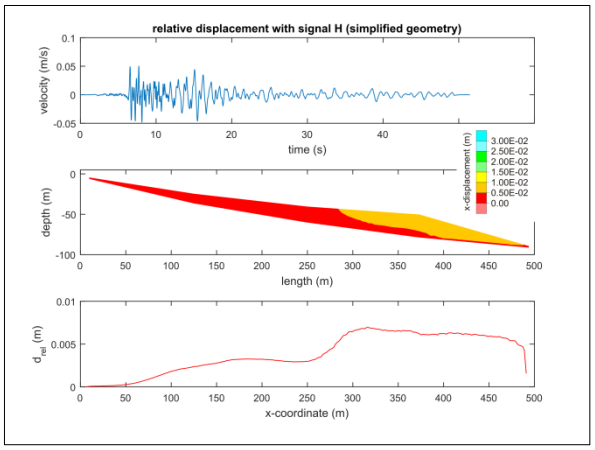
relative displacement with signal H (simplified geometry)
velocity (m/s)
time (s)
depth (m)
length (m)
x-displacement (m)
3.00E-02
2.50E-02
2.00E-02
1.50E-02
1.00E-02
0.50E-02
0.00
d_rel (m)
x-coordinate (m)

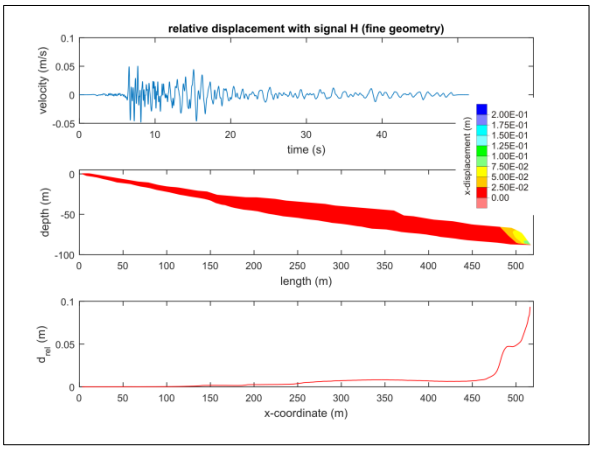
relative displacement with signal H (fine geometry)
velocity (m/s)
time (s)
depth (m)
length (m)
x-displacement (m)
2.00E-01
1.75E-01
1.50E-01
1.25E-01
1.00E-01
7.50E-02
5.00E-02
2.50E-02
0.00
d_rel (m)
x-coordinate (m)

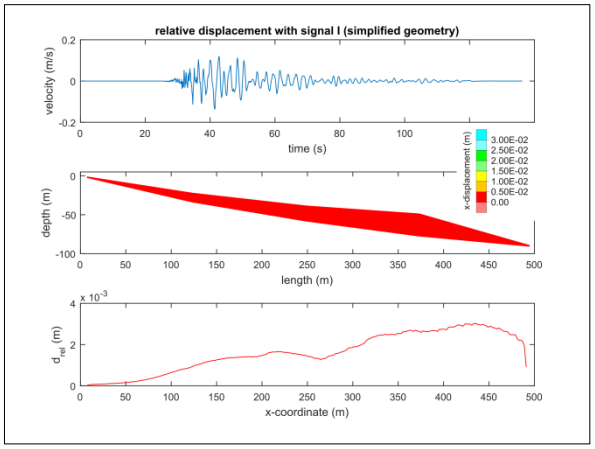
relative displacement with signal I (simplified geometry)
velocity (m/s)
time (s)
depth (m)
length (m)
x-displacement (m)
3.00E-02
2.50E-02
2.00E-02
1.50E-02
1.00E-02
0.50E-02
0.00
x 10^-3
d_rel (m)
x-coordinate (m)

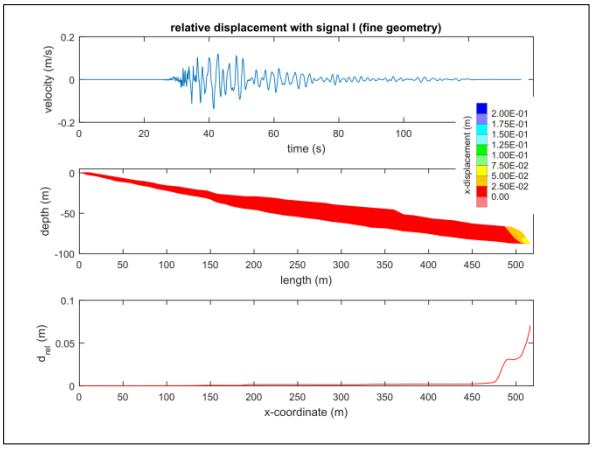
relative displacement with signal I (fine geometry)
velocity (m/s)
time (s)
depth (m)
length (m)
x-displacement (m)
2.00E-01
1.75E-01
1.50E-01
1.25E-01
1.00E-01
7.50E-02
5.00E-02
2.50E-02
0.00
d_rel (m)
x-coordinate (m)

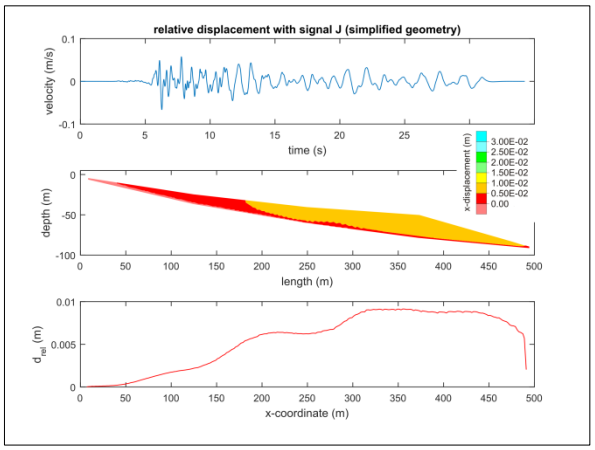
relative displacement with signal J (simplified geometry)
velocity (m/s)
time (s)
depth (m)
length (m)
x-displacement (m)
3.00E-02
2.50E-02
2.00E-02
1.50E-02
1.00E-02
0.50E-02
0.00
d_rel (m)
x-coordinate (m)

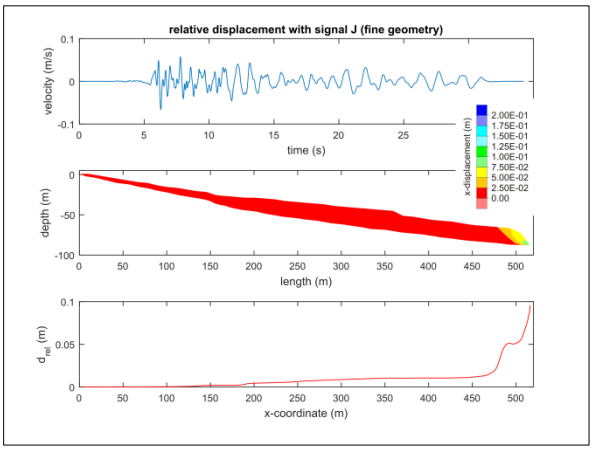
relative displacement with signal J (fine geometry)
velocity (m/s)
time (s)
depth (m)
length (m)
x-displacement (m)
2.00E-01
1.75E-01
1.50E-01
1.25E-01
1.00E-01
7.50E-02
5.00E-02
2.50E-02
0.00
d_rel (m)
x-coordinate (m)

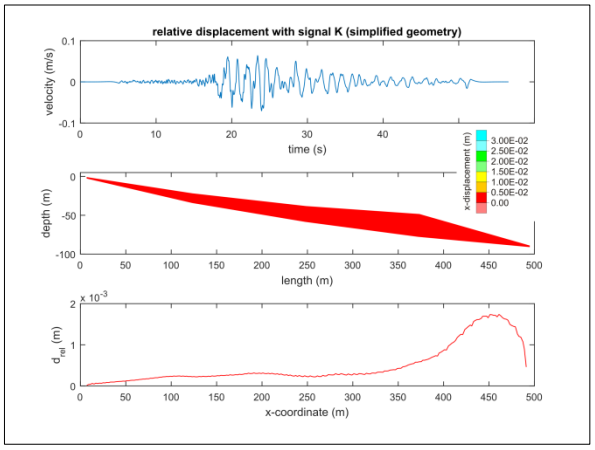
relative displacement with signal K (simplified geometry)
velocity (m/s)
time (s)
depth (m)
length (m)
x-displacement (m)
3.00E-02
2.50E-02
2.00E-02
1.50E-02
1.00E-02
0.50E-02
0.00
x 10^-3
d_rel (m)
x-coordinate (m)

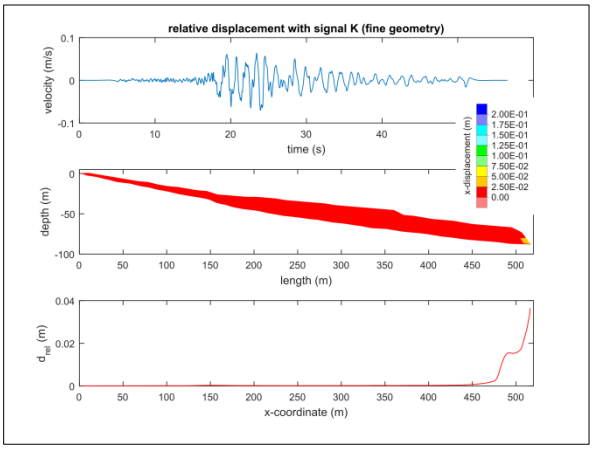
relative displacement with signal K (fine geometry)
velocity (m/s)
time (s)
depth (m)
length (m)
x-displacement (m)
2.00E-01
1.75E-01
1.50E-01
1.25E-01
1.00E-01
7.50E-02
5.00E-02
2.50E-02
0.00
d_rel (m)
x-coordinate (m)

```
% PLOT OF SITE EFFECTS IN 2D
%
% ------------------------------------------------------------------
%
% -> Exported velocity time-histories must be stored in a folder
%    "vel" next to this MATLAB-function.
% -> Exported velocity time-histories must be named "1.dat",
%    "2.dat", etc. according to their node position along the ground
%    surface from the left to the right side of the model.
% -> With the velocity time-history export from FLAC comes along a
%    file called "xy.out";
%    it must be placed next to this MATLAB-function.
% ->  Two MATLAB-functions must be downloaded from
%    https://mathworks.com/matlabcentral/fileexchange/;
%    "natsort.m" and "natsortfiles.m" (COBELDICK, 2012) must be
%    placed next to this MATLAB-function.
%
% ------------------------------------------------------------------

% LOAD GEOMETRY

load xy.out;                              % for topography
                                          % (contains full model length)
%load SG_fine.inp;   sg=SG_fine;          % for fine sliding surface
                                          % (on model length)
 load SG_simple.inp; sg=SG_simple;        % for simple sliding surface
                                          % (on model length)

% LOAD SIGNAL

load Ricker6Hz_NH.inp;                    % signal file with no header
                                          % (therefore extension "NH")

% READ ALL FILES FROM FOLDER "VEL"

read = dir('vel/*.dat');
sortedNames = natsortfiles({read.name});

% DEFINITION OF PARAMETERS FOR FFT

L = length(dlmread(strcat('vel/', read(1).name), '', 4, 0));

ps = 0.___;                 % sampling period (insert time-steps!)[s]
fs = 1/ps;                  % sampling frequency                   [Hz]
time = (L-1)*ps;            % time of record                       [s]
t =(0:ps:time);             % time vector
f = fs*(0:(L/2))/L;         % frequency vector
tS =(0:0.___:time);         % time vector for signal
                            % (insert time-steps!)

% CREATE 3 MATRICES THAT WILL BE FILLED

DATA = zeros(L, length(read));        % will contain the
                                      % velocity time-histories
```

```
FFT  = zeros(L/2 + 1, length(read));  % will contain the FFTs of
                                      % these velocity time-histories

TRF  = zeros(L/2 + 1, length(read));  % will contain the
                                      % transfer functions

% MAKE MATRICES DATA & FFT

for r = 1:length(sortedNames)

     M = dlmread(char(strcat('vel/', sortedNames(r))), '', 4, 0);
     % skip 4 first lines and 0 columns

     DATA(:,r) = M(:,2);         % filling DATA matrix per reading

     ffTmp = fft(M(:,2));
     ffA2 = abs(ffTmp/L);
     FFT(:,r) = ffA2(1:L/2+1);  % filling FFT matrix per reading
end

% MAKE MATRIX TRF

for p = 1:size(FFT,2)
      TRF(:,p) = FFT(:,p)./FFT(:,1);             % 1st   FAS = ref.
     %TRF(:,p) = FFT(:,p)./FFT(:,___);           % ___th FAS = ref.
     %TRF(:,p) = FFT(:,p)./FFT(:,size(FFT,2));   % last  FAS = ref.

end

% CREATE PLOT

subplot(4,1,1:2);     % subplot occupying place 1 & 2 of 4

contourf(TRF(1:150,:),200,'edgecolor','none'),
xlabel('length (m)'), ylabel('frequency (Hz)')
c = colorbar('northoutside');
c.Label.String = 'amplitude (-)';
colormap(jet)

subplot(4,1,3);       % subplot occupying place 3 of 4

plot(sg(:,1), sg(:,2),'-k'), hold on
plot(xy(:,1), xy(:,2),'-r'),
xlabel('length (m)'), ylabel('depth (m)')
xlim([xy(1,1) xy(length(xy),1)])

subplot(4,1,4);       % subplot occupying place 4 of 4

plot(tS, Ricker6Hz_NH,'-k'),
xlabel('time (s) of applied signal'), ylabel('velocity (m/s)')

% GO TO PLOT, EDIT AXES AND SAVE THE PLOT
```

A.10. MATLAB-Procedure for Site Effect Plots in 2D – Axes Labeling

Initially the plot of the transfer functions is labeled with the indices of the matrix; i.e. there must be a "manual translation" for both axes. The model of the Diezma Landslide serves as example.
The model has a length of 950 m, and hence – with a spacing of 1 m between nodes – there are 951 nodes where a velocity time-history can be registered. Effectively, only 950 velocity time-histories are exported which do not include the one of the very last node. Due to the big number of available records and the relatively small spacing between their locations it is, however, legitimate to stretch the plot to cover all 951 nodes. One can thus rename the ticks according to the first axis of the second subplot containing the longitudinal cross section.
More difficult is the relabeling of the second axis. Since each column of the TRF-matrix contains as many entries as one Fourier Amplitude Spectrum (FAS), the relabeling is related to the spacing of the carrying frequency vector. From the code (cf. A.7.) it is visible that:

$$f = \frac{1}{ps} \cdot \underbrace{\left(0{:}\,1{:}\,\frac{L}{2}\right)}_{\substack{definition\ of \\ range\ with\ steps \\ (in\ MATLAB)}} /L$$

Respectively, for the simplified and the fine geometry the frequency vectors are defined as follows and by chance both have the spacing of 0.1:

$$f = \frac{1}{0.00005} \cdot \left(0{:}\,1{:}\,\frac{2000000}{2}\right) /2000000 = (0{:}\,0.1{:}\,10000)$$

$$f = \frac{1}{0.001} \cdot \left(0{:}\,1{:}\,\frac{10000}{2}\right) /10000 = (0{:}\,0.1{:}\,500)$$

This means that, for instance, one needs 10 steps (of 0.1Hz each) to reach 1Hz (at the 11th point); and therefore the translation of "points to Hertz" is carried out by:

1.	reading the index on the second axis	e.g. 140 (#)	or	1 (#)
2.	subtract 1	e.g. 139	or	0
3.	multiply by 0.1 (= spacing of the frequency vector)	e.g. 13.9 (Hz)	or	0 (Hz)

With this procedure, the axis can be relabeled regardless of how many rows of the TRF-matrix should be displayed. (The code in A.7. displays only the first 150 rows.)
It should be noted that, due to the narrowness of the plot, the subtraction of 1 was skipped in Fig. 7.13 and Fig. 7.14; the index 140 was directly relabeled with 14 Hz.
In case one would like to use the code for other site effect plots, the legitimacy of those two slightly "incorrect" ways of relabeling must be used with caution. Especially when the available data is scarce, shifted plots might be the result and interpretations may be wrong.

A.11. Ranking- and Tendency-Relationships

Of all 17 ranking- and tendency-relationships only 14 are shown here. The diagram of the duration defined by TRIFUNAC & BRADY (1975) serves as example in the text body (cf. 8.3.). The two diagrams of the ratios of the characteristic site periods (T_s/T_m and T_l/T_m) differ from the one of the characteristic site frequency (F_m) only by a translation of the red line as the characteristic site periods (T_s and T_l) are constant for 300 m/s; this shift does not influence the ranking or the tendency.
The seismic moment (M_0) and the two magnitudes (M_W and M_S) were tested in logarithmic and non-logarithmic form, but no ranking or tendency could be recognized.
The lowest NEWMARK-value appears in the plot of the mean FAS.

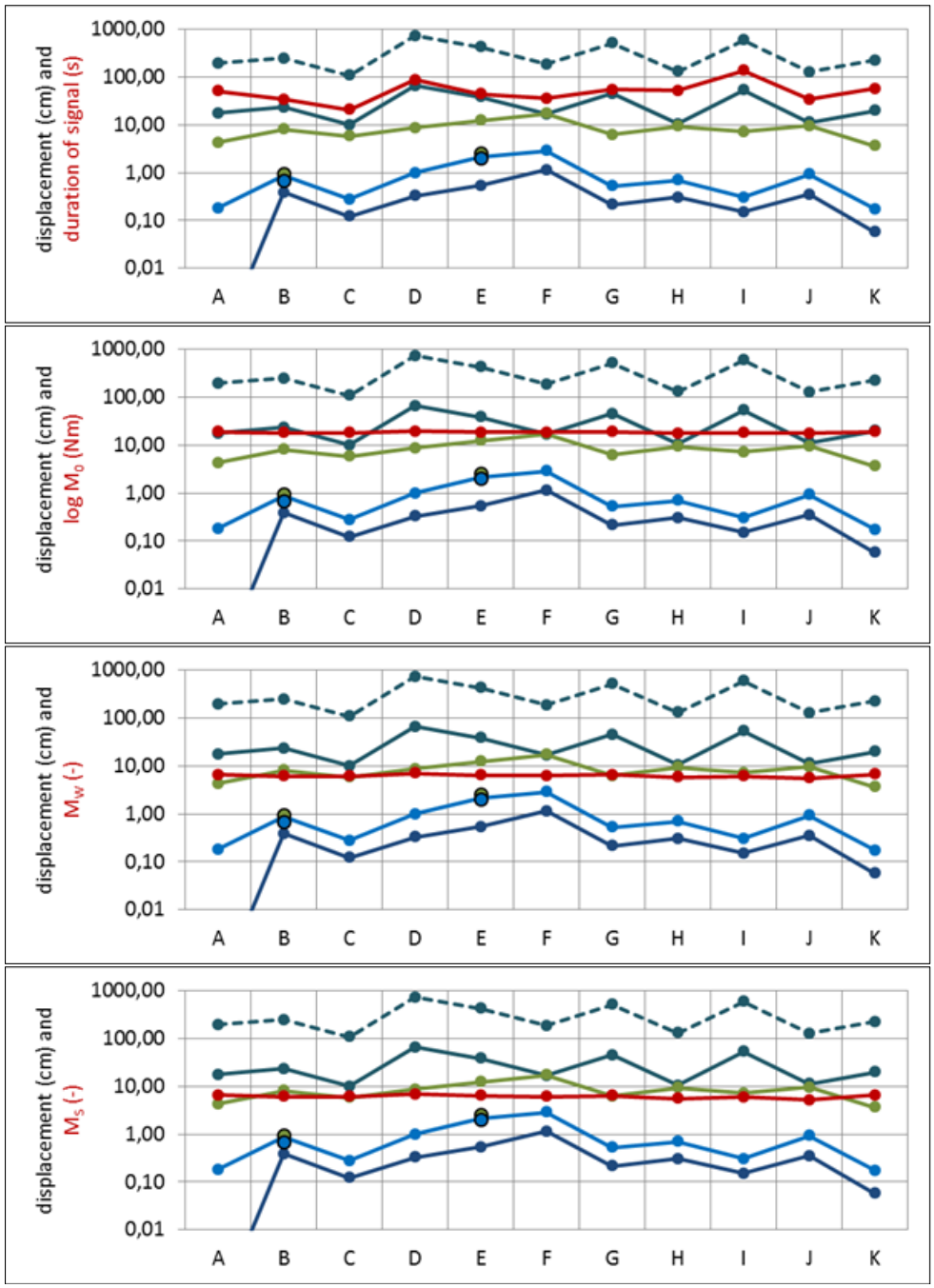

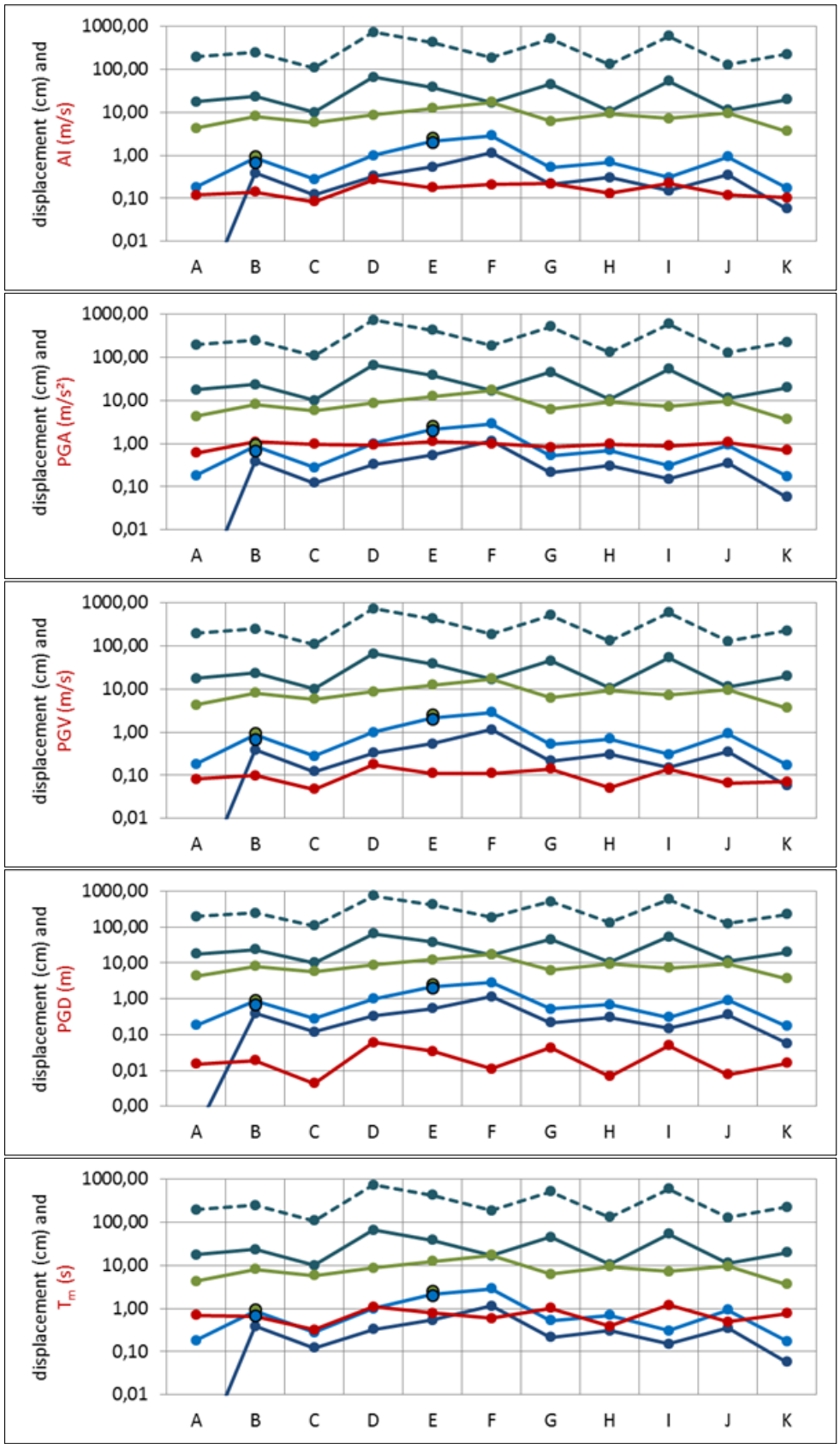
displacement (cm) and AI (m/s)
displacement (cm) and PGA (m/s²)
displacement (cm) and PGV (m/s)
displacement (cm) and PGD (m)
displacement (cm) and T_m (s)
1000,00
100,00
10,00
1,00
0,10
0,01
0,00
A B C D E F G H I J K

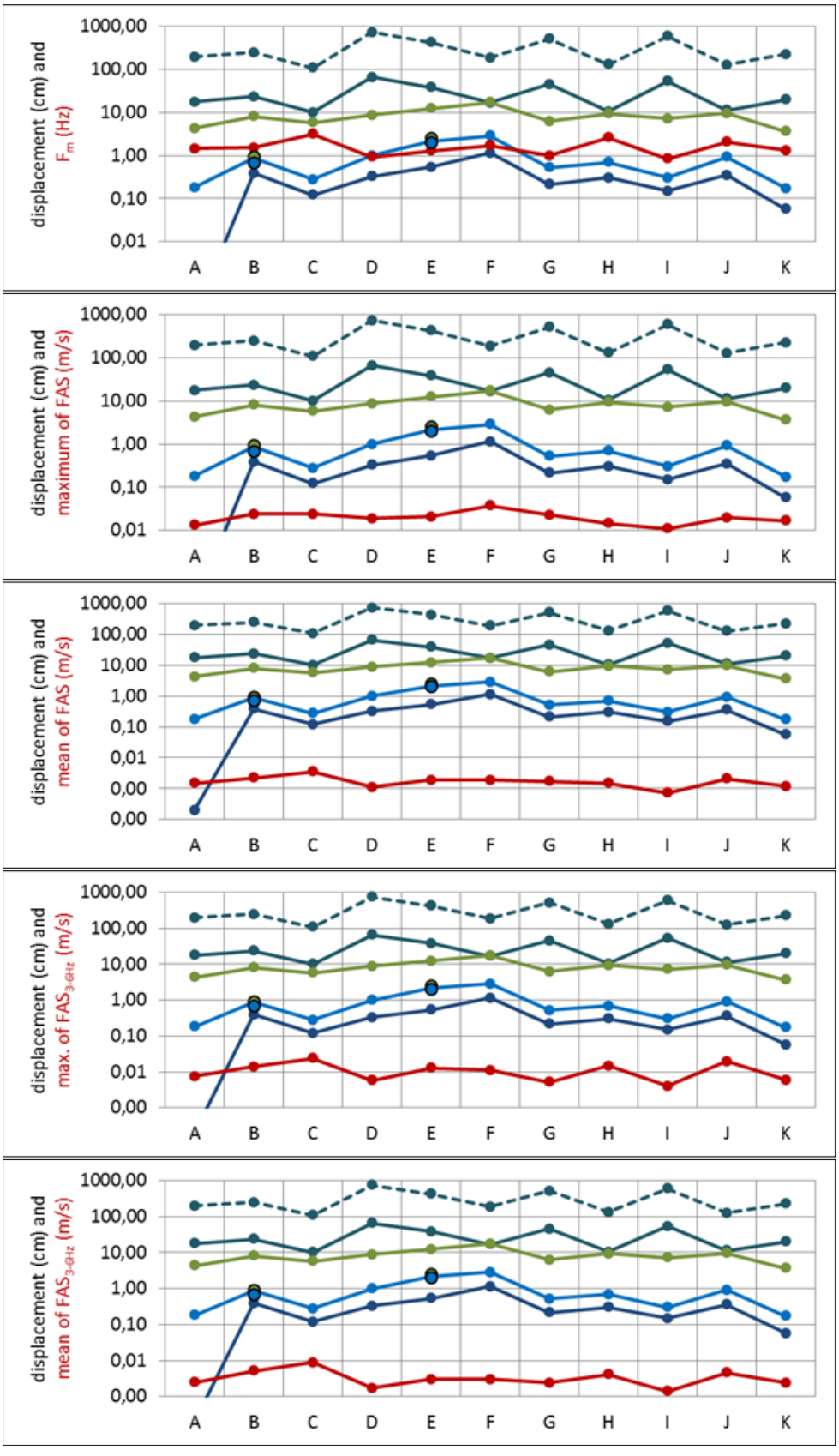
displacement (cm) and F_m (Hz)
displacement (cm) and maximum of FAS (m/s)
displacement (cm) and mean of FAS (m/s)
displacement (cm) and max. of $FAS_{3\text{-}6Hz}$ (m/s)
displacement (cm) and mean of $FAS_{3\text{-}6Hz}$ (m/s)
1000,00
100,00
10,00
1,00
0,10
0,01
0,00
A B C D E F G H I J K

A.12. Schematic Model Layout for CESAR and FLAC

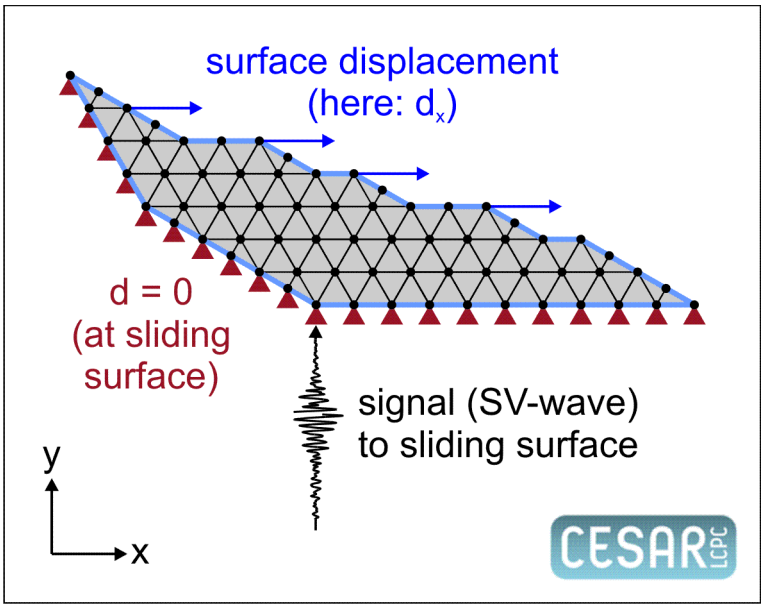

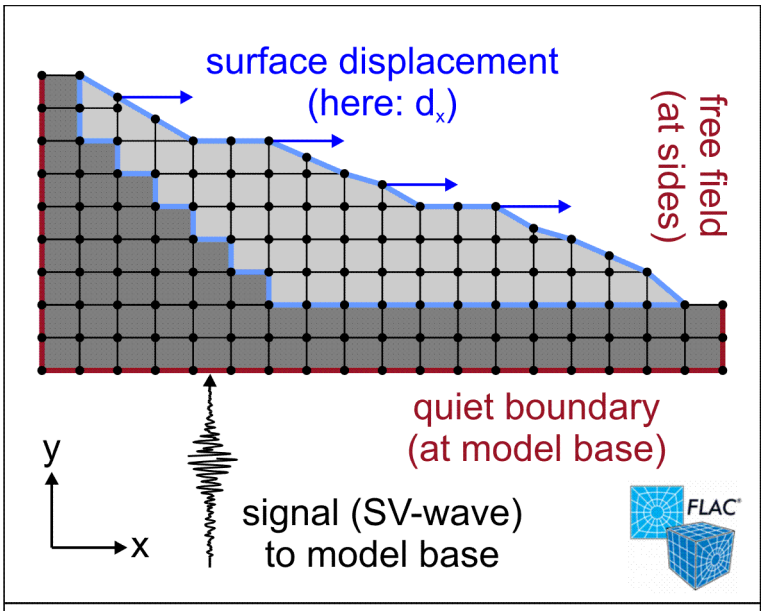

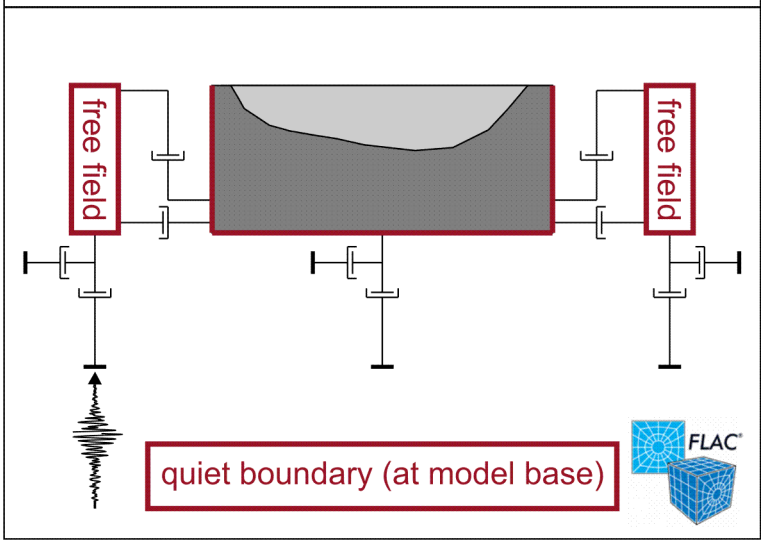

ABSTRACT

Seismically induced slope deformation is a worldwide common phenomenon that poses an increasing and considerable threat to fast expanding urbanization, and a great number of catastrophic events throughout the past attest thereof. For this reason, displacement predictions allowing for proper slope surveillance became a major concern.

Early attempts to relate slope failures to seismic parameters are of empirical nature and date back to the 1980s. Although having proven stable, these relations are frequently disturbed by site effects causing outliers in terms of smaller or greater displacements than expected.

The first part of this thesis presents a newly build chronological database of 277 globally distributed seismically and non-seismically induced landslides. A comprehensive statistical analysis was conducted on the data of this database with the main result that – statistically seen – the average geometrical shapes of landslides differ only proportionally.

The second part of the thesis is dedicated to a comparative slope stability analysis of the Diezma Landslide (Spain) by means of three methods: the limit-equilibrium based NEWMARK-Method (1965) in 2D under elasto-perfectly-plastic conditions; finite-difference analysis in the time domain with the code FLAC in 2D and 3D under visco-elasto-perfectly-plastic conditions; and modal recombination analysis in the frequency domain with the finite-element code CESAR-LCPC in 2D and 3D under visco-elastic conditions.

Located in a seismically active region, the Diezma Landslide is likely to be affected by earthquakes and was therefore considered as a suitable model case. A broad analysis of expected displacements was conducted using eleven strong-motion seismic scenarios. Moreover, the thesis searches for potential relations between macro-seismic parameters of the applied earthquake scenarios and the predicted deformations obtained from the three methods.

It appeared that – due to the functionality of the methods – results differ quantitatively as well as qualitatively, and so does their suitability. Major findings are: (a) Results from the three methods are of different orders of magnitude and, thus, can easily lead to over- or under-estimations of displacements; (b) Both numerical methods reveal a strong influence of the model-geometry on the predicted displacements, whereas a scenario-dependent slope behavior manifested itself only within the finite difference analysis; (c) The switch from 2D to 3D does not necessarily result in a similar performance in each dimension and results must be critically judged before further use; (d) The NEWMARK-Method (1965) has proven itself once more to be appropriate for first slope assessments but not for sophisticated evaluations of ground response to seismic shaking.

RÉSUMÉ

Les phénomènes d'instabilité générés par les séismes dans les pentes représentent un risque naturel majeur à l'échelle mondiale. Ce risque a, de plus, tendance à croître du fait d'une urbanisation croissante dans des zones à fort aléa, comme en témoignent de nombreux évènements catastrophique à travers le passé. Pour garantir la sécurité des personnes et des biens face à ce type d'aléa, il faut améliorer les prédictions des déplacements générés par les séismes dans les pentes.

Les premiers travaux scientifiques visant à corréler les caractéristiques des instabilités dans les pentes aux paramètres sismiques sont de nature empirique et remontent aux années 1980. Ces méthodes ne permettent pas d'expliquer tous les mouvements de terrain observés à travers le monde, notamment lorsque les effets de site modifient sensiblement la distribution des mouvements dans les pentes et génèrent des déplacements plus grands ou plus petits que ceux prédits par les lois empiriques qui négligent les effets de site.

La première partie de cette thèse présente une nouvelle base de données mondiale de 277 glissements de terrain d'origine sismique ou non. L'analyse statistique conduite sur les données de cette base a montré que la forme géométrique moyenne des glissements de terrain reste stable lorsque le volume des instabilités augmente.

La deuxième partie de la thèse est dédiée à l'analyse de la stabilité du glissement de terrain de Diezma (Espagne) au moyen de trois méthodes : la Méthode de NEWMARK (1965) basée sur le principe de l'équilibre limite en 2D qui suppose des conditions elasto-parfaitement-plastiques ; l'analyse par différences finies dans le domaine temporel avec le code FLAC en 2D et en 3D qui suppose des conditions visco-elasto-parfaitement-plastiques ; et l'analyse par recombinaison modale dans le domaine fréquentiel avec le code CESAR-LCPC en 2D et en 3D qui suppose des conditions visco-élastiques.

Situé dans une région sismiquement active, le glissement de terrain de Diezma est susceptible d'être affecté par des séismes. Une analyse des déplacements induits dans ce versant par onze signaux sismiques différents a été menée dans l'objectif d'établir des corrélations entre les paramètres macro-sismiques des scenarios sismiques appliqués et les déformations calculées par les trois méthodes.

Les résultats montrent des différences marquées à la fois qualitatives et quantitatives. Les conclusions principales sont : (a) Les déplacements obtenus par les trois méthodes ont des ordres de grandeur différents et peuvent donc conduire à une surestimation ou à une sous-estimation des déplacements ; (b) Les deux méthodes numériques montrent que les déplacements sont fortement conditionnés par la géométrie des modèles ; seule la méthode par différences finies fait apparaître une réponse en termes de déplacements qui dépend du scénario sismique considéré; (c) Les résultats des simulations2D et 3D ne sont pas comparables ; des analyses complémentaires doivent encore être menées pour guider l'utilisateur dans le choix de la méthode la plus appropriée; (d) La Méthode de NEWMARK (1965), dont l'utilisation reste très répandue de nos jours, est tout à fait appropriée à l'étude de cas simples mais elle peut se révéler inexacte lorsque la structure géologique / topographique du versant conduit à un fort effet de site car ce dernier n'est pas pris en compte par cette méthode.

> create 1 CLEO26
(never name with '_' since this is reserved to distinguish models with '_M1' etc.)
> set geometry
(with absolute points in [m] using coordinates defining the landslide; close surface completely)
> save
> set mesh
(mark all points, lines and surfaces and set fixed length density to 0.5m; finished when mesh appears)
> apply-save
> to set properties at least 1 dynamic model must exist
(insert for first model ρ in [kg/m³], E in [MN/m²] and ν in [-], then export to XML and call later again for other models via the import of properties)
> save

DiezmaGEO.cleo26
(base file)

duplicate

for all models:

> set properties (to surface)
> apply-show-save
> set boundary conditions (to lines; imposed U and V)
> apply-show-save

ADiezma.cleo26
> add 7 MODE models (to solve all 7 at once)

BDiezma.cleo26
> add 7 MODE models (to solve all 7 at once)

CDiezma.cleo26
> add 5 MODE models (to solve all 5 at once)

(1) create data file

for all models:

> set full renumbering for analysis
> apply
> create input file for solver (calculate option 1; tick correct model ID)
> save

(prefixes A, B and C are needed to distinguish groups)

ADiezma_M1.data
...
ADiezma_M7.data

BDiezma_M1.data
...
BDiezma_M7.data

CDiezma_M1.data
...
CDiezma_M5.data

(2) modify & solve

for all DATA:

> control E
(search for "COND")
> modify last lines
(cf. code page a))
> open CLEO26 and verify modified DATA
> solve for existing input files
(calculate option 3; tick correct model ID)
> save

ADiezma_M1.rst
...
ADiezma_M7.rst

ADiezma_M1.list
...
ADiezma_M7.list

BDiezma_M1.rst
...
BDiezma_M7.rst

BDiezma_M1.list
...
BDiezma_M7.list

CDiezma_M1.rst
...
CDiezma_M5.rst

CDiezma_M1.list
...
CDiezma_M5.list

results

for all LIST:

> read first 20 resonance frequencies (search for "FREQ" and 3rd column)
> plot with Matlab

after step 1:
3 CLEO26
3 ENV
3 RESU
19 DATA
19 LIST
19 MESG
19 RST
19 RSV4

Step 1 (MODE) Eigenfrequencies

---

duplicate

(as in step 1)

bound. cond.: lines to ground surface

SURFDiezma.cleo26
> add 1 MODE model

(1) create data file

(as in step 1)

(properties can be any of the 19 options; step 2 searches only IDs of ground surface and rupture surface)

SURFDiezma_M1.data

results

for this DATA:

> read IDs of points for displacement (search for "NUL", cf. code page b))
> save to **TXT**

after step 2:
1 CLEO26
1 DATA
1 ENV

Step 2 IDs of Points

DiezmaGEO.cleo26
> add 1 SUMO model

> keep geometry and mesh
(recreating the mesh might result in a slightly different arrangement with different knot positions and IDs)
> reduce 7 MODE models to 1
(called '_M1'; preserving the imported properties)
> add 1 SUMO model
(called '_M8'; reading later the properties)
> save

Procedure of 2D Modal Superpositon with CESAR-LCPC
- Diezma Landslide
- v_s: 100-1000 m/s²
- 11 signals

duplicate

> create 209 CLEO26 (containing 1 MODE and 1 SUMO; only SUMO for further analysis)

for all models:

> set geometry and boundary conditions (as in step 1)
> set loads (gravity force factores to gx=1 and gy=0; to everything)
> apply-show-save

Diezma100K.cleo26
Diezma100J.cleo26
Diezma100I.cleo26
Diezma100H.cleo26
Diezma100G.cleo26
Diezma100F.cleo26
Diezma100E.cleo26
Diezma100D.cleo26
Diezma100C.cleo26
Diezma100B.cleo26

Diezma100A.cleo26
Diezma150A.cleo26
Diezma200A.cleo26
Diezma250A.cleo26
Diezma300A.cleo26
Diezma350A.cleo26
Diezma400A.cleo26
Diezma450A.cleo26
Diezma500A.cleo26
Diezma550A.cleo26
Diezma600A.cleo26
Diezma650A.cleo26
Diezma700A.cleo26
Diezma750A.cleo26
Diezma800A.cleo26
Diezma850A.cleo26
Diezma900A.cleo26
Diezma950A.cleo26
Diezma1000A.cleo26

(1) create data file

for all models:

> set full renumbering for analysis
> apply
> create input file for solver (calculate option 1; tick correct model ID)
> save

(prefixes A, B and C are not any more needed because every CLEO26 hosts only one model)

Diezma100K_M8.data
Diezma100J_M8.data
Diezma100I_M8.data
Diezma100H_M8.data
Diezma100G_M8.data
Diezma100F_M8.data
Diezma100E_M8.data
Diezma100D_M8.data
Diezma100C_M8.data
Diezma100B_M8.data

Diezma100A_M8.data
Diezma150A_M8.data
Diezma200A_M8.data
Diezma250A_M8.data
Diezma300A_M8.data
Diezma350A_M8.data
Diezma400A_M8.data
Diezma450A_M8.data
Diezma500A_M8.data
Diezma550A_M8.data
Diezma600A_M8.data
Diezma650A_M8.data
Diezma700A_M8.data
Diezma750A_M8.data
Diezma800A_M8.data
Diezma850A_M8.data
Diezma900A_M8.data
Diezma950A_M8.data
Diezma1000A_M8.data

(2) modify & solve

for all DATA:

> control E
(search for "COND")
> modify last lines
(cf. code page c))

This DATA includes information about:
- the **resonance frequencies** of the landslide
- the **points** in which the **displacement** will be estimated
- the **applied signal** as displacement time history in [m]

> open CLEO26 and verify modified DATA
> solve for existing input files
(calculate option 3; tick correct model ID)
> save

strong motion signals (A-K)

Diezma100K_M8.list
Diezma100J_M8.list
Diezma100I_M8.list
Diezma100H_M8.list
Diezma100G_M8.list
Diezma100F_M8.list
Diezma100E_M8.list
Diezma100D_M8.list
Diezma100C_M8.list
Diezma100B_M8.list

Diezma100A_M8.list
Diezma150A_M8.list
Diezma200A_M8.list
Diezma250A_M8.list
Diezma300A_M8.list
Diezma350A_M8.list
Diezma400A_M8.list
Diezma450A_M8.list
Diezma500A_M8.list
Diezma550A_M8.list
Diezma600A_M8.list
Diezma650A_M8.list
Diezma700A_M8.list
Diezma750A_M8.list
Diezma800A_M8.list
Diezma850A_M8.list
Diezma900A_M8.list
Diezma950A_M8.list
Diezma1000A_M8.list

results

for all LIST:

> read estimated displacements in [m] (search for "VALEURS"; if exported in English search for "WITH")
> export IDs (1st column), displacement in x (2nd column) and displacement in y (3rd column)
> plot with Matlab

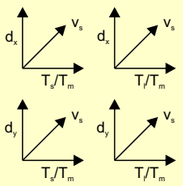

after step 3 (per signal):
19 CLEO26
19 DATA
19 ENV
19 LIST
19 MESG
19 RESU
19 RSV4

Step 3 (SUMO) Modal Superposition & Displacement Evaluation

> create 1 CLEO36
(never name with '_' since this is reserved to distinguish models with '_M1' etc.)
> set geometry
(with absolute points in [m] using coordinates defining the landslide; close surface completely)
> save
> set mesh
(mark all points, lines and surfaces and set fixed length density to 1.1m; finished when mesh appears)
> apply-save
> to set properties at least 1 dynamic model must exist
(insert for first model ρ in [kg/m³], E in [MN/m²] and ν in [-], then export to XML and call later again for other models via the import of properties)
> save

Diezma3DGEO.cleo36
(base file)

Diezma3DGEO.cleo26
> add 1 SUMO model

> keep geometry and mesh
(recreating the mesh might result in a slightly different arrangement with different knot positions and IDs)
> keep 1 MODE model (called '_M1'; preserving the imported properties)
> add 1 SUMO model (called '_M2'; reading later the properties)
> save

Procedure of 3D Modal Superpositon with CESAR-LCPC
- Diezma Landslide
- v_s: 300 m/s²
- 11 signals

duplicate

for this model:

> set properties (to surface)
> apply-show-save
> set boundary conditions (to tiles; imposed U, V and Z)
> apply-show-save

Diezma3D.cleo36
> add 1 MODE model

(1) create data file

for this model:

> set full renumbering for analysis
> apply
> create input file for solver
(calculate option 1; tick correct model ID)
> save

Diezma3D_M1.data

(2) modify & solve

for this DATA:

> control E
(search for "COND")
> modify last lines
(cf. code page a))
> open CLEO36 and verify modified DATA
> solve for existing input files
(calculate option 3; tick correct model ID)
> save

Diezma3D_M1.rst

Diezma3D_M1.list

results

for this LIST:

> read first 20 resonance frequencies
(search for "FREQ" and 3rd column)
> plot with Matlab

after step 1:

1 CLEO36	1 DATA
1 ENV	1 LIST
1 RESU	1 MESG
	1 RST
	1 RSV4

Step 1 (MODE) Eigenfrequencies

---

duplicate

(as in step 1)

bound. cond.:
SURFlcs → lines to LCS,
SURFplane → tiles to topography

SURFlcsD...3D.cleo36
> add 1 MODE model
(for displ. along LCS)

SURFplaneD...3D.cleo36
> add 1 MODE model
(for displ. on topography)

(1) create data file

(as in step 1)

(properties can be 300m/s or any of the 19 options; step 2 searches only IDs of ground surface and rupture surface)

SURFlcsD...3D_M1.data

SURFplaneD...3D_M1.data

results

for both DATA:

> read IDs of points for displacement
(search for "NUL", cf. code page b))
> save to **TXT**

after step 2:
2 CLEO36
2 DATA
2 ENV

Step 2 IDs of Points

---

duplicate

> create 22 CLEO36 (containing 1 MODE and 1 SUMO; only SUMO for further analysis)

for all models:

> set geometry and boundary conditions (as in step 1)
> set loads (gravity force factores to gx=1, gy=0 and gz=0; to everything)
> apply-show-save

D...3DlcsA.cleo36
D...3DlcsB.cleo36
D...3DlcsC.cleo36
D...3DlcsD.cleo36
D...3DlcsE.cleo36
D...3DlcsF.cleo36
D...3DlcsG.cleo36
D...3DlcsH.cleo36
D...3DlcsI.cleo36
D...3DlcsJ.cleo36
D...3DlcsK.cleo36

D...3DplaneA.cleo36
D...3DplaneB.cleo36
D...3DplaneC.cleo36
D...3DplaneD.cleo36
D...3DplaneE.cleo36
D...3DplaneF.cleo36
D...3DplaneG.cleo36
D...3DplaneH.cleo36
D...3DplaneI.cleo36
D...3DplaneJ.cleo36
D...3DplaneK.cleo36

(1) create data file

for all models:

> set full renumbering for analysis
> apply
> create input file for solver
(calculate option 1; tick correct model ID)
> save

D...3DlcsA_M2.data
D...3DlcsB_M2.data
D...3DlcsC_M2.data
D...3DlcsD_M2.data
D...3DlcsE_M2.data
D...3DlcsF_M2.data
D...3DlcsG_M2.data
D...3DlcsH_M2.data
D...3DlcsI_M2.data
D...3DlcsJ_M2.data
D...3DlcsK_M2.data

D...3DplaneA_M2.data
D...3DplaneB_M2.data
D...3DplaneC_M2.data
D...3DplaneD_M2.data
D...3DplaneE_M2.data
D...3DplaneF_M2.data
D...3DplaneG_M2.data
D...3DplaneH_M2.data
D...3DplaneI_M2.data
D...3DplaneJ_M2.data
D...3DplaneK_M2.data

(2) modify & solve

for all DATA:

> control E
(search for "COND")
> modify last lines
(cf. code page c))

This DATA includes information about:
- the **resonance frequencies** of the landslide
- the **points** in which the **displacement** will be estimated
- the **applied signal** as displacement time history in [m]

> open CLEO36 and verify modified DATA
> solve for existing input files
(calculate option 3; tick correct model ID)
> save

strong motion signals (A-K)

D...3DlcsA_M2.list
D...3DlcsB_M2.list
D...3DlcsC_M2.list
D...3DlcsD_M2.list
D...3DlcsE_M2.list
D...3DlcsF_M2.list
D...3DlcsG_M2.list
D...3DlcsH_M2.list
D...3DlcsI_M2.list
D...3DlcsJ_M2.list
D...3DlcsK_M2.list

D...3DplaneA_M2.list
D...3DplaneB_M2.list
D...3DplaneC_M2.list
D...3DplaneD_M2.list
D...3DplaneE_M2.list
D...3DplaneF_M2.list
D...3DplaneG_M2.list
D...3DplaneH_M2.list
D...3DplaneI_M2.list
D...3DplaneJ_M2.list
D...3DplaneK_M2.list

results

for all LIST:

> read estimated displacements in [m]
(search for "VALEURS"; if exported in English search for "WITH")
> export IDs (1st column), displacement in x (2nd column), displacement in y (3rd column) and displacement in z (4th column)
> plot with Matlab

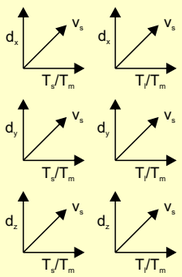

after step 3 (per signal):

2 CLEO26	2 MESG
2 DATA	2 RESU
2 ENV	2 RSV4
2 LIST	

Step 3 (SUMO) Modal Superposition & Displacement Evaluation